Volume 135
2008

EDITORS
F. Kremer
W. Richtering

Colloid and

Progress in Colloid and Polymer Science

Recently Published and Forthcoming Volumes

Colloids for Nano- and Biotechnology
Volume Editors: Hórvölgyi, Z. D., Kiss, É.
Vol. 135, 2008

Surface and Interfacial Forces –
From Fundamentals to Applications
Volume Editors: Auernhammer, G. K., Butt, H.-J., Vollmer, D.
Vol. 134, 2008

Smart Colloidal Materials
Volume Editor: Richtering, W.
Vol. 133, 2006

Characterization of Polymer Surfaces and Thin Films
Volume Editors: Grundke, K., Stamm, M., Adler, H.-J.
Vol. 132, 2006

Analytical Ultracentrifugation VIII
Volume Editors: Wandrey, C., Cölfen, H.
Vol. 131, 2006

Scattering Methods and the Properties
of Polymer Materials
Volume Editors: Stribeck, N., Smarsly, B.
Vol. 130, 2005

Mesophases, Polymers, and Particles
Volume Editors: Lagaly, G., Richtering, W.
Vol. 129, 2004

Surface and Colloid Science
Volume Editor: Galembeck, F.
Vol. 128, 2004

Analytical Ultracentrifugation VII
Volume Editors: Lechner, M. D., Börger, L.
Vol. 127, 2004

Trends in Colloid and Interface Science XVII
Volume Editors: Cabuil, V., Levitz, P., Treiner, C.
Vol. 126, 2004

From Colloids to Nanotechnology
Volume Editors: Zrinyi, M., Hórvölgyi, Z. D.
Vol. 125, 2004

Aqueous Polymer Dispersions
Volume Editor: Tauer, K.
Vol. 124, 2004

Trends in Colloid and Interface Science XVI
Volume Editors: Miguel, M., Burrows, H. D.
Vol. 123, 2004

Aqueous Polymer – Cosolute Systems
Volume Editor: Anghel, D. F.
Vol. 122, 2002

Molecular Organisation on Interfaces
Volume Editor: Lagaly, G.
Vol. 121, 2002

Lipid and Polymer-Lipid Systems
Volume Editor: Nylander, T.
Vol. 120, 2002

Progress in Colloid and Polymer Science

Editors: F. Kremer, Leipzig and W. Richtering, Aachen

Volume 135 · 2008

Colloids for Nano- and Biotechnology

Volume Editors:
Zoltán D. Hórvölgyi
Éva Kiss

Springer

ISSN 0340-255X
ISBN-10 3-540-85133-X
ISBN-13 978-3-540-85133-2
e-ISBN 978-3-540-85134-9
DOI 10.1007/978-3-540-85134-9
Library of Congress Control Number 2008934041
Springer Berlin, Heidelberg, New York

Springer is a part of Springer Science + Business Media

http://www.springer.com

Cover design: eStudio Calamar S. L.,
F. Steinen-Broo, Pau/Girona, Spain

Typesetting and production:
le-tex publishing services oHG, Leipzig

Printed on acid-free paper

Progr Colloid Polym Sci (2008) 135: V

Preface

Over the past decades the application of nano- and biomaterials has substantially grown in high-tech industries. A colloidal approach to nano- and biotechnology was one of the main topics of the 2007 meeting organized by the Hungarian Chemical Society in cooperation with leading Hungarian universities and the Hungarian Academy of Sciences. The goal of the 9th Conference on Colloid Chemistry and the previous meetings was to bring together scientists, engineers from universities, industries and research institutions to exchange views on the latest developments and perspectives in the applications of colloidal systems.

The scientific programme of the conference included 71 oral lectures and 70 posters. Participants came from 23 countries mainly from Europe but researchers visited us from the countries of other continents, from Israel, Japan, Thailand and from the United States. The meeting also gave opportunity for many young researchers (40 students) to present their work and join the scientific community. Three poster prizes were issued, two of them in memory of the late Hungarian colloid chemists, *Ferenc Szántó* and *Ervin Wolfram*.

During the three–day meeting the most important aspects of science, technology and applications of colloid chemistry were presented in specified sessions: "Nanoparticles" and their "Colloid Systems", "Nanolayers, Drug Delivery Systems", "Porous Systems, Surfaces" and "Polymers, Gels, Biocolloids".

Listening the oral presentations and studying the posters it repeatedly turned out that "The world of neglected dimensions" should not be neglected at all in modern material sciences and technologies.

This volume contains a selection of the contributions demonstrating the progress of the field and new possibilities in materials science and biomedical applications.

Zoltán D. Hórvölgyi
Éva Kiss

Progr Colloid Polym Sci (2008) 135: VI–VIII

CONTENTS

Progr Colloid Polym Sci (2008) 135: 1–9
DOI 10.1007/2882_2008_091

Published online: 29 August 2008

André Ayral

Colloid Science for Functional Nanomaterials: Application to Oxide Ceramic Membranes

André Ayral (✉)
Institut Européen des Membranes,
CNRS-ENSCM-UM2, Université
Montpellier 2, Place E. Bataillon,
34095 Montpellier cedex 5, France
e-mail: andre.ayral@iemm.univ-montp2.fr

Abstract The basic principles of colloid science are usually applied for preparing functional nanomaterials by wet chemistry routes. This subject is here illustrated with the development of sol–gel-derived nanoporous oxide ceramic membranes.

A current trend is to prepare tailor-made nanoporous membranes. A first aspect is the choice of the most suitable solid phase to manage the fluid-membrane chemical and physical interactions. A second aspect is concerned with the control of the nanoporous texture (porosity, pore size and pore size distribution, connectivity and tortuosity of the pore network).

By adding amphiphilic molecules in the starting sols, lyotropic liquid crystal mesophases can be obtained by self-assembly during the layer deposition. The templating effect of these mesophases enables to generate an ordered mesoporosity. Stable complex organic-inorganic hybrid suspensions can also be formulated to develop membranes exhibiting a hierarchical porosity.

Keywords Ceramic membrane · Colloidal route · Hierarchical porosity · Ordered mesoporosity

Introduction

A membrane can be defined as a thin and selective barrier which enables the transport or the retention of compounds between two media. Different types of driving forces can be at the origin of the transport across the membranes. For baromembrane processes, the driving force is a pressure gradient between the feed and strip compartments (transmembrane pressure). The treated phases can be liquids or gas (Table 1). A lot of separation operations are currently performed using membranes both for production processes and environmental applications. Environmental considerations like massive scale air and water pollution and also the gradual rarefaction of the fossil energy resources gave rise to the concept of sustainable growth and to related strategies like the process intensification, the reuse of water and solvents at their point of use, the hydrogen as energetic vector (requiring H_2 production and using fuel cells as electric generators). Membranes will have a key part to play in the new technologies associated with these strategies. Intensive efforts of R&D are now engaged everywhere in the world to develop high performance membranes for these emerging applications, in particular nanoporous membranes for high efficiency separation of small molecules or ions.

The interest of the ceramic membranes is first related to the intrinsic characteristics of the used materials: mechanical strength allowing large pressure gradients without significant strain; chemical resistance which permits applications in corrosive aqueous media or in organic solvents; refractarity for using at high temperatures. Other specific properties are the ability to counter-pressure cleaning, to sterilization and their insensibility to bacterial attacks.

Moreover, the conventional ceramic processing enables to easily produce macroporous supports and layers, whereas mesoporous or microporous layers can be achieved by the

Table 1 Characteristics of the main baromembrane processes

Process	Nature of feed/strip	Pore size	Origin of selectivity	Pressure gradient	Elemental operation
Microfiltration MF	liquid/liquid	10–0.1 μm	Sieving effect	1–3 bar	Clarification, debacterisation, separation
Ulltrafiltration UF		0.1 μm–2 nm		3–10 bar	Clarification, purification, concentration
Nanofiltration NF		< 2 nm	Sieving + specific interactions with the membrane	10–40 bar	Purification, water softening, separation, concentration
Reverse osmosis RO		dense	Retention of solutes and permeation of solvent	> osmotic pressure	Purification, water desalination
Pervaporation PV	liquid/gas	< 2 nm	Sieving + additional specific interactions	1 bar	Separation
Gas filtration GF		100 μm–10 nm	Sieving effect	0.1–5 bar	Separation, dusting
Gas separation GS	gas/gas	few nm–dense	Sieving + additional specific interactions	0.1–50 bar	Separation, extraction, purification
Gas separation GS		dense	Ionic conduction of O^{2-} by oxides	$\Delta P(O_2)$	Air separation, selective transport of O_2
Gas separation GS		dense	Ionic conduction of H^+ by oxides, H transport by metals	$\Delta P(H_2)$	Selective, transport of H_2

Table 2 Characteristics of the intermediate and of the separative top layers (from [1])

Process	Average number of layers	Thickness of the separative layer	Pore size in the separative layer	Nature of the porosity
Microfiltration	1–3	few ten μm	5–0.1 μm	macroporosity
Ultrafiltration	3–4	few μm	5 nm	mesoporosity
Nanofiltration/gas separation	4–5	< 1 μm	1 nm	microporosity

sol–gel route. The used pore size classification is that recommended by IUPAC (micropores with a size less than 2 nm, mesopores with a size in the range from 2 to 50 nm, macropores with a size more than 50 nm).

The overall performance of membranes is related to two main characteristics of such separative layers, their permeability and their permselectivity (separation ability). For porous membranes, the selectivity and the membrane cut-off depend on the pore size and on the pore size distribution of the separative layer. In the case of the smallest pores (mesopores and micropores) the developed area is very large and the permeability is very low. Thus, the thickness of the separative layer must thin enough to reach attractive fluxes with experimentally acceptable transmembrane pressures. On the other hand, the mechanical strength of the membrane must be large enough to withstand the applied pressure. These considerations led to the concept of asymmetric structure based on a macroporous support and successive layers with decreasing thickness and pore size (Table 2, Fig. 1).

The latest developments in ceramic membranes are closely related to recent advances in materials science [2],

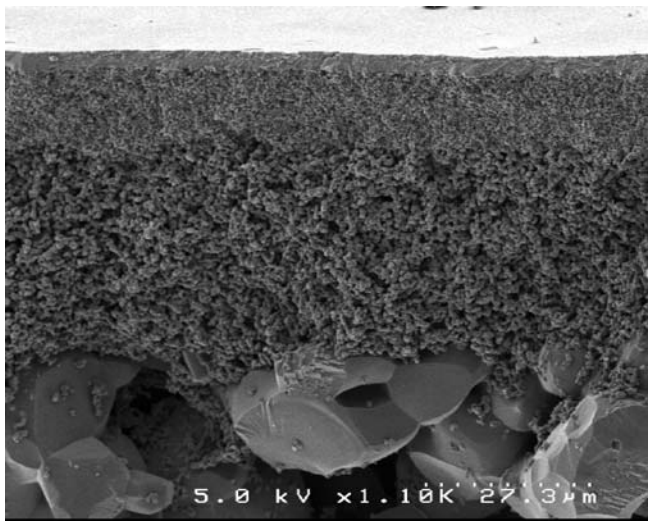

Fig. 1 Scanning electron microscope image of the cross-section of a commercial UF alumina membrane (Pall Exekia). The average pore size of the support, of the two intermediate layers and of the separative top layer are 10 μm, 0.8 μm, 0.2 μm and 5 nm, respectively

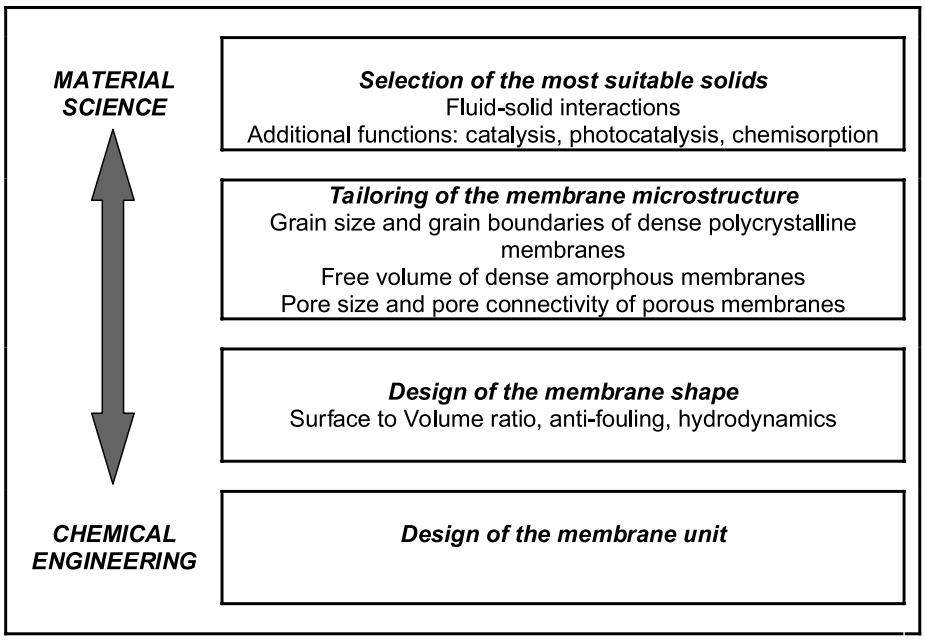

Fig. 2 Role of materials science in membrane science

in particular in the development of nanomaterials by innovative sol–gel or hydrothermal routes. In correlation with chemical engineering and transport modeling considerations, several complementary strategies are adopted in term of material engineering (Fig. 2). The first one is the selection of the most suitable solid phase to manage the fluid-membrane interactions. Layers exhibiting specific physical or chemical properties can be advantageously prepared. Multifunctional membranes coupling separation with functionality like catalysis, photocatalysis or adsorption can also be designed. A second aspect deals with the tailoring of the nanoporous texture (porosity, pore size and pore size distribution, connectivity and tortuosity of the pore network). The third point concerns the design of the membrane shape to increase the surface-to-volume ratio, to promote anti-fouling and hydrodynamics properties.

Tailoring of the porosity is very important because the porosity, the pore size distribution, the connectivity and tortuosity of the pore network are parameters which both define the permselectivity and the permeability of the porous membranes. The sol–gel process is a convenient method to prepare mesoporous or microporous supported membranes. The porosity of sol–gel derived layers drastically depends on the various synthesis parameters (Table 3) [3, 4].

With conventional sol–gel routes, the pore size distribution is usually broad and the tortuosity of the pore network is important with the presence of constrictions. Thus ordered interconnected pore networks with constant and tunable pore size are strongly attractive (Fig. 3). Hierarchical porosity and adaptive porosity are also fascinating approaches to increase or manage the permeability of ceramic membranes. This paper presents a short review of approaches developed in our laboratory for the preparation of innovative porous ceramic membranes by colloidal routes.

Table 3 Tools to tailor the initial porosity of sol–gel derived layers

Stage	Parameters
Choice of the elemental bricks	Size, shape, size distribution
Preparation of the sol before deposition	Conditions of polymerization/destabilization
	Sol aging
Reinforcement after deposition and before drying	Thermal aging
	Chemical post treatments
Drying method	Freeze-drying, hypercritical drying, ...

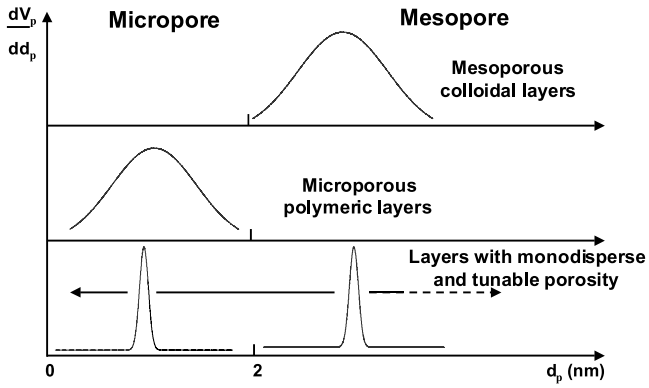

Fig. 3 Pore size distributions for sol–gel derived layers

Mesophase Templating and Ordered Mesoporosity

Extension of the microporous molecular sieves like zeolites to the mesoporosity range is possible using lyotropic liquid crystal mesophases (Fig. 4) as removable templates. These mesophases result from the self-assembly of surfactants or amphiphilic molecules and can be thermally or chemically eliminated after the formation of the inorganic network. This approach enables the preparation of materials exhibiting an ordered mesoporosity with pores usually ranging from two to more than ten nanometers. The pioneering work of Beck et al. [6, 7] has detailed the use of the templating effect to produce ordered mesoporous aluminosilicates. Divided materials have been prepared by phase separation and precipitation under hydrothermal conditions. Since these first articles, many investigations were carried out on this new class of materials, in particular for the preparation of sol–gel derived silica layers exhibiting hexagonal, cubic or lamellar structures using cationic surfactant of alkyltrimethylammonium halide type [8–16]. At the same time, this synthesis method was extended to the use of non-ionic surfactants [17, 18] and of block copolymers [19–21]. The preparation of other mesoporous oxides was also demonstrated [22, 23].

The formation of film is based on "evaporation-induced self-assembly" of the surfactant molecules [24]. The synthesis process is schematically shown in Fig. 5. The synthesis rules to prepare continuous layers without extra-porosity were initially investigated in the case of silica [16, 25]. The two main parameters are: (1) the size

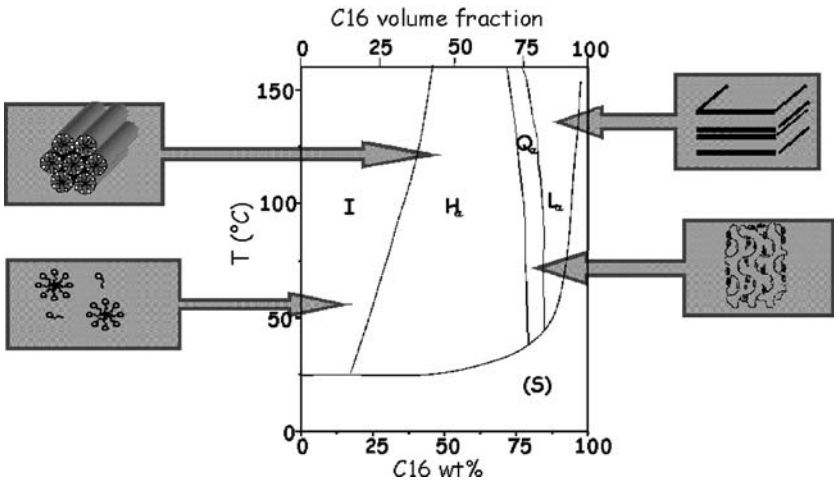

Fig. 4 Water-hexadecyltrimethylammonium bromide (from [5]). I: micellar solution; H_α: 2D hexagonal mesophase; Q_α: bicontinuous cubic mesophase; L_α: lamellar mesophase

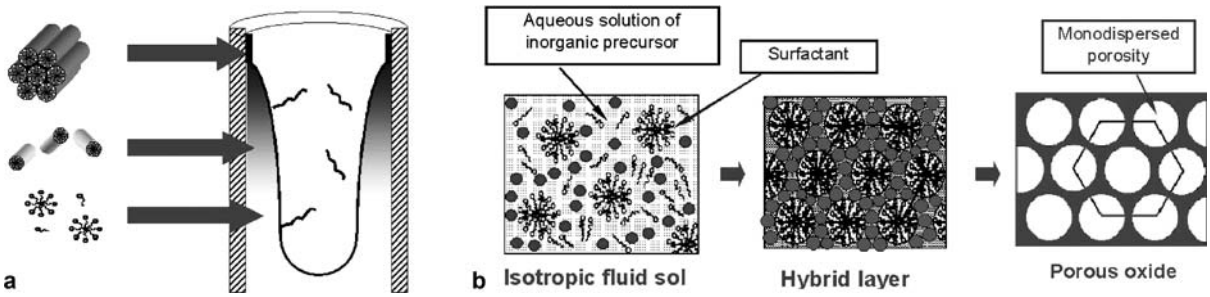

Fig. 5 Schematic representation of the formation of membranes with an ordered mesoporosity resulting from self-assembly of amphiphilic molecules. **a** Deposition by slip-casting in a tubular subtrate and solvant evaporation. **b** Various stages of the synthesis process

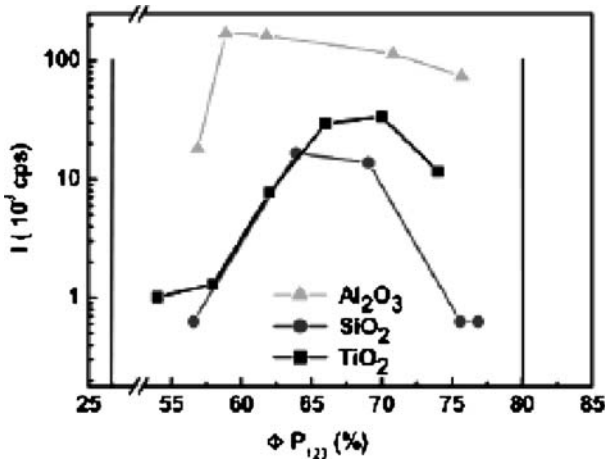

Fig. 6 Evolution of the intensity of main diffraction peak associated to ordered mesoporosity as a function of the volume fraction of triblock copolymer (P123). The limits of the hexagonal phase at 30 °C in the water-P123 binary diagram are reported as *vertical lines* (from [29])

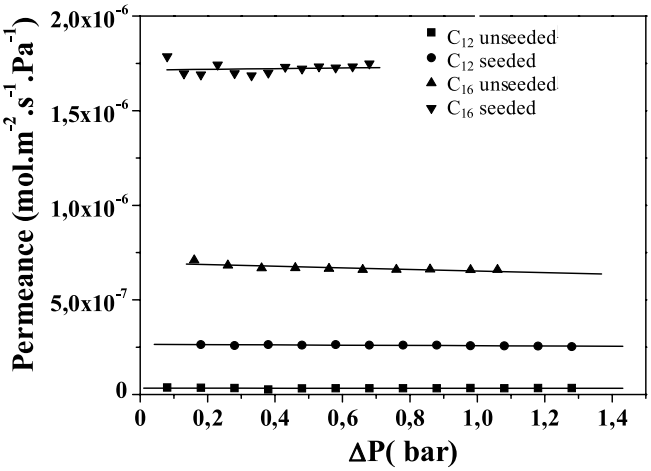

Fig. 8 Nitrogen permeance versus applied pressure difference for unseeded and seeded membranes, C16 and C12 (from [30])

of the inorganic clusters or nanoparticles which must be small enough to enable the self-assembly process; (2) the surfactant volume fraction in the dried layer which must be in agreement with the aimed mesostructure. This approach was successfully extended to the preparation of thin layers and membranes of oxides like Al_2O_3 and TiO_2 (Fig. 6) [25–29].

Mesoporous Silica Membranes

2D and 3D hexagonal mesoporous silica membranes were successfully prepared according to the synthesis procedures reported in [30, 31]. Only the 2D hexagonal membranes shown in Fig. 7 will be discussed here. These membranes were obtained using tetraethoxysilane as silica precursor and alkyltrimethylammonium bromides ($C_nH_{2n+1}(CH_3)_3N^+$, Br^- with $n = 12$ or 16) as surfactant [30]. The corresponding samples will be later labeled C16 and C12 in respect of the used surfactant.

The 2D mesoporous structures consist of a hexagonal packing of cylindrical pores. Previous studies [32, 33] evidenced the role of both the solid–solution and air–solution interfaces in the formation of 2D hexagonal mesophases and their alignment parallel to these interfaces. A seeding strategy with amorphous silica nanoparticles (12 nm-sized) or maghemite (γ-Fe_2O_3) nanoparticles was used to promote heterogeneous nucleation of the templating mesophase by creating additional interfaces inside the hybrid gelling solution [34].

The variations of nitrogen permeance as a function of the applied pressure difference are shown in Fig. 8,

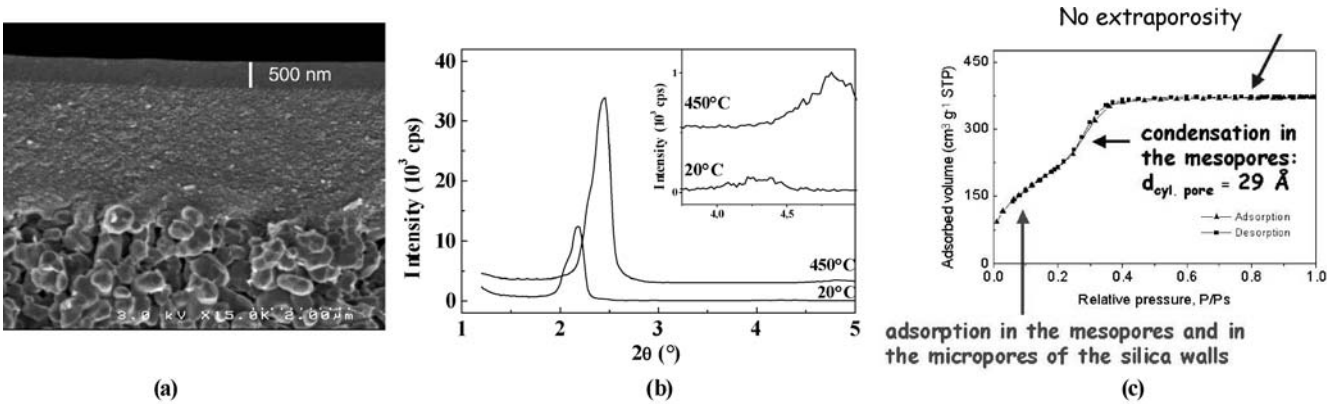

Fig. 7 **a** SEM cross-section image of a 2D hexagonal mesoporous C_{16} layer deposited on an asymmetric porous substrate with a 5 nm pore-sized γ-alumina top-layer. **b** X-ray diffraction patterns for unseeded C_{16} thin layers dried at 20 °C and thermally treated at 450 °C. **c** N_2 adsorption–desorption isotherms of a calcined unseeded C_{16} thin layer

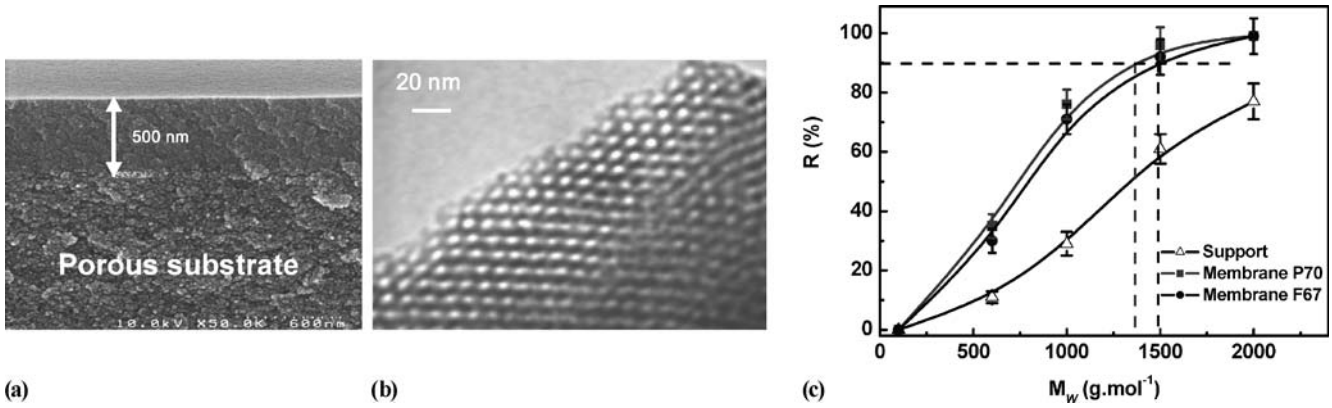

Fig. 9 SEM cross-section image (**a**) and TEM image for a P70 layer (**b**); Rejection rates R% versus PEG molecular weight for P70 and F67 membranes

for unseeded and seeded membranes C16 and C12. The measured permeance does not vary with the applied pressure difference (ΔP) as it is the case for a viscous flow gas transport. The permeance Π_{N_2} measured for the unseeded C16 membrane is very weak. The seeding with silica nanoparticles induces a clear increase of Π_{N_2}. The permeance of the unseeded and seeded C12 membranes is higher. In all cases, the nanoparticle seeding induces an increase of the membrane permeance by one order of magnitude. In unseeded C16 layers, the cylindrical mesopores are preferentially aligned parallel to the substrate, and so perpendicular to the gas flow. N_2 molecules are consequently forced across the microporous silica walls. Silica seeding, which induces a random orientation of the ordered domains, promotes a decrease of the tortuosity and an increase of the permeability associated to a larger statistic contribution of mesopores to gas transport. The permeability for the unseeded C12 layer is in the same range as the permeability of the seeded C16 layer. This result is explained by a less important alignment of the ordered domains and the absence of a very well aligned superficial area at the air–layer interface for the C12 membranes, as previously shown by X-ray diffraction measurements. The introduction of nanoparticles in the C12 layers increases the disorder in the orientation of ordered domains, which increases the membrane permeability.

Mesoporous Titania Membranes

Mesoporous titania membranes and coatings are attractive for coupling both separation and photocatalyzed reaction [35]. Mesoporous thin layers and membranes were synthesized from an anatase hydrosol using the templating effect of liquid crystal mesophases, as detailed in [28, 29]. The selected amphiphilic molecules were triblock copolymers, poly(ethylene oxide)-poly(propylene oxide)-poly(ethylene oxide): $EO_{20}PO_{70}EO_{20}$ and $EO_{106}PO_{70}EO_{106}$, labeled P123 and F127, respectively. The samples obtained without any surfactant were labeled WS and those obtained with the P123 or F127 copolymer were labeled P70 and F67, respectively. The membranes were prepared by slip-casting on asymmetric tubular alumina supports with a 5 nm pore-sized γ-alumina top-layer.

Crack-free and homogeneous layers were observed by SEM (Fig. 9a). The mesostructures of P70 and F67 layers are of 2D hexagonal and cubic types, respectively [29]. The ordering of mesopores is clearly evidenced from transmission electron microscope images (Fig. 9b).

The permeability of the mesostructured membranes was determined experimentally by water permeation measurements. These measured data are in good agreement with values calculated from the Carman–Kozeny equation and the membrane porous characteristics [35] (Table 4).

The membrane molecular weight cut-off (MWCO) was measured from the retention curves shown in Fig. 9c. In both cases, the MWCO is around 1.5 kDa which corresponds to a pore size of about 1.6 nm, as estimated from literature data [36]. This value is lower than the mesopore size experimentally determined from adsorption measurements: 4.2–4.8 nm. The retention is in fact defined by the smallest porosity existing inside the anatase walls.

Hierarchical Porosity

It can be advantageous to generate extraporosity at a larger scale in the separative layer in order to increase its permeability. The main condition which has to be respected is that the additional porosity must not be directly interconnected in order to preserve the cut-off fixed by the porosity of the continuous phase. The extra porosity can also be used to generate an additional functionality by insertion of specific catalysts or adsorbents at pre-defined locations inside the layer. This approach is here illustrated for sol–gel derived multifunctional ceramic membranes with a hierarchical porosity.

Table 4 Calculated values of intrinsic permeability for titania membranes

Sample	Pore type	Specific surface area ($m^2\ g^{-1}$)	Porosity (%)	Theoritical permeability (m^2)
Without any template/WS	Micro	25	10	2.7×10^{-20}
With P123 only/P70	Micro + meso	95	26.5	5.3×10^{-20}
With F127 only/F67	Micro + meso	97	27.5	4.8×10^{-20}
With P123 and PS/TLP	Micro + meso	100	26	4.4×10^{-20}
	Micro + meso + macro	100	36	1.5×10^{-19}
With F127 and PS/TLF	Micro + meso	105	27.5	5.0×10^{-20}
	Micro + meso + macro	105	37.5	1.7×10^{-19}

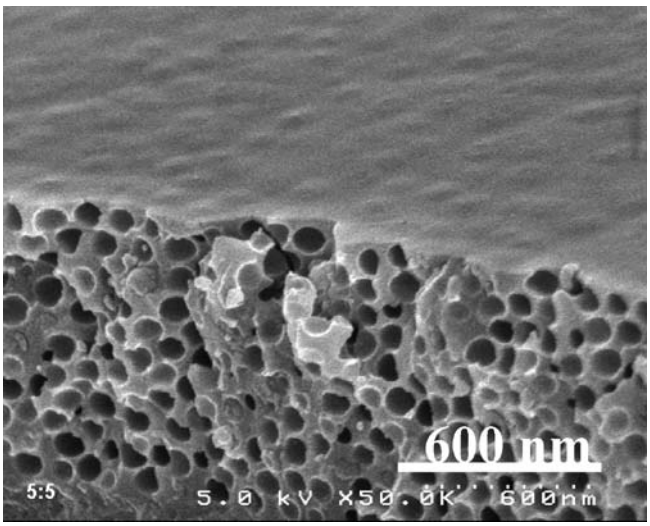

Fig. 10 SEM cross-section images of silica layers containing isolated obtained after a 2 h thermal treatment at 300 °C in air

Templating by polystyrene latex was previously used to produce individual macropores inside silica layers (Fig. 10) [37–39]. It was also applied to prepare membranes with other oxides [40, 41]. In addition, the presence of dispersed micron-sized or submicron-sized particles inside the starting suspensions modifies their rheology and decreases their ability to infiltrate the porous substrates. This strategy can be used to reduce the number of intermediate layers in asymmetric ceramic membranes. It must be noted that dispersion of dense and unremovable particles like oxide powders inside conventional sols enabled us to deposit homogeneous thick layers (from few μm to few tens μm thick) on macroporous substrates [42, 43].

Taking benefit of this experience, stable complex organic-inorganic hybrid suspensions were successfully prepared by mixing a polystyrene latex aqueous suspension, non-ionic triblock copolymers (poly(ethylene oxide)-poly(propylene oxide)-poly(ethylene oxide): $EO_xPO_yEO_x$) and titania or silica sols. Titania samples prepared from such suspensions were labeled TLP (when obtained from P123: $EO_{20}PO_{70}EO_{20}$) and TLF (when obtained from F127: $EO_{106}PO_{70}EO_{106}$) [44]. Homogeneous porous layers with a thickness equal to ~ 1.2 μm were prepared by slip-casting on asymmetric tubular alumina supports with a 0.2 μm pore-sized top-layer. The macropores, the mesopores and the nanocrytalline TiO_2 anatase walls with interconnected micropores are shown in Fig. 11 in the case of a TLP hierarchical anatase layer. N_2 adsorption–desorption isotherms of powders corresponding to different titania sol formulations are reported in Fig. 12a. The direct analysis of the porosity in the thin TLP layer was possible using a home-made environmental μ-balance and adsorption–desorption of ethanol at room temperature. The resulting isotherms (Fig. 12b) fit with those of the equivalent powder. From the main porosity characteristics, it was possible to predict the permeability values of the corresponding layers using the Carman–Kozeny equation [44]. The calculated permeabilities for the TLP and TLF samples are one order of magnitude higher than

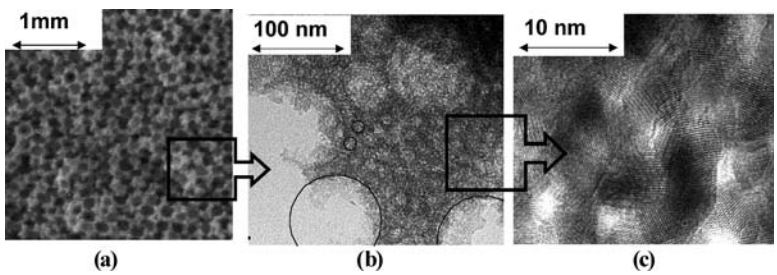

Fig. 11 **a** SEM and (**b**, **c**) TEM images of a TLP hierarchical anatase layer after thermal treatment up to 410 °C in air

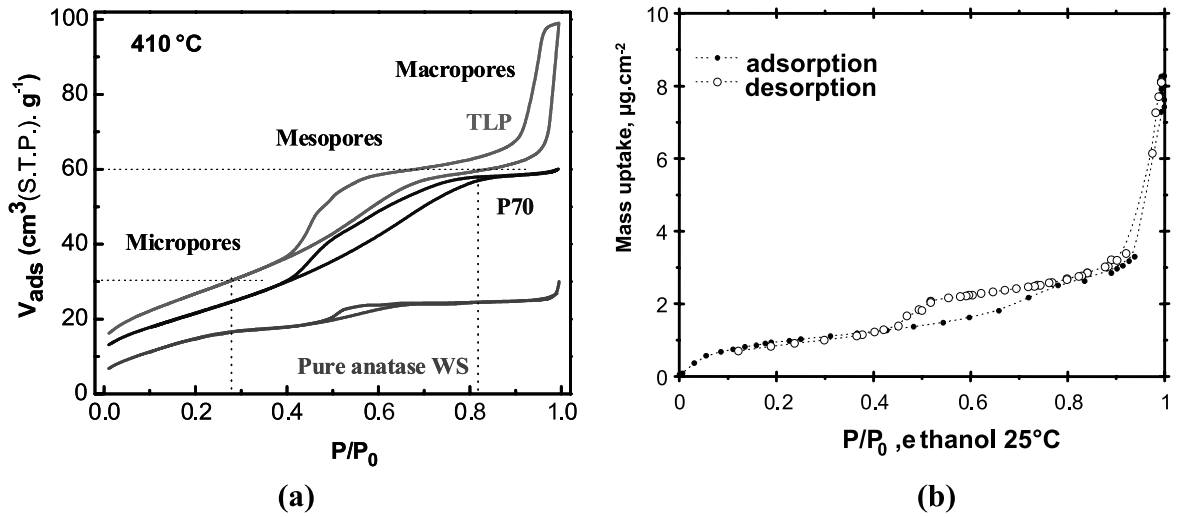

Fig. 12 **a** N_2 adsorption–desorption isotherms of TLP, P70 and WS powders thermally treated up to 410 °C in air; **b** Direct analysis of the porosity in the TLP thin layer using the environmental μ-balance and adsorption–desorption of ethanol at room temperature

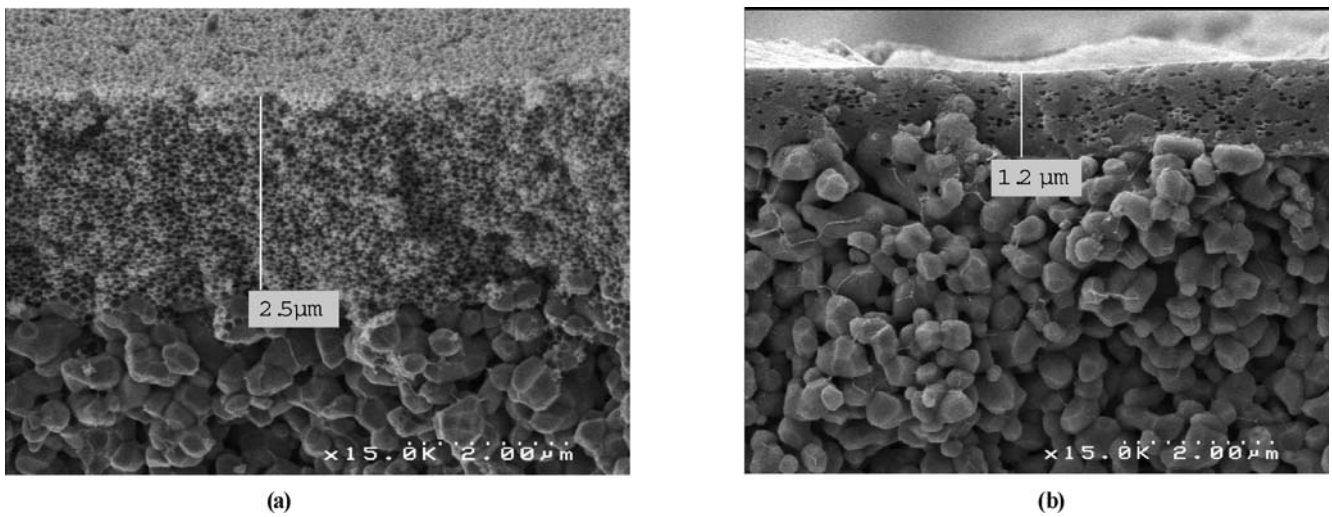

Fig. 13 SEM cross-section images of hierarchical silica membranes deposited on the 0.2 µm pore-sized α-alumina top-layer of an asymmetric porous alumina substrate. **a** Without or, **b** with pre-treatment of the substrate with a polymer to prevent sol infiltration, and thermally treated for 2 h at 450 °C in air

those calculated for a purely microporous anatase sample (Table 4). It must be underlined that the TLP and TLF layers can be directly deposited on a macroporous support, whereas a conventional microporous layer requires an additional intermediate mesoporous layer which significantly lowers the whole membrane permeance.

More recently silica layers with a hierarchical porosity were prepared by mixing a polystyrene latex aqueous suspension, a non-ionic triblock copolymer (F68: $EO_{80}PO_{30}EO_{80}$) and tetraethylorthosilicate (TEOS) [45]. SEM cross-section images of hierarchical silica membranes deposited on the 0.2 µm pore-sized α-alumina top-layer of an asymmetric porous alumina substrate are shown in Fig. 13. A pre-treatment of the substrate with a polymer prevents partial sol infiltration and enables to maintain the same volume fraction of macropores as for layers deposited on dense substrates. Indeed, the infiltration of the liquid phase within the support porosity induces close-packing for the latex particles on the support surface and finally yields to connected macropores (Fig. 13a). The membrane quality is strongly improved when sol infiltration is avoided (Fig. 13b). Gas permeation experiments and incorporation of metal nanoparticles are in progress with these original supported membranes exhibiting a hierarchical porosity.

Conclusion

Emerging membrane applications related to the treatment of liquids or gas require nanoporous ceramic membranes exhibiting a high thermal and chemical stability, and/or coupled functionalities like catalysis, photocatalysis or adsorption activity.

This article illustrates innovative approaches developed in our laboratory for the preparation of such membranes by colloidal routes.The templating effect of lyotropic liquid crystal mesophases enables to generate an ordered nanoporosity. Stable complex organic-inorganic hybrid suspensions can also be formulated to develop membranes exhibiting a hierarchical porosity or a nanocomposite ultrastructure.

Acknowledgement The author warmly thanks his Ph.D. students who were or are still involved in this research area: Thierry Dabadie, Michaela Klotz, Noureddine Idrissi-Kandri, Florence Bosc and Christelle Yacou.

References

1. Bonekamp BC (1996) Preparation of asymmetric ceramic membrane supports by dipcoating. In: Burgraff AJ, Cot L (eds) Fundamentals of Inorganic Membrane Science and Technology. Membrane Science and Technology Series, 4. Elsevier, Amsterdam, pp 141–225
2. Ayral A, Julbe A, Guizard C (2005) Ceramic Membrane Processing; New approaches in their design and applications. In: Lee BI, Komarneni S (eds) Chemical Processing of Ceramics, 2nd edn. Taylor and Francis Group, Boca Raton, USA, pp 629–666
3. Ayral A, Julbe A, Guizard C, Cot L (1997) J Korean Chem Soc 41:566
4. Klotz M, Ayral A, Guizard C, Cot L (1999) Bull Korean Chem Soc 20:879
5. Wärnheim T, Jönsson A, Sjöberg M (1990) Progr Colloid Polym Sci 82:271
6. Kresge CT, Leonowicz ME, Roth WJ, Vartuli JC, Beck JS (1992) Nature 359:710
7. Beck JS, Vartuli JC, Roth WJ, Leonowicz ME, Kresge CT, Schmitt KD, Chu CTW, Olson DH, Sheppard EW, McCullen SB, Higgins JB, Schlenker JL (1992) J Am Chem Soc 114:10834
8. Ogawa M (1994) J Am Chem Soc 116:7941
9. Dabadie T, Ayral A, Guizard C, Cot L, Robert JC, Poncelet O (1994) Mat Res Soc Symp Proc 346:849
10. Dabadie T, Ayral A, Guizard C, Cot L, Robert JC, Poncelet O (1994) Ma YH (ed) Proc 3rd Int Conference on Inorganic Membranes. Worcester Polytechnic Institute, Worcester, pp 411–419
11. Ayral A, Balzer C, Dabadie T, Guizard C, Julbe A (1995) Catal Today 25:219
12. Ogawa M (1996) Chem Commun, p 1149
13. Dabadie T, Ayral A, Guizard C, Cot L, Lacan P (1996) J Mater Chem 6:1789
14. Bruinsma PJ, Hess NJ, Bontha JR, Liu J, Baskaran S (1997) Mat Res Soc Symp Proc 443:105
15. Lu Y, Ganguli R, Drewien CA, Anderson MT, Brinker CJ, Gong W, Guo Y, Soyez H, Dunn B, Huang MH, Zinks JI (1997) Nature 389:364
16. Klotz M, Ayral A, Guizard C, Cot L (2000) J Mater Chem 10:663
17. Tanev PT, Pinnavaia TJ (1995) Science 267:865
18. Bagshaw SA, Prouzet E, Pinnavaia TJ (1995) Science 269:1242
19. Templin M, Franck A, Du Chesne A, Leist H, Zhang Y, Ulrich R, Schädler V, Wiesner U (1997) Science 278:1795
20. Zhao D, Yang P, Melosh N, Feng J, Chmelka BF, Stucky GD (1998) Adv Mater 10:1380
21. Zhao D, Huo Q, Feng J, Chmelka BF, Stucky GD (1998) J Am Chem Soc 120:6024
22. Sayari A, Liu P (1997) Microporous Mater 12:149
23. Yang P, Zhao D, Margolese DI, Chmelka BF, Stucky GD (1999) Chem Mater 11:281
24. Brinker CJ, Lu Y, Sellinger A, Fan A (1999) Adv Mater 11:579
25. Klotz M, Idrissi Kandri N, Ayral A, Guizard C (2000) Mat Res Soc Symp Proc 628:CC7.4.1.
26. Idrissi Kandri N, Ayral A, Klotz A, Albouy PA, El Mansouri A, van der Lee A, Guizard C (2001) Mater Lett 50:57
27. Ayral A, Guizard C (20001) Mater Transact 42:1641
28. Bosc F, Ayral A, Albouy PA, Guizard C (2003) Chem Mater 15:2463
29. Bosc F, Ayral A, Albouy PA, Datas L, Guizard C (2004) Chem Mater 16:2208
30. Klotz M, Ayral A, Guizard C, Cot L (2000) Separation Purif Technol 25:71
31. Klotz M, Besson S, Ricolleau C, Bosc F, Ayral A (2003) Mat Res Soc Symp Proc 752:123
32. Yang H, Kuperman N, Coombs N, Mamiche-Afara S, Ozin GA (1996) Nature 379:703
33. Yang H, Coombs N, Sokolov I, Ozin GA (1996) Nature 381:589
34. Klotz M, Albouy PA, Ayral A, Menager C, Grosso D, van der Lee A, Cabuil V, Babonneau F, Guizard C (2000) Chem Mater 12:1721
35. Bosc F, Ayral A, Guizard C (2005) J Membrane Sci 265:13
36. Nishiyama N, Saputra H, Park DH, Egashira Y, Ueyama K (2003) J Membrane Sci 218:165
37. Ayral A, Guizard C, Cot L (1994) J Mater Sci Lett 13:1538
38. Ayral A, Julbe A, Guizard C, Cot L (1997) J Korean Chem Soc 41:566
39. Klotz M, Ayral A, Guizard C, Cot L (1999) Bull Korean Chem Soc 20:879
40. Guliants VV, Carreon MA, Lin YS (2004) J Membrane Sci 235:53
41. DeFriend KA, Barron AR (2003) J Membrane Sci 212:29
42. Gwak J, Ayral A, Rouessac V, Cot L, Grenier JC, Jang ES, Choy JH (2004) Mater Chem Phys 84:348
43. Pintault B, Ayral A (2008) J Porous Materials DOI 10.1007/s10934-007-9170-y
44. Bosc F, Lacroix-Desmazes P, Ayral A (2006) J Colloid Interf Sci 304:545
45. Yacou C, Fontaine ML, Ayral A, Lacroix-Desmazes P, Albouy PA, Julbe A (2008) J Mater Chem DOI: 10.1039/b807029f

Progr Colloid Polym Sci (2008) 135: 10–15
DOI 10.1007/2882_2008_122

Published online: 13 September 2008

Ferenc Horkay

Biopolymer Gels: Nanostructure and Macroscopic Properties

Ferenc Horkay (✉)
Section on Tissue Biophysics and Biomimetics, Laboratory of Integrative and Medical Biophysics, NICHD, National Institutes of Health, 13 South Drive, Bethesda, MD 20892, USA
e-mail: horkayf@mail.nih.gov

Abstract Small-angle neutron scattering (SANS) has been used to investigate the effect of salts (NaCl and $CaCl_2$) on the structure of DNA and polyacrylic acid (PAA) gels. In the absence of salt a distinct correlation peak is observed in the SANS spectra of both systems indicating that electrostatic interactions play an important role in the organization of the polymer chains. When the salt concentration is increased, the peak position shifts to smaller values of the scattering vector q, and progressively vanishes. Osmotic swelling pressure measurements show that Ca ions reduce the swelling pressure and lead to the collapse of these gels. The Ca/Na ion exchange process does not affect the shear modulus of PAA gels. However, the shear modulus of DNA gels decreases with increasing Ca ion concentration at high swelling degrees, and increases at low swelling degrees. The results indicate that changing the ionic composition provides a simple way to control the nanoscale structures and properties in polyelectrolyte gels.

Keywords DNA · Gel · Polyelectrolyte · Shear modulus · Small-angle neutron scattering

Introduction

Colloids, polymers and biomaterials are increasingly important, from both fundamental and applied viewpoints. The demand for materials with controlled structure and morphology at all dimensions from nanoscale to macroscale is growing rapidly. Nanostructures may confer beneficial properties on biomaterials with advanced functionality. Living organisms tailor biological materials into highly complex functional structures exerting control on composition, interactions and architecture. Biological systems operate at the cellular and subcellular levels; therefore, material properties including structure, osmotic and mechanical properties must be determined to dimensions below 100 nm.

An emerging area of practical significance relates to biomimetic polymer networks and gels. Recently designed synthetic polymers mimic the hierarchical structure and function of biological macromolecules, such as DNA, proteins, as well as biological membranes and cells. Understanding the underlying physical characteristics of these systems enables molecular and nanometer scale manipulation with the aim of engineering useful and novel properties. Examples of applications include responsive biomaterials in tissue repair, e.g., "smart hydrogel scaffolds" for tissue engineering, medical implants for diagnosis and therapy, and in-vivo drug-delivery.

The main focus of our research is on the roles that nanoscale structures and interactions play in determining the macroscopic properties of polyelectrolyte gels. In hydrogels different kind of interactions (electrostatic, van der Waals, hydrophobic interactions, hydrogen bonding, etc.) play a role in driving the formation of complex hierarchical structures. These interactions are governed by a combination of structural properties at the micro- and nanoscale as well as by macroscopic physical parameters such as ionic strength and solvent quality. It is well known that many natural and synthetic polyelectrolytes

(e.g., DNA, polyacrylic acid) exhibit a strong sensitivity to ionic strength and, in particular, to counterion valence. Changes in the ionic environment impact the structure and dynamic properties of these polymers and, at high ionic strength lead to their precipitation. The complexity of the behavior of charged macromolecular systems necessitates an investigation of the structure and physical properties on all length scales from the atomic to the macroscopic level. Small-angle neutron scattering (SANS) and small-angle X-ray scattering (SAXS) are well-suited methods for such studies since enhanced spatial resolution is crucial. These techniques allow us to investigate biopolymer molecules and assemblies in their natural environment and to correlate the changes in environmental conditions (e.g., ionic composition, solvent quality) with physical properties.

We developed a multiscale approach to examine the structural hierarchy, phase behavior and equilibrium properties of polymer gels. In the present work we report SANS measurements that probe the structure over a wide range of length scales (1–500 nm) and provide insight into the hierarchical organization of polymer gels. A comparison is made between the main structural features of a synthetic (polyacrylic acid sodium salt) (PAA) and a biopolymer (DNA) gel. Osmotic swelling pressure measurements and shear modulus measurements are used to determine the macroscopic properties of the same gels.

Theory

The total free energy change, ΔF, associated with the swelling of a covalently cross-linked polymer network can be given as a sum of three terms [1]

$$\Delta F = \Delta F_{\text{mix}} + \Delta F_{\text{el}} + \Delta F_{\text{ion}} \,, \tag{1}$$

where ΔF_{mix} is the mixing, ΔF_{el} is the elastic, and ΔF_{ion} is the ionic contribution of the free energy.

In weakly cross-linked gels the elastic contribution can be approximated by the Gaussian theory of rubber elasticity [1–3]. In polyelectrolyte gels, in the presence of large amount of added salt, the electrostatic interactions are screened, and the ionic term is not expected to play a significant role. However, ionic interactions may modify the mixing free energy contribution. For neutral polymer gels the mixing pressure can be given by the Flory–Huggins theory [1], based on the lattice model of polymer solutions

$$\begin{aligned} \Pi_{\text{mix}} &= -\frac{1}{v_1}\frac{\partial \Delta F_{\text{mix}}}{\partial n_1} \\ &= -\frac{RT}{v_1}\left[\ln(1-\varphi)+\varphi+\chi_0\varphi^2+\chi_1\varphi^3\right] \,, \end{aligned} \tag{2}$$

where φ is the volume fraction of the polymer, v_1 is the molar volume of the solvent, n_1 is the number of the moles of the solvent, R is the gas constant, T is the absolute temperature, and χ_0 and χ_1 are constants that depend on the polymer–solvent interactions.

The neutron scattering intensity of a neutral semi-dilute polymer solution can be described by a Lorentzian function [4]

$$I(q) = \frac{A}{\left(1+q^2\xi^2\right)} \,, \tag{3}$$

where A is a constant, ξ is the polymer–polymer correlation length, and q is the scattering vector.

The scattering intensity from gels contains another contribution due to structural features frozen in by the cross-links [4–6]. Thus, the gel signal is given by

$$I(q) = \frac{A}{\left(1+q^2\xi^2\right)} + B(q) \,, \tag{4}$$

where the functional form of the second term is defined by the details of the gel structure.

Experimental

Gel Preparation

Polyacrylic acid (PAA) gels were prepared by free-radical polymerization in aqueous solution from partially neutralized acrylic acid monomers at 30% (w/w) monomer concentration in the presence of 0.3% *N*,*N*′-methylenebis(acrylamide) cross-linker as described previously [7]. After gelation the remaining acrylic acid units were neutralized by 0.1 M NaOH solution.

DNA gels were made from deoxyribonucleic acid sodium salt (Sigma). The molecular weight determined by ultracentrifugation was 1.3×10^6 Da. DNA gels were prepared [8] from a 3% (w/w) solution by cross-linking with ethyleneglycol diglycidyl ether at pH = 9.0 using TEMED to adjust the pH.

Both PAA and DNA gels were swollen in NaCl solution, and then the concentration of the $CaCl_2$ in the surrounding NaCl solution was gradually increased.

Small-angle Neutron Scattering

SANS measurements were made on gels using the NG3 instrument [9] at the National Institute of Standards and Technology (NIST, Gaithersburg MD). Gel samples were placed into standard NIST sample cells. The sample cell consisted of 1 mm thick quartz windows separated by a 2 mm thick spacer. The q range explored was $0.003\ \text{Å}^{-1} \le q \le 0.2\ \text{Å}^{-1}$, and counting times from twenty minutes to two hours were used. D_2O was the solvent. After radial averaging, detector response and cell window scattering were applied. The neutron scattering intensities were calibrated using absolute intensity standards. All experiments were carried out at 25 ± 0.1 °C.

Swelling Pressure and Elastic Modulus Measurements

Swelling pressure measurements were made by equilibrating the gels with aqueous solutions of poly(vinyl pyrrolidone) ($M_n = 29$ kDa) of known osmotic pressure [10, 11]. The penetration of the polymer into the swollen network was prevented by a semipermeable membrane.

Elastic (shear) modulus measurements were carried out on cylindrical gel samples using a TA.XT2I HR Texture Analyser (Stable Micro Systems, UK). Swollen networks were uniaxially compressed (at constant volume) between two parallel flat plates. The stress-strain isotherms were determined in the range of the deformation ratio $0.7 < \Lambda < 1$.

The data were analyzed using the relation [2]

$$\sigma = G\left(\Lambda - \Lambda^{-2}\right) , \tag{5}$$

where G is the shear modulus and σ is the nominal stress (related to the undeformed cross-section of the gel cylinder). The absence of volume change and barrel distortion was checked by measuring the dimensions of the deformed and undeformed gel cylinders.

Results and Discussion

Small-Angle Neutron Scattering Measurements

Figure 1 shows the SANS spectra of DNA and PAA gels (inset) measured in D_2O at different NaCl concentrations. All the spectra exhibit two common features: low-q clustering and high-q solvation. The upturn in $I(q)$ at approximately $q < 0.01$ Å^{-1} indicates domain formation generally observed in polyelectrolyte solutions [12–14]. The size of the clusters exceeds the resolution of the SANS experiment. Solvation is governed by the thermodynamic interactions between the polymer and the solvent molecules [15].

In the salt-free solutions the scattering curves for both gels exhibit a distinct correlation peak at a finite value of q, a behavior typical of weak polyelectrolyte systems. In the DNA gel the peak occurs at $q_0 \approx 0.07$ Å^{-1} corresponding to an average distance of $d_0 = 2\pi/q_0 \approx 90$ Å between the charged domains. In the PAA gel the polyelectrolyte peak is not well resolved from the low-q clustering feature. In salt solutions ions screen the charges, and the polyelectrolyte peak position is shifted towards lower values of q. In the DNA gel the correlation peak moves from $q_0 \approx 0.07$ Å^{-1} (without salt) to $q_o \approx 0.04$ Å^{-1} (in 10 mM NaCl solution) indicating that the size of the charged domains increases by roughly 80%. In 40 mM NaCl solution the polyelectrolyte peak has completely disappeared and the curve only exhibits a shoulder at $q \approx 0.04$.

The SANS data can be analyzed using a simple equation that reproduces the main characteristic features of the scattering curves [14, 15]

$$I(q) = \frac{A}{1 + |q - q_0|^2\,\xi^2} + \frac{B}{q^m} + C\,. \tag{6}$$

In this equation q_0 is the peak position. A, B, C and m are constants. C is mostly due to incoherent "background" scattering, which is independent of q. The dashed lines show the fits of Eq. 6 to the SANS spectra. For small values of q (< 0.01 Å^{-1}) both DNA and PAA gels exhibit a power law behavior with a slope $-3.4 < m < -4$, that can be attributed to scattering from interfaces. Rough colloids give slopes between -3 and -4, whereas smooth colloids give slope of -4 (Porod scattering) [16, 17]. In the intermediate q-range (0.01 Å$^{-1} < q < 0.08$ Å^{-1}) the first term of Eq. 6 satisfactorily describes the experimental data. In the high q-region ($q > 0.08$ Å^{-1}) the scattering intensity is governed by the local geometry of the polymer molecules. We note that small ions are not visible in the SANS experiment; only their influence on the polymer conformation and the thermodynamic properties of the system is detectable.

The upper curve in Fig. 1 shows the SANS spectrum of a DNA gel measured in 40 mM NaCl containing 0.2 mM $CaCl_2$. Ca/Na ion exchange modifies the electrostatic interactions between the DNA strands and affects their organization. In the low-q region Ca ions only slightly influence the slope of the scattering curve. In gels covalent

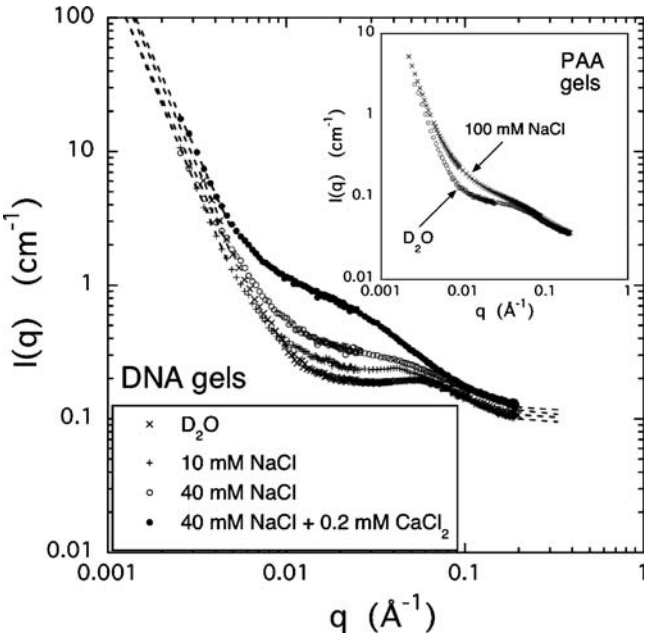

Fig. 1 SANS intensity from DNA gels in equilibrium with D_2O solutions containing NaCl (0, 10 and 40 mM) and NaCl + $CaCl_2$ (40 mM NaCl + 0.2 mM $CaCl_2$). The *inset* shows the SANS spectra of PAA gels in pure D_2O (*lower curve*) and in 100 mM NaCl (in D_2O) (*upper curve*)

cross-links lead to a local decrease in chain mobility, and prevent significant structural reorganization. At intermediate length scales the scattering intensity from the Ca-containing gel significantly exceeds that from the other three samples. The increase of intensity is consistent with a system approaching phase separation. The present DNA gel undergoes phase separation at approximately 0.3 mM $CaCl_2$ concentration (in the surrounding 40 mM NaCl solution). In the high-q region calcium ions do not influence the SANS signal, indicating that the chain geometry (cross-section of the DNA molecule) remains unchanged.

Osmotic Pressure and Shear Modulus Measurements

In this section we focus on the macroscopic elastic and osmotic properties of PAA and DNA gels, and relate the macroscopic behavior to structural features identified by SANS.

The dependence of the swelling degree ($1/\varphi$) on the $CaCl_2$ concentration for DNA and PAA gels swollen in 10 mM NaCl solution is plotted in Fig. 2. With increasing $CaCl_2$ concentration both systems display an abrupt volume change. The sharp variation of the swelling degree indicates that this transition is a highly cooperative process.

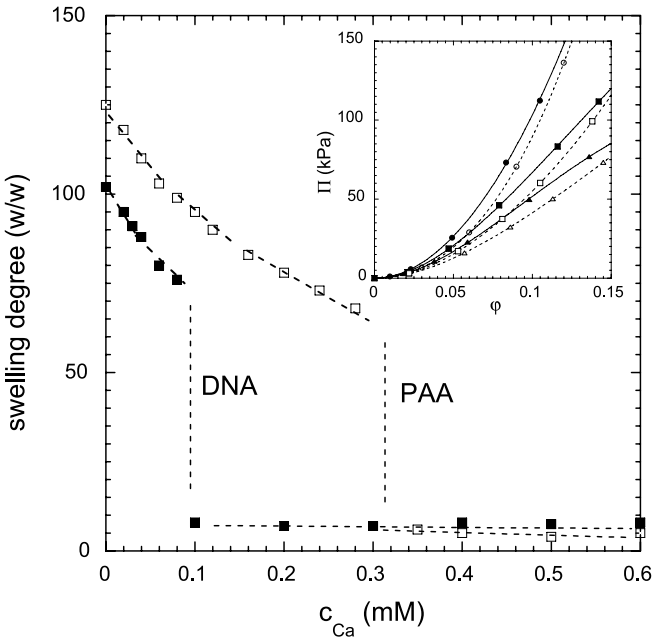

Fig. 2 Dependence of the swelling degree of DNA and PAA gels on the $CaCl_2$ concentration of the surrounding 10 mM NaCl solution. *Inset* shows the variation of the osmotic pressure with the polymer volume fraction for the same gels at three different calcium concentrations (DNA gels: ● 0 mM $CaCl_2$, ■ 0.03 mM $CaCl_2$, ▲ 0.06 mM $CaCl_2$; PAA gels: ○ 0 mM $CaCl_2$, □ 0.1 mM $CaCl_2$, △ 0.2 mM $CaCl_2$)

Equation 1 predicts that the swelling pressure of the gel Π_{sw} is the sum of elastic (Π_{el}), mixing (Π_{mix}) and ionic (Π_{ion}) pressure contributions [1]

$$\Pi_{sw} = \Pi_{el} + \Pi_{mix} + \Pi_{ion} \,. \tag{7}$$

In what follows we investigate the effect of ions on the individual terms of Eq. 7.

The elastic contribution can be estimated from the shear modulus G of the gel [2]

$$\Pi_{el} = -G = -KRT\nu\varphi^n \,, \tag{8}$$

where ν is the concentration of the elastic chains in the swollen network, and K is a constant that depends on the functionality of the cross-links. According to the classical theory of rubber elasticity the value of the exponent n is $1/3$ [1, 2].

The inset in Fig. 2 illustrates the dependence of the osmotic pressure Π_{mix} on the polymer volume fraction φ for DNA (continuous curves) and PAA (dashed curves) gels. Each data set was measured at constant $CaCl_2$ concentration. The osmotic pressure gradually decreases as Ca ions replace Na ions, which implies that the osmotic compression modulus $K_{os}(=\varphi\partial\Pi_{sw}/\partial\varphi)$ also decreases with increasing Ca concentration. The decrease in K_{os} is reflected by an increase in the SANS intensity (see Fig. 1). We note that at the phase transition both scattering intensity and correlation length (ξ) diverge.

Figures 3 and 4 show the variation of the shear modulus as a function of the polymer volume fraction for PAA

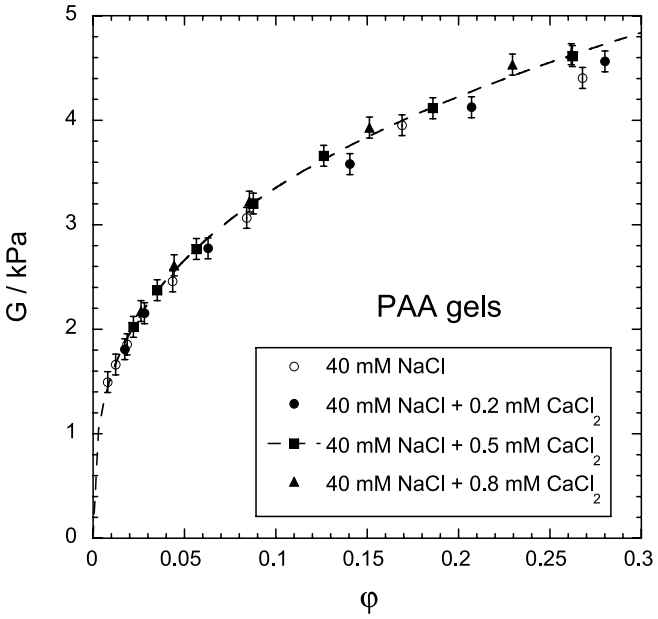

Fig. 3 Variation of the shear modulus of PAA gels with the polymer volume fraction in salt solutions containing 40 mM NaCl and different amounts of $CaCl_2$. *Dashed curve* is a power law fit to Eq. 8 ($n = 0.34$)

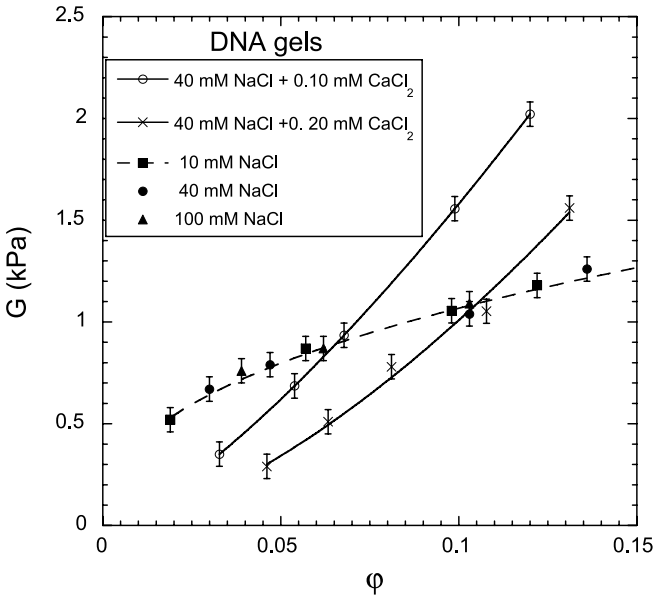

Fig. 4 Variation of the shear modulus in DNA gels with the DNA volume fraction in salt solutions containing different amounts of NaCl and $CaCl_2$. The *dashed line* through the 10 mM NaCl data is a power law fit to Eq. 8 ($n = 0.42$)

and DNA gels swollen in NaCl solutions containing different amounts of $CaCl_2$. In PAA gels G is practically independent of the ion concentration and ion valence, implying that Ca ions do not form additional "cross-links" between the negatively charged PAA chains. The dashed curve through the experimental points is the fit of Eq. 8 to the data. The value 0.34 obtained for the exponent is close to that predicted by the theory of rubber elasticity. In DNA gels G is hardly affected by the NaCl concentration. However, addition of Ca ions modifies G. It is well known that dissolved DNA spontaneously forms liquid crystalline regions (mesophases). SANS measurements show that Ca ions only slightly affect the gel structure in the low-q region (see Fig. 1). Replacing Na with Ca ions reduces the electrostatic repulsion between the charged domains producing an increase in the elastic modulus. This is observed at high DNA concentration where the elastic moduli of the Ca-containing gels exceed that of the Ca-free gels. However, at low DNA concentration the elastic modulus decreases with increasing Ca content. In highly swollen gels the DNA-rich zones become separated by regions of lower DNA concentration. The elastic modulus of such systems is governed by the properties of the "soft" regions as indicated by the decrease of G.

Conclusions

SANS and osmotic pressure measurements reveal similarities between the structure and macroscopic properties of PAA and DNA gels. In the absence of added salt the SANS spectra of both systems exhibit a correlation peak which progressively disappears as the salt (NaCl) concentration increases at constant polymer concentration. The data also show that on addition of salt the position of the correlation peak shifts to the lower q-region.

Ca ions reduce the osmotic swelling pressure and induce volume transition in both gel systems. Addition of Ca ions enhances the scattering intensity as expected upon approaching phase transition.

Shear modulus measurements reveal important differences between the elastic properties of PAA and DNA gels. In PAA gels the shear modulus is practically independent of the $CaCl_2$ concentration of the surrounding solution indicating that Ca ions do not form cross-links. The shear modulus of Ca-containing DNA gels is smaller at low DNA concentration, and greater at high DNA concentration than that of the corresponding Ca-free DNA gels.

The results illustrate that changing the ionic environment in polyelectrolyte gels allows us to modify the organization of the polymer segments at the nanoscale level without significantly influencing the network structure at larger length scales.

Acknowledgement This research was supported by the Intramural Research Program of the NICHD, NIH. The authors acknowledge the support of the National Institute of Standards and Technology, U.S. Department of Commerce for providing access to the NG3 small angle neutron scattering instrument used in this experiment. This work utilized facilities supported in part by the National Science Foundation under Agreement No. DMR-0454672.

References

1. Flory PJ (1953) Principles of Polymer Chemistry. Cornell University, Ithaca
2. Treloar LRG (1976) The Physics of Rubber Elasticity. Clarendon, Oxford
3. Horkay F, McKenna GB (2007) Mark JE (ed) Gels, Physical Properties of Polymers Handbook. Springer, New York
4. Bastide J, Candau SJ (1996) Cohen Addad JP (ed) Physical Properties of Polymeric Gels. Wiley, Chichester
5. Horkay F, Hecht AM, Mallam S, Geissler E, Rennie AR (1991) Macromolecules 24:2896
6. Horkay F, Grillo I, Basser PJ, Hecht AM, Geissler E (2002) J Chem Phys 117:9103
7. Horkay F, Tasaki I, Basser PJ (2000) Biomacromolecules 1:84
8. Horkay F, Basser PJ (2004) Biomacromolecules 5:232
9. NIST Cold Neutron Research Facility (1999) NG3 and NG7 30-meter SANS Instruments Data Acquisition Manual, January 1999
10. Vink H (1971) Eur Polym J 7:1411

11. Horkay F, Zrínyi M (1982) Macromolecules 15:1306
12. Moan M (1978) J Appl Cryst 11:519
13. Prabhu VM, Muthukumar M, Wignall GW, Melnichenko YB (2003) J Chem Phys 119:4085–4098
14. Hammouda B, Horkay F, Becker M (2005) Macromolecules 38:2019
15. Hammouda B, Ho D, Kline S (2004) Macromolecules 37:6932
16. Bale HD, Schmidt PW (1984) Phys Rev Lett 53:596
17. Glatter O, Kratky O (1982) Small Angle X-ray Scattering. Academic Press, New York

Progr Colloid Polym Sci (2008) 135: 16–20
DOI 10.1007/2882_2008_121

Published online: 9 September 2008

R. Koeppe
A. Fuchsbauer
S. Lu
N. S. Sariciftci

Energy Transfer from CdSe/ZnS Nanocrystals to Zinc-Phthalocyanine for Advanced Photon Harvesting in Organic Photovoltaics

R. Koeppe (✉) · A. Fuchsbauer · S. Lu · N. S. Sariciftci
Linz Institute for Organic Solar Cells (LIOS), Johannes Kepler University Linz, Altenbergerstr. 69, 4040 Linz, Austria
e-mail: robert.koeppe@jku.at

S. Lu
Present address:
Institute for Organic Solar Energy Opto-Electronic Materials, College of Biological and Chemical Engineering, Zhejiang University of Science and Technology, 310012 Hangzhou, China

Abstract Due to the limited spectral width of absorption in organic dyes, it is necessary to look for strategies to enhance the spectral photon harvesting in organic solar cells. Investigations of the energy transfer between zinc-phthalocyanine (ZnPc) and CdSe/ZnS core shell nanocrystals are performed and show a highly efficient energy transfer and no sign of a competing charge transfer mechanism. The dependence of the energy transfer efficiency on the length of the alkyl spacers around the nanoparticles is investigated. The integration of semiconductor nanoparticles into a photodiode based on ZnPc yields increased sensitivity of the device in the green spectral range.

Keywords Energy transfer · Organic solar cells · Phthalocanine · Semiconductor nanocrystals

The large scale availability of organic semiconductors now enables technological photonic applications such as organic light emitting diodes (OLEDs) and organic solar cells [1–3]. One of the most attractive properties of organic semiconductors is the possibility to combine and chemically alter the materials to fit a specific application.

Another material class allowing precise tailoring of optical and electronical properties are colloidal semiconductor nanomaterials. They exhibit strong optical absorption and high photoluminescence yield as well as solution processability. These properties can be tuned by changing the material, the size and the shape of the nanocrystals [4, 5]. The chemical properties of these nanoparticles are mostly determined by a shell of organic ligands that provide good compatibility with organic solvents and organic semiconductor matrices.

In bulk heterojunction organic solar cells, a solid state blend of a donor and an acceptor material is used, between which an ultrafast photoinduced charge transfer mechanism takes place. This photoinduced charge transfer facilitates the separation of excitations into free charge carriers [6]. Both materials are usually active in charge transfer and charge transport and at least one of the materials has to be highly absorptive in the spectral range of the solar irradiation (chromophore). Especially a high absorption in a broad spectral region requires thick layers, but then the charge transport is likely to limit the solar cell performance. Since the mobilities are on the order of $\mu \approx 10^{-2}$–$10^{-4}\,\mathrm{cm^2\,V^{-1}\,s^{-1}}$, the thickness is usually limited to around 100 nm.

Advanced photon harvesting concepts in which light absorption is separated from the materials providing charge generation and transport can overcome this problem. Resonant energy transfer from antenna molecules onto the photoactive components can play a major role in those concepts. Especially the long range energy transfer mechanism as described by the Förster theory [7] is applicable to funnel photon energy from light absorbing antenna materials onto the electrically active species. Exactly this strategy is implemented in natural photosynthesis systems using antenna molecules to absorb and funnel the energy into the photosynthetic reaction cen-

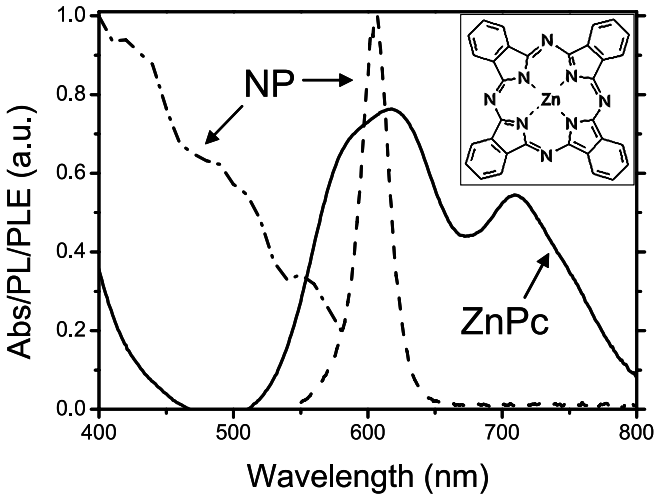

Fig. 1 Absorption spectra of a thin film of ZnPc (*solid line*), together with the photoluminescence (*dashed*) and photoluminescence excitation (*dash-dotted*) spectra of the CdSe/ZnS nanocrystals showing the possibility of energy transfer from the nanocrystals to the ZnPc due to the overlap between nanoparticle emission with the ZnPc absorption. *Inset*: the chemical structure of ZnPc

ter. Several reports exist in the literature using different approaches to combine energy transfer systems with photoinduced charge transfer [8–10] or to directly use natural photosynthetic complexes [11] in a solar cell.

Zinc-phthalocyanine (ZnPc) as photoinduced electron donor molecules can provide power conversion efficiencies above 3% in combination with C_{60} fullerene as an electron acceptor [12–14]. ZnPc forms polycrystalline films upon vacuum evaporation which are semiconducting with strong absorption bands around 400 nm and between 600 and 800 nm. This material has an absorption lack around 500 nm (Fig. 1). Therefore, antenna systems absorbing wavelengths around 500 nm are fitting to this absorption profile of ZnPc.

As a photon harvesting antenna system, we use CdSe/ZnS nanocrystals with a high absorption cross section in the desired wavelength range as well as a strong luminescence above 600 nm, required for the energy transfer to the ZnPc. A second advantage is the organic ligand shell around the nanocrystals, electrically insulating them from the surrounding matrix. This ensures that the leading mechanism between the nanoparticles and the surrounding ZnPc matrix is energy transfer and not the charge transfer [16]. Charge transfer is not desirable, as the transport of the charges remaining on the nanocrystals is usually unfavourable.

In this work, we use steady state absorption and fluorescence spectroscopy to study the interaction between the two species. The nanoparticle ligands are altered to probe the dependence of the transfer efficiency on the distance between donor particle and acceptor matrix. Photodiodes with and without an intermediate nanoparticle layer are compared and a significant spectral sensitization around 500 nm is observed.

The CdSe/ZnS nanocrystals were purchased as solution in toluene from NN-labs Inc. (www.nn-labs.com). Nominal diameter of the particles is 3.0 nm and the emission maximum in solution is at 605 nm. The CdSe core is epitaxially coated alternately with zinc (4 layers) and sulphur (3 layers) to passify surface states. The PL quantum yield in solution is approximately 40%. The original octadecylamine (ODA) ligands providing solubility were exchanged with a standard ligand exchange procedure [14] to n-alkanethiols of different length: $n = 18$ (T18), 16 (T16), 12 (T12), 9 (T9), 6 (T6).

Absorption spectra were taken with a Varian Cary 3G UV-Vis Spectrophotometer. The luminescence of the films was measured with a M.U.T "Tristan light" fiber spectrometer using a Coherent "Innova 400" Ar^+-laser as 514 nm excitation source.

The energy transfer samples were produced by thermally evaporating 20 nm of ZnPc in high vacuum ($p < 10^{-5}$ mbar) onto a clean glass slide, followed by dropcasting of approximately 30 µl solution of T12-coated nanocrystals and subsequent evaporation of another 20 nm thick film of ZnPc. A 40 nm thick film of ZnPc was evaporated under the same conditions onto a clean glass slide as reference.

The scattered nanoparticle samples were prepared by putting one drop of a solution of 2 mg nanoparticles (T18, T16, T12, T9 or T6) in 1 ml of toluene onto a clean glass slide ($1.5 \times 1.5\,cm^2$) rotating at 6000 rpm. Subsequently, on one half of the glass slide, a layer of 20 nm ZnPc is thermally evaporated in high vacuum. The quenching ratio was determined by averaging the nanoparticle photoluminescence of 5 points each on the parts of the glass slides with and without covering of ZnPc. The luminescence of the nanoparticles did not change significantly during several repetitions of the experiment independent of the coverage with ZnPc. Spincoating the nanoparticles on top of a ZnPc film yielded similar quenching ratios, indicating that the deposition of ZnPc onto the nanoparticles does not alter the intrinsic PL efficiency.

The photodiodes were prepared by spincoating a layer of PEDOT:PSS (Baytron PH) onto an ITO-covered glass slide. These substrates were coated with a layer of 40 nm ZnPc by thermal evaporation in high vacuum. On some samples, approximately 25 µl of T12 coated nanoparticle solution was dropcast. Then another 20 nm of ZnPc and 75 nm Al were evaporated to finish the diode structure. Charge separation in this photodiodes is not very efficient, but yields enough photocurrent to record the spectrally resolved photocurrent.

The Incident Photon to Collected Electron conversion efficiency spectra (IPCE) were measured by illuminating the active area of the samples with monochromatised and chopped light from a tungsten halogen lamp. The resulting

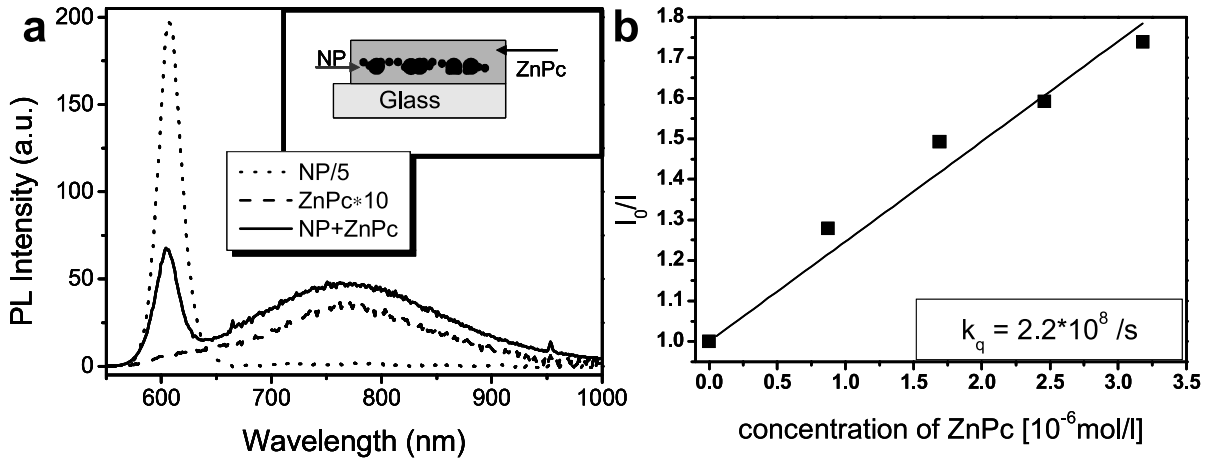

Fig. 2 **a** Photoluminescence spectra of a dropcast film of nanocrystals (*dotted line* 5×), a 40 nm thick evaporated film of ZnPc (*dashed line* 10×) and a 40 nm thick evaporated film of ZnPc with nanocrystals dropcast after 20 nm. Strong quenching of the nanocrystal luminescence and a significant increase of the ZnPc luminescence indicates efficient energy transfer. **b** Stern–Volmer plot of the quenching of the nanoparticle luminescence by addition of ZnPc molecules into the nanoparticle solution

modulated photocurrent is recorded by a lock-in amplifier. The lamp power is recorded with a silicon diode powermeter (Thorlabs PM100) and is between 3–20 μW over the measured spectral range.

In Fig. 1, the extinction spectra of thin films of ZnPc on glass can be seen as well as the photoluminescence and photoluminescence excitation spectra of thin nanoparticle films. The absorption spectrum of the evaporated film of ZnPc (solid line) measured against a clean glass slide as reference shows a strongly broadened Q-band in the red and near infrared part of the spectrum. This is due to a π–π interaction of the ZnPc molecules in a close packed film that leads to a Davydov splitting and broadening of the absorption peak. The antireflection effect of the thin ZnPc film on the glass slide leads to the negative values for the extinction around 470 nm.

The nanoparticle films (dashed line) show a very strong and narrow luminescence centered at 605 nm with a photoluminescence excitation spectrum extending in the blue region of the spectrum. Noticeable is the strong overlap of the nanoparticle luminescence with the ZnPc absorption, a prerequisite for efficient resonant energy transfer. The nanoparticle films can be efficiently excited in the range of low absorption of the ZnPc, as can be seen in the photoluminescence excitation spectra of the nanoparticles.

In order to quantify the possible resonant energy transfer interaction between the molecules, a quenching experiment was performed in dilute solution. The photoluminescence of a nanoparticle solution was monitored during the stepwise addition of small amounts of ZnPc. A linear increase of the inverse luminescence intensity change on the molar concentration of the ZnPc is observed (Fig. 2b), indicating quenching according to the Stern–Volmer formalism. The quenching rate k_q can be thus obtained via the gradient of the inverse luminescence intensity K_{sv} with the Stern–Volmer formula

$$K_{sv} = k_q \times \tau_F \, .$$

The resulting quenching rate constant calculates to around 10^8 s, with the measured nanoparticle luminescence lifetime τ_F of about 7 ns (amplitue averaged) and a calculated nanoparticle molar mass of 75×10^3 g/mol. Therefore, an efficient quenching process has to be present in the system.

Thermally evaporated films of ZnPc, such as used in the fabrication of organic solar cells, show packing induced intermolecular π–π-interactions which strongly quench the ZnPc luminescence, as radiative transitions from the lower Davydov-level are forbidden. The weak luminescence of a 40 nm thick film of evaporated ZnPc is broadened and featureless, as can be seen in Fig. 2a (dashed line, magnified 10×). After the addition of nanoparticles to the film, the luminescence signal (solid line) of the ZnPc in the range of 800 nm increases by a factor of approximately 15, indicating a transfer of energy from the nanoparticles to the ZnPc. The nanoparticles show a much higher absorption at the excitation wavelength of 514 nm than the pure ZnPc layer. At the same time, the luminescence of the nanoparticles is considerably quenched as compared to a layer of similar thickness deposited on clean glass (dotted line, divided by 5). The increase of luminescence in the ZnPc-layer is a strong indication that there is a resonant energy transfer rather than charge transfer occuring between the ZnPc and the nanoparticles.

Another way of identifying and quantifying resonant energy transfer is to study the dependence of the donor luminescence quenching on the thickness of the insulating

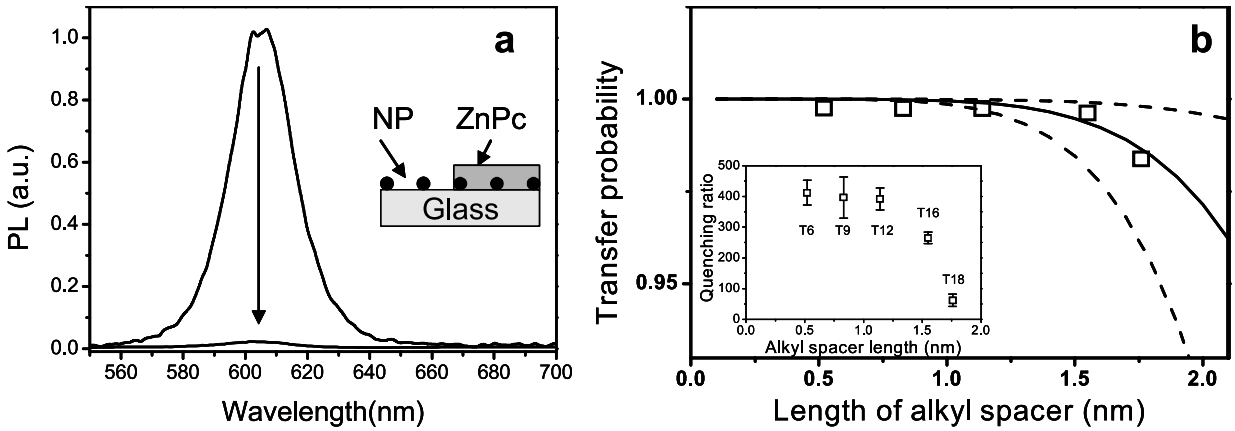

Fig. 3 **a** Photoluminescence spectrum of nanocrystals scattered on a glass slide before and after evaporation of a 20 nm thick layer of ZnPc. **b** Evolution of the transfer probability and the quenching ratio (*inset*) with different lengths of the ligand on the nanocrystal surface. The *lines* indicate different calculations according to Förster's theory with R_0 set to 3.6 nm (*solid line*) as well as 3 and 5 nm (*dashed lines*)

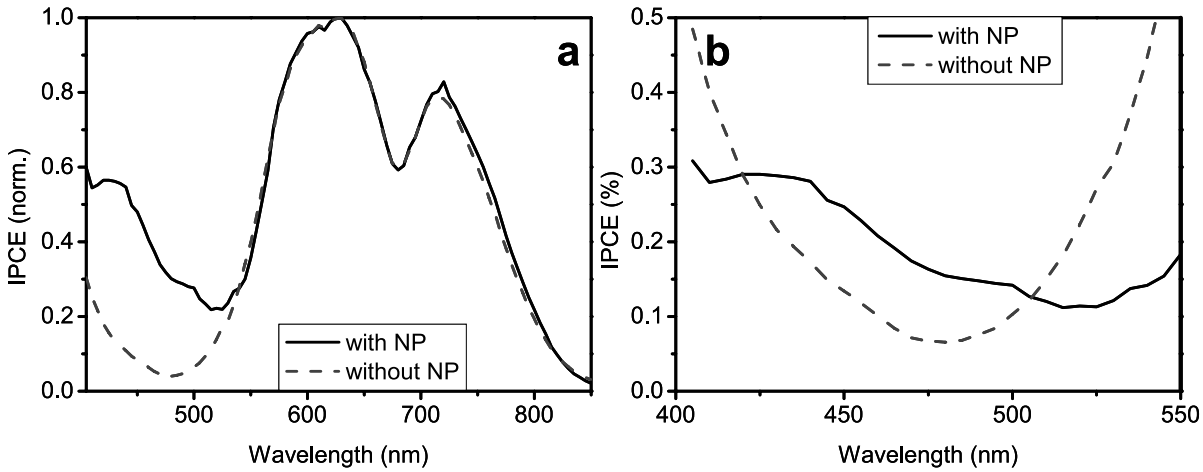

Fig. 4 **a** Normalized incident photon to converted electron efficiency spectrum of ZnPc photodiodes with (*solid line*) and without (*dashed line*) nanocrystals dropcast into the ZnPc layer. **b** Absolute values of IPCE in the spectral region of sensitization

shell between donor and acceptor matrix. For this reason, nanoparticles are scattered from dilute solution on a glass substrate with subsequent evaporation of ZnPc. Thus we can make sure that almost all of the nanoparticles are in close contact with ZnPc molecules held at a distance by the ligand shell. As expected, the nanoparticle luminescence is strongly quenched (Fig. 3a).

The inset of Fig. 3b shows the dependence of the nanoparticle luminescence quenching ratio on the length of the ligands covering the particles, assuming they are tightly packed and therefore fully elongated. 514 nm laser excitation leads to a strong photoluminescence signal of the nanoparticles which then is significantly quenched in the presence of ZnPc on top of the nanoparticles. As expected, the quenching ratio increases with smaller shell thickness, but saturates at spacer lengths of less than 1 nm. The quenching ratio is then over 400 : 1.

The donor–acceptor distance dependence of the energy transfer probability according to Förster's theory can be described by the following formula

$$P = \frac{1}{1 + \left(\frac{R}{R_0}\right)^6} .$$

R_0, the so-called Förster radius, is the donor–acceptor distance at which the transfer probability is 50%. In well-tuned energy transfer systems it can reach values of around 5 nm.

Comparing calculations according to Förster's theory with the measured data, we can roughly estimate an effective Förster radius between 3 and 5 nm. Figure 3b shows the data points together with the calculated behaviour for a Förster radius of 3.6 nm (solid line, best fit) as well as 3.0 and 5.0 nm (dashed lines).

Charge transfer between the compounds therefore seems unlikely, because an overlap of the wavefunctions is required [16]; calculations show that in a model system of two conjugated polymers only at donor-acceptor distances much less than 1 nm efficient charge transfer can be expected [17].

Figure 4a shows the incident photon to electron conversion efficiency (IPCE) versus the wavelength of the incident light of a ZnPc photodiode with (solid line) and without (dashed line) nanocrystals deposited into the ZnPc layer normalized to the peak efficiency at 635 nm. The introduction of the nanoparticles into the active layer of the photodiode shows a distinst sensitization of the photocurrent generation in the spetral range of low ZnPc absorption around 500 nm. Above 580 nm, the nanoparticles do not absorb any light and the IPCE spectrum of both samples shows the same shape.

The absolute values of the IPCE shown in Fig. 4b indicate that the overall conversion efficiency is decreasing, most probably due to the hindered transport in the ZnPc film with interspersed nanocrystals. Around 500 nm though, a significant increase of the absolute quantum efficiency values can be observed due to the absorption of the nanocrystals with subsequent energy transfer to the ZnPc. The difference between the conversion spectra of photodiodes with and without nanoparticles resembles the nanoparticle excitation spectrum plotted in Fig. 1, with a decrease in the area of strong absorption in the ZnPc. There, a competition takes place between the absorption in the ZnPc and direct charge generation and the absorption in the nanoparticles and subsequent energy transfer. The second process is less efficient, as it only introduces a further step. So an enhancement of the conversion efficiency can only be expected where the absorption in the nanoparticle layer significantly exceeds the absorption in the ZnPc layer.

We investigate the photophysical interactions between zinc-phthalocyanine and CdSe/ZnS nanocrystals. Photoluminescence measurements on thin ZnPc films with and without added nanocrystals indicate that resonant energy transfer is taking place. Further quantification of the resonant energy transfer is performed by changing the thickness of the shell of organic ligands around the nanoparticles. The luminescence is quenched very efficiently even with a nearly 2 nm thick shell. This indicates long range resonant energy transfer as quenching mechanism. We conclude that for photon harvesting purposes, usual ligand shell thicknesses between 1 and 2 nm will not reduce the efficiency of the energy transfer to the matrix significantly.

ZnPc photodiodes show a significant change of the IPCE spectrum upon addition of nanocrystals into the active layer. An increase of the quantum efficiency in the range of 500 nm is observed where there is a low absorption of the ZnPc but a strong absorption of the nanoparticles. Further work will have to be put in the device design to allow the nanoscale integration of the photon harvesting structure without deterioration of the charge transport processes [18].

Acknowledgement The authors want to acknowledge financial support from the Austrian Science Foundation (FWF NFN Project S9711-N08) and the EU via the Molycell project.

References

1. Dennler G, Sariciftci NS (2005) Proc IEEE 93(8):1429
2. Tang CW, Van Slyke SA (1987) Appl Phys Lett 51(12):913
3. Tang CW (1986) Appl Phys Lett 48:183
4. Scher EC, Manna L, Alivisatos AP (2003) Philos Trans R Soc London A 361:241
5. Finlayson CE, Ginger DS, Marx E, Greenham NC (2003) Philos Trans R Soc London A 361:363
6. Sariciftci NS, Smilowitz L, Heeger AJ, Wudl F (1992) Science 258:1474
7. Förster T (1959) Discuss Faraday Soc 27:7
8. Calzaferri G, Huber S, Maas H, Minkowski C (2003) Angew Chem Int Ed 42(32):3732
9. D'Souza F, Smith PM, Zandler ME, McCarty AL, Itou M, Araki Y, Ito O (2004) J Am Chem Soc 126(25):7898
10. Neugebauer H, Loi MA, Winder C, Sariciftci NS, Cerullo G, Goulomis A, Vazquez P, Torres T (2004) Sol Engerg Mater Sol Cells 83(2/3):201
11. Das R, Kiley PJ, Segal M, Norville J, Yu AA, Wang LY, Trammell SA, Reddick LE, Kumar R, Stellacci F, Lebedev N, Schnur J, Bruce BD, Zhang SG, Baldo M (2004) Nano Lett 4(6):1079
12. Drechsel J, Mannig B, Kozlowski F, Pfeiffer M, Leo K, Hoppe H (2005) Appl Phys Lett 86(24):244102
13. Wohrle D, Meissner D (1991) Adv Mater 3:129
14. Koeppe R, Sariciftci NS, Troshin PA, Lyubovskaya RN (2005) Appl Phys Lett 87(24):244102
15. Hikmet RAM, Talapin DV, Weller H (2003) J Appl Phys 93(6):3509
16. Rice MJ, Gartstein YN (1996) Phys Rev B 53:10764
17. Wu MW, Conwell EM (1998) Chem Phys 227:11
18. Koeppe R, Bossart O, Calzaferri G, Sariciftci NS (2007) Sol Energ Mater Sol Cells 91:986

Progr Colloid Polym Sci (2008) 135: 21–28
DOI 10.1007/2882_2008_096

Published online: 30 August 2008

Erzsébet Szabó-Bárdos
Zoltán Zsilák
Ottó Horváth

Photocatalytic Degradation of Anionic Surfactant in Titanium Dioxide Suspension

Erzsébet Szabó-Bárdos · Zoltán Zsilák · Ottó Horváth (✉)
Institute of Chemistry, Department of General and Inorganic Chemistry, University of Pannonia, 158, 8201 Veszprém, Hungary
e-mail: otto@vegic.uni-pannon.hu

Abstract In TiO_2-based photocatalytic degradation of an anionic detergent (lauryl benzenesulfonate) initial pH of 5.0 proved to be most appropriate for high efficiency of surfactant conversion, although lower pHs were more favorable for the adsorption on the surface of the catalyst. A catalyst concentration of 1 g dm^{-3} was optimum for the mineralization of this pollutant. After decreasing the surfactant concentration below the limit of foaming in a closed photoreactor utilizing H_2O_2 as electron acceptor, total mineralization of the pollutant could be achieved by a longer-time irradiation in a second, air-bubbled reactor. The activity of the photocatalyst proved to be constant even after several reusages. The temperature increase promoted the photoassisted degradation of the anionic detergent in the range of 20–50 °C measured in a home-built pilot equipment. The progress of mineralization became faster only after the conversion of surfactant reached 80–85%. There was found an optimum concentration of the oxidizer, H_2O_2, above which the efficiency of degradation could not be significantly enhanced.

Keywords Detergent · Mineralization · Photocatalysis · Titanium dioxide · Wastewater treatment

Introduction

A significant part of the man-made pollutants getting into our natural environment is toxic and/or biologically nondegradable. Some of these materials upset the balance of the biosphere in the soils and natural waters, or spoil the resources of drinking water [1]. Generally, microorganisms relatively fast destroy natural, organic materials, with rather few exceptions. The situation, however, is quite different in the case of numerous synthetic organic compounds. Besides, also organic pollutants of natural origin (such as proteins) may cause serious environmental problems if their concentration is too high to be degraded in wastewater plants within a reasonable period of time.

Photocatalytic methods have been proved to offer efficient solutions for treatment of waters contaminated with organic and inorganic pollutants [2–7]. For example, a variety of pesticides can be completely mineralized by photocatalytic procedures [8]. One of the most promising type of these procedures is based on photoactive semiconductors. The most frequently applied semiconducting material for photocatalytic purposes is titanium dioxide [9–13]. The combination of the TiO_2-based photocatalysis with sonolysis proved to be a promising technique too for mineralization of organic pollutants [14]. TiO_2-mediated photodegradation was also applied for decomposition of various amino acids [15–17]. Similarly, oil spills could be successfully treated by photoassisted oxidation utilizing titanium dioxide and solar energy [18].

Several detergents belong to the pollutants of our environment because of their industrial and domestic use. Although these compounds are not directly toxic, they hinder both the dissolution of atmospheric oxygen into natural waters and the sedimentation of floating particles. In alkylsulfonic acids a sulfonate group serves as the hydrophilic part. Until the early 1960s, alkyl benzene sulphonates

were the most common surfactants used. Since these compounds were, however, very slowly biodegradable, due to their branched-chain structure, they were replaced by linear alkyl sulfonates [19].

TiO_2-mediated photocatalysis proved to be an efficient and simple method also for surfactant decontamination [20–26]. In this work we have studied the TiO_2-based photoassisted degradation of lauryl benzenesulfonate (LAS, as a linear alkyl sulfonate) in both laboratory-scale reactors and a pilot equipment. The effects of pH, catalyst and oxidizer concentrations on the efficiency of decomposition were investigated. The reusage of the catalyst was also realized.

Experimental Sections

Materials

The titanium dioxide sample used in all experiments was Degussa P25 (70% anatase, 30% rutile; with a surface area of $50\,m^2\,g^{-1}$). The initial pH of the reaction mixture was adjusted using H_2SO_4 and NaOH of pure reagent grade. Sodium lauryl benzenesulfonate (LAS) of same purity was purchased from Aldrich. The other materials, such as methylene blue or chloroform were also reagent grade. H_2O_2 as an oxidizer was introduced into the reaction mixtures from 30% stock solution. The high purity water used in the experiments was double distilled and then purified with the Milli-Q system.

Photoreactors and Photocatalytic Experiments

Photochemical experiments were performed using both laboratory-scale reactors with $3\,dm^3$ effective volume and a 200-dm^3 reactor in a pilot equipment (all were home-built). In one of the laboratory-scale reactors, the heterogeneous reaction mixture (TiO_2 suspension) was circulated by continuously fed air with a flow rate of $40\,dm^3\,h^{-1}$ and described in a previous paper [10]. Beside stirring, air also served as electron acceptor (i.e., oxidizer) as well. The photon flux of the internal light source (40 W, $\lambda_{max} = 350$ nm) was determined by tris(oxalato)ferrate(III) chemical actinometer. It was estimated to be 1.45×10^{-5} einstein s^{-1}.

In the first stage of photocatalytic degradation of surfactants, however, air-bubbling cannot be used for introducing oxygen as electron acceptor in this system because of the strong foaming. Instead, addition of hydrogen peroxide was applied for this purpose in another, closed 3-dm^3 reactor, in which reaction mixture was circulated by a liquid pump.

For larger-scale experiments, a 200-dm^3 closed, thermostated reactor was used, as a part of a home-developed pilot equipment containing a 3-stage reactor cascade (1 pumped and 2 air-bubbled reactors) [27]. In such a reactor, 31 light tubes with emission properties similar to those of the light source in the laboratory-scale reactors were applied for irradiation. Hydrogen peroxide solution (30%) was continuously introduced with an appropriate liquid pump of variable rate.

Analytical Procedures

For analyses, $4\,cm^3$ samples were taken from the reactors through a septum with a syringe. The solid phase of samples, when necessary, was separated by centrifugation and subsequent filtration using Millipore Millex-LCR PTFE 0.45 μm.

The concentration of lauryl benzenesulfonate was photometrically determined. $0.2\,cm^3$ of the sample was diluted by distilled water up to $100\,cm^3$. $25\,cm^3$ were added to the diluted sample from the following solution. $30\,cm^3$ of a $1\,g\,dm^{-3}$ methylene blue aqueous solution, $6.8\,cm^3$ cc H_2SO_4 and 50 g $Na_2HPO_4 \cdot H_2O$ were mixed and diluted by distilled water to $1\,dm^3$. $10\,cm^3$ chloroform was also added to this mixture. Methylene blue and lauryl benzenesulfonate form a complex, which dissolves in chloroform (organic phase). After the extraction, the absorbance of the organic phase was measured at 652 nm in a 0.5-cm quartz cell.

The absorption spectra were recorded on a Specord S 100 diode array spectrophotometer, using 1-cm quartz cuvettes. Mineralization was followed by measuring the total organic carbon (TOC) concentration, utilizing a Thermo Electron Corporation TOC TN 1200 apparatus. Chemical oxygen demand (COD) was determined by dichromate method.

Results and Discussion

Adsorption of Anionic Detergent on the Surface of TiO_2 Catalyst

Earlier results clearly indicated that adsorption of the substrate on the surface of the catalyst is one of the crucial properties detetermining the efficiency of the photoassisted degradation [28, 29]. The surfactant to be degraded is negatively charged, hence its adsorption on the catalyst particulates may significantly depend on the pH affecting their surface charge. The pH_{zpc} for TiO_2 is about 6.5 (for anatase [30]). Above this value the surface of the catalyst is negatively charged, which hinders the adsorption of the anionic detergent. On the other hand, lower pH values may considerably promote the adsorption of these species on the oppositely charged surface of TiO_2 particulates as Fig. 1 unambiguously demonstrates. The adsorption % vs. pH plot shows a monotonous decrease from 33.8% at $pH = 2$ down to 4.2% at $pH = 10$. According to this observation, lower values of pH (i.e., acidic condition) are favorable for the adsorption and, thus, for the degradation of anionic surfactants. However, other factors in the photocatalytic system may also pH dependent, besides, the cost

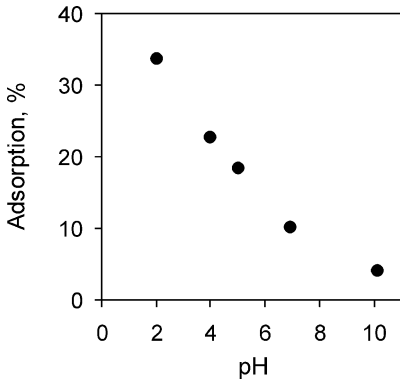

Fig. 1 The pH effect on the adsorption of lauryl benzenesulfonate on TiO_2 particulates in aqueous suspension (1 g dm^{-3} TiO_2, 300 mg dm^{-3} LAS)

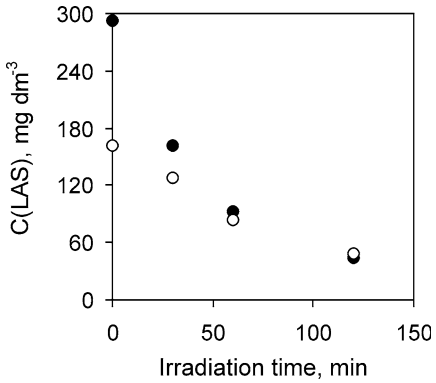

Fig. 2 The change of the surfactant concentration during the irradiation of the TiO_2 suspension, measured with (○) and without (●) removal of the colloidal catalyst (pH = 2.5, 1 g dm^{-3} TiO_2, 300 mg dm^{-3} LAS)

of the adjustment of the initial pH should be taken into consideration too.

The time factor may also play a significant role in the case of adsorption, i.e., how fast can be reached the adsorption equilibrium in this system under continuous stirring. As our experimental results showed, the equilibrium state in this system was reached within 20 min. This observation suggests that the system during the longer-time irradiation is always close to equilibrium in the respect of adsorption, which is favorable for the degradation of the surfactant.

Photoassisted Degradation of the Anionic Surfactant

Experiments at Lower Concentration of Surfactant. In order to follow the progress of the conversion of the detergent during the irradiatiation, a spectrophotometric method was utilized after an extraction step. A comparison was made for studying how the adsorption affects the results of this analysis. The samples taken during the photolysis were divided into two parts. One part was extracted after removal of the TiO_2 catalyst by centrifugation and filtration, while in the case of the other part directly the suspension was treated by extraction. Thus, in the previous case, the concentration of the unconverted detergent was lower by the amount of the tensid adsorbed. As Fig. 2 indicates, at higher concentrations of the detergent, especially in the beginning of the irradiation, the difference between the results of the two methods is very significant. Later on, however, at concentrations less than 50 mg dm^{-3}, this deviation is negligible, even at pH = 2.5. Thus, below this concentration value removal of the colloidal catalyst is superfluous during the preparation of the samples.

During the preliminary experiments, at pH = 2.5 300 mg dm^{-3} surfactant with 1 g dm^{-3} TiO_2 was irradiated. In the beginning of the photolysis 30 cm^3 30% H_2O_2 was given to the 3-dm^3 reaction mixture, then 10–10 cm^3 in every 15-min interval (altogether 220 cm^3). As shown in Fig. 3 (plot a) after a 6-h irradiation the conversion of the detergent is almost 100% (the rest of it is 1.30 mg dm^{-3}). For sake of saving acid, it was checked on if higher pH (pH = 4.0) is enough for a similar efficiency. As Fig. 3 (plot b) indicates, also in this case the conversion is practically 100% (the rest is 1.50 mg dm^{-3}). This can be explained by the significant pH decrease during the photolysis, reaching the value of 3.0 till the end of the 6-h reaction time. The considerable pH decrease can be attributed to the formation of proton in the oxidation process

$$–CH_2– + 6h^+ + 2H_2O \longrightarrow CO_2 + 6H^+ ,$$

where –CH_2– designates one unit of the reducing hydrocarbon chain of the surfactant, while h^+ represent photogenerated hole. The effect of the decreasing pH partly compensates the moderately diminished adsorption in the initial period of the photocatalysis.

Also for sake of saving the oxidative agent, H_2O_2, another experiment was carried out at pH = 4.0. In this case no H_2O_2 was initially added. Thus, the conversion of the

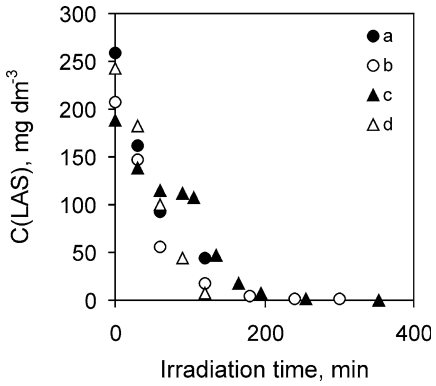

Fig. 3 The change of the surfactant concentration during the irradiation of the TiO_2 suspensions of various compositions: (a) pH = 2.5, 220 cm^3 H_2O_2; (b) pH = 4.0, 220 cm^3 H_2O_2; (c) pH = 4.0, 40 cm^3 H_2O_2; (d) pH = 5.0, 50 cm^3 H_2O_2 (1 g dm^{-3} TiO_2, 300 mg dm^{-3} LAS)

detergent significantly slowed down after 60 min. Hence, 30 cm^3 H_2O_2 was added at this point, than 10 cm^3 at the 260th minute (Fig. 3, plot c). Thus, it was managed to reach the oxidation efficiency of the previous experiment (using more H_2O_2).

In order to decrease the acid consumption, experiment was carried out also at initial pH of 5.0. A similarly good result was observed as in the case of pH = 4.0 (Fig. 3, plot d). It can be partly attributed to the gradual pH decrease during the progress of the photoassisted oxidation of the anionic detergent.

As the comparison of the experiments at different pH values indicates, the fastest conversion of the detergent was observed at initial pH of 5.0. Thus, in the following experiments 5.0 was adjusted as initial pH in the system (for saving acid).

Experiments at Higher Concentration of Surfactant. Since in industrial wastewaters anionic surfactants can exist also at higher concentrations, experiments with solutions of 1.2 g dm^{-3} lauryl benzenesulfonate were also carried out. In the first series of this type, initially 30 cm^3 30% H_2O_2 was added, then at the 120th and 250th minutes additional 10–10 cm^3.

As Fig. 4 shows, the photoassisted oxidation proved to be efficient in this case too. After 300-min irradiation the conversion was 98%, giving a rest of 20.9 mg dm^{-3} detergent. In the reaction mixture, initially the foaming was extremely strong, while after 4 h, it became almost negligible, giving a visual manifestation of the progress of degradation.

At higher detergent concentration (1 g dm^{-3}) it was reasonable to study if an increase in the concentration of the TiO_2 photocatalyst accelerates the degradation. According to the data of Fig. 5, neither 2 g dm^{-3} nor 5 g dm^{-3} TiO_2 concentration gave better results than 1 g dm^{-3}. In the later case H_2O_2 was only added in the

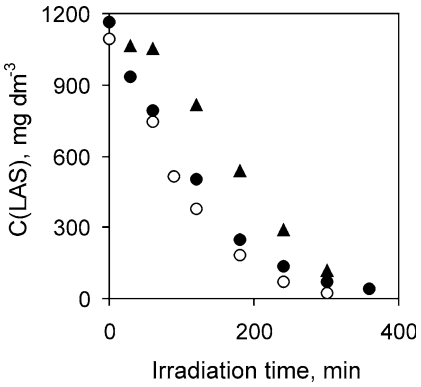

Fig. 5 The change of the surfactant concentration during the irradiation of the TiO_2 suspensions at different catalyst concentrations: (○) 1 g dm^{-3}, (●) 2 g dm^{-3}, (▲) 5 g dm^{-3} (pH = 5.0, 1 g dm^{-3} LAS, 50 cm^3 H_2O_2)

75th minute, clearly indicating that the initial lack of H_2O_2 significantly hinders the reaction.

In the case of 1 g dm^{-3} TiO_2 concentration, the effect of a decrease in the amount of H_2O_2 added was also studied. Instead of addition of 30 + 10 + 10 cm^3 H_2O_2 15 + 5 + 5 cm^3 H_2O_2, were added. It was observed that for the same conversion 2 h longer irradation was necessary than with the bigger amount of H_2O_2 added. (Fig. 6). The spectral change in this case, after removal of the colloidal catalyst, clearly demonstrates the progress of the detergent conversion (Fig. 7). A characteristic bands gradually disappeared, and the featureless spectrum of the very simple intermediates of the mineralization remained.

A more concentrated sample with 2.2 g dm^{-3} surfactant was also treated photocatalytically. In this case, a longer irradiation time (8–9 h) and more added oxidant (H_2O_2, 0.15 mol dm^{-3} total concentration) was necessary to cease the foaming in this system. Continuing the irradiation of the same reaction mixture (involving the totally

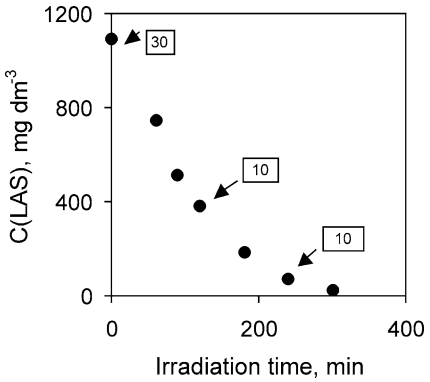

Fig. 4 The change of the surfactant concentration during the irradiation of the TiO_2 suspension (pH = 5.0, 1 g dm^{-3} TiO_2, 1 g dm^{-3} LAS, 50 cm^3 H_2O_2, volume (in cm^3) of addition is indicated in *squares*)

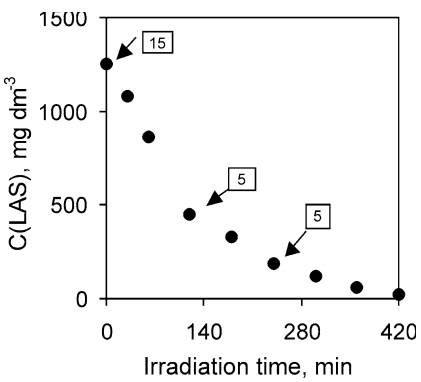

Fig. 6 The change of the surfactant concentration during the irradiation of the TiO_2 suspension (pH = 5.0, 1 g dm^{-3} TiO_2, 1 g dm^{-3} LAS, 25 cm^3 H_2O_2, time and volume (in cm^3) of addition is indicated in *squares*)

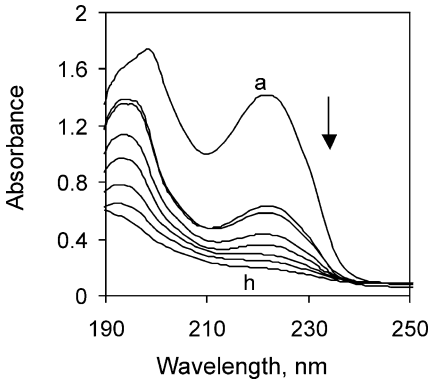

Fig. 7 Spectral change during the irradiation of the TiO_2 suspension (pH = 5.0, 1 g dm^{-3} TiO_2, 1 g dm^{-3} LAS, 25 cm^3 H_2O_2) from 0 min (a) to 420 min (h)

converted detergent), after its transfer into the air-bubbled reactor (i.e., in reactor 2), also the value of chemical oxygen demand (COD) decreased further, indicating the progress of mineralization of the pollutant. In Fig. 8 it is unambiguously seen that in spite of the total conversion of the detergent the COD value was still high even after a 8–9-h irradiation in the second reactor. Thus, for further decrease of COD, a longer photoassisted treatment of the pollutant was necessary in the air-bubbled reactor.

It can be established that even at relatively high concentration, the pollutant (surfactant) can be degraded in two reactors. In the first (closed) one, where the circulation of the reaction mixure is realized by a liquid pump, using H_2O_2 as electron acceptor, the concentration of the rest of the surfactant can be diminished below the limit of foaming (ca. 1 mg dm^{-3}), making the application of air-bubbled reactor possible. In the next stage, in the second reactor, air is used for both continuous stirring and as oxidant.

Reusage of the TiO_2 Catalyst

In the previous experiments in each case fresh (unused) TiO_2 catalyst was applied. After the irradiations, the suspended catalyst was removed by sedimentation and filtration. For decreasing the cost of the TiO_2 consumption and for enviromental protection, it was also studied how efficiently can function the already used catalyst in another photoassisted treatment of the detergent. (If a two stage experiment was carried out, the suspension was directly transferred into the second reactor, without changing the catalyst.)

For this experiment, as a comparison, a concentrated sample of surfactant was used. The conditions were practically the same as in the previous experiments. As Fig. 9 shows, neither the previous usage of the catalyst nor the decrease of the amount of oxidant added diminished significantly the efficiency of the conversion of the anionic detergent. The rate of the conversion in the first reactor, however, was higher (but less than 10%), probably due to the more peroxide added, at the end of the total irradiation period (7–9 h) the extents of the degradation were the same.

Experiments in Pilot Equipment

On the basis of the results regarding the 3-dm^3 laboratory scale reactor, a pilot equipment containing a 3-stage thermostated photocatalytic reactor cascade was built. Each reactor has an effective volume of 200 dm^3, the irradition of which serve 31 pieces of 40 W light tubes with the emission maximum at 350 nm. Similary to the laboratory scale reactors, in the first reactor the TiO_2 suspension is circulated by a liquid pump and H_2O_2 is the only oxidizer is the system. The further experiments were carried out in this reactor.

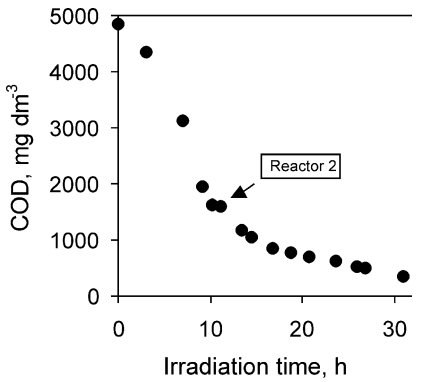

Fig. 8 The change of the chemical oxygen demand (COD) in the TiO_2 suspension (pH = 5.0, 1 g dm^{-3} TiO_2, 2.2 g dm^{-3} LAS, 0.15 M H_2O_2) irradiated in both the closed and the air-bubbled (indicated in the *square*) reactor

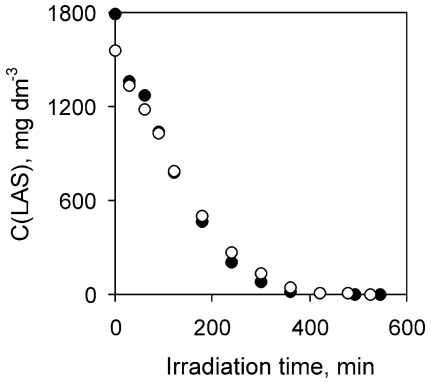

Fig. 9 The change of the surfactant concentration during the irradiation of the TiO_2 suspension (pH = 5.0, 1 g dm^{-3} TiO_2, 1.6 g dm^{-3} LAS): (●) with fresh catalyst and 80 cm^3 H_2O_2, (○) with reused catalyst and 50 cm^3 H_2O_2

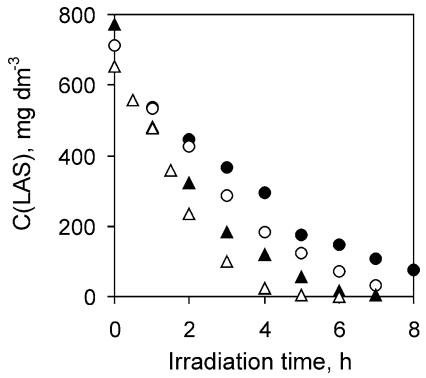

Fig. 10 The effect of temperature on the change of the surfactant concentration during the irradiation of the TiO_2 suspension in the pilot equipment (pH = 5.0, 1 g dm^{-3} TiO_2, 1 g dm^{-3} LAS, 227 cm^3 h^{-1} H_2O_2): (●) 20 °C, (○) 30 °C, (▲) 40 °C, (△) 50 °C

Temperature Effect. The effect of the temperature on the efficiency of the detergent degradation was studied in this system. The range of 20–50 °C was chosen, taking the economic technological possibilities (low-cost cooling or heating) into consideration. As it could be expected, increasing the temperature, the conversion rate was enhanced (Fig. 10). At 50 °C, within a 5-h irradiation time, total conversion of the surfactant took place, while at 20 °C not even an 8-h period of experiment was enough. Of course, the progress of mineralization (the decrease of TOC) is much slower than the conversion of the surfactant, but the tendency regarding the temperature effect is the same (Fig. 11). On the basic of these observations, 40 °C was chosen for technological purpose, and thus, for the further experiments.

It can also be seen that an intense decrease of TOC begins only above 80–85% conversion of surfactant. This indicates that in the first stage of the mechanism of the degradation the oxidation ceases the surface active property of this pollutant, either removing the hydrophylic sulfonate "head" at the detergent or the hydrophobic "tail" is converted to be polar. According to our independent experiments with similar surfactants, desulfonation is the predominant step in the first period of degradation, followed by the oxidation and cleavage of the longer hydrocarbon tails.

H_2O_2 Effect. Also in this case the optimum amount of H_2O_2 to be added was determined. Similarly to the observation with the laboratory-scale experiments, there is no mean increasing the oxidizer concentration above a certain limit, because it results in no further increase in the degradation efficiency, or the enhancement reached in this concentration range is not cost-effective any more. As Fig. 12 shows, the highest rate of peroxide addition (796 cm^3 h^{-1}) practically did not increase the conversion efficiency any more compared to the effect of the lower rate the value of which (378 cm^3 h^{-1}) is less than half of the highest one applied. However, at lower values of rate the decrease in the conversion efficiency is significant.

A somewhat different observation was made regarding the TOC decrease in the same range of rate of H_2O_2 addition (Fig. 13). Since generally the progress of mineralization becomes stronger after the conversion of most of the detergents, the effect of the oxidizer concentration can only be experienced after 5–6 h of irradiation. Deviating from this tendency, at the highest rate after one hour reaction time a significant (and close to linear) progress of mineralization can be observed.

However, above 5 h even at lower rate (378 cm^3 h^{-1}) a faster TOC decrease begins. This phenomenon confirms that application of lower concentration of H_2O_2 is enough for an efficient degradation.

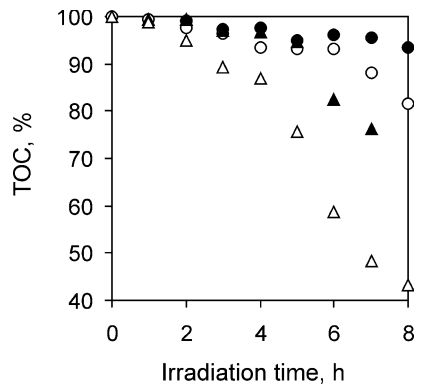

Fig. 11 The effect of temperature on the change of TOC during the irradiation of the TiO_2 suspension in the pilot equipment (pH = 5.0, 1 g dm^{-3} TiO_2, 1 g dm^{-3} LAS, 227 cm^3 h^{-1} H_2O_2): (●) 20 °C, (○) 30 °C, (▲) 40 °C, (△) 50 °C

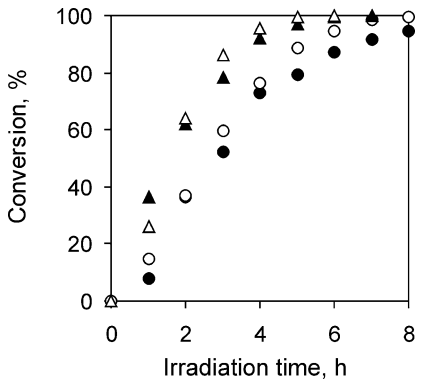

Fig. 12 The effect of the rate of H_2O_2 addition on the change of the surfactant concentration during the irradiation of the TiO_2 suspension in the pilot equipment (pH = 5.0, 1 g dm^{-3} TiO_2, 1 g dm^{-3} LAS): (●) 98.6 cm^3 h^{-1}, (○) 227 cm^3 h^{-1}, (▲) 378 cm^3 h^{-1}, (△) 796 cm^3 h^{-1}

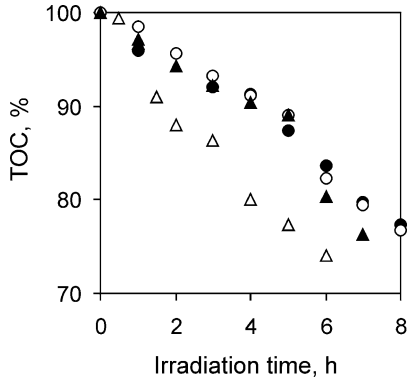

Fig. 13 The effect of the rate of H_2O_2 addition on the change of TOC during the irradiation of the TiO_2 suspension in the pilot equipment (pH = 5.0, 1 g dm^{-3} TiO_2, 1 g dm^{-3} LAS): (●) 98.6 cm^3 h^{-1}, (○) 227 cm^3 h^{-1}, (▲) 378 cm^3 h^{-1}, (△) 796 cm^3 h^{-1}

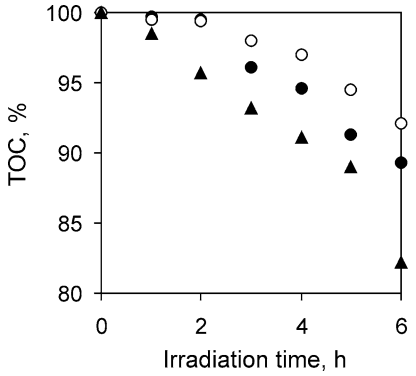

Fig. 14 The effect of the catalyst concentration on the change of TOC during the irradiation of the TiO_2 suspension in the pilot equipment (pH = 5.0, 1 g dm^{-3} TiO_2, 1 g dm^{-3} LAS, 227 cm^3 h^{-1} H_2O_2): (●) 0.5 g dm^{-3}, (▲) 1.0 g dm^{-3}, (○) 2.0 g dm^{-3}

TiO_2 Effect. Also in the pilot equipment was the effect of the photocatalyst concentration on the degradation efficiency studied. Somewhat deviating from the case of the laboratory-scale reactor, in the pilot equipment the detergent conversion did not depend on the TiO_2 concentration, although in a narrower range of 0.5–2.0 g dm^{-3}. In the 200-dm^3 reactor also the effect on the TOC decrease was measured. In this respect, i.e., regarding the progress of mineralization, however, the TiO_2 concentration of 1 g dm^{-3} gave unambiguously the best results (Fig. 14), in accordance with the previous observations in other systems [28].

Conclusion

An anionic detergent (lauryl benzenesulfonate) was successfully degraded by TiO_2-based photocatalytic method. Although low pH (2.0) proved to be most favorable for the adsorption on the surface of the catalyst particulates, initial pH of 5.0 was found to be appropriate because the photoassisted redox reactions gradually decrease pH during the irradiation, and the adsorption equilibrium is reached relatively fast. On the other hand, at pH = 5.0 was the highest effiency of the detergent conversion.

A catalyst concentration of 1 g dm^{-3} proved to be most favorable even at higher concentration of surfactant from the viewpoints of both the conversion and the mineralization (TOC decrease). After the concentration of the rest of surfactant has been decreased below the limit of foaming, air can be used for homogenizing the reaction mixture and as oxidizer as well. Total mineralization of the pollutants can be reached by a longer-time irradiation in air-bubbled reactor. It has been proved that previously used photocatalyst can be recycled, i.e., it provided as good efficiency as the freshly used one did. The temperature effect measured in the pilot system clearly indicated that, as expected, the photoassisted degradation of the anionic detergent is faster at higher temperature in the range of 20–50 °C. The progress of mineralization begins to be stronger only after the conversion of surfactant has reached 80–85%. There is an optimum concentration of the H_2O_2 electron acceptor, above which there is no further significant enhancement in the efficiency of degradation. Experiments are in progress for optimizing the whole procedure of degradation at industrial scale.

Acknowledgement Supports of this work by Henkel Hungary Ltd and LightTech Lamp Technology Ltd are gratefully acknowledged.

References

1. Manahan SE (2000) Fundamentals of Environmental Chemistry. Lewis Publishers, Boca Raton, pp 721–758
2. Horváth O, Huszánk R (2003) Photochem Photobiol Sci 2:960
3. Kanki T, Yoneda H, Sano N, Toyoda A, Nagai C (2004) Chem Eng J 97:77
4. Kajitvichyanukul P, Ananpattarachai J, Pongpom S (2005) Sci Technol Adv Mater 6:344
5. Kajitvichyanukul P, Ananpattarachai J, Pongpom S (2005) Sci Technol Adv Mater 6:352
6. Horváth O, Bodnár E, Hegyi J (2005) Colloids Surf A 265:135
7. Gkika E, Troupis A, Hiskia A, Papaconstantinou E (2006) Appl Catal B 62:28
8. Devipriya S, Yesodharan S (2005) Sol Energ Mater Sol Cells 86:309
9. Fujishima A, Rao TN, Tryk DA (2000) J Photochem Photobiol A 1:1
10. Szabó-Bárdos E, Czili H, Horváth A (2003) J Photochem Photobiol A 154:195
11. Szabó-Bárdos E, Czili H, Megyery-Balog K, Horváth A (2004) Progr Colloid Polym Sci 125:42
12. Fabbri D, Bianco Prevot A, Pramauro E (2006) Appl Catal B 62:21

13. Patsoura A, Kondarides DI, Verykios EX (2007) Catal Today 124:94
14. Peller J, Wiest O, Kamat PV (2004) J Phys Chem 108:10925
15. Hidaka H, Hirokoshi S, Ajisaka K, Zhao J, Serpone N (1997) J Photochem Photobiol A 108:197
16. Matsushita M, Tran TH, Nosaka AY, Nosaka Y (2006) Catal Today 120:240
17. Szabó-Bárdos E, Pétervári E, El-Zein V, Horváth A (2006) J Photochem Photobiol A 184:221
18. Heller A, Brock JR (1994) Accelerated Photooxidative Dissolution of Oil Spills. In: Helz GR, Zepp RG, Crosby DG (eds) Aquatic and Surface Photochemistry. Lewis Publishers, Boca Raton, pp 427–436
19. Fellenberg G (2000) The Chemistry of Pollution. Wiley, Chichester, pp 67–99
20. Zhang R, Gao L, Zhang Q (2004) Chemosphere 54:405
21. Lizama C, Bravo C, Caneo C, Ollino M (2005) Environ Technol 26:909
22. Kimura T, Yoshikawa N, Matsumura N, Kawase Y (2004) J Environ Sci Health A 39:2867
23. Zhang H, Quan X, Chen S, Zhao H, Zhao Y (2006) Appl Surf Sci 252:8598
24. Zhang T, Oyama T, Horikoshi S, Zhao J, Serpone N, Hidaka H (2003) Appl Catal B 42:13
25. Hegyi J, Horváth O (2004) Progr Colloid Polym Sci 125:10
26. Lea J, Adesina AA (1998) J Photochem Photobiol A 118:111
27. Horváth O, Zsilák Z, Szabó-Bárdos E (2007) Photocatalytic degradation of surfactants in reactors for wastewater treatment. In: XXIIIth International Conference on Photochemistry, Cologne, 29 July–3 August, Book of Abstracts, P272, p 517
28. Bahnemann D (1999) Photocatalytic Detoxification of Polluted Waters. In: Boule P (ed) The Handbook of Environmental Chemistry, vol 2 part L Environmental Photochemistry. Springer, Berlin, Heidelberg, New York, pp 285–351
29. Horváth O, Hegyi J (2001) Progr Colloid Polym Sci 117:211
30. Sun B, Reddy EP, Smirniotis PG (2005) Environ Sci Technol 39:6251

Progr Colloid Polym Sci (2008) 135: 29–37
DOI 10.1007/2882_2008_111

Published online: 9 September 2008

A. Hajdú
E. Tombácz
E. Illés
D. Bica
L. Vékás

Magnetite Nanoparticles Stabilized Under Physiological Conditions for Biomedical Application

A. Hajdú · E. Tombácz (✉) · E. Illés
Department of Colloid Chemistry,
University of Szeged, Aradi Vt. 1,
6720 Szeged, Hungary
e-mail: tombacz@chem.u-szeged.hu

D. Bica · L. Vékás
Center of Fundamental and Advanced
Technical Research, Romanian
Academy-Timisoara Division, Romania

Abstract The biomedical application of water based magnetic fluids (MFs) is of great practical importance. Their colloidal stability under physiological conditions (blood pH ∼ 7.2–7.4 and salt concentration ∼ 0.15 M) and more in high magnetic field gradient is crucial. Magnetite or maghemite nanoparticles are used in general. In the present work, magnetite nanoparticles were stabilized with different compounds (citric acid (CA) and phosphate) and sodium oleate (NaO) as the most used surfactant in the stabilization of MFs. The adsorption and overcharging effect were quantified, and the enhancement in salt tolerance of stabilized systems was studied. Adsorption, electrophoretic mobility and dynamic light scattering (DLS) measurements were performed. The electrolyte tolerance was tested in coagulation kinetic measurements. Above the adsorption saturation, the nanoparticles are stabilized in a way of combined steric and electrostatic effects. The aim was to research these two important effects and demonstrate that none of them alone is enough. The phosphate was not able to stabilize the ferrofluid in spite of our expectation, but the other two additives proved to be effective stabilizing agents. The magnetite was well stabilized by the surface complexation of CA above pH ∼ 5, however, the salt tolerance of citrate stabilized MFs remained much below the concentration of physiological salt solution, and more the dissolution of magnetite nanocrystals was enhanced due to Fe-CA complexation in aqueous medium, which may cause problems in vivo. The oleate double layers were able to stabilize magnetite nanoparticles perfectly at pH ∼ 6 preventing particle aggregation effectively even in physiological salt solution.

Keywords Electrosteric stabilization · Magnetite · Surface complexation · Surfactant double layers · Water-based magnetic fluid

Introduction

Preparation of stable water based magnetic fluids (MFs) is of renewed interest nowadays due especially to biomedical applications. Many important applications in the fields of biotechnology and biomedicine, such as cell labeling and separation, magnetic resonance imaging (MRI) contrast agent [1, 2], enzyme and protein separations, targeted drug delivery, magnetic ferrofluids hyperthermia are known [3–6]. Magnetic nanoparticles are of magnetite and maghemite dominantly, because iron oxides are excreted via the liver after the treatment. Most of these applications require the magnetic nanoparticles to be non-toxic, chemically stable, uniform in size, and well-dispersed under physiological conditions. The magnetic characteristics and colloidal stability are overemphasized, since particle ag-

gregation must be excluded in magnetic field during application with the reference to the risk of blood clots in blood vessel. To fulfill the stability criterion different coatings on the surface of particles are developed to prevent their aggregation and to improve their colloidal and chemical stability. In biocompatible MFs, coatings with biocompatible molecules such as dextran, polyethylene glycol (PEG), polyvinyl alcohol (PVA) and phosopholipids, recently by dendrimers and silica have been developed, all of which have been used on iron oxide nanoparticles [7–10].

In general, colloidal stabilization of magnetic nanoparticles in aqueous medium is assigned to the surface accumulation (adsorption) of appropriate dissolved species forming the innermost layer on particle surface due to either i) physical interaction (e.g. ions by Coulombic attraction, non-ionic polymers (PEG, PVA, dextran) and surfactants (Pluronics) by van der Waals forces) or ii) chemical interaction, i.e., chemical bond formation on active sites of surface such as surface complexation, e.g. –COOH groups (of fatty acids, citric acid or polyacrylic acid (PAA)) on ≡FeOH sites. In several cases, a second layer has to be built to enhance colloidal stability in general, but especially in biomedical applications, to provide biocompatibility by inert coating (e.g. PEG, PEO) or to functionalize magnetic particles for specific interactions with antibodies. The second layer formation may take place due to either i) physical such as hydrophobic interactions (e.g. fatty acid double layers) or ii) chemical, profoundly covalent binding (e.g. streptavidin, protein A).

A variety of complexants seems to be appropriate stabilizers of magnetite/maghemite particles in aqueous medium. However, significant change in the pH dependent stability of magnetic fluids occurs, if different ligands like hydroxyl or thiol polycarboxilic acids (e.g. tartaric, gluconic, dimercaptosuccinic acids) and arginine hydroxamate are used. Only tartaric and dimercaptosuccinic acids stabilized MFs showed high resistance against pH above pH ~ 4 [11].

Earlier studies from Matijevic's group [12, 13] have shown that oxalic and citric acids bind to the iron oxide (hematite) surface through chemisorption, which is highly pH dependent. It was inferred from zeta potential measurements that citric acid is bound either as a bidentate or a tridentate surface complex. The latter is not likely to form for simply geometric reason. It was assumed in a recent paper [14] that citric acid may be adsorbed on the surface of magnetite nanoparticles by coordinating ≡FeOH sites via one or two of the carboxylate functionalities depending on the steric necessity and the curvature of the surface. Citric acid (CA) is one of the widely accepted stabilizing agent in water based magnetic fluids. CA can prevent the aggregation of magnetic particles effectively owning to the steric and electrostatic repulsive barrier of the ionized layer of citrate coating on magnetite or maghemite [14–19].

Surfactants are often used to disperse nanoparticles entirely in an appropriate medium. Coating of single-domain magnetic particles, usually magnetite/maghemite, with a single or double layers of surfactants in non-polar or polar mostly water carriers, respectively, results in magnetic fluids or may be called as surfacted ferrofluids [20]. The formation of first layer is specific, often involves chemical bonds, Coulombic attraction, so it depends on the quality and density of active sites on the surface of particles (e.g. ≡FeOH on magnetite, 5–10 sites/nm^2 [21]) and chemical composition of polar head group (e.g. –COOH in fatty acids). The second layer forms on the hydrophobic shell of oriented surfactant molecules via hydrophobic interaction. The surfactant double layer coated particles are hydrophilic, and their surface charge character is determined by the quality of polar head group in the second surfactant layer. For example, pH-dependent negative charges exist due to dissociation of bound groups, $S-COOH \rightleftharpoons S-COO^- + H^+$ ($pK \sim 4$) in a fatty acid second layer. Coating of particle surface can effectively prevent the adhesion of colliding particles during thermal motion. Covering particles with adsorption layer usually results in enhanced resistance against the particle aggregation. In aqueous medium, electrostatic, steric and combined stabilization layers can develop [22]. The thicker coating such as the double surfactant layers provides better stability, especially in the case of magnetic fluids, since the spacing (typically 2–3 nm) between magnetic domains is important, if magnetic field is applied [23].

While colloidal stability of MFs, especially that focusing on particle aggregation in strong magnetic field has been studied extensively, less attention was paid to the adsorption of different stabilizers, the charge neutralization and re- or overcharging of the surface of magnetite nanoparticles. The effect of MF dilution and the common parameters in aqueous solutions such as pH and salt concentration have also remained in the background, although these are the most important factors in biomedical application. In this work, based on our previous experiences on the colloidal stability, surface and charge characterization, as well as their modification in different systems [24, 25], we attempted to clear up some basic questions studying on citrate and phosphate monolayer and oleate double layer stabilized magnetite nanoparticles in details.

Experimental

Materials

Co-precipitation method was used to prepare superparamagnetic magnetite with particle size below 10 nm. The most common surfactant the sodium oleate (NaO) and the well-known complexants (citric acid (CA) and phosphate) were used for coating magnetite nanoparticles with double or single layers in order to be dispersed in water. The details of preparation and the characterization of magnetite itself and the surfacted nanofluids can be found in the papers published before [24, 26–28].

All experiments were performed at room temperature (25 ± 1 °C). All reagents were of analytical grade product apart from the technical grade surfactants and Milli-Q water was used.

Methods

Adsorption. The adsorption data for different stabilizers were determined by batch method at pH $\sim$ 6. The magnetite suspensions (the solid/liquid ratio was 1 g/l) were equilibrated with the series of oleate solutions up to 3 mmol/l concentration in closed test tubes for 24 h, at room temperature. The NaCl concentration was kept constant at 0.01 M. The pH was adjusted to 6 ± 0.1 by adding small portions of either NaOH or HCl solutions and checked after adsorption time for 24 h, as well. The equilibrium concentration of oleate was determined by measuring the absorbance of supernatants at appropriate wavelength after perfect separation of the solid particles by centrifuging at 13 000 rpm for 1 h and using a permanent magnet completed with a membrane filtration (0.22 μm MILLEX-GP) at higher oleate concentrations. The adsorption isotherm of citric acid was determined at pH $\sim$ 6, where both acidic form and dissociated citrate exist. The conditions above were adopted for the CA experiments.

Electrophoretic Mobility – Laser Doppler Electrophoresis. Electrophoretic mobilities of the pure magnetite samples and that containing different stabilizers were measured at 25 ± 0.1 °C in a disposable zeta cell (DTS 1060) of NanoZS (Malvern, UK) apparatus. The setting of the instrument was checked by measuring a standard latex sample with the zeta potential of -55 ± 5 mV. To obtain the optimal condition for measurements, the intensity of scattered light has to be at a medium level ($\sim 10^5$ counts per seconds). Therefore, the dilution series of pure magnetite sol were tested prior to the detailed studies on the effects of pH and stabilizer loading on the electrophoretic mobility of magnetite nanoparticles. According to this preliminary measurement, the optimal condition was reached at 0.05 g/l magnetite content. The pH was adjusted in the range of about 4 to 10 by HCl or NaOH solutions, and after waiting an hour to reach equilibrium, it was measured directly before introducing the samples into the zeta cell. The effect of the increasing loading of different stabilizers on magnetite sols was measured up to reaching high overcharging.

Particle Sizing and Aggregation – Dynamic Light Scattering (DLS). The pH-dependence of particle size and aggregation was measured in pure magnetite sols and in the presence of different stabilizers. Dilute sols (0.05 g/l magnetite, 0.01 M NaCl) were measured in the range of pH 4 to 10. The effect of oleate and citrate loadings over broad range from 0.1 to 2 mmol/g was investigated. The Z average sizes calculated from 3rd order cumulant fits of the measured correlation functions at a given kinetic stage (measured 50 s after the ultrasonication) are presented. The salt tolerance of magnetite nanoparticles coated by different stabilizers was tested in coagulation kinetic measurements by using Zetasizer 4 (Malvern, UK) apparatus. NaCl concentration was changed gradually from 0.01 to 0.4 M at pH $\sim$ 6. The optimal measuring condition was reached at 0.0025 g/l magnetite content. DLS method was used to follow the size evolution of aggregates in time. In a typical experiment, the data were accumulated for an hour with a time resolution of 2 min.

Results and Discussion

pH-Dependent Surface Charging of Magnetite

Magnetite is an amphoteric solid, which can develop charges in the protonation ($\equiv\mathrm{FeOH} + \mathrm{H}^+ \rightleftharpoons \equiv\mathrm{FeOH_2}^+$) and deprotonation ($\equiv\mathrm{FeOH} \rightleftharpoons \equiv\mathrm{FeO}^- + \mathrm{H}^+$) reactions of $\equiv$FeOH sites on surface. These surface reactions can be interpreted as specific adsorption of H^+- and OH^--ions at hydrated solid/water interface. The net proton surface excess amount ($\Delta n^\sigma = n^\sigma_{\mathrm{H}^+} - n^\sigma_{\mathrm{OH}^-}$), which is proportional to the surface charge density ($\sigma_{0,\mathrm{H}} = F\Delta n^\sigma / a^\mathrm{S}$, F Faraday constant, a^S specific surface area) is experimentally accessible from potentiometric acid–base titration of oxide suspensions [29–31]. The point of zero charge (PZC) could be determined as the intersection point of the Δn^σ vs. pH curves at different ionic strengths, since it coincides with $n^\sigma_{\mathrm{H}^+} = n^\sigma_{\mathrm{OH}^-}$, where surface charge density is also zero $\sigma_{0,\mathrm{H}} = 0$. Several experimental data of PZC for iron oxides are available in the literature, the values fall between 3.8 and 9.9 for magnetite [21, 31, 32]. The pH-dependent surface charging of magnetite used in this work has been characterized [28, 33], and both the intersection point of experimental curves and the surface complexation modeling resulted in a PZC at pH 7.9 ± 0.1. In the absence of specific adsorbing ions like citrate, phosphate and carboxylate anions in the present work, the pure oxide surface is positively charged at pHs lower than the PZC, while it has negative charges above it. The net surface proton excess amounts varied from +0.3–0.1 mmol/g measured at pH $\sim$ 4 to −0.1–0.15 mmol/g at pH $\sim$ 10 in 1 to 0.01 M NaCl solutions, and hence the surface charge densities also ranged over the same values (from +0.3–0.1 C/m^2 at pH $\sim$ 4 to −0.1–0.15 C/m^2 at pH $\sim$ 10) considering the specific surface area of magnetite sample 95.3 m^2/g [28]. These values show that less than 2 $\equiv$FeOH sites from the 5–10/nm^2 can only become charged in agreement with the literature [29–31]. The amount of the available $\equiv$FeOH surface sites 0.8 mmol/g can be estimated, if the $\equiv$FeOH site density 5 sites/nm^2 is assumed and the measured specific surface area (95.3 m^2/g) is considered. We have also concluded that the dissolution of magnetite nanocrystals

can be neglected in the studied pH range, since the activity of dissolved Fe(III) species remains below $\sim 10^{-5}$ M between pH ~ 4 and ~ 10 in the absence of complexing or reducing agents [21].

Adsorption of Different Stabilizers on Magnetite

Oleic acid or oleate is the most often used surfactant in MF stabilization; however, its adsorption on magnetite nanoparticles has not studied yet to the best of our knowledge. It is used in a general way, empirical doses are simply added to magnetite just after precipitating nanoparticles and its excess related to the monolayer coverage is removed by washing solid with ethanol or acetone [26, 34, 35], and the organic coated particles are ready to disperse spontaneously in organic carriers. If water based MFs are prepared, the second layer development is followed by visual observation of dispersing solid particles in aqueous medium. Unfortunately the empirical way is preferred in the preparation of not only the surfacted MFs, but also in the case of any other stabilizers like citrate, dextran or PEG/PEO. Since the oleate and citrate are the most often used stabilizers and their adsorption mechanism is highly different, we measured their adsorption on magnetite nanoparticles at pH ~ 6 in the presence of 0.01 M NaCl.

Double layers of oleate are adsorbed on magnetite as explained in details [36]. Monolayer coverage is completed below specific amount ~ 1 mmol/g, while the saturation value ~ 2 mmol/g indicates the completion of double layer formation. Oleate is chemisorbed in the first layer due to the surface complex formation between the $-COO^-$ groups of oleate and the $\equiv$FeOH sites on the surface of magnetite as assumed [35, 37, 38]. This interaction is not Coulombic, the positive surface potential on magnetite particles at pH ~ 6 enhances only the formation of surface complexes [30]. A second layer of oleate anions can be adsorbed on the hydrophobic shell of oriented surfactant molecules via hydrophobic interaction.

Citric acid (CA) is also applied in MF stabilization without studying on adsorption. In general, empirical doses, sometimes huge amounts [14, 15, 19] are simply added to magnetite just after precipitating nanoparticles, and the products are interpreted as CA surface coating, which provides good/excellent stability of water based MFs. Our adsorption study showed that monolayer surface coverage is reached at ~ 0.1 mmol CA on 1 g magnetite, which is fairly above the positive charge density of magnetite 0.044 mmol/g under same condition, but much below the amount of the available $\equiv$FeOH surface sites 0.8 mmol/g, even supposing that all three carboxylic groups of CA molecules could be bound on $\equiv$FeOH sites. In fact, only one or two carboxylate groups of CA can be bound to the $\equiv$FeOH sites forming surface complexes on magnetite particles [14, 16, 17]. It should be noted that dissolution of iron oxides is enhanced in the presence of complexant like CA [13]. In the adsorption series, the dissolution of the Fe(III)-ions from magnetite crystals with increasing CA loading became evident from the rising yellowish color of supernatants, in which the iron concentration up to 0.45 mmol/l was measured by ICP method.

The adsorption of phosphate on magnetite was not studied because phosphates are not used in MF preparation, although they are well known peptizing agents forming mono- or bidentate complexes on iron oxide surface [39]. Under the condition similar to ours (pH ~ 6, 0.01 M indifferent electrolyte) phosphate coverage 0.002 mmol/m^2 on goethite surface was measured, and assuming inner-sphere surface complexes half-and-half bidentate nonprotonated and bidentate protonated surface species were identified by fitting data with CD-MUSIC model. Considering the value 0.002 mmol/m^2 and the specific surface area of magnetite sample 95.3 m^2/g, phosphate coverage 0.19 mmol/g can be estimated for the magnetite sample. The stabilizing effect of phosphate on magnetite nanoparticles was only compared with that of oleate and citrate.

The Effect of Different Stabilizers on Magnetite Particle Charge

The influence of the different stabilizers on the charge state of magnetite particles was studied in parallel with the adsorption measurements. Electrophoretic mobility was determined in the presence of increasing concentration of additives at pH ~ 6. The change in electrophoretic mobility with increasing loading of citrate, phosphate and oleate is plotted in Fig. 1. Each curve starts at a fairly well defined positive value indicating the dominance of positive charges on magnetite at pH ~ 6 below the pH of PZC (~ 8) [24]. The density of positive charges on naked magnetite surface is ~ 0.05 mmol/g in 0.01 M NaCl solution at pH ~ 6 [28]. The mobility values remain in the positive region, i.e., cationic particles exist up to the different concentrations of anionic stabilizers. However, above these concentrations the sign of measured electrophoretic mobility values reversed. The electrophoretic mobility reversal occurring with increasing loading of stabilizers indicates the reversal of the charge sign at shear plane of magnetite particles due to the specific adsorption of anionic compounds. The neutralization of positive surface charges occurs at greater (~ 0.15 or ~ 0.25 mmol/g) or much greater (~ 0.75 mmol/g) specific amounts of added anions than the amount of positive charges (~ 0.05 mmol/g) on magnetite surface. However, the charge neutralization points reach the amount of the available $\equiv$FeOH surface sites 0.8 mmol/g, but never go above this limitation. The latter supports the chemisorption of these anions on the surface of magnetite particles. The charge neutralization point of CA at ~ 0.15 mmol/g is above its monolayer coverage ~ 0.1 mmol/g identified in adsorption measurements. The same trend seems to be valid for phosphate comparing the charge neutralization point at ~ 0.25 mmol/g with its

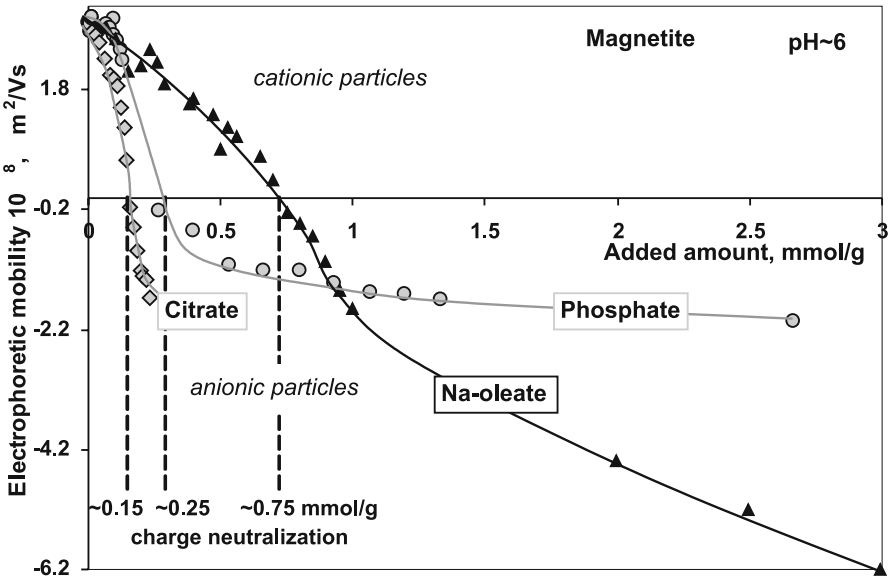

Fig. 1 Effect of different stabilizers on charge state of magnetite nanoparticles. Dilute 0.05 g/l magnetite sols contain 0.01 M NaCl and pH was adjusted to ~ 6

surface coverage 0.19 mmol/g estimated above. The specific amount of the added oleate is ~ 0.75 mmol/g at this charge neutralization point in fairly good agreement with the amount of oleate adsorbed in the first layer [36]. The positive magnetite particles at pH ~ 6 (below the pH of PZC ~ 8) became negative, i.e. anionic particles formed above the charge neutralization points due to the excess charges accumulated in the adsorption layers. In the case of oleate, the formation of second layer via hydrophobic interaction starts with increasing loading, in which the dissociated carboxylate groups (S-COO$^-$, p$K \sim 4$) are oriented toward the aqueous medium. The packing density of adsorbed oleate (5 per nm^2) becomes doubled in the second layer related to that (2.5 per nm^2) in the first layer. Therefore, the amount of negative charges carried by magnetite particles increases significantly, particles become overcharged, and so unusually great electrophoretic mobility values can be measured in the negative region with increasing oleate loading. Such huge negative mobility values were never reached in the presence of citrate and phosphate, even if they were added in high excess, because these stabilizers are adsorbed only in monolayer forming mono- or bidentate complexes on the surface iron oxides [14, 16, 17, 39] and the amount of carried charges above the adsorption saturation depends on the dissociation degree of their unbound negative groups. Both stabilizers are able to dissociate in three steps forming uni-, bi- then trivalent anions with increasing pH. Since the deprotonation of 2nd and 3rd carboxylic group of citric acid (p$K_1 = 2.86$, p$K_2 = 4.47$, p$K_3 = 5.82$) takes mostly place at pH ~ 6, ~ 2.5 negative charges exist on each molecule, while only ~ 1.5 negative charge can be estimated on each phosphate ion because its suppressed dissociation state (p$K_1 = 2.16$, p$K_2 = 7.21$, p$K_3 = 12.33$) at pH ~ 6. Considering the specific amounts of citrate and phosphate (~ 0.15 and ~ 0.25 mmol/g, respectively) belonging to the neutralization of positive surface charges and the ionization state of these anions (~ 2.5 and ~ 1.5, respectively), not more than 2.5 negative charges per nm^2 can be estimated on the surface of magnetite above its charge reversal, which is about half of the carboxylate density (5 per nm^2) in the outer layer of double oleate layer coating.

The Effect of Oleate and Citrate Loading on the pH-dependent Charge State and Aggregation of Magnetite

The electrophoretic mobility measured in pure magnetite sols and in the presence of different amounts of oleate and citrate, respectively, over a broad range of pH can be seen in Fig. 2(upper panel). It is obvious that the naked magnetite particles (open squares) are positively charged below pH ~ 8, and have negative charges above it due to the protonation and deprotonation reactions on $\equiv$FeOH sites as discussed above. The electrophoretic mobility values decrease with increasing pH and their sign reverses at pH ~ 8, which may be identified as the isoelectric point (IEP) of magnetite in good agreement with PZC in the absence of complex forming agents. The IEP of synthetic magnetite determined by different methods falls between 7 and 9 [21, 29].

The effect of oleate and citrate on the surface charge properties of magnetite was examined at several concentrations. The measured data at two characteristic loadings, one below somewhat the charge neutralization points (Fig. 1) and the other in the high excess of stabilizers,

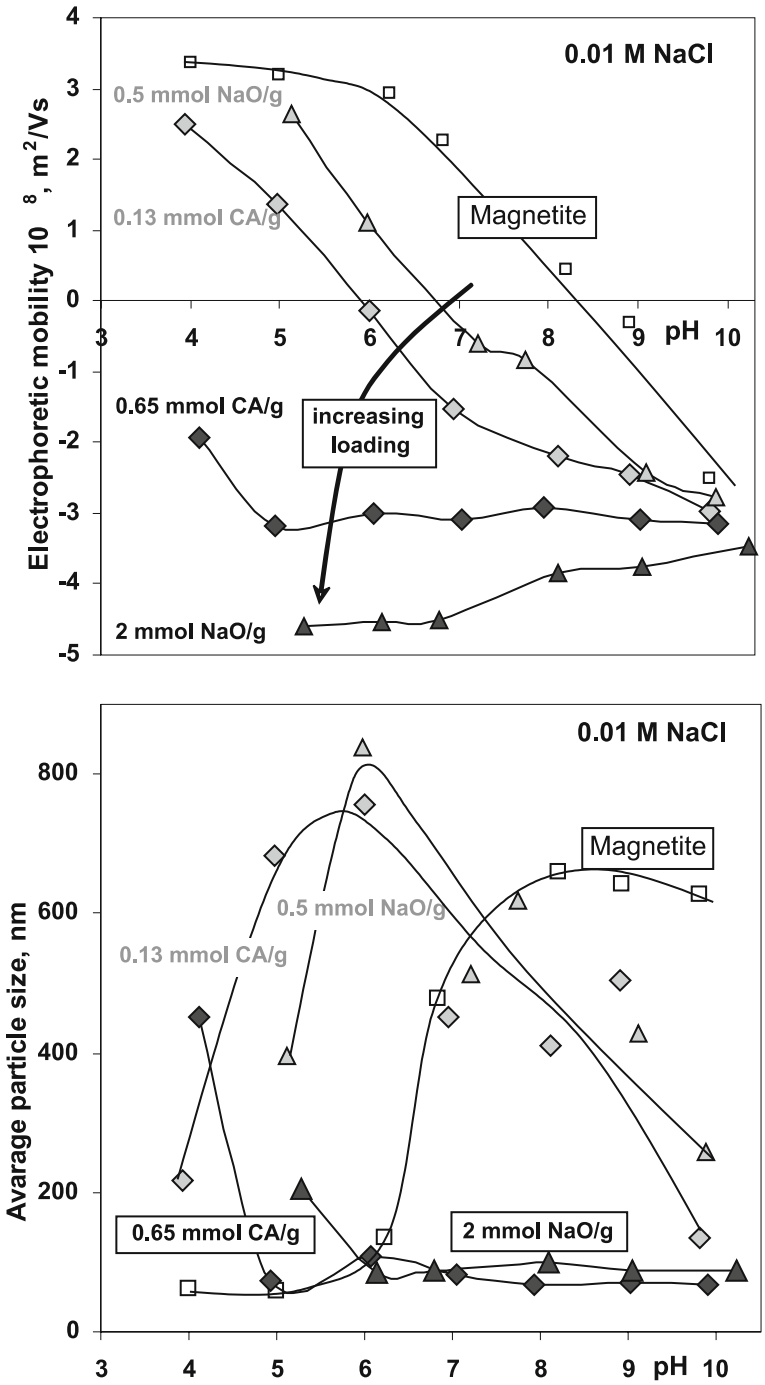

Fig. 2 Effect of Na-oleate (NaO) and citric acid (CA) loading on pH-dependent charge state (*upper panel*) and aggregation (*lower panel*) of magnetite nanoparticles in 0.01 M NaCl solutions at 25 ± 0.1 °C. (The reproducibility of electrophoretic mobility was not better than $\pm 0.4 \times 10^{-8}$ m^2/V s. Reproducible size values below ~ 100 nm were measured in stable sols. The larger values even measured under the same kinetic condition show only the presence of larger aggregates in unstable systems)

are shown in Fig. 2(upper panel). It can be seen that electrophoretic mobility decreases gradually with both increasing oleate and citrate loadings over the whole range of pH. The IEP values belonging to the smaller concentrations (0.5 mmol NaO/g and 0.13 mmol CA/g) shift by 1–2 units to the lower pHs showing that surface coverage of magnetite particles has not completed yet, since the specific adsorption of anions was able to neutralize the positive charges of magnetite only in part. At the higher loadings, however, magnetite becomes negatively charged

even at low pHs, since particles are covered completely in the high excess of stabilizers. In the case of oleate, the 2nd adsorption layer is built up and magnetite nanoparticles become overcharged at 2 mmol NaO/g loading. Due to the close packed structure of oleate anions in the 2nd of the double layer on magnetite particles, the measured values become more negative than that in the alkaline pH region in the absence of surfactant. Citric acid is adsorbed only in monolayer binding to magnetite surface via one or two carboxylate groups even in its high excess (0.65 mmol CA/g), and so the overcharging of particles is limited, the negative charge density on CA covered magnetite is smaller than that on the oleate double layer coated particles as explained above. Therefore, all the measured electrophoretic mobilities of citrate coated magnetite are smaller negative values than that of oleate stabilized sample (Fig. 2 upper panel). The pH-dependence of mobility shows that the charge state of citrate coated magnetite is almost independent of pH except a significant change below pH $\sim$ 5 due to the suppressed dissociation of carboxylic groups on CA ($pK_1 = 2.86$, $pK_2 = 4.47$, $pK_3 = 5.82$).

In parallel, the pH-dependent particle aggregation was measured by dynamic light scattering, which can be used even in coagulating system [40] and particle size data provide information on the colloidal stability of systems. In the pure magnetite sols, only the electric double layer exists far from the PZC, which is able to stabilize particles at low salt concentration, so the measured average hydrodynamic sizes remained below 100 nm (Fig. 2 lower panel, open squares). However, in the absence of electrostatic stabilization near the pH of PZC, large aggregates form even at low 0.01 M salt concentration. The formation of large aggregates was also observed near to the IEP (pH $\sim$ 6) of magnetite covered imperfectly by anions at the smaller loadings of both oleate (0.5 mmol/g) and citrate (0.13 mmol/g), where positive charges of magnetite surface were partially neutralized, and so the colliding particles adhered for the lack of electrostatic repulsion. Far away from the pH of IEP, the efficiency of particle adhesion in random collisions was much worse and only smaller aggregates could form in both acidic and alkaline regions during the given time of measurements. When perfectly coated anionic particles are dispersed at either oleate (2 mmol/g) or citrate (0.65 mmol/g) loadings, reproducible hydrodynamic size values smaller then $\sim$ 100 nm were measured independently of the pH above pH $\sim$ 6. The outermost hydrophilic shell on the double layer coated magnetite particles contains carboxylate groups. Therefore, pH-dependent negative charges exist due to the dissociation of bound groups, $S{-}COOH \rightleftharpoons S{-}COO^- + H^+$ ($pK \sim 4$) on the surface of the oleate double layer coated magnetite particles. Fully dissociated carboxylate groups above pH $\sim$ 6 provide electrostatic repulsion between colliding particles besides the steric hindrance of double layer. However, the dissociation degree starts to decrease with decreasing pH below pH $\sim$ 6, and so not only the electrostatic repulsion declines, but also particles become less hydrophilic in the acidic region. In the same way, a significant decline in the stability of citrate coated magnetite samples occurs only below pH $\sim$ 5, where dissociation of CA begins to suppress as explained above. Therefore, a significant decrease in colloidal stability, i.e., formation of aggregates can be predicted in acidic medium for both oleate and citrate stabilized MFs.

Salt Tolerance of Dilute Magnetic Fluids Stabilized by Different Agents

The salt tolerance of the phosphate and citric acid monolayer as well as the oleic acid double layer stabilized magnetic nanofluids was investigated in dilute systems at pH $\sim$ 6 to test particle aggregation in time, whether the combined electrostatic and steric stabilization provides suitable colloidal stability under physiological condition. We should note that the salt tolerance of naked magnetite particles is very low ($\sim$ 0.001 M NaCl) under this condition. Coagulation kinetics measurements were performed to determine quantitatively the efficiency of different agents in the stabilization of magnetite particles dispersed in more and more concentrated salt solutions. The size evolution of aggregates in time was followed by dynamic light scattering and the coagulation rate was calculated from the slope of kinetic curves as explained before [22, 24]. The stability ratio (W) was calculated from the initial slopes of kinetic curves belonging to the slow and fast coagulation as suggested in literature [40]. The lowest salt concentration inducing fast coagulation called as critical coagulation concentration (CCC) is usually determined from the $\log_{10} W$ versus $\log_{10}$ electrolyte concentration function. The different stabilizers were applied in high excess and the CCC values determined at different loadings of phosphate, citrate and oleate are summarized in Table 1. The data show an increasing resistance against salt with increasing loading of phosphate and citrate, however, none of them was able to provide a suit-

Table 1 The critical coagulation concentration (CCC) values determined in dilute magnetite sols stabilized by increasing loadings of different stabilizers at pH $\sim$ 6. (The concentration of physiological salt solution is 150 mM)

Stabilizer	Amount added mmol/g	Electrophoretic mobility 10^{-8} m^2/Vs	CCC mM
Citrate	0.65	–2.61	40
	1		60
	1.5	–2.85	80
	4.5		90
Oleate	1.5	–3.15	200
	2	–4.52	200
Phosphate	26.64	–2.63	40

able salt tolerance expected under physiological condition, since the measured CCC values (40–90 mM) remained much below 150 mM even in their huge excess (30 and 100 times as charge neutralization points of citrate and phosphate, respectively). It should be noted that such high CA loadings enhance the dissolution of magnetite crystals to a great extent. The oleate double layer can hinder effectively the aggregation of magnetite particles due to the combined steric and electrostatic stabilization. The latter is supported by the greater electrophoretic values of oleate loaded samples than that of citrate and phosphate contained systems in Table 1. The resistance of magnetite sols stabilized by oleate double layers against electrolytes is enhanced above the critical salt tolerance (> 0.150 M) expected under physiological condition.

Conclusion

The aim of this work was to clear up some basic questions related to the stabilization of magnetite nanoparticles in aqueous medium, namely the adsorption of different anionic stabilizers, the charge neutralization and the reverse sign or overcharge of magnetite surface, as well as the effect of the pH and salt concentration on particle aggregation. The latter parameters are common in aqueous colloidal systems, but their effect is still not investigated in water based MFs literature, although these are the most important factors in biomedical application.

Chemisorption of each stabilizer studied here results in monolayer coverage on magnetite nanoparticles. Mostly bidentate type surface complexes form between carboxylate groups or phosphate ions and ≡FeOH surface sites in the innermost layer. The only oleate is able to form a second layer via hydrophobic interaction between long alkyl chains. In each case, the ionized groups either carboxylate or phosphate in the outer layer, are contact with aqueous medium. The surface density and dissociation state of these anionic groups determine the overall charge density on particle surface, which govern the electrostatic repulsion between colliding particles. It seems the closed packed structure in the second layer of oleate double layer results in about double density of carboxylate groups as that in the citrate monolayer, which was almost the same as the estimated surface density of phosphate groups. Anionic magnetic particles formed with increasing loading of each stabilizer, so each stabilizer was able to reverse the sign of positive charges on magnetite surface after their neutralization, however, overcharging occurred only at high loading of oleate (> 1.5 mmol/g) due to the high surface density of carboxylate groups dissociated well at pH ~ 6. Although protective layer on magnetite nanoparticles formed from each stabilizer and both steric and electrostatic stabilization exist in all cases; the only oleate double layers are able to hinder the aggregation of magnetite particles effectively in physiological salt solution. This work gave evidence that the salt tolerance of CA stabilized system like any dilute citrated MF remains much below as it is expected, and so CA coating used frequently in aqueous MF is not enough effective to hinder aggregation of magnetite particles under physiological condition. In turn, oleate double layers on magnetite nanoparticles results in effective electrosteric stabilization in water based MF, which seems to deserve further in vitro investigation.

Acknowledgement This work was supported by the Hungarian National Office of Research and Technology (NKTH) under contract no. OMFB-01604/2006 and NKTH-OTKA (A7-69109/2007), as well by the Romanian Authority for Scientific Research through the CEEX research projects MAGMED and NANOFUNC.

References

1. Halavaara J, Tervahartiala P, Isoniemi H, Höckerstedt K (2002) Efficacy of Sequential Use of Superparamagnetic Iron Oxide and Gadolinium in Liver MR Imaging. Acta Radiol 43:180–185, doi:10.1034/j.1600-0455.2002.430216.x
2. Benderbous S, Corot C, Jacobs P, Bonnemain B (1996) Session 7 Superparamagnetic Agents: Physicochemical Characteristics and Preclinical Imaging Evaluation. Acad Radiol 3, Suppl. 2:292–294
3. Babincová M, Sourivong P, Leszczynska D, Babinec P (2000) Blood-specific whole-body electromagnetic hyperthermia. Med Hypotheses 55(6):459–460, doi: 10.1054/mehy.2000.1089
4. Brigger I, Dubernet C, Couvreur P (2002) Nanoparticles in cancer therapy and diagnosis. Adv Drug Deliv Rev 54:631–651, doi:10.1016/S0169-409X(02)00044-3
5. McNeil SE (2005) Nanotechnology for the biologist. J Leukoc Biol 78:585–594, doi:10.1189/jlb.0205074
6. Berry CC, Curtis ASG (2003) Functionalisation of magnetic nanoparticles for applications in biomedicine. J Phys D: Appl Phys 36:R198–R206, PII: S0022-3727(03)38650-4
7. Pankhurst QA, Connolly J, Jones SK, Dobson J (2003) Applications of magnetic nanoparticles in biomedicine. Top Rev, J Phys D: Appl Phys 36:R167–R181, PII: S0022-3727(03)40035-1
8. Bahadur D, Giri J (2003) Biomaterials and magnetism. Sadhana 28(3/4):639–656, doi: 10.1007/BF02706451
9. Saiyed ZM, Telang SD, Ramchand CN (2003) Application of magnetic techniques in the field of drug discovery and biomedicine. Biomagn. Res Technol 1:2, doi:10.1186/1477-044X-1-2
10. Gupta AK, Gupta M (2005) Synthesis and surface engineering of iron oxide nanoparticles for biomedical applications. Biomaterials 26:3995–4021, doi:10.1016/j.biomaterials.2004.10.012
11. Fauconnier N, Bée A, Roger J, Pons JN (1999) Synthesis of aqueous magnetic liquids by surface complexation of maghemite

nanoparticles. J Molec Liq 83:233–242, doi:10.1016/S0167-7322(99)00088-4
12. Kallay N, Matijević E (1985) Adsorption at Solid/Solution Interfaces. 1. Interpretation of Surface Complexation of Oxalic and Citric Acids with Hematite. Langmuir 1:195–201
13. Zhang Y, Kallay N, Matijević E (1985) Interaction of Metal Hydrous Oxides with Chelating Agents. 7. Hematite-Oxalic Acid and -Citric Acid Systems. Langmuir 1:201–206
14. Goodarzi A, Sahoo Y, Swihart MT, Prasad PN (2004) Aqueous Ferrofluid of Citric Acid Coated Magnetite Particles. Mater Res Soc Symp Proc 789:6.6.1–6.6.6
15. Lacava ZGM, Azevedo RB, Martins EV, Lacava LM, Freitas MLL, Garcia VAP, Rébola CA, Lemos APC, Sousa MH, Tourinho FA, Da Silva MF, Morais PC (1999) Biological effects of magnetic fluids: toxicity studies. J Magn Magn Mater 201:431–434 Bibliographic Code: 1999JMMM..201..431L
16. Sahoo Y, Goodarzi A, Swihart MT, Ohulchanskyy TY, Kaur N, Furlani EP, Prasad PN (2005) Aqueous Ferrofluid of Magnetite Nanoparticles: Fluorescence Labeling and Magnetophoretic Control. J Phys Chem B 109:3879–3885
17. Bee A, Massart R, Neveu S (1995) Synthesis of very fine maghemite particles. J Magn Magn Mater 149:6–9, doi: 10.1016/0304-8853(95)00317-7
18. Morais PC, Santos RL, Pimenta ACM, Azevedo RB, Lima ECD (2006) Preparation and characterization of ultra-stable biocompatible magnetic fluids using citrate-coated cobalt ferrite nanoparticles. Thin Solid Films 515:266–270, doi:10.1016/j.tsf.2005.12.079
19. Rãcuciu M, Creang DE, Airinei A (2006) Citric-acid-coated magnetite nanoparticles for biological applications. Eur Phys J E 21:117–121, doi:10.1140/epje/i2006-10051-y
20. Scherer C, Figueiredo Neto AM (2005) Ferrofluids: Properties and Applications. Braz J Phys 35(3A):718–727, doi: 10.1590/S0103-97332005000400018
21. Cornell RM, Schwertmann U (1996) The Iron Oxides. VCH, Weinheim
22. Hunter RJ (1987) Foundations of Colloid Science. Vol I, Clarendon Press, Oxford
23. Odenbach S (2003) Ferrofluids-magnetically controlled suspensions. Colloids Surf A 217:171–178, doi:10.1016/S0927-7757(02)00573-3
24. Illés E, Tombácz E (2006) The effect of humic acid adsorption on pH-dependent surface charging and aggregation of magnetite nanoparticles. J Colloid Interf Sci 295:115–123, doi:10.1016/j.jcis.2005.08.003
25. Tombácz E (2003) Effect of environmental relevant organic complexants on the surface charge and the interaction of clay mineral and metal oxide particles. In: Bárány S (ed), Role of Interfaces in Environmental Protection. NATO ASI Series IV: Earth and Environmental Sciences Vol 24, Kluwer Academic Publisher, Dordrecht, pp 397–424
26. Vékás L, Bica D, Marinica O (2006) Magnetic nanofluids stabilized with various chain length surfactants. Rom Rep Phys 58(3):217–228
27. Bica D, Vékás L, Avdeev MV, Marinica O, Balasoiu M, Garamus VM (2007) Sterically stabilized water based magnetic nanofluids: synthesis, structure and properties. J Magn Magn Mater 311(1):17–21, doi:10.1016/j.jmmm.2006.11.158
28. Tombácz E, Illés E, Majzik A, Hajdú A, Rideg N, Szekeres M (2007) Ageing in the inorganic nanoworld: example of magnetite nanoparticles in aqueous medium. Croat Chem Acta 80:503–515
29. James RO, Parks GA (1982) Characterization of Aqueous Colloids by Their Electrical Double-Layer and Intrinsic Surface Chemical Properties, in: Matijević E (ed), Surface and Colloid Science, Vol 12, Plenum, New York, pp 119–216
30. Tombácz E (2002) Adsorption from electrolyte solutions, in: Tóth J (ed), Adsorption: Theory, Modeling, and Analysis, Marcel Dekker, New York, pp 711–742
31. Kosmulski M (2001) Chemical Properties of Material Surfaces. Marcel Dekker, New York, p 753
32. Sun Z, Su F, Forsling W, Samskog PJ (1998) Surface Characteristics of Magnetite in Aqueous Suspension. Colloid Interf Sci 197:151–159, doi:10.1006/jcis.1997.5239
33. Illés E, Tombácz E (2003) The role of variable surface charge and surface complexation in the adsorption of humic acid on magnetite. Colloids Surf A 230(1–3):99–109, doi:10.1016/j.colsurfa.2003.09.017
34. Wooding A, Kilner M, Lambrick DB (1991) Studies of the double surfactant layer stabilization of water-based magnetic fluids. J Colloid Interf Sci 144:236–242
35. Chen K, Bakuzis AF, Luo W (2006) Improving surfactant grafting in magnetic colloids. Appl Surf Sci 252:6379–6382, doi:10.1016/j.apsusc.2005.12.160
36. Tombácz E, Bica D, Hajdú A, Illés E, Majzik A, Vékás L (2008) Surfactant double layer stabilized magnetic nanofluids for biomedical application. J Phys Condens Matter 20:204103 (6pp) doi: 10.1088/0953-8984/20/20/204103
37. Wooding A, Kilner M, Lambrick DB (1992) "Stripped" magnetic particles. Applications of the double surfactant layer principle in the preparation of water-based magnetic fluids. J Colloid Interf Sci 149:98–104
38. Hong RY, Zhang SZ, Han YP, Li HZ, Ding J, Zheng Y (2006) Preparation, characterization and application of bilayer surfactant-stabilized ferrofluids. Powder Technol 170:1–11, doi:10.1016/j.powtec.2006.08.017
39. Antelo J, Avena M, Fiol S, López R, Arce F (2005) Effects of pH and ionic strength on the adsorption of phosphate and arsenate at the goethite–water interface. J Colloid Interf Sci 285:476–486, doi:10.1016/j.jcis.2004.12.032
40. Schudel M, Behrens SH, Holthoff H, Kretzschmar R, Borkovec M (1997) Absolute Aggregation Rate Constants of Hematite Particles in Aqueous Suspensions: A Comparison of Two Different Surface Morphologies. J Colloid Interf Sci 196:241–253, doi:10.1006/jcis.1997.5207

Progr Colloid Polym Sci (2008) 135: 38–43
DOI 10.1007/2882_2008_099

Published online: 9 September 2008

László Trif
Gyula Tolnai
István Sajó
Erika Kálmán

Preparation and Characterization of Hexagonal W-type Barium Ferrite Nanoparticles

László Trif (✉) · Gyula Tolnai · Erika Kálmán
Institute of Surface Chemistry and Catalysis, Chemical Research Center of the Hungarian Academy of Sciences, Pusztaszeri street 59–67, 1025 Budapest, Hungary
e-mail: ltrif@chemres.hu

István Sajó
Institute of Structural Chemistry, Chemical Research Center of the Hungarian Academy of Sciences, Pusztaszeri street 59–67, 1025 Budapest, Hungary

Abstract New chemical synthesis procedure for preparation of nickel-zinc doped W-type hexagonal, nickel-zinc doped barium ferrite nanoparticles has been developed, using the nitrate-citrate sol–gel auto-combustion method (NCSAM). The crystalline phase attributes, microstructure, morphology, thermal behavior of the as-burnt phase and the sintered powders were characterized using XRD, SEM, TG-DTA, FT-IR measurements. The pure W-type ferrite phase is formed during 4 h annealing at a temperature of 1200 °C.

Keywords Ceramics · Hexaferrite · Nanoparticle · Self-combustion · Sol–gel

Introduction

Hexagonal ferrites are a wide family of ferromagnetic oxides, with peculiar and useful properties. The crystal structure of the different known types of hexagonal ferrites (M, W, X, Y, Z, and U) is very complex and can be considered as a superposition of R and S blocks along the hexagonal *c* axis, RSR*S* for M-type and RSSR*S*S* for W-type, where R is a three-oxygen-layer block with composition $BaFe_6O_{11}$, S (spinel block) is a two-oxygen-layer block with composition Fe_6O_8, and the asterisk means that the corresponding block has been turned 180° around the hexagonal axis [1, 2]. Among the hexagonal ferrites W-type compounds with a general formula $AMe_2Fe_{16}O_{27}$ (A = alkali earth metals, usually Ba, Sr, Ca, and Me = *d*-block metals, Zn, Co, Ni, etc.) have created interest due to the main magnetic parameter values, that are more suitable for microwave applications than those of other hexagonal ferrites [3].

A variety of techniques have been developed to synthesize W-type hexaferrites. The most used method for the preparation of barium ferrite in industrial and technical application is the classical ceramic method, which results in a material that is inhomogeneous at a microscopic scale [4]. The conventional mechanical grinding [5] and glass crystallization method [6] for W-type hexaferrites preparation have disadvantages such as time consuming and introducing impurities into material composition. Furthermore, the high calcination temperature (≥ 1300 °C) results in the formation of coarse aggregation and the vaporization of some volatile components. Nowadays, new wet chemical methods have been developed for the preparation of nanograined hexagonal W-type ferrites. Various advantages such as low processing cost, energy efficiency and high production rate [7] are among the benefits of the sol–gel combustion synthesis method, which has been applied to the preparation of various high performance materials including ceramics, intermetallics, and composites [8, 9]. In this paper, sol–gel auto-combustion method has been used to synthesize nanocrystalline, nickel and zinc doped W-hexaferrite. The synthesis process and characterizations of nanocrystalline ferrite is reported.

Experimental

Materials

Nickel-zinc W-type barium hexaferrite powders were prepared by nitrate-citrate sol–gel auto-combustion method (NCSAM). The starting materials were $Ba(NO_3)_2$ ($\geq 99\%$), $Ni(NO_3)_2 \cdot 6H_2O$ ($\geq 97\%$), $Zn(NO_3)_2 \cdot 6H_2O$ ($\geq 99\%$), $Fe(NO_3)_3 \cdot 9H_2O$ ($\geq 97\%$), citric acid anhydrous ($\geq 99.5\%$) and ammonia ($\sim 25\%$), all of analytical purity. All the reagents were purchased from Fluka, and were used without any further purification.

Preparation

The preparation process can be described as follows. The stoichiometric amounts of barium, nickel, zinc nitrates and iron nitrates were dissolved together in distilled water, under continuous stirring during 30 min. The calculated amount of citric acid was poured into this mixture, changing the colour of the solution from orange to brownish-yellow. The metal nitrates to citric acid molar ratio were chosen to be 1 : 2. After a subsequent 30 min of stirring, the pH was adjusted to the value of 2, by adding concentrated ammonia solution, followed by 6 h of continuous stirring at room temperature. The dark green coloured clear sol was heated on a hot plate at circa 110 °C under continuous stirring, until the 3/4 volume of the water evaporated, and suddenly the gelation occurred, resulting a viscous dark green gel, which was further dried in a drying chamber at 140 °C. During this process, the gel burnt in a self-propagating combustion manner (Fig. 1) to form a dark-grey colored fluffy, loose powder, which was heat-treated in air atmosphere at various temperatures between 900–1200 °C.

(a) (b)

Fig. 1 **a** Gel and **b** the product after completion of the reaction

Characterization

X-ray Diffraction Spectroscopy (XRD). XRD patterns of the samples treated at various temperatures were recorded in the range of $2\theta = 10$–$70°$, with a scanning speed of $0.04° \text{ min}^{-1}$ on a Philips PW 105 diffractometer, operated at 40 kV, 35 mA and using Cu K_α radiation. The average crystallite size in the sample was calculated using the Scherrer equation:

$$D = \frac{K\lambda}{h_{1/2} \cos \Theta}, \quad (1)$$

where D = average size of the crystallites, K = Scherrer constant, λ = wavelength of radiation (1.54186 Å), $h_{1/2}$ = peak width at half height and Θ corresponds to the peak position.

Elemental Analysis by Inductively Coupled Plasma Spectroscopy (ICP). The stoichiometry analysis of the heat treated powders was carried out using a inductively coupled plasma spectrometer. The results were almost equal with the initial, calculated composition.

Transmission Electron Spectroscopy (TEM). The micrograph and the crystallite size of the calcined samples were examined using a MORGAGNI 268D TEM (100 kV; W filament, top-entry; point-resolution = 0.5 nm) transmission electron microscope.

Fourier Transformed Infrared Spectroscopy (FT-IR). The infrared spectra of the samples were recorded using a THERMO Nicolet AVATAR 320 FT-IR spectrometer (laser frequency $15\,798.8 \text{ cm}^{-1}$) in the range of 4000–400 cm^{-1}. The number of sample and background scans was 32 each. The recorded spectra were evaluated with the spectrometer's software (EZ OMNIC version 6.1a). Sample preparation included mixing ~ 0.7 mg powdered sample with 250 mg dried KBr and pressing them into pellets.

Scanning Electron Microscopy (SEM). Scanning electron micrographs and analysis of the morphology of the samples were carried out on a JEOL JSM-6100 scanning microscope, operated at 15 kV high voltage, with EDAX EDS detector system.

Thermogravimetry and differential thermal analysis (TG-DTA). The thermal behavior of the powders was investigated with thermo gravimetric analysis (TG) and differential thermal analysis (DTA), using a Setaram Setsys 16/18 TG-DTA instrument. Experimental conditions were: flowing synthetic air atmosphere (80% N_2, 20% O_2), in the temperature range 25–1300 °C, with a heating rate of 10 K/min, using 100 µl Al_2O_3 crucibles. The spectra were evaluated using the thermogravimeter's software (SETSOFT, ver. 1.54).

Results and Discussion

The X-ray diffraction (XRD) patterns of the studied $Ba(Ni_{0.5}Zn_{0.5})_2Fe_{16}O_{27}$ ferrite samples heat treated at various temperatures are shown in Fig. 2.

In the case of the sample annealed during 4 h at 900 °C (Fig. 2a), the main constituent is $BaFe_{12}O_{19}$ M-type hexaferrite, contaminated with magnetite and hematite. When increasing the calcination temperature, the magnetite and hematite content decreases. During 4 h annealing at 1200 °C, the formation of the pure $Ba(Ni_{0.5}Zn_{0.5})_2Fe_{16}O_{27}$ W-type ferrite phase can be observed (Fig. 2b). The crystalline size of the W-type ferrite, calculated using Scherrer's formula (Eq. 1), and found to be 110 nm. It can be concluded, that the formation of W-type ferrite occurs at high temperatures through complex solid-state reactions, in which the melted, previously formed M-type ferrite dissolves the remained unreacted iron, nickel and zinc oxides, to form pure $Ba(Ni_{0.5}Zn_{0.5})_2Fe_{16}O_{27}$ ferrite phase. The annealing temperature and time greatly influences the amount of W-type ferrite phase.

The FT-IR spectrum of an as burnt powder, and a sintered sample at 1200 °C, 4 h is shown in the Fig. 3.

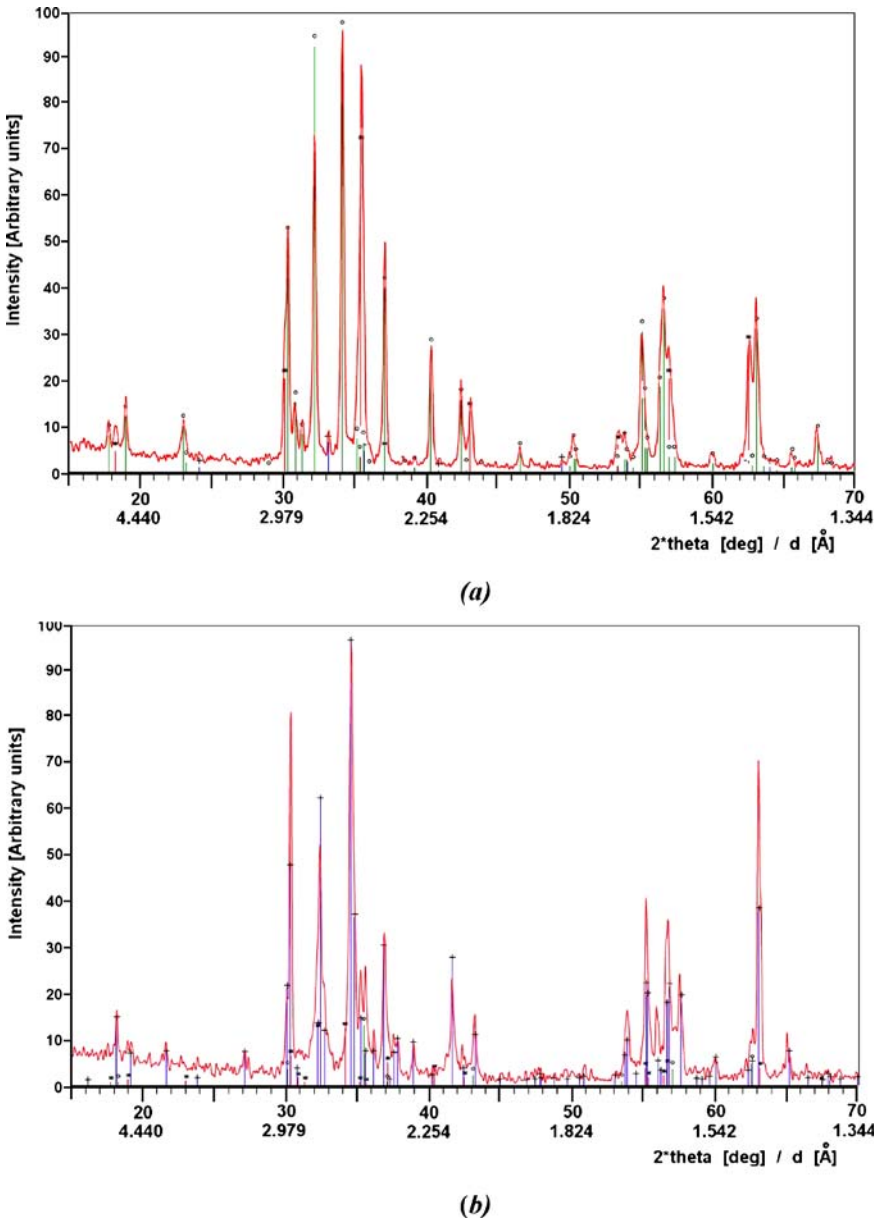

Fig. 2 XRD pattern of hexaferrite powders sintered (**a**) 4 h at 900 °C and (**b**) 4 h at 1200 °C

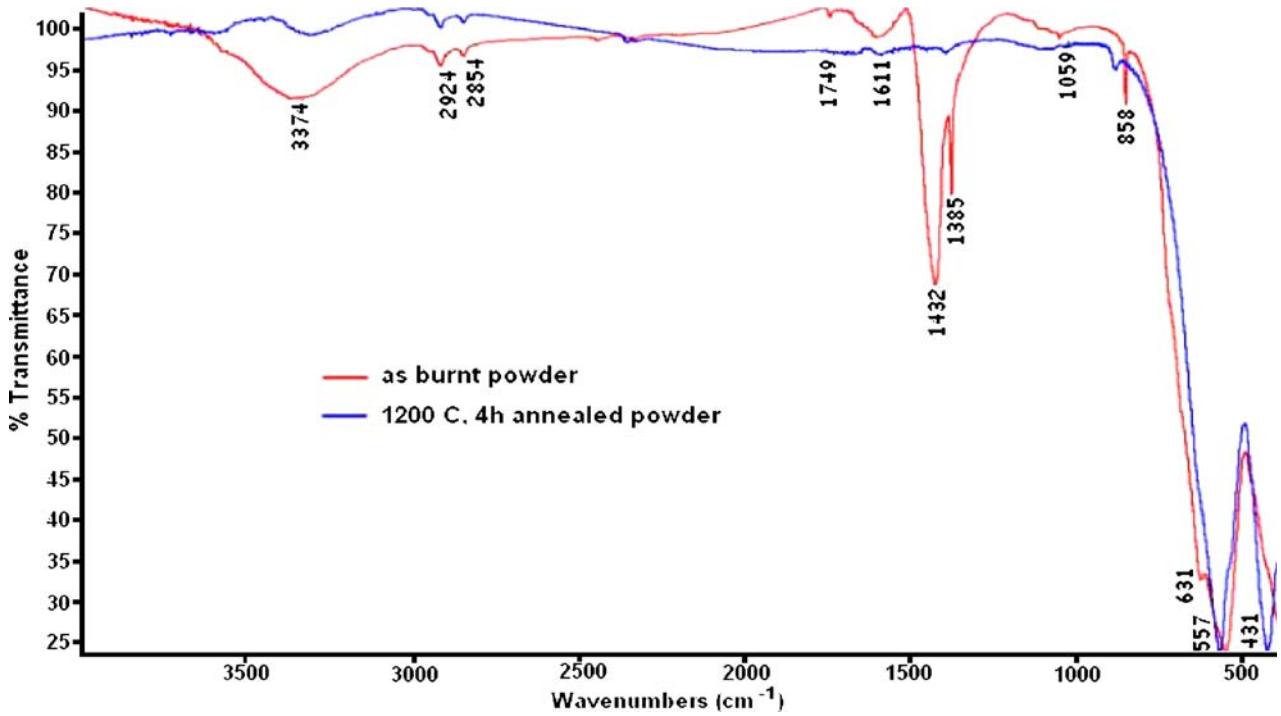

Fig. 3 FT-IR spectra of the as burnt and sintered powder

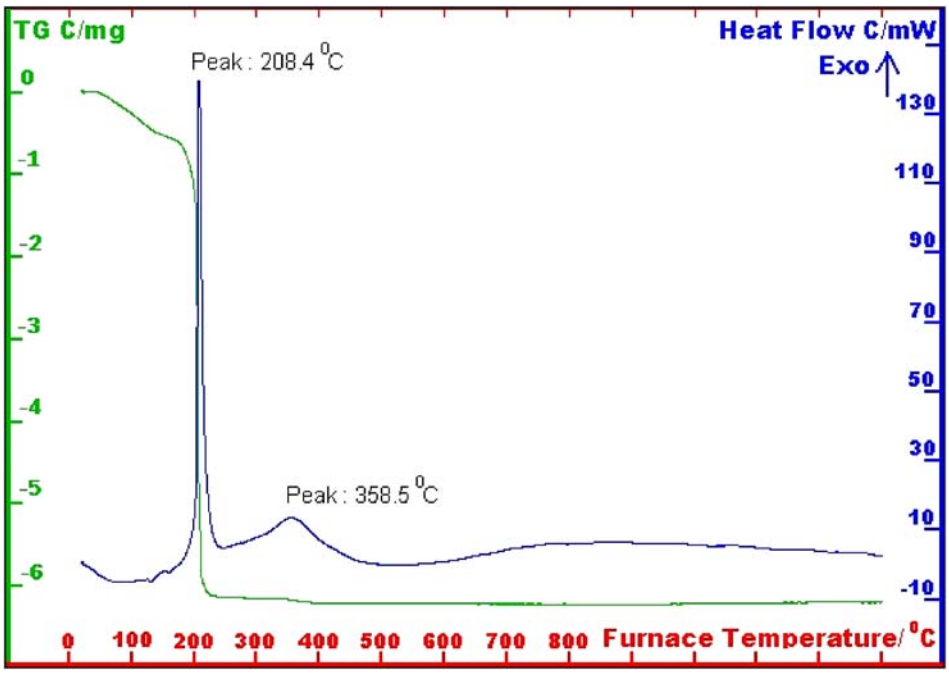

Fig. 4 TG and DTA curves of the gel dried at 110 °C

On the as burnt powder spectrum, the broad absorption band around 3370 cm^{-1} is a characteristic stretching vibration of hydroxyl group (O–H), and absorption peaks around 1600 cm^{-1} and 1390 cm^{-1} are assigned to asymmetrical and symmetrical stretching vibration of carboxylate groups coordinated to metallic ions. Peak localized at 1059 cm^{-1} is assigned to symmetrical stretching vibration of C–O–C group, and the band at $\sim$ 1430 cm^{-1} is charac-

teristic of the presence of CO_3^{2-} anion. The sharp peak localized at 850 cm^{-1} is assigned to deformation vibration of C–H group. In the range 1000–100 cm^{-1}, the IR bands of solids are usually assigned to vibration of ions in the crystal lattice [10]. Two main broad metal-oxygen bands are seen in the IR spectra of ferrites, which can be found on both curves in the Fig. 3. The highest one usually located in the range of 600–550 cm^{-1}, corresponds to stretching vibrations of metal ions at the tetrahedral site, whereas the lowest, observed in the range 450–370 cm^{-1} is assigned to stretching vibrations in octahedral sites. It could be concluded that after completion of the self-combustion reaction, the resulting powder's main components are metal oxides and carbonates, but a small amount of unreacted organic material also can be found. In the spectra of the annealed powder only the peaks assigned to vibration of ions in the crystal lattice can be seen, so it could be concluded, that metal oxides are exclusively present, which is also proved by the XRD measurements.

The TG-DTA results are shown in the Fig. 4. Measurements were carried out on small amounts of solid samples, obtained by drying the gel at ∼ 110 °C in a drying chamber, followed by pulverization in an agate mortar. Evaluating the spectra, it can be seen, that a broad endothermic peak with two small shoulders located at 130.7 and 160.9 °C respectively can be found in the temperature range room temperature (25 °C)– ∼ 160 °C, accompanied by a mass loss of approximately 6.67%, which can be attributed to the vaporization of planar and inner water.

The largest sharp exothermal peak at 208.4 °C, accompanied by a drastic mass loss (∼ 66%) in the temperature range of 160–260 °C, is due to the autocatalytic oxidation-reduction reaction between the metal nitrates (particularly the nitrate anions) and citric acid. In this reaction citric acid acts not only as chelating agent but also as fuel. The broader exothermic peak with the maximum at 358.5 °C is accompanied only by a small weight loss. This is the result of the decomposition of the remaining organic matter, but also the decomposition of metal carbonates formed during the self-combustion reaction. In the temperature region 400–1300 °C no significant mass loss occurs.

A SEM micrograph of a ferrite sample heat treated 4 h at 1200 °C is shown in Fig. 5. The particle size estimated from the photograph is ∼ 1–3 μm, and homogenous well-formed hexagonal-shaped crystals can be seen. Increasing the temperature the grain size of the ferrite increases also, which is in accordance with the results of Kishan Reddy et al. [11].

The microstructure of the ferrite powder obtained at 1200 °C is shown in Fig. 6. It was observed, that the crystallites were more or less uniform in size with an average size of 100 nm, which is in good agreement with the calculated results obtained by the XRD measurements. The selected area electron diffraction (SAED) pattern is shown in the insert of Fig. 6, corresponding to that of a W-type ferrite phase.

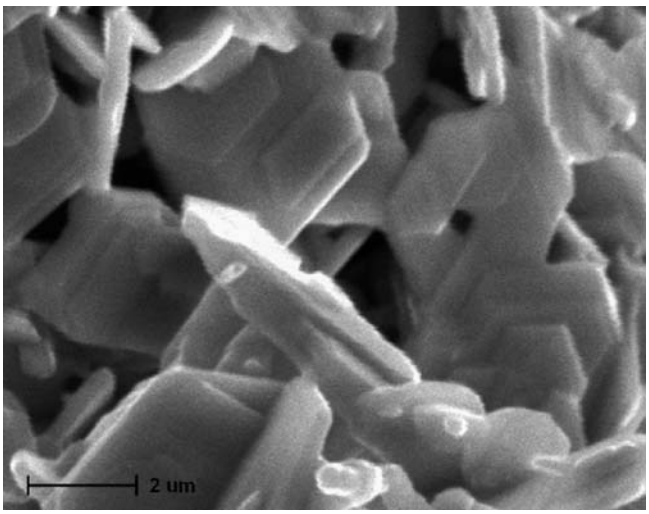

Fig. 5 SEM micrograph of the hexaferrite powder sintered 4 h at 1200 °C (scale bar is 2 μm)

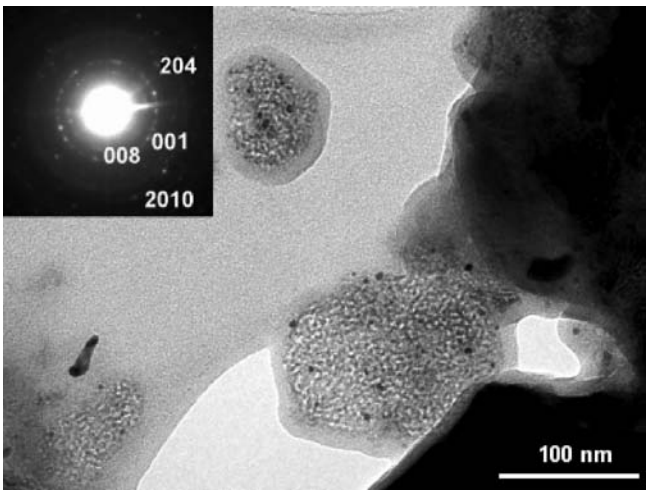

Fig. 6 TEM micrograph of the hexaferrite powder sintered 4 h at 1200 °C (scale bar is 100 nm)

The ICP spectroscopy stoichiometry analysis result of a 1200 °C calcined powder is summarized in Table 1. It can be seen that the elemental composition of the ferrite does not differ from the calculated theoretical values.

Table 1 Elemental composition of the 4 h 1200 °C sintered ferrite powder

m/m %	Ba	Ni	Zn	Fe
Theoretical composition	8.65	3.69	4.12	56.30
Sintered powder	8.82	3.75	3.99	56.41

Conclusion

The sol–gel auto-combustion method is convenient for the synthesis of nano-sized nickel-zinc doped W-type barium hexaferrites. The main components of the resulting powder, after the completion of self-combustion reaction, are metal oxides and carbonates. The formation of pure W-type ferrite occurs at relatively lower temperature (1200 °C) than in the case of classical ceramic synthesis route. Magnetic measurements will be carried out on the pure materials in order to investigate their magnetic properties.

Acknowledgement The authors are grateful to the financial support of the Hungarian National Office for Research and Technology (NKTH) in the frame of the NKFP-3/A 2004 (NANOFERRIT) project. László Trif wishes to thank to Patrizio Madau (ULB, Brussels, Belgium) for the SEM measurements and for the Bay Zoltán Foundation for Applied Research, Institute for Materials Science and Technology for the TG-DTA investigations.

References

1. Smit J, Wijn HPJ (1959) Ferrites. Philips Technical Library
2. Valenzuela R (2005) "Magnetic ceramics", Chemistry of Solid State Materials. Cambridge University Press, Cambridge
3. Leccabue F et al. (1988) Mater Res Bull 33:263
4. Haneda K et al. (1974) J Am Ceram Soc 57:68
5. Abo El Ata AM et al. (1999) J Magn Magn Mater 204:36
6. Sürig C et al. (1995) J Magn Magn Mater 150:270
7. Crider JF (1982) Ceram Eng Sci Proc 3:519
8. Avakyan PB et al. (1996) Am Ceram Soc Bull 75:50
9. Munir ZA (1988) Ceram Bull 67:342
10. Brabers VAM (1969) Phys Stat Solidi 33:563
11. Kishan Reddy N et al. (2002) Mater Chem Phys 76:75–77

Progr Colloid Polym Sci (2008) 135: 44–47
DOI 10.1007/2882_2008_100

Published online: 10 September 2008

Nikoletta Molnár
Gyula Tolnai
Sándor Mészáros
Erika Kálmán

Preparation and Characterization of Y-Fe-Al Garnet Nanostructured Materials

Nikoletta Molnár (✉) · Gyula Tolnai · Erika Kálmán
Institute of Surface Chemistry and Catalysis, Chemical Research Center of the Hungarian Academy of Sciences, Pusztaszeri street. 59–67, 1025 Budapest, Hungary
e-mail: niki@chemres.hu

Sándor Mészáros
Institute of Nuclear Research of the Hungarian Academy of Sciences, Bem tér, 18/c, 4001 Debrecen, Hungary

Abstract Aluminium doped yttrium-iron garnet (YIG) nanoparticles ($Y_3Al_xFe_{5-x}O_{12}$, $x = 0$, 1,5, 1,55, 1,575, 1,6) have been prepared by the nitrate-citrate sol–gel auto-combustion method (NCSAM). Our goal was to prepare YIG nanopowders with different aluminium content, furthermore to investigate the variation of the Curie temperature of the samples in function of the amount of dopant cations. The crystalline phase attributes, microstructure, morphology, surface area, Curie temperature (T_C) and permeability of the sintered powders were characterized using X-ray diffraction spectroscopy (XRD), scanning electron microscopy (SEM), surface area measurement (BET) and ac magnetic permeability with frequency shift. The results show, that the sintered powders exhibit a spongy-like morphology with relatively high surface area. Furthermore it has been confirmed, that the ac magnetic permeabilities are strongly depending on the chemical composition.

Keywords Ceramics · Nanoparticles · Self-combustion · Sol–gel · Yttrium-aluminium-iron garnet

Introduction

The garnet ferrites are the basis of materials for many high-technology devices for magneto-optical information storage [1], microwave, and memory applications [2], and recently they have found applications for instance in medicine and biology [3].

The general formula of ferrite garnets is $A_3B_5O_{12}$, where "A" is a rare-earth trivalent cation, or Y, and "B" is usually Fe^{3+}, Al^{3+}, etc. The crystal structure has cubic symmetry and is relatively complex. The unit cell is formed by eight formula units (160 atoms) and belongs to the space group O_h^{10}–$Ia3d$. In contrast to spinels, the O sublattice is not a close packed arrangement, and it can be described as a polyhedra combination. The O polyhedra define three kinds of cation site: dodecahedral (eight-fold), octahedral (six-fold) and tetrahedral (four-fold). Rare earths, "A", occupy the largest, dodecahedral sites, while "B" cations enter the octahedral and tetrahedral sites. The notation for the site occupancy is as follows: $\{A_3\}[B_2](B_3)O_{12}$, where { } denotes dodecahedral sites, also known as *c* sites. There are 24*c* sites in the unit cell; [ ] denotes octahedral sites, also designated as *a* sites, with 16*a* sites per unit cell; and ( ) means tetrahedral sites or *d* sites and there are 24*d* sites in each unit cell [4, 5].

The usual method for preparing YIG particles in micrometer range [6] or substituted YIG ones [7, 8] requires a long annealing time at high temperatures followed by a grinding operation, yielding large particles of several tens of micrometers. New methods to prepare submicron diameter YIG and doped YIG particles are the hydroxide coprecipitation [9] coprecipitation in microemulsion [10], metal alkoxides hydrolysis [11], glycothermal synthesis [12], glass-crystallization [13] or the citrate gel process [14].

In this paper, a new sol–gel auto-combustion method has been used to synthesize nanocrystalline aluminium doped yttrium-iron garnets. The synthesis process and

characterizations of nanocrystalline ferrite materials are reported.

Experimental

Materials

Aluminium doped yttrium-iron garnet powders were prepared by nitrate-citrate sol–gel auto-combustion method (NCSAM). The starting materials were $Y(NO_3)_3 \cdot 6H_2O$ (99.9%, Fluka), $Al(NO_3)_3 \cdot 9H_2O$ (p.a., Reanal, Hungary), $Fe(NO_3)_3 \cdot 9H_2O$ (> 97.0%, Fluka), $C_6H_8O_7 \cdot H_2O$ (p.a., Reanal, Hungary) and concentrated ammonia (25%, Reanal, Hungary).

Preparation

The stoichiometric amounts of yttrium, aluminium and iron nitrates were dissolved together in distilled water under continuous stirring for 15 min at room temperature. After this the suitable amount of citric acid was added, to obtain a fully transparent solution, followed by 30 min stirring at room temperature. The pH was adjusted to the value of 2 using concentrated ammonia solution. After stirring over 3 h, the intense green coloured solution was heated on a hot plate, until the 3/4 volume of the water evaporated, and the gelation occurred, resulting a viscous dark green gel, which was dried at 140 °C. During this process, the gel burnt in an auto-combustion manner to form a dun, fluffy, loose powder, which was further sintered at 1000 °C. Five samples were prepared, varying the aluminium content, namely $Y_3Al_{1.5}Fe_{3.5}O_{12}$ denoted as "A", $Y_3Al_{1.55}Fe_{3.45}O_{12}$ denoted as "B", $Y_3Al_{1.575}Fe_{3.425}O_{12}$ denoted as "C", $Y_3Al_{1.6}Fe_{3.4}O_{12}$ denoted as "D", and a pure, undoped yttrium aluminium garnet (YIG) $Y_3Fe_5O_{12}$ denoted as "E", as control material. Stoichiometry analysis of the heat treated powders was measured by inductively coupled plasma (ICP). The results were almost equal with the initial, theoretical calculated composition.

Characterization

Scanning Electron Microscopy (SEM). Scanning electron micrographs and analysis of the morphology of the samples was carried out on a JEOL JSM-6100 scanning electron microscope, with EDAX EDS, operated at 15 kV high voltage.

X-ray Diffraction Spectroscopy (XRD). XRD patterns of the heat treated samples were recorded in the region of $2\theta = 25$–$50°$, with a scanning speed of $0.06° \, min^{-1}$, on a Siemens Kristalloflex Diffraktometer D5000, using Cu K_α radiation.

Surface Area Measurement by BET. The specific surface area of the powders was determined by the single point BET method, using a gas mixture of 30% by molar volume nitrogen gas and 70% by molar volume helium, in a Micromeritics FLOWSORB II 2300, DESORB 2300 instrument. The samples were degassed at 150 °C, overnight. The measured powder weights were ~ 0.1 g.

Results and Discussion

The morphology of crystal grains of the Al doped yttrium-iron garnets, with different amounts of aluminium was studied by SEM and the results are shown in Fig. 1.

The powders were sintered for 4 h, at 1000 °C. The morphology of both powders shows a spongy-like structure, with larger pores in the case of the lower aluminium content (Fig. 1a) and smaller pore sizes in the case of the sample containing a higher content of doping cations (Fig. 1b). When the aluminium content increases not only

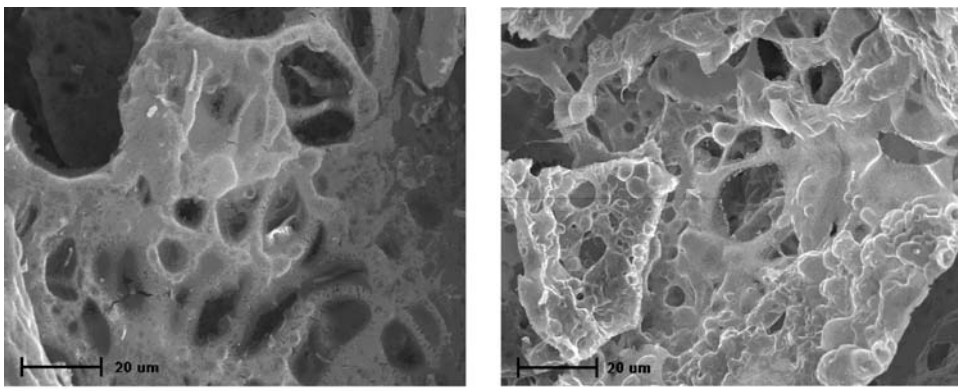

(a) $Y_3Fe_{3,5}Al_{1,5}O_{12}$ (*A*) (b) $Y_3Fe_{3,425}Al_{1,575}O_{12}$ (*C*)

Fig. 1 SEM micrographs of the $Y_3Al_xFe_{5-x}O_{12}$ samples, with $x = 1.5$ (**a**) and $x = 1.575$ (**b**)

the pore diameter will be changed, but number of the larger pores will be decreased too.

The X-ray diffraction (XRD) patterns in Fig. 2. show that $Y_3Al_xFe_{5-x}O_{12}$ oxides crystallizes in a cubic crystal with the unit cell dimension (a) between the values of 12.307 Å (belonging to the $Y_3AlFe_4O_{12}$ formula), and 12.237 Å respectively (belonging to the $Y_3Al_2Fe_3O_{12}$ garnet). Analyzing the figure, we can see, that pure garnet phase is present in the case of all four powders, with no other contaminating crystalline phases.

The BET surface areas of the $Y_3Al_xFe_{5-x}O_{12}$ powders measured using single point BET method are displayed in Table 1. Evaluating the results no significant difference can be observed and the values are relatively low for a highly porous structure, as observed in the SEM micrographs. This could be a consequence of the measurement inaccuracy, due to the too small quantity of the used powder (0.1 g).

Temperature dependence of ac magnetic permeability of the samples was measured by placing about 10 mg of sample powder into the coil of an audio frequency oscillator. The coil is part of a parallel resonator of an LC oscillator.

The frequency shift and oscillation amplitude were monitored as the temperature was swept at a rate of 0.5 K/min up to well above the expected Curie temperature. Temperature was measured and controlled by a Lake Shore Model 331 temperature controller with a standard 100 Ω platinum resistance thermometer. The frequency shift and amplitude reduction are directly proportional to the real and imaginary part of the magnetic permeability respectively. The arrangement is suitable to obtain the temperature dependence but no quantitative information was gained on the absolute values. Curie temperatures could be determined from the measured data. In addition some important features of the magnetic properties of the samples could be extracted from the measurements: the peaking up of the real part (Fig. 3) of ac susceptibility indicates some kind of 'melting' of the magnetic domains. From the point of view of medical applications the important magnetic characteristic is the temperature dependence of the energy absorption per cycle, which is contained in the temperature dependence of the imaginary component of the permeability (Fig. 4). Increasing the aluminium content of the doped garnets shifts the maximum of the curves to lower temperatures, so we can conclude, that modifying the amount of dopant cations, this also is changing the Curie temperature of the product.

Table 1 Specific surface area of the powders of $Y_3Al_xFe_{5-x}O_{12}$

X	1.5	1.55	1.575	1.6
S_{BET} (m^2g^{-1})	4.75	4.77	4.42	4.65

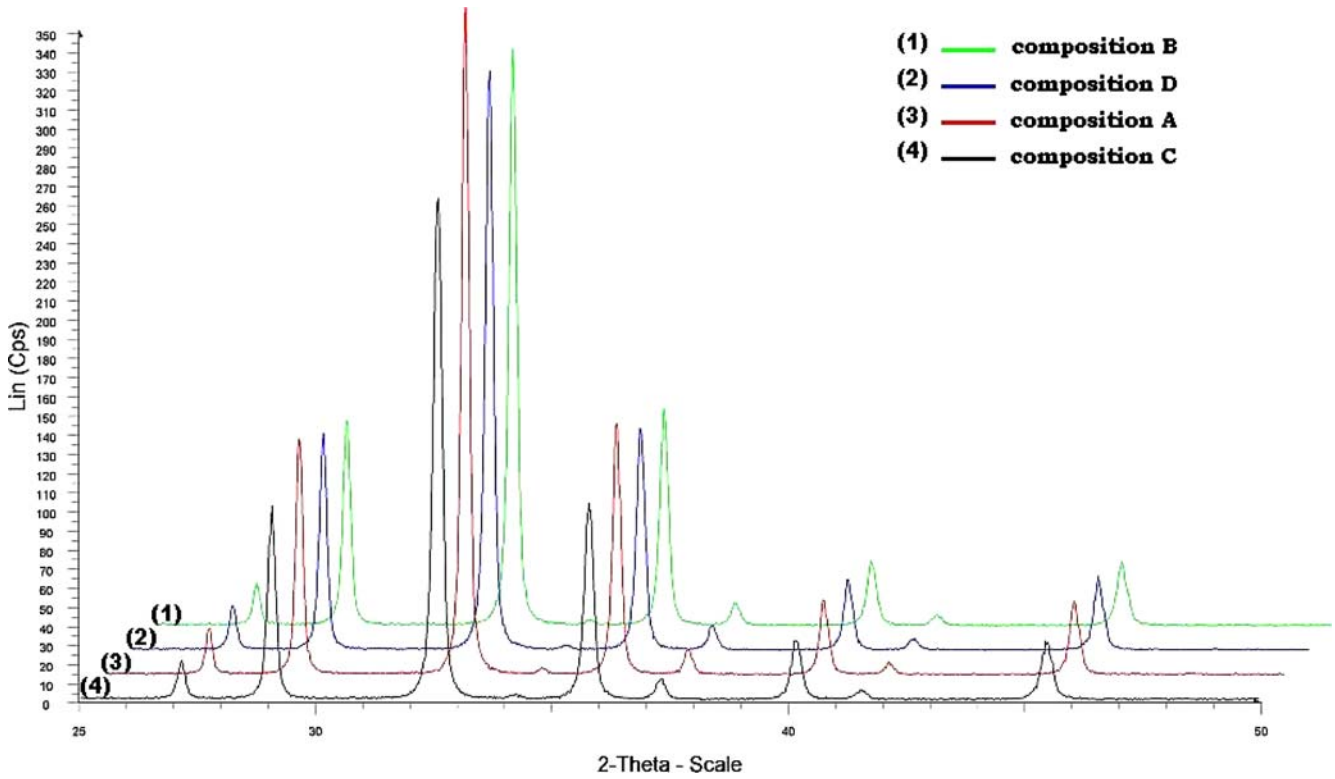

Fig. 2 XRD patterns of the four heat-treated doped garnets

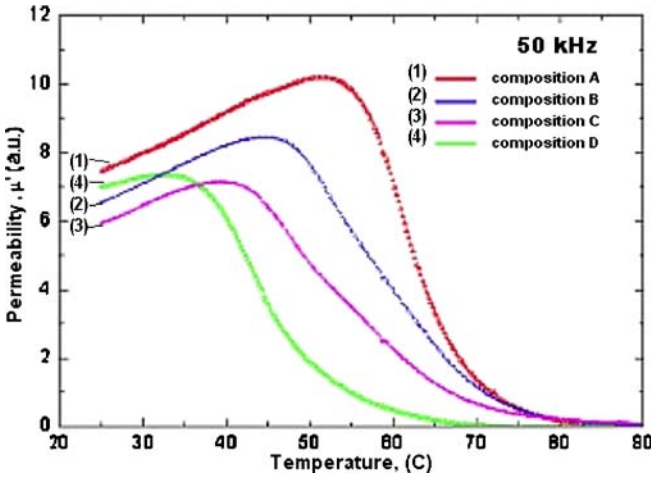

Fig. 3 Real part of the permeability

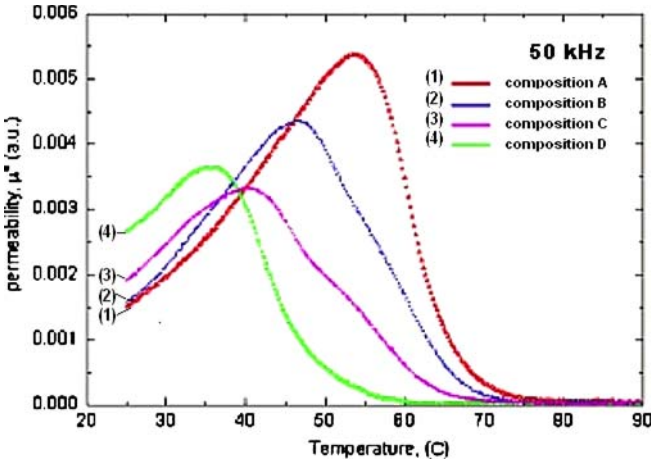

Fig. 4 Imaginary part of the permeability

Conclusion

A preparation process for aluminium doped yttrium iron garnets, based on the nitrate-citrate sol–gel autocombustion method (NCSAM) was successfully developed, and the formation of pure garnet phase during a 4 h sintering at 1000 °C has been demonstrated. The results of the magnetic measurements are showing that the samples may be good candidates of self-regulating magnetic heating substances. More quantitative measurements of magnetic properties are necessary to get data for this design in temperatures range: 35–55 °C.

Acknowledgement The authors are grateful to the financial support of NKFP 5-0006/2005 (MAGNESOM) project. Nikoletta Molnár wishes to thank to Titiana Segato (ULB, Brussels, Belgium) for the XRD measurements and for the fruitful discussions, for Patrizio Madau (ULB, Brussels, Belgium) for the SEM and BET measurements and for Prof. Marie Paule Delplancke-Ogletree (ULB, Brussels, Belgium) for the hospitality and the Excell FP6-NOE 515-703-2 project for support.

References

1. Taketomi S et al. (2000) J Magn Magn Mater 222:54
2. Wohlfahrt EP (ed) (1982) Ferro-Magnetic Materials, Vol 3. North-Holland Publishing Company, Amsterdam
3. Grasset F et al. (2001) J Magn Magn Mater 234:409–418
4. Smit J, Wijn HPJ (1959) Ferrites. Philips Technical Library
5. Raul V (2005) Chemistry of Solid State Materials. Cambridge University Press, Cambridge
6. Pauthenet R (1958) J Appl Phys 29:253
7. Miller CE (1961) J Phys Chem Solids 17:229
8. Vladikova D et al. (1996) Phys Stat Solidi A 156:461
9. Grosseau P et al. (1996) J Therm Anal 46:1633
10. Vaqueiro P et al. (1997) J Mater Chem 7:501
11. Taketomi S et al. (1993) J Magn Magn Mater 122:6
12. Inoue M et al. (1998) J Mater Chem 13:856
13. Bahadur D et al. (1982) J Mater Sci Lett 1:106
14. Vaqueiro P et al. (1997) Chem Mater 9:2836

Progr Colloid Polym Sci (2008) 135: 48–56
DOI 10.1007/2882_2008_116

Published online: 13 September 2008

Petar Dokić
Ljubica Dokić
Tamara Dapčević
Veljko Krstonošić

Colloid Characteristics and Emulsifying Properties of OSA Starches

Petar Dokić (✉)
Institute for Food Technology, University of Novi Sad, Bul. Cara Lazara 1, 21000 Novi Sad, Serbia
e-mail: petardok@uns.ns.ac.yu

Ljubica Dokić · Tamara Dapčević
Faculty of Technology, University of Novi Sad, Bul. Cara Lazara 1, 21000 Novi Sad, Serbia

Veljko Krstonošić
Faculty of Medicine, University of Novi Sad, Hajduk Veljkova 3, 21000 Novi Sad, Serbia

Abstract The objective of this paper was to characterize commercially available octenyl-succinate starches (OSA starches), Purity Gum 2000 and Hi-cap 100, by determining their viscous behaviour and characteristics and molecular mass, as well as to examine their emulsifying properties in corn oil-in-water emulsion system.

Huggins equation and extrapolation procedure were employed to determine intrinsic viscosity and Huggins constant of OSA starches in water, KOH and various electrolyte solutions, as well as in dimethylsulfoxide (*DMSO*). The viscosity-average molecular mass was calculated. Emulsifying properties were evaluated analysing the rheological behaviour, particle size distribution and creaming stability of the emulsions as a function of emulsification time, dispersed phase content, emulsifier concentration and combination with micro molecular emulsifier polyoxyethylene (20) sorbitan monooleate (Tween 80).

Intrinsic viscosities as well as molecular mass of Purity Gum 2000 were higher than ones determined for Hi-cap 100. Emulsions prepared with Purity Gum 2000, compared to those containing Hi-cap 100, had better stability and higher viscosity, which increased with the increase in dispersed phase and emulsifier concentration. The stability of the emulsions prepared combining OSA starches with surfactant Tween 80 was largely dependent of the emulsification time, while the emulsions stabilized only with OSA starches were not significantly influenced by this factor.

Keywords Emulsions · Octenylsuccinate starch · Rheology · Stability · Viscosity

Introduction

In addition to its value in human nutrition starch has been used for its functional properties in many industrial areas. That is way starch has been the subject of very intensive investigation for many years, probably to a greater extent than any other biopolymer [1].

Nowadays, the application of native starches is limited due to their process and storage instability. Recently, an increasing number of innovative modifications to starches have been developed to alter many aspects of starch performance [2, 3]. Since their development in 1940s, modified starches have become a leading class of ingredients that satisfy consumers demand for products containing naturally derived raw materials, but also with sophisticated performance [4].

Starch modification includes physical and chemical modification of native starch [5]. By chemical modifica-

tion, octenyl-succinate starches are produced by esterification of starch with anhydrous octenylsuccinic in aqueous suspension at pH 7.0–9.0. There are few papers available about preparative conditions [6–10]. Also, modification can be conducted in an organic medium. In that case the granules are ruptured, while during the reaction in aqueous medium the granular structure is maintained. Products from an organic medium did show an increase in activity with concentration, while for the products from aqueous medium the activity was largely independent of the concentration of the substrates. The molecular mass for products from organic medium seemed to be lower as suggested by viscometry [11].

By introduction of hydrophobic octenylsuccinate group the starch molecule acquires amphiphilic nature and thus surface-active properties. Measurements of interfacial tension prove that these octenyl-succinate starches, called OSA starches, are surface active substances [11, 12]. The main stabilizing mechanism is a steric hindrance [12].

OSA starches, have found varieties of applications in food, pharmaceutical [11, 13, 14], cosmetics and other industries as emulsifiers and stabilizing agents. They are used in the products such as flavour emulsions, salad dressings, body powders and lotions, as beverage clouding agents [15], and as flavours and fragrances encapsulating agents [16, 17]. It is a special advantage that OSA starches are cold water soluble. Also these starches are colourless and tasteless in solutions since most oral surfactants are bitter what can lead to problems like vomiting [11]. Other reasons for modifying starches are that they are readily available and thus can provide an economic advantage in applications where higher priced items such as gum arabic, casein and gelatine otherwise must be used. Also, OSA starches could be used as emulsifiers instead of egg yolk, providing cholesterol free products. Emulsifying properties of different OSA starches are already examined in suspensions [11], beverage emulsions [15] and even in water-in-oil emulsions (cosmetics) [18].

OSA starches are polyelectrolytes bearing charged groups such as free COO^- groups present in octenylsuccinic chain [19]. Such polyion chains undergo different conformations responding to change of environment, mainly the ionic strength and the solvent quality. When good solvent conditions are present, chains adopt extended, rigid conformations. In solvent referred as bad or "poor" solvent the conformation of chain is coil like in order to minimize the contact with solvent [20]. The quality of solvent can be monitored measuring the viscosity of solutions. Namely, the fact that OSA starches are water soluble is well known, but commercially available products are very complex, containing different salts and organic solvents, what can greatly modified expected properties of used macromolecular emulsifier and thus lead to often undesirable changes in product quality. So the investigation of the viscosity of OSA starches in other solutions is of great importance.

Commercially available OSA starches (Purity Gum 2000 and Hi-cap 100), used in this study, are known to be derived from waxy maize starch composed of nearly 100% amylopectin, so they can be considered as derivatives of amylopectin only but there is relatively little information about their properties.

One of the aims of this study was to investigate solubility of OSA starches in different solvents and determine solutions viscosities. Viscosity-average molecular mass was calculated for both samples.

Concentrated corn oil-in-water emulsions with OSA starches and with mixtures of OSA starch and Tween 80 as emulsifier were prepared in order to determine their emulsifying efficiency. Emulsifying properties were evaluated by rheological behaviour, particle size distribution and creaming stability of the emulsions as a function of emulsification time, dispersed phase content and emulsifier concentration.

Experimental

Materials

Octenyl succinate modified starches (E1450) – Purity Gum 2000 (PG 2000) and Hi-cap 100 (HC 100) were obtained from National starch and Chemical GmbH, Germany. Non-ionic surfactant polyoxyethylene (20) sorbitan monooleate (E433) – Tween 80 was purchased from J.T. Baker, Holland. For preparation of oil-in-water emulsions cold pressed corn oil ($\eta = 68$ m Pas, 20 °C; $\rho = 0.9231$ g/cm^3, 20 °C), purchased from local market, and double-distilled water were used. All chemicals were of reagent grade and were used as such.

Intrinsic Viscosity and Molecular Mass Determination

Viscosity measurements, using a Cannon capillary viscometer with suspended level, were performed. Water efflux time was 247.5 s at 20 °C. Temperature was kept constant at 20 ± 0.1 °C using a HAAKE thermostatic bath.

Stock solutions of OSA starches were prepared by dissolving 1.5 g in 100 cm^3 of proper solvent without heating. The following solvents were used: double-distilled water, 0.1% NaCl, 0.1% KCl, 0.1% $CaCl_2$, 2% NaCl, 2% $CaCl_2$ and dimethylsulfoxide (*DMSO*). Solutions of this concentration were used to prepare series of stock solutions dilutions of concentrations ranging from 0.3 to 1.5 g/cm^3. Viscosity measurements of OSA starch solutions were done immediately after preparation.

Viscometric parameters were determined by measuring the efflux time of seven concentrations of the samples solutions. All the measurements were done as triplicates and the average values were reported.

In order to calculate molecular mass, solutions of OSA starches were prepared in 1M KOH as solvent and measured at 35 °C since literature data [21] for constants K

and a used in Mark's variation of Staudinger's formula are given for this particular conditions.

Intrinsic viscosity $[\eta]$ was determined according to Huggins and Kraemer equations Eq. 1 and Eq. 2:

$$\frac{\eta_{sp}}{c} = [\eta] + k' [\eta]^2 c \quad (1)$$

$$\frac{\ln \eta_{rel}}{c} = [\eta] - k'' [\eta]^2 c \,, \quad (2)$$

where: $\eta_{rel} = t/t_0$ is relative viscosity or viscosity ratio (efflux time ratio between the solution, in a determined concentration, and the solvent); η_{sp} is specific viscosity ($\eta_{sp} = \eta_{rel} - 1$); k', k'' are Huggins and Kraemer coefficients, respectively and c is concentration of solution.

The viscosity-average molecular mass was calculated using the Mark's variation of Staudinger's formula Eq. 3:

$$[\eta] = KM^a \,, \quad (3)$$

where K and a are constants specific to the solvent and temperature used in the measurements.

Preparation of Emulsions

All emulsions were prepared by homogenizer Ultra-Turrax T25 basic (IKA-Werke, Germany) at 9500 rpm. The emulsification was achieved by shearing for 60 min at 30 °C, and samples for rheological measurements, creaming experiments and droplet size distribution were taken after 5, 10, 20, 40 and 60 min of homogenization. Corn oil-in-water emulsions with oil concentration 40, 50 and 60% (w/w) were stabilized using different emulsifiers. Continuous phase for emulsions from the first group were prepared by dissolving 3, 5, 10 and 20% (w/w, calculated on oil phase mass) of OSA starch (Purity Gum 2000 or Hi-cap 100) in cold double-distilled water, while the second group contained 3% (w/w) Tween 80 and 2% (w/w) OSA starch. Control emulsions were prepared with Tween 80 as surfactant following the same emulsification procedure.

Rheological Measurements

Rheological characteristics of emulsions and 30% solutions of OSA starches were measured by rotational viscometer HAAKE Rheo Strees 600 (Thermo Electron Corporation, Karlsruhe, Germany). All measurements were performed with cone-plate C60/1Ti sensor at 20 ± 0.1 °C. Continuous hysteresis loop tests were carried out. Shear rate continually increased form 0–500 s^{-1}, was kept constant at 500 s^{-1} and decreased to 0s^{-1}, 180 s was duration of each step. The obtained flow curves show shear thinning behaviour and can be presented by the Ostwald Reiner power law model Eq. 4:

$$\tau = K\dot{\gamma}^n \,, \quad (4)$$

where the coefficient K is the measure of consistency of the system and n is the flow behaviour index.

Emulsions Stability

For stability experiments emulsions were stored in 10 cm^3 graduated glass cylinders for 9 days at room temperature. Creaming of emulsion samples was monitored visually and the extent of creaming was characterized by the creaming index H, Eq. 5.

$$H = \frac{100 H_C}{H_E} (\%) \,, \quad (5)$$

where H_C is the volume of transparent serum layer at the bottom of the cylinder and H_E is the total volume of emulsion sample.

Obtained curves were fitted using a Boltzmann sigmoidal function of the form (Eq. 6):

$$y = \frac{A_1 - A_2}{1 + e^{(x - x_0)/\mathrm{d}x}} + A_2 \,, \quad (6)$$

where A_1 and A_2 are the initial values, left and right horizontal asymptote, respectively, x_0 is the centre of the fitted curve and dx is the gradient of the slope at x_0.

Particle Size Distribution

The emulsions prepared were polydisperse. The droplet size distribution was determined from microphotography, after 24 h. The surface area frequencies percent data were plotted against the particle diameter. Values for surface area frequencies were calculated using the Eq. 7:

$$f = \frac{n_i d_i^2}{\sum n_i d_i^2} \,, \quad (7)$$

where n_i is the number of droplets of d_i diameter.

The average droplet size was expressed as the volume-surface mean diameter (Sauter diameter) Eq. 8:

$$d_{vs} = \frac{\sum n_i d_i^3}{\sum n_i d_i^2} \,, \quad (8)$$

where n_i is the number of droplets of d_i diameter.

Results and Discussion

Comparison of Two Commercially Available OSA Starches – Purity Gum 2000 and Hi-cap 100

The results of intrinsic viscosities and Huggins constants for both OSA starches are given in Table 1. The values for intrinsic viscosity in water are in agreement with literature results [10]. The data indicated that *DMSO* is worse solvent for OSA starch than water, so in *DMSO* the conformation is more compact because of present association, while in water it is extended. The addition of electrolytes decreased the intrinsic viscosity, which indicated a reduction in the hydrodynamic size of the molecule since the

Table 1 Intrinsic viscosities and Huggins constants of OSA starches in different solvents at 20 °C

Solvent	Purity Gum 2000		Hi-cap 100	
	Intrinsic viscosity ($100\,cm^3/g$)	Huggins constant	Intrinsic viscosity ($100\,cm^3/g$)	Huggins constant
Water	0.2363	0.4248	0.1171	1.2864
0.1% NaCl	0.1496	0.6072	0.1105	1.3382
0.1% KCl	0.1556	0.5022	–	–
0.1% $CaCl_2$	0.1648	0.1337	–	–
2% NaCl	0.1540	0.3040	–	–
2% $CaCl_2$	0.1705	0.2523	–	–
DMSO	0.3175	0.5347	–	–

charge screening reduced the influence of electrostatic origin repulsion forces on the polymer conformation.

The Huggins parameter k' gives information about the solvent quality and formation of molecular aggregates. Huggins constants were calculated form Eq. 1 and the ones for the Purity Gum 2000 solutions were observed to be lower than for the solutions of Hi-cap 100 for the same solvent. Values between 0.3 and 0.7 have been suggested for perfect solutions, whereas values of $k' \geq 1$ would encourage aggregate formation. This indicated that macromolecules of Hi-cap 100 were more self-associated.

The intrinsic viscosities were also calculated in 1 M KOH (Fig. 1).

The obtained values were $[\eta] = 0.2568$ ($100\,cm^3/g$) for Purity Gum 2000 and $[\eta] = 0.1457$ ($100\,cm^3/g$) for Hi-cap 100 and that values were used for determination of their molecular mass. The calculation of constants K and a, using the literature available data for acetylated amylopectin fractions from the starches of various botanical origins is shown in Fig. 2 [21].

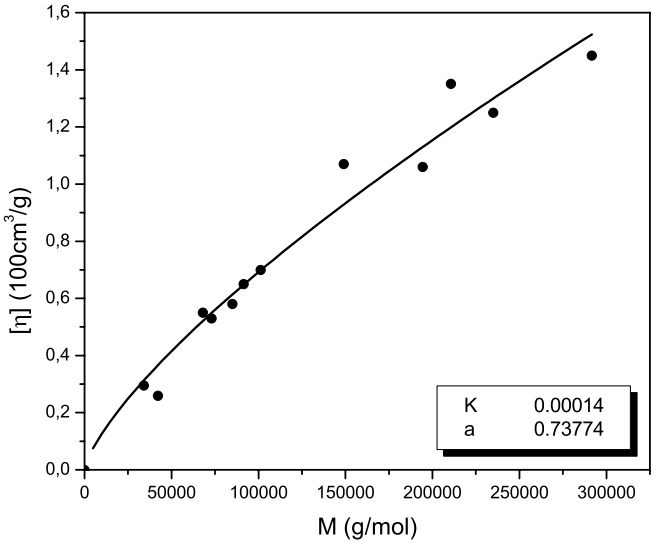

Fig. 2 Plot of intrinsic viscosity versus molecular mass for acetylated amylopectin fractions from the starches of various botanical origins

The values $K = 0.00014$ and $a = 0.73774$ were obtained by direct fitting of the experimental data using Mark's variation of Staudinger equation. According to these results molecular masses for Purity Gum 2000 and Hi-cap 100 were $M = 26\,521.64$ g/mol and $M = 12\,336.07$ g/mol, respectively.

The steady-shear behaviour of 30% solution of OSA starches is given in Fig. 3.

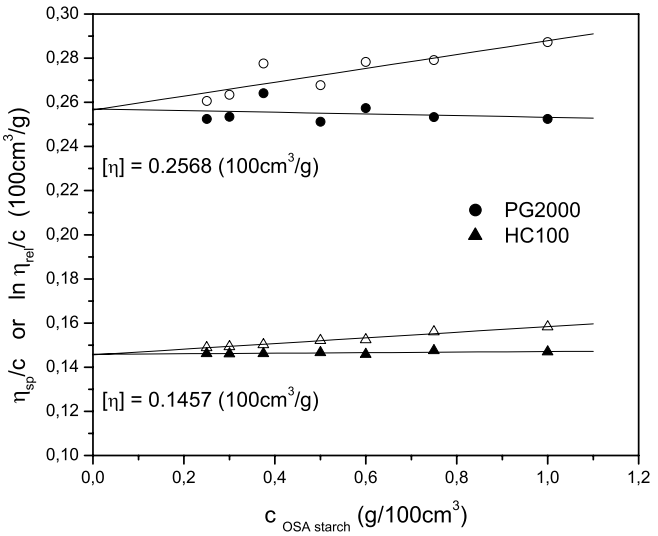

Fig. 1 Determination of intrinsic viscosity of OSA starches in 1 M KOH

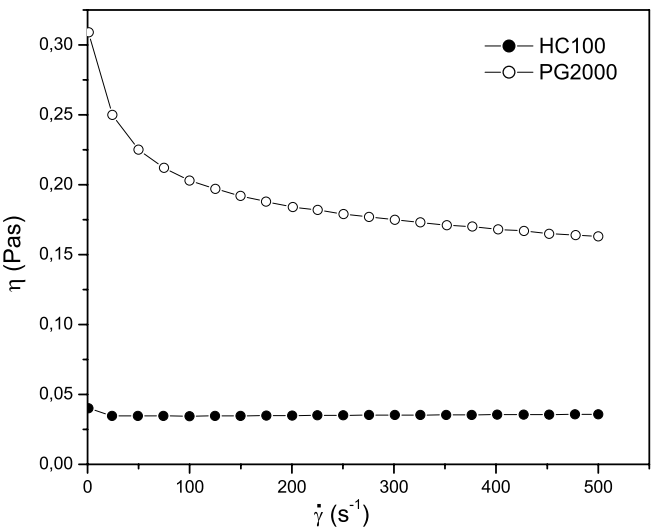

Fig. 3 Dependence of the viscosity on the shear rate for 30% solutions of OSA starches

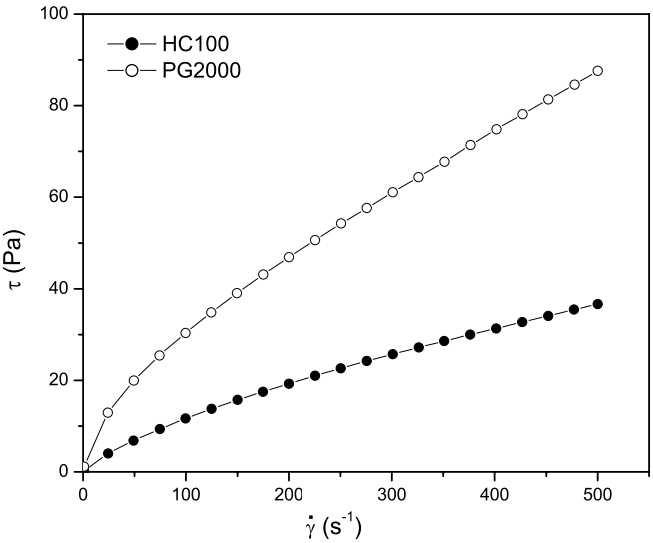

Fig. 4 Flow curves of 50% emulsions stabilized with 20% of different OSA starches

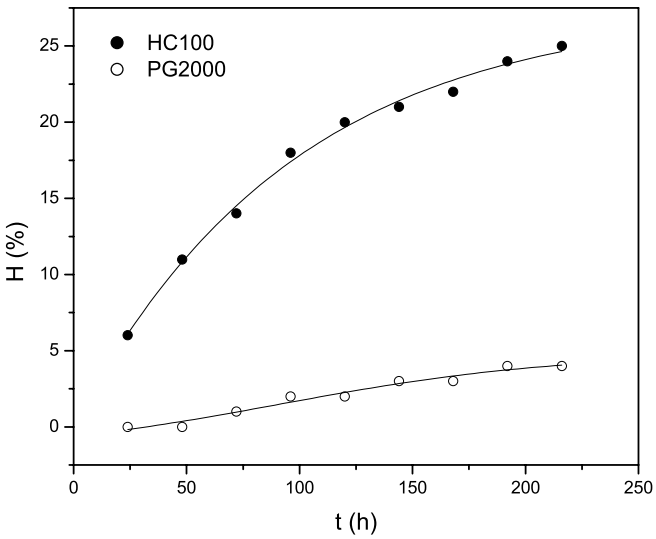

Fig. 5 Creaming index of 50% emulsions with 20% of OSA starch as a function of storage time

Both flow curves exhibited sheer thinning behaviour, but solution of Hi-cap 100 was less viscous which is in agreement with values of calculated molecular mass obtained using the capillary viscometer.

To determine the influence of the OSA starch type on the emulsification process, flow behaviour (Fig. 4), stability (Fig. 5) and particle size measurements of 50% emulsions containing 20% of OSA starches homogenized for 20 min were carried out.

Emulsions exhibited sheer thinning behaviour, which means the addition of oil did not cause changes in flow types, which remained the same as one of continuous phases. Emulsions with Purity Gum 2000 had better stability, shown on Fig. 5 as creaming index. They almost did not cream during the observed time. As for the emulsions stabilized with Hi-cap 100 rapid separation of the cream phase took place at the early stage and then, the creaming process became slower.

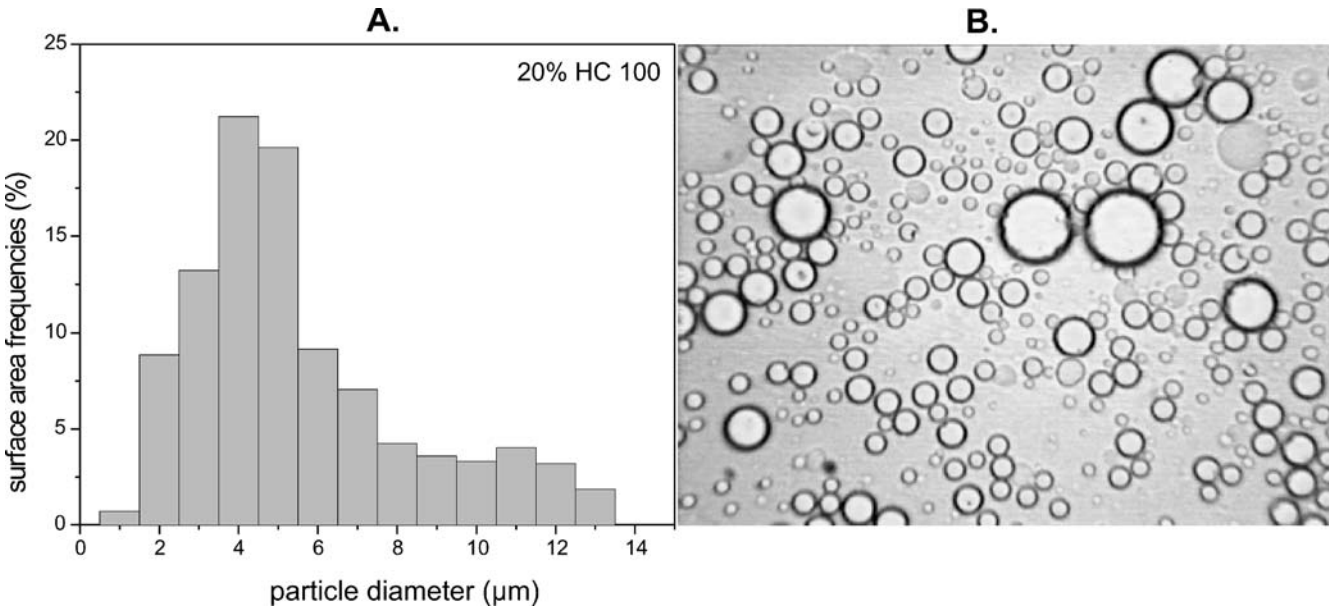

Fig. 6 Particle size distribution (**A**) and microphotography (**B**) for 50% emulsion with 20% of Hi-cap 100

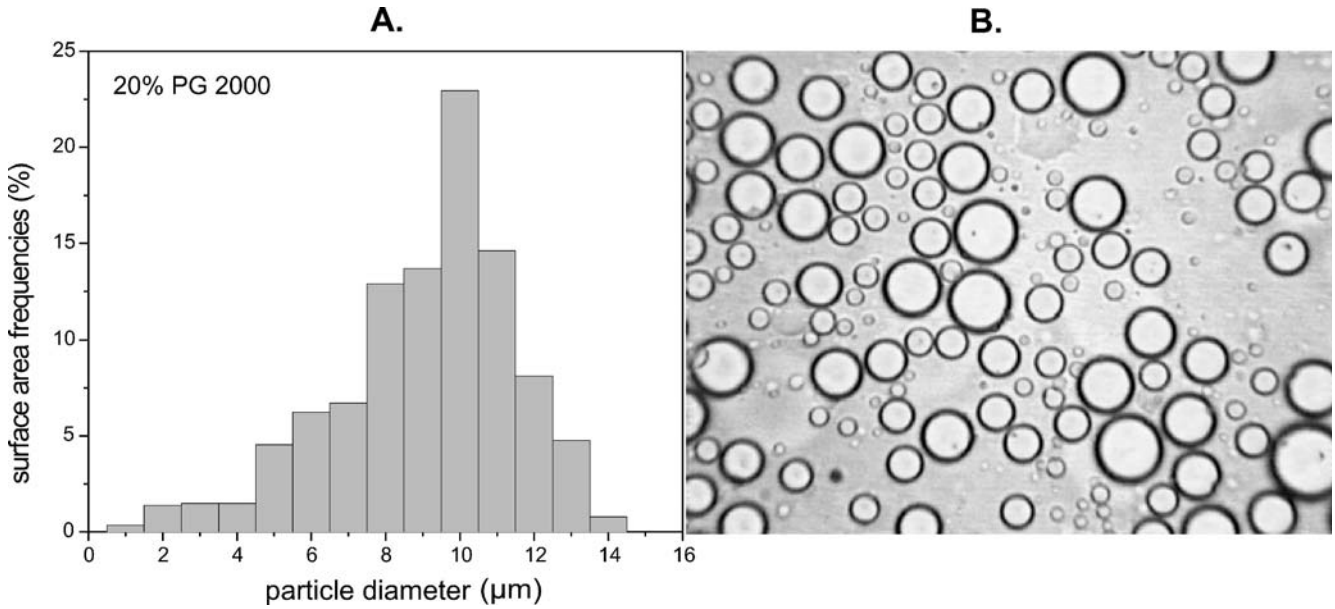

Fig. 7 Particle size distribution (**A**) and microphotography (**B**) for 50% emulsion with 20% of Purity Gum 2000

The particle size distributions and microphotographs of emulsions containing 20% of Hi-cap 100 and Purity Gum 2000 are shown in Figs. 6 and 7, respectively. The surface area frequencies percent data were plotted against the particle diameter. Average droplets sizes for emulsions with Purity Gum 2000 and Hi-cap 100 were $d_{vs} = 9.1\ \mu m$ and $5.5\ \mu m$, respectively, what indicated that increasing in emulsions stability was governed by increasing in the length of starch molecule chain and not by decreasing in particle diameter.

The most predominant diameters for emulsions with Hi-cap 100 were 4–5 μm (40.8%) and for emulsions with Purity Gum 2000 was 10 μm (22.9%).

Influence of Emulsifier Concentration and Dispersed Phase

Influence of emulsifier concentration on shear stress values at shear rate $500\ s^{-1}$ and stability is given at Fig. 8.

Shear stress at shear rate $\dot{\gamma} = 500\ s^{-1}$ and the stability of emulsions increased with increasing concentration of OSA starch. As concentration of emulsifier increased from 3 to 20%, changes both in shear stress and stability were more asserted for higher concentrations of OSA starch. The results for Hi-cap 100 were alike.

Figure 9 presents the influence of dispersed phase content on emulsion stability and values of shear stress obtained at shear rate $\dot{\gamma} = 500\ s^{-1}$.

Increasing in oil concentration increased both stability and shear stress what is related to more tightly packed oil droplets in concentrated systems. The results for Purity Gum 2000 were alike. These results are in an agreement with results given in literature for beverage cloud coconut oil-in-water emulsions [15].

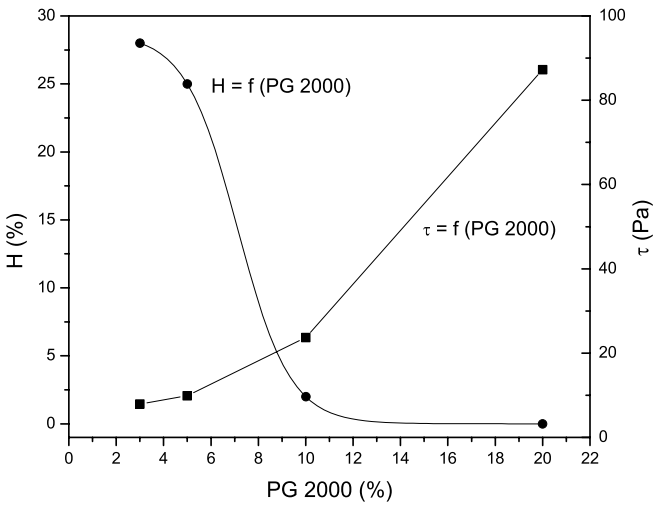

Fig. 8 Values of creaming index and shear stress ($\dot{\gamma} = 500\ s^{-1}$) of 50% emulsions with Purity Gum 2000 homogenized 60 min as a function of OSA starch concentration

Comparison of Emulsion with OSA Starch with Emulsions with Tween 80 and Their Combination

Verification of modified starches ability to stabilize the emulsions was done by comparing properties of samples prepared with Purity Gum 2000, Hi-cap 100, Tween 80 and mixtures of OSA starch and Tween 80.

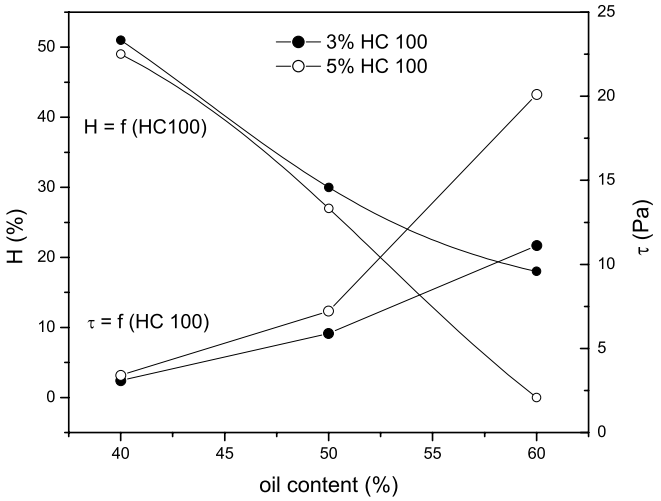

Fig. 9 Values of creaming index and shear stress of 50% emulsions with 3 and 5% Hi-cap 100 homogenized 60 min as a function of dispersed phase content

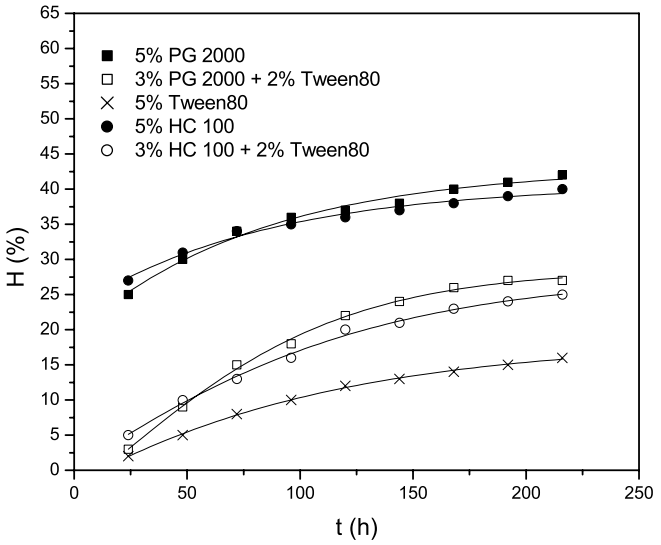

Fig. 10 Effect of different emulsifiers on creaming rate of 50% emulsions homogenized 20 min

Emulsions prepared using the starch system showed higher values of creaming index (Fig. 10) and volume-surface mean diameter (Table 2) than those with Tween 80, while emulsions containing both emulsifiers (Tween 80 and OSA starch) showed same properties as those with Tween 80. This indicated that the more surface-active Tween 80 [12] competitively displaced the larger starch macromolecules between droplets what led to increase in viscosity of continuous phase, and the viscosity of whole system (Fig. 11).

This presumption is supported by the values of parameters of power-law equation, K and n, which are listed in Table 2. Emulsions with OSA starches had higher consistency coefficient, K than emulsions with Tween 80. Also

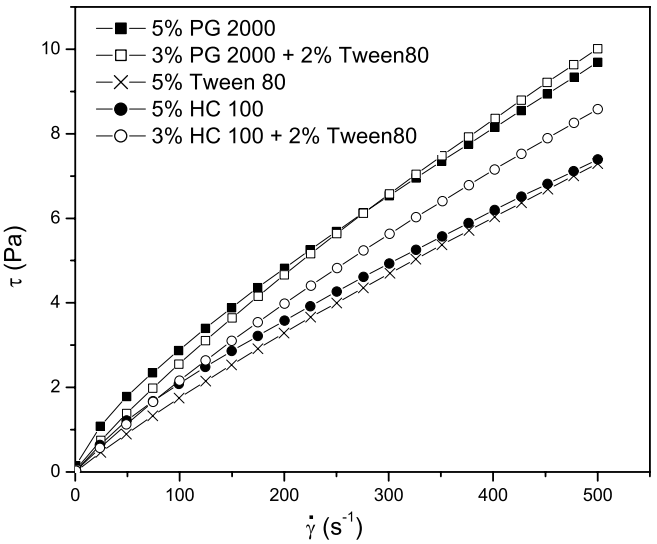

Fig. 11 Flow curves of 50% emulsions stabilized with different emulsifiers homogenized 20 min

Table 2 Droplets mean diameters d_{vs} and parameters of flow curves for emulsions with 50% of oil

Emulsifier	d_{vs} (μm)	K	n
5% Purity Gum 2000	27.75	0.0914	0.7492
3% Purity Gum 2000 + 2% Tween 80	5.26	0.0538	0.8417
5% Tween 80	5.23	0.0308	0.8801
5% Hi-cap 100	17.37	0.0555	0.7868
3% Hi-cap 100 + 2% Tween 80	6.16	0.0437	0.8504

they had lower values of the degree of non-Newtonian behaviour, n what indicate that the shear thinning behaviour was more pronounced. The results for emulsions containing both Tween 80 and OSA starch were alike to those containing only Tween 80.

Influence of Emulsification Time

It is evident from Fig. 12 that the changes in emulsion stability with emulsification time were more pronounced in the emulsions containing Tween 80 and combination of emulsifiers (Tween 80 and OSA starch), indicating that after the optimal homogenization time (20 min) the pre-emulsification effect occurred.

Results present in Fig. 13 which shows the influence of emulsification time on droplet diameter were in accordance with those in Fig. 12.

Although the effect of increase in droplet size is present even in the case of emulsions containing only Tween 80, it

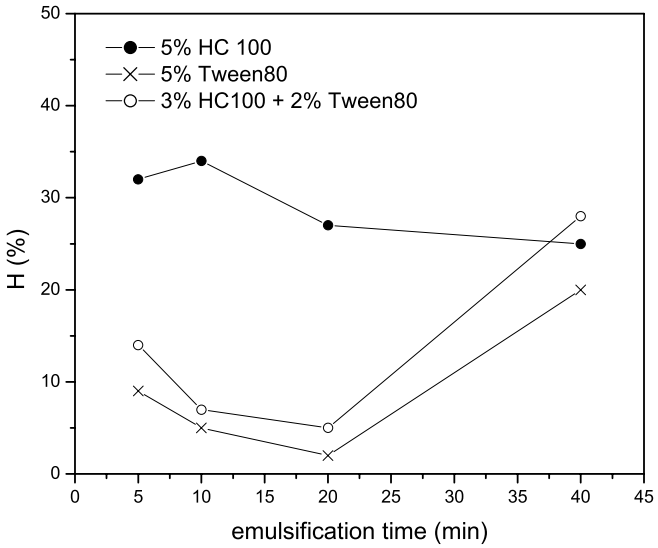

Fig. 12 Creaming index of 50% emulsions with different emulsifiers as a function of emulsification time

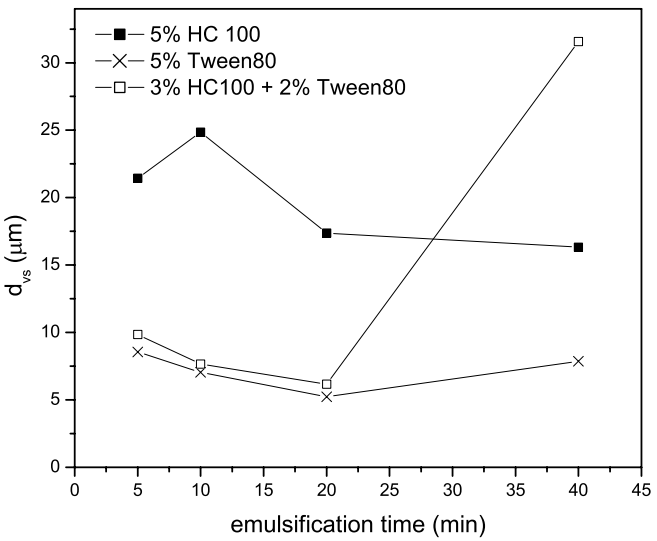

Fig. 13 Droplets mean diameter of 50% emulsions with different emulsifiers as a function of emulsification time

is more pronounced in emulsions containing both emulsifiers, while in emulsions stabilized only with OSA starch it does not occur. Specific increase in droplet size after 20 min of emulsification, for emulsions containing the combination of two emulsifiers, requires further studies.

Conclusion

Both OSA starches even thought derivatives of waxy-maize starch differ in viscosity of their solutions. Intrinsic viscosity measurements and calculated Huggins constants in different solvents showed that their conformations changed from extended in water as solvent to coil like in organic solvent such as dimethylsulfoxide. Determined values for the viscosity-average molecular mass for Purity Gum 2000 and Hi-cap 100 were $M = 26\,521.64$ g/mol and $M = 12\,336.07$ g/mol, respectively. This difference influenced their behavior as emulsifying agents. Emulsions containing Purity Gum 2000 were more viscous and stable, but had droplets with higher volume-surface mean diameter, than those with Hi-cap 100 which indicated that their better stability was governed by increasing in viscosity of their continuous phase. Increasing in oil and emulsifier concentration increased both stability and viscosity, especially in the range of high concentrations. Changes in values of creaming index, volume-surface mean diameter and parameters of power-law equation, K and n, for emulsion containing combination of OSA starch and Tween 80 in comparison with emulsions containing only OSA starches showed that there was competition between emulsifiers in the absorption layer around oil droplets. The more surface-active Tween 80 competitively displaced the larger OSA starch macromolecules. Also, stability and values of droplet size of the emulsions prepared combining OSA starches with micro molecular surfactant Tween 80 were largely dependent of the emulsification time, while the emulsions stabilized only with OSA starches were not significantly influenced by this factor. All the fluctuated factors (emulsification time, dispersed phase content, emulsifier concentration and combination with micro molecular emulsifier, such as Tween 80) did not influence on the flow type which remains shear thinning. These experiments suggest that even small changes in composition of system can lead to significant changes in its properties.

Acknowledgement This work was financially supported by the Ministry of Science of the Republic of Serbia.

References

1. Banks W, Greenwood CT (1975) Starch and its Components. Edinburgh University Press, Edinburgh, p 1
2. Light JM (1989) Modified Food Starches: Why, What, Where and How. Symposium on Modified Food Starches at AACC's, 74th Annual Meeting in Washington, DC, October 29–November 2
3. Dokić-Baucal L, Dokić P, Jakovljević J (2004) Influence of different maltodextrins on properties of O/W emulsions. Food Hydrocolloids 18:233–239

4. Daniels R (2001), Galenic Principles of Modern Skin Care Products, Issue 25. Skin Care Forum
5. Thomas DJ, Atwell WA (1999) Starches. Eagan Press, St. Paul, pp 35–36
6. Bao J, Xing J, Phillips DL, Corke H (2003) Physical Properties of Octenyl Succinic Anhydride Modified Rice, Wheat and Potato Starches. J Agric Food Chem 51:2283–2287
7. Song X, He G, Ruan H, Chen Q (2006) Preparation and Properties of Octenyl Succinic Anhydride Modified Early Indica Rice Starch. Starch/Stärke 58:109–117
8. Viswanathan A (1999) Effect of Degree of Substitution of Octenyl Succinate Starch on the Emulsification Activity on Different Oil Phases. J Environ Polym Degrad 7(4):191–196
9. Park S, Chung MG, Byoungseung Y (2004) Effect of Octenylsuccinylation on Rheological Properties of Corn Starch Pastes. Starch/Stärke 56:399–406
10. Shogren R, Biresaw G (2007) Surface properties of water soluble maltodextrin, starch acetates and starch acetates/alkenylsuccinates. Colloids Surf A Physicochem Eng Aspects 298:170–176
11. Kuentz M, Egloff P, Röthlisberger D (2006) A technical feasibility study of surfactant-free drug suspensions using octenyl succinate-modified starches. Eur J Pharm Biopharm 63:37–43
12. Tesch S, Gerhards C, Schubert H (2002) Stabilization of emulsions by OSA starches. J Food Eng 54:167–174
13. Baydoun L, Furrer P, Gurny R, Müller-Goymann CC (2004) New surface-active polymers for ophtalmic formulations: evaluation of ocular tolerance. Eur J Pharm Biopharm 58:169–175
14. Heacock PM, Hertzler SR, Wolf B (2004) The glycemic, inulinemic, and breath hydrogen responses in humans to a food starch esterified by 1-octenyl succinic anhydride. Nutrition Res 24:581–592
15. Taherian AR, Fustier P, Ramaswamy HS (2006) Effect of added oil and modified starch on rheological properties, droplet size distribution, opacity and stability of beverage cloud emulsions. J Food Eng 77:687–696
16. Spicer PT, Small WB, Lynch ML, Burns JL (2002) Dry powder precursors of cubic liquid crystalline nanoparticles (cubosomes). J Nanoparticle Res 4:297–311
17. Loksuwan J (2007) Characteristics of microencapsulated β-carotene formed by spray drying with modified tapioca starch, native tapioca starch and maltodextrin. Food Hydrocolloids 21:928–935
18. Carey JM, Law MR, Marks GP (2000) Improved high internal phase emulsions using alkenyl succinic anhydride based emulsifiers. Proceedings, CESIO 5th World Surfactants Congress, Florence, Italy, May 29–June 2, Vol 2, pp 883–888
19. Shih FF, Daigle KW (2003) Gelatinization and pasting properties of rice starch modified with 2-octen-1-ylsuccinic anhydride. Nahrung/Food 47(1):64–67
20. Bordi F, Cametti C, Gili T, Sennato S, Zuzzi S, Dou S, Colby RH (2005) Solvent quality influence on the dielectric properties of polyelectrolyte solutions: A scaling approach. Phys Rev E 72:031806(10)
21. Kerr RW, Cleveland FC, Katzbeck WJ (1951) The Molecular Magnitude of Amylopectin. J Am Chem Soc 73:111–117

Progr Colloid Polym Sci (2008) 135: 57–64
DOI 10.1007/2882_2008_103

Published online: 11 September 2008

Árpád Figyelmesi
Béla Pukánszky Jr.
Kristóf Bagdi
Zsuzsa Tóvölgyi
József Varga
Lajos Botz
Stephan Hudak
Tamás Dóczi
Béla Pukánszky

Preparation and Characterization of Barium Sulfate Particles as Contrast Materials for Surgery

Árpád Figyelmesi · Béla Pukánszky Jr. · Kristóf Bagdi · József Varga · Béla Pukánszky (✉)
Laboratory of Plastics and Rubber Technology, Department of Physical Chemistry and Materials Science, Budapest University of Technology and Economics, P.O. 91, 1521 Budapest, Hungary
e-mail: bpukanszky@mail.bme.hu

Árpád Figyelmesi · Béla Pukánszky Jr. · Kristóf Bagdi · Béla Pukánszky
Institute of Materials and Environmental Chemistry, Chemical Research Center, Hungarian Academy of Sciences, P.O. 17, 1525 Budapest, Hungary

Zsuzsa Tóvölgyi · Lajos Botz
Department of Pharmaceutics and University Pharmacy, Medical School, University of Pécs, P.O. 99, 7601 Pécs, Hungary

Stephan Hudak · Tamás Dóczi
Department of Neurosurgery, Medical School, University of Pécs, P.O. 99, 7601 Pécs, Hungary

Abstract Barium sulfate particles were prepared from $BaCl_2$ and Na_2SO_4 under various conditions to explore their potential application as contrast material in endovascular surgery. Ethanol was added for the stabilization of the suspension obtained. Particle characteristics of the samples were determined by SEM and light scattering, while the stability of the suspensions was characterized by sedimentation experiments. Particle characteristics were shown to depend very much on reaction conditions. Particles were obtained in spherical and plate like shape and in a variety of sizes. Primary particles of nanometer size formed aggregates in most cases. Some of the samples had bimodal particle size distribution. Particle characteristics determined from SEM micrographs, by laser light scattering measurements and calculated from sedimentation experiments often differed from each other. The discrepancy could be explained by the dissimilar behavior of various fractions and the different sensitivity of the measurements to them. Some of the samples showed aging phenomena in DMSO leading either to the formation of larger particles or to the break down of aggregates.

Keywords Barium sulfate · Contrast · Embolization · Particle characterization · Sedimentation

Introduction

Acute problems can originate from the formation of aneurysms or arterio-venosus malformations (vein tumors) in the blood vessels. The walls of the vessels become weak at certain places and the burst of the veins may result in bleeding. Such malformations can form anywhere in the body, but they are extremely dangerous in the brain. 50% of the patients who have a bleeding (stroke) do not survive, and even in the case of a successful treatment there is a high chance of permanent brain damage [1–3]. The early way to prevent bleeding in these cases was open surgery, which was extremely dangerous and showed high mortality rate [4, 5]. Aneurysm and artero-venous malformations are treated more and more frequently by endovascular techniques [6–9]. These methods, in which

the treatment takes place directly in the blood vessel, show better results than micro-neurosurgical methods. Micro balloons and spirals are frequently applied [10–13], but liquid embolizing agents are the newest materials used for the treatment [14, 15]. These are less invasive than earlier methods and result in very high recovery ratios, but appropriate contrast is needed to carry out the operation [16–19].

Several contrast materials are used in medical practice. The degree of contrast and the suitability of a material for surgical purposes depend on its electron density [20–22] and on the stability of the suspension. Gold, tantalum and barium sulfate ($BaSO_4$) are added the most frequently to improve contrast in the body during endovascular surgery [20, 23–25]. Gold is extremely expensive, while a larger amount of $BaSO_4$ is needed in order to achieve the necessary contrast. Barium sulfate suspension in water is the universal contrast medium used also for the examination of the upper gastrointestinal tract [26]. However, a simple barium sulfate/water mixture has several undesirable properties including the tendency to sediment. $BaSO_4$ particles are also the principal additive used to adjust the density of drilling mud for controlling the pressure gradients in drilling operations, where it is very important to avoid it completely [27]. Flocculation and sedimentation of suspended solids in a liquid phase are one of the most central problems in colloid science. A number of studies have been devoted to the understanding of the stability of colloidal suspensions and especially on aggregation [28–32] or settling phenomena [33] from a fundamental point of view. Information on particle size, packing density and the mechanism of settling for both flocculated and deflocculated systems have been discussed by several authors [34–36]. Different approaches have been proposed to describe the settling process; some of them extend the hydrodynamic calculations developed for macroscopic particles to flocculated suspensions. Accordingly, the stability of the suspension is determined by particle size and density, and by the viscosity of the dispersion [37, 38]. The contrast materials available in the open market come in various particle sizes. The stability of the suspension prepared with them is very often not sufficient; the particles frequently separate from the dispersion by sedimentation. Separation of the contrast material in the body is very dangerous, since the operation cannot be safely completed; the contrast material may block the arteries and cause damage [39–41]. The proper adjustment of the above mentioned factors, i.e. electron density, particle characteristics, solution viscosity and density, may result in more efficient contrast materials than those available presently.

The goal of our research was to explore the possibility of finding efficient and economically viable materials for contrasting purposes. We also wanted to investigate the effect of the main factors on contrast and dispersion stability. Since gold and tantalum are very expensive and $BaSO_4$ is also used in medical practice, we decided to prepare such particles under different conditions and to characterize them with various methods. In this report we discuss the effect of reaction conditions on particle characteristics and on the stability of suspensions.

Experimental

In this study $BaSO_4$ particles were prepared from solution by mixing barium chloride (99.0%, Spektrum 3D, Hungary) and sodium sulfate (99.5%, Reanal, Hungary). The reagents were used as received. The reaction was carried out under various conditions; we changed the concentration of the solutions, reaction temperature, the order and way of mixing. The solution of the reactants was either put into dropping funnels or into the collection beaker in which the reaction took place. The conditions of the reactions are summarized in Table 1. Ethanol (96%, Spektrum

Table 1 The conditions of the preparation of $BaSO_4$ particles for contrasting purposes

Sample	T (°C)	c_{sol}^{a} (mol/dm^3)	Beaker[b]	Funnel 1[b]	Funnel 2[b]	EtOH[c]
B1	30	1.00	–	$BaCl_2$	Na_2SO_4	After
B2	30	1.00	$BaCl_2$	–	Na_2SO_4	After
B3	30	1.00	Na_2SO_4	$BaCl_2$	–	After
B4	30	1.00	–	$BaCl_2$	Na_2SO_4	–
B5	30	0.10	–	$BaCl_2$	Na_2SO_4	After
B6	30	0.01	–	$BaCl_2$	Na_2SO_4	After
B7	50	1.00	–	$BaCl_2$	Na_2SO_4	After
B8	10	1.00	–	$BaCl_2$	Na_2SO_4	After
B9	30	1.00	–	$BaCl_2$	Na_2SO_4	Before

[a] concentration of the $BaCl_2$ and Na_2SO_4 solutions
[b] content of the beaker and the funnels before the reaction
[c] conditions of the addition of ethanol

3D, Hungary) was added to the suspension in order to prevent aging either at the beginning (before) or at the end (after) of the reaction (see last column of Table 1). Always 50 ml was used from both reactants and the suspension was stabilized with 100 ml ethanol. Altogether 9 samples were prepared and characterized in this study.

Since we found that the dried particles cannot be resuspended again for further study, we used solvent exchange to transfer the particles from water to other suspension liquids. The solid particles were separated in a centrifuge, water was removed from the upper phase and it was exchanged to the required solvent. Separation in the centrifuge did not change the morphology of the particles in any visible way and they could be easily resuspended after separation. The particles were suspended in the new solvent by vigorous stirring and then separated again. Solvent exchange was repeated three times in order to achieve perfect exchange of the solvent. Even a superficial visual inspection indicated significant differences among the prepared particles; the sample prepared without ethanol could be resuspended much easier than the others. Commercial barium sulfate particles were used as reference contrast materials; one is offered specifically for medical purposes (BR1), while the other, a general purpose sample, was purchased from Aldrich (BR2).

The size of the particles was determined by scanning electron microscopy (SEM) and laser light scattering. 1 g material was suspended in 100 ml ethanol for SEM. One droplet was placed on a sample holder, the solvent was evaporated and the particles were coated with gold. Micrographs were taken with a JEOL JSM-6380 apparatus. Dynamic laser light scattering measurements were done using a Brookhaven BI 9000 apparatus at 90° scattering angle in ethanol and DMSO, the solvents used in endovascular surgery. The concentration of the suspension was 0.1 g/100 ml and the suspension was treated with ultrasound for 10 min before the measurement. The sedimentation of the particles was studied by recording the movement of the sedimentation front. The initial rate of sedimentation and the sedimentation volume were used for their characterization. 1 g material was suspended in 10 ml solvent in a closed graduated cylinder and the suspension was shaken vigorously for 5 min before the measurement. The movement of the sedimentation front was followed by a camera, visualized with the Vision GS software, recorded by Bulent's Screen Recorder and evaluated by the BSR Movie Lab software. Sedimentation was studied in water, ethanol and DMSO.

Results and Discussion

The results of the measurements are presented in three sections. First we describe the size and shape of the particles and the effect of reaction conditions on them. Then we discuss the results of the light scattering measurements and finally the stability of the suspensions, which is extremely important from the medical point of view.

Particle Size and Shape

The particle size and shape of the contrast material strongly influences the stability of the suspensions. As mentioned before, different reaction conditions resulted in various particle sizes and shapes. A few examples are shown in Fig. 1. The reference samples (BR1, BR2) are also included for

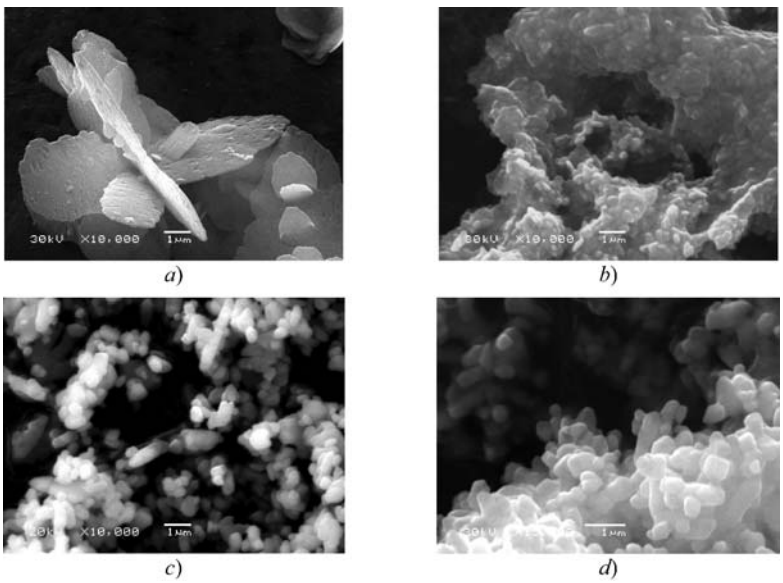

Fig. 1 Size and shape of selected $BaSO_4$ samples; **a** B3, **b** B6, **c** medical grade (BR1), **d** general purpose (BR2)

Table 2 Particle size and shape of the prepared $BaSO_4$ particles determined by various methods

Sample	Shape	Particle size (μm)		
		SEM	Light scattering measured in	
			EtOH	DMSO
BR1	Sphere	0.7	1.49 ± 0.19	1.12 ± 0.55
BR2	Sphere	0.5	1.15 ± 0.17	1.71 ± 0.86
B1	Sphere	0.1	–	1.97 ± 1.56
B2	Sphere	0.1	–	0.43 ± 0.43
B3	Plate	10.0	0.74 ± 0.42	1.06 ± 0.45
B4	Sphere	0.2	0.45 ± 0.05	0.35 ± 0.15
B5	Sphere	0.3	0.61 ± 0.14	–
B6	Ellipsoid	0.5	–	–
B7	Sphere	0.2	–	0.75 ± 0.55
B8	Sphere	0.1	–	0.42 ± 0.24
B9	Sphere	0.2	–	0.19 ± 0.07

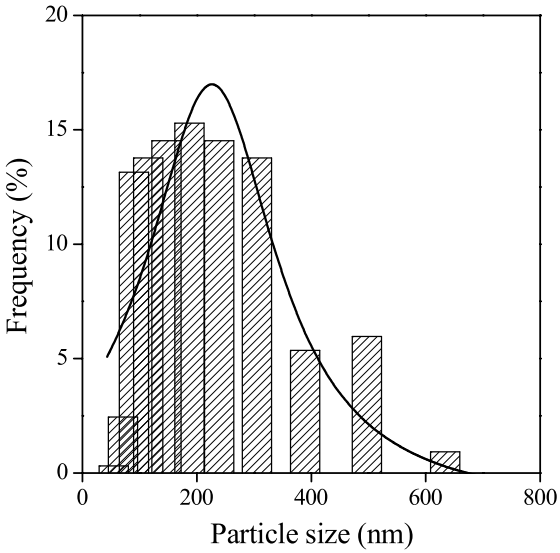

Fig. 2 Particle size distribution of sample B8 determined by laser light scattering in DMSO

comparison. The size and shape of both the particles and the aggregates differ significantly from each other. Sample B3 deviates considerably from the other particles prepared; it has a plate-like geometry (Fig. 1a), while all the others possess more or less spherical shape (see Fig. 1b). The main difference here is the drop-wise addition of $BaCl_2$ into Na_2SO_4, while in all other experiments the two solutions were introduced to the collecting vessel simultaneously or sodium sulfate was added to barium chloride. The large size and plate-like shape of the particles must influence sedimentation rate and the stability of the suspension. The primary particles of the medical grade $BaSO_4$ (BR1) are also spherical, just like those of the commercial product purchased from Aldrich (BR2) (Fig. 1c and d, respectively). Most of the products form large aggregates consisting of smaller primary particles (see Fig. 1b).

The characteristic size of the primary particles, as well as their shape were determined by SEM and the results are listed in Table 2. Aggregates were not considered in this evaluation. As mentioned above, most of the particles have spherical shape. The size of the primary particles is always below 1 micron, but they form aggregates of different sizes. The estimation of aggregate size is very difficult from the micrographs, although they determine the sedimentation characteristics and stability of the dispersions. Since simple visual inspection and semi-quantitative characterization of the particles do not give any information about the behavior of the suspensions, further characterization was carried out by methods which offer information about the behavior of the samples in bulk.

Particle Size Distribution

The size distribution of the particles was determined by laser light scattering in DMSO and ethanol. The measurements could not be carried out in all cases, either because the size of the particles was outside the range of the equipment (4 μm) or because the particles and/or aggregates sedimented too fast. This latter happened especially frequently in ethanol, since both the viscosity and the density of this solvent are small compared to our other solvent, DMSO. A typical particle size distribution is presented in Fig. 2. The continuous line was created by fitting a Gausian function to the experimental data. The distribution range is relatively wide from 50 to 650 nm. On the other hand, the average particle size is still rather small especially if we compare it to that of commercial fillers or to the reference $BaSO_4$ obtained from Aldrich (BR2). Most of the particles produced by us had a similar particle size distribution, although average particle sizes varied.

Two of the samples showed bimodal particle size distribution. One of them was the general purpose commercial reference sample purchased from Aldrich (BR2), while the other was sample B1. The particle size distribution of the former is presented in Fig. 3. The distribution shows two distinct peaks with maximums at around 400 and 1250 nm. The bimodal size distribution is clearly disadvantageous for our purpose, because the suspension separates very easily with the fast sedimentation of the larger particles. The bimodality of sample B1 was not as strong as that of the commercial sample mentioned above (BR2), but it could be definitely observed. The reason for the development of such a distribution is unclear; it must be determined again by the reaction conditions, which should be analyzed for a more exact explanation.

Average particle size and its standard deviation are collected in Table 2. Only two samples could not be characterized in DMSO, but the size of more than half of the samples could not be determined in ethanol. Average particle sizes cover approximately one decade from 0.19 nm

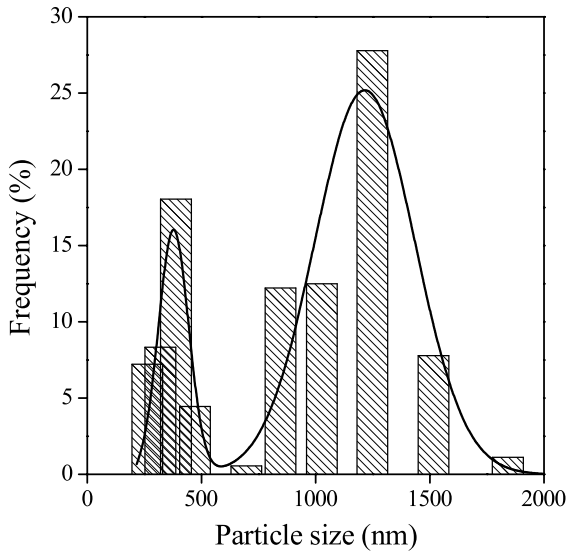

Fig. 3 Bimodal size distribution of the commercial $BaSO_4$ sample (BR2) obtained from Aldrich. Laser light scattering in DMSO

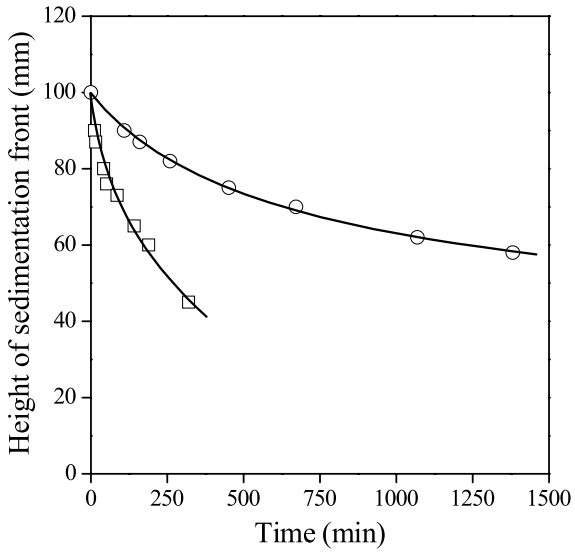

Fig. 4 Rate of sedimentation of samples B3 and B8 in ethanol. Symbols: (□) B3, (◯) B8

for sample 9 to 1.97 nm for the commercial reference sample. The width of the distribution also varies, but it seems to depend on the actual value of particle size. These results indicate that at least some of the particles will form stable suspensions and can be applied as contrast material in endovascular surgery.

It is also worth to compare the results obtained by the two different methods, i.e. SEM analysis and laser light scattering. The general tendency between the quantities determined by the two techniques compares well, but the exact values are quite different and considerable contradictions can be also observed occasionally. Large sizes were determined for both reference samples (BR1, BR2), as well as for sample B3 by both methods. On the other hand, the size of the B1 particles proved to be very large in the light scattering measurement, while the SEM study yielded a much smaller value. This apparent contradiction can be easily explained by the fact that primary particles were determined by SEM, while light scattering cannot differentiate between these and the aggregates. Finally we must mention here that much smaller aggregates formed in DMSO than in ethanol. The observation was later confirmed by the sedimentation experiments described below. The different aggregation tendency of the samples must be related to dissimilar surface characteristics and interactions, but we did not investigate them in this study.

Sedimentation, Suspension Stability

As a first approximation the sedimentation rate of spherical particles can be predicted by Stokes' law:

$$v_s = \frac{d^2 g(\rho_p - \rho_s)}{18\eta}, \quad (1)$$

where v_s is the sedimentation rate of the particles, g gravitational acceleration, ρ_p and ρ_s is the density of the particles and the solvent, respectively, and η is the dynamic viscosity of the suspension. Equation 1 clearly shows that the main factors determining sedimentation are the size of the particles, the density difference between the particles and the liquid, and the viscosity of the media. Particle size has an especially dominating effect on sedimentation rate since it appears on the square in the equation. In the case of small particles, the solvate layer adsorbed onto the surface of the particles also influences particle size and must be taken into consideration. The results and their analysis presented above clearly show that the size of our particles cover a wide range thus we may expect considerable differences in the stability of the suspensions.

Sedimentation experiments were carried out in water, ethanol and DMSO. Occasionally we could not measure the sedimentation characteristics of the samples because a homogeneous suspension could not be prepared or because sedimentation was excessively fast (samples BR1, B5 and B6). We present two typical sedimentation curves in Fig. 4, which show the progress of the sedimentation front as a function of time. The SEM micrograph taken from sample B3 (see Fig. 1a) clearly showed the platelike particle geometry and large size of this sample. The sedimentation curve agrees well with these observations, the rate of sedimentation is relatively fast, the particles rapidly fall to the bottom of the vessel. Both microscopy and light scattering experiments indicated that the particle size of sample B8 is much smaller. The particle characteristics of this sample can be observed quite well in Fig. 5. We see that the primary size of the particles is relatively small and they form small aggregates. This aggregate formation appears in the light scattering experiments

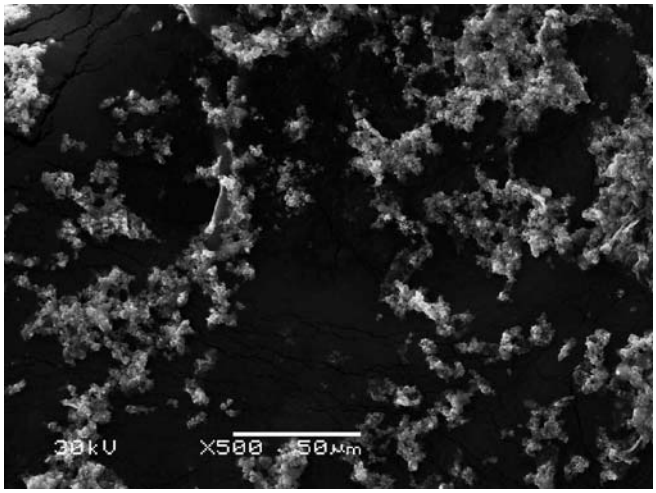

Fig. 5 Particle characteristics and aggregation tendency of sample B8

as a relatively large size, i.e. 0.42 ± 0.24 µm compared to the value determined by SEM. In spite of some aggregation, the size of B8 particles is much smaller than that of the B3 sample thus its sedimentation proceeds significantly slower.

Initial sedimentation rates were determined in the three media for all samples and they are presented in Table 3. The relative order of the samples is more or less the same in the three solvents. Apart from the commercial $BaSO_4$ sample purchased from Aldrich (BR2), only the B3 sample sediments faster than the others. The larger viscosity and density of DMSO is clearly seen in the values of the table; in most cases sedimentation is significantly slower in this solvent than in the other two.

DMSO differs from the other two solvents in other respects as well. On several occasions, independently of the propagation of the sedimentation front, a sediment consisting of larger particles appeared in the vessel used for the experiments. This sediment could not be suspended any more in the same way as at the beginning of the experiments. These samples are indicated with an asterisk in Table 3. The phenomenon might be caused by some aging process, by the transformation of the material, aggregation, or recrystallization. We did not carry out further experiments to find an unambiguous and exact explanation for the process. Nevertheless, we must draw the conclusion that $BaSO_4$ particles cannot be stored infinitely in DMSO, i.e. the embolization suspension must be freshly prepared if $BaSO_4$ is used for contrasting or some other solution must be found for the stabilization of the suspension. Such an approach might be the application of a mixture of DMSO and ethanol, which is frequently used in endovascular surgery anyway in order to decrease the level of toxic DMSO load on the patient [42–44].

In other cases just the opposite phenomenon was observed. Instead of the formation of a sediment with increased particle size, the sedimentation front proceeded much slower than expected. The slower rate could not be justified by the difference in density and viscosity compared to ethanol or water. This phenomenon indicated the partial decomposition of the aggregates formed during the production of the samples. The observed phenomena prove again that preparation conditions strongly influence the final characteristics of the samples, including particle characteristics and stability. Moreover, in certain media the $BaSO_4$ particles may undergo further transformation, which changes these characteristics.

Table 3 Sedimentation rate of the studied $BaSO_4$ particles in various media

Sample[a]	Sedimentation rate (mm/h) in		
	Water	EtOH	DMSO
BR2	390	360	288
B1	3	6	0.50*
B2	5	15	0.10
B3	10	60	0.10
B4	2	4	0.05
B7	4	15	0.25*
B8	3	2	0
B9	4	10	0.08*

[a] Reliable data could not be obtained for samples BR1, B5 and B6, since sedimentation was too fast

The particle size of the samples can be indirectly determined also from the initial rate of sedimentation using Stokes' law (see Eq. 1). All parameters necessary are

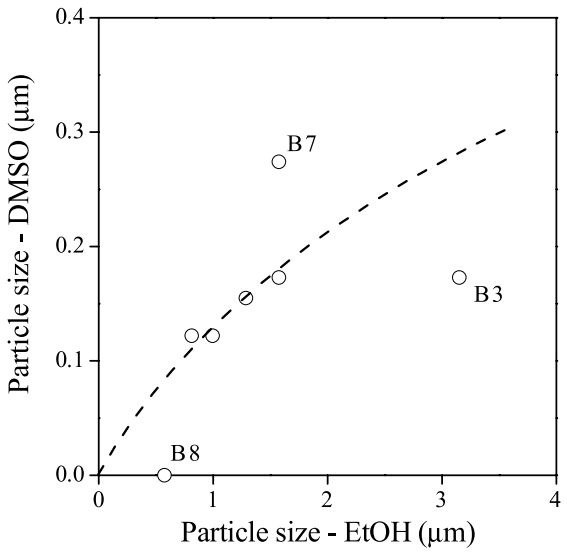

Fig. 6 Demonstration of the aging of $BaSO_4$ particles occurring in DMSO by the comparison of particle sizes calculated from sedimentation rates determined in ethanol and DMSO, respectively

known and the average particle size can be calculated. This calculation was carried out and we compare particle sizes derived from results obtained in ethanol and DMSO in order to study the aging phenomena further. The results are presented in Fig. 6 for those samples which could be studied by this technique, i.e. by sedimentation, at all. The commercial BR2 sample was omitted from the correlation, since the much larger value obtained for it would have dominated the correlation pushing the rest of the values closely together. Although the number of points is rather small, a general tendency can be established in the figure. The large difference in the absolute values must be assigned to the inadequacy of the model used (Stokes' law), since it is supposed to take into account changes in the density and viscosity of the solvents used. The deviation from the general tendency must be related to the aging phenomena mentioned above, which occur in DMSO. Samples falling above the tendency consist of larger, while those below it contain smaller particles than in ethanol indicating aggregation or disaggregation, respectively. These results further support our observations about the aging of $BaSO_4$ particles in DMSO, which might considerably influence the stability of the suspension. Moreover, the deviations from the general tendency call the attention to the fact that the results of all measurements must be treated with the utmost care, since some of them can be biased by various factors.

The results presented here unambiguously prove that commercial contrasting agents, like the medical reference sample used in this study (BR1), are not always optimal and the stability of the suspensions prepared from them might be poor. On the other hand, by the selection of the reaction conditions properly, barium sulfate particles can be prepared with proper shape and particle size, which completely fulfill the strict requirements of medical application and yield a suspension with appropriate stability. The contrasting efficiency of the samples, their effect on the viscosity of the embolizing fluid and the concentration necessary for surgical application requires further study and optimization.

Conclusions

In this study barium sulfate particles were prepared under various conditions to explore their potential application as contrast materials in endovascular surgery. The results showed that the particle characteristics of the samples depend very much on reaction conditions. Particles were obtained in spherical and plate-like shape and in a variety of sizes. Primary particles of nanometer size formed aggregates in most cases. Some of the samples had bimodal particle size distribution. Particle characteristics determined from SEM micrographs, by laser light scattering measurements and calculated from sedimentation experiments often differed from each other. The discrepancy could be explained by the different behavior of various fractions and by the dissimilar sensitivity of the measurements to them. Some of the samples showed various aging phenomena in DMSO leading either to the formation of larger particles or to the break down of aggregates. The experiments also proved that the appropriate selection of preparation conditions results in particles yielding stable suspensions, which can be used in the intended application.

Acknowledgement The project was financed by the National Bureau of Research and Development (NKFP Grant No. 1/0027/2005) and the National Scientific Research Fund of Hungary (OTKA Grant No. K 68748); their support is highly appreciated.

References

1. Valtonen S (2000) Oper Tech Neurosurg 3:231
2. Wiebers DO (2000) Oper Tech Neurosurg 3:166
3. Karhunen PJ (1991) Forensic Sci Int 51:13
4. Vajkoczy P, Horn P, Schmiedek P (1999) Oper Tech Neurosurg 2:106
5. Sekhar LN, Kalavakonda C (1999) Oper Tech Neurosurg 3:129
6. Alleyne CH Jr, Baskin JJ, McDougall CG (1998) Oper Tech Neurosurg 1:189
7. Niimi Y, Berenstein A (2000) Oper Tech Neurosurg 3:195
8. Buz S, Zipfel B, Mulahasanovic S, Pasic M, Weng Y, Hetzer R (2008) Eur J Cardio-Thorac 33:143
9. Levy MM, Baum RA, Carpenter JP (1998) J Vasc Surg 28:995
10. Guglielmi G (2000) Oper Tech Neurosurg 3:191
11. Serbinenko A (1974) J Neurosurg 41:125
12. Murayama Y, Vinulea FJ, Tateshima K, Gonzalez NR, Wallace MP (2001) J Neurosurg 94:454
13. Hampikian JM, Heaton BC, Tong FC, Zhang Z, Wong CP (2006) Mater Sci Eng Solid B 26:1373
14. Mottu F, Gailloud P, Massuelle D, Ruk DA, Doelker E (2000) Biomaterials 21:803
15. Tokunaga K, Kinugasa K, Meguro T, Sugiu K, Nakashima H, Mandai S, Ohmoto T (2000) J Clin Neurosci 7:1
16. Christiansen C (2005) Toxicology 209:185
17. Brinker J (2005) Rev Cardiovasc Med 4:S19
18. Mullan FB, Madsen MT, Messerle L, Kolesnichenko V, Kruger J (2000) Acad Radiol 7:4
19. Sovak M (1988) Int J Radiat Appl Instrum B 15:3
20. Grainger RG (1986) Clin Radiol 37:199
21. Montgomery DP, Clamp SE, Dombal FT, Chennells PM, Parkin GJS, Lintott DJ, Simpkins KC (1982) Clin Radiol 33:265
22. Briggs RW, Liebig T, Ballinger JR, Ros PR (1993) Magn Reson Imaging 11:635
23. Briggs RW, Liebig T, Ballinger R, Ros PR (1993) Magn Reson Imaging 11:635

24. Li KCP, Tart RP, Fitzsimmons JR, Storm BL, Mao J, Rolfes RJ (1991) Magn Reson Imaging 9:141
25. Marti-Bonmati L, Vilar J, Paniagua JC, Talens A (1991) Magn Reson Imaging 9:259
26. Sutton D (1980) A textbook of Radiology and Imaging. Churchill Livingstone, London
27. Balastre M, Argillier JF, Allain C, Foissy A (2002) Colloid Surf A 211:145
28. Allain C, Cloitre M, Parisse F (1996) J Colloid Interf Sci 178:411
29. Jullien R (1992) Croatica Chem Acta 65:215
30. Stenius P, Jarnstrom L, Rigdahl M (1990) Colloids Surf 51:219
31. Stoll S, Perfferkorn E (1992) J Colloid Interf Sci 152:247
32. Weitz DA, Huang JS, Lin MY, Sung (1984) J Phys Rev Lett 53:1657
33. Russel WB, Saville DA, Schowalter WR (1989) Colloidal Dispersion. Cambridge University Press, New York
34. Davies L, Dollimore D, McBride GB (1977) Powder Technol 16:45
35. Glasrud GC, Navarrete RC, Scriven LE, Macosko CW (1993) AIChE J 39:560
36. Stenour HH (1944) Ind Eng Chem 36:618
37. Parfitt GD (1973) Dispersion of powders in liquids. Appl Sci Publ, London
38. Azema N (2006) Powder Technol 165:133
39. Erffmeyer JE, Siegle RL, Lieberman P (1985) J Allergy Clin Immun 75:401
40. Strickland NH, Rampling MW, Dawson P, Martin G (1992) Clin Radiol 45:240
41. Lieberman P (2002) J Allergy Clin Immun 110:S64
42. Willson JE, Brown DE, Timmens EK (1965) Toxicol Appl Pharm 7:104
43. Jacob SW, Wood DC (1967) Am J Surg 114:414
44. Worthley EG, Schott CD (1969) Toxicol Appl Pharm 15:275

Progr Colloid Polym Sci (2008) 135: 65–69
DOI 10.1007/2882_2008_115

Published online: 9 September 2008

Teresa Chambino
Anabela Correia
Sandor Barany

Aluminium Salts Hydrolysis Products from Industrial Anodising Sludges in Wastewater Treatment

Teresa Chambino (✉) · Anabela Correia
Dep. of Materials and Production Technologies, INETI, Est. do Paço do Lumiar 22, 1649-038 Lisboa, Portugal
e-mail: teresa.chambino@ineti.pt

Sandor Barany
Institute of Chemistry, University of Miskolc, 3515 Miskolc-Egyetemváros, Hungary

Abstract The wastewaters resulting from industrial aluminium anodising processes must be treated in a wastewater treatment plant usually involving the main operations of neutralisation, flocculation, settling and filtration with a press-filter. In Portugal the annual quantity of sludges, resulting from these wastewaters treatment, is estimated in 15 000 t/year (2002) and in the EU a large quantity is also involved. No use has been found for these sludges and they are sent to landfills or disposed of in uncontrolled places. Recycling is an economical and environmentally friendly way to handle hazardous wastes, reducing the amounts disposed in landfills. So the effect of the anodising sludge as flocculant of municipal wastewaters instead of inorganic salts commonly used was studied.

Sludges from nine industrial units were characterised and used as flocculant. The efficiency of the sludge aluminium salts hydrolysis products in the removal of suspended particles and organic matter was demonstrated.

Keywords Anodising · Coagulation · Recycling · Sludge · Waste

Anodising Sludge Origin

Along the anodising surface treatment processes several wastewaters are generated. The wastewaters come basically from rinsing operations or cleaning of concentrated chemical baths containing sodium hydroxide and sulphuric acid. Some of the wastewaters can be alkaline, generated during the rinsing performed after the pickling operation with sodium hydroxide. They can also be acid resultant from the rinsing of anodised articles coming from anodising baths formed usually by a solution of sulphuric acid.

The wastewaters must be treated in a wastewater treatment plant usually involving the main operations of neutralization, flocculation, settling and filtration with a press-filter. The alkaline and acid wastewaters are collected separately and are sent in a controlled flow to the industrial wastewater plant so that a neutralization process occurs. A final pH adjustment can be necessary usually with lime or sulphuric acid. Next the wastewaters are submitted to a coagulation process followed by a settling period. The sludge from the settling tank, usually with a solid concentration up to 10% SS, is transferred to a filter press where it is concentrated up to 30% SS.

In Portugal the annual quantity is estimated, by the industrial sector association, in 15 000 t/year (2002) and in the EU around 300 000 t/year (2006), an average of 16 t per installation [1].

Aluminium recycling is being studied [2] but solutions are still needed concerning many wastes from different aluminium processes that otherwise will be sent to landfills. This is also the case of anodising sludges because no use has been found for these sludges and they are sent to landfills or disposed of in uncontrolled places. Research in order to find new recycling possibilities for these wastes is a promising and environmentally interesting subject.

The anodising sludge resulting from the wastewater treatment has a variable composition according to the

anodising processes used but has a certain amount of aluminium compounds. Aluminium salts have been used for long in the treatment of municipal wastewaters as coagulant for the removal of suspended solids, turbidity, colour or algae that can be present as colloidal particles. In this work it is intended to use this chemical characteristic of the anodised sludge and study its capacity as coagulant of municipal wastewaters instead of inorganic salts commonly used.

Materials and Methods

Anodising Sludge

Sludge Sampling and Characterisation. Nine industrial units were selected for this study being a group of the more representative units regarding the quantitative production of the anodising sector. The sludge was recovered at the press filter discharge. A representative composite sample was recovered, well homogenised so that a homogeneous sample was produced and analysed.

The composition of the solid fraction consists especially of aluminium (18–35%), sulphates and organic matter [3]. Sodium, calcium, chromium and iron collectively make less than 3% and the other elements appear in even lower quantities.

Sludge Preparation. The sludge was tested as coagulant with two different physical forms: as powder and as a suspension.

To prepare the powder form the sludge samples were well homogenised, submitted to a process of drying at room temperature and grinded with a grid of 0.5 mm so that a homogeneous powder of constant characteristics was produced. Along the drying process successive humidity determinations were made until constant weight loss determination was achieved.

The suspension was prepared as a homogenised mixture of sludge and water according to an established procedure and defined solids content. Stable suspensions were obtained with solids content from 5 to 15%. Suspensions with solids content of 5% were used, in this study, being easier to handle.

Municipal Plant Wastewater

A wastewater from a large municipal wastewater plant was selected to test the efficiency of the anodised sludge as coagulant. In other studies we have also studied the use of the anodising sludge in the treatment of paint, paper-mill and textile wastewaters [3–5]. Several samples were recovered, along the work, at the entrance of the primary treatment formed by the primary settler and after the initial grit removal where the elimination of coarse suspended matter, oils and grease takes place. This effluent contains considerable organic matter, high suspended solids concentration and turbidity. The physical and chemical characteristics of the wastewaters were determined and are indicated in Table 1.

Table 1 Wastewater characterisation

Parameter	Municipal wastewater average values	Max–min values	Emission limits*
COD ($mg\,l^{-1}$ O_2)	771	980–560	125
TSS ($mg\,l^{-1}$)	356	490–160	35
Aluminum Al ($mg\,l^{-1}$)	3.5	5.2–0.34	
Turbidity (NTU)	243	283–205	
pH	7.5	8.2–6.8	

* Portuguese Legislation regarding the discharge of Urban Wastewater Treatment Plants, D.L. 152/97, 2007

Coagulation Experiments with the Anodising Sludge

In many water and wastewater treatment processes particle removal is important because the particles are pollutants that have to be removed. Particles are usually very small and can not be separated in reasonable time periods. Interparticle forces also can contribute to the suspension stability. The particle characteristics can be modified through aggregation in a coagulation process. Coagulation causes the formation of aggregates of particles (flocs) more easily removed. Coagulation tests have been intensely used in order to establish the best conditions of floc formation. The tests structure can vary according to the author's objectives [4] but the more important parameters to be controlled during the experiments are coagulant dose, mixing conditions (intensity and duration of mixing phases and type of stirring device), settling time, turbidity and final pH.

Coagulation tests were performed in order to study the coagulation effect of the anodising sludge. The coagulation experiments were conducted by first adding the selected amount of sludge to wastewater samples. The samples were then submitted to a rapid stirring phase followed by a slower one. Afterwards the coagulated suspension was allowed to settle. At the end of the settling period samples were taken from the supernatant. The samples were chemically analysed and the influence of the experimental parameters was studied through several tests. The optimum coagulation conditions were established based on the removal efficiency of wastewater contaminants, on the final turbidity and chemical oxygen demand (COD) of the supernatant samples. The coagulation conditions used in the tests are indicated in Table 2.

Table 2 Coagulation conditions

Parameters		
Coagulant dose		0.05; 0.1; 0.2; 0.4; 1
Rapid mixing phase	Stirring speed	100; 300; 800 rpm
	Stirring time	5; 15 min
Slow mixing phase	Stirring speed	50; 80 rpm
	Stirring time	30 min
Settling		30 min; 1 h
Stirring system		Type of impeller

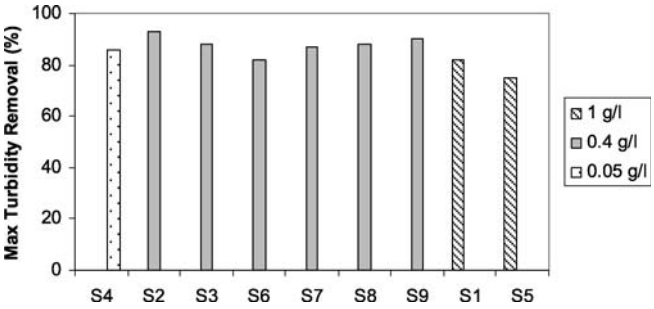

Fig. 2 Maximum turbidity reduction, powder coagulant

Experimental Results

Coagulant dose is a very important parameter regarding the coagulation process efficiency. Different coagulant doses were tested in order to establish the more favourable conditions. The results regarding the lower and higher doses tested, using the coagulant as powder form, are indicated in Fig. 1. The maximum turbidity removal achieved with a coagulant dose of 0.05 g/l oscillated from 69 to 88%. For the case of the higher dose of 1 g/l, the turbidity removal reached 75 to 92%, for the different sludges.

The maximum turbidity reduction obtained with different coagulant doses for the nine sludges, used as powder, is indicated in Fig. 2. High turbidity removal is achieved, between 75 to 93%. Most sludges reach the highest removal with the intermediate dose of 0.4 g/l.

Higher or lower values of coagulant dose do not improve turbidity removal. So, increasing coagulant dose improves turbidity removal only up to a certain quantity. When the maximum removal is reached to increase the dose will lead to a poorer supernatant clarification.

Blank tests were performed, involving only the settling process of wastewater samples, without any coagulant, and an average turbidity removal of 61%, with 30 min settling time, was reached. These values are in agreement with known bibliography values that, comparatively, indicate that a well dimensioned primary settling tank without chemicals addition removes 50 to 70% of the total suspended solids (TSS), 25 to 40% of the biochemical oxygen demand (BOD) and 25 to 75% of the bacteria [6].

The sludge was also used as a suspension. Even higher values of turbidity removal were achieved in this case. The maximum turbidity removal achieved with a coagulant dose of 0.05 g/l oscillated from 79 to 89% and for the case of the higher dose of 1 g/l, the turbidity removal reached 92 to 99%, for the different sludges, Fig. 3.

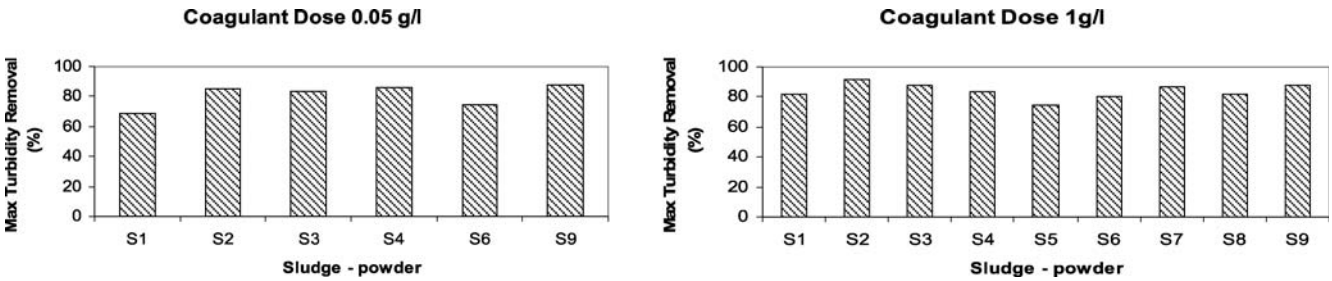

Fig. 1 Maximum turbidity reduction with powder coagulant for two different doses

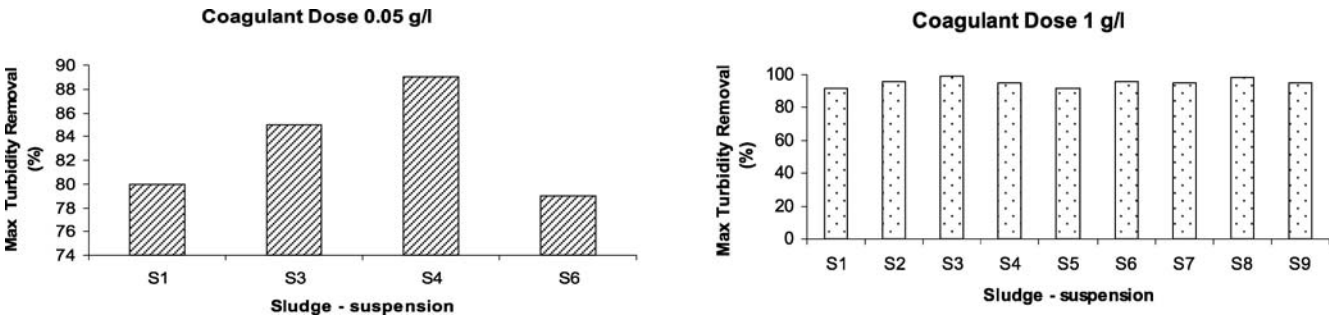

Fig. 3 Maximum turbidity reduction with suspension coagulant for two different doses

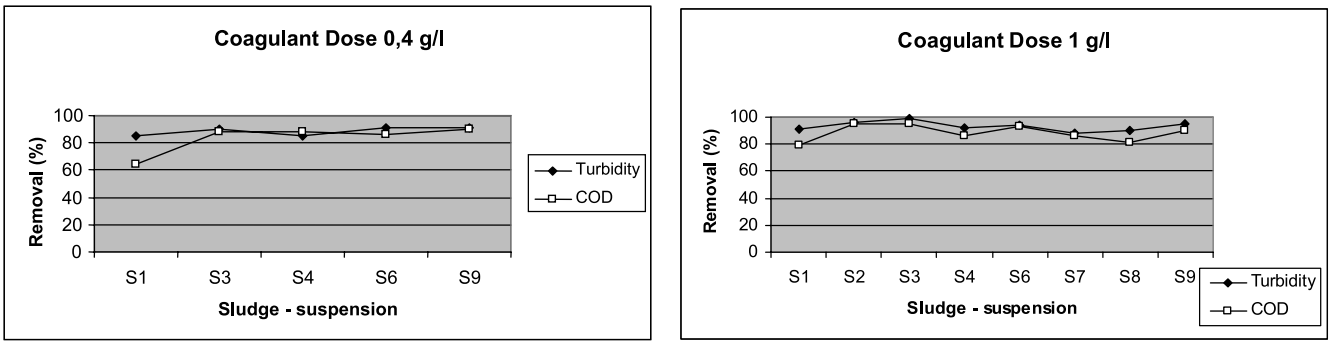

Fig. 4 Maximum turbidity and COD reduction with suspension coagulant for two different doses

For the coagulation with the suspension, the maximum removal was obtained with the dose of 1 g/l. So, in this case, the turbidity removal continued its increase with increasing coagulant doses up to 1 g/l.

Nevertheless in order to select the more adequate conditions for the wastewater treatment an equilibrium must be chosen between contaminant removal and coagulant dose. Although the highest removal was achieved with the dose of 1 g/l, an average dose of 0.4 g/l allows already good results for wastewater treatment, as can be seen in Fig. 4. The coagulation conditions that showed higher removal were selected as a rapid mixing phase (300 rpm; 15 min) and a slow mixing phase (50 rpm; 30 min). The results presented, in Fig. 4, regard turbidity and COD removal under these selected coagulation conditions. Considering the dose of 0,4 g/l, turbidity removal of 85 to 91% and COD removal of 64 to 90% were achieved. With the coagulant dose of 1 g/l the turbidity removal of 88 to 99% and COD removal of 79 to 95% for these selected coagulation conditions.

Discussion

The coagulation process with the anodising sludge was very efficient. The pollutant removal, detected through turbidity and COD measurements, reached high percentage levels. After the treatment the wastewater contaminant levels were below the legislation emission limits, in most tests. The classical wastewater treatment involves coagulation with aluminium salts followed by a neutralisation process for pH adjustment. In the coagulation with the anodising sludge the neutralisation step is suppressed. In fact during the coagulation experiments the final pH oscillates from initial to final pH. The pH change is not very noticeable and the supernatant can be considered included in the neutral pH range not needing a final adjustment for neutral range.

Anodising sludge is a more complex product than traditional coagulants. So its mode of action is still being studied. Nevertheless the destabilisation process, when using the anodising sludge as coagulant, can be explained by two mechanisms: sweep flocculation and charge neutralisation. The relative importance of the two mechanisms will depend on the coagulant dose and the pH [7]. Several aquocomplexes are formed during the process. Hydrolysis products are mainly cationic and coagulation can proceed by charge neutralisation.

When this mechanism is predominant there is a stoichiometric relationship between particle and coagulant concentration. Also if the neutralisation mechanism is involved there is a narrow range for the optimum coagulation dose that must be very precise. This does not happen using the anodising sludge as coagulant. Although the optimum coagulation dose is found during the experiments, nevertheless reasonable contaminant removal can be achieved over a broader coagulant range. As pH increases, although around neutral pH, the formation of a hydroxide precipitate will occur. Contaminants may be enmeshed or adsorbed, for the case of soluble contaminants, in the precipitate and be removed by sweep flocculation [8]. Heterocoagulation can occur between positive precipitate particles and colloidal negatively charged contaminants involving also the charge neutralisation mechanism. Aluminium precipitates will be positively charged at pH below 8 or 9 according to different authors. The presence of sulphates, as it is the case of the complex anodising sludge, can produce large precipitate flocs over a wider pH range [9]. During our sludge coagulation experiments the final pH range was 8–9 and precipitates should be positive. So according to the conditions of the coagulation experiments with the anodising sludge the main mechanism will be sweep flocculation enhanced with heterocoagulation.

The coagulant dose was the decisive parameter regarding the contaminant removal results. Nevertheless several stirring conditions were tested, with different impeller systems, and optimised coagulation conditions were established. The higher contaminant removal was not obtained for the same stirring conditions for all the sludges probably due to differences in their composition and granulometry. However the higher turbidity and COD removal was obtained with the same dose for all the sludges, in the case of suspension coagulant, reinforcing the importance of the coagulant dose regarding

the other coagulation parameters. Data analysis of the coagulation results was performed according to the statistical Taguchi method and has also confirmed the previous statement. This analysis will be presented in a following paper.

The anodising sludge was tested as a powder or a suspension. Good coagulant efficiency was obtained with both forms but higher contaminant removal was achieved with the suspension form. This form possibly permits an easier contact coagulant–contaminant.

References

1. European Commission (2006) Ref. Doc. On Best Available Techniques for the Surface Treatment of Metals and Plastics
2. Shinzato MC, Hypolito R (2005) Waste Manag 25(1):37–46
3. Bartolomeu F, Chambino T, Correia A et al (2006) Industria e Ambiente 42:31–35
4. Correia A, Chambino T et al (2005) Desalination 185(1–3):341–350
5. Chambino T, Correia A et al (2001) Int. Water Assoc. (IWA) 2nd World Water Congress, Proceedings in CD-rom. IWA Publishing, Berlin
6. Metcalf, Eddy (1995) Wastewater Engineering– Treatment, Disposal and Reuse. Mcgraw-Hill, Tata
7. Johnson P, Amirtharajah A (1983) JAWWA 75:232–239
8. Dempsey B (1984) CRC Crit Rev Env Control 14(4):311–331
9. Duan J, Gregory J (2003) Adv Colloid Int Sci 100–102:475–502

Progr Colloid Polym Sci (2008) 135: 70–76
DOI 10.1007/2882_2008_107

Published online: 9 September 2008

Renáta Mészáros
Sándor Bárány

Strength of Flocs Formed from Aluminium Sulfate Hydrolysis Product Particles

Renáta Mészáros · Sándor Bárány (✉)
Department of Chemsitry, University of Miskolc, 3515 Miskolc-Egyetemvaros, Hungary
e-mail: akmbsab@uni-miskolc.hu

Abstract The kinetics of aggregation of aluminium sulfate hydrolysis product particles (AS HPP) formed in two model waters with different pH and alkalinity values, at different shear conditions in a flow system has been studied. The effect of the hydrolyzing salt dose, ionic strength of the solution and the mode and rate of stirring the system on the growth, destruction and regrowth of HPP aggregates has been investigated. The comparison of the results obtained with our previous data on the electrokinetic potential and hydration of AS HPP [7] testifies that the aluminium sulfate hydrolysis product particles formed in a model water with parameters that facilitate appearance of small particles with relatively high charge and zeta-potential values, low degree of hydration and interaction of primary particles predominantly in the primary minimum (water II: pH 7.5, alkalinity 1 mmol/l, average particle radius 6–7 nm, $\zeta = 26$–29 mV), are more stable and possess higher ability for reconstruction after their destruction during intensive stirring, than aggregates built of particles with lower charge, higher initial particle size and hydration, aggregating in the secondary minimum (water I: pH 9.3, alkalinity 3 mmol/l, average particle radius 10–11 nm, $\zeta = 16$–18 mV).

Keywords Aggregates · Aluminium sulfate · Destruction · Growth · Hydrolysis products · Reconstruction · Shear intensity

Introduction

Aggregation of dispersed particles plays an important role during phase separation processes, in particular in the course of water conditioning and treatment, mineral processing, etc. [1, 2]. Typically, these processes are initiated or enhanced by adding hydrolysing salts or high-molecular polymeric flocculants to dispersion or water to be treated. Depending on the balance of main variables operating in the system, the size of aggregates formed, their strength and packing density as well as the changes of these parameters during the aggregation process can be varied in a broad interval [3–5].

Special interest represents information about the laws and kinetics of aggregates formation from the aluminium salts hydrolysis product particles (HPP) widely used in water treatment [5–7]. The course of these processes as well as the size, density and strength of aggregates depends not only on the coagulant nature but also on the system variables such as pH, ionic strength and alkalinity. By changing these parameters, the colloid-chemical properties of primary particles of the hydrolysis product, the size and density of aggregates formed and their mechanical strength, i.e. ability for destruction and following reconstruction after termination of the acting physical and mechanical forces can be regulated.

Recently several papers have been published on the problem of destruction/reconstruction of aggregates formed under the action of coagulants or polymeric flocculants [8–11]. Different ideas about the mechanisms of

these processes have been proposed but none of these assumptions has got detail experimental confirmation.

Mixing conditions can have a very significant effect on the performance of coagulants and flocculants. The first requirement is for the additive to be distributed uniformly among the particles in suspension. This is usually achieved by some form of rapid mixing. The particles then need to collide in order to form aggregates and this process can be assisted by gentle agitation. When flocs are subjected to an increased shear rate, breakage can occur. Breakage depends greatly on the intensity of shear and on the flocs strength. The latter is determined by the nature of the interaction between particles, i.e whether they are aggregating in the primary or secondary minimum, and the average number of bonds per particle (or on the floc density). In practice, floc strength is often approached in an empirical manner, usually by observing the limiting floc size under given shear conditions. After floc breakage, its re-growth may occur on restoring the previous low shear conditions. There have been only limited studies on this aspect and the influence of mixing conditions on the re-formation of flocs has not been yet properly evaluated.

The aim of this study is to investigate the effect of the coagulant dose, ionic strength and alkalinity of the water as well as the mixing conditions on formation, breakage and re-formation of aggregates formed from aluminum sulfate (AS) hydrolysis product particles (HPP), and to establish an interconnection between the surface properties and stability of flocs at different (mentioned) variables of the system. A continuous optical monitoring method, with controlled mixing and stirring conditions, was used.

Materials and Methods

As hydrolysing salt (coagulant) commercial product of aluminium sulfate has been applied. A working solution of concentration 0.1% (as for Al_2O_3) was prepared from 1% stock solution that was stored in a refrigarator at 5 °C. Doses of AS from 5 to 30 mg/l (as Al_2O_3) have been used.

Model "waters" prepared from distilled water, containing different amounts of HCl or KOH and $NaHCO_3$ to adjust the required pH and alkalinity values (= $[HCO_3^-]$, mol/l), have been applied. The ionic strength of the system (I) was varied between 10^{-3} and 5×10^{-2} mol/l by adding KCl solution. Two samples of "model" water were used: water I with pH 9.3 and alkalinity 3 mmol/l and water II with pH 7.5 and alkalinity 1 mmol/l.

Experiments on the kinetics of formation, destruction and subsequent re-formation of aggregates were performed in a flowing cell using PDA-2000 dispersion Analyzer (Rank Brothers, UK) that permits to determine the relative size of forming aggregates [9–12]. One hundred ml of the model water with adjusted pH, alkalinity and ionic strength values was placed in a beaker and the stirring by a mechanic stirrer immediately started at 50 (or other) rpm. The water was pumped in a transparent flexible tube through the measuring unit of the PDA instrument by a peristaltic pump. The magnitude of the light flux passing through the suspension was continuously registered by the sensitive photodetector capable to transfer a light signal into an electrical one. It was shown [12] that the root-mean-square values of the fluctuating signal (rms) is a characteristic of the number-averaged concentration and size of the suspended particles. The rms signal converted into an electric one is given in millivolts (mV). The values of V_{rms} are significantly increased at the onset of aggregation, and decreased while aggregates are broken After reaching a permanent value of V_{rms}, the designated amount of the aluminium sulfate solution was added and the output signal characterising the degree of flocculation was immediately recorded during 3000 s. At certain stages of the process indicated below, an intensive stirring of 500 rmp during 20 s has been applied, followed by stirring the system with previous velocity (50 rpm). By this manner we followed the dynamics of increase and subsequent destruction/restoration of the aluminium sulfate HPP aggregates.

Experimental

Kinetics of the AS HPP Aggregation

It has been shown by authors [5, 7, 13, 14] that by changing the pH, ionic strength and alkalinity values, the colloid-chemical characteristics of HPP, such as size of primary particles, their electrokinetic potential and degree of the surface hydration, can be regulated. It has been found that with increasing pH, the electrokinetic potential of AS HPP particles decreases while the hydration of their surfaces and the diameter of primary particles increases. This results in an increase of the density of aggregates. An increase in the ionic strength and alkalinity of the system also gives a rise to the density of packing of particles in aggregates.

Figure 1 shows how the V_{rms} parameter for aluminium sulfate HPP formed in water I (pH 9.3, alkalinity 3 mmol/l) with ionic strength of $I = 1 \times 10^{-3}$ mol/l, depends on the duration of the process. The formation of aggregates was periodically interrupted by intensive stirring of the system for 20 s (indicated by arrows), with subsequent restoration of the previous stirring velocity. It is seen that the initial rate of HPP aggregates formation substantially increases with the dose of the coagulant. For example, at AS dose of 5 mg/l, the aggregation is rather slow: the maximum V_{rms} value is attainded only during 800 s after adding the salt, and the V_{rms} value is 0.45 mV only. With increasing the salt concentration the first and subsequent maxima on the curves, i.e. the degree of aggregation increases, and the time necessary to reach the maximum decreases. At coagulant dose of 30 mg/l, the maximum of V_{rms} (1.25 mV) is reached for about 200 s. At

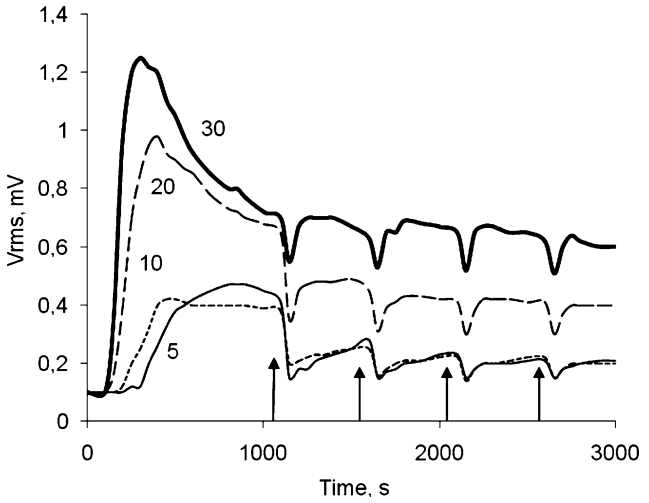

Fig. 1 Kinetics of V_{rms} variation for aggregates of aluminium sulfate hydrolysis products particles in model water I. $I = 1 \times 10^{-3}$ g ion/l. Here and further the *numbers* near the curves indicate the coagulant doses, and the *arrows* show the onset of intensive stirring (500 rpm) and aggregate breakage

low AS contents the maxima are rather extended, and with increasing the coagulant dose, on the $V_{rms}(t)$ curves after a sharp rising part a subsequent decrease is observed. This decrease steeper, the coagulant dose higher.

Similar dependencies have been obtained for HPP aggregates formation in model water II (pH 7.5, alkalinity 1 mmol/l), see Fig. 2. The general laws of formation and destruction of HPP aggregates in water II obey the same regularities that were observed for the previous system, i.e. larger V_{rms} values, with an increase of the steepness of the rising part of curves with increasing coagulant dose and the decrease of this parameter during intensive stirring the system. For this water no differencies in the form of peaks on $V_{rms}(t)$ plots, both for small and large AS doses have been registered. But also some differences in the behavior of these two systems can be seen: (1) for water II, the increase of the degree of aggregation (V_{rms}) as a function of time is slower, (2) the duration of the induction period is longer, (3) the size of aggregates formed until the beginning of intensive stirring does not decrease in contrast to the water I, but even increases. This increase is observed both for primary (initial) aggregates and for aggregates that are restored after every cycle of intensive stirring of the dispersion. It means that aggregates in this system are more stable toward stirring than aggregates arising in water with lower pH and alkalinity (cp. Figs. 1 and 2).

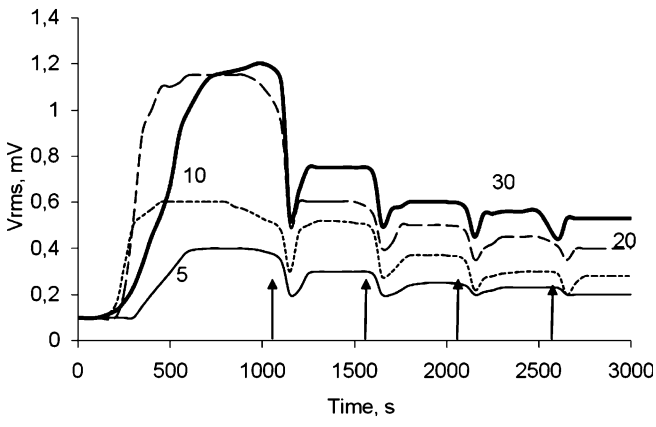

Fig. 2 Kinetics of V_{rms} variation for aggregates of aluminum sulfate hydrolysis products particles in model water II. Mixing as usual. $I = 5 \times 10^{-2}$ g ion/l

Effect of the Ionic Strength

The $V_{rms}(t)$ dependencies for the water I or II, with higher ionic strength values of 10^{-2} and 5×10^{-2} mmol/l are similar to those shown on Figs. 1 and 2 (for $I = 10^{-3}$ mmol/l), but in these cases higher V_{rms} values were observed, especially at high coagulant doses (Figs. 3 and 4). This shows that the size of forming HPP aggregates increases not only with increasing the AS concentration but also with the ionic strength of the solution. There are also other similarities in the behaviour of the two systems: at relatively high coagulant content (20 and 30 mg/l) the heights of the primary and subsequent maxima on $V_{rms}(t)$ curves increase with electrolyte concentration in both system (Figs. 3 and 4), whereas at low AS doses these dependences are more complex. For example, for water I, with increasing the ionic strength the $V_{rms(max)}$ values for the first peak slightly increase, while for the water II, the first V_{rms} values with rising ionic strength go through a maximum. Also the subsequent V_{rms} reveal big differences. These differences as well as the high $V_{rms(max)}$

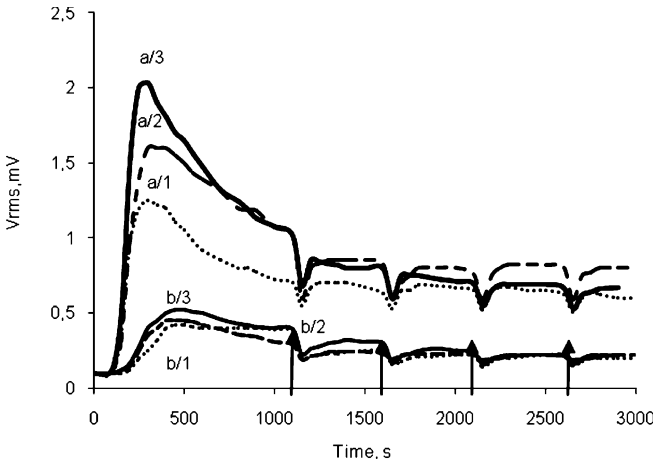

Fig. 3 Kinetics of V_{rms} variation for aggregates of aluminium sulfate hydrolysis product particles for two AS doses and different ionic strength values. Model water I, AS doses: a – 30 mg/l, b – 10 mg/l, ionic strengths: 1 – $I = 1 \times 10^{-3}$ g ion/l; 2 – $I = 1 \times 10^{-2}$ g ion/l and 3 – $I = 5 \times 10^{-2}$ g ion/l

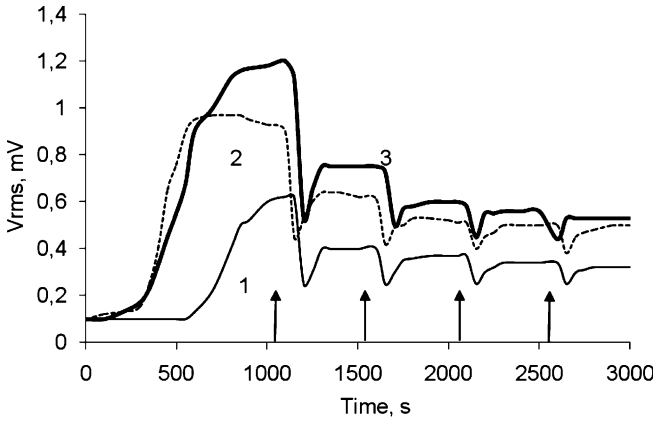

Fig. 4 Kinetics of V_{rms} variation for aggregates of aluminium sulfate hydrolysis product particles in water II for AS dose 30 mg/l and different ionic strength values: 1 – $I = 1 \times 10^{-3}$ g ion/l; 2 – $I = 1 \times 10^{-2}$ g ion/l and 3 – $I = 5 \times 10^{-2}$ g ion/l

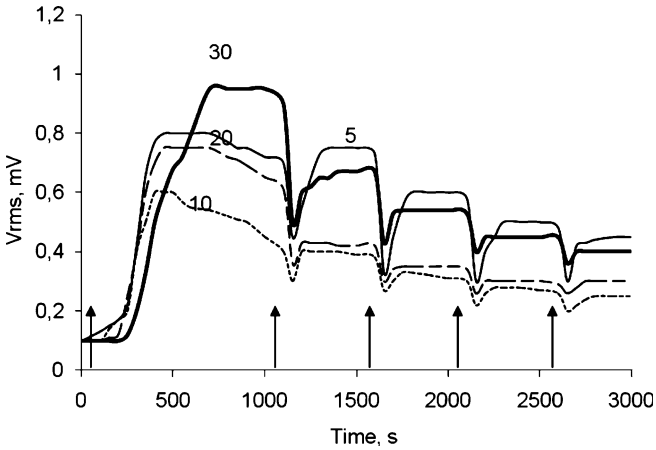

Fig. 5 Kinetics of V_{rms} variation for aggregates of aluminium sulfate hydrolysis products particles in model water II. The mixing rate 500 rpm was used during the first 30 s. $I = 5 \times 10^{-2}$ g ion/l

values typical for low AS doses and intermediate ionic strengths indicate the considerable stability of HPP aggregates even after several intensive stirring periods.

Effect of the Mode and Duration of Stirring

The regularities described above are an evidence of the strong dependence of the size and structure of HPP aggregates on the water parameters and applied shear. In all cases studied, the primary aggregates were formed at low stirring, so probably their structure was rather diffuse. We performed a comparative study of the kinetics of formation/destruction/reconstruction of AS HPP aggregates in water II, at conditions described above and with initial slow (50 rpm) and intensive (500 rpm) stirring of the system during 30 s. In the event of slow initial stirring the system (Figs. 1–4), the peak values of V_{rms} increase proportionally with the AS dose, i.e. the packing density of particles in aggregates can be considered approximately the same. It is line with a decrease in the height of peaks for HPP at different AS doses at subsequent intensive stirring the system.

Quite different picture was observed when initially an intensive stirring of the system was applied (Fig. 5): the rapid stirring during first 30 s resulted in formation of large, low-density aggregates of arbitrary, probably non-equilibrium structure due to the high frequency of particles collision. This effect is most pronounced for low AS dose (5 mg/l), when the interparticle distance is relatively big. At this dose, with slow initial stirring, the maximum size of aggregates is characterized by V_{rms} about 0.4 mV (Fig. 1), while with fast initial stirring of the system, the V_{rms} value reaches 0.8 (Fig. 5). In the course of subsequent fast stirring intervals, these aggregates undergo deformation but they remain large and diffuse. The aggregates formed at higher coagulant doses at slow stirring rates, are even larger but more resistant to breakage.

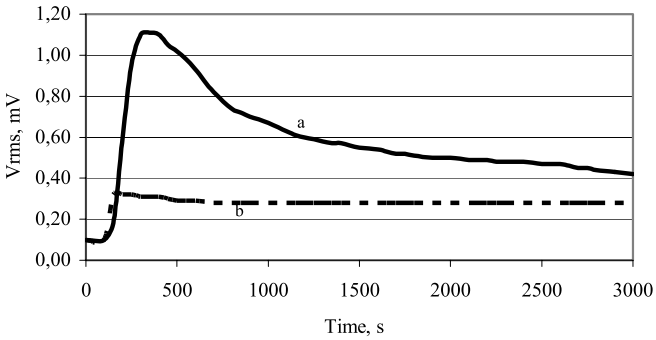

Fig. 6 Kinetics of V_{rms} variation for aggregates of aluminium sulfate hydrolysis products particles under condition of constant slow (a) and fast (b) mixing in model water I. AS dose 20 mg/l, $I = 5 \times 10^{-2}$ g ion/l

Also we have measured the kinetics V_{rms} variation for aggregates of aluminium sulfate hydrolysis product particles under condition of continuous fast (Fig. 6, curve a) and slow (Fig. 6, curve b) stirring of the system. It is seen that the initial parts of V_{rms} vs. t curves during the first 20 s from the beginning of the process coincide for both cases. After this period constant V_{rms} values for the "fast stirring" process and a steep rise in V_{rms} with subsequent decrease, for the "slow stirring" process are observed. It should be noted that in the event of slow stirring the V_{rms} "final" value reaches 0.4 mV to the 3000 s from the beginning of the process which corresponds to the magnitude of V_{rms} for aggregates restored after many-fold stirring at the same coagulant dose (20 mg/l). It is interesting that the coordinates of peaks on this curve (before the intensive stirring period) are the same as the coordinates of peaks on V_{rms} vs. t curves shown in Fig. 2. Also the coordinates of the minima of this dependence (Fig. 2) that appear as a result of fast stirring (after 1600 s) entirely coincide with the

6b curve, and the curve a is asymptotically approaching to the V_{rms} dependence shown in Fig. 2.

Discussion

The size and structure of aggregates of HPP depends on the parameters of the water such as pH, ionic strength and alkalinity as well as the reagent dose. The aggregates can be either in equilibrium or in non-equilibrium state. To the equilibrium the HPP aggregates approach with different rate, depending on the way of stirring.

To compare the strength of aggregates and the efficiency of their breakage/reconstruction, we have calculated the so-called strength factor (F_1), that characterizes the tendency for their destruction, and re-formation factor (F_2), which characterizes the ability of aggregates for reconstruction, using the ideas developed by Gregory [10]:

$$F_1 = (V_2/V_1) \times 100\,,$$
$$F_2 = [(V_3 - V_2)/(V_1 - V_2)]/100\,,$$

where V_1 is the value of V_{rms} maximum of aggregates formed on the given stage of the process; V_2 – the V_{rms} value for aggregates destructed after intensive stirring; V_3 – the same for aggregates reconstructed after intensive stirring.

Examples of the variation of F_1 and F_2 of AS HPP aggregates at different coagulant dose are given in Tables 1 and 2. The F_1 vs. AS dose dependences obtained can be summarized as follows:

1. The least stable aggregates are formed in waters I and II before their intensive stirring and after each subsequent stirring the aggregates become more and more stable;
2. Maximum differencies between the strength of initially formed aggregates and those on the next stages of formation (after the following intensive stirring) are observed for the relatively big doses of aluminium sulfate (10–20 mg/l);
3. For all systems studied the destruction factor of aggregates varied after the first intensive stirring from 30 to 50%, while after the next intensive stirrings it varied from 50 to 80%;
4. The mechanical impact is the most pronounced factor affecting the formation/destruction of the primary AS HPP aggregates;
5. The strength of aggregates both at high and low ionic strength values is higher in water II with relatively low pH and alkalinity values than in water II;
6. In most cases, especially at high electrolyte concentrations, the aggregates' strength decreases with an increase of the coagulant dose, i.e. with an increase of the HPP concentration in the system that is accompanied by a decrease of the inter-particle distances.

The factor of aggregates reconstruction (F_2) varies in similar direction in both model systems (Table 2): F_2

Table 1 Strength factors (F_1) for AS HPP at different coagulant doses and at different stages of the aggregation/de-aggregation process

	Strength factors [%] at $I = 5 \times 10^{-2}$ g ion/l, for AS doses [mg/l]							
	5	10	20	30	5	10	20	30
Number of peaks on V_{rms} vs. t curve	Water I				Water II			
1st peak	54	43	33	33	50	51	42	41
2nd peak	65	56	64	65	67	57	66	63
3rd peak	67	60	69	70	80	60	71	78
4th peak	70	74	78	77	82	66	79	77

Table 2 Renewal factors (F_2) for AS HPP at different coagulant doses and at beginning of the aggregation/de-aggregation process

	AS doses in water [mg/l]							
	5	10	20	30	5	10	20	30
	Renewal factors [%] for waters with $I = 5 \times 10^{-2}$ g ion/l							
	Water I				Water II			
1st peak	58	28	14	10	50	74	29	37
	Renewal factors [%] for waters with $I = 10^{-3}$ g ion/l							
	Water I				Water II			
1st peak	40	25	21	21	32	53	40	40

for the aggregates formed before the turbulent stirring decreases at growth of the coagulant dose from 10 to 30 mg/l and with changing from the model water II to the water I. Aggregates formed at minimal (5 mg/l) dose of aluminium sulfate represent an exception: their F_2 factor is lower than that at AS dose 10 mg/l, and the F_2 value is minimal at lows ionic strengths (Table 2). No direct relationship has been found between F_1 and F_2 factors, i.e. the aggregates could be stable enough against destruction, but possess weak ability for reconstruction after ceasing the mechanical force, i.e. stirring the system.

Comparative data on physical-chemical parameters of AS HPP aggregates in waters I and II are presented in [5, 7, 13]. They testify that aluminum sulphate hydrolysis product particles formed in model water I, are larger ($r =$ 10–11 nm), with lower ζ-potential value (16–19 mV) and more hydrated (especially at low coagulant doses) than those formed in model water II ($r = 6$–7 nm) and having higher ζ ($= 26$–29 mV). Based on these data and parameters of the inter-particle interaction energy vs. distance curves (calculated by the DLVO theory using the measured electrokinetic potential of particles and primary aggregates) [7, 14, 15] one can conclude that at the first step, the interaction of HPP primary aggregates' in water I occurs in the secondary minimum, with depth about 8–10 kT, and there is no potential barrier between particles in this case. The interaction of aggregates in water II may occur both in primary and secondary minimum, i.e. the depth of these minima is only 1–2 kT. Formation of bigger aggregates in this water, compared to water II, means that the aggregates in the second system are more diffuse (loose). Nevertheless, we consider that probably it is not the looseness of aggregates (low amount of particles in a unit volume) is the main factor that determinates the aggregates' strength, and their ability to destruction and reconstruction.

Among other factors affecting the size and strength of the HPP aggregates, the kinetics and mechanism of aggregate formation at conditions of slow stirring should be taken into account. Relatively large and weakly charged particles in the first water interact quickly enough (the time of interaction corresponding to $V_{\mathrm{rms(max)}}$, is only 200–250 s). At these conditions, large aggregates of random structure which is probably far from the equilibrium, are formed. As the time of slow stirring increases, aggregates are not really destructed, but are getting "worn" and re-formed gradually, approaching to an energetically more favorable structure. Destruction as such takes place only after a series of consecutive stirring at turbulent conditions ($n = 500$ rpm). Such a slight "weariness", and formation of aggregates with more stable structure is probably due to the interaction of primary aggregates and those of the next orders in the secondary minimum. Owing to this rearrangement, the aggregates are becoming looser, and their structure approaches to the most energetically favorable value. The less the partial concentration in the aggregating dispersion, the slower the aggregates' structure formation and it is closer to the equilibrium. That is why the time $\tau_{\max}$, corresponding to $V_{\mathrm{rms(max)}}$, increases and the effect of "weariness" of aggregates decreases with a decrease of the AS dose, and at dose 5 mg/l it disappears at all (Fig. 1), in line with the mentioned speculations.

Formation of HPP aggregates in water II at similar conditions occurs somewhat different. Smaller, weakly hydrated and higher charged particles of the AS hydrolysis products aggregate rather slowly ($\tau_{\max} = 1000$–1200 s) that is due to considerable repulsion energy between particles. This enables particles to form aggregates with structure close to equilibrium. The diameter of these aggregates is somewhat smaller than that for the system II, and the "weariness" effect for them is absent.

Based on the effects analyzed, bonds in the aggregate structure in water II can be considered to be weaker, that makes these aggregates sensitive to modest but prolonged stirring.

At turbulent conditions (high-velocity stirring), an abrupt break of bonds between particles in aggregates in both cases may occur, followed by spasmodic decrease of V_{rms} values. On the other hand, the aggregates in the system II do not deform substantially, before the beginning of rapid stirring. It means that in the first case rapid stirring only accelerates the changes occurring within the aggregates during slow stirring, while in the second case it provokes these changes. At the same time the destruction factor for the aggregates in water I is lower than that in water II. Probably this difference can be explained by the influence of the HPP surface hydration: in water I the particles are more (almost an order of magnitude) hydrated than in water II, which facilitates the processes of the aggregates' rearrangements. This factor complicates the processes of reconstruction of the aggregates' structure after ceasing the stirring. The data presented signify the sufficiently reversibility of the processes of aggregates' destruction, especially at water II conditions (40%).

Thus, the investigations described testify that AS HPP aggregates formed in a model water with parameters that facilitate appearance of small particles with relatively high charge and zeta-potential values, low degree of hydration and interaction of primary particles predominantly in the primary minimum, are more stable and can be more easily reconstructed during intensive stirring, than aggregates built of particles with lower charge, higher initial particle size and hydration, aggregating in the secondary minimum.

Acknowledgement The authors are grateful to Prof. J. Gregory for ideas of such studies and useful discussions, and to Dr. I. Solomentseva for performing some experiments and participation in the evaluation of the results. We also thank the Hungarian TeT Agency for support of this study in the frame of the Hungarian-Portuguese TeT Project P 11/03.

References

1. Zapolsky AK, Baran AA (1987) Coagulants and Flocculants in Water Treatment. Khimiya, Leningrad (in Russian)
2. Amirtharajah A, O'Melia CR (1990) AWWA. In: Pontius FW (ed) In Water Quality and Treatment. McGraw-Hill, New York, p 269
3. Tambo N, Watanabe Y (1979) Water Res 13:409
4. Goncharuk VV, Solomentseva IM, Teselkin VV (2001) Sov J Water Chem Technol 23:227
5. Solomentseva IM, Gerasimenko NG, Barany S (1999) Colloids Surf 151:113
6. Duan J, Gregory J (2003) Adv Colloid Interf Sci 100–102:475
7. Solomentseva IM, Barany S, Gregory J (2003) Colloids Surf A 230:117
8. Blaser S (1999) Colloids Surf A 1–3:215
9. Yukselen MA, Gregory J (2002) Environ Eng Sci 19(4):229
10. Yukselen MA, Gregory J (2003) Int J Miner Process 1659:435
11. Yukselen MA, Gregory J (2004) J Chem Technol Biotechnol 79:782
12. Gregory J (1985) J Colloid Interf Sci 105:357
13. Gerasimenko NG, Solomentseva IM, Zapolsky AK (1998) Sov J Water Chem Technol 20:329
14. Goncharuk VV, Solomentseva IM, Gerasimenko NG (1999) Sov J Water Chem Technol 21:52
15. Solomentseva IM, Gerasimenko NG, Shilov VV (1994) Sov J Water Chem Technol 16:606

Progr Colloid Polym Sci (2008) 135: 77–86
DOI 10.1007/2882_2008_098

Published online: 30 August 2008

J. Telegdi
T. Rigó
É. Pfeifer
T. Keszthelyi
E. Kálmán

Nanolayer Coatings

J. Telegdi (✉) · T. Rigó · É. Pfeifer · T. Keszthelyi · E. Kálmán
Institute of Surface Chemistry and Catalysis, Department of Surface Modification and Nanostructures, Chemical Research Center, Hungarian Academy of Sciences, P.O. Box 17, 1525 Budapest, Hungary
e-mail: telegdi@chemres.hu

Abstract Langmuir–Blodgett and self assembled molecular layers of hydroxamic and phosphonic acids deposited onto metal surfaces were studied in corrosive aqueous solution with and without corrosion relevant microorganisms. The role of intermolecular interaction, molecular layer thickness, self assembled molecular layer (SAM) formation time as well as the alkyl chain length in the anticorrosion processes and in the microbiological adhesion was in the focus of our experiments. Langmuir films characterized by isotherms and Brewster angle microscopy (BAM) were deposited as Langmuir–Blodgett (LB) layers onto copper and iron surfaces. The SAM layer formation was followed by sum frequency vibration (SFG) and infrared (IRRAS) spectroscopy, the morphology of the LB and SAM films was visualized by atomic force microscopy (AFM), and the change in the wettability was characterized by contact angle values measured in pure water on metals (with and without nanocoatings). The anticorrosion efficiency of the nanofilms was confirmed by electrochemical as well as by AFM measurements. The decrease in the microbial adhesion caused by the nanolayers was visualized by epifluorescence microscopy and enumerated by microbiological technique. Correlation was found between the metal surface energy and the number of adhered corrosion relevant microorganisms.

Keywords Anticorrosion efficacy · Hydroxamic and phosphonic acids · Inhibition of microbial adhesion · Intermolecular interaction · Langmuir · Langmuir–Blodgett · SAM layers

Introduction

The importance of nanolayers in different technologies (coatings, sensors etc.) has increased in the last decades. Mainly two types of nanofilm are discussed in the literature, the Langmuir–Blodgett and the self assembled layers. The early literature on Langmuir monomolecular layers on LB films was reviewed by Gaines [1] and Petty [2]. Roberts also contributed to the LB film topic [3]. Ulman who has discussed both the LB and SAM layers has given an introduction to many characterization techniques [4], and Schwartz has presented a review on LB film structures [5]. The preparation, characterization and application of LB films have been surveyed by several authors [6–9]. All these papers discuss not only the molecules which can form nanofilms but also the techniques applicable for investigation of molecular layers. Over the last two decades the sensitivity of a number of experimental techniques has been increased. These techniques include photoelectron spectroscopy, X-ray diffraction and reflection, neutron reflection, infra red and Raman spectroscopy, electron diffraction and different scanning probe microscopy. By

fluorescence and Brewster angle microscopy larger structures of nanolayers can be observed, and in special cases the quartz crystal nanobalance can also provide important information on film formation. All these methods help in understanding the LB and SAM layer formation and, on one hand, in elucidating the binding forces between solids and nanolayers, and, on the other hand, in showing the conformation of the amphiphiles in nanolayers.

In our experiments two types of amphiphilic molecules were used for nanolayer preparation. Phosphonic acids have often discussed in the literature [10–16]. First Lossen reported the existence of hydroxamic acids (acyl hydroxylamines) in 1868 [17]. Biological activities of natural hydroxamic acids were also demonstrated by several authors [18–21]. Extended research on water soluble mono- and dihydroxamic acids were done by Farkas and her co-workers [22–25]. The corrosion inhibiting efficiency of benzohydroxamic acid derivatives and dihydroxamic acids in aqueous solution were also studied [26, 27], but on nanolayers of hydroxamic acids only limited publications are available. The first experiments on hydroxamic acid SAM nanolayers were reported by Folkers et al. [28] who have demonstrated that the SAM layers of alkyl hydroxamic acids are more stable on metal oxide surfaces than the similar carboxylic and phosphonic acids. The most recent publication on alkyl hydroxamic acids [29] discusses monomer and polymer hydroxamic acid in SAMs.

In our previous publications we have shown how can the pH and the subphase temperature influence the molecular layer structure [30] and in some cases the application of these nanolayers was also demonstrated [31, 32]. In this paper intermolecular constants calculated for L monolayers of hydroxamic acid amphiphiles as well as comparative analysis of anticorrosion efficiency of LB and SAM films produced from the same amphiphiles will be presented. Additionally, the influence of the solid surface energy of metals (with and without nanocoatings) on the microbial adhesion will be discussed.

Experimental

Chemicals: alkyl hydroxamic acids (decanoyl (C10N), lauroyl (C12N), palmitoyl (C16N) and stearoyl (C18N) hydroxamic acids) synthesized from the proper alkyl acid chloride and hydroxyl amine [33] were re-crystallized from ethyl acetate. Octadecanoyl phosphonic acid (C18P) was the product of a Michaelis–Arbusov reaction. Melting points, thin layer chromatography, elemental analysis and IR spectroscopy were applied for purity control.

Metal surface finishing: copper (99.99%) and iron (99.99%) surfaces ground with emery paper (200–1200 grit SiC) and polished with Al_2O_3 paste (0.3 μm), were washed with water, degreased with acetone and let it dry under atmospheric conditions.

Nanolayer Preparation

Langmuir and Langmuir–Blodgett Molecular Films

Nanolayers at the air/water interface prepared by spreading a solution of the amphiphiles (dissolved in chloroform) on an ultra pure aqueous subphase were investigated in LB trough (NIMA Technology 611D) equipped with Wilhelmy plate pressure sensor. After spreading and evaporation of the solvent (10 min) the monolayer was compressed and transferred to the polished solid metal surfaces under accurate automatic control of surface pressure which is essential for proper LB deposition, as during film transfer the area of the monolayer is reduced continuously in order to keep the surface pressure at a constant value. To produce high quality LB films the deposition speed is also an essential factor (20 mm/min). The morphology of the Langmuir monomolecular layers were characterized by Brewster angle microscopy (BAM, miniBAM, Göttingen). This technique is a well established method to visualize nanolayers with different structures (condensed domains, scattered molecules etc.). The principle of the operation of BAM is that p-polarized light at the Brewster angle is not reflected from the interface. The water surface is very smooth and has an optically well-defined background signal at the Brewster angle. The areas of different brightness are due to different molecular layer densities on the surface. A single molecular layer is resolved in high contrast. This is an ideal instrument for on-line visualization of homogeneity and of domain structure in nanolayers. In our experiments at different pH and temperature values of the subphase in situ BAM images were taken at the gas-, liquid- and solid phases as well as after the collapse of the molecular layers.

SAM Layer Preparation

Polished, washed and degreased copper and iron coupons were dipped into the solution of amphiphilic materials dissolved in tetrahydrofuran (Merck). The completeness of a compact layer formation was followed by infra red (Nicolet Magna 750 FTIR spectrometer equipped with a liquid nitrogen cooled MCT detector) and sum frequency vibration spectroscopy (EKS-PLA, Vilnius Lithuania). The maximum intensity of peaks in SFG spectra has proven the compactness of the nanolayers.

The solid surface morphology (with and without nanocoatings) were visualized by atomic force microscopy (AFM, Digital Instruments, NanoScope III).

Electrochemical Experiments

In a three-necked cell filled with 300 ml sodium sulphate electrolyte (0.1 M; pH = 3.5 (copper); pH = 7.0 (iron); room temperature) were immersed the working electrode

(copper or iron with and without nanolayers), the counter electrode (Pt) and the reference (saturated calomel) electrode. The corrosion potential and the polarisation curves were registered in a potentiostat (Radiometer PG-201). Polarization resistance values were calculated from electrochemical impedance spectra (EIS).

Microbial Adhesion Experiments

Metal coupons with or without nanolayers were immersed either into cooling water (with mixed population of corrosion relevant microorganisms) or into pure culture of *Desulfovibrio desulfuricans*, *Acidithiobacillus ferrooxidans* and *Leptospirillum ferrooxidans*. The presence of adhered microbes was demonstrated by epifluorescence microscope (Zeiss) after acridine orange staining (0.01% acridine orange in water).

Results and Discussion

Several experimental techniques have enabled us to obtain detailed information on Langmuir and Langmuir–Blodgett films. The influence of pH and temperature of the subphase is important to know in order to find the most proper conditions for the preparation of the most compact Langmuir and LB layers.

Isotherms Measured at Different pH and Temperature

After spreading long-chain hydroxamic acids on pure water sub-phase, the Langmuir monolayers were characterized by surface pressure/area (Π/A) isotherm at different temperatures (Fig. 1). The slope of the isotherms is temperature dependent, different phase transitions can be observed if the temperature varies, similarly to results given in the literature for other molecules [34, 35].

On pure water surface the pressure/area isotherms show three distinct regions, which can be described as gas-, liquid- and solid-phase. The transition pressure between liquid and solid phase is 20 mN/m in the case of the C16 N, and 18 mN/m at C18 N. For the sake of comparison similar value of the stearic acid is 23 mN/m [36]. This transition is temperature-dependent, and the molecules need larger surface area at higher temperature. The decrease in the temperature results in a more rigid Langmuir monolayer. The collapse pressure of the monolayers on pure water sub-phase at pH 5.6 decreases with increasing temperature. This is in accordance with the results mentioned in the literature on others type of molecules [36]. All important information about the monolayers under investigation is summarized in Table 1.

Our investigation on hydroxamic acid monolayers was not confined to their non-dissociated state but at increased pH values on the dissociated form, too. The monolayer pressure-area isotherms of palmitoyl and stearoyl hydroxamic acids on pure water sub-phase at different pH values can be correlated with the length of the carbon chain. As expected, under identical conditions the molecule with longer carbon chain gives a more rigid film than the shorter one. The stability of the C18HA monolayer increases with the increase of sub-phase pH from acidic to near neutral values up to about the pK value. At pH 5.6, a stable, compact film is obtained.

This behavior is supported by the surface demand of the C18HA molecules at different pH values. The pH dependence of the molecular area has shown a minimum at about 5.5. At extreme pH values, i.e., at acidic and espe-

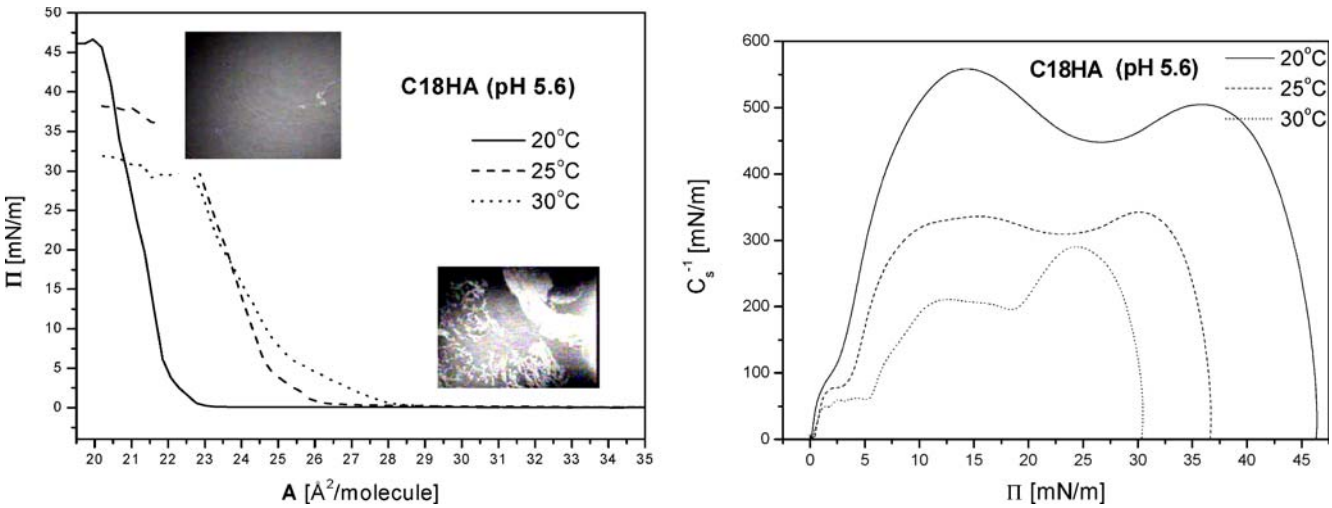

Fig. 1 Temperature dependent isotherms and compression modulus of the stearoyl hydroxamic acid; BAM images taken at the "gas" phase as well as after collapse are inserted [30]

Table 1 Characteristic parameters of three amphiphiles

pH	Collapse pressure [mN/m]		
	C16N monolayer	C18N monolayer	C18P monolayer
2.0	35	35	31
4.0	29	33	27
5.6	28	33	29
8.0	27	33	31
10.0	26	34	–
T [°C]			
20	38	46	34
25	34	37	30
30	27	31	24
Molecular area [Å^2/molecule]	27	21	31

cially at alkali pH values these molecules occupy larger surface area, which may be due to the structure of the head group. Alkyl hydroxamic acid monolayers can dissociate at higher pH. The pK measured in solution is shifted in some cases to higher values on the water subphase [37].

As these hydroxamic compounds are weak acids, when the sub-phase is acidified to pH 2, their ionization is completely suppressed and they behave like neutral molecules. At this low pH (protonated structure, non-dissociated neutral molecules) the C(O)NHOH groups are switched by intermolecular hydrogen bonding, which gives 2D net of molecules. At a little higher pH value hydrogen ions dissociate from the hydroxamic acid and hydroxamate ions are involved into the molecular film. With increasing pH in the sub-phase, the dissociation of the individual molecule as well as the ratio of deprotonated groups increases. The hydrogen bond between protonated (–OH) and deprotonated groups (negatively charged O^-) is stronger, around pH = 6 the head groups of the molecules require smaller area on the sub-phase. Competition between the hydrogen bond and electrostatic repulsion can be observed. At pH around the pK value the molecular area has a minimum, which may be due to the shorter intermolecular distance between protonated and deprotonated oxygen atoms. At higher pH values repulsion between charged head groups predominates, and the electrostatic repulsion counteracts with the van der Waals forces between the long carbon chains; the consequence is that the molecules require more area. The pH-dependent molecular area curve is asymmetric (Fig. 2).

The transition pressure between liquid and solid phases varies with the pH values of the sub-phase. At increasing pH values the transition pressure decreases, but the collapse pressure (when multi-layers are formed) is not significantly affected by it (Table 1).

In the first theoretical description of the Π/A isotherms given by De Boer [38] the van der Waals equation for non-

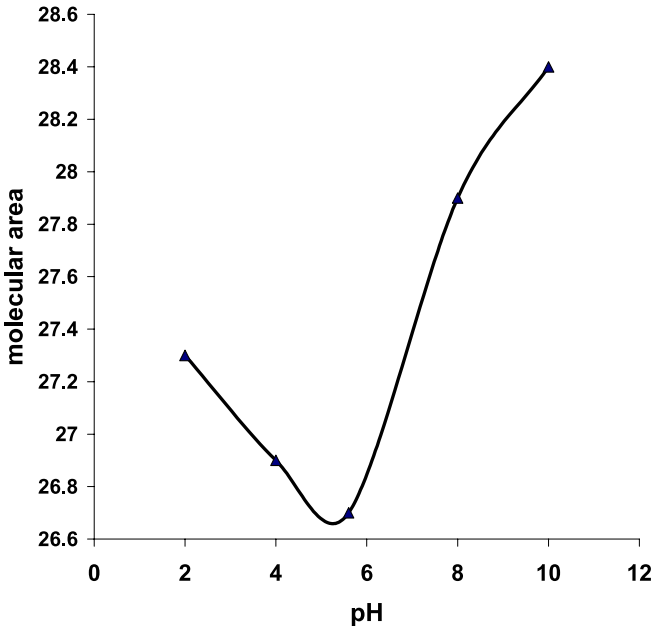

Fig. 2 pH-dependent molecular areas in case of stearoyl hydroxamic acid

ideal two-dimensional gases is the follow

$$\Pi = RT/(A-\omega) - a/A^2\,, \tag{1}$$

(where R: gas constant, T: temperature, ω: the area per one molecule of the amphiphile in the extremely compressed monolayer, A: area available for molecules during two-dimensional condensation, a = molecular constant).

This predicts the existence of metastable state for the high values of the molecular constant a which is valid when the area available for molecules decreases but the surface pressure remains unchanged. When the surface pressure increases, the equation [39] is valid, when $A \geq A(\mathrm{c})$

$$\Pi = RT/(A-\omega) - B\,,$$
(B: intermolecular constant) (2)

$A(\mathrm{c})$ is the area available for the molecules at liquid-expanded/liquid-condensed state.

The pH- and temperature-dependent surface pressure/molecular experimental isotherms were used for the quantitative determination of intermolecular constants. The intermolecular constants calculated from Eq. 2 are summarized in Tables 2 and 3.

Not only the van der Waals interaction and hydrogen bond formation but electrostatic interactions also play important role in monolayer formation. According to the calculated intermolecular constants the van der Waals force increases with increasing alkyl chain. Table 3 summarizes the effect of pH on the intermolecular constants. At low pH a weaker hydrogen bond, at higher pH values the elec-

Table 2 Temperature-dependent intermolecular constants

	B [mN/m]		
	20 °C	25 °C	30 °C
C16N	–0.0129	–0.0607	–0.1019
C18N	–0.0291	–0.1393	–0.1747

Table 3 The pH-dependent intermolecular constants

	B [mN/m]			
	pH = 2	pH = 4	pH = 5.6	pH = 8
C16N	–0.6771	–0.1639	–0.0607	–0.7766
C18N	–0.6833	–0.2933	–0.1393	–0.6084

trostatic repulsion modifies the van der Waals attraction. At pH 2 a lateral hydrogen bond network links the internal groups in the monolayer. At near neutral pH values stronger mutual forces lead to stable films. At alkaline pH range, because of strong electrostatic repulsion, the nanolayer structure shows less ordering, the aggregates are in small lace-like domains.

Characterization of the Nanolayers

Significant increase in contact angles has proven the successful layer deposition (Table 4). According to the literature [40], when the contact angle value of a nanolayer coated surface is less than 110°, the film on the solid is partly disordered or there are defect places in it. In our cases these values significantly exceed the 110° that prove the presence of films on metals with hydrophobic character and the existence of tightly packed methyl groups.

Infra red spectroscopic techniques are accepted methods for studying nanolayers as they provide information on the binding mode and on the molecular conformation and orientation. The time-dependent measurement of infra red reflectivity can also be used to monitor the adsorption. Our measurements were completed by IRRAS and SFG measurement. The first technique has proven a successful layer-by-layer deposition (Fig. 3). On copper or iron substrates in case of monolayer a perpendicular molecular arrangement and a tilted one in multi-layers (up to 9) was observed. The average tilt angle is around 23°. Linear relationship was observed between the number of layers and the asymmetric and symmetric CH_3 stretching band intensity (with $R^2 = 0.9992$). The other type of well-ordered structure is involved into SAM layers. The chain-length and deposition time-dependent increase in intensity got by these techniques has helped to prepare compact SAM layers (Figs. 4 and 5). These methods are very complementary because not only the adsorption and the layer-by-layer deposition are detected but also the completeness of the SAM process is demonstrated. The SFG reflectivity gives information about secondary processes like increasing ordering in the nanolayers at the surface [41, 42]. In the nanolayers of hydroxamic acids (like in the case of fatty acids [43, 44]) the alkyl chains are in all-trans conformation with their long axis normal to the substrate.

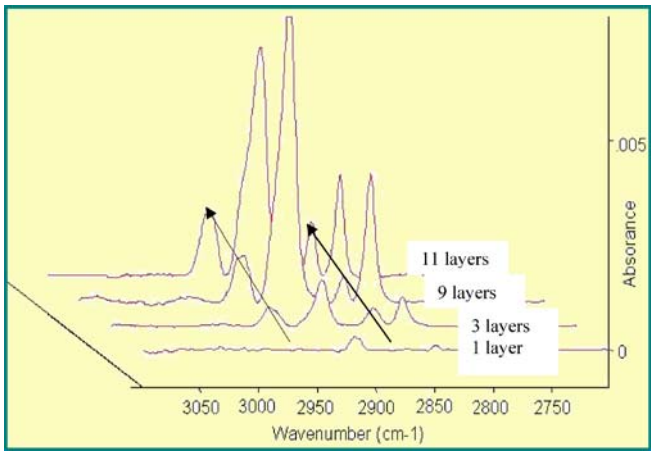

Fig. 3 IRRAS spectra of LB nanolayers of stearoyl hydroxamic acid deposited onto copper

Table 4 Contact angles measured in water on copper and iron surface with and without nanolayers

Surface	Control	Stearoyl hydroxamic acid LB monolayer	Octadecanoyl phosphonic acid LB monolayer
	Θ dyn adv./retr.	Θ dyn adv./retr.	Θ dyn adv./retr
Copper	78°/31°	128°/95°	124°/88°
Iron	68°/32°	123°/72°	126°/95°

Electrochemical Measurements

The anticorrosion efficiency of the nanolayers measured by electrochemical polarisation is demonstrated in Table 5.

The efficiency data show that the hydroxamic acid nanolayers both in LB and SAM films decrease the corrosion processes and their influence slightly depends on the length of carbon chain of the amphipiles.

Results of other electrochemical technique (EIS; Fig. 6) support the efficiency data got by polarization measurement. The polarization resistance (R_p) data (which are the measure of the nanolayer resistance in the corrosion process) increase significantly with increasing layer formation time. These films form insulating films between the aqueous aggressive environment and the metal surface

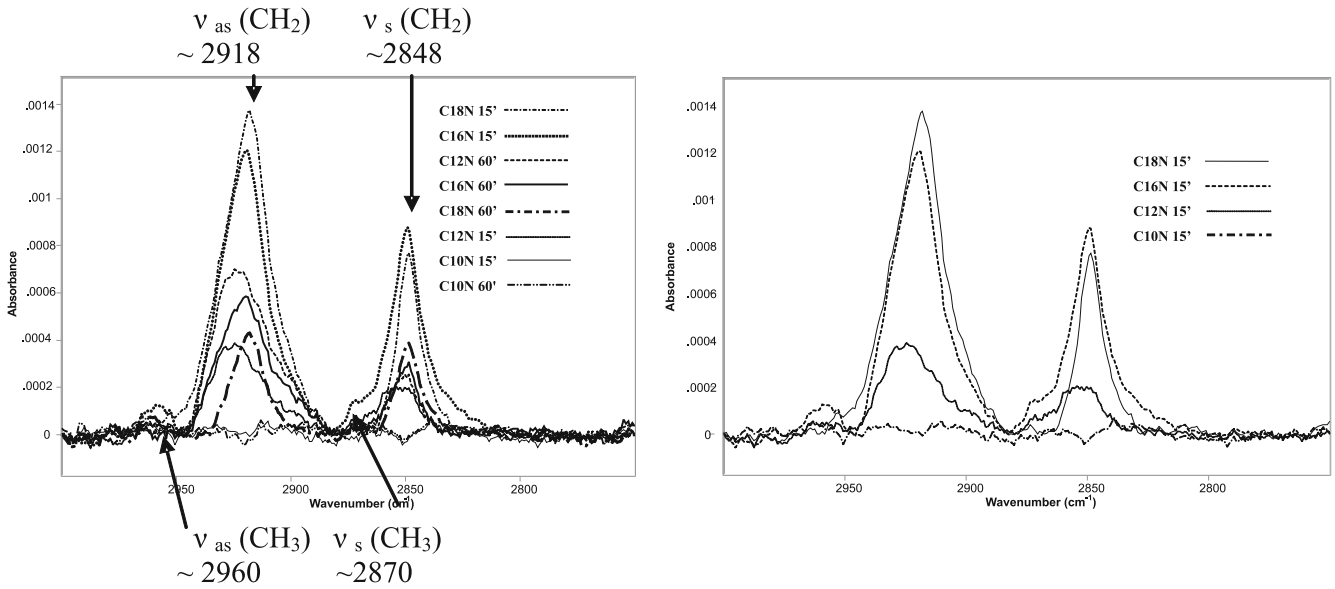

Fig. 4 SAM layers on copper surface; chain-length and time-dependent IRRAS spectra (0° polarization)

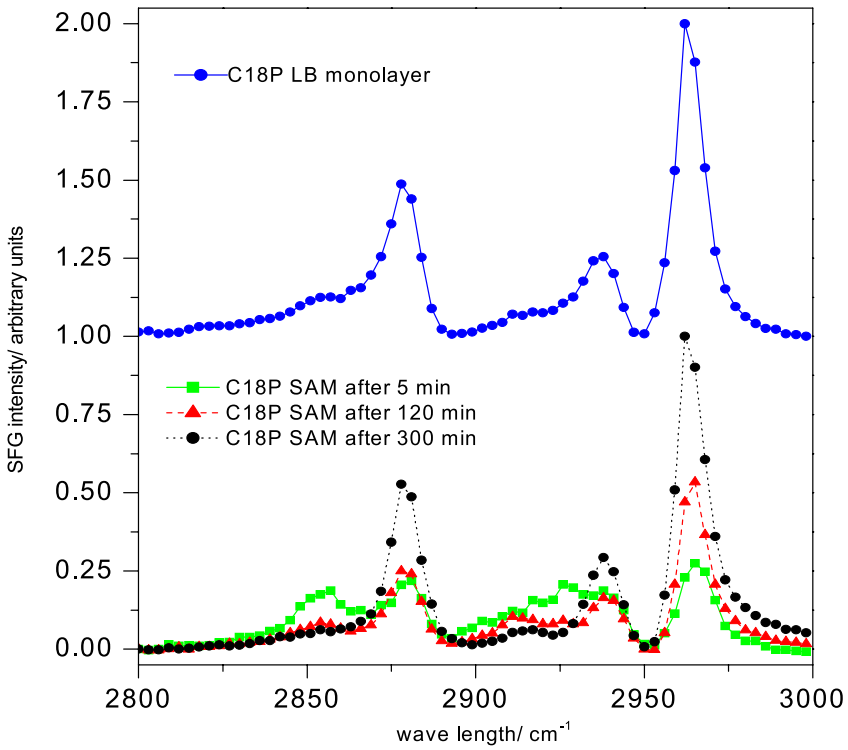

Fig. 5 SFG spectra of the octadecanoyol phosphonic acid in LB and time-dependent SAM layer deposited onto iron surface

and block the active places. Higher R_p values mean less porosity of the layer.

Control of Microbial Adhesion by Nanolayers

Desulfovibrio desulfuricans can much less adhere to nanocoated metal surfaces then to pure copper or iron coupons (Fig. 7). Similar experimental results were observed on pyrite in the presence of *Acidithiobacillus ferrooxidans* and *Leptospirillum ferrooxidans* (Fig. 8; these microorganisms are responsible for bioleaching processes). The example of experiments carried out by pyrite coupons shows the effectiveness of multilayers in comparison with a monomolecular film. On copper and

Table 5 Results of anticorrosion experiments got in the presence of LB monomolecular films and SAM layers developed from hydroxamic acids, deposited onto copper electrodes (0.1 M Na_2SO_4, pH = 3; 23 °C; η = efficiency)

	E_{corr} [mV]	j_{corr} [μA cm^{-2}]	η [%]
Copper	–26	0.91	–
Cu + LB:palmitoyl hydroxamic acid	–29	0.35	62
Cu + LB:stearoyl hydroxamic acid	–31	0.25	73
Cu + SAM:decanoyl hydroxamic acid	–36	0.13	76
Cu + SAM:lauroyl hydroxamic acid	–38	0.17	81
Cu + SAM:palmitoyl hydroxamic acid	–39	0.16	82
Cu + SAM:stearoyl hydroxamic acid	–40	0.14	85

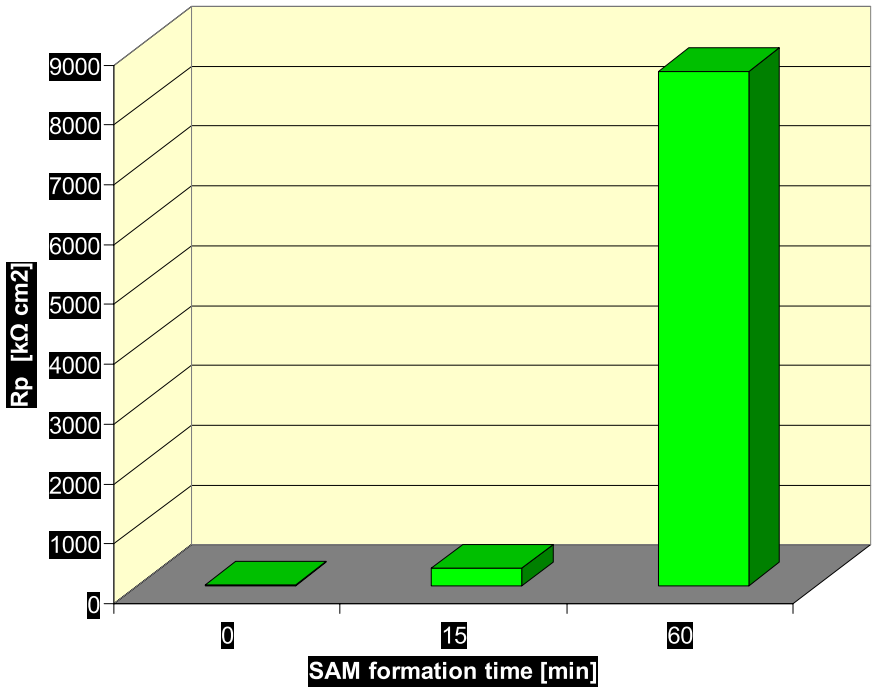

	Rp [kΩcm^2]	
Measuring time [h] →	**1**	**20**
SAM formation time [min]		
5	**5**	**15**
15	**106**	**305**
60	**2564**	**8596**

Fig. 6 Results of electrochemical impedance spectroscopic measurements with copper electrodes with and without SAM layers developed from decanoyl hydroxamic acid

iron coupons with and without nanocoatings after dipping into cooling water (Table 6), the number of the orange colored (dead) cells and green colored (vial) cells show how effectively the nanolayer could repel the microorganisms from the surface. The increase in SAM formation time and LB monomolecular layer number enhance the layer quality (ordering, compactness, porosity), a more hydrophobic film can better inhibit the adhesion of microorganisms.

We tried to find a quantitative correlation between the surface properties and the number of adsorbed microorganisms. Table 6 summarizes the metal surface energies got from the contact angle values and the number of the microorganisms irreversible adsorbed onto the solids (with

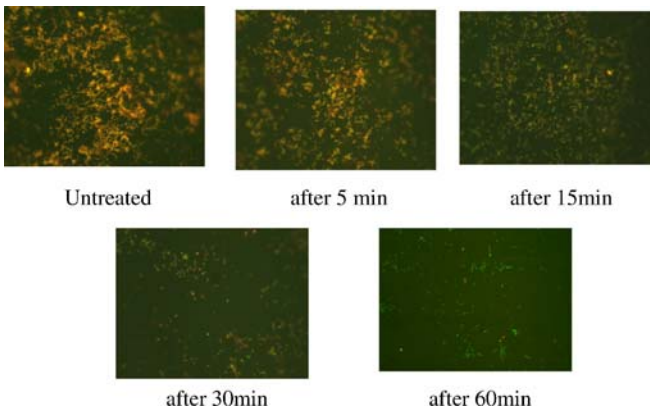

Fig. 7 Adhesion of *Desulfovibrio des*. on copper surface covered by SAM layer; influence of SAM layer formation time; the amphiphile is lauroyl hydroxamic acid

and without nanocoatings). The number of microorganisms of cooling water adhered to pure metal surfaces are larger with order of magnitudes than those measured on nanocoated surfaces. The only exception is the iron coated by C18P monolayer, which effectively inhibit the corrosion processes, but the adsorption of microorganisms is little decreased. From the measured contact angle values the surface energies were derived. It is well known that the surface energy of pure metals is high. Hydrophobic nanocoatings decrease this value. According to our experimental results the corrosion relevant microbes, which are covered by ionic biocoating, dislike the hydrophobic surface. Increase in surface energy results in decreased microbial number on the surface.

Conclusion

This paper has presented results on amphiphilic molecules in LB and SAM layers. The change in the pH and

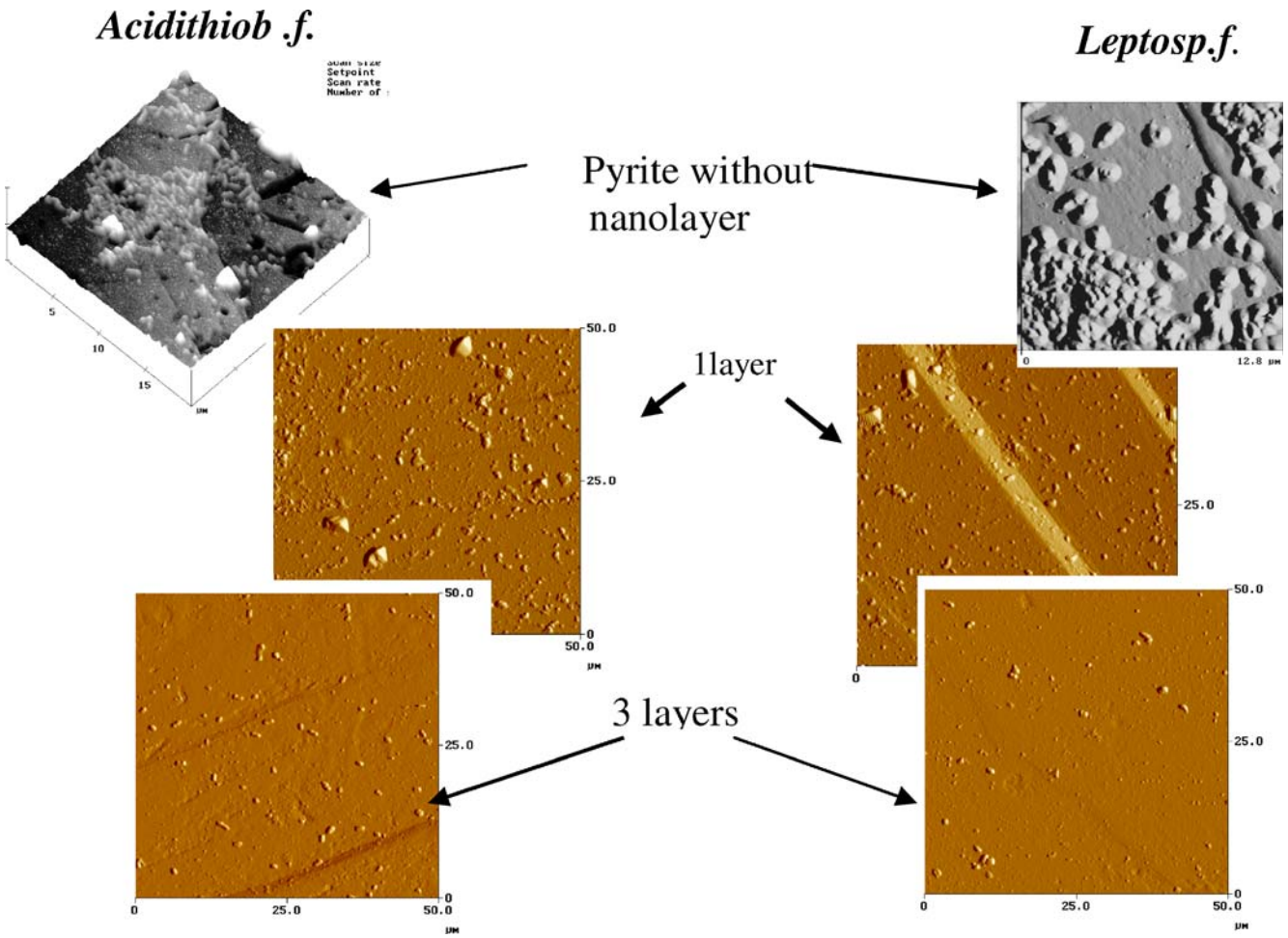

Fig. 8 Pyrite surfaces after immersion into media inoculated with *Acidothiobacillus ferrooxidans* and *Leptospirillum ferrooxidans*; influence of nanolayers onto the microbial adhesion

temperature values was reflected in isotherms of Langmuir monomolecular layer which allowed us to calculate characteristic parameters (molecular area, intermolecular constants etc.) of the hydroxamic and phosphonic acid amphiphiles. Contact angles, SFG and IRRAS techniques have rendered possible to characterize LB layers, to ascertain the most proper SAM layer formation time. By electrochemical measurements the anticorrosion effectiveness of these nanolayers has been proven. Positive correlation was found between the efficacy of nanofilms and

1. the molecular layer number in LB films;
2. the SAM layer developing time;
3. the carbon chain length in the amphiphiles.

These nanolayers could control not only the corrosion processes but the microbial adhesion too, that was ascertained by the correlation between the surface energy and the number of adhered microorganisms.

Acknowledgement This work was supported by Marie Curie Research Training Network (CHEXTAN). The authors convey their sincere thanks to Katalin Tímár for the synthetic work.

Table 6 Correlation between the surface energy and the microbial invasion on different, coated and uncoated surfaces (iron, copper, nanolayers, coupons in cooling water with for 5 days)

Metal	Surface energy [erg cm^{-2}]	Microorganisms in biofilm [cell cm^{-2}]	
Fe	62.99	5.2×10^5	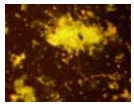
Fe + LB:stearoyl hydroxamic acid	25.06	3.6×10^3	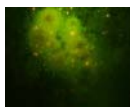
Fe + LB:octadecanoyl phosphonic acid	42.39	1.6×10^5	
Cu	56.67	1.2×10^5	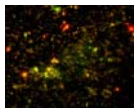
Cu + LB:stearoyl hydroxamic acid	25.66	6.8×10^2	

References

1. Gaines GL (1966) Insoluble Nanolayers at liquid/gas interfaces. Interscience, New York
2. Petty MC (1996) Langmuir–Blodgett films. An Introduction. Cambridge Univ Press, Cambridge
3. Roberts GG (1990) Langmuir–Blodgett Films. Plenum Press, New York
4. Ulman A (1991) An Introduction to Ultrathin Organic Films, from LB to Self Assembly. Academic Press, San Diego
5. Schwartz DK (1997) Surf Sci Rep 27:241
6. Roberts GG (1985) Adv Phys 34:475
7. Swalen JD, Allara DL, Andrade JD et al. (1987) Langmuir 3:932
8. Petersen IR (1994) In: Mahler G, May V, Schreiber M (eds) The Molecular Electronic Handbook. Marcel Decker, New York
9. Mohai M, Kiss É, Tóth A, Szalma J, Bertóti I (2002) Surf Interf Anal 34:772
10. Allara DL, Nuzzo RG (1985) Langmuir 1:45 and 52
11. Slotter NE, Porter MD, Bright TB, Allara DL (1986) Chem Phys Lett 132:93
12. Thoughton EB (1988) Langmuir 4:365
13. Laibinis PE (1991) J Am Chem Soc 113:7152
14. Laibinis PE, Whitesides AM (1992) J Am Chem Soc 114:9022
15. Jennings GK, Munkro JM, Yong TH, Laibinis PE (1998) Langmuir 14:6130
16. Van Alsten JG (1999) Langmuir 15:7605
17. Lossen H (1869) Justus Liebigs Ann Chem 150:134
18. Miller MJ (1989) Chem Rev 89:1563
19. Nagarajan K, Rajappa S, Rajagopalam P et al. (1991) Indian J Chem B 30:222
20. Nakamura S, Inouye Y (1989) Kagaku Zokan (Kyoto) 116
21. Schmetzer J, Stetter J, Hammann I, Homeyer B (1982) Eur Pat 50, p 283
22. Farkas E, Megyeri K, Somsák L, Kovács LJ (1998) Inorg Biochem 70:41
23. Farkas E, Enyedi ÉA, Csóka H (1999) Polyhedron 18:23910
24. Farkas E, Enyedi ÉA, Csóka H (2000) J Inorg Biochem 79:205
25. Farkas É, Enyedi A, Zékány L, Deák G (2001) J Inorg Biochem 83:107
26. Shaban A, Kálmán E, Telegdi J (1998) J Electrochim Acta 43:159
27. Alaghta A, Felhõsi I, Telegdi J, Bertóti I, Kálmán E (2007) Corr Sci 49:2754
28. Folkers JP, Gorman CB, Laibinis PE et al. (1995) Langmuir 11:813
29. Deng H, Nanjo H, Qian P et al. (2008) Electrochim Acta 53:2972
30. Telegdi J, Rigó T, Kálmán E (2005) J Electroanal Chem 582:191
31. Telegdi J, Rigó T, Kálmán E (2004) Corr Eng Sci Technol 39:65
32. Telegdi J, Rigó T, Beczner J, Kálmán E (2005) Surf Eng 21:1
33. Hauser CR, Renfrow WB (1971) Org Synth Collect 2.67
34. Baret F, Hasmonay H, Firpo J et al. (1982) Chem Phys Lipids 30:177
35. Seoane R, Miòones J, Conde O et al. (2000) J Phys Chem B 104:7735
36. Kang YS, Lee DK, Kim YS (2001) Synth Met 117:165
37. Betts JJ, Pethica BA (1956) Trans Faraday Soc 52:1581

38. De Boer JH (1945) The Dynamical Characters of Adsorption. Oxford Univ Press, London
39. Jasper JJ (1972) J Phys Chem Ref Data 1:841
40. Engelking J, Wittemann M, Rehahn M, Menzel H (2000) Langmuir 16:3407
41. Schnitter M, Engelking J, Heise A, Miller RD, Menzel H (2000) Macromol Chem Phys 201:1504
42. Umemura J, Takeda S, Hasegawa T, Takenaka T (1993) J Mol Struct 297:57
43. Kimura F, Umemura J, Takenaka T (1986) Langmuir 2:96
44. Holland RF, Nielsen JR (1962) J Mol Spectrosc 9:436

Progr Colloid Polym Sci (2008) 135: 87–92
DOI 10.1007/2882_2008_117

Published online: 12 September 2008

K. Hill
C. B. Pénzes
B. G. Vértessy
Z. Szabadka
V. Grolmusz
É. Kiss

Amphiphilic Nature of New Antitubercular Drug Candidates and Their Interaction With Lipid Monolayer

K. Hill · C. B. Pénzes · É. Kiss (✉)
Laboratory of Interfaces and Nanostructures, Institute of Chemistry, Eötvös University, P.O. Box 32, 1518 Budapest 112, Hungary
e-mail: kissevak@ludens.elte.hu

B. G. Vértessy
Institute of Enzymology, Hungarian Academy of Sciences, Budapest, Hungary

Z. Szabadka · V. Grolmusz
Protein Information Technology Group, Institute of Mathematics, Eötvös University, Budapest, Hungary

Z. Szabadka · V. Grolmusz
Uratim Ltd., Nyíregyháza, Hungary

Abstract Tuberculosis remains a major problem throughout the world causing large number of deaths, more than that from any other single infectious disease [1]. The treatment of the chronic inflammatory caused by *Mycobacterium tuberculosis* (*Mtb*) requires prolonged chemotherapy often associated with unwanted side effects and developing resistant bacterium strains [2]. Introduction of new in silico identified drug candidates which are expected to be specific inhibitor of dUTPase [3] a vital enzyme of *Mtb* presents a novel approach in the combat with the disease. Three of those drug candidates – ligand 3, 4 and 69 – were compared in the present study considering their interfacial properties, polarity, amphipatic character and lipid affinity which are relevant in pharmaceutical function.

Langmuir monolayers were prepared from the ligands and their mixture with phospholipon as a simple model material of cell membrane. Analysis of the isotherms showed than ligand 3 and 44 presents significant affinity to the lipid building into the monolayer. The penetration ability of the drug candidates were also characterized by measuring the increase of surface pressure of the lipid monolayer following their injection to the subphase at two initial lipid densities. The results were in accordance with the order of log P_{app} values determined for the three compounds as well as with their dynamic surface activity although the highest difference amongst the three ligands was observed in the penetration ability which is of paramount importance in the selection of promising therapeutic agent.

Keywords Langmuir monolayer · Lipid affinity · Membrane model · Penetration of drug · Surface activity

Introduction

Pulmonary tuberculosis is a chronic respiratory transmitted inflammatory disease. One third of the human population of the world is infected. *Mycobacterium tuberculosis* (*Mtb*) causes 8 million new cases and nearly two million people die every year [4]. The problems and difficulties of the antitubercular therapy include the prolonged duration of treatment, the dose related drug toxicity and unwanted side effects like the damage of liver and kidney. The aim is to improve patient compliance and reduce harmful effects decreasing the duration of treatment. The emergence of drug resistant strains of *Mtb* has made the search for new drugs more urgent [3, 5, 6].

One of the new approaches to find more effective drugs is based on the inhibition of bacterial enzymes and hence killing the bacteria. A number of possible specific inhibitor of dUTPase, an enzyme of *Mtb* essential for cell viability [7] were identified by simulation methods [8, 9]. The selection, physico-chemical, biological, pharmaceutical characterization of these new drug candidates and

introduction of the best ones might be an effective means to treat tuberculosis infections in humans.

Drugs have to be transported through several membranes to reach the infected target cell therefore the interaction of drug with lipid membrane is in the focus of research. Among the membrane models the Langmuir monolayer of lipids is the most simplified but well defined system [10]. Although much less complex than biological membranes it is excellent model because various parameters like density, packing and nature of lipid as well as the subphase composition and temperature can been varied [11–13]. The monomolecular layer of oriented and close packed lipid molecules is prepared at water/air surface in a Langmuir balance. Quantitative information can be obtained on the influence of drugs on the stability, structure and permeability of lipid film as well as on drug's penetration behaviour. Affinity and compatibility of drug to the lipid membrane can be assessed analysing the area–surface pressure isotherms [11].

The monolayer technique became a widespread method in the last decades characterizing the molecular interaction between drug candidates and membrane forming lipids and other components [12, 14, 15]. Jablonowska and coworker studied the effect of the ibuprofen at various concentrations on dipalmitoyl-phosphatidylcholine, DPPC, monolayer [16]. The lipid layer was condensed at low concentration while higher amount of ibuprofen led to opposite effect perturbing the ordered structure of lipid monolayer which change is related to membrane function. Fa and coworkers obtained similar results with azithromycin which increased the fluidity and permeability of membrane layer [17]. The presence of cholesterol additive generally stabilizes the lipid layer hindering the drug penetration [18, 19]. The Langmuir technique applying functional monolayer components was used to reveal the mechanism of antifungal agent comparing toxic and less toxic derivatives [20].

The main component of lung surfactant mixture besides other important proteinous compounds is also a lipid, namely DPPC. Their role in inhibiting or improving the lung function was systematically investigated [21]. The understanding the mode of incorporation of drug into DPPC monolayer can help to design stable liposomes as drug carrying system [5, 22].

New drug candidates which are expected to be specific inhibitor of dUTPase [3, 23] a vital enzyme of *Mtb* were identified in silico [7, 8]. Three of those – ligand 3, 4 and 69 – were compared in the present study considering their interfacial properties, polarity, amphipatic character and lipid affinity which are relevant in pharmaceutical function. Langmuir monolayers were prepared from the ligands and their mixture with phospholipon as a simple model material of cell membrane. Interaction and compatibility with lipid is evaluated from the analysis of the isotherms. The penetration ability of the drug candidates were also characterized by measuring the increase of surface pressure of the lipid monolayer following their injection to the subphase at two initial lipid densities. The amphiphilicity of the three ligands were assessed using log P_{app} and dynamic surface activity values and related to the results of monolayer experiments.

Experimental

Materials

Phospholipon 100H containing 85 wt. % distearoyl-phosphatidylcholine DSPC and 15 wt. % dipalmitoyl-phosphatidylcholine DPPC, respectively was obtained from Nattermann GmbH (Germany).

The in silico identified selective inhibitor molecules of the dUTPase marked as ligand 3, 44 and 69 have chemical composition $C_{25}H_{38}N_4O$, $C_{25}H_{28}N_2O_5$ and $C_{15}H_{16}N_4O$, respectively. The important data of the three drug candidate compounds are given in Table 1.

Chloroform (purity > 99.8%) from Fisher Chemicals and methanol (purity ≥ 99.9%) from Sigma-Aldrich Kft. Hungary were used for preparing spreading solutions. Dichloromethane (purity ≥ 99.9%) from Spectrum-3D Kft. Hungary was used for cleaning the Langmuir trough. *n*-octanol from Reanal, Hungary, was used for log P_{app} determination. Double distilled water was checked by its conductivity (< 5 mS) and surface tension (> 72.0 mN/m at 23 ± 0.5 °C) values.

Methods

Determination of log P_{app}. The *n*-octanol/water partition coefficient (P) is the ratio of the concentration of the drug in *n*-octanol and water in equilibrium. The *n*-octanol and water in 1 : 1 volume ratio was shaken for 12 h to saturate both phases with each other. Then the drug was dissolved in the aqueous phase ($C_1 = 3 \times 10^{-5}$ M) and was shaken with equal volume of octanol phase for 1 h to achieve the partition equilibrium. Centrifugation was required to separate the two phases (2000 rpm, 10 min). After separation the absorbance of the aqueous phase was determined from

Table 1 Molecular data (molecular weight M, number of charges and molecular area A_m) of drug candidates from ZINC database [29] and the measured values: logarithm of apparent partition coefficient log P_{app} and static surface tension γ_{stat} (mN/m) of aqueous solution with concentration of 8×10^{-5} M

Drug candidates	M	Charges	A_m (A^2)	log P_{app}	γ_{stat} (mN/m)
Ligand 3	413.6	3	81.2	0.94 ± 0.05	70.0 ± 0.3
Ligand 44	438.5	2	156.2	0.89 ± 0.05	70.1 ± 0.5
Ligand 69	268.0	–	157.7	0.61 ± 0.05	71.6 ± 0.4

which the concentration was determined (C_2) using the calibration curve. Calibration curves were determined by absorbance at 227, 398 and 352 nm for ligand 3, 44 and 69, respectively. The drug concentration in octanol is $C_1 - C_2$.

$$\log P_{\text{app}} = \log([\text{drug}]_o/[\text{drug}]_{\text{w}}) = \log(C_1 - C_2)/C_2 \,,$$

where the $[\text{drug}]_o$ and $[\text{drug}]_{\text{w}}$ are the equilibrium concentrations of drug in octanol and water, respectively. Apparent partition coefficient P_{app} was obtained since pK values of the compounds were not taken into consideration for correction [24].

Static and Dynamic Surface Tensions. The surface tensions of drug solutions were determined with an accuracy of 0.1 mN/m by the axisymmetric drop shape analysis [25] using the OCA15+ instrument (Dataphysics, Germany). Drop of 10 µl of the aqueous solution of ligand 3, 44 and 69 with concentration of 8×10^{-5} M was formed on the tip of a Teflon coated capillary of a Hamilton syringe at a rate of 2 µl/s. Measuring adsorption at air/water surface the drop was immersed into a glass cuvette saturated with water vapour. All measurements were performed for each drug candidate as triplicate at 23 ± 0.1 °C. The surface tension values were reproduced with a scatter less then ±0.5 mN/m. The profile of capillary surface required to determine the surface tension is obtained by analysing the shape of the pendent drop using a CCD camera coupled to a video profile digitalizer board connected to a personal computer. Static surface tension was measured after 15 min. The instrument allows the programmed decrease or increase the volume/area of the pendent drop. After drop formation the volume of the drop was decreased slowly [26–28] with the rate of 0.1 µl/s, until the 50% of the initial area was reached. The surface tension response for the area decrease was recorded simultaneously with 120 frames/min frequency. From these data the dynamic surface tension as a function of surface area change was obtained.

Langmuir Film Experiments. The experiments were performed by using automated Langmuir balance (18 × 6 × 0.6 cm). The spread monolayer can be compressed by means of a movable barrier while the surface pressure and the area are continuously recorded. Surface pressure is measured tensiometrically with an accuracy of ±0.05 mN/m using a Wilhelmy plate made from chromatography paper (Whatman Chr1) connected to a force transducer. The surface pressure/area isotherm was recorded at a barrier speed of 10 cm^2/min at 23 ± 0.5 °C and there was no wait period between compression and expansion. For the monolayer studies the pure lipid and the pure drugs (0.1 g/l) as well as lipid–drug mixtures (5 : 1 molar ratio) were spread at water surface. The spreading solvent was 3 : 1 v/v chloroform/methanol mixture, 50 µl solution was applied dropwise by a Hamilton syringe to form the monolayer. Before compression the solvent was allowed to evaporate for 15 min. The compression/expansion isotherms were recorded five times consecutively. The trough was made of Teflon while the barrier from POM [14] and cleaned carefully with dichloromethane and bidistilled water.

In the first type of experiments isotherms of pure lipid and pure drug candidates then that of the two-component mixture monolayer were recorded. To get the mixed monolayer the components were premixed in the spreading solvent. The difference between the pure lipid and lipid–drug films were investigated to presume the incorporation of the drug into the lipid monolayer. In the second type of experiments penetration of drug into the lipid layer was detected by the change of surface pressure. As a first step pure lipid monolayer was formed and following one compression/expansion cycle the layer was compressed to a given value of surface pressure (15 and 20 mN/m). At that position the barrier was stopped and a fixed amount of aqueous solution of the drug was injected into the subphase to obtain a final drug concentration of 2×10^{-6} M. The change in surface pressure as the indicator of drug penetration was recorded as a function of time for one hour.

Results and Discussion

Amphiphilicity of Drug Candidates

The logarithm of *n*-octanol/water partition coefficient serves as a quantitative descriptor of lipophilicity (hydrophobicity) and is one of the key determinants of pharmacokinetic properties. Hydrophobicity affects drug adsorption, bioavailability, hydrophobic drug–receptor interactions, metabolism of molecules, as well as their toxicity. Partition coefficient is useful in estimating distribution of drugs within the body. Hydrophobic drugs with high partition coefficients are preferentially distributed to hydrophobic compartments such as lipid bilayers of cells while hydrophilic drugs (low partition coefficients) preferentially are found in hydrophilic compartments such as blood serum. The equilibrium organic and aqueous phases of *n*-octanol/water system contain 2.3 M of water and 4.5×10^{-8} M *n*-octanol, respectively. This is a widely accepted model for the estimation of distribution of a drug molecule to the cell membrane.

The solubility/amphiphilicity of the three drug candidates were characterized by partition experiment and determining their surface activity. These results and some other data of the ligands are summarized in Table 1. The log P_{app} values obtained indicated a medium hydrophobicity of the ligands. Considering the standard deviation of data ligand 44 and ligand 3 presented similar hydrophobicity while ligand 69 proved to be less hydrophobic although the difference is rather small.

Changing of water surface tension gives also information on the amphiphilic properties of dissolved drugs. If the molecules adsorb at air/water surface the surface

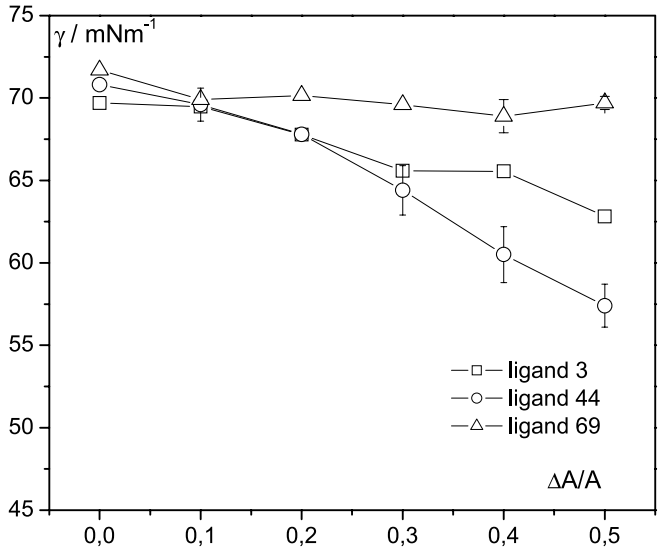

Fig. 1 Dynamic surface tension γ (mN/m) of aqueous solutions of ligand 3, 44 and 69 with a concentration of 8×10^{-5} M as a function of reduction of surface area $\Delta A/A$. (The scatter of surface tension values are shown when exceeding the size of symbol)

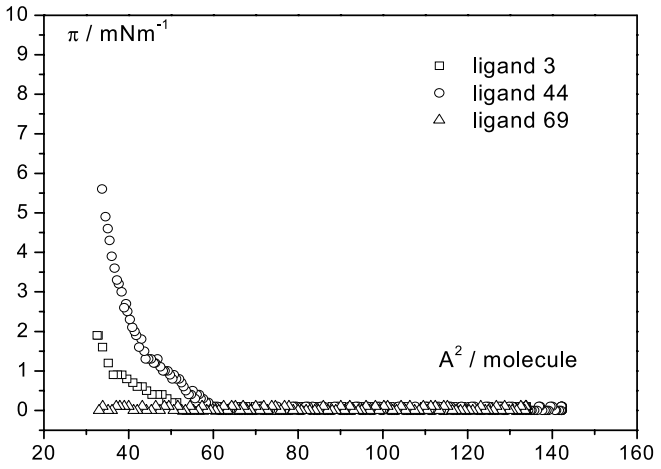

Fig. 2 Surface pressure π (mN/m) area A (A^2/molecule) isotherms for spread monolayer of pure ligand 3, 44 and 69

tension is reduced. There was detected neither static nor dynamic surface activity of any of the ligands at concentration used in the penetration experiment (2×10^{-6} M). Increasing the concentration 40 fold (8×10^{-5} M) small but significant reduction was obtained for ligand 3 and 44 (Table 1) in the static surface tension. Ligand 69 did not show surface active behaviour under the same circumstances. Measuring the dynamic surface tension of the same solutions much higher effect and difference between the three compounds were obtained. Dynamic surface tension as a function of area reduction of the drop was plotted in Fig. 1. A marked decrease of surface tension was observed from app. 30% of area reduction due to the considerable accumulation of the adsorbed ligand 3 and 44 molecules on the water surface. This decrease of surface tension maintains decreasing the area further with more pronounced effect for ligand 44. On the contrary, the surface tension remains almost unchanged in the presence of ligand 69. According to the surface tension measurements the increasing order of amphiphilicity of the drug candidates is ligand 69 < ligand 3 < ligand 44.

Monolayer Experiments

Isotherms of Pure Drug Candidates. Compression isotherm of spread layer determined with the Langmuir balance are plotted for the three ligands in Fig. 2. The shape of the isotherms reflect the instability of the monolayer of the pure ligands. A fraction – or in the case of ligand 69 almost the whole amount – of the spread molecules are probably squeezed out from the air/water surface during the compression. This result could be due to high water solubility of the drug candidates. A difference however, can be seen between the three ligands. A significant surface pressure was detected at high compression for ligand 3 while an even higher value for ligand 44.

Lipid + Ligand Monolayers. Isotherms of lipid + drug candidate mixed monolayers are shown in Fig. 3. The surface pressure/area isotherms are compared to the isotherm of pure lipid monolayer. The lipid : ligand molecular ratio was 5 : 1 in the spreading solution. Both the pure lipid and the mixed isotherms are presented in a form that the area corresponds to one lipid molecule, hence the shift of the isotherm directly indicates the presence of ligand in the mixed layer.

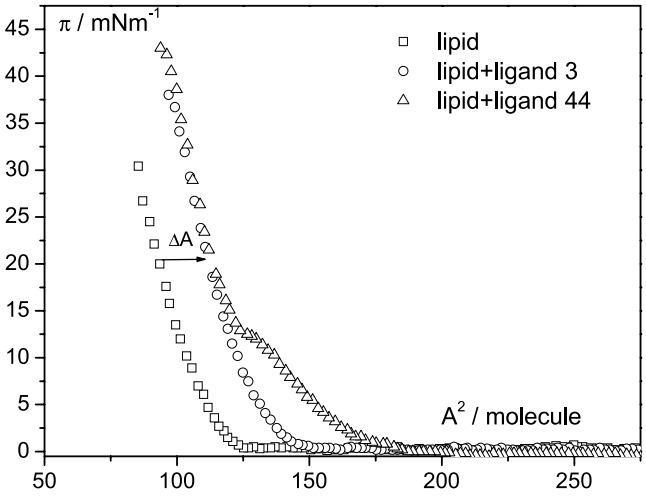

Fig. 3 Surface pressure π (mN/m) area A (A^2/molecule) isotherms for spread monolayer of pure lipid, lipid + ligand 3 and lipid + ligand 44 mixed films with lipid : ligand molar ratio of 5

The mixed isotherm overlaps with that of pure lipid in the case of ligand 69. From that we can conclude that there is no interaction between ligand 69 and lipid molecules, the ligand is most likely migrates into the aqueous subphase from the air/water surface. The mixed films with ligand 3 and 44 show the quite opposite behaviour. Their isotherms are shifted to higher area which is the consequence of the formation of mixed monolayer at the air/water surface where the ligand molecules between the lipid molecules occupy an additional area. Determining this additional area ΔA the amount of ligands present in the mixed film can be estimated at various surface pressures π. As a first approximation the highest molecular area of the ligands representing the planar orientation at the air/water surface were taken into consideration (Table 1). The results of this calculation expressed as lipid : ligand molecular ratio R are given in Table 2.

The behaviour of ligand 44 is similar to that of ligand 3 considering the affinity to lipid. At low surface pressures the molar composition of the two mixed layers are comparable. Lipid : ligand ratio $4 < R < 5$ was obtained in the expanded part of the isotherms. This is probably due to less compressed state of the mixed monolayer.

The section of the isotherm with high slope corresponds to compressed monolayer with close packed molecules (Fig. 3). Above surface pressure of 15 mN/m the molar area is getting nearly constant in this region. For ligand 3 the calculated molar ratios were in good accordance with the composition of the spreading solution characterized by lipid : ligand ratio of 5. This denotes that the ligand molecules remained in the lipid film during compression in spite of the solubility of the ligand in the subphase. That is the clear evidence for the ligand's affinity to lipid.

The R values for lipid films with ligand 44 are different at various compression states of the film. Above surface pressure of 10 mN/m $R \geq 7.5$ indicates that less ligand molecules are present at the air/water surface or the spread amount of molecules occupy less area. The former case is not probable because repeating the compression/expansion cycles overlapping isotherms could be detected. It is reasonable to assume that the structural change is related of the orientation of the ligand molecule in the lipid monolayer. The sign of this behaviour recognized as structural change was observed on the shape of the isotherm at $\pi = 12$ mN/m (Fig. 3). In order to estimate the possible orientation of ligand 44 molecules the calculated R values supposing the vertical orientation of the molecules to the air/water surface are also given in Table 2. The comparison reveals that the ligand 44 molecules are incorporated into the lipid layer in a way that occupy the area which corresponds an orientation between the planar and the vertical ones. The ligand 44 molecules can be tilted or partially submerged into the aqueous phase. Any of them occur the process was found reversible changing the compression of the monolayer and verifies the lipid–ligand interaction.

Table 2 Lipid to ligand ratios R in the mixed monolayers for ligand 3 and 44 assessed from the shift of the isotherms ΔA compared to that of pure lipid at various surface pressures π. Values in brackets were obtained supposing vertical orientation of ligand molecule in the lipid monolayer

π (mN/m)	Ligand 3 ΔA (A^2)	R	Ligand 4 ΔA (A^2)	R
5	20	4.1	38.0	4.2
10	18.3	4.4	32.5	4.8
15	16	5.1	20.8	7.5 (2.4)
18	15.6	5.2	19.5	8.0 (2.6)
20	15.2	5.3	18.7	8.3 (2.7)

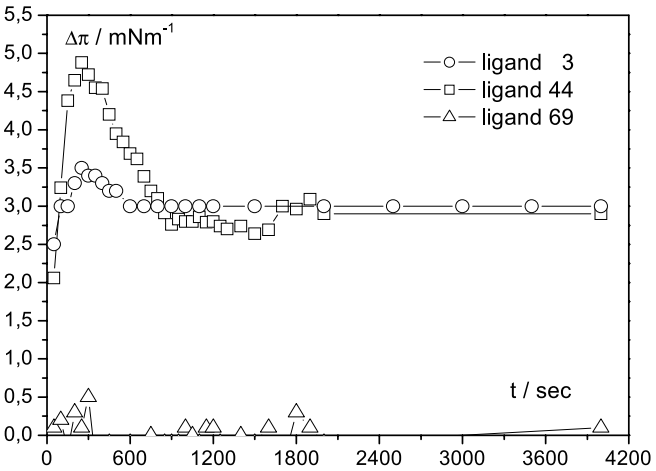

Fig. 4 Increase of surface pressure $\Delta\pi$ (mN/m) due to penetration of ligand 3, 44 and 69 into lipid monolayer with initial surface pressure of 15 mN/m as a function of time t (s)

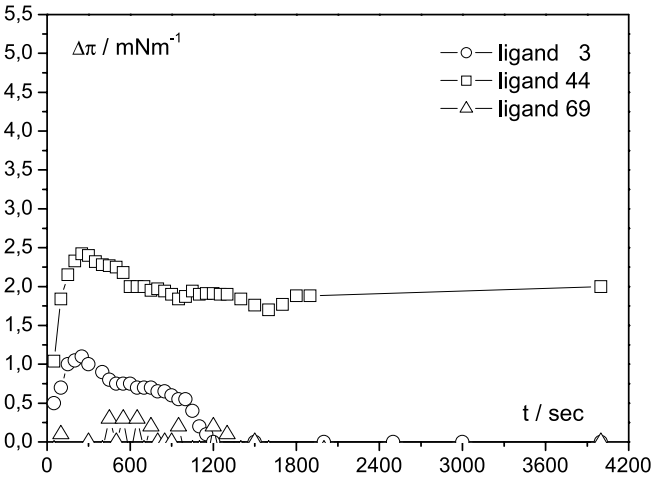

Fig. 5 Increase of surface pressure $\Delta\pi$ (mN/m) due to penetration of ligand 3, 44 and 69 into lipid monolayer with initial surface pressure of 20 mN/m as a function of time t (s)

Penetration. The lipid monolayer was compressed in the Langmuir balance to reach surface pressure of 15 and 20 mN/m and then the barrier was stopped. After the drug candidate solution had been injected into the subphase the change of surface pressure was recorded for an hour. The results of these penetration experiments were summarized in Figs. 4 and 5.

The fast increase of surface pressure observable in the first period is probably connected to the locally high concentration of ligands in the subphase. Therefore the static values developed after appr. 1200 s and maintained for more than an hour were applied for comparison. Considering the lipid film wih surface pressure of 15 mN/m the degrees of penetration are similar for ligand 3 and 44, presenting 3 mN/m as a static increase of surface pressure. The penetration however, into the more dense lipid layer with 20 mN/m is weaker. Nevertheless the ligand 44 produced static increase of surface pressure even of the lipid film with 20 mN/m reflecting the most pronounced affinity to lipid monolayer. The ligand 69 does penetrate neither the less nor the more dense monolayer exhibiting no affinity to lipid.

Conclusion

Three in silico identified drug candidates – ligand 3, 44 and 69 – were characterized and compared in the present work considering their hydrophobicity and membrane affinity. Octanol/water partiton as well as static and dynamic surface activity of the compounds were determined while the membrane affinity was studied in Langmuir film experiments. Results of the three kinds of measurements were in accordance concerning the hydrophobic/amphiphilic character of the three ligand molecules although, the most pronounced differences between the drug candidates were obtained in the dynamic surface tension measurements and investigating their interaction with lipid layers.

Despite the good water solubility of the molecules studied here we found considerable differences in their amphiphatic character and their affinity to lipid monolayer. Ligand 69 being the less hydrophobic showed no interaction with lipid, while the ligand 44 presented a substantial affinity to lipid monolayer being the most hydrophobic and most surface active compound.

It was demonstrated that amphiphilicity and affinity of a drug candidate to model membrane can be reasonably estimated using the Langmuir monolayer and penetration experiments in combination with the characterization of surface activity and hydrophobicity of the given compounds. These results might be promising for the future assessment whether the drugs possess ability to interact with the biomembrane models.

Acknowledgement Research was supported by National Science Foundation OTKA 60197, 68120, 68358, K 68229, Howard Hughes Medical Institutes (#55005628 and #55000342), National Office for Research and Technology TB_INTER

References

1. Raja A (2004) Indian J Med Res 120:213
2. Kaufmann SHE (2004) Ann Rheum Dis 63:50
3. Chan S, Segelke B, Lekin T, Krupka H, Cho US, Kim M, So M, Kim CY, Naranjo CM, Rogers YC, Park MS, Waldo GS, Pashkov I, Cascio D, Perry JL, Sawaya MR (2004) J Mol Biol 341:503
4. World Health Organization (2002) Report 2002
5. Chimote G, Banerjee R (2005) Respir Physiol Neurobiol 145:65
6. Tripathi RP, Tewari N, Dwivedi N, Tiwari VK (2004) Med Res Rev 25:93
7. Barabás O, Pongrácz V, Kovári J, Wilmanns M, Vértessy BG (2004) J Biol Chem 279:42907
8. Varga B, Migliardo F, Takacs E, Vértessy BG, Magazù S, Mondelli C (2008) J Chem Phys 345:250
9. Varga B, Migliardo F, Takacs E, Vértessy BG, Magazù S (2008) J Mol Struct 886:128
10. MacRitchie F (1990) Chemistry of Interfaces. Academic Press, San Diego
11. Brezesinski G, Möhwald H (2003) Adv Colloid Interf Sci 100–102:563
12. Maget-Dana R (1999) Biochem Biophys Acta 1462:109
13. Deleu M, Paquot M, Nylander T (2005) J Colloid Interf Sci 283:358
14. Hardy NJ, Richardson TH, Grunfeld F (2006) Colloid Surf A 284–285:202
15. Kiss É, Varga A, Vargha-Butler E (2004) Phys Chem Chem Phys 6:1575
16. Jablonowska E, Bilewicz R (2007) Thin Solid Films 515:3962
17. Fa N, Ronkart S, Schanck A, Deleu M, Gaigneaux A, Goormaghtigh E, Mingeot-Leclercq MP (2006) Chem Phys Lipids 144:108
18. Pickholz M, Oliveira ON JR, Skaf MS (2007) Biophys Chem 125:425
19. Zhao L, Feng SS (2006) J Colloid Interf Sci 300:314
20. Hac-Wydro K, Dynarowicz-Latka P, Grzybowska J, Borowski E (2005) Biophys Chem 116:77
21. Serrano AG, Perez-Gil J (2006) Chem Phys Lipids 141:105
22. Minones J Jr, Gomez-Serranillos IR, Conde O, Dynarowicz-Latka P (2006) J Colloid Interf Sci 301:258
23. Varga B, Barabas O, Takacs E, Vértessy BG (2008) Biochem Biophys Res Commun 373:8
24. Takácsné Novák K, Völgyi G (2005) Magy Kém Foly 4:169
25. Rotenberg Y, Boruvka L, Neumann AW (1983) J Colloid Interf Sci 93:169
26. Miller R, Sedev M, Schano KH, Ng C, Neumann AW (1993) Colloid Surf A 69:209
27. Miller R, Policova Z, Sedev R, Neumann AW (1993) Colloid Surf A 76:179
28. Hill K, Horváth-Szanics E, Hajós G, Kiss É (2008) Colloid Surf A 319:180
29. Irwin JJ, Shoichet KB (2004) J Chem Inf Model 45:177

Progr Colloid Polym Sci (2008) 135: 93–100
DOI 10.1007/2882_2008_120

Published online: 11 September 2008

András Süle
Ferenc Csempesz

Complexation of Statins with β-Cyclodextrin in Solutions of Small Molecular Additives and Macromolecular Colloids

András Süle · Ferenc Csempesz (✉)
Laboratory of Colloid and Supramolecular Systems, Institute of Chemistry, Eötvös University, P.O. Box 32,
1518 Budapest 112, Hungary
e-mail: csf@chem.elte.hu

Abstract The solubility of lovastatin and simvastatin (inevitable drugs in the management of cardiovascular diseases) was studied by phase-solubility measurements in multicomponent colloidal and non-colloidal media. Complexation in aqueous solutions of the highly lipophilic statins with β-cyclodextrin (β-CD) in the absence and the presence of dissolved polyvinyl pyrrolidone, its monomeric compound, tartaric acid and urea, respectively, were investigated. For the characterization of the CD-statin inclusion complexes, stability constants for the associates have been calculated.

It was shown that complexation might lead to considerable improvement of the aqueous solubilities of both statins. In binary systems dominantly statin-β-CD associates of 1 : 1 molar ratios form, which exhibit considerable surface activity.

In statin-CD-additive ternary systems the solubility of the statins could be further improved. The enhanced drug solubilities in the solutions of small molecular mass solutes are likely related due to the peculiar feature of the additives to destroy the H-bonding system of β-CD. In polymer-containing systems statin-CD-polymer associates of supramolecular structure may presumably form in a way that portions of surface-active statin-β-CD complexes are anchored at the macromolecular chains.

Keywords Cyclodextrins · Dissolution · Inclusion complexes · Macromolecular colloids · Statins · Supramolecular associates

Introduction

A great challenge of the current research in pharmaceutical sciences and the related fields is to reveal ways of improving the efficacy and safety of existing drugs. This claim stems from that more than 40% of developed drug molecules exhibit poor biopharmacological properties, partly because of their diminished dissolution and/or inadequate permeability [1]. In order to achieve decent bioavailability, a pharmacon must be absorbed in a way that sufficient drug level arises at the pharmacologically active sites.

Extensive studies show that, among indispensable drugs, statins provide crucial benefits when used in either lipid lowering treatment or coronary heart disease (CHD) therapy. Dissolved statins inhibit the rate-limiting steps in cholesterol synthesis. Their 3-hydroxy-3-methylglutaryl-like domain may attach to the appropriate binding site of the reductase enzyme and therefore, sterically prevent the natural substrates to bind [2]. Chemically different statins mostly differ in their absorption parameters and they may exhibit varied efficacy in reducing the low-density lipoprotein (LDL) cholesterol levels even at the same dosages. Schematic molecular structure of two basic statins is illustrated in Fig. 1.

A hard obstacle in statin therapy is the extremely low aqueous solubility of most derivatives. Their bioavailabil-

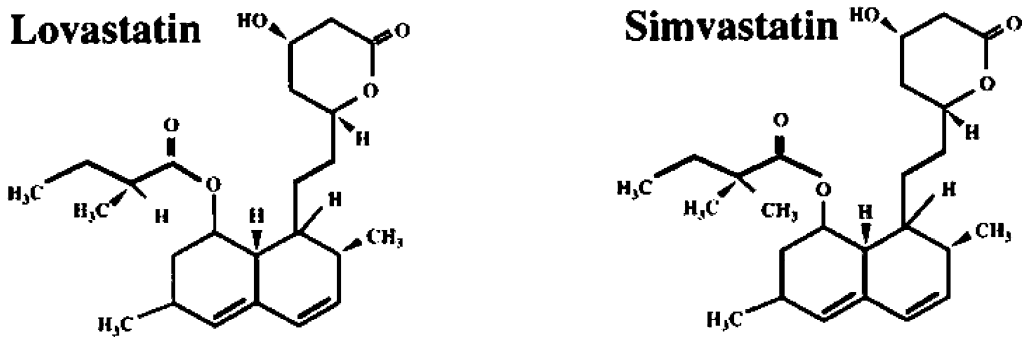

Fig. 1 Chemical structure of lovastatin and simvastatin

ity is, therefore, also low and may exhibit high variability in individuals [3, 4]. In addition, known food and drug interactions usually tend to increase the prevalence of statin-related side effects. Despite of these shortcomings, monotherapy with either lovastatin or simvastatin is proven to be safe, but concerning their interactions in complex delivery systems, many questions may arise [5, 6].

Cyclodextrins (CDs) are peculiar cyclic oligomers of α-D-glucose. Their shapes resemble truncated cones with primary and secondary hydroxyl groups located around their narrower and wider rim, respectively [7] (Fig. 2).

The most widely used natural cyclodextrins consist of 6–8 glucose units and according to the number of monomers in the macrocycle, they are named as α-, β- and γ-cyclodextrin. Due to this special molecular structure, CD molecules have a hydrophobic inner cavity, where lipophilic guest molecules (or molecule parts) of the appropriate size can be encapsulated, forming inclusion complexes [9].

The large number of hydroxyl groups on the outer surface makes CD molecules water-soluble. Suitable modification of the chemical structure of CDs, for example, by esterification of the 2-, 3- and 6-hydroxyl groups or introducing other functional groups at these sites, may remarkably perturb the internal hydrogen-bond network of β-CDs, resulting in an elevated water-solubility [10]. Enhanced aqueous solubility β-cyclodextrin was observed in solution of some hydroxy acids, as well [11].

Native cyclodextrins are referred to as biologically safe and biocompatible compounds. They are efficient pharmaceutical solubilizers and used, for example, as complexing agents for prostaglandins and non-steroidal anti-inflammatory drugs (NSAIDs). However, parenteral administration may be harmful, since at moderately high doses of some CDs, haemolysis may occur. Moreover, the low water-solubility of β-CD leads to its precipitation in the kidneys, resulting in renal tubule damage.

Recently, there has been a growing interest in the cyclodextrin-based pharmaceutical formulae, but few is known about how usually needed additives may affect the physico-chemical and pharmacological behaviour of drugs and their non-covalent interactions in complex delivery systems. Much less attention has been paid to the relevance and the role of colloidal additives in inclusion drug complexation. Possible use of water-soluble polymers to improve inclusion properties of CDs is well documented by Loftsson et al. [12]. Nevertheless, possible differences in the effect of non-colloidal and colloidal ad-

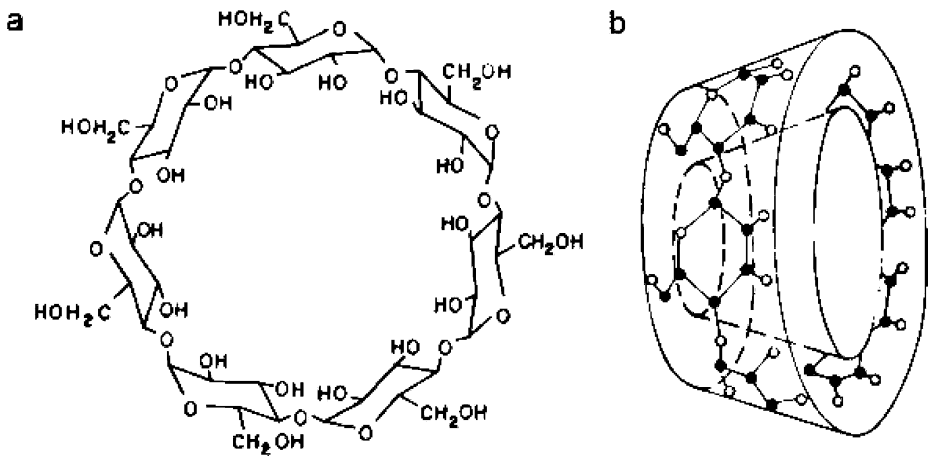

Fig. 2 Computer-simulated model of β-cyclodextrin [8]

ditives on the complex formation between cyclodextrins and pharmacons, and in their interactions with the formed supramolecules have not been revealed in detail.

Complexation of statins in aqueous cyclodextrin solutions in the absence and the presence of colloidal and non-colloidal additives is in the focus of the present study. The solubility enhancing effect of β-CD and hydroxypropylated-β-CD has been well described in the literature [13–15]. In this study, solubility of lovastatin and simvastatin with β-cyclodextrin, and comparison of the effects of a water-soluble polymer, its monomeric analogue compound, urea and a hydroxy acid, respectively, on the formation of supramolecular complexes has been investigated. Ways of enhancing the aqueous solubility of the drugs in binary and ternary solutions have been discussed.

Materials and Methods

Materials

Lovastatin and simvastatin of USP23-grade (Chiesi Farmaceutici SpA, Italy), β-cyclodextrin as well as different additives, such as tartaric acid, carbamide (Reanal Chem. Ltd, Budapest, Hungary), 1-ethyl-2-pyrrolidinone (Sigma-Aldrich Chemie GmbH, Germany) and PVP K30 polyvinyl pyrrolidone (Fluka AG, Buchs SG, Switzerland) were used in the experiments. Cyclolab R&D Ltd., Budapest, Hungary, manufactured the pharmaceutical grade β-cyclodextrin. The chemicals used were of analytical grade.

Solubility Measurements

Phase-solubilities of the statins in binary solutions of β-cyclodextrins were studied according to the Higuchi–Connors procedure [16]. Various amounts of CD were generally dissolved in distilled water and lovastatin or simvastatin was added to the solutions in vast excess. 24 h of temperature-programmed incubation period in a refrigerated bath (HAAKE PhoenixII C35P instrument) was ensured for the dissolution of the pharmacon at 25 °C. After longer dissolution times, no definite increase in drug solubilities could be detected. After removing the non-dissolved statin from the solutions with Millipore type GS 0.22 μm membrane filter, the absorption spectra of the dissolved pharmacon were then taken in the range of 190–400 nm wavelengths.

The statin content of the solutions was determined with a UV-spectrophotometric assay based on the PhEur directives [17]. The absorbance of lovastatin and simvastatin was measured at 236 and 240 nm, respectively. For these measurements a computer-controlled spectrophotometer (Perkin-Elmer Lambda Series 2S instrument) was used and the raw spectra were evaluated by OriginLab Origin 7.0 software suite. The solubility isotherms were calculated by using calibration curves determined with ethanolic statin solutions of known concentrations.

For the preparation of statin-CD-additive ternary systems, a specially controlled thermal program was used. The appropriate mixtures were put in a computer-driven refrigerated bath, where the samples were heated up to 70 °C and held at this elevated temperature for 2 h. After that, the solutions were cooled down to 25 °C and kept at this temperature for 22 h. UV-spectra of solutions indicated that such a rapid thermal treatment does not cause alterations in the molecular structure of the statins.

Results and Discussion

Solubility of Pharmacons in Aqueous Media

The solubility of both lovastatin and simvastatin in water is extremely poor ($S_{\text{lovastatin}} = 1.5$ μg/ml, $S_{\text{simvastatin}} = 2.0$ μg/ml). In mildly acidic media the solubilities of both statins only slightly increase [13]. Improving their aqueous solubility might offer also much better biological availability of the pharmacons. In Fig. 3, solubility isotherms for lovastatin and simvastatin in solutions of β-cyclodextrin are shown.

These results demonstrate about 5 and 8-fold increase in the solubility of the statins at higher β-CD concentrations. The observed improvement of drug solubilities can be reasonably attributed to the formation of inclusion complexes between the statin and the β-CD molecules [10]. The linear section of the isotherms supports this notion and suggests that at these CD concentrations, the dissolved cyclodextrin and statin molecules presumably form molecular associates of 1 : 1 molar ratio. It should be noted here that β-CD itself has a rather low aqueous solubility at 25 °C ($\sim$ 18.5 mg/ml). Nevertheless, some increase in the drug solubilities at above the solubility limit of the pure β-CD could be detected. During complexation, slight enhancement of the solubility of β-CD may also occur. In the solution, a part of the dissolved β-CD is in complexed form, which shifts the association equilibrium towards higher values of the total CD concentrations. Therefore, the observed increase in the drug solubilities at higher β-CD concentrations can be ascribed to the improved solubility of the complexing agent, as well.

For the characterization of the assumed complexation equilibrium, stability constants have been calculated from the solubility curves using an approach offered by Iga et al. [18].

$$K_{11} = \frac{m1}{S_0(1-m1)},$$

(where K_{11} is the stability constant of 1 : 1 assemblies, m_1 is the slope of the linear section of the solubility curve, S_0 its intersection with the ordinate axis). Stability constants for statin-CD associates assuming the formation of their complexes with more complicated stoichiometry have also

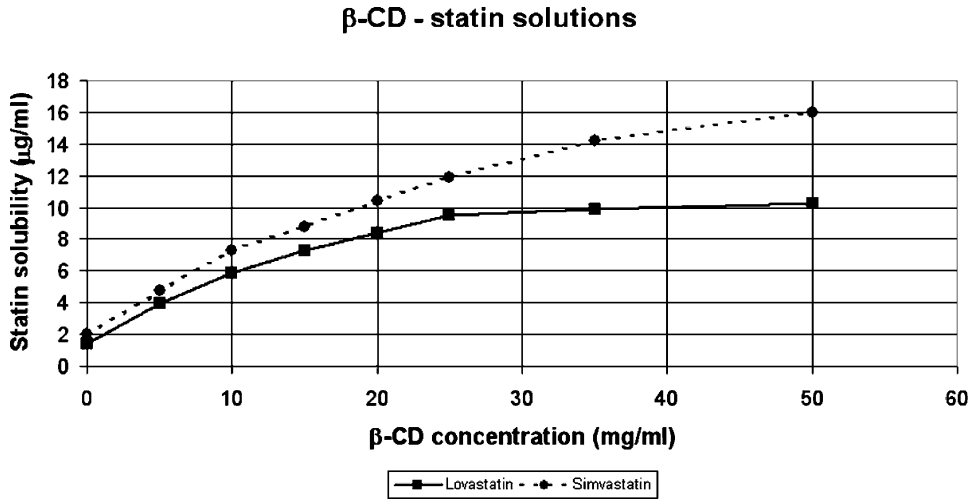

Fig. 3 Phase-solubility curves of simvastatin and lovastatin in β-CD solutions at 25 °C

Table 1 Stability constants of CD-statin complexes of 1 : 1 molar ratio, $T = 25$ °C

Binary system	K_{11} $\times 10^2$ [M^{-1}]	K^*_{11} $\times 10^2$ [M^{-1}]
Lovastatin-β-CD	1.9	1.9
Simvastatin-β-CD	2.1	2.92

been calculated by using an iterative computation program [19]. For comparison purposes, the K_{11} association constants and those obtained for statin-β-CD complexes of 1 : 1 molar ratio by the iteration procedure (K^*_{11}) are shown together in Table 1.

These data suggest the formation of somewhat more stable complex of simvastatin with β-CD, but do not inform about the possible mechanism of the inclusion of these drugs. The corresponding K_{11} and K^*_{11} constants are in line, but estimation of the stability constants from the phase solubility isotherms provided slightly higher values.

Complexation in Ternary Systems

Small molecular additives and macromolecular substances are widely used in pharmaceutical applications, mostly with the aim of improving physico-chemical and/or pharmacological behaviour of active ingredients. When a third component is added to a binary statin-CD solution, in principle it may induce a conventional competition for the CD cavities between the pharmacon and the additive. Revealing the effects of relevant small molecular solutes and of colloidal components on inclusion complexation, may therefore offer reasonable alternatives of controlling the formation of supramolecular associates, as well.

In ternary (drug-CD-additive) systems, the effect of polyvinyl pyrrolidone (PVP), a chemically analogous compound of PVP monomer (1-ethyl-2-pyrrolidinone (NEP)), urea and tartaric acid, respectively, on the dissolution of the statins was studied.

In Figs. 4 and 5, changes in the solubilities of lovastatin in β-CD solutions due to various amounts of the monomeric substance and the polymer, respectively, are shown. (The changes in drug solubilities represented by the columns are number average mean values obtained from at least 3 simultaneous measurements.)

As can be seen, without cyclodextrin the added NEP decreased the solubility of the pharmacon to a lesser degree, but the dissolved β-CD markedly reduced it. The higher is the concentration of the small molecular mass additive at constant CD concentration, the higher is the reduction in the solubility of the drug. These results strongly support the notion that in competition of the drug and the additive for the CD cavities, complexation of NEP over the statin is preferred. In other words, NEP molecules presumably form more stable complexes with β-CD than that of the pharmacon and therefore, drug complexation with the CD is hindered.

In polymer-containing systems, just an opposite effect of the macromolecular colloid on the solubility of the statins could be observed. Figure 5 well demonstrates that under the specified experimental conditions, the solubility of the drug in the solutions of β-CD-lovastatin-polyvinyl pyrrolidone definitely increased.

In the absence of cyclodextrin only slight improvement of drug solubilities could be detected, but at higher CD-concentrations the dissolved polymer resulted in 15–20% increase in the solubility of lovastatin. It is important to note here, that the complex systems containing either of the additives were subjected to a heat treatment as described in the experimental methods. The polymer-containing samples stored at 25 °C for 24 h showed no significant increase in the solubility of the statins. Heat treatment proved to be a crucial step, since the drug solubility

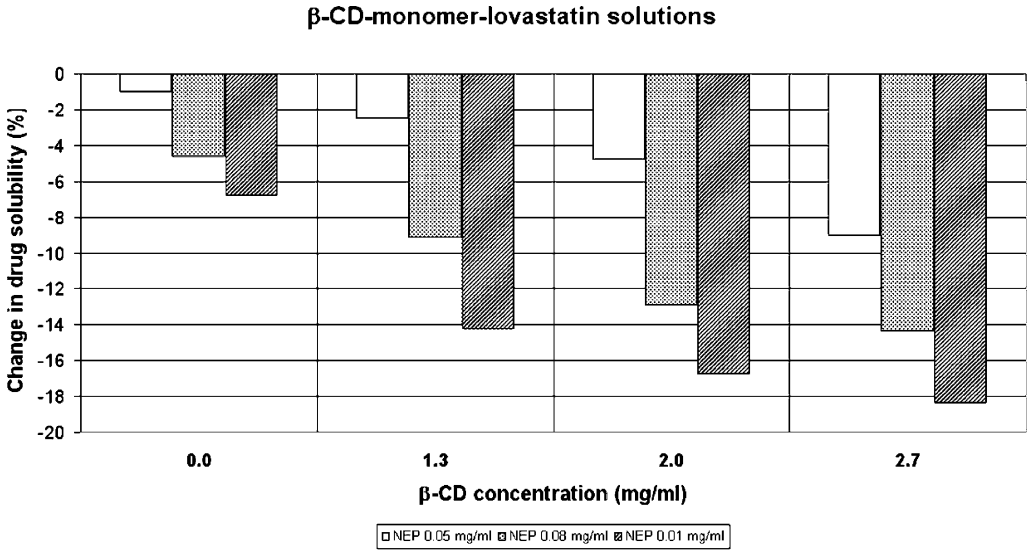

Fig. 4 Effect of 1-ethyl-2-pyrrolidinone on the solubility of lovastatin in solutions of β-cyclodextrin, $T = 25\,^{\circ}\mathrm{C}$

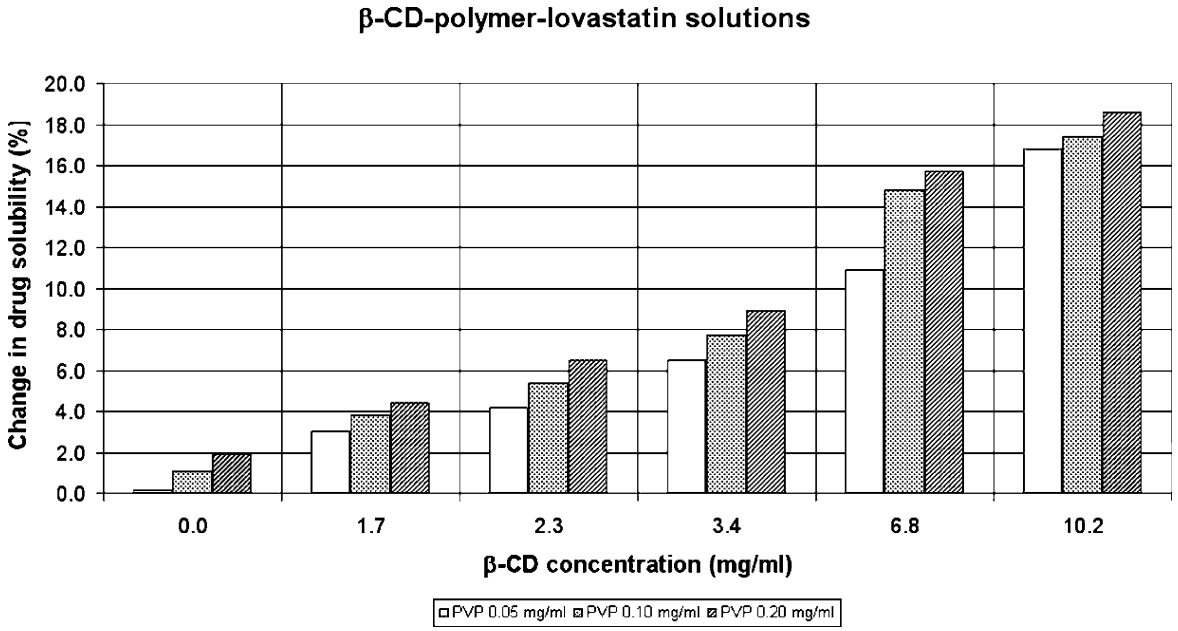

Fig. 5 Effect of PVP on the solubility of lovastatin in solutions of β-cyclodextrin, $T = 25\,^{\circ}\mathrm{C}$

could be enhanced only even when a short "thermal jump" in the storage regimen was implied. In the studied temperature range, the increase in the statin solubility seems to be proportional to the extent of "heat treatment". On the other hand, such enhance of the drug solubilities without polymer could not be observed.

Much similarity to the effect of the polymer on the drug solubilities could be revealed in the ternary systems of lovastatin-β-CD and the tartaric acid or the carbamide. The columned graphs shown in Figs. 6 and 7 well demonstrate that both of these small molecular mass additives brought about definite improvement of drug solubilities in their CD-containing ternary systems.

It was documented by Pharr et al. [20] that carbamide itself can enhance the low solubility of β-CD. In drug-cyclodextrin complex systems, the tartaric acid and the urea improved the drug solubilities by 20–25% and 50–60%, respectively, but in the solutions of the hydroxy acid, the concentrations of both the β-CD and the additive were much lower. More importantly, enhanced drug solubilities could be detected in ternary systems of these additives even when the thermal treatment in the dissolution proced-

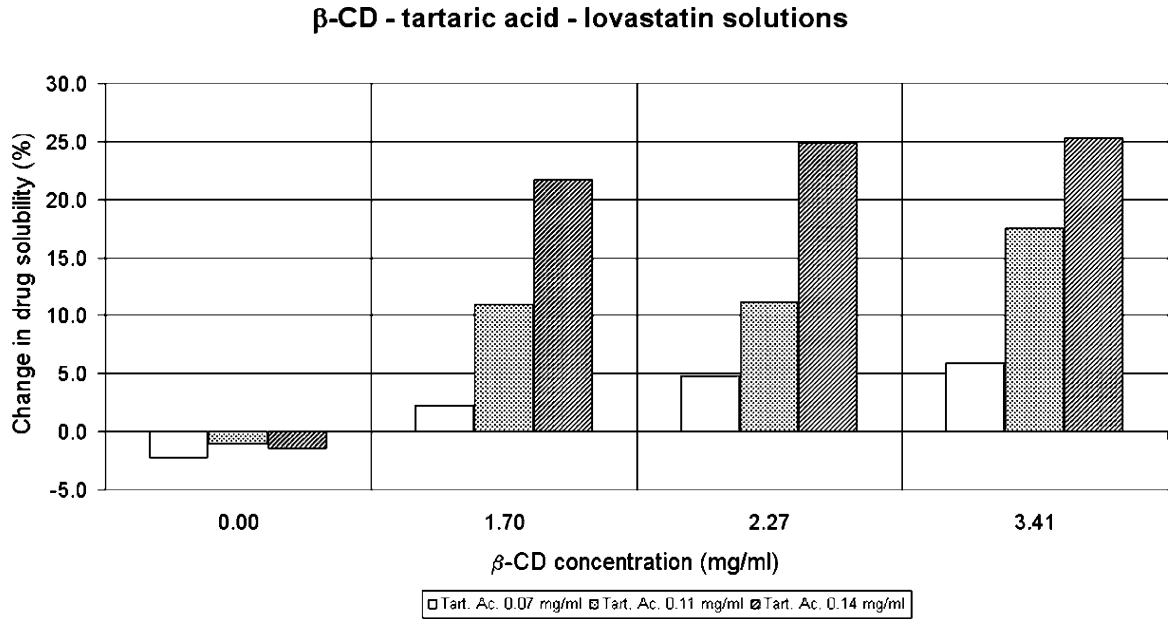

Fig. 6 Effect of tartaric acid on the solubility of lovastatin in solutions of β-cyclodextrin, $T = 25\,^{\circ}\mathrm{C}$

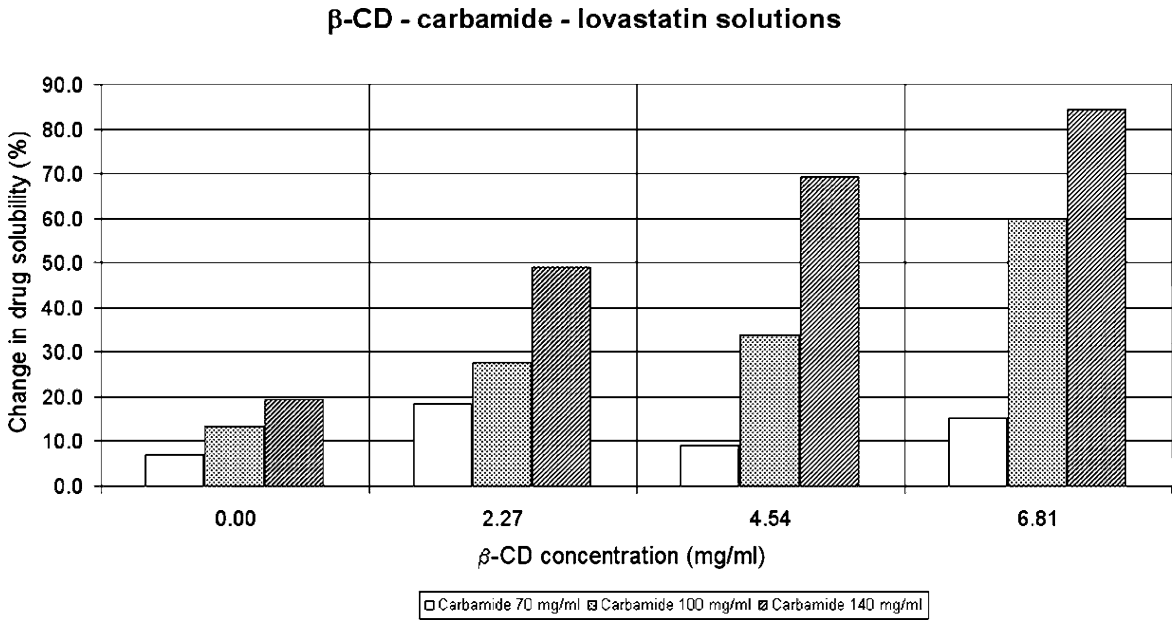

Fig. 7 Effect of carbamide on the solubility of lovastatin in solutions of β-cyclodextrin, $T = 25\,^{\circ}\mathrm{C}$

ure was omitted i.e. when the solutions were kept steadily at 25 °C for 24 h. The solubility of simvastatin in their CD-containing solutions could also be improved [21].

Remarkably enhanced solubilities of other sparingly soluble drugs in aqueous multicomponent systems of tartaric acid have also been observed [22]. It was also shown [11] that hydroxy acids at higher concentrations enhance the aqueous solubility itself of the β-CD, as well. The solubilizing power of tartaric acid was attributed to its (weak) inclusion complexation with β-CD and also, to the capability of the hydroxy acid groups to modify the intra- and intermolecular hydrogen-bond system of β-CD. This third component does not only act as a ternary guest, associated probably on the surface of β-CD units, but also acts as an inhibitor of the self-association of preformed statin/β-CD 1 : 1 complexes in water.

The effectiveness of the urea can be understood in similar manner. Solubility enhancing effect of carbamide

molecules might also rely on their "hydrogen-bond destroying" feature in aqueous media of the β-CD.

In order to evaluate of the results obtained in multicomponent solution, formation of ternary complexes with supramolecular structure can be reasonably assumed [23]. Nevertheless, no unquestionable answer can be given from these results concerning the structure of the supramolecular assemblies. Despite of the similar effects due to the different additives, the formation mechanism and the structure of the ternary complexes developed in the CD-solutions of the small molecular additives and of the polymeric component, are very likely different. Nevertheless, a peculiar feature of the stain-CD complexes might also have relevance in the explanation of the enhanced drug solubilities. Preliminary surface activity measurements performed in aqueous statin-CD solutions showed that the dissolved β-CD itself did not cause detectable reduction of the surface tension of water, but the statin β-CD complexes exhibited marked surface activity. In lovastatin β-CD solutions as high reduction as 24–25 mJ/m^2 in the surface tension of water could be measured, indicating that the complexation of stain led to the development of solutes with definitely amphiphilic solutes.

Taking all these into account, the enhanced drug solubilities may be likely ascribed to the formation of ternary associates. In solutions of statin-CD-small molecular mass additive, demolition of the hydrogen-bond system of β-CD (which leads to disintegration of β-CD aggregates improving hereby their aqueous solubility, as well) may play a role [11, 24, 25]. In addition, these "hydrotropes" may attach to the "surface active" statin–β-CD complexes as second-sphere ligands [26]. Somewhat differently, the amphiphilic complexes may anchor by their hydrophobic part at the macromolecular chains forming in a way ternary statin- β-CD – polymer assemblies of supramolecular structure.

Using macromolecular colloids may involve a better adsorption of such ternary assemblies to biological membranes, as well. Accordingly, cyclodextrin-based "nanoencapsulation" of statins might offer reasonable benefit of controlled drug delivery for the standard antihiperlipidemic therapy [23].

Acknowledgement This work was supported by Cyclolab R&D Ltd., Budapest, Hungary.

References

1. Prentis RA, Lis Y, Walker SR (1988) Pharmaceutical innovation by seven UK-owned pharmaceutical companies (1964–1985). Br J Clin Pharmacol 25:387–396
2. Istvan ES, Deisenhofer J (2001) Structural mechanism for statin inhibition of HMG-CoA reductase. Science 292:1160–1164
3. Maron DJ, Fazio S, Linton MF (2000) Current perspectives on statins. Circulation 101:207–213
4. Kang BK, Lee JS, Chon SK, Jeong SY, Yuk SH, Khang G, Lee HB, Cho SH (2004) Development of self-microemulsifying drug delivery systems (SMEDDS) for oral bioavailability enhancement of simvastatin in beagle dogs. Int J Pharm 274:65–73
5. Bradford RH, Shear CL, Chremos AN, Dujovne CA, Franklin FA, Grillo RB et al. (1994) Expanded Clinical Evaluation of Lovastatin (EXCEL) study results: two-year efficacy and safety follow-up. Am J Cardiol 74:667–673
6. Haria M, McTavish D (1997) Pravastatin: a reappraisal of its pharmacological properties and clinical effectiveness in the management of coronary heart disease. Drugs 53:299–336
7. ME Brewster, Loftsson T (2007) Cyclodextrins as pharmaceutical solubilizers. Adv Drug Deliv Rev 59:645–666
8. Loftsson T, Brewster M (1996) Pharmaceutical applications of cyclodextrins. I. Drug solubilization and stabilization. J Pharm Sci 85(10):1017–1025
9. Liu L, Guo QX (2002) The Driving Forces int he Inclusion Complexation of Cyclodextrins. J Incl Phenom Macrocycl Chem 42:1–14
10. Szejtli J (1982) Cyclodextrins and Their Inclusion Complexes. Akadémiai Kiadó, Budapest, Hungary
11. Fenyvesi E, Vikmon M, Szeman J, Redenti E, Delcanale M, Ventura P, Szejtli J (1999) Interaction of Hydroxy Acids with β-Cyclodextrin. J Incl Phenom Macrocycl Chem 33:339–344
12. Loftsson T, Friðriksdóttir H, Sigurðardóttir AM, Ueda H (1994) The effect of watersoluble polymers on drug-cyclodextrin complexation. Int J Pharm 110:69–177
13. Süle A, Szente L, Csempesz F (2005) Ciklodextrinek és sztatinok kölcsönhatásának in vitro vizsgálatai. Acta Pharm Hung 75:9–13
14. Jun SW, Kim M-S, Kim J-S, Park HJ, Lee S, Woo J-S, Hwang S-J (2007) Preparation and characterization of simvastatin/hydroxypropyl-b-cyclodextrin inclusion complex using supercritical antisolvent (SAS) process. Eur J Pharm Biopharm 66:413–417
15. Patel RP, Patel MM (2007) Physico-Chemical Characterization & In Vitro Dissolution Behavior of Simvastatin-Cyclodextrin Inclusion Compounds. Drug Deliv Technol 7(5):50–56
16. Higuchi T, Connors KA (1965) Phase-Solubility Techniques. Adv Anal Chem Instrum 4:117
17. European Directorate for the Quality of Medicines & HealthCare (EDQM) (ed) (2007) European Pharmacopeia 5th Edition 5.8 Supplement

18. Iga K, Hussain A, Kashihara T (1981) New direct calculation of K1 : 1 and K1 : 2 complexation constants using solubility method. J Pharm Sci 70(1):108–109
19. Buvári-Barcza Á, Barcza L (2000) Changes in the Solubility of β-Cyclodextrin on Complex Formation: Guest Enforced Solubility of β-Cyclodextrin Inclusion Complexes. J Incl Phenom Macrocycl Chem 36:355–380
20. Hinze WL, Pharr DY, Fu ZS, Burkert WG (1989) Thin-layer chromatography with urea-solubilized β-cyclodextrin mobile phase. Anal Chem 61:422
21. Süle A, Csempesz F (2005) Hatóanyag-oldékonyság szabályozása ciklodextrinekkel és kolloidokkal. Abst. Semmelweis Egyetem PhD Tudományos Napok, Budapest, Hungary, p 64
22. Redenti E, Selva A, Pasini A, Ventura P, Casetta B (1994) Proc 7th Int Symposium on Cyclodextrins, Tokyo, p 184
23. Loftsson T, Stefánsson E, Friðriksdóttir H, Kristinsson JK (1996) Novel CD-based Drug Delivery System. Proc 8th Int Symposium on Cyclodextrons, pp 407–412
24. Pioger E, Wouessidjewe D, Douchene D, Bogdanova S (1998) Effects of Some Hydrotropic Agents on the Formation of Indomethacin/β-Cyclodextrin Inclusion Compounds. J Incl Phenom Macrocycl Chem 30:151–161
25. Guo R, Quan S, Qian J (2004) Hydrotrope and hydrotrope-solubilization action of cephanone in CTAB/n-$C_5H_{11}OH$/H_2O system. Colloid Polym Sci 283:15–23
26. Stoddart FJ, Zarzycki R (1998) Cyclodextrins as second-sphere ligand for transition metal complexes. Rec Trav Chim Pays-Bas 107:515–528

Progr Colloid Polym Sci (2008) 135: 101–106
DOI 10.1007/2882_2008_113

Published online: 12 September 2008

Joakim Balogh
Jan Skov Pedersen

Investigating the Effect of Adding Drug (Lidocaine) to a Drug Delivery System Using Small-Angle X-Ray Scattering

Joakim Balogh
Departamento de Quimica da Universidade de Coimbra, Rua Larga, 3004-535 Coimbra, Portugal

Joakim Balogh (✉)
Physical Chemistry 1, Center for Chemistry and Chemical Engineering, Lund University, Getingev. 60, 22100 Lund, Sweden
e-mail: Joakim.Balogh@Fkem1.lu.se

Jan Skov Pedersen
Department of Chemistry and iNANO interdisciplinary Nanoscience Center, University of Aarhus, 8000 Aarhus C, Denmark

Abstract The effect on a model drug delivery system when adding a drug, lidocaine, has been studied. Temperature and concentration dependence of a nonionic microemulsion with part of the oil, 1 and 10 vol. %, substituted with drug has been investigated. A nonionic oil-in-water microemulsion consisting of $CH_3(CH_2)_{11}(OCH_2CH_2)_5OH$, ($C_{12}E_5$), decane, water and the drug (lidocaine) that has been used to substitute part of the oil was studied. The microscopic differences have been derived from small-angle X-ray scattering (SAXS) data and the results are compared with light scattering data. Using these results together with the macroscopic differences, as observed in the phase diagram (lowering of phase boundaries), between the systems with and without lidocaine can be explained.

Keywords $C_{12}E_5$ · Drug-containing · Lidocaine · Nonionic microemulsion · Temperature dependence

Introduction

This work deals with microemulsions as a model drug delivery system and the effects of adding a drug to these systems. The advantage of a microemulsion compared with an emulsion is that it is thermodynamically stable and hence self-assembling and not depending on mixing process. Using nonionic surfactants, microemulsions can be made without addition of co-solvents, co-surfactants or salts [1, 2]. Microemulsions are typically structured on length scales of the order of 5–20 nm, and can have many different morphologies. In general, the structures consist of water and oil separated by a surfactant film [1, 3, 4], which is traditionally modelled as a fluid flexible film [5–9]. The curvature elasticity of the surfactant film describes the film properties. The curvature free energy, G_c, is given by the surface integral $G_c = \int \mathrm{d}A g_c$, of the curvature energy density, g_c, over the area, A. Within the harmonic approximation this is often written according to the Helfrich model [10] as

$$g_c = 2\kappa(H - H_0)^2 + \bar{\kappa}K\,, \tag{1}$$

where H_0 is the spontaneous curvature, κ is the bending rigidity, and $\bar{\kappa}$ is the saddle splay modulus. κ and $\bar{\kappa}$ are on the order of a few k_BT. The principal curvatures, c_1 and c_2, enter H, the mean curvature, as $(c_1 + c_2)/2$, and enter K, the Gaussian curvature, as $c_1 \times c_2$. For $\bar{\kappa} < 0$ discrete aggregates are preferred and for $\bar{\kappa} > 0$ saddle-like structures are preferred. $H_0 = 0$, represents a lamellar structure, L_α, i.e. a flat structure with $c_1 = c_2 = 0$ or a bilayer bicontinuous microemulsion, L_3, with local saddle structure with the curvature of equal size but opposite sign ($c_1 = -c_2$).

The temperature, T, can in nonionic microemulsions with C_iE_j surfactants be used to change H_0. One has found [11, 12] that

$$H_0 = \alpha(T_0 - T) \, . \tag{2}$$

Here T_0 is the temperature for which the spontaneous curvature is zero, known also in literature as the phase inversion temperature, (PIT) and α is a temperature coefficient. This approximation holds for a range of 20 K below and above T_0 [11–13] in nonionic microemulsions with C_iE_j surfactants.

The microemulsions have in general a region where small globular droplets are stable. The region is surrounded by upper and lower boundaries known as emulsification failure boundaries. It is often easiest to study these systems at the temperature of the lower emulsification failure boundary, T_{EFB}, since the microemulsion droplets are often spherical here.

This present work describes the effects of a drug, lidocaine, on a model drug delivery system as observed in the phase diagrams and in the micro structure determined by SAXS. The model drug delivery system is the well-known nonionic ternary microemulsion system composed of $C_{12}E_5$, decane, and water with fixed surfactant to oil volume ratio of 0.85 : 1. This system has been studied previously amongst others by Olsson and co-workers [14–27]. We therefore have access to SANS, NMR and light scattering data for the microemulsion without drug. From above literature it is known that the system consists of spherical oil droplets covered with surfactant with a radius of 80 Å at the lower emulsification boundary and the droplets grow with temperature and to a small degree also with concentration. The growth gives aggregates with volume that increases, but to maintain the area to volume ratio of the droplets, they need to change shape when growing. In this particular case the growth is one-dimensional and often described as prolate aggregates. The ratio of the large axis to the small axis gives the axial ratio and it describes the shape of the prolate. Generally the particles only grow to an axial ratio less than 6 before they become bicontinuous microemulsion or phase separate at the upper emulsification boundary. These oil filled system therefore never change structure into wormlike micelles or similar structures. The change into a bicontinuous structure comes at lower temperatures when increasing the droplet concentration. For the system with added drug there have just recently been published data from light scattering (static and dynamic) [28] on the systems as well as a partial phase diagram [29]. We will compare these results with our present findings as well as with the general findings for the system without drug.

The use of microemulsions as drug delivery systems is a well studied field [30–38]. Microemulsion systems are generally designed for topic (skin, dermal) drug delivery [39–42]. The use of non-ionic microemulsions as enhancers for transdermal drug delivery of lidocaine has been studied by Sarpotdar and Zatz [43].

Materials and Methods

Materials

Decane (99%+), and 2-diethylamino-*N*-(2,6-dimethylphenyl)acetamide (lidocaine) (98%) TLC were purchased from Sigma-Aldrich Chemie (Germany). The nonionic surfactant $CH_3(CH_2)_{11}(OCH_2CH_2)_5OH$, abbreviated as ($C_{12}E_5$), was purchased from Nikko Chemicals (Japan). The chemicals were used without further purification. The water used was treated with a Millipore-Q water purification system.

Sample Preparation

A drug containing oil was made of decane and 1 or 10% of lidocaine, respectively. The drug containing oils were heated until a transparent solution was obtained and then stored above 303 K to avoid lidocaine precipitating. Stock solutions of "oil" (decane and lidocaine) and surfactant were then prepared. These solutions were stable at room temperature. The samples for the measurements were prepared from the stock solutions by dilution with water, mixed using a vortex mixer at 308 K, and then mixed while cooling to the microemulsion phase and kept there until measuring.

Phase Diagram Determination

The samples were studied in a thermostated water bath. Phase-boundary temperatures were determined by visual inspection, including the use of crossed polarizers. The phase boundaries were determined both for increasing and decreasing temperatures.

SAXS

The experiments were performed at the newly established SAXS setup at the I711 beamline in MAX-Lab, Lund, Sweden. The details of the beamline is described by Cerenius et al. [44]. The setup has three slits, two beam defining ones and an anti-scattering slit in front of the sample for removing background. Typical beam size at the sample position is 0.3 mm. The range of scattering vectors $\boldsymbol{q}$ is roughly 0.007–0.25 $Å^{-1}$. Here $\boldsymbol{q} = (4\pi/\lambda)\sin(\theta)$, where λ is the radiation wavelength and 2θ is the scattering angle. The samples are kept in a vacuum chamber to reduce background. The capillary holder insures good thermal contact with the thermostated block. The capillary is inserted directly into the vacuum so that no extra windows are needed.

Results

A partial phase diagram for the system with fixed surfactant to "oil" (decane and lidocaine) ratio of 0.85 : 1 with the droplet volume fraction, Φ, ranging from 0.01 to 0.2 is shown in Fig. 1 including data taken from [29]. The figure shows the phase boundaries for the three systems with 0, 1 and 10% of the volume of the oil substituted with lidocaine. Lidocaine has low solubility in water, less than 0.5%, and even at high temperatures (360 K) it is not possible to solubilize 1% in water. The solubility in decane for lidocaine is around 10% by volume at the temperature we used and increasing with temperature. The solubility in the surfactant is not known exactly but with the addition of the surfactant to the oil–lidocaine solution the stability range was increased to temperatures at least 10 K below the limit without surfactant. If we assume that the drug is solubilized in the oil, we would have constant surfactant to "oil" ratios in the systems. This would give similar size of the droplets at T_{EFB}. The change with a substitution of 1% oil for lidocaine is small or negligible while the change with 10% substitution results in major changes in the phase boundaries. The lower emulsification failure boundary T_{EFB} is lowered by 5 K and the upper phase boundary by 3 K. The lowering of the phase boundaries with 10% lidocaine compared with the system without lidocaine could be the result of either better penetration of the drug into the surfactant tail or lower amount of oil, if lidocaine is not solubilized in the oil phase but in the surfactant phase. The latter could either be with an effective change in the area per headgroup of the surfactant (also known as effective cross-sectional area per surfactant) or without. If it is without a change in the area per headgroup, it implies that the area per surfactant is the same but that the lidocaine acts as a surfactant and gives effectively bigger "surfactant area". If the lidocaine is not taken into consideration when calculating the area per headgroup, it results in an apparent change of area per headgroup.

The SAXS data were masked and converted to one dimension intensity distribution as a function of q using the program Fit2D [45]. The data were later fitted with a model of core–shell ellipsoids with polydispersity of the size. The structure factor is included in a decoupling approximation with an effective hard-sphere structure factor. We have not done attempts to use the advanced model by Arleth and Pedersen [46] since it is highly nonlinear in the parameters and therefore also much more difficult to fit to the data. The scattering data and fit for the 1% lidocaine system at T_{EFB} are shown in Fig. 2 and it shows that the fit describes the data well. The scattering data and fits for three temperatures for the droplet volume fraction $\Phi = 0.011$ with 1% lidocaine are shown in Fig. 3. The figure shows that the aggregates change shape and by that size with temperature. The fits provide the change in shape. The axial ratios, ρ as a function of temperature are shown in Fig. 4. The figure shows

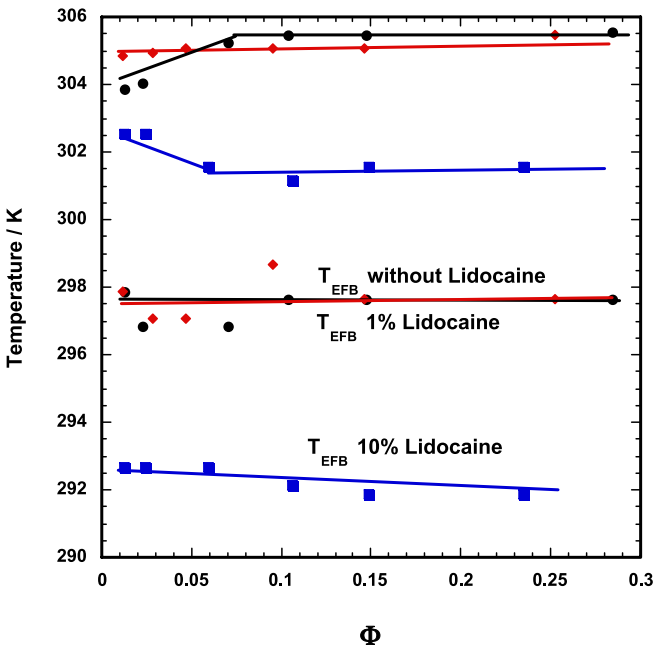

Fig. 1 Partial phase diagram for the three systems with 0, 1 and 10% of the oil volume substituted with lidocaine. The *circles*, *diamonds* and *squares* are, respectively, for the systems with 0, 1 and 10% lidocaine. The *lines* represent the temperature of emulsification failure boundary T_{EFB} and the upper phase boundary. Data taken from [29] are included

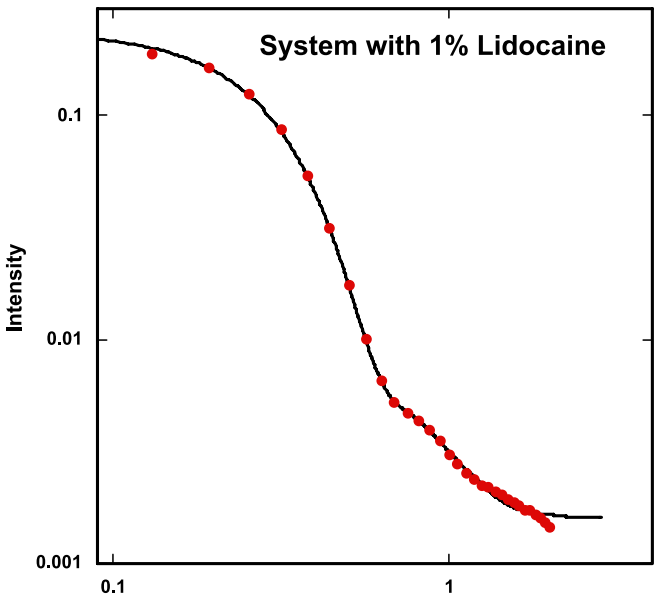

Fig. 2 The fit, *full curve*, and the data, *selected points*, shown for the system with 1% of the oil volume substituted by lidocaine and with droplet volume fraction of $\Phi = 0.011$ at T_{EFB} presented as log intensity vs. log q

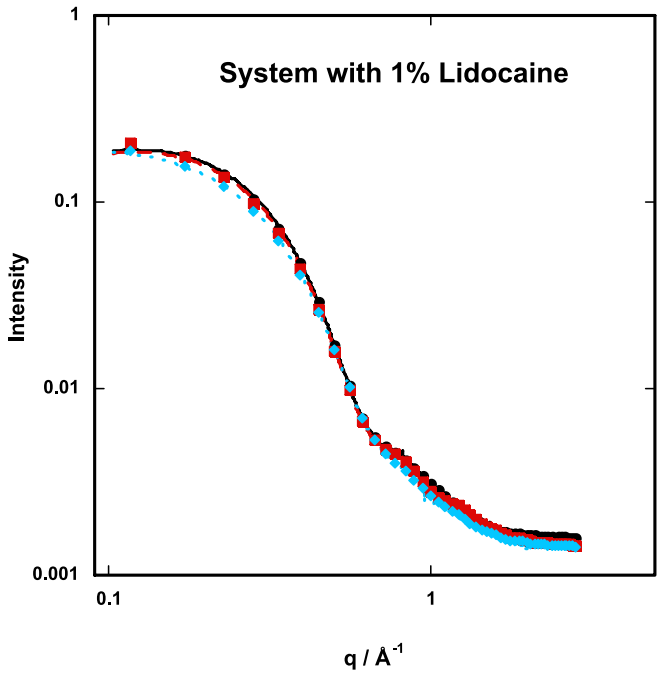

Fig. 3 SAXS data for the system with 1% of the oil volume substituted by lidocaine and with droplet volume fraction of $\Phi = 0.011$ at three temperatures $T_{EFB} = 298$ K (*circles*), 300 K (*squares*) and 302 K (*diamonds*) with their fits shown as respectively *full*, *dashed* and *dotted curves*

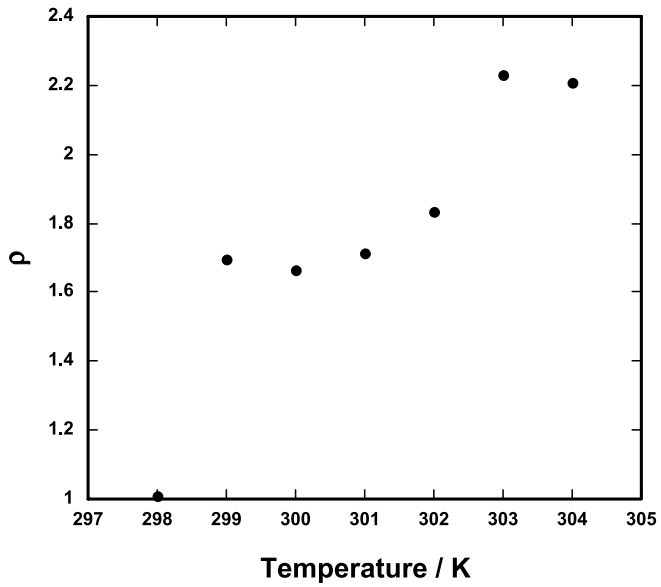

Fig. 4 The axial ratio ρ of the droplets as a function of temperature for the system with 1% of the oil volume substituted by lidocaine and with droplet volume fraction of $\Phi = 0.011$

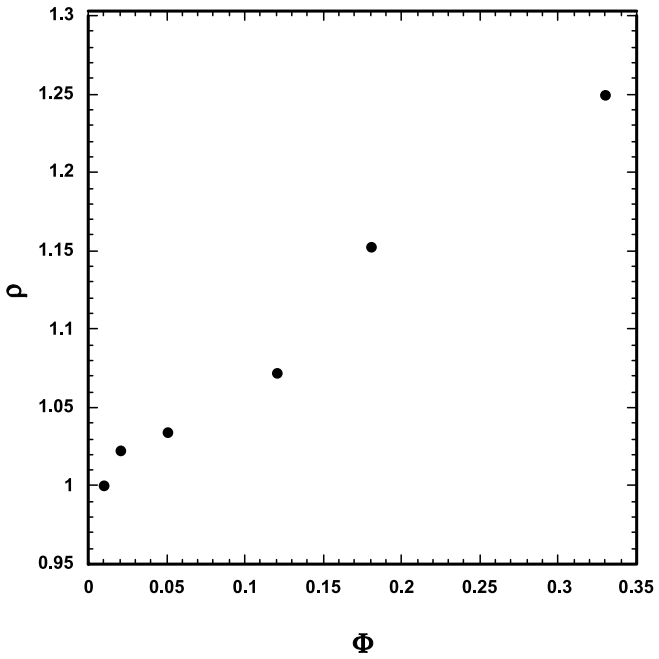

Fig. 5 The axial ratio ρ as a function of volume concentration of droplets as observed for the system without lidocaine at T_{EFB} measured in a previous study [22]

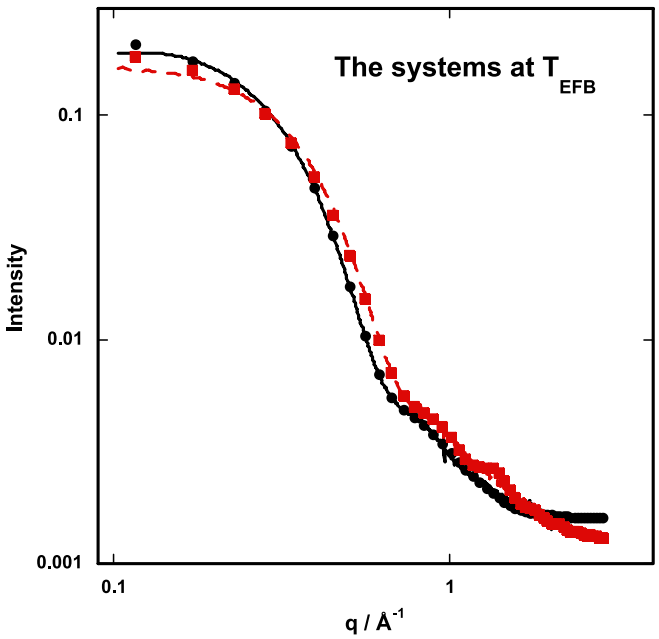

Fig. 6 The scattering data of the systems with droplet volume fraction of $\Phi = 0.011$ with 1% of the oil volume substituted with lidocaine (*circles*) and 10% substituted with lidocaine (*squares*) at T_{EFB} 298 and 292 K, respectively, and the corresponding fits as, respectively, *continuous* and *dashed curves*

that the droplets grow. Figure 5 displays the growth of the droplets with concentration for the system without lidocaine where the effective volume-equivalent radius is plotted versus droplet volume fraction [22]. The figure shows that the aggregates also grow with increasing concentration. Figure 6 displays the differences between the systems with different amount of lidocaine. The 10% lidocaine system has higher axial ratio even at T_{EFB}, 1.7 compared to 1 for the 1% system. Comparison with static and dynamic light scattering gives good agreement for the sizes that are increasing with temperature. It furthermore shows that the droplets in the system with 10% lidocaine are smaller at T_{EFB}. The decrease in size is so large that it can not be explained by having less oil due to lidocaine being solubilized in the surfactant phase, so either the lidocaine change the area per surfactant headgroup or it acts as surfactant itself with a constant area of the surfactant headgroup. It can also be a combination where part of the lidocaine is in the oil and increase the oil volume and part of it is solubilized in the surfactant and increase the "surfactant" volume/area. We believe it is the second case with most of the oil in the surfactant layer.

Conclusion

Substituting part of the oil with lidocaine in a model microemulsion influences the macroscopic properties, phase boundaries, and microscopic properties, particle size (shape) as well as concentration and temperature dependence. We believe this to be due to lidocaine being solubilized into the surfactant film and either acts as a surfactant or increases the area per headgroup of the surfactant. This is supported by phase behaviour and particle size. If the lidocaine would act as surfactant with the same headgroup area per volume as the surfactant $C_{12}E_5$, not all of the lidocaine would be in the surfactant film but rather two thirds would be in the surfactant film and one third in the oil. Most likely lidocaine is not as effective as a surfactant so even less than one third of the lidocaine would be solubilized in the oil.

Acknowledgement The authors would like to thank H. Wennerström and B. Lindman for valuable discussions. J.B. thanks FCT Post-Doc Fellowship (SFRH/BPD729511/2006) for financial support. Finally, we thank Matti Knaapila for assistance during the SAXS measurements and with the Fit2D program.

References

1. Evans DF, Wennerström H (1999) The Colloidal domain: where physics, chemistry, biology and technology meet. John Wiley & Sons Inc, New York, NY
2. Holmberg K, Jönsson B, Kronberg B, Lindman B (2003) Surfactants and Polymers in Aqueous Solution. John Wiley & Sons Ltd, Chichester
3. Anderson D, Wennerström H, Olsson U (1989) J Phys Chem 93:4243–4253
4. Chen SJ, Evans DF, Ninham BW, Mitchell DJ, Blum FD, Pickup S (1986) J Phys Chem 90:842–847
5. Wennerström H, Olsson U (1993) Langmuir 9:365–368
6. Safran SA (1992) Microemulsions: an ensemble of fluctuating interfaces. In: Chen S, Huang JS, Tartaglia P (eds) Structures and Dynamics of Strongly Interacting Colloids and Supramolecular Aggregates in Solution. Kluwer Academic Publishers, Dordrecht, The Netherlands, p 237
7. Daicic J, Olsson U, Wennerström H, Jerke G, Schurtenberger P (1995) J Phys 5:199–215
8. Roux D, Nallet F, Coulon C, Cates ME (1996) J Phys 6:91–93
9. Daicic J, Olsson U, Wennerström H, Jerke G, Schurtenberger P (1996) J Phys 6:95–96
10. Helfrich W (1973) Naturforschung 28c:693–703
11. Strey R (1994) Colloid Polym Sci 272:1005–1019
12. Olsson U, Wennerström H (1994) Adv Colloid Interf 49:113–146
13. Le TD, Olsson U, Wennerström H, Schurtenberger P (1999) Phys Rev E 60:4300–4309
14. Olsson U, Schurtenberger P (1993) Langmuir 9:3389–3394
15. Olsson U, Schurtenberger P (1997) Progr Colloid Polym Sci 104:157–159
16. Olsson U, Bagger-Jörgensen H, Leaver M, Morris J, Mortensen K, Strey R, Schurtenberger P, Wennerström H (1997) Progr Colloid Polym Sci 106:6–13
17. Leaver MS, Olsson U, Wennerström H, Strey R, Wurz U (1995) J Chem Soc Faraday Trans 91:4269–4274
18. Leaver M, Furo I, Olsson U (1995) Langmuir 11:1524–1529
19. Leaver MS, Olsson U (1994) Langmuir 10:3449–3454
20. Leaver MS, Olsson U, Wennerström H, Strey R (1994) J Phys 4:515–531
21. Bagger-Jörgensen H, Olsson U, Mortensen K (1997) Langmuir 13:1413–1421
22. Balogh J, Olsson U, Pedersen JS (2006) J Dispers Sci Technol 27:497–510
23. Balogh J, Olsson U (2007) J Dispers Sci Technol 28:223–230
24. Balogh J, Kaper H, Olsson U, Wennerström H (2006) Phys Rev E 73:041506
25. Balogh J, Olsson U, Pedersen JS (2007) J Phys Chem B 111:682–689
26. Balogh J (2008) To be submitted for publication
27. Wennerström H, Balogh J, Olsson U (2006) Colloid Surf A 291:69–77
28. Balogh J, Schillen K, Miguel M (2007) Investigating a nonionic oil-in-water microemulsion containing a hydrophobic drug (Lidocaine). In: Valente A, Seixas de Melo J (eds) 2nd Iberic Meeting of Colloids and Interfaces (RICI2). Sociedade Portuguesa de Quimica, Coimbra, Portugal, p 311–319
29. Balogh J, Schillen K, Miguel MD (2007) AAPS J 9:W4179
30. Bagwe RP, Kanicky JR, Palla BJ, Patanjali PK, Shah DO (2001) Crit Rev Ther Drug 18:77–140

31. Trotta M, Gasco MR, Morel S (1989) J Control Release 10:237–243
32. Kreilgaard M (2002) Adv Drug Deliv Rev 54:S77–S98
33. Lawrence MJ, Rees GD (2000) Adv Drug Deliv Rev 45:89–121
34. Vandamme TF (2002) Prog Retin Eye Res 21:15–34
35. Spernath A, Aserin A (2006) Adv Colloid Interface 128:47–64
36. Krafft MP, Chittofrati A, Riess JG (2003) Curr Opin Colloid Interface Sci 8:251–258
37. Malmsten M (2007) J Dispers Sci Technol 28:63–72
38. Malmsten M (2006) Soft Matter 2:760–769
39. Trotta M, Morel S, Gasco MR (1997) Pharmazie 52:50–53
40. Sarpotdar PP, Zatz JL (1986) Drug Dev Ind Pharm 12:1625–1647
41. Sarpotdar PP, Zatz JL (1987) Drug Dev Ind Pharm 13:15–37
42. Lee PJ, Langer R, Shastri VP (2003) Pharm Res 20:264–269
43. Sarpotdar PP, Zatz JL (1986) J Pharm Sci 75:176–181
44. Cerenius Y, Stahl K, Svensson LA, Ursby T, Oskarsson A, Albertsson J, Liljas A (2000) J Synchrotron Radiat 7:203–208
45. Hammersley AP, Svensson SO, Hanfland M, Fitch AN, Hausermann D (1996) High Press Res 14:235–248
46. Arleth L, Pedersen JS (2001) Phys Rev E 63:061406

Progr Colloid Polym Sci (2008) 135: 107–118
DOI 10.1007/2882_2008_123

Published online: 12 September 2008

Lívia Naszályi Nagy
Nóra Ábrahám
Attila L. Kovács
Arie van der Lee
Vincent Rouessac
Didier Cot
André Ayral
Z. Hórvölgyi

Zinc Oxide LB Films with Improved Antireflective, Photoactive and Mechanical Properties

Lívia Naszályi Nagy · Nóra Ábrahám · Z. Hórvölgyi (✉)
Department of Physical Chemistry and Materials Science, Centre for Colloid Chemistry, Budapest University of Technology and Economics, 1521 Budapest, Hungary
e-mail: zhorvolgyi@mail.bme.hu

Attila L. Kovács
Department of Anatomy, Cell and Developmental Biology, Cell Physiology Laboratory, Loránd Eötvös University, P.O. Box 120, 1518 Budapest, Hungary

Arie van der Lee · Vincent Rouessac · Didier Cot · André Ayral
Institut Européen des Membranes, CNRS-ENSCM-UM2, cc047, Université Montpellier 2, Place Eugène Bataillon, 34095 Montpellier cedex 5, France

Abstract Multifunctional Langmuir–Blodgett films were prepared using sol–gel derived ZnO and silica nanoparticles synthesized by the procedure of Seelig et al. [1] and Stöber et al. [2], respectively. High inherent porosity was observed for ZnO particles (30–40%) by pycnometry, scanning angle reflectometry, N_2 adsorption–desorption and ellipsometric porosimetry methods. Water contact angle of ZnO nanoparticles was determined from the non-dissipative part of the obtained surface pressure-surface area isotherms, and by scanning angle reflectometry measurements in a Wilhelmy film balance. Antireflective and photocatalytically active coatings of ZnO particles were deposited on glass, conductive glass and silicon substrates. The antireflectivity of ZnO LB films was improved by the integration of silica nanoparticles in the LB film. The photocatalytic activity and the mechanical stability of the samples were enhanced by means of surface modification with 3-methacryloxypropyl(trimethoxy)silane.

Keywords Antireflectivity · Langmuir–Blodgett films · Mechanical stability · Photocatalysis · ZnO nanoparticles

Introduction

The development of new, energy-saving applications is a great challenge of nanotechnology. The use of small quantity nanomaterials in coatings [3, 4], the coupling of functionalities in one device [5] and the use of renewable energies (photodegradation [6–8], solar cells [9–11]) are highly recommended strategies.

Wet chemistry synthesis routes offer cheap and versatile preparation methods for these materials. Large-area optical coatings e.g. were obtained for the reduction of energy-losses in high-power lasers by dip coating technique [12, 13]. Layer-by-layer (LBL) deposition methods would be also favourable for the control of optical properties through the precise control of film structure. Therefore the Langmuir–Blodgett (LB) technique is a suitable candidate for the development of optical coatings from nanoparticles. Basic research work has been carried out for the preparation of antireflective (AR) LB films using silica nanoparticles [4, 14, 15]. In the recent years, ultrathin LB films (3–20 nm) of ZnO nanoparticles were also fabricated on the surface of silicon and fused silica slides [16]. These films showed excellent transparency in the visible range, however, antireflective effect could not be induced because of unsuitable thickness of the films and high refractive index of crystalline ZnO (2.01, [17]). To the best of our knowledge, no report has been published on the preparation of pure ZnO AR films. Only complex LB films of silica and ZnO nanoparticles with AR effect were reported [18].

Sol–gel derived ZnO films were studied in photocatalytic degradation of organic dyes, ZnO being a high band gap ($E_g = 3.3$ eV) semiconductor material whose photoactivity is similar to that of titania. ZnO was even found to be more effective in the degradation of organic dyes in studies using solar light [19, 20].

The aim of the present study was to prepare pure and complex ZnO LB films with AR property and to characterize their activity for photocatalysis (multifunctional coatings). As the stability of LB films towards mechanical impacts is generally poor, which is unfavourable for applications, we made attempts to improve it by adapting a previously described surface modification procedure. The method of Rohe et al. [21] elaborated for the linkage of ZnO nanoparticles in aqueous sol was based on the idea of developing siloxane bridges (≡Si−O−Si≡) between the ZnO particles. They irradiated the hydrosol of ZnO nanoparticles by UV light after surface modification of the particles in methanolic solution of 3-methacryloxypropyl(trimethoxy)silane (MTS). We aimed at establishing similar siloxane chains between ZnO particles in LB films as well as between the particles and the glass substrate providing improved mechanical stability for the coatings.

Optical and photocatalytic properties of the ZnO LB films were studied in parallel and found to be improved by the incorporation of silica nanoparticles and surface modification, respectively.

Experimental

Reagents, Solvents and Substrates

Particle Preparation. Zinc acetate dihydrate (> 98% A.C.S. reagent, Aldrich), tetraethyl orthosilicate (> 98% GC, Merck), ammonia (25% aqueous solution a.r., Reanal), absolute ethanol (a.r. > 99.7%, Reanal) and diethylene glycol (DEG, purum, Reanal) were used as received.

Film Balance Experiments. Chloroform (ultra-resi analyzed, > 99.8%, Baker) was used as spreading liquid. Distilled water was purified in a Millipore Simplicity 185 system (18.2 MΩcm).

Preparation and Characterization of LB Films. Microscope glass slides, conductive (ITO) glass slides and silicon substrates have been used for film preparation. The substrates were thoroughly cleaned prior to use. The glass slides were immersed into persulphuric acid (2 : 1 vol. % of sulphuric acid (96%, ISO-for analysis, Carlo-Erba) and hydrogen peroxide (30% in aqueous solution, puriss., Reanal)) for 1 h, then rinsed with distilled water, ethanol and, finally, dried at room temperature. The ITO glass was cleaned in diluted NaOH and then in acetone ultrasonic bath and finally rinsed with Millipore water and abs. ethanol. The silicon wafers were immersed into 2% aqueous HF solution (diluted from 40% HF, a.r., Reanal) for 30 s to remove the native oxide layer, then washed with distilled water, ethanol and finally, dried at room temperature.

3-methacryloxypropyl(trimethoxy)silane (MTS, > 98%, Sigma) and hexane (for synthesis, 96%, Merck) were used for the surface modification of LB films.

Methyl orange (MO, spec., Reanal) in 5.5 mg l^{-1} aqueous solution was used in photocatalytic experiments.

Experimental Methods

Preparation of Alcosols and Powders. According to transmission electron microscopy (TEM) investigations, ZnO particles of 110 ± 16 nm, 172 ± 24 nm, 225 ± 10 nm, 267 ± 26 nm and 360 ± 15 nm diameter were synthesized in diethylene glycol (DEG) according to the procedure of Seelig et al. [1]. 2.2 g zinc acetate dihydrate was rapidly heated to 160 °C in 100 ml of DEG. After 3 h of reaction a white slurry was obtained that was separated from the supernatant in a centrifuge (4200 rpm, 3 h). A second reaction was then carried out heating up rapidly the same amount of starting reagents. When 150 °C was reached 10 ml of the primary supernatant was added to the second reaction, and temperature was allowed to rise up to 160 °C for 1.5 h. The resulting stable, white sol was finally cooled down and stored at room temperature. The samples were named according to their mean particle size (e.g. Z110).

Nearly spherical silica particles with mean diameter of 96 ± 13 nm [4] were used in this study. The sample name was S96.

Chloroform as spreading liquid was used in a vol. ratio of 1 : 1 for ZnO sols in DEG and 2 : 1 for silica sols.

Mixed spreading sols were prepared from Z110 and S96 alcosols. The ratio of ZnO particles over silica particles was estimated using $\rho_{SiO_2} = 2.06\ g\ cm^{-3}$ [22] density data and $\rho_{p,ZnO} = 2.77\ g\ cm^{-3}$ (density measurement of Z172). The six mixtures were named Z110-R17, Z110-R10, Z110-R3, Z110-R1.6, Z110-R0.8 and Z110-R0.25 according to the number ratio of ZnO particles to silica particles. Equal volume of chloroform was added to the mixture of particles in their original media. Aliquots of ZnO alcosols were transferred into chloroform. After centrifuging (4200 rpm, 60–120 min) the supernatant was discarded and the particles were redispersed in chloroform.

Aliquots of Z172 and Z360 were washed five times with chloroform and then dried at 60 °C to yield equivalent powders. An aliquot of the sol sample was centrifuged, the supernatant was discarded, and the particles were redispersed in fresh chloroform. This procedure was repeated four times.

Characterization of Alcosols and Powders. The solid content of samples was determined on 3×500 µl aliquots of sols dried at 120 °C for 3 h.

Images taken by a JEOL JEM-100 CXII transmission electron microscope (TEM) were used for the determination of particle sizes. Samples were taken from the Langmuir films of particles at moderate surface pressures using Formvar coated copper grids.

The porous texture of powders dried from Z172 and Z360 was investigated by N_2 adsorption–desorption (Micromeritics, ASAP 2010), pycnometry (manual, 10 ml using ethanol solvent) and H_2O adsorption–desorption (Quantachrome Instruments, Hydrosorb 1000 3.14) techniques.

Preparation of Langmuir Films. Langmuir films were prepared in a Wilhelmy trough filled with Millipore water the surface of which was cleaned before each experiment. The particles were spread at the air–water interface after 1 min of ultrasonication. 5 min elapsed before recording the surface pressure (Π)–surface area (A) isotherms during compression of the area from maximum (235 cm^2) to minimum (40 cm^2) at constant barrier speed of 33.2 $cm^2\,min^{-1}$. A NIMA PS4 forcemeter was used with paper plate, cut from Whatmans Chr1 chromatography paper.

Characterization of Langmuir Films. Evaluation of the Π–A isotherms was done by the determination of contact cross-sectional area (CCSA, A_K) of particles. The area occupied by one single particle in the Langmuir film (A_1) could be calculated by

$$A_1 = \frac{A_K}{N}\,, \tag{1}$$

and

$$N = 6\frac{m}{\bar{d}^3\pi\rho}\,, \tag{2}$$

where N is the number of particles forming the Langmuir film, m is the mass of oxide particles spread (obtained from the solid content of spreading sol), ρ is the density of particles and $\bar{d}^3$ is the average particle volume (obtained from the particle sizes). In the case of ZnO particles, the density measured for Z172 with a pycnometer was used for the calculations (2.77 g cm^3). If particles form hexagonal close-packed structure upon compression, the area occupied theoretically by one single particle can be expressed by the area of a hexagon including the particle

$$A_{H,1} = \frac{\sqrt{3}}{2}\bar{d}^2\,, \tag{3}$$

where $\bar{d}^2$ is the average particle cross section area calculated from size distribution function. This expression was used to correlate the effective refractive index of the particles and the LB monolayers, and to calculate the water contact angle of Z172 and Z267 particles from the non-dissipative part of the isotherm using the expression [23, 24]

$$W^1 = \gamma_{LF} r^2 \pi (1 - \cos(\Theta))^2 = \frac{1}{2}(A_1 - A_{c,1})\Pi_c\,, \tag{4}$$

where W^1 is the adhesion work, γ_{LF} is the surface tension of the subphase, r is the mean particle radius, Θ is the contact angle of the particle on the subphase, Π_c is the collapse pressure and $A_{c,1}$ is the collapse area computed for one single particle. The calculated water contact angle shows a nearly linear dependence on the spread amount because of the existence of surface pressure gradient in the particulate layer during anisotropic compression [25, 26]. The intrinsic water contact angle of the particles was obtained by extrapolation of this linear function to zero amount of material [27].

Scanning angle reflectometry (SAR) measurements were performed in the Wilhelmy trough illuminated with a *p*-polarized laser beam (Melles-Griot 17 mV He-Ne laser, $\lambda = 632.8$ nm) as described previously [15]. A silicon photodiode detector (PD200 Edmund Industrial Optics) was used for the detection of reflected light intensity as a function of the angle of incidence. The angle of incidence was changed by steps of 0.1° in the range between 50 and 58° (around the Brewster angle of water–air interface). The intensity curves obtained for the Langmuir films were converted into reflectance curves [15]. These were evaluated using a previously described optical model (*hexagonal model*) for hexagonal close packed particles partially immersed into the subphase (in-depth refractive index profile) at the air–water interface [15, 28]. Parameters of this model are: *particle refractive index* ($n_{p,eff}$), *interparticulate distance* (assumed to be d in this case), *particle diameter* (d, layer thickness) and *immersion depth* (h) or *immersion ratio* (h/d) (Fig. 1). Starting value of particle refractive index computation is the refractive index (RI) evaluated from the intersection of film reflectance curve and water reflectance curve. The water contact angle of the particles can be evaluated from the *immersion ratio* with a simple geometrical relation assuming that the water

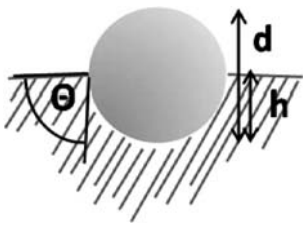

Fig. 1 Accomodation of a partially wettable particle at the air–water interface. Θ is the water contact angle, d is the particles diameter and h is the immersion depth

surface is not distorted by the weight of the particle (Fig. 1):

$$\cos \Theta = 2\frac{h}{d} - 1 \,. \tag{5}$$

Preparation of LB Films. The trough of the Wilhelmy film balance was filled with Millipore water, and the water surface was cleaned. The substrate was immersed into the water prior to the spreading of the particles. A continuous Langmuir film was formed on the water surface slowly decreasing the available area. Withdrawal of the substrate was launched at ca. 50% of the collapse pressure. The deposited layers were dried at ambient temperature. In the case of multilayered LB films the above procedure was repeated 1–4 times. The obtained films were finally dried at 105 °C in air. The samples were denominated indicating the spreading mixture (in the subscript) and the number of deposited layers e.g. $F_{Z110\text{-}R31}$ (monolayer of Z110-R3 mixed spreading sol – Table 1). In the case of complex LB films containing S96 and Z110 particles in separate monolayers, they are labelled according to the sequence of layers starting from the substrate e.g. F_{ZS} is a two-layered complex LB film with one layer of Z110 particles deposited on the surface of the substrate and a second layer of S96 particles deposited on the surface of the Z110 layer.

Surface Modification of LB Films. $F_{Z110}1$, $F_{S96}1$ and F_{SZ} films were immersed for 1 min into a 1 vol. % solution of 3-methacryloxypropyl(trimethoxy)silane in hexane, followed by irradiation for 15 min under UV light (Philips CleoHPa 400 W, maximum intensity at 375 nm) in the presence of water vapours (samples kept above a beaker containing hot water during the irradiation). Samples were labelled with letter M after the sample name e.g. $F_{Z110}1M$ (Table 1).

Table 1 Name and characteristics of the prepared LB films. Each number in brackets corresponds to a discrete sample

LB film	Sample name	No. of layers	Surface modified
Pure ZnO	$F_{Z110}(1, 2, 3, 4)$,	1–4	$F_{Z110}1M$
	$F_{Z(172,225,267,360)}1$	1	–
Pure SiO_2	$F_{S96}1$	1	$F_{S96}1M$
Mixed[a]	$F_{Z110\text{-}R(17,\ 10,\ 3)}1$	1	–
	$F_{Z110\text{-}R10+R3}2$	2	–
Complex[b]	F_{SZ}	2	$F_{SZ}M$
	F_{ZS}	2	–

[a] Mixed LB films are prepared using mixed spreading sols Z110-R17, Z110-R10 and Z110-R3.
[b] Complex LB films are deposited using pure SiO_2 and ZnO spreading sols.

Structural Characterization of LB Films. Information about the structure and morphology of deposited, multilayered films images was obtained by a Hitachi S-4500 scanning electron microscope (SEM). Glass slides and silicon wafers were used as substrates. X-ray diffraction (XRD) was performed on $F_{Z267}1$ LB film with a PanAlytical X'pert Pro instrument using wavelength $\lambda(Cu_{K\alpha})$.

Ellipsometric porosimetry (EP) (ellipsometer Plasmos SD2300) measurements were performed on silicon supported films $F_{Z110}1$, $F_{Z172}1$, $F_{Z225}1$, $F_{Z267}1$ and $F_{Z360}1$. The angles of incidence (and detection) of He-Ne laser light ($\lambda = 632.8$ nm) were 70°. Ethanol was chosen to be the probe molecule. First, the bare substrate (Si) was put into a home-made, controllable vapour-pressure cell. Its refractive index (≈ 3.40) and extinction coefficient (≈ -0.28) was evaluated on the basis of a few tens of measurements at atmospheric pressure (software SD 6.5). The thin supported film was put in the way of light, and then the sample cell was sealed and put under vacuum ($p \approx 10$–3 mbar). Ethanol vapour pressure was increased step by step over the sample opening and closing a valve. The temperature (26–28 °C) was noted and the values of relative pressure p/p_0 were calculated accordingly.

Functional Characterization of the LB Films. UV-Vis spectroscopy method using an Agilent 8453 spectrophotometer was used to study the *antireflective property* (transmittance) of the LB films in the wavelength range between 300–1100 nm. The reference was air in every case.

The *photocatalytic activity* of complex LB films was studied by determining the degradation of MO in 5.5 mg l^{-1} aqueous solution. The irradiating light source was a Philips CleoHPA lamp (400 W, max. intensity at 375 nm). The supported catalyst film (5.5–6.8 ± 0.3 cm^2 of area) was immersed in 10 ml of the MO solution kept at 25 °C under magnetic stirring during the experiment. Absorbance of the organic dye in solution was observed at 464 nm as a function of the irradiation time. Before each absorbance measurement, the volume of the MO solution was readjusted to 10 ml with distilled water because there was a slight evaporation of the solvent during the photocatalytic test. Specific degradation vs. irradiation time diagrams were obtained from photocatalytic measurements. Specific degradation corresponds to the decrease in MO absorbance at 464 nm per cm^2 of sample area. This specific value enables to take into account the variation of sample area (5.5–6.8 ± 0.3 cm^2) in contact with a fixed volume of dye solution (10 ml). It was calculated as follows:

$$D_{\mathrm{sp}} = 100\frac{A_0 - A_{\mathrm{t}}}{A_0 S} \,, \tag{6}$$

where A_0 is the absorbance of MO solution at the beginning of the test, A_{t} is the absorbance value after t illumination time and S is the area of solid supported film.

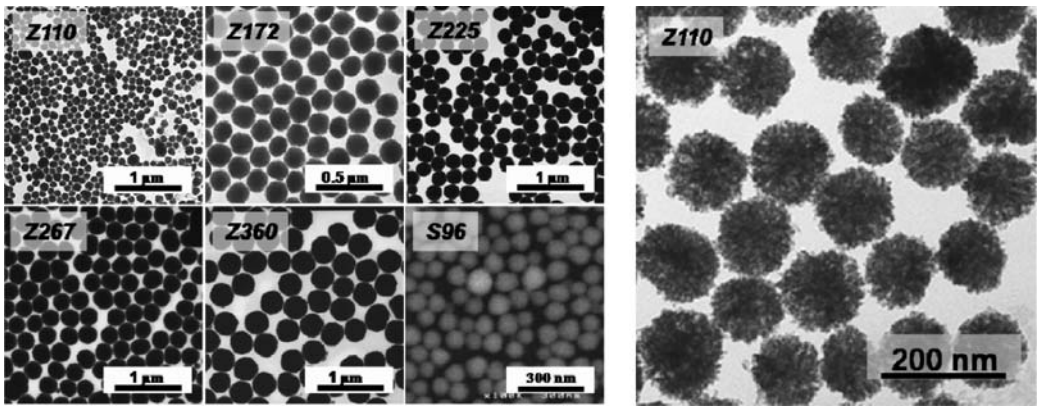

Fig. 2 Transmission electron micrographs of ZnO particles and scanning electron micrograph of silica nanoparticles

UV-Vis spectroscopy was used to evaluate the changes induced in the film composition during *mechanical stability* test. Estimation could be given to the ZnO content of the film observing the absorption edge of ZnO at about 360 nm. Transmittance spectra of the samples were taken directly after film preparation, then after the surface modification of the sample and, finally, after various times of ultrasonication in ethanolic bath (ultrasound frequency = 37 kHz).

Results and Discussion

Structural Characterization of Materials

ZnO Particles. ZnO particles prepared by the procedure of Seelig et al. [1] were mainly spherical according to TEM pictures (Fig. 2). The polycrystalline nature of the ZnO particles was reported by the authors of the synthesis, but the particle porosity was not investigated. However, porosity can be expected, since in a similar reaction the formation of porous ZnO particles in diol solutions was observed by Uekawa et al. [29]. We investigated the porosity of particles and resulting films by pycnometry, N_2 and H_2O adsorption–desorption, ellipsometric porosimetry, scanning angle reflectometry techniques applying suitable models. The density of Z172 powder was found to be 2.77 g cm^{-3} by pycnometry. The density of bulk ZnO is 5.67 g cm^{-3} [30], which means that the porosity

Table 2 Porosity of Z110, Z172, Z267 and Z360 particles evaluated from pycnometry, N_2 adsorption–desorption, scanning angle reflectometry (SAR) and ellipsometry measurements

Technique	Sample	P (%)
Pycnometry	Z172	51
N_2 ads.–des.	Z172	16
	Z360	32
SAR	Z110	43
	Z172	38
	Z267	40
Ellipsometry	Z110	59
	Z172	37

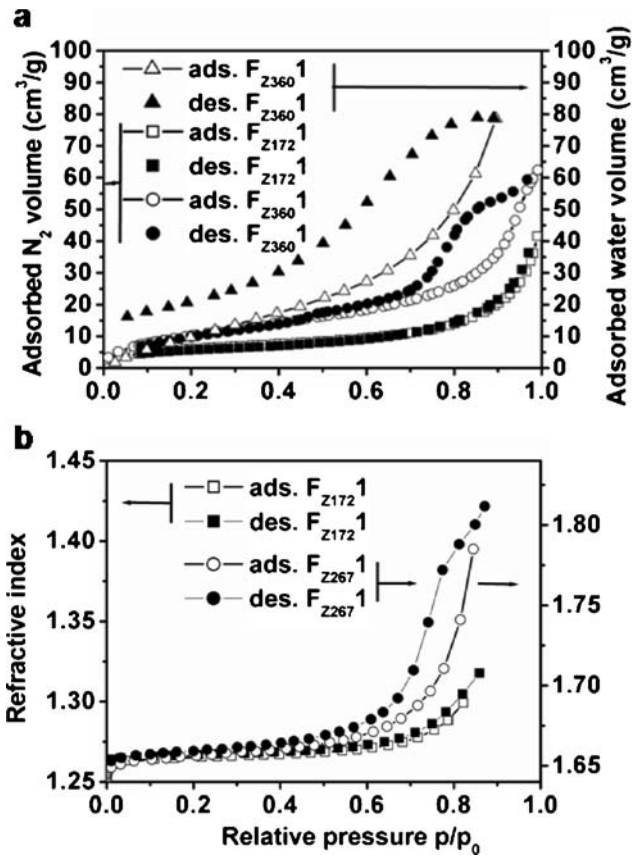

Fig. 3 **a** N_2 and H_2O adsorption–desorption isotherms on ZnO particles; **b** ellipsometric porosimetry measurements: evolution of the effective refractive index of silicon supported ZnO LB monolayers during ethanol adsorption–desorption

of particles may be 51% (Table 2). However, the nitrogen adsorption–desorption measurement evidenced only 16% of porosity in powder Z172 and 32% in powder Z360 (Fig. 3a). Furthermore, the shape of Z172 isotherm did not show open mesoporosity (absence of hysteresis loop on the isotherm). The discrepancy between the results of pycnometry and N_2 adsorption measurements can be explained by assuming mainly closed porosity. The pores of Z360 particles were at least partially open to nitrogen molecules. The mean pore size of 10 nm corresponded to the pores between the small primary ZnO particles that formed large secondary spheres [29]. Therefore, we presume aggregation-type growth mechanism in the reaction described by Seelig et al. The shape of the water adsorption–desorption isotherm performed on Z360 powder was very different from that obtained with N_2 probe molecules, though the degassing process was the same. This "irreversible loop"-type isotherm was previously observed for mesoporous oxides with partially hydroxylated surface and was attributed to chemisorption of water molecules [31].

ZnO Particles at the Air–Water Interface. All ZnO samples produced isotherms with well-defined solid region, which enabled us to evaluate A_K (A_1), A_c ($A_{c,1}$) and Π_c values (Fig. 4a). The value of A_K depended linearly on the spread volume of the sol. Nevertheless, when A_K values were plotted against the mass of the spread ZnO particles (Fig. 4b), it appeared that more than twice of the ZnO amount was spread from a mixture of diethyleneglycol and chloroform (hollow symbols) as compared to the amount spread from pure chloroform (plain symbols) to have the same surface covered. This means that diethyleneglycol (miscible with water) pulls the particles into the subphase during spreading and, therefore, the amount of ZnO at the air–water interface cannot be determined.

Mixed spreading sols of Z110 and S96 particles (samples Z110-R(17-0.25)) were spread at the air–water interface. At low concentrations (ZnO/silica number ratio > 3), the introduction of silica particles in the ZnO Langmuir film made no difference in the film structure, but at higher silica content a significant cohesiveness was observed. This could be confirmed by repeated compression-decompression (inset in Fig. 5b as compared to Fig. 5a) of mixed systems: anomalous changes occur in the surface pressure, indicating a highly cohesive system [32]. Segregation of silica and ZnO particles in samples with ZnO/ silica number ratio ≥ 3 was evidenced by TEM pictures (Fig. 6). Furthermore, isotherms of samples containing silica particles in excess (Z110-R(0.8-0.25)) had neither linear region nor shoulder (the total number of particles spread was similar for each isotherm, $(1.3–1.6 \times 10^{18})$. These isotherms presented no similarity to that of either pure ZnO or silica particulate films. The interpretation of the phenomena observed in hybrid and mixed Langmuir films of ZnO particles needs further investigation.

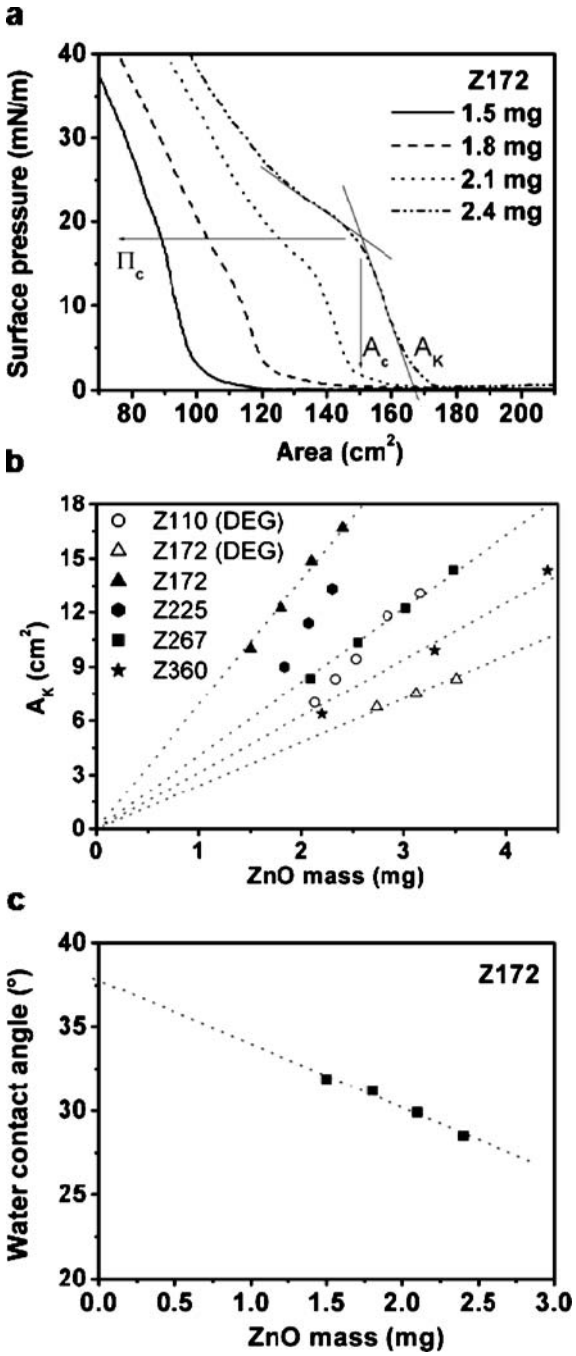

Fig. 4 Evaluation of Π–A isotherms; **a** isotherms of Z172 particles transferred into chloroform and determination of characteristic parameters (contact cross sectional area (A_K), collapse area (A_c) and collapse pressure (Π_c)); **b** A_K values vs. the ZnO mass spread from mixtures of DEG: chloroform $= 1 : 1$ vol. ratio (*hollow symbols*) and from pure chloroform (*plain symbols*); **c** determination of characteristic water contact angle of particles Z172 by extrapolation to zero amount of ZnO

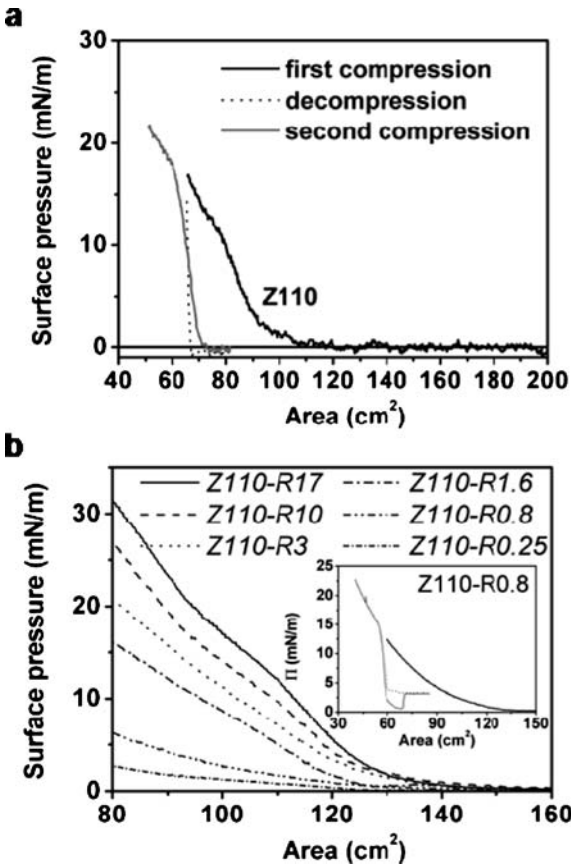

Fig. 5 Isotherms and repeated compression–decompression cycles of Langmuir films of **a** Z110 particles and **b** mixed samples Z110-R(17-0.25) (repeated compression-decompression of Z110-R0.8 in the *inset*)

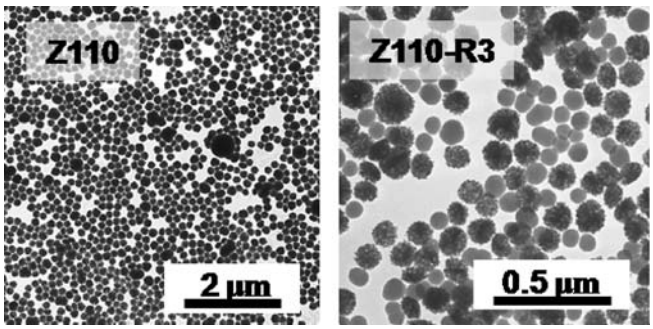

Fig. 6 Transmission electron micrographs of Z110 and Z110-R3 Langmuir films. *Black and spongy spheres* are ZnO particles, *grey and smooth spheres* are silica particles

Optical Properties – SAR Measurement. SAR measurements performed at the air–water interface and following optical model fitting (described elsewhere [15, 28]) provided us values of particle refractive index ($n_{p,eff}$), film thickness (d) and immersion depth of particles in the subphase (h) (Fig. 1) for samples Z110, Z172 and Z267 (Fig. 7, Table 3). According to the computation, the

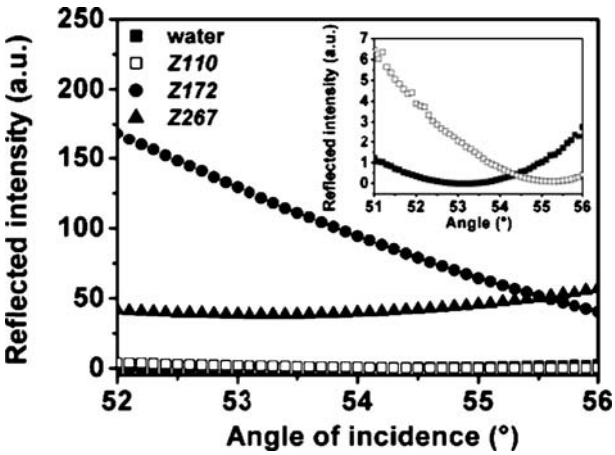

Fig. 7 Scanning angle reflectometry curves obtained from pure water surface and from Z110, Z172 and Z267 particulate Langmuir films. The curves of water and Z110 Langmuir film are enlarged in the *inset*

Table 3 Optical properties of Z110, Z172 and Z267 particulate films at the air–water interface evaluated from scanning reflectometry measurements by fitting with the hexagonal model [27]. χ^2 is the sum of deviation squares

Sample	d	h/d	$n_{p,eff}$	$\chi^2(\times 10^{-8})$
Z110	119	0.719	1.486	0.004
Z172	188	0.945	1.531	0.10
Z267	291	0.936	1.515	0.07

particle refractive index was 1.486 for Z110, 1.531 for Z172 and 1.515 for Z267. For hexagonal close-packed LB films [15], this would yield film refractive indices of 1.277 for $F_{Z110}1$, 1.300 for $F_{Z172}1$ and 1.292 for $F_{Z267}1$ (calculated with the *Lorentz–Lorenz formula*). The porosity values calculated from particle refractive indices are shown in Table 2. These values are between the porosity values measured by pycnometry and N_2 adsorption–desorption technique showing an "optical" porosity of 38–43%.

Estimation of Water Contact Angle. The irreversible removal of the particles from the air–water interface during compression is confirmed by repeated compression-decompression of the particulate film (Fig. 5a). Therefore, computation could be assessed for the water contact angle of particles spread from pure chloroform (all ZnO samples except for Z110) using Eqs. 1, 2, and 4). The characteristic water contact angle was the value extrapolated at zero amount of ZnO (Fig. 4c).

The water contact angle of the particles Z110, Z172 and Z267 was calculated from SAR measurements with Eq. 5 assuming that particles do not distort the water surface. The water contact angles evaluated from SAR meas-

Table 4 Water contact angle of ZnO particles evaluated from surface pressure–surface area isotherms (Π–A) and scanning angle reflectometry measurements (SAR)

Technique	Z110	Z172	Z225	Z267	Z360
Π–A	–	37°	40°	34°	35°
SAR	65°	27°	–	29°	–

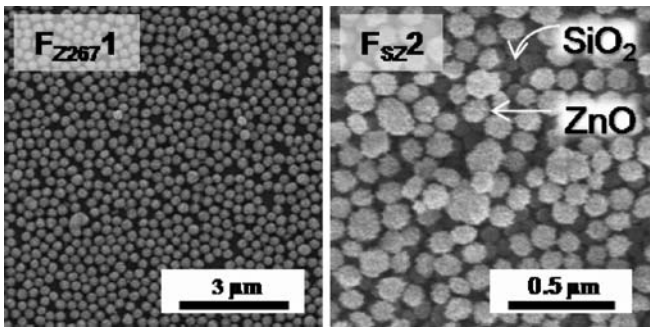

Fig. 8 Scanning electron micrograph of LB monolayer of Z267 particles ($F_{Z267}1$) and two-layered complex LB film composed of an S96 sublayer and a Z110 top layer ($F_{SZ}2$)

urements and Π–A isotherms are summarized in Table 4. They are in reasonable agreement with each other and show a partially wettable ZnO surface.

Langmuir–Blodgett Films of ZnO Nanoparticles. The arrangement of the ZnO particles in mono- and multilayered LB films was studied in SEM pictures (Fig. 8). The ZnO particles formed small domains for samples with low polydispersity (Z225, Z267, Z360), but at higher polidispersity, the packing of the particles was irregular, though continuous (e.g Z110 layer on the top of closely packed S96 particles for $F_{SZ}2$ in Fig. 8).

XRD diffraction performed on $F_{Z267}1$ revealed the presence of crystallised ZnO with hexagonal wurtzite structure.

Functional Characterization of ZnO LB Films

Optical Properties.

Ellipsometry Measurements. Ellipsometric porosimetry (EP) measured the changes in the refractive index of a thin film during adsorption and desorption of solvent vapours. Accurate mesopore size calculation requires having the *t*-curve (thickness of adsorbed probe molecules on the solid surface) in the case of the ethanol-ZnO system [33]. Such t-curve was not found in the literature. The shape of isotherms performed on LB monolayers is similar to that obtained with the traditional N_2 adsorption technique for powders. The shape of isotherms obtained from EP revealed that smaller particles (Z110, Z172, Z225) contained mainly closed porosity, while larger ones (Z267 and Z360) had available mesopores for ethanol (hysteresis loop on the isotherm). The values of film refractive index (1.192 for Z110, 1.305 for Z172, 1.508 for Z225, 1.642 for Z267 and 2.550 (physically unrealistic) for Z360) have to be interpreted with caution: at larger particle size light scattering becomes more and more important. Unrealistic values of film thickness were observed for particles larger than 172 nm, therefore only data obtained for Z110 and Z172 have been accepted as reliable.

Particle refractive index and further particle porosity was computed using the *Lorentz–Lorenz formula* of refractive index mixing, assuming a hexagonal closely packed arrangement of the spherical ZnO particles in the LB film [15]. The obtained values are summarized in Table 2. 59 and 37% internal porosity was calculated for Z110 and Z172 particles, respectively. These values may overestimate the actual particle porosity if the arrangement of the particles in the LB film is less closely packed (for particles with polydispersity over 7% [25]). Comparison was made between the LB film refractive index measured by EP and the film refractive index calculated from particle refractive index obtained with SAR measurement in Langmuir films. The LB film refractive index obtained for $F_{Z172}1$ (1.305) was in excellent agreement with that assessed from SAR measurement (1.300). The discrepancy between the values for $F_{Z110}1$ (1.192 from EP and 1.277 from SAR measurements) was perhaps due to a less closely packed structure of the particles in the LB film. However, for Z267 the discrepancy between the results of these two measurements was too high to be reasonable, therefore the value measured with ellipsometry was not given credit. Our conclusion is that particles should reasonably contain 30–50% internal porosity of which 10–20% might be closed.

UV-Vis Measurements. LB films of ZnO particles with mean diameter between 110 and 225 nm possess antireflective property in the visible-near infrared wavelength range when coated on the surface of glass (Fig. 9a,b) and conductive glass slides (Fig. 9c), in spite of the high refractive index of ZnO bulk phase. This finding can be explained by the high internal porosity (30–50%) of the particles demonstrated above and the special nanostructure of the LB film. The antireflective effect is higher for smaller particle size and lower layer thickness (depending on particle size and the number of LB layers). The best transparency was, therefore, observed for one-layered LB film of Z110 particles with AR wavelength range between 580–1100 nm. At larger particle size, the interference phenomena cause the appearance of high reflection band (at 400 nm for sample $F_{Z267}1$ and at 510 nm for sample $F_{Z360}1$). Coloured reflection can be seen in Fig. 9b (inset).

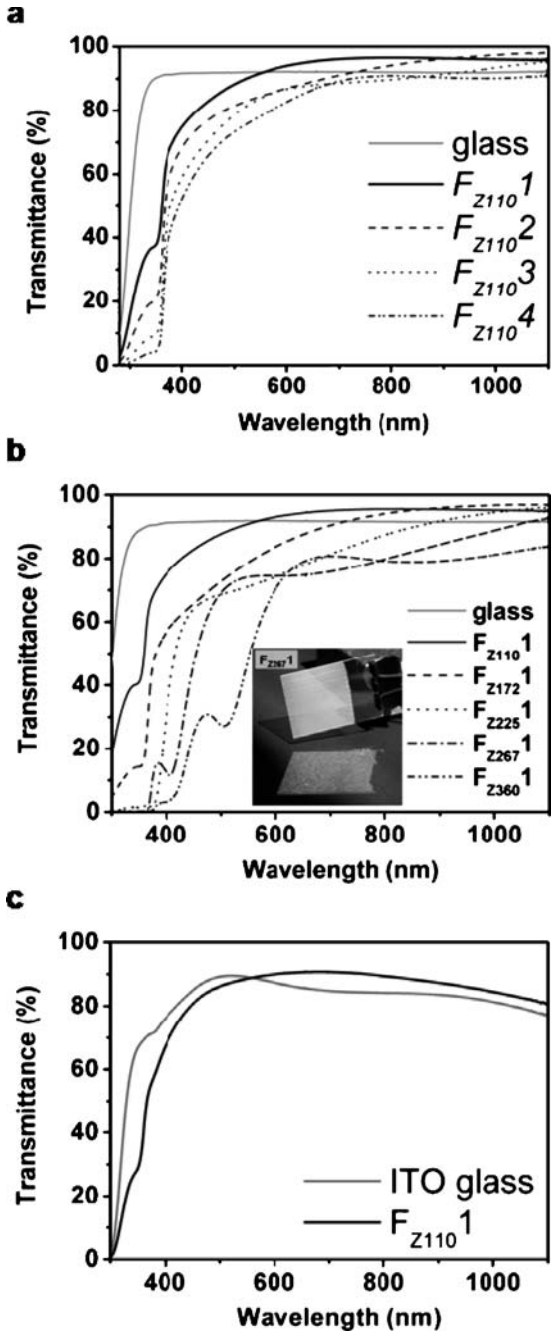

Fig. 9 UV-Vis transmittance spectra of **a** 1–4 layers of Z110 particles on the surface of glass substrate, **b** one layer of different size ZnO nanoparticles on the surface of glass substrate, **c** one layer of Z110 particles on the surface of ITO conductive glass substrate

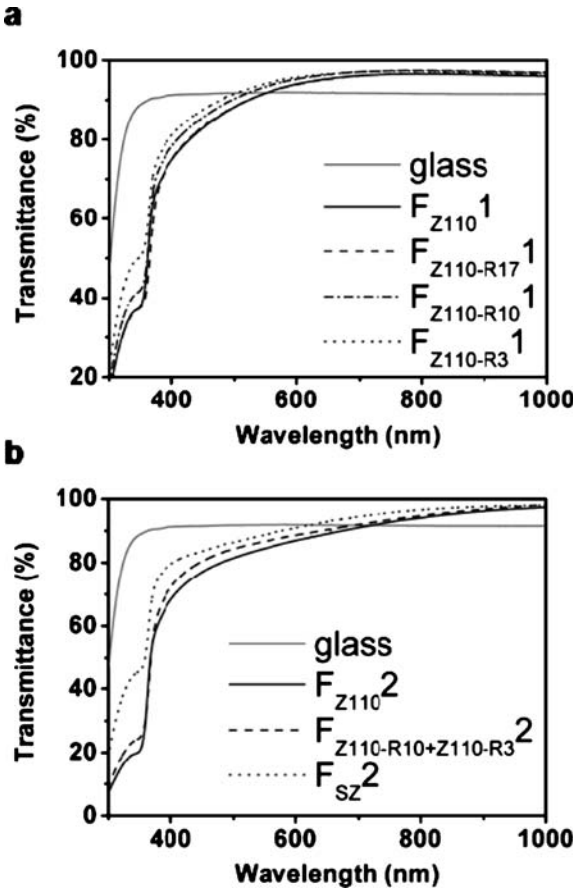

Fig. 10 UV-Vis transmittance spectra of **a** pure (Z110) and mixed (Z110-R(17-3)) LB monolayers and; **b** two-layered LB films of pure (Z110) and mixed (Z110-R10 and Z110-R3) systems shown together with a complex LB film ($F_{SZ}2$) on the surface of glass substrate

Attempts were made for the improvement of inherent ZnO LB film antireflectivity by mixing silica particles to ZnO particles. S96 silica particles were incorporated in the spreading liquid of Z110 particles to have homogeneously mixed LB films. The transparency of these mixed LB films ($F_{Z110\text{-}R(17\text{-}3)}1$) is better than that of pure Z110 particles (broadening of AR wavelength range, Fig. 10a). Besides, the maximum transmittance wavelength shifted from 793 nm ($F_{Z110}1$) to 760 nm ($F_{Z110\text{-}R3}1$). More important effect could have been achieved at higher silica content, but the cohesiveness of Langmuir films of samples Z110-R(1.6-0.25) prevented the deposition of continuous LB films for these samples: separate flakes of the cracked film were seen on the solid substrate. The reasons of cohesiveness are not yet understood, further study should reveal them. Nevertheless, the surface modification of one or both types of nanoparticles may enable the preparation of homogeneous mixed LB films with higher silica content.

Two layered film of mixed LB layers ($F_{Z110\text{-}R10+R3}2$) was deposited to induce gradient refractive index by diminishing the ZnO content of the film from the substrate to the air (in general advantageous for AR property). The AR property was slightly improved as compared to $F_{Z110}2$ (Fig. 10b). LB film of silica particles was deposited under and over the ZnO LB film of Z110 nanoparticles. Both of

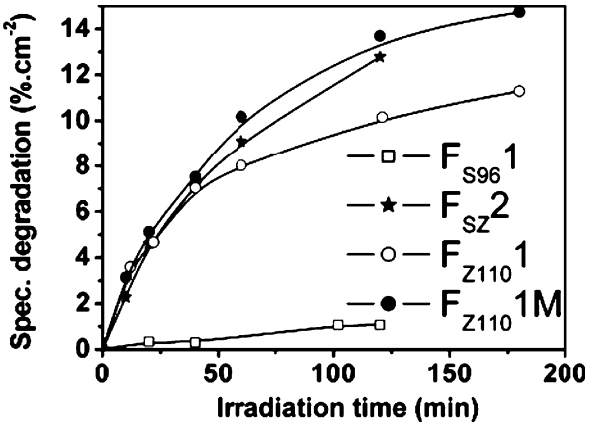

Fig. 11 Photocatalytic degradation of methyl orange dye in 5.5 mg ml^{-1} aqueous solution under UV irradiation of 0–180 min and in contact with $F_{S96}1$, $F_{SZ}2$, $F_{Z110}1$ and $F_{Z110}1M$ LB films. Specific degradation values are obtained using Eq. 6

the obtained complex LB films ($F_{SZ}2$ and $F_{ZS}2$) showed better AR property than the two-layered LB film of Z110 particles with similar film thickness (Fig. 10b). Hence, we could achieve slight improvement of AR effect and slight shift of maximum transmittance wavelength (fine tuning) of ZnO LB films by the incorporation of silica particles.

Photocatalytic Properties. The photocatalytic activity of $F_{Z110}1$ and $F_{Z225}1$ LB films was investigated in photodegradation experiments. The supported films immersed into the aqueous solution of methyl orange were irradiated with intense UV light. The comparison of the photocatalytic activity of slightly different size samples was possible by the calculation of specific degradation values (degraded amount of MO (%) over the surface area of the film (cm^2)). Typical specific degradation values of 11 and 12 % cm^{-2} were found for samples $F_{Z110}1$ and $F_{Z225}1$, respectively after 120 min of irradiation. Higher specific degradation value was obtained for the complex LB film $F_{SZ}2$ (13% cm^{-2} at 120 min of irradiation) (Fig. 11). We assume that this is due to the better availability of the ZnO surface when deposited on the top of a porous LB structure.

Mechanical Stability

The mechanical stability of native ZnO LB films was poor. Immersed into ethanol ultrasonic bath no ZnO absorption

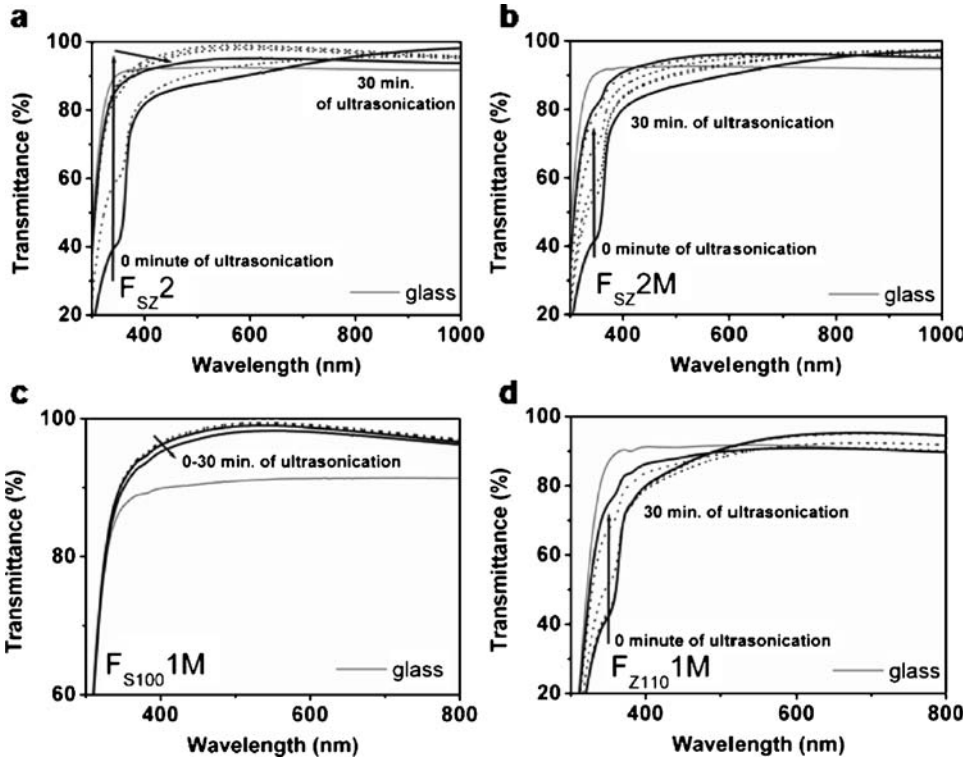

Fig. 12 Mechanical stability tests. Evolution of UV-Vis transmittance spectra of **a** $F_{SZ}2$; **b** $F_{SZ}2M$; **c** $F_{S100}1M$ and **d** $F_{Z110}1M$ LB films during ethanolic ultrasonication of 0 min (*solid black line*), 1–15 min (*dotted black lines*) and 30 min (*solid black line*)

could be detected after more than 2 min. of ultrasonication. The stability of the silica films was better, antireflective effect was lowered, but still present after 30 min of ultrasonication. In the case of the complex LB film $F_{SZ}2$, the disappearance of ZnO absorption is demonstrated after 5 min of ultrasonication, and then slow decrease of AR property can be seen together with the deterioration of the silica LB layer (Fig. 12a). This indicates the rapid removal of the top ZnO LB layer followed by a slow removal of the silica particulate sublayer.

The effect of surface modification is striking (Fig. 12b): the ZnO absorption, and at the same time strong AR property, are still present at 30 min of ultrasonication. The increased resistance of the particulate film towards mechanical impact suggests the linkage of silica particles to the surface. Furthermore, the ZnO particles in the top layer are supposed to be linked to the silica particles in the sublayer providing increased stability. As a result, the ablation of the two layers proceeds together and in a slower rate than it was previously observed for either ZnO or silica LB films. Surface modification was achieved also on single LB films $F_{S96}1$ and $F_{Z110}1$. Excellent stability was observed for $F_{S96}1M$ (Fig. 12c), and stability improvement was provided for $F_{Z110}1M$ (Fig. 12d).

Effect of Surface Modification on Functional Properties of LB Films. The antireflectivity of LB films was slightly decreased by surface modification (1–2% of loss in transmittance), but an increase was observed in their photocatalytic activity (14 % cm^{-2} at 120 min of irradiation) (Fig. 11). We conclude, therefore, that surface modification results in higher mechanical stability and has a beneficial effect on the photocatalytic properties of these ZnO LB films.

Conclusion

The preparation of functional Langmuir and LB films was reported using silica and ZnO nanoparticles. The ZnO LB films showed AR property in the wavelength range between 580-1100 nm as a consequence of the high internal porosity of the particles and special LB structure. The fabrication of mixed and complex LB films from silica and ZnO nanoparticles gave an entry into the fine tuning of light transmission. Surface modification of the particles by adapting the method of Rohe et al. [21] resulted in slightly reduced AR property, but it increased the photocatalytic activity and the mechanical stability of simple and complex LB films.

Wilhelmy film balance experiments permitted the estimation of water contact angle of ZnO particles both from the non-dissipative part of surface pressure–surface area isotherms and scanning angle reflectometry measurements. Additionally, film balance investigations on mixed films revealed interesting structuring phenomena due to interactions between silica and ZnO nanoparticles. A thorough investigation of these findings could lead to a better understanding and control of complex interfacial systems.

Acknowledgement We are indebted to E. Hild and K. László for optical model fitting and water adsorption-desorption isotherms, respectively. The authors thank the French Ministry of Foreign Affairs (for the mobility grant of L.N.) and the financial support of the Hungarian Scientific Research Fund (OTKA T049156). This work was achieved in the scope of a specific support action of EU FP 6 (Hungarian Network of Excellent Centers on Nanosciences) and of a cooperation program, BALATON (TéT F-20/04) sponsored by the Hungarian Ministry of Science and Technology and the French Embassy in Budapest. The Öveges program accorded to Z.H. is greatly acknowledged.

References

1. Seelig EW, Tang B, Yamilov A, Cao H, Chang RPH (2003) Mater Chem Phys 80:257
2. Stöber W, Fink A, Bohn E (1968) J Colloid Interface Sci 26:62
3. Ozin GA (1992) Adv Mater 4(10):612
4. Deák A, Bancsi B, Tóth AL, Kovács AL, Hórvölgyi Z (2006) Colloid Surf A 278:10
5. Bosc F, Naszályi L, Ayral A (2007) An example of innovative strategies in the application and the design of ceramic membranes: the photocatalytic membranes. In: Nechifor G, Barboiu M (eds) Materials, membranes and processes. Editura Printech, Bucharest, pp 66–97
6. Bosc F, Ayral A, Guizard C (2005) J Membr Sci 265:13
7. Pal B, Sharon M (2002) Mater Chem Phys 76:82
8. Liao S, Donggen H, Yu D, Su Y, Yuan G (2004) J Photochem Photobiol A 168:7
9. Kay A, Grätzel M (2002) Chem Mater 14:2930
10. Kim SS, Yum JH, Sung YE (2005) J Photochem Photobiol A 171:269
11. Beek WJE, Wienk MM, Janssen RAJ (2005) J Mater Chem 15:2985
12. Floch H, Belleville P, Pegon P (1996) Annual Symposium on Optical Materials for High Powers Lasers, Boulder City (USA). SPIE Proc Ser 2714:521
13. Belleville P, Pegon P (1997) Annual Symposium on Optical Materials for High Powers Lasers, Boulder City (USA). SPIE Proc Ser 2966:204
14. Szekeres M, Kamalin O, Schoonheydt RA, Wostyn K, Clays K, Persoons A, Dékány I (2002) J Mater Chem 12:3268
15. Deák A, Hild E, Kovács AL, Hórvölgyi Z (2007) Mater Sci Forum 537/538:329
16. Naszályi L, Deák A, Hild E, Ayral A, Kovács AL, Hórvölgyi Z (2006) Thin Solid Films 515:2587
17. Weast RC (1972) CRC Handbook of Chemistry and Physics. Chemical Rubber Co., Cleveland
18. Hild E, Deák A, Naszályi L, Sepsi Ö, Ábrahám N, Hórvölgyi Z (2007) J Opt A Pure Appl Opt 9:920
19. Hariharan C (2006) Appl Catal A 304:55
20. Dindar B, Içli S (2001) J Photochem Photobiol A 140:263

21. Rohe B, Veeman WS, Tausch M (2006) Nanotechnology 17:277
22. Kabai-Faix M (1996) Magy Kem Foly 102(1):33
23. Bordács A, Agod A, Hórvölgyi Z (2006) Langmuir 22:6944
24. Deák A, Hild E, Kovács AL, Hórvölgyi Z (2007) Phys Chem Chem Phys 9:6359
25. Agod A, Deák A, Hild E, Kálmán E, Kovács AL, Tolnai Gy, Hórvölgyi Z (2004) J Adhes 80(10/11):1055
26. Meunier J, Henon S (1991) Prog Polymer Colloid Sci 84:194
27. Máté M, Fendler JH, Ramsden JJ, Szalma J, Hórvölgyi Z (1998) Langmuir 14:6501
28. Hild E, Hórvölgyi Z (2006) Basics of scanning angle reflectometry and application for nanoparticulate films In: Ayral A, Rouessac V (eds) Techniques innovantes pour la caractérisation optique microstructurale de couches minces. CNRS Éditions, Paris, pp 127–141
29. Uekawa N, Iahii S, Kojima T, Kakegawa K (2007) Mater Lett 61:1729
30. Norton DP, Heo YW, Ivill MP, Ip K, Pearton SJ, Chisholm MF, Steiner T (2004) Mater Today 7(6):34
31. Gregg SJ, Sing KSW (1982) Adsorption, Surface area and Porosity. Academic Press, London
32. Hórvölgyi Z, Németh S, Fendler JH (1996) Langmuir 12:997
33. Rouessac V, Ayral A (2006) Analysis of heterogeneities and porosity by ellipsometry In: Ayral A, Rouessac V (eds) Techniques innovantes pour la caractérisation optique microstructurale de couches minces. CNRS Éditions, Paris, pp 49–72

Progr Colloid Polym Sci (2008) 135: 119–129
DOI 10.1007/2882_2008_097

Published online: 30 August 2008

F.O. Costa-Balogh
E. Sparr
J.J.S. Sousa
A.A.C.C. Pais

Drug Release and Skin Permeation from Lipid Liquid Crystalline Phases

F.O. Costa-Balogh · J.J.S. Sousa
Centro de Estudos Farmacêuticos, Laboratório de Galénica e Tecnologia Farmacêutica, Faculdade de Farmácia, Universidade de Coimbra, 3000-295 Coimbra, Portugal

F.O. Costa-Balogh (✉) · E. Sparr
Department of Physical Chemistry 1, Chemical Center, Lund University, 124, 22100 Lund, Sweden
e-mail: Fatima.Costa@fkem1.lu.se

A.A.C.C. Pais
Departamento de Química, Universidade de Coimbra, Codex 3004-535 Coimbra, Portugal

Abstract We have studied drug release and skin permeation from several different liquid crystalline lipid formulations that may be used to control the respective release rates. We have studied the release and permeation through human skin of a water-soluble and amphiphilic drug, propranolol hydrochloride, from several formulations prepared with monoolein and phytantriol as permeation enhancers and controlled release excipients. Diolein and cineol were added to selected formulations. We observed that viscosity decreases with drug load, wich is compatible with the occurrence of phase changes. Diolein stabilizes the bicontinuous cubic phases leading to an increase in viscosity and sustained release of the drug. The slowest release was found for the cubic phases with higher viscosity. Studies on skin permeation showed that these latter formulations also presented lower permeability than the less viscous monoolein lamellar phases. Formulations containing cineol originated higher permeability with higher enhancement ratios. Thus, the various formulations are adapted to different circumstances and delivery routes. While a slow release is usually desired for drug sustained delivery, the transdermal route may require a faster release. Lamellar phases, which are less viscous, are more adapted to transdermal applications. Thus, systems involving lamellar phases of monoolein and cineol are good candidates to be used as skin permeation enhancers for propranolol hydrochloride.

Keywords Drug release · Enhancers · Lipid liquid crystalline phases · Monoolein · Phytantriol · Propranolol hydrochloride · Skin permeation

Introduction

Sustained release formulations have the advantage of reducing the dosing frequency and producing controllable and sustained plasma levels which tend to minimize the risk of undesirable side effects. Additionally, for transdermal formulations, the avoidance of the hepatic first-pass metabolism is an obvious advantage. In this work, we investigate different formulations based in lipid liquid crystalline phases composed of monoolein (MO) or phytantriol (PHY) doped with diolein (DO) or cineol.

The drug used is propranolol hydrochloride (PHCl), a water soluble cationic amphiphilic drug. PHCl is a non-selective β-adrenoreceptor blocker that is widely used in the treatment of many cardiovascular diseases like hypertension, angina pectoralis, cardiac arrythmia and myocardial infarction. However, propranolol is subject to an extensive and highly variable hepatic first pass metabolism following oral administration. Its oral bioavailability was reported to be between 15 and 23% [1]. This clearly motivates the growing interest for developing systems for transdermal delivery of this drug [2–4].

Nevertheless this route presents unique chalenges. The greatest obstacle is the stratum corneum, the outermost layer of the skin which is considered to form the primary rate-limiting barrier to the permeation of drugs across the skin [5]. It consists of dead, flattened cells, filled with keratin, that are embedded in a lipid matrix [6]. The stratum corneum has been described as hydrophilic protein "bricks" in a hydrophobic mortar of lipid bilayers [7].

Several strategies have been employed to circumvent this natural barrier. One of the most used strategies employs penetration enhancers, molecules that reversibly reduce the barrier properties of skin by affecting the properties of the different components, such as lipids and corneocytes, in a way that the barrier properties are altered [8]. Penetration enhancers may incresase the permeability of a drug by affecting the intercellular lipids of the stratum corneum and/or by increasing the partitioning of the drug into the stratum corneum [9].

Monoolein (MO) is a polar lipid that is considered a penetration enhancer [10] and presents the extraordinary ability of forming several different liquid crystalline phases in contact with water. Bicontinuous cubic phases are formed (space groups *Ia*3*d* and *Pn*3*m*) for water contents between 20 and 40 wt %. These cubic phase possess a transparent, stiff, gel-like appearance and constitutes a three-dimensional network of curved lipid bilayers separated by a network of congruent water channels [11]. Such charactheristics have been used to sustain the delivery of various water soluble and insoluble drugs including peptides [12], and through several different administration routes including the oral, periodontal, mucosal and vaginal [13] ones. Transdermal delivery [14] and in vivo topical administration have also been reported [10].

Phytantriol (PHY) or tetramethyl hexadecanetriol is a well-known active ingredient for the cosmetics industry in hair and skin care. It is considered to improve the properties of moisture retention of skin and hair and act as a penetration enhancer of panthenol, vitamins and amino acids. PHY shows the same type of phase sequence as MO and may be seen as an alternative ingredient in certain applications of the cubic liquid crystalline phases [15], in particular. As shown in PHY/water phase diagram [15], PHY forms bicontinous cubic phases at lower water contents than MO. The possibility of using both lipids, MO and PHY, in mixed systems was also referred [16], taking advantage of this difference in water swelling.

In this work, formulations based on MO or PHY where doped with DO or cineol in order to tune the phase behaviour and the viscosity. The addition of DO to MO or PHY, leads to the formation of a reversed hexagonal phase in excess water [17]. This phase is not formed in the binary MO-Water system nor in the binary PHY-water system at room temperature [15, 16, 18, 19]. On the other hand, the addition of the amphiphilic drug PHCl promotes the formation of normal structures

Cineol is an essential oil (monoterpen) also known as eucalyptol, that has been reported as a penetration enhancer that increases the drug diffusivity in the skin. The enhancing effect has been attributed to disruption of the highly ordered intercellular lipid structure of the stratum corneum [4]. Furthermore this stratum corneum-cineol interaction is reversible [7] and terpenes are generally regarded as safe, with low cutaneous irritancy [20].

The growing interest in transdermal delivery of PHCl, together with the fact that both MO and PHY are considered skin penetration enhancers [10], motivates further investigations of the formulations characteristics and drug release from these systems, and this forms the major goal of the present study. We aim to check the possibility of using these lipids as vehicles (matrix) in transdermal delivery systems of PHCl, and investigate phase behaviour, viscosity, drug release and permeation through human skin.

Materials and Methods

We have used Propranolol hydrochloride (Becpharma, Batch No. PRP 190), as a water-soluble model drug. Monoolein (Rylo MG 19 Pharma ID98-027, a thecnical grade constituted by 90% monoolein, 5% of other monoglycerides and 5% of mainly diglycerides, fatty acids and free glycerol, Danisco Ingredients, Denmark,), diolein (Danisco Ingredients, Denmark) and phytantriol (BASF, Germany, Lot: 40356188QO) were used without further purification. The water used was de-ionized and purified (Milli-Q water system).

Preparation of Formulations

MO was melted at 45 °C and PT at 50 °C. Appropriate amounts of these lipids were weighted into different glass vials. Water, DO and drug were also weighted into the vials as appropriate (see Table 1). The vials were then sealed and centrifuged back and forth several times at 45 or 50 °C, for MO and PT containing formulations, respectively. They were then left to equilibrate for 7 days at 23 ± 2 °C.

Visual Inspection

Crossed polarizers were used to examine the homogeneity of formulations. Only the homogeneous samples, isotropic and anisotropic, were considered for further studies.

Formulations pH

A pH meter (pH526, WTW, Germany) was used for the determination.

Table 1 Formulations codes and composition. The non-homogeneous (phase separated) formulations were rejected from further studies

Formulation code	Composition [wt %]				Homogeneity
	PHCl	Lip[a] : w	Lip[a] : DO	Cineol	
MO (blank)	0	65 : 35	–	–	yes
MO2	2	65 : 35	–	–	yes
MO5	5	65 : 35	–	–	no
MO10	10	65 : 35	–	–	yes
MO15	15	65 : 35	–	–	yes
MOD1 (blank)	0	65 : 35	92 : 8	–	yes
MO2D1	2	65 : 35	92 : 8	–	yes
MO5D1	5	65 : 35	92 : 8	–	no
MO15D1	15	65 : 35	92 : 8	–	yes
MOD2 (blank)	0	65 : 35	88 : 12	–	yes
MO2D2	2	65 : 35	88 : 12	–	yes
MO5D2	5	65 : 35	88 : 12	–	yes
MO15D2	15	65 : 35	88 : 12	–	yes
MOC5 (blank)	–	65 : 35	–	5	no
MOC10 (blank)	–	65 : 35	–	10	no
MO15C5	15	65 : 35	–	5	yes
MO15C10	15	65 : 35	–	10	yes
PHY (blank)	0	73 : 27	–	–	yes
PHY2	2	73 : 27	–	–	yes
PHY5	5	73 : 27	–	–	yes
PHY15	15	73 : 27	–	–	no
PHYD1 (blank)	0	73 : 27	92 : 8	–	yes
PHY5D1	5	73 : 27	92 : 8	–	yes
PHY15D1	15	73 : 27	92 : 8	–	no
PHYD2 (blank)	0	73 : 27	88 : 12	–	yes
PHY5D2	5	73 : 27	88 : 12	–	yes
PHY15D2	15	73 : 27	88 : 12	–	no

[a] Lipid: MO or PHY, depending if the formulation code starts by MO or PHY respectively.

Small-Angle X-ray Scattering (SAXS)

The measurements were performed on a Kratky compact small-angle system equipped with a position sensitive detector (OED 50 M from M. Braun, Graz, Austria) containing 1024 channels with 53.0 μm width. Cu K_α radiation of wavelength 1.542 Å was provided by a Seifert ID300 X-ray generator operating at 55 kV and 40 mA. A 10 μm thick nickel filter was used to remove the K_β radiation, and a 1.55 mm tungsten filter was used to protect the detector from the primary beam. The sample-to-detector distance was 277 mm. The volume between the sample and the detector was kept under vacuum during data collection in order to minimize the background scattering. Samples were measured in a sample holder with mica windows at 32 °C. Temperature was kept constant (±0.1 °C) with a Peltier element.

Viscosity

Viscosity measurements were performed on a controlled stress Physica UDS 200 rheometer using a 1° cone-and-plate geometry (25 mm diameter). All measurements were performed within the linear viscoelastic region, which was checked for each sample (1 g). This was placed on the plate held at 32 °C. Oscillatory tests were made in the angular frequency range of 0.05 to 5 Hz. The above experimental procedure allowed the recording of the complex viscosity (η^*) as function of the angular frequency of oscillation.

In Vitro Dissolution Studies

Dissolution was conducted using Teflon supports in a USP rotating paddles apparatus, at a speed of 50 rpm, in 6×900 ml of de-ionized water, maintained at 32 ± 0.5 °C, using an automated assembly which consisted of a water bath fitted with a variable-speed stirrer (Dissolutest Prolabo, France), a peristaltic pump (Ismatec IPN, Switzerland), a UV/Vis spectrophotometer (Perkin Elmer Lambda 2, Germany) with an automatic multicell programer (Perkin Elmer B012-7391, Germany). The released propranolol hydrochloride absorbance was recorded automatically at 290 nm every 12 min for 48 h. A total of

5 dissolution curves were obtained for each formulation, which were back-correlated with the respective blank (see Table 1). Mean dissolution times (MDT) at different time points were determined from the mean profiles obtained from these 5 curves, as described in [21].

In vitro permeation studies

Permeation studies through the epidermis of human cadaver skin were performed using modified vertical Franz cells during 48 h, immersed in a bath at 37 °C and also connected to a spectrophotometer ($\lambda = 290$ nm). The permeation area was of 1.767 cm^2 and the total volume was 19 ml. The epidermis was separated from the dermis with a pair of tweezers after heating at 60 °C for 60 s. Subsequently, it was cut and placed on the Franz cells receiver chamber filled with phosphate buffer saline (PBS) pH 7.4 with the outer layer facing up. Care was taken to avoid entrapment of air bubbles. Formulations (150 mg with parafilm as support) were then placed on top. Finally donor cells were clamped closing the system. The permeation of selected formulations was studied in comparison with aqueous solutions containing 2 and 5% drug.

Results and Discussion

Phase Characterization

The phase behaviour of the different formulations were characterised by means of small-angle X-ray scattering (SAXS) and visual inspection in cross-polarized light. It is known [11] from the MO/water and PHY/water systems phase diagrams, that, the phase sequence with increasing water content at room temperature and at 32 °C (temperature of the skin surface and at which all experiments were performed), is reversed micellar (L_2), lamelar (L_α), reversed bicontinuous cubic of space group $Ia3D$ and reverse bicontinuous cubic of space group $Pn3m$. PHY needs less water than MO to form the bicontinuous cubic phases [15]. The addition of Diolein (DO) to the MO or to the PHY, leads to the formation of a reversed hexagonal phase upon hydration . This phase is not formed in the binary MO-water system nor in the binary PHY-water system [15, 17].

Our blank samples (MO/water 65 : 35 wt % and PHY/water 73 : 27 wt %) form the $Pn3m$ cubic phase. This phase is not stable to the addition of the amphiphilic drug, and the successively increasing drug loads leads to the phase changes to the $Ia3d$ cubic phase and to the lamellar (L_α) phase, which is also consistent with previous studies [22]. The changes in phase behaviour caused by the addition of DO and/or PHCl can be understood in terms of the packing concept of amphiphilic molecules [23]. DO promotes structures with negative curvature, like the reversed hexagonal phase, and PHCl promotes normal, lamellar, structures. When both DO and PHCl are added to the MO/water cubic phase, these opposing effect can compensate for each other, and the cubic phase might be the most stabile structure.

After visual inspection using crossed polarizers, some samples were eliminated from further consideration because they were phase separated (Table 1). The samples considered for further characterization are summarized in Table 2. The pH values determined for the formulations vary between 5 and 6, which is perfectly compatible with the normal skin pH in healthy people that is 4 to 6.5 [24].

Viscosity of the Different Formulations

The viscosity of the different formulations are presented in Table 2. A general observation is that the viscosity is mainly determined by the phase behaviour. PHY formulations generally present higher viscosity than the MO counterpart, but in both systems we can observe that the drug load induces a decrease of viscosity, related with phase changes (Table 1). It should be noted, however, that PHY is more resistant to a phase transition upon drug load (PHY5 is still a homogeneous cubic phase while MO5 is not). This is likely explained by that PHY forms the cubic phases at lower water contents than MO. The decrease in viscosity with PHCl was also observed by

Table 2 Formulations, liquid crystalline phase, and η, viscosity ($n = 3$)

Formulations	Phase	η Pa s
MO (blank)	Cubic $Pn3m$	$1.13 \times 10^6 \pm 3.21 \times 10^4$
MOD1 (blank)	H_{II}	$6.29 \times 10^4 \pm 2.12 \times 10^2$
MOD2 (blank)	H_{II}	$1.35 \times 10^4 \pm 3.54 \times 10^2$
MO2	Cubic $Ia3d$	$3.09 \times 10^5 \pm 2.00 \times 10^3$
MO10	L_α	$3.02 \times 10^3 \pm 4.00 \times 10^1$
MO15	L_α	$2.66 \times 10^3 \pm 7.07 \times 10^1$
MO2D1	Cubic $Ia3d$	$5.49 \times 10^5 \pm 2.00 \times 10^3$
MO10D1	L_α	$1.12 \times 10^3 \pm 2.00 \times 10^1$
MO15D1	L_α	$2.23 \times 10^3 \pm 6.35 \times 10^1$
MO2D2	Cubic $Ia3d$	$5.80 \times 10^5 \pm 9.71 \times 10^3$
MO5D2	Cubic $Ia3d$	$4.01 \times 10^5 \pm 1.20 \times 10^3$
MO10D2	L_α	$2.46 \times 10^3 \pm 1.04 \times 10^2$
MO15D2	L_α	$2.30 \times 10^3 \pm 3.51 \times 10^1$
MO15C5	L_α	$2.31 \times 10^3 \pm 5.45 \times 10^1$
MO15C10	L_α	$2.02 \times 10^3 \pm 3.68 \times 10^1$
PHY (blank)	Cubic $Pn3m$	$6.02 \times 10^6 \pm 7.07 \times 10^4$
PHYD1 (blank)	H_{II}	$4.25 \times 10^5 \pm 4.25 \times 10^2$
PHYD2 (blank)	H_{II}	$6.54 \times 10^4 \pm 8.49 \times 10^2$
PHY2	Cubic $Ia3d$	$2.59 \times 10^6 \pm 3.51 \times 10^4$
PHY5	Cubic $Ia3d$	$8.16 \times 10^5 \pm 2.45 \times 10^3$
PHY2D1	Cubic $Ia3d$	$2.04 \times 10^6 \pm 4.93 \times 10^4$
PHY5D1	Cubic $Ia3d$	$8.45 \times 10^5 \pm 3.25 \times 10^3$
PHY2D2	Cubic $Ia3d$	$3.47 \times 10^6 \pm 4.16 \times 10^4$
PHY5D2	Cubic $Ia3d$	$1.83 \times 10^6 \pm 2.08 \times 10^4$

other authors [25]. Cineol also decreased the viscosity, and the cineol-containing lamellar phases MO15C5 and MO15C10 present lower viscosity than the correspondent lamellar formulation without cineol, MO15.

When adding DO to the MO and PHY formulations, we observed, in general, the opposite effect on viscosity compared to when adding the drug. DO increases the relative volume of the hydrophobic region, which favours the transition to the reverse hexagonal phase instead of lamellar phase, and gives a higher viscosity when in comparison with formulations without DO. However, when we add a small amount of PHCl together with DO, we have also the presence of an amphiphile that promotes normal structures, and the combined effect is the stabilisation of the more viscous cubic phase. This can be exemplified by comparing the formulations MO15D1, MO15D2, MO5D2 and MO5. In formulations MO15D1 and MO15D2 we observe mainly the effect of PHCl in changing the structure and affecting the curvature of the interface inducing a lamellar phase (with lower viscosity). In contrast, for MO5D2, DO stabilize the Ia3D cubic phase phase (high viscosity) (Table 2). We note that among the PHY formulations we do not observe such strong effects on the phase behaviour and viscosity uppon addition of DO and PHCl. However, with drug loadings above 5% phase separation is observed (Table 1).

Figure 1 shows formulations viscosities versus their lattice spacing obtained from SAXS measurements for the different phases. Here, we have considered both the influence of drug and DO on phase behaviour and the lattice parameter. It is observed that the PHY cubic phases present higher viscosities and lower lattice spacing values than the MO cubic phases. This can be explained by the lower water content in the PHY cubic phases. Finally, the lattice spacing of both MO and PHY *Pn*3*m* cubic phases (blanks), respectively of 97.2 and 67.1 Å are in close agreement with values previously determined by other authors [15, 26].

In Vitro Dissolution Studies

The release properties of the different formulations were investigated. Figure 2 shows the dose percentage of Propranolol HCl transferred into bulk solution in 48 h from the different MO and PHY formulations. The release is highly correlated with the phase behaviour, and, not independently, with the viscosity of the formulation. The MO formulations with lower drug load (MO2, MO2D1, MO2D2 and MO5D2), which form a cubic phase, present a slow and incomplete release. In fact, these formulations, do not attain 80% of drug release in 48 h. The incomplete release indicates that the amphiphilic drug has to some extent partitioned into the lipid bilayers and is thereby retained longer in the formulation. PHCL is an amphiphilic molecule that contains a hydrophobic and a cationic moiety. In aqueous solution, PHCL form micellar-like aggregates with an aggregation number of 10 [27]. We therefore expect a strong interaction also with the lipid bilayers in the formulations, explaining the observed incomplete release. Some authors [22] refer that the cationic drug can form complexes with oppositely charged fatty acids that might be present in the lipid samples (see material section). Such complexation could be responsible for the sustained and incomplete drug release. However, if this was

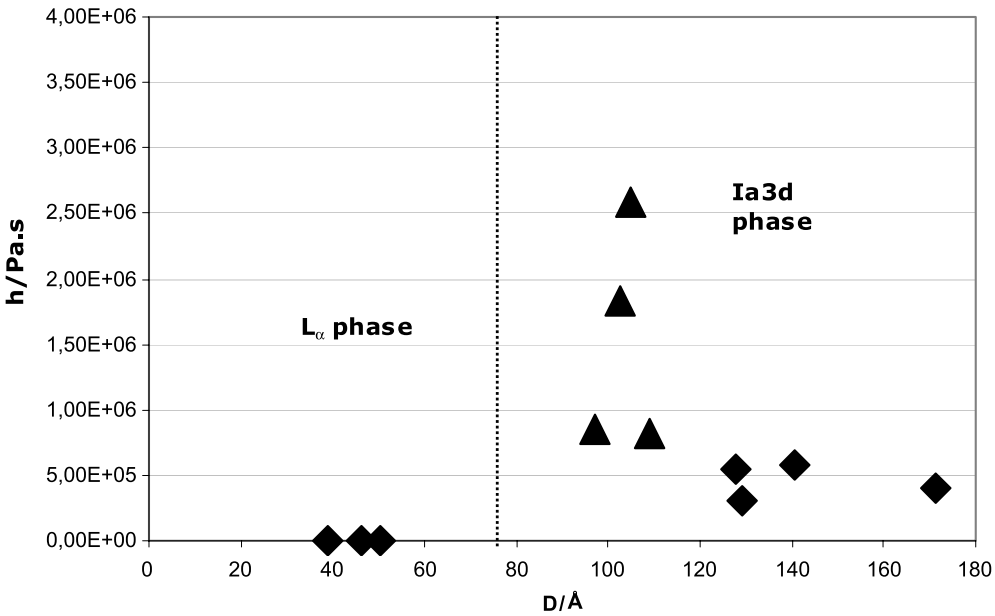

Fig. 1 Formulations viscosities, η, versus lattice spacing, D, obtained with SAXS measurements. PHY cubic phases present higher viscosities and lower D values than MO cubic phases. The lamellar, L_α, phases present much lower viscosity. ◆ MO formulations; ▲ PHY formulations

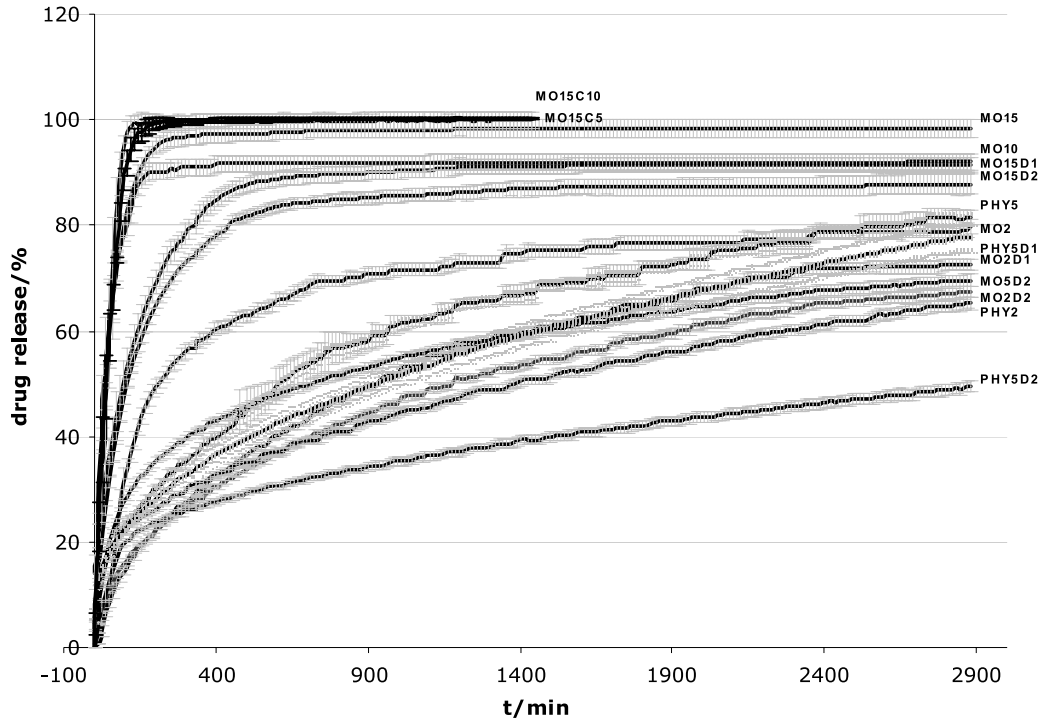

Fig. 2 Dose percentage of propranolol hydrochloride released in 48 h from MO and PHY formulations

the case, we would expect the same effect of incomplete drug release for the lamellar phases. As shown in Fig. 2, the formulations that are in the lamellar phase, e.g. MO15, show almost complete drug release over 48 h, and complexation alone can thus not explain our results.

The addition of DO to the formulations affects the drug release (Fig. 2). In the formulations containing DO the release is slower than in those in which this component is absent. A general observation upon the introduction of DO is an increased viscosity (Table 2), which may explain the observed effects. DO helps to preserve the shape and tortuosity of the aqueous channels and hinders the diffusion of both drug and water.

The PHY formulations investigated are very viscous and they all form a reverse cubic phase of space group *Ia*3*d*. These formulations present a slower release than MO formulations. The addition of DO has a strong effect in both sustaining the release and retaining the drug. This effect might be also related with the fact that these formulations have lower water content. The decrease in water content is accompanied by a decrease in the size of water channels, and therefore, results in a lower diffusivity and a lower release of the amphiphilic drug.

Figure 3 presents the viscosity of formulations viscosity versus mean dissolution time (MDT) values at 48 h. Here it is possible to observe a clear relation between viscosity and MDT, and therefore also with the drug release rate. In general, the formulations with highest MDT present also the highest viscosity values. From the above release and viscosity results we draw the general conclusion that, for a certain lipid and drug load the viscosities correlates inversely with the drug release, and that the introduction of DO retards the release.

The most important factor to the release control in these systems appear to be the phase behavior of the lipid formulation, where the lamellar, less viscous phases display a faster release of the drug than the reverse cubic ones. However, it should be pointed out that, for the lamellar phases, the drug load is higher, and thus the gradient that is the driving force for diffusion is also larger. In spite of the latter remark, note that MO15D2 $\gg$ MO5D2 $\sim$ MO2D2, which suggests that the observations canot only be explained from the differences in drug concentration, but that the release is also strongly dependent on the formation of a lamellar phase

After 48 h dissolution tests the lipid liquid crystalline phases were characterized again with SAXS. This showed that, after dissolution, the formulations form the same phases as the blank drug-free formulations. In other words, the MO and PHY formulations that contain DO form a hexagonal phase after the dissolution test, and the MO and PHY formulations without DO form the *Pn*3*m* cubic phases, which is the fully swollen cubic phase again after the dissolution test. The formation of these phases in excess of water, which is the final state of this experiment, is also consistent with the phase diagrams of MO and PHY [15, 25]. This means that during this process the lipid/water systems undergo through phase changes that

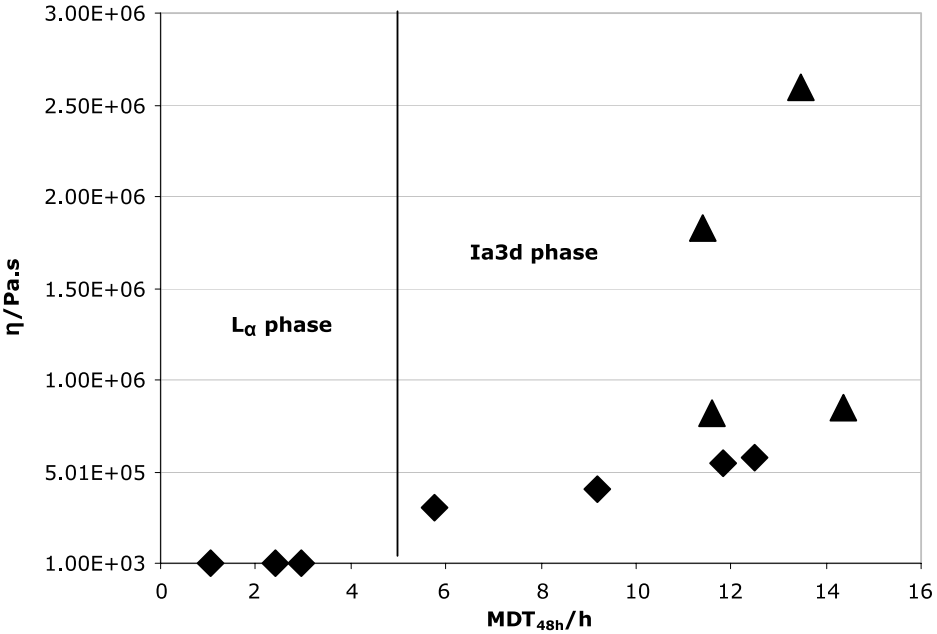

Fig. 3 Formulations viscosity, η, versus MDT values at 48 h for MO and PHY formulations. ◆ MO formulations; ▲ PHY formulations

may influence the rate and mechanism of drug release. Lamellar phases change into cubic or hexagonal phases (except for the ones with cineol that phase separate after drug release) and there must be intermediate inhomogeneous stages. Also the reverse *Ia*3*D* cubic phases change to the more swollen *Pn*3*m* cubic phase or to hexagonal phases (except PHY5D2 that after 48 h is still a mixture of phases, lamellar and hexagonal). These phase transition cannot be detected in our PHCL release curves.

In summary, concerning release, we can say that DO can prevent the formation of the less viscous phases and, for the lower drug loads, it stabilizes the MO cubic phases and retards release. In general, formulations with higher viscosity present a slower drug release, especially for a certain lipid and drug load. PHY formulations present a slower drug release than MO formulations and PHCl is not completely released from the formulations. This effect was strongest for the formulations that contained DO. This is explained by the drug partitioning into the lipid bilayers due to its amphiphilic nature.

Skin Permeation

For the in vitro permeation studies we have chosen to study skin permeation of PHCl from 8 of the formulations (Table 3); two cubic phases with low amount of drug (MO2 and PHY2), the MO and PHY formulations that show the fastest release of the drug (MO15, MO10 and PHY5), the formulation in which DO has the strongest stabilizing effect upon the cubic phase (MO5D2), and the formulations that contain cineol (MO15C5 and MO15V10). The permeation from these formulations were compared to the permeation from aqueous solutions of 2 and 5% PHCl in water.

Figure 4A shows the cumulative amount of drug permeated from these formulations during 48 h. Naturally, the thermodynamic activity of the drug may vary in the different formulations. This aspect is most relevant in the comparison between aqueous solutions and the lipid formulations.

We first note that MO and PHY have a similar performance. The permeation from the different formulations strongly relates to their phase behavior, and the lowest amount permeated in 48 h was observed for the simple aqueous solutions. The lamellar phases (MO10 , MO15, MO15C5 and MO15C10), present much higher permeation rates than the cubic phases (MO15, MO10, PHY5 and MO5D2).

Table 3 also shows the water/drug ratio present in each formulation. We observe that the transdermal flux increase with the decrease of water/drug ratio, within each group of formulations (MO and PHY based). The water/drug ratio depends directly on the amount of drug, so we can say that the drug load affect directly the transdermal flux. Also phase behaviour and viscosity affect transdermal flux. The lamellar phases MO10 and MO15 present a flux much higher than the cubic MO5D2 (7 and 10 times higher respectively) and the drug load increases only 2 or 3 times (MO10 and MO15 respectivelly).The formulations MO15, MO15C5 and MO15C10 have the same amount of drug and their water/drug ratio present minimal differences, but their transdermal fluxes are very different, showing the effect of cineol.

The most striking observation from the permeation studies (Fig. 4), is that cineol displays a paramount effect in enhancing the permeation rate of PHCl, which increases

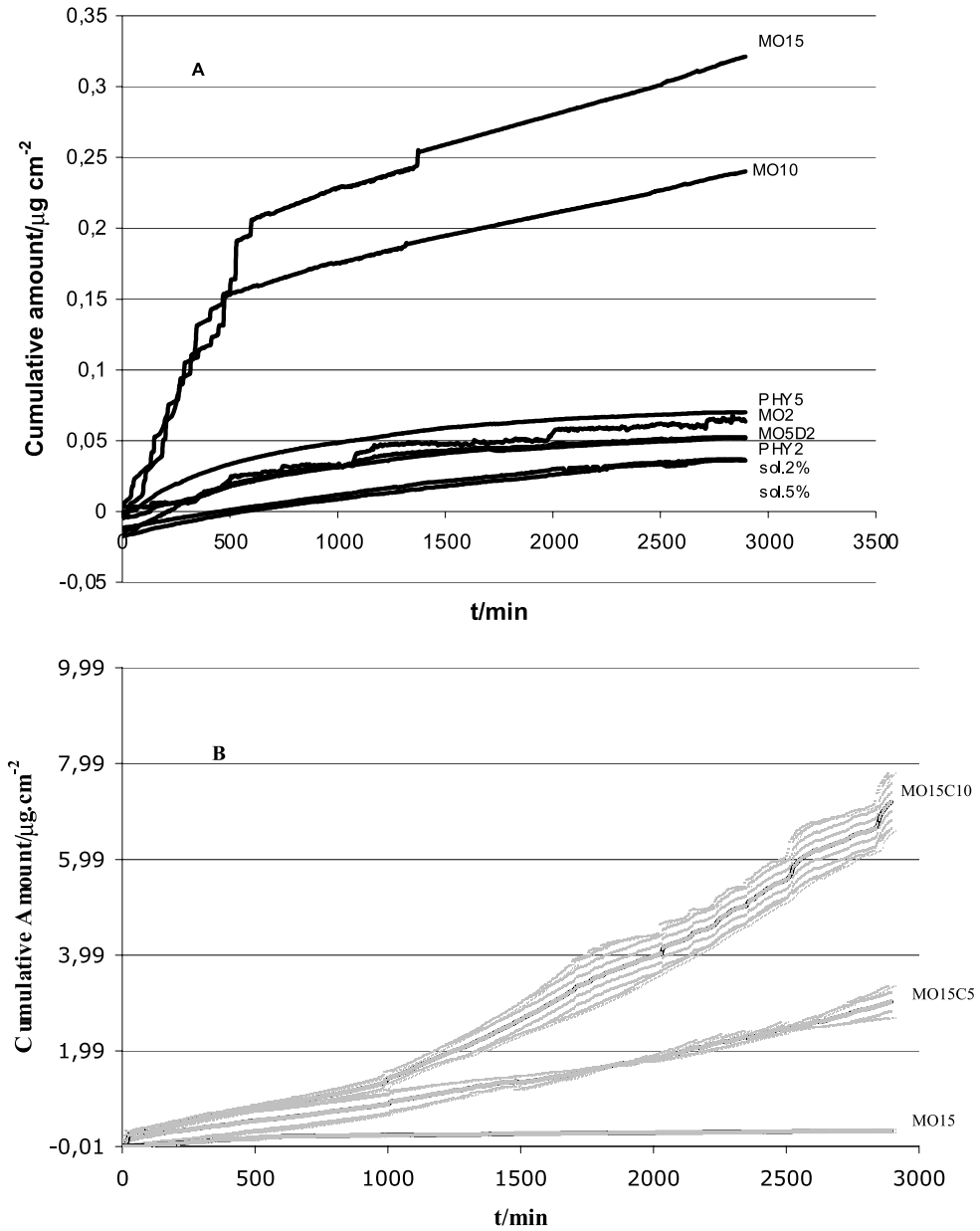

Fig. 4 Cumulative amount of PHCl permeated through human epidermis during 48 h ($n = 3$, **A** with standard deviation between 5 and 10%, not shown for clarifying reasons, **B** shows standard deviations)

more than 50 times (Table 3). This is a higher enhancement effect than previously described in the literature for this drug and cineol [4]. This might indicate a synergistic effect of cineol and MO in the lamellar phase in PHCl permeation enhancement. The cumulative amount of drug permeated from the cineol-containing lamellar formulations are shown in Fig. 4B together with the corresponding data for the lamellar MO formulation MO15, which showed the highest release among the formulations that does not contain cineol.

The formulations that do not contain cineol show much lower fluxes. Still there are significant differences between these formulations. The permeation from the cubic phases do not differ significantly from the permeation from the simple aqueous solutions, with the exception of MO5D2 (ER = 2), where DO shows some enhancer effect. For the PHY formulations (high viscous cubic phases), as for the simple aqueous drug solutions, the permeation rate does not change much with drug load showing a limit of diffusion. The permeation from the lamellar formulations without cineol is several times higher than the flux from the cubic phases, again indicating that the phase behavior is an important factor for the performance of these formulations.

Table 3 Epidermis permeation parameters of PHCl formulations: J–transdermal flux; P–permeability; Q_{24}–cumulative amount per area unit in 24 h and ER–enhancement ratio = transdermal flux from formulation/transdermal flux from drug solution. Present also the water/drug ratio for comparison

Formulations	J [$\mu g\,h^{-1}cm^{-2}$]	P [$cm\,h^{-1}$]	Q_{24} [$\mu g\,h^{-1}cm^{-2}$]	ER	Water/drug ratio
MO2	1.09 ± 0.090	$5.43 \times 10^{-5} \pm 4.5 \times 10^{-6}$	0.048 ± 0.004	1.04	17.15
MO5D2	2.22 ± 0.155	$4.44 \times 10^{-5} \pm 3.1 \times 10^{-6}$	0.043 ± 0.003	2.00	6.65
MO10	16.38 ± 0.821	$1.64 \times 10^{-4} \pm 8.3 \times 10^{-6}$	0.192 ± 0.001	7.38[a]	3.15
MO15	23.05 ± 0.713	$1.54 \times 10^{-4} \pm 4.7 \times 10^{-6}$	0.257 ± 0.008	6.92[b]	1.98
MO15C5	67.57 ± 4.971	$4.50 \times 10^{-4} \pm 3.3 \times 10^{-5}$	1.330 ± 0.099	20.29[b] 2.93[c]	1.87
MO15C10	181.83 ± 6.181	$1.21 \times 10^{-3} \pm 4.1 \times 10^{-5}$	2.474 ± 0.084	54.60[b] 7.89[c]	1.75
PHY2	1.25 ± 0.143	$6.22 \times 10^{-5} \pm 7.5 \times 10^{-6}$	0.040 ± 0.006	1.19	13.23
PHY5	1.52 ± 0.194	$3.03 \times 10^{-5} \pm 3.9 \times 10^{-6}$	0.058 ± 0.003	1.37	5.13
2% solution	1.05 ± 0.050	$5.35 \times 10^{-5} \pm 2.5 \times 10^{-6}$	0.021 ± 0.001	–	49.00
5% solution	1.11 ± 0.112	$2.22 \times 10^{-5} \pm 2.2 \times 10^{-6}$	0.017 ± 0.002	–	19

[a] Enhacement in relation with 2 times transdermal flux of 5% solution,
[b] Enhacement in relation with 3 times transdermal flux of 5% solution,
[c] Enhancement in relation with MO15 transdermal flux.

Figure 5 show the cumulative amount of drug permeated in 24 h, Q_{24}, versus MDT values at 24 h (A) and versus viscosity, η (B). The highest permeation rates correspond to the formulations that present a faster drug release (lower MDT).

The most viscous formulations (cubic phases), present the lowest permeation rate. The phase behaviour and the viscosity of the formulation affects the diffusivity of the drug causing both a slower release, and a lower permeation rate.

To summarize the release and skin permeation data, the slowest release was found for the cubic phases with the higher viscosity (PHY, PHY:DO, MO and MO:DO with 2 and 5% drug load). The skin permeation studies have further shown that the latter formulations presented lower permeability (1.31×10^{-5} to 2.67×10^{-5} cm/h) than the less viscous MO lamellar phases (1.54×10^{-4} and 1.64×10^{-4} cm/h). The formulations with 5 and 10% cineol originated a higher permeability (4.5×10^{-4} cm/h and 1.21×10^{-3} cm/h respectively). These, when compared with the 15% MO formulation yield enhancement ratios (ERs) of 2.9 and 7.9, respectively, and when compared with the 5 and 10% water solutions yield ERs of 20.3 and 54.6, respectively.

Conclusions

Controlled slow drug release is frequently a desired characteristic for drug sustained delivery. However, this feature seems to be undesirable in transdermal delivery. A low viscosity formulation may favour the contact between vehicle and skin and thereby, drug permeation through the skin. A high drug concentration will also facilitate drug release, and thereby skin permeation. Still, the present study clearly shows that the drug concentration is not the major factor in determining the release and permeation from these formulations. This demonstrate that the formulation plays a very important role, and that one needs to consider several molecular aspect of the lipid-drug formulation in the interpretation of such data. The partitioning of the amphiphilic drug between lipid and water regions of the vehicle, as well as the partitioning between the formulation and the lipid lamellae in the skin are very important factors. Also important are the diffusion characteristics of the drug in the tortuous bicontinuous cubic liquid crystalline phases, and the anisotropic charactheristics of the lamellar liquid crystalline phases.

In this work we have investigated phase behaviour, viscosity, drug release and skin permeation of PHCl from a range of different lipid formulation based on different liquid crystalline phases. The major conclusions are:

- The phase behavior and the viscosity of the liquid crystalline formulations clearly affect both the release of the drug and the skin permeation. In general, formulations with higher viscosity present a slower drug release, especially for a certain lipid and drug load.
- DO can prevent the formation of the less viscous phases and, for the lower drug loads, it stabilizes the MO cubic phases and retards release, resulting

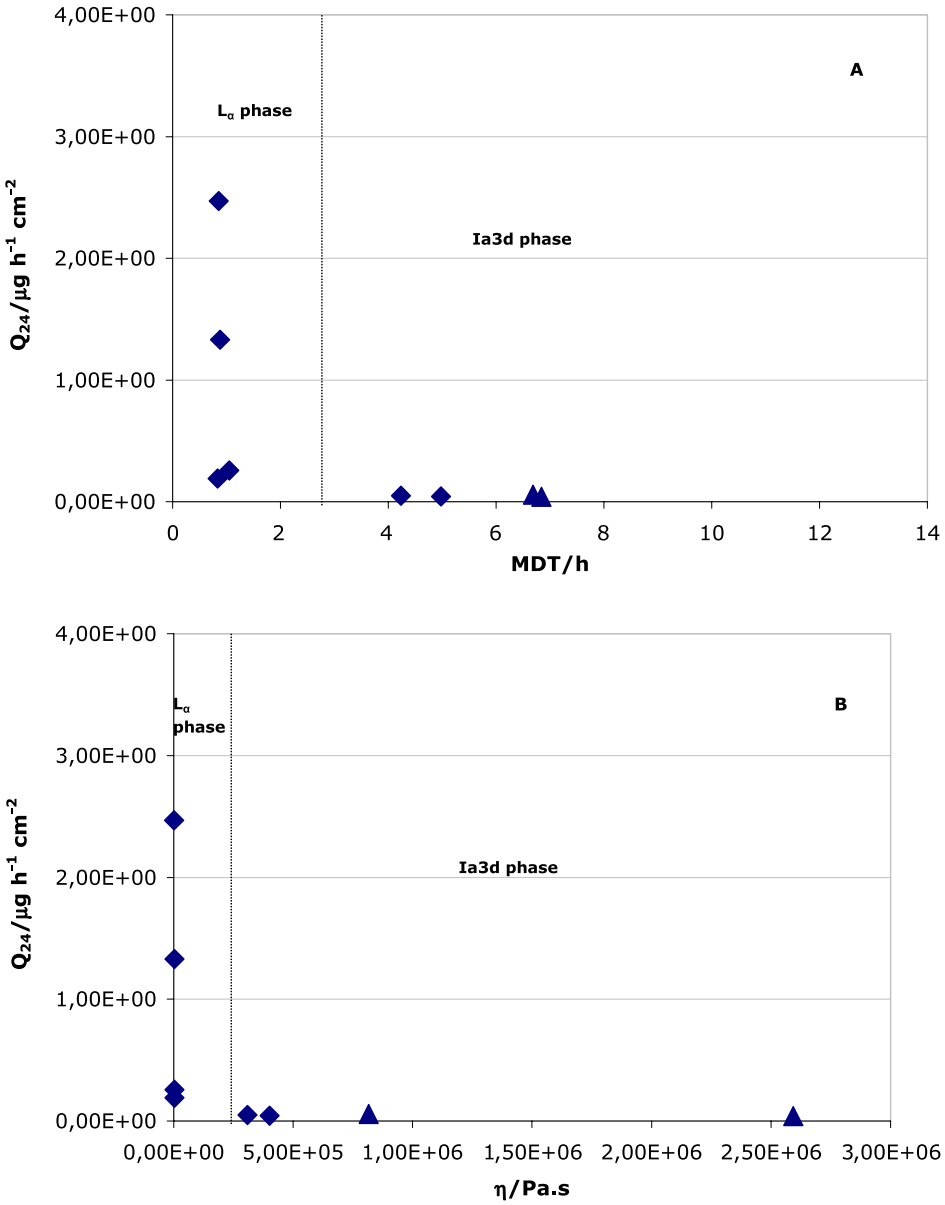

Fig. 5 Cumulative amount of drug permeated in 24 h, Q_{24}, versus MDT values at 24 h (**A**) and versus viscosity, η (**B**) . ◆ MO formulations; ▲ PHY formulations

in a substantial control over the respective release rate;

- PHY formulations present a slower drug release than MO formulations;
- PHCl is not completely released from the formulations. This effect is strongest for the formulations that contained DO. This is explained by the drug partitioning into the lipid bilayers due to its amphiphilic nature;
- The formulations with cineol present the highest permeability, much above the permeability of the other lamellar formulations in study.
- Lamellar phases, which are less viscous and favour faster release, are more adapted to transdermal drug delivery. Thus, with this work we demonstrated that systems involving lamellar phases of monoolein and cineol are good candidates to be used as skin permeation enhancers for propranolol hydrochloride and be possible to use in transdermal delivery systems of this drug.

Acknowledgement The "Fundação para a Ciência e a Tecnologia", Portugal is acknowledged for financial support (Ref. SFRH/BD/10306/2002). ES acknowledges the Swedish Research Council.

References

1. Guyot M, Fawaz F (2000) Int J Pharm 204:171–182
2. Verma PRP, Iyer SS (2000) Drug Dev Ind Pharm 26:471–476
3. Rao PR, Reddy MN, Ramakrishna S, Diwan PV (2003) Eur J Pharm Biopharm 56:81–85
4. Amnuaikit C, Ikeuchi I, Ogawara K, Higaki K, Kimura T (2005) Int J Pharm 289:167–178
5. Elias PM (1991) J Control Release 15:199–208
6. Bouwstra JA, Dubbelaar FE, Gooris GS, Weerheim AM, Ponec AM (1999) Biochim Biophys Acta 1419:127–136
7. El-Kattan AF, Asbill CS, Kim N, Michniak BB (2001) Int J Pharm 215:229–240
8. Williams AC, Barry BW (2004) Adv Drug Del 56:603–618
9. Zhao K, Singh J (1999) J Control Release 62:359–366
10. Bender J, Ericson MB, Merclin N, Iani V, Rosén A, Engström S (2005) J Moan J Control Release 106:350–360
11. Engström S, Engström L (1992) Int J Pharm 79:113–122
12. Clogston J, Caffrey M (2005) J Control Release 107:97–111
13. Shah JC, Sadhale Y, Chilukuri DM (2001) Adv Drug Del Rev 47:229–250
14. Carr MG, Corish J, Corrigan OI (1997) Int J Pharm 157:35–42
15. Barauskas J, Landh T (2003) Langmuir 19:9562–9565
16. Wadsten-Hindrichsen P, Bender J, Unga J, Engström S (2007) J Coll Interf Sci 315:701–713
17. Borné J, Nylander T, Khan A (2000) Langmuir 16:10044–10054
18. Hyde S, Andersson S, Ericson B, Larsson KZ (1984) Z Kristallogr 168:213–219
19. Briggs J, Chung H, Caffrey MJ (1996) J Phys II France 6:723–751
20. Krishnaiah YSR, Al-Saidan SM (2006) Drug Dev Ind Pharm 32:423–435
21. Costa FO, Sousa JJS, Pais AACC, Formosinho SJ (2003) J Control Release 89:199–212
22. Chang C-M, Bodmeier R (1997) Int J Pharm 147:135–142
23. Israelachvili JN, Marcelja S, Horn R (1980) Q Rev Biophys 13:121–200
24. Yosipovitch G, Hu J (2003) Skin Aging 11:88–93
25. Chang C-M, Bodmeier R (1998) Int J Pharm 173:51–60
26. Qiu H, Caffrey M (2000) Biomaterials 21:223–234
27. Mosquera V, Ruso JM, Attwood D, Jones MN, Prieto G, Sarmiento F (1999) J Coll Interf Sci 210:97–102

Progr Colloid Polym Sci (2008) 135: 130–138
DOI 10.1007/2882_2008_094

Published online: 29 August 2008

K. Sinkó
A. Meiszterics
L. Rosta

Comparative Study of Calcium Silicate Bulk Systems Produced by Different Methods

K. Sinkó (✉) · A. Meiszterics
Institute of Chemistry, L. Eötvös University, Pazmany P. st. 1/a, 1117 Budapest, Hungary
e-mail: sinkokata@ludens.elte.hu

L. Rosta
Neutron Spectroscopy Department, Research Institute for Solid State Physics and Optics of the Hungarian Academy of Science, Budapest, Hungary

Abstract The aim of this study is to prepare bulk calcium silicate system that exhibits suitable properties to be used for biomedical applications. Glass-ceramics of composition $CaO \cdot SiO_2$ were produced by sol–gel technique starting from tetraethoxysilane and calcium nitrate tetrahydrate and by melt-quenching technique using a mixture of $CaCO_3$ and SiO_2. The traditional power technology requires 1500 °C temperature to produce ceramic bulks; contrarily the sol–gel technique 700 °C. Their structures were compared by means of thermoanalysis, X-ray diffraction, and small angle X-ray scattering. In the melt-quenched samples, the crystalline feature is dominated; the gel-derived samples are rather amorphous. The mechanical property of the calcium silicate materials obtained by different preparation routes were characterized by Brinell hardness test. The melt-quenching technology provides the glass-ceramics product with high mechanical strength at 1500 °C; the gel derived products achieve this mechanical strength already after a heat treatment at 700 °C. The gel derived product prepared with ammonia catalyst proved to be the hardest, most compact matter.

Keywords Bioceramic · Calcium silicate · Melting · Sol–gel method

Introduction

The bioactive glass-ceramics and composites have been successfully used for the repair, reconstruction, and replacement of diseased or damaged parts of the body, especially bone. Bioactive materials form a biologically active layer on the surface of the implant, which provides the implanted materials with good connection to the natural tissues [1, 2]. The calcium silicate ceramic materials can be applied for biomedical applications due to the bioactive character in a simulated body fluid environment. First bioactive glasses were prepared by classic quenching of melts comprising SiO_2 and P_2O_5 as network formers and CaO and Na_2O as network modifiers. The early publications on the $CaO–SiO_2$ systems describe the expected phases of the binary system. Kautz et al. found only CaO as a new phase up to 1100 °C [3]. According to Kröger, there is already an equilibrium between $CaSiO_3$, Ca_2SiO_4, and $3CaO \cdot 2SiO_2$ below the dissociation temperature of limestone (770–870 °C) [4]. Tamman and Oelsen [5] detected wollastonite ($CaO \cdot SiO_2$) formation at 1010 °C, while Wilburn and Thomasson [6, 7] identified meta- and orthosilicates depending on the chemical composition. If SiO_2 was in excess, metasilicate ($CaSiO_3$) could be demonstrated as main product at 1200 °C. If $CaCO_3$ was in excess, the main product was orthosilicate (Ca_2SiO_4) formed above 1400 °C. The starting materials in the classic quenching process reported recently are generally analytical grade reagents $CaCO_3$, and SiO_2 and the required temperature is around 1500 °C [8–10].

In the early 1990s the sol–gel procedure was introduced for the synthesis of bioactive glasses. One of the most important advantages of the sol–gel technique is the low energy requirement, much lower than that of con-

ventional powder technology. In addition, the sol–gel processing allows one to produce gel glasses with compositions lying within the liquid–liquid immiscibility dome of the $CaO–SiO_2$ system. As with many multicomponent glasses, only a certain range of $CaO–SiO_2$ compositions can be melt derived. The sol–gel chemistry involved in the process is generally based on the inorganic polymerization reactions of metal alkoxide precursors (e.g. $Si(OR)_4$, $Ca(OR)_4$). Hayashi and Saito, who first prepared gels in the binary $CaO–SiO_2$ system, used calcium ethylate ($Ca(OEt)_4$) [11]. Several works reported on the successfully use of calcium nitrate tetrahydrate [$Ca(NO_3)_2 \cdot 4H_2O$] as a calcium source in the sol–gel process [12–19]. Catauro and Laudisio applied calcium acetate as the cation precursor [20]. Perruchot at al. have produced Ca-Si-containing gels with various compositions from the solution of sodium metasilicate and calcium chloride [21]. The hydrolysis of alkoxides precursors requires acidic or basic catalysis. The generally used catalyst is the nitric acid [13–17]. There are also exemplars for application of ammonia and acetic acid catalyst [18, 19].

Catauro and Laudisio prepared calcium silicate glasses by melt-quenching technique from a mixture of $CaCO_3$ and SiO_2 at 1550 °C and by sol–gel route starting from tetramethoxysilane (TMOS), calcium nitrate tetrahydrate and water in order to compare the structures of various calcium silicate glasses [22, 23]. The sol–gel derived sample was not completely amorphous owing to the presence of some amount of alite (Ca_3SiO_5) microcrystals. Smaller amounts of $CaO \cdot SiO_2$ crystals and larger amount of alite together with cristobalite form in the gel-derived sample as compared to the melt-quenched glass. Alemany and co-workers also compared the calcium silicate glass-ceramic materials produced by two different routes; by ceramizing a glass, via powder technology route, and by heat treatment of a gel prepared by sol–gel method [24–28]. Both procedures lead to a good bioactivity although the glass-ceramic obtained from a gel exhibits faster bioactivity [24]. Wollastonite phase can be detected in the melt-quenched sample at 1000 °C which phase is transforming into pseudowollastonite at 1300 °C. Gel-derived sample is amorphous up to 1000 °C, where the wollastonite phase appears. At 1300 °C a new phase forms beside the pseudowollastonite; rankinite ($3CaO \cdot 2SiO_2$).

The aim of this study is to develop ceramics in calcium silicate systems that exhibit suitable properties to be used for biomedical applications. Sol-gel derived calcium silicate materials are reported to be more bioactive than ceramics prepared by quenching of melts [24, 29]. In this work, ceramics of composition $CaO \cdot SiO_2$ were prepared by two methods: sol–gel technique and conventional melt-quenching process in order to compare their structure. The starting materials were $CaCO_3$ and SiO_2 in the powder technology and calcium nitrate tetrahydrate and TEOS in the sol–gel method. In gelation process acetic acid and ammonia were applied as catalysts with various compositions. Comparison of calcium silicate glass-ceramics synthesized by two preparation methods was carried out by means of thermoanalysis (DTA, TG), small angle X-ray scattering (SAXS), X-ray diffraction (XRD), and Brinell hardness test.

Experimental

Preparation Processes

The sol–gel syntheses of calcium silicate glasses were carried out by hydrolysis and polycondensation in an organic solution of stoichiometric amounts of the precursors; TEOS and $Ca(NO_3)_2 \cdot 4H_2O$ (Fig. 1). The rate of hydrolysis of TEOS is very slow in neutral solutions and requires an acid (99–100 wt.% acetic acid and diluted by 25 wt.%) or base (25 wt.% ammonia) catalyst. The gelation, aging as well as drying processes were performed at 80 °C [30].

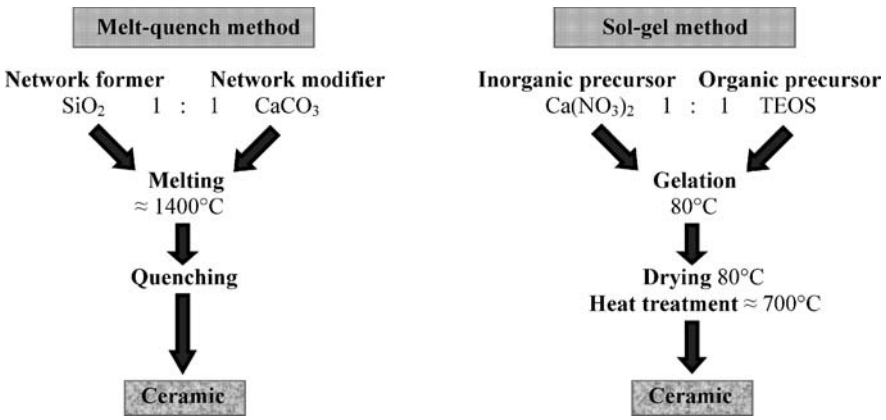

Fig. 1 Preparation routes for calcium silicate ceramic

The experiments of the heat treatment were conducted in the range of 100–1300 °C. A calcium silicate sample of the same composition was also prepared by melting analytical grade reagents $CaCO_3$ and SiO_2 in a platinum crucible in an electrical oven for 3 h at > 1000 °C (Fig. 1). The particle size was less than 53 and 71 μm, respectively.

Structure Characterization

Thermogravimetric analysis (TG/DTA) was used in order to investigate the processes occurred during the heat treatment. TG and DTA curves were recorded with Derivatograph-C System (MOM, Hungary) under dynamic air-flow at a heating rate of 6 °C min^{-1} on crushed bulk specimens from room temperature to 1000–1500 °C.

X-ray Diffraction (XRD) is a powerful non-destructive technique for characterizing crystalline materials. The structure and concentration of the crystalline nucleation centrums were followed by high resolution powder X-ray diffraction in quartz capillaries of 1 mm in diameter ($\lambda =$ 0.695277 Å), and with a measurement time of 10–60 s using a synchrotron radiation on a beamline of HASYLAB at DESY in Hamburg. The XRD instrument was provided with heating cell. The heating rate was 6 °C min^{-1}.

Small-angle X-ray scattering (SAXS) measurements were conducted on several instruments. The laboratory equipment was operated with a 12 kW rotating anode X-ray generator and a pinhole X-ray camera with variable distance (20.5–98.5 cm) from the sample to the two-dimensional detector (Bruker, AXS, Karlsruhe). The gels were covered in vacuum tight foil. The two dimensional spectra were corrected for parasitic pinhole scattering, as well as for the foil scattering. X-ray scattering experiments were also recorded on the JUSIFA beamline of HASYLAB at DESY in Hamburg. All the measured intensities have been normalized to a constant value of incident X-ray flux. In the evaluation of SAXS data, the fractal dimensions (D) can be obtained from the slope (μ) of SAXS curves in the Porod's region using a simple power law expression; $I(q) \sim q^{-D}$ [31, 32]. ($I =$ intensity; $q =$ scattering vector.) The surface roughness of the particles can be characterized by surface fractal dimension, D_s. ($D_s = 6 + \mu$, if $\mu < -3$.) A smooth, nonporous surface is described by $D_s = 2.0$.

The following approximation was used to interpret the scattering data for aggregate systems:

$$y = y_0 + D(x - xc) + \left(\frac{A}{w\sqrt{(\pi/2)}}\right) \times \exp\left(-2\left(\frac{x - xc}{w}\right)^2\right), \quad (1)$$

($D =$ the slope of a linear; $xc =$ the maximum of peaks; $A =$ the intensity of peaks; $w =$ standard deviation.) The particle size can be derived from q of the maximum of peaks; $R = 2\pi/q$.

Brinell hardness (HB) measurements were carried out on an automatic penetrometer (Labor MIM, Hungary). The hardness values were determined by the measure of the depth of the indentation resulted by the load of a body with precise geometry. The load was 466 mN. The results were compared to the Brinell hardness value of the silicate xerogels.

Result and Discussion

Preparation Routes

Sol–gel procedure. The aim of the experiments of sol–gel method was to develop a new low energy-consuming technique and to increase the bioactivity of calcium silicate ceramics. According to the literature, the sol–gel derived calcium silicate materials are more bioactive than ceramics prepared by quenching process [24, 29]. By sol–gel method it is not possible to obtain any gel system from TEOS and Ca nitrate without the presence of water and catalyst. The use of nitric acid leads to a precipitation in our experiments, although it is a common catalyst in the sol–gel procedure of Ca silicate. Without any catalysis, elastic homogeneous gel structures form. These gels need a long drying time and the gel samples are fragile. The materials produced by acetic acid catalysis in various dilutions proved to be homogeneous gel systems. The porosity of gel samples prepared with acetic acid catalyst depends strongly on the water content of the initial gelling solutions. From a diluted system, a porous monolith gel forms, the concentrated solutions turns into a more compact gel system [30]. Using ammonia catalysis resulted in a colloidal basic calcium silicate precipitate. This precipitate can be most easily compressed to compact monolith system comparing with the samples prepared with acidic catalyst and dried at 80 °C. The drying process at 80 °C yields a powder-like product independently of the applied catalyst. At acetic acid catalysis, surfactants are needed to compress the particles due to the strong electrostatic repulsion. TEOS proved to be most suitable to decrease electrostatic effect. The white powder – pressed in vacuum under pressure of 3 GPa – was sintered at varied temperature from 500 to 1300 °C. Between 300 and 500 °C, appearance of $CaCO_3$ phase has to be taken into account (see the XRD measurements on Fig. 6!). The calcite phase destroys the structure and reduces strongly the mechanical strength.

Melt-quenching Process. Only powder-like product could be obtained by melting process without use of quenching technique even at 1500 °C. By quenching of melt product, a compact, hard ceramic bulk formed at 1500 °C, the samples melt-quenched below 1500 °C proved to be crumbling.

Table 1 Thermoanalytical data (DTA) of calcium silicate samples prepared by sol–gel and melting processes

Preparation method		Temperature-range of DTA-peaks (°C)								
		initial	max	final	initial	max	final	initial	max	final
Melt-quenching		560	566	572	638	841	860	1421	1437	1447
Sol–gel	Ac	25	71	114	535	586	602	629	639	654
	Ac_{dil}	25	74	160	527	605	619	–	–	–
	NH_3	25	81	122	535	548	564	–	–	–

The mole ratio of $SiO_2/CaCO_3$ is 1. Ac – calcium silicate gel sample catalyzed with acetic acid; Ac_{dil} – catalyzed with diluted acetic acid; NH_3 – catalyzed with aqueous solution of ammonia

Structures of Calcium Silicate Ceramics Prepared by Different Routes

In ceramic procedures, there is very important task to find out the processes occurred during the heating, to come to know the temperature range of these processes. In the $CaCO_3$–SiO_2 mixture, the first alteration is the α–β polymorphic transformation of SiO_2 during the heating. This transformation occurs between 560 and 575 °C according to thermoanalysis (Table 1, Fig. 2) and by X-ray diffraction between 500 and 550 °C. The $SiO_2/CaCO_3$ ratio has no effect on the α–β polymorphism. The decarboxylation of calcite starts at ≈ 600 °C. The decarboxylation is denoted by DTA between 640–870 °C. The increase of the amount of SiO_2 significantly accelerates the decarboxylation process. The temperature range of decomposition is reduced from 850 to 780 °C by growing the mole ratio of $SiO_2/CaCO_3$ from 0.3 to 15.0. The X-ray data proved that SiO_2 reacts not with $CaCO_3$, but with CaO. New phases could be detected only after the complete decarboxylation, but already below 1000 °C. By means of XRD, only dicalcium silicate (orthosilicate) and a trace of monocalcium silicate (cyclowollastonite) were identified as new phases, independently of the quantitative composition of the binary system (Fig. 3). The predominance of orthosilicate in the diffractograms is induced by the not enough time for the equilibration at the heating rate of 6 °C min^{-1} (industrial conditions). The kinetic control is more effective. This fact is supported by the diffractogram of the sample (≥ 1 mole ratio of $SiO_2/CaCO_3$) heated at

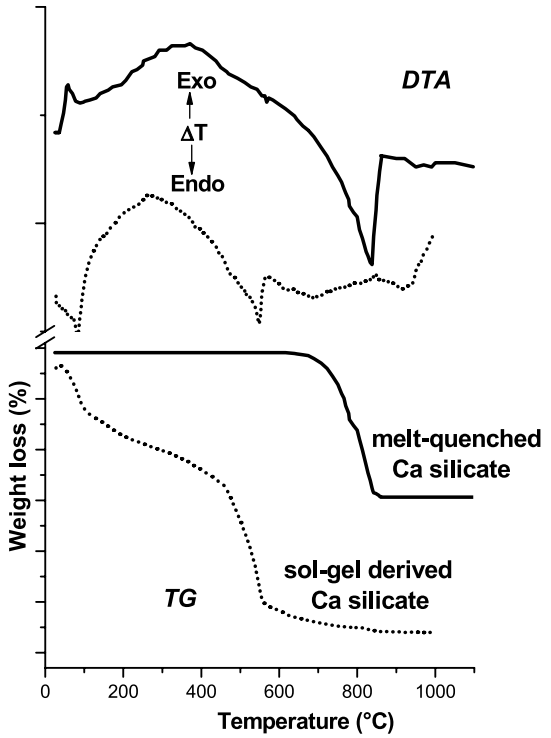

Fig. 2 DTA and TG curves for calcium silicate glasses produced by different preparation routes

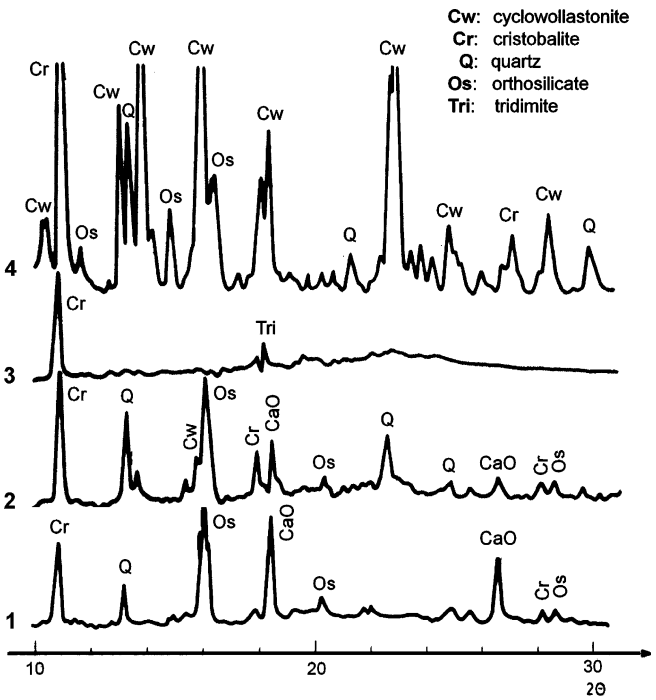

Fig. 3 XRD patterns of melt-quenched sample. 1: heat treated at 1200 °C; 2: 1375 °C; 3: 1400 °C; 4: cooled down to RT

Table 2 Thermoanalytical data (TG) of calcium silicate samples prepared by sol–gel and melting processes

Preparation method		Weight loss/TG					
		Temp. range °C	Weight loss wt.%	Temp. range °C	Weight loss wt.%	Temp. range °C	Weight loss wt.%
Melt-quenching		590–840	27	–	–	–	–
Sol–gel	Ac	20–100	6	250–325	16	500–600	26
	Ac_{dil}	20–100	4.5	–	–	530–650	43
	NH_3	29–230	14	–	–	240–560	35

The mole ratio of $SiO_2/CaCO_3$ is 1. Ac – calcium silicate gel sample catalyzed with acetic acid; Ac_{dil} – catalyzed with diluted acetic acid; NH_3 – catalyzed with aqueous solution of ammonia

1400 °C and cooled down to room temperature indicating monocalcium silicate phase as main component (Fig. 3). If $CaCO_3$ is in excess γ-dicalcium silicate will be dominated. CaO disappears from the system only far above 1300 °C, the quartz phase can be detected up to 1400 °C. Above 1400 °C, a sharp and intensive melting process takes place (Fig. 3).

The weight loss in the $CaCO_3$–SiO_2 mixture occurs in one step (590–840 °C); in the *calcium silicate wet gels* in two (or three) steps (Table 2). The weight loss of gel-derived samples in the first step (20–100 °C) can be attributed to the loss of residual water and propanol. The second main step ($\approx$ 200 to $\approx$ 600 °C) belongs to the evaporation of organic compounds and nitrogen-containing molecules after the loss of pore liquid. The TG curves indicate the fastest evaporation of the vaporizable phases in the gel sample prepared with ammonia catalyst (Fig. 2). The decomposition processes finish at 560 °C in the gel-derived sample synthesized in the presence of ammonia; at 600 °C in the sample of acetic acid catalyst; at 650 °C in the sample of diluted acetic acid catalyst; and at 841 °C in the $CaCO_3$–SiO_2 mixture (Table 2). On the basis of TG curves, the heat treatment of Ca silicate gel systems should be carried out at about 600 °C. The mass loss reaches more than 90% until 560 or 600 °C in the samples prepared with ammonia or acetic acid catalysis, respectively. The thermoanalysis indicates considerable changes between 500–600 °C in the gel-derived samples. These changes have been resulted by the decomposition of silicate network and the appearance of calcium silicate phase. The changes have been verified by FTIR, SAXS, and XRD measurements as well [30]. The first step of the gelation process is the development of a silicate network connected by Si–O–Si bonds containing dissociated Ca^{2+} and nitrate ions [30]. This gel structure survives up to 300–500 °C depending on the solvent content of gel samples. At 500 °C the nitrate content escapes, the amorphous silica network decomposes and the bond system of Ca silicate starts developing. The chemical bond systems of calcium silicate system prepared by traditional melting process and by sol–gel technique are presented in Figs. 4 [33] and 5, respectively. All geometry were performed using Gauss View [34] and considering the published values for Si–O–Si bond angles and bond length [35, 36].

The XRD measurements cannot reveal any well defined homogeneous crystalline phase in the gel-derived sample containing acetic acid catalyst, these materials

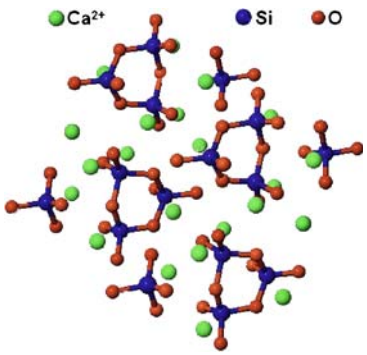

Fig. 4 Chemical bond system of calcium silicate produced by traditional melting process [33]

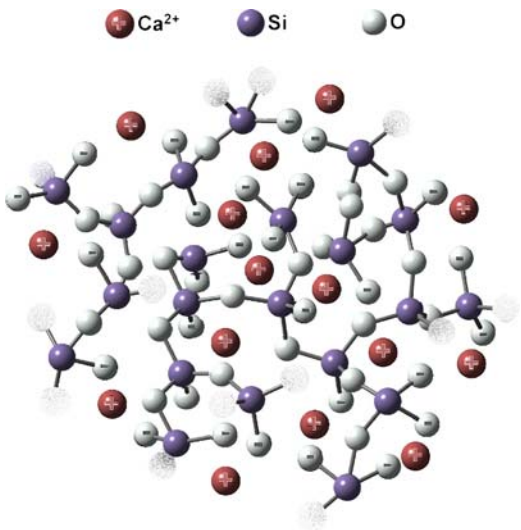

Fig. 5 Chemical bond system of calcium silicate produced by sol–gel method

are mostly amorphous up to about 1000 °C. The XRD diffractograms depict slight volume of SiO_2 between 100–300 °C in the sample catalysed by acetic acid, and $CaCO_3$ between 300–500 °C as a temporary phase. The crystalline phase of calcium silicate can be observed from 400 °C. Their wide diffraction peaks mean quasi amorphous feature, the size of crystalline particles is less than 10 nm. Slight amount of cyclowollastonite can be observed in the sample heated at 1300 °C and cooled down to room temperature. The system prepared with ammonia catalyst keeps the amorphous character during the whole heat treatment except in the range of 200–450 °C (Fig. 6). A crystalline phase of $CaCO_3$ appears temporarily in this temperature range as in the gel-derived sample of acetic acid catalyst. The volume of calcite phase is smaller in the substance obtained with ammonia catalyst due to the basic character of sample. The material containing acetic acid can strongly adsorb CO_2 molecules. Calcium silicate crystalline phase can not be demonstrated by XRD up to 800 °C in the gel system catalyzed with ammonia. On its XRD diffractogram, a wide peak indicates the presence of an amorphous calcium silicate phase. The XRD measurements don't verify the presence of any crystalline wollastonite phases in the gel-derived samples of present study. Otherwise the wollastonite is a typical crystalline phase of the Ca silicate systems [19].

In order to compare the structures obtained by different preparation routes we investigated the calcium silicate systems heat treated at 700, 1000, and 1300 °C. The conventional melt-quenching process requires > 1000 °C temperatures. The nano-scale structures were studied by SAXS measurements. The gel-derived samples heat treated at 700 °C show different structural characters (Fig. 7). The samples catalyzed by acetic acid are built up from aggregates. The aggregate structure defines a random packing of colloidal particles. The aggregate units can be characterized by 2.6–2.7 surface fractals (D_s). The size of aggregates produced by diluted acetic acid (Ac_{dil}) is smaller (50–60 nm) than that of aggregates of concentrated acetic acid catalyst (Ac, 80–90 nm). The aggregates with smooth surface provide the structure of the samples prepared in water without any catalyst (W). The slope of the SAXS curve is −4.0 in log–log plot. These aggregates (W) are the smallest; 30–35 nm. The SAXS data for samples prepared in the presence of ammonia catalyst (NH_3) denote fractal-like structural characters ($\mu = -2.9$), the fractal-like clusters are built up from compact 3-D units ($D_s = 2.7$). The size of clusters could not be determined by means of this SAXS data, the SAXS curve is straight in whole measuring range. The heat treatment at ≥ 1000 °C destroyed the gel structures and the various unique structural features disappeared. The SAXS curves for melt, melt-quenched, and sol–gel derived samples heat treated at ≥ 1000 °C are very similar proving the presence of aggregates in every sample (Figs. 8 and 9). The aggregates of gel network have been slightly crumbled by effect of the heat treatment at 1000 °C. The aggregates of system produced by concentrated acetic acid catalyst (Ac) remained the largest; 50–60 nm, the size of other aggregates reduced to 40–45 nm (Fig. 8). The heat treatment

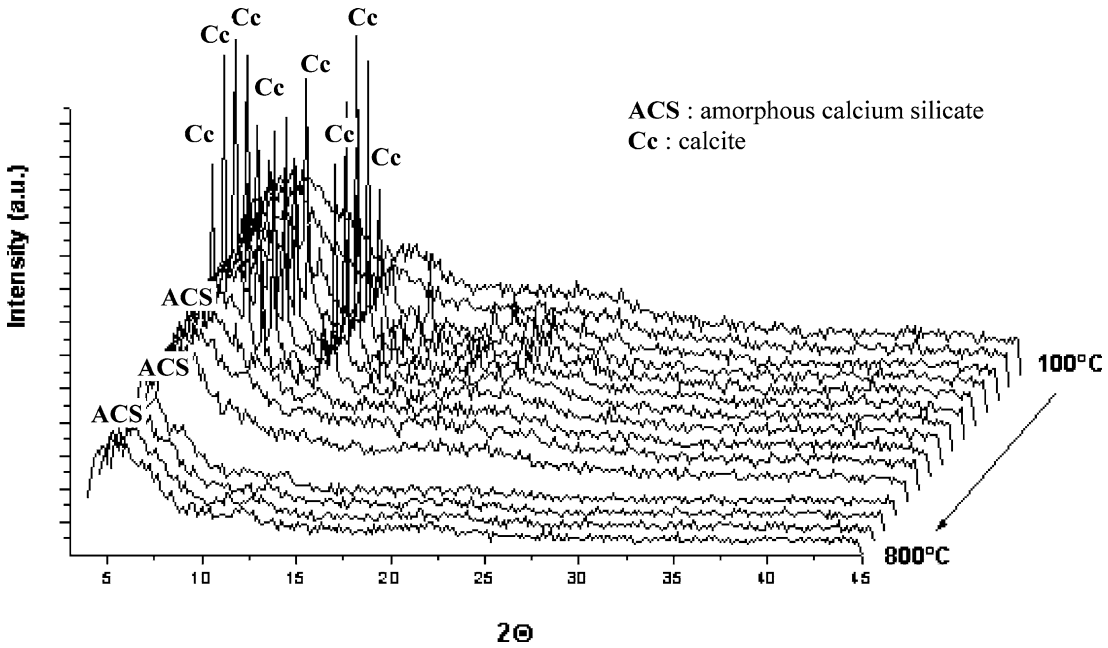

Fig. 6 XRD patterns of gel-derived sample prepared with ammonia catalyst

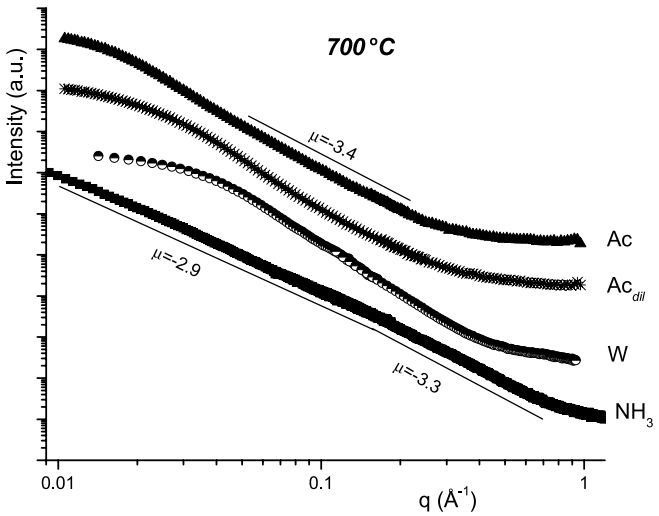

Fig. 7 SAXS curves for gel-derived calcium silicates heated at 700 °C. Ac – calcium silicate gel sample catalyzed with acetic acid; Ac_{dil} – with diluted acetic acid; NH_3 – with aqueous solution of ammonia

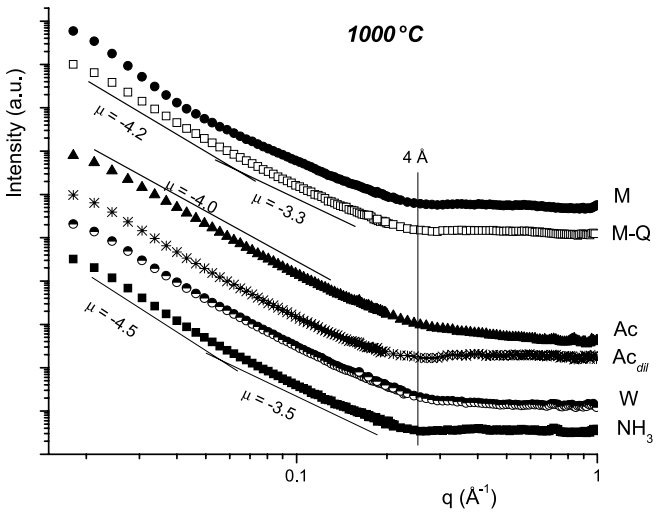

Fig. 8 SAXS curves for calcium silicate systems produced by melt-quenching method and by sol–gel method with various catalysts, heated at 1000 °C. M – melted calcium silicate; Ac – calcium silicate gel sample catalyzed with acetic acid; Ac_{dil} – with diluted acetic acid; NH_3 – with aqueous solution of ammonia; MQ – melt-quenched calcium silicate

at 1300 °C crumbled more the aggregates (Fig. 9). For example the aggregate size of melted sample decreased from 55–60 nm (1000 °C) to 35–40 nm and from ≈ 45 nm (1000 °C) to ≈ 40 nm in the melt-quenched sample. In the q-range < 4 Å, the scattering intensity is very low in every sample heated at ≥ 1000 °C, thus the number of scattering units in this size range is slight. The scattering curves don't show the presence of any characteristic lengths. The aggregates can be characterized by surface fractals (D_S)

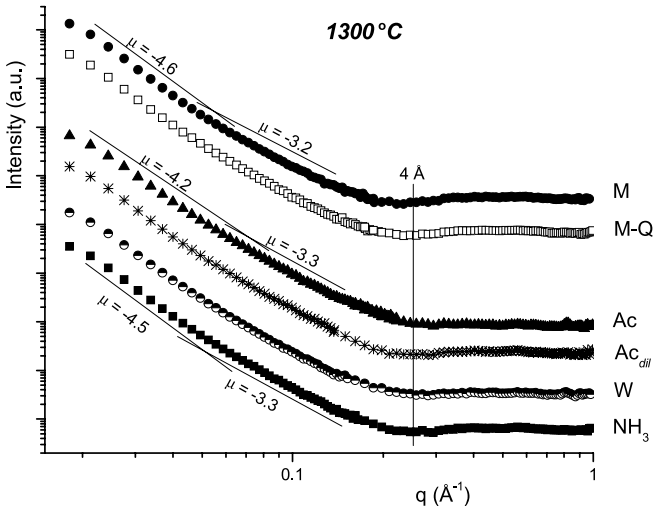

Fig. 9 SAXS curves for calcium silicate systems produced by melt-quenching method and by sol–gel method with various catalysts, heated at 1300 °C. M – melted calcium silicate; M-Q – melt-quenched calcium silicate; Ac – calcium silicate gel sample catalyzed with acetic acid; Ac_{dil} – with diluted acetic acid; NH_3 – with aqueous solution of ammonia

of 2.5–2.7 and 2.7–2.8 in the samples heat treated at 1000 and 1300 °C, respectively. The concentrated acetic acid and ammonia catalyst provides the sol–gel derived sample with the most homogeneous structure in this preparation series.

Mechanical Strength of Calcium Silicate Systems Prepared by Different Routes

The mechanical strengths were detected by Brinell hardness test. The data are relative values compared to the silicate glass-like xerogel obtained by dried at 100 °C. The Brinell hardness data also prove the changes above 500 °C in the gel derived samples (Table 3). Brinell test detected the best values for mechanical property in the gel derived samples prepared by ammonia catalyst (NH_3-700 °C); without catalyst (W-700 °C); and melt-quenched sample heated at 1500 °C (MQ-1500 °C). These ceramic products proved to be too hard to Brinell test (Table 3). The Vickers test did not result in exact, reliable data due to the pores, but it made differences between the ceramic samples. The samples prepared by sol–gel method in the presence of ammonia catalyst provide the greatest hardness. The melt-quenched product was too crumbling to the Vickers test. In the case of the samples catalyzed by acetic acid, a TEOS treatment before the sintering increased efficiently the mechanical strength. Raising the temperature of heat treatment above 700 °C does not improve the hardness of gel derived products any more.

Table 3 Brinell hardness (HB) test of calcium silicate samples prepared by sol–gel and melting processes

Preparation method	Treatment	Relative HB values
Melt-quenching	1000 °C	0
	1300 °C	0
	1500 °C	∞
Sol–gel method	W-80 °C[1]	0
	W-500 °C[2]	0
	W-700 °C[3]	∞
	Ac-80 °C[4]	0
	Ac-500 °C[5]	0
	Ac-700 °C[6]	8.6 ± 2.3
	Ac + TEOS-700 °C[7]	17.7 ± 4.7
	NH_3-80 °C[8]	0
	NH_3-500 °C[9]	∞
	NH_3-700 °C[10]	∞
Comparison samples	Silicate alcogel 80 °C	0
	Silicate xerogel 100 °C	1 ± 1
	Epoxy resin	0.3 ± 0.1
	Porcelain	∞

Samples prepared without any catalysis:
[1] dried at 80 °C,
[2] sintered at 500 °C,
[3] at 700 °C.
Samples catalysed with concentrated acetic acid:
[4] at 80 °C,
[5] sintered at 500 °C,
[6] at 700 °C.
[7]Samples catalysed with concentrated acetic acid, dried at 80 °C and heat treated with TEOS, sintered at 700 °C.
Samples catalysed with ammonia:
[8] at 80 °C,
[9] sintered at 500 °C, [10] at 700 °C

Conclusions

Ca silicate ceramics are intended to apply as implant materials, usually for bone substitution. According to the published results the bioactivity of the sol–gel derived calcium silicate glass-ceramics is unambiguously better than that of ceramics prepared by quenching of melts. Glass-ceramics of composition $CaO \cdot SiO_2$ were synthesized by different preparation routes; by traditional power technique from $CaCO_3$ and SiO_2 as well as by sol–gel method from TEOS and Ca nitrate. The aim of this study was to compare the required temperature of preparation processes and the structures of products. The catalyst, the compositions, and the temperature of heating processes were varied in the sol–gel synthesis. The effect of composition and temperature of heat treatment were investigated on the product of melt-quenching procedure.

The sol–gel procedure requires 700 °C to produce bulk ceramics, the conventional power technology > 1300 °C. By sol–gel method the decomposition processes finish by 600 °C; the calcium silicate bond system evolves above 500 °C; the temporary phase of calcium carbonate disappears until 500 °C; and the mechanical strength increase considerably above 500 °C. The decarboxylation reaction occurs between 600 and 850 °C in the melted samples. The melt-quenched products proved to be crystalline materials containing mostly cyclowollastonite phase; the gel derived samples rather amorphous ordered in aggregate structures up to 1000 °C. The heat treatment of ≥ 1000 °C destroys the structure of gel-derived products. The calcium silicate phases can be identified by XRD from 400 °C in the melt-quenched products and from 800–1000 °C in the gel-derived samples as a weekly detectable crystalline phase. The melt-quenching technique requires temperature of 1500 °C, the sol–gel method only 700 °C for getting a high mechanical strength. Using a sol–gel method and ammonia catalyst provide the greatest hardness.

Advantages of the use of ammonia catalyst are the fastest evaporation of vaporizable phases, the lowest temperature range of decomposition processes, the small volume of the calcite phase, the homogeneous structure, the most compact structure, and the greatest hardness. The homogeneous structure and the more emphatic calcium silicate bond system can be taken into account as advantages of catalysis with acetic acid.

Acknowledgement This study has been supported by OTKA T 043636 funds, and I-04-009 EU in HASYLAB, DESY.

References

1. Hench LL (1991) J Am Ceram Soc 74:1487
2. Hench LL (1998) J Am Ceram Soc 81:1705
3. Kautz K, Stromburg G (1969) Glastechn Ber 42:309
4. Kröger C, Ziegler G (1953) Glastechn Ber 26:346
5. Tamman G, Oelsen W (1930) Z Anorg Allg Chem 193:245
6. Wilburn FW, Thomasson C (1961) Phys Chem Glass 2:126
7. Warburton R, Wilburn FW (1963) Phys Chem Glass 4:91
8. Frantz JD, Mysen BO(1995) Chem Geolog 121:155
9. Branda F, Arcobello-Varlese F, Costantini A, Luciani G (1999) J Non-Cryst Solids 246:27
10. De Aza PN, Luklinska ZB, Anseau MR, Guitian F, De Aza S (1999) J Dentistry 27:107
11. Hayashi T, Saito H (1980) J Mater Sci 15:1971
12. Bansal NP (1990) J Am Ceram Soc 73:2647
13. Izquierdo-Barba I, Salinas AJ, Vallet-Regí M (1999) J Biomed Mater Res 47:243

14. Martínez A, Izquierdo-Barba I, Vallet-Regí M (2000) Chem Mater 12:3080
15. Vallet-Regí M, Ragel CV, Salinas AJ (2003) Eur J Inorg Chem 6:1029
16. Saravanapavan P, Hench LL (2003) J Non-Cryst Solids 318:1
17. Vallet-Regí M, Salinas AJ, Martínez A, Izquierdo-Barba I, Pérez-Pariente J (2004) Solid State Ionics 172:441
18. Iimori Y, Kameshima Y, Okada K, Hayashi S (2005) J Mater Sci 16:73
19. Chrysafi R, Perraki T, Kakali G (2007) J Eur Ceram Soc 27:1707
20. Catauro M, Laudisio G (1998) J Mater Sci Lett 17:311
21. Perruchot A, Massard P, Lombardi J (2003) CR Geosience 335:951
22. Catauro M, Laudisio G, Costantini A, Fresa R, Branda F (1997) J Sol–Gel Sci Technol 10:231
23. Laudisio G, Catauro M, Costantini A, Branda F (1998) Thermochim Acta 322:17
24. Alemany MI, Velasquez P, de la Casa-Lillo MA, De Aza PN (2005) J Non-Cryst Solids 351:1716
25. De Aza PN, Guitian F, De Aza S (1994) Scr Met Mater 31:1001
26. De Aza PN, Guitian F, De Aza S (1995) Adv Sci Technol 12:19
27. De Aza PN, Luklinska ZB, Anseau MR, Guitian F, De Aza S (1996) J Microsc 182:24
28. De Aza PN, Luklinska ZB, Martinez A, Anseau MR, Guitian F, De Aza S (2000) J Microsc 197:60
29. Kokubo T (1992) Bol Soc Esp Ceram Vid, Proc XVI Int Cong Glass, Madrid, 1:119
30. Meiszterics A, Sinkó K (2008) Colloids Surf A 319:143
31. Porod G (1982) General theory. In: Glatter O, Kratky O (eds) Small Angle X-Ray Scattering. Academic Press, London
32. Martin JE (1986) J Appl Cryst 19:25
33. http://www.3dchem.com/inorganicmolecule
34. GaussView, Version 3.09, Dennington II R, Keith T, Millam J, Eppinnett K. Hovell W L, Gilliland R, Semichem, Inc., Shawnee Mission, KS (2003)
35. Lee SK (2004) J Phys Chem B 108:18228
36. Criscenti LJ, Brantley SL, Mueller KT, Tsomaia N, Kubucki JD (2005) Geochim Cosmochim Acta 69:2205

Progr Colloid Polym Sci (2008) 135: 139–147
DOI 10.1007/2882_2008_104

Published online: 9 September 2008

Orsolya Czakkel
Imre Miklós Szilágyi
Erik Geissler
Nick Kanellopoulos
Krisztina László

Morphological Characterization of Oxidized and Metal Impregnated Spherical Carbons

Orsolya Czakkel · Krisztina László (✉)
Department of Physical Chemistry and Materials Science, Budapest University of Technology and Economics, P.O. Box 92, 1521 Budapest, Hungary
e-mail: klaszlo@mail.bme.hu

Imre Miklós Szilágyi
Materials Structure and Modelling Research Group of the Hungarian Academy of Sciences, Budapest University of Technology and Economics, Department of Inorganic and Analytical Chemistry, Szt. Gellért tér 4, 1111 Budapest, Hungary

Erik Geissler
Laboratoire de Spectrométrie Physique CNRS UMR 5588, Université J. Fourier de Grenoble, BP 87,
38402 St. Martin d'Hères cedex, France

Nick Kanellopoulos
MESL – Institute of Physical Chemistry N.C.S.R. "Demokritos". Terma Patriarchou Grigoriou, Agia Paraskevi, Attiki,
15310 Athens, Greece

Abstract The surface of microporous spherical carbon ($S_{BET} = 1457\,m^2/g$, pH = 7.9) was modified by nitric acid treatment and by Cu^+, Cu^{2+} and Sn^{2+} salt impregnation. The morphology and the surface properties of the samples were characterized by SEM/EDS, low temperature nitrogen adsorption and small angle X-ray scattering. The surface chemistry of the samples was investigated under wet conditions.

Oxidation by nitric acid changed the pH to 3.4 and slightly reduced the accessible porosity, but not the morphology or the Cu^{2+} adsorption capacity. Surface chemistry, morphology and the species of the anion and of the metal were found to influence the result of the impregnation. The most remarkable change occurred in the pore size range < 14 Å due to pore blocking. This effect was a linear function of Cu^{2+} loading below the saturation capacity. When $SnCl_2$ was used instead of Cu^{2+} salts in aqueous phase, a redox reaction seemed to take place, resulting in greater surface roughness. Metal ions were not detected on the surface of the particles. Treatment with solid CuCl produced a practically complete CuCl film on the surface of the particles and metallic copper was formed as a by-product.

Keywords Cu^+-impregnation · Cu^{2+}-impregnation · Low temperature nitrogen adsorption · Sn^{2+}-impregnation · Surface oxidation

Introduction

CO_2 emission is a major problem with regard to global climate change. Modified combustion techniques cannot reduce CO_2 formation, but dependence on fossil fuels over the coming decades could be reconciled with our climate change commitments by developing CO_2 capture and sequestration technologies. Among the competing solutions, separation techniques for CO_2 are well placed. Carbon monoxide, however, is a valuable raw material for the synthesis of a large variety of chemicals. Separation of CO from gas mixtures by adsorption is therefore of great importance.

Solid adsorbents have been used for gas separation and purification since the early stages of gas adsorption applications. The most commonly used adsorbent is activated

carbon (AC) either in powdered (PAC) or in granular form (GAC). Activated carbon fibres (AFC) have also received increasing attention in recent years for separation of gas mixtures. The great advantage of activated carbons is their ability to separate gas mixtures at very low concentrations by virtue of their high adsorption capacity. Nevertheless, the CO_2/CO separation potential of carbon sorbents has not received the attention it deserves.

Further exploitation of solid/gas processes has revealed that the chemical properties of the adsorbent surface play an important role in addition to their porosity. Chemical oxidation, for example, may enhance the sorption of polar species. For air purification, e.g., to remove formaldehyde, oxidized carbons are found to perform well [1].

Impregnation by metals, especially transition metal salts, can also increase their receptive capacity, especially for gases of low molecular weight, low boiling point and appreciable polarizability. Impregnation with $CuCl_2$ and $PdCl_2$ has been found to increase CO adsorption by between 8 and 20-fold [2]. Those authors attempted to interpret qualitatively the CO uptake of the impregnated carbons using the perturbation energy, as the electronic states of both the adsorbate and adsorbent play an important role in the adsorption interaction.

Activated carbon-supported metals are believed to adsorb CO through complex formation between CO and the highly dispersed metal halides on the surface of the adsorbents [3]. Cu^+ can also selectively modify the CO adsorption on porous supports [4]. Since Cu^+ ions on the surface can form coordination bonds with CO and weaken the basicity of the surface, adsorbents displaying greater capacity and selectivity for CO than for CO_2 could be obtained. $SnCl_2$ impregnation was found to be also effective in increasing the adsorption ability of activated carbon. It acts in the form of SnO_2, since, on account of its relatively low melting point (313.6 K), $SnCl_2 2H_2O$ can easily be oxidized to Sn^{4+}, making it a suitable agent for CO adsorption [5].

In this paper, a set of carbon-based samples, intended for use in CO/CO_2 separation, is characterized. The samples were prepared to study the influence of the surface oxidation, metal ion loading and the species of the metal and anion on the morphology of the resulting adsorbent.

Experimental

Sample Preparation

Microporous spherical carbon (SC) based on vinyl-pyridine – divinylbenzene co-polymer was used as starting material [6]. The particle size of the carbon varies between 500 and 1320 μm. The SCOX sample was prepared by treating SC with aqueous HNO_3 (cc HNO_3 : water = 1 : 1 by volume) in a Soxhlet apparatus.

Samples impregnated with Cu^{2+} and Sn^{2+} were prepared by soaking SC or SCOX in aqueous solutions of their salts. Impregnation was performed at room temperature, from 0.03 or 0.3 M metal salt solutions. The amount of aqueous solution was 16, 8, or 4 ml/g carbon. No pH setting was applied.

Cu^+ impregnated samples were prepared according to the method of Xie by mixing the carbon with freshly synthesized CuCl at a mass ratio of 2 : 1 in a rotating glass reactor at 623 K for 4 h under N_2 atmosphere [4].

A commercial mesoporous carbon, F400 (Calgon Carbon Corp. Pittsburg, PA, USA), was used as received, for comparison.

SEM/EDS

The morphology and surface composition of the samples were examined with a SEM/EDS JEOL 5500 electron microscope in combination with a secondary electron detector.

Low Temperature Nitrogen Adsorption

Nitrogen adsorption isotherms were measured at 77 K (Autosorb-1, Quantachrome). The apparent surface area was derived from the BET model. Micropore analysis was carried out according to the Dubinin–Radushkevich (DR) equation. The pore size distribution (PSD) was calculated with the Quantachrome software using both the nonlinear density function (NLDFT) and the Barrett, Joyner and Halenda (BJH) methods, respectively.

SAXS

SAXS measurements were made at the BM2 beam line at the European Synchrotron Radiation Facility in Grenoble, working at 18 keV in the transfer wave vector range 10^{-2} Å$^{-1} \leq q \leq 1$ Å^{-1} [7].

2.5 pH

The carbons studied are characterized by the pH of their aqueous suspension, detected under standardized conditions [8]. As the carbon surfaces are decorated only with O-containing heteroatoms, the functional groups of different pK_a range were determined by Boehm titration [9].

Cu^{2+} Adsorption

Cu^{2+} adsorption isotherms were measured at room temperature, by soaking SC or SCOX in an aqueous solution of $Cu(CH_3COO)_2$. The contact time was three days. The concentration of the aqueous solutions was measured by UVIKON 930 UV/Vis spectrophotometer at 766 nm.

Results and Discussion

The acidic treatment erodes the surface as shown in the SEM micrographs of Fig. 1.

The reversible low temperature nitrogen isotherms (Fig. 2) reveal the microporous character of the SC carbon, which was also retained during the oxidative treatment. Parameters deduced from the adsorption/desorption isotherms are listed in Table 1.

The PSD of all these samples are very similar in the micropore range. Figure 3a reveals a broad distribution with maxima at 7, 11, 15 and 18.5 Å. The oxidative treatment affects only the microporous region of the SC carbon. Porosity in the mesopore range was detected only in F400 (Fig. 3b). The slight upturn observed for SC and SCOX at the higher end of the mesopore range, owing to their smaller particle size, may be due to interparticle porosity.

In Fig. 4, the SAXS response of the SC and SCOX samples at low wave vector q exhibits power law behaviour, the slope of which is characteristic of scattering from a rough surface [10].

The pronounced shoulder for both SCs at $q \approx 0.1$ Å^{-1} is the result of the microporous structure. By plotting the data in a Guinier representation ($\log(I(q)$ vs. q^2), not shown here) [11], the radius of gyration of the micropores were found to be 10.9 and 12.3 Å for SC and SCOX respectively. Comparison of the surface area, calculated by the method of Porod [11] (1560 and 1390 m^2/g, respectively), with the nitrogen adsorption data reveals only limited inaccessible porosity [12].

The equivalent slope for F400 is smaller than 3, which indicates scattering from a volume that contains a densely branched structure. For this reason, in this sample the microporous behaviour appears much less pronounced, producing a scattering feature that is too weak to permit more detailed evaluation.

The SC and the F400 carbons have slightly basic character, as reflected in the values of pH in Table 2. Nevertheless, the distribution of the surface functionalities of different pK_a values must be very different. The high concentration of basic surface groups in the SC carbon originates from the nitrogen functionalities. In spite of the presence of nitrogen, the acidic treatment significantly reduces the pH of this carbon.

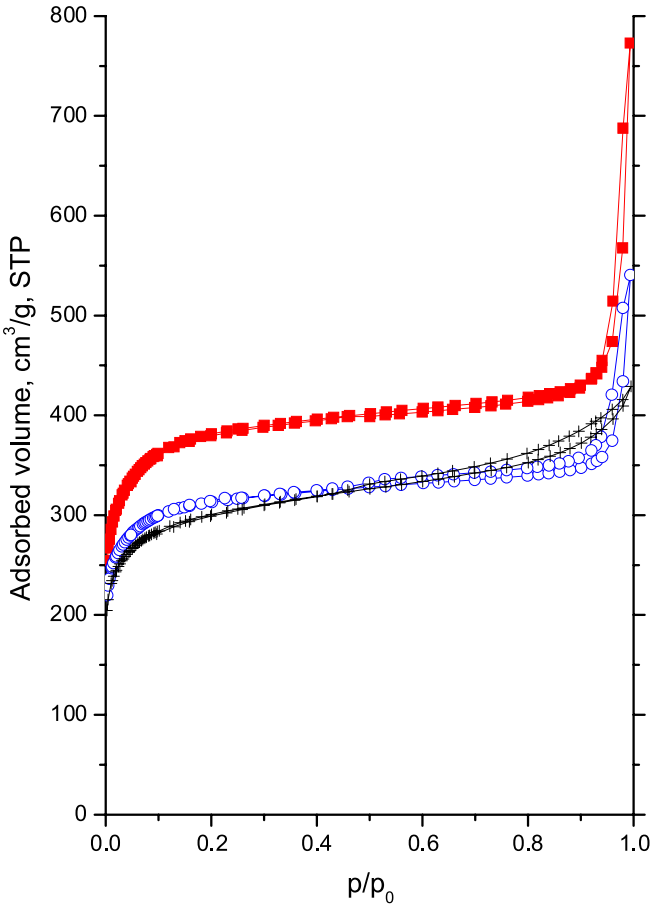

Fig. 2 N_2 (77 K) adsorption/desorption isotherms of the SC (■), SCOX (○) and F400 (+) carbons

To study the interaction between the carbon surface of different chemistry and the metal cations, Cu^{2+} adsorption isotherms were measured for SC and SCOX from aqueous solutions of $Cu(CH_3COO)_2$. The isotherms,

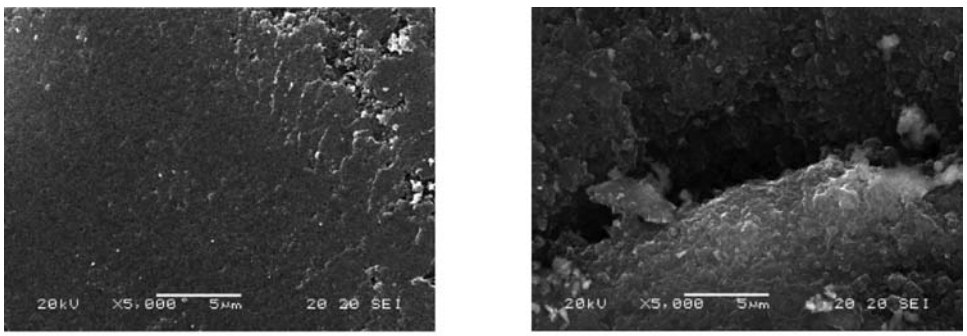

(a) (b)

Fig. 1 Scanning electron micrographs of SC **a** and SCOX **b** ; magnification: 5000 ×, scale bar: 5 μm

Table 1 Morphology data from low temperature N_2 adsorption measurements of the non-impregnated carbons

Sample	S_{BET} (m^2/g)	V_{TOT} (cm^3/g)	d_{ave} (Å)	W_0 (cm^3/g)	w (Å)	W_0/V_{TOT} (%)
SC	1457	0.69	9.47	0.58	9.1	84
SCOX	1176	0.55	9.35	0.46	7.8	84
F400	1081	0.66	24.0	0.42	6.9	64

S_{BET} is the apparent surface area, V_{TOT} is the total pore volume from the isotherm at $p/p_0 = 0.94$, $d_{ave} = 2V_{tot}/S_{BET}$; W_0 and w are the volume and the average width of the micropores, respectively.

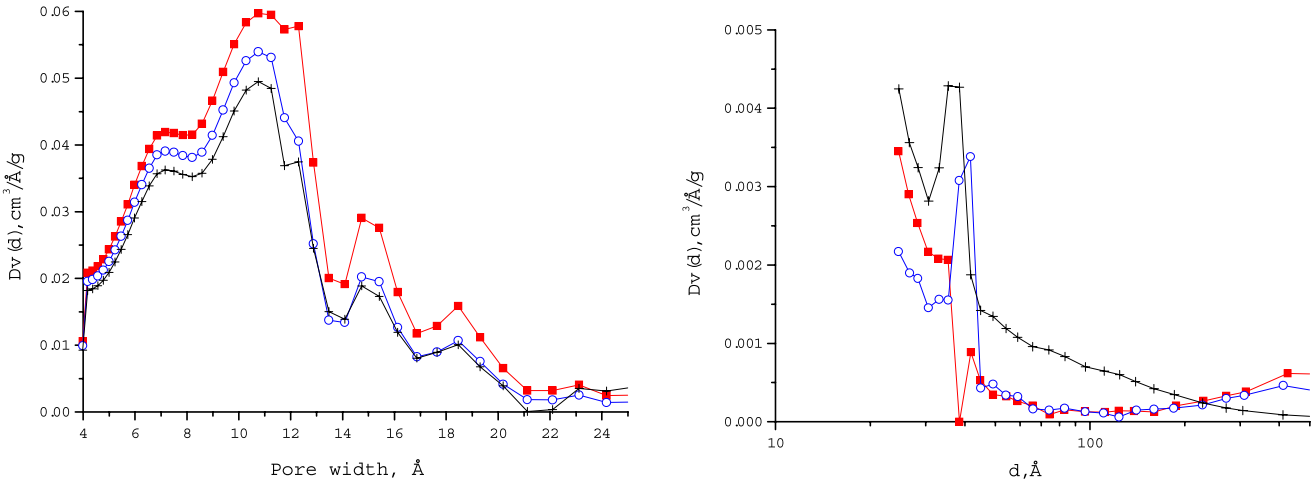

Fig. 3 PSD of the carbon samples from the N_2 adsorption isotherms **a** by the NLDFT method **b** by the BJH method (■ SC, ○ SCOX, + F400)

which belong to type L in the Giles classification [13], were evaluated from the linear Langmuir plot (Table 3). The cation exchange capacity of SC and SCOX, measured by Boehm titration (Table 2), was found to be about an order of magnitude smaller than the corresponding copper uptake. This may be explained by the nitrogen-containing functional groups present, which may react as complexing agents and increase the copper adsorption.

SC and F400 were treated with aqueous $Cu(CH_3COO)_2$ solution under identical conditions to study the influence of the pore structure. The metal uptake for the microp-

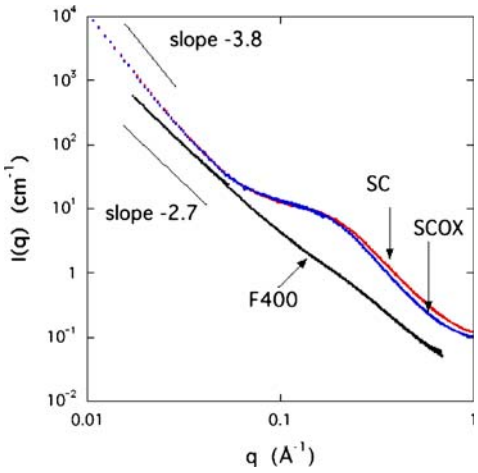

Fig. 4 SAXS response of the SC, SCOX and F400 carbons

Table 2 Surface chemical properties of SC, SCOX and F400 in aqueous phase

	SC	SCOX	F400
pH	7.9	3.4	7.8
Acidic functional groups (μeq/g)	273	838	210
Basic functional groups (μeq/g)	538	223	–*

* The amount of the basic functional groups in the surface could not be determined for this sample by the Boehm titration method

Table 3 Parameters of the Langmuir equation* for SC and SCOX

	n_m (mmol/g)	K	R^2
SC	2.2	14.5	0.9511
SCOX	2.1	18.8	0.9578

* n_m is the monolayer capacity, K is the interaction parameter and R is the regression coefficient of the fit

orous SC was 1.9 mmol/g, and 1.1 mmol/g for F400. The PSDs and the structural parameters derived from the N_2 adsorption/desorption isotherms are displayed in Fig. 5 and Table 4, respectively.

These data show that metal impregnation causes partial blocking of the porosity and reduces the contact surface area and the volume of the accessible pores. The PSDs indicate that the ions are accommodated mainly within pores either smaller than 14 Å or larger than 50 Å. EDS results also confirmed that adsorption takes place within the pores [14], since no copper was detected on the outer surface of the impregnated particles. As has been reported in the literature [15], this increases the microporous character of the mesoporous carbon and leads to the increase of w and d_{ave} in both carbons.

The sensitivity of the small pores to metal impregnation is also apparent upon comparing the porosity of SCOX carbons with different loadings (Fig. 6, Table 5).

For metal loading below the saturation capacity of SCOX (2.1 mmol/g, Table 3), the monotonic decrease in pores of size smaller than 14 Å visible in Fig. 6a is accompanied by a corresponding reduction of both the surface area and the pore volume that is proportional to the loading. The microporous character and the accessibility of the larger pores, however, are unaffected. When the loading exceeds 2.1 mmol/g a dramatic change in the structural parameters occurs.

When SCOX was loaded from the 0.03 M aqueous solutions of copper salts (16.0 ml/g carbon) with various anions at room temperature, different uptakes of copper ion were observed (Table 6). This finding indicates that the size and the charge of the anions and their different state of hydration may influence the sorption of the cations [16]. It should be noted that the effect of the anions on the pH was not investigated.

According to the EDS analysis, treatment with freshly prepared CuCl at elevated temperature in an inert atmosphere yielded spherical carbons with a CuCl-covered sur-

Table 4 Structural parameters from low temperature N_2 adsorption measurements for the microporous and mesoporous carbon

Sample (Cu loading, mmol/g)	S_{BET} (m^2/g)	V_{TOT} (cm^3/g)	W_0 (cm^3/g)	w (Å)	W_0/V_{TOT} (%)	d_{ave} (Å)
SC	1457	0.69	0.58	9.10	84	9.47
SC/Cu (1.9)	722	0.36	0.28	10.4	78	19.9
F400	1081	0.66	0.42	6.90	64	24.0
F400/Cu (1.1)	484	0.34	0.24	11.0	71	28.1

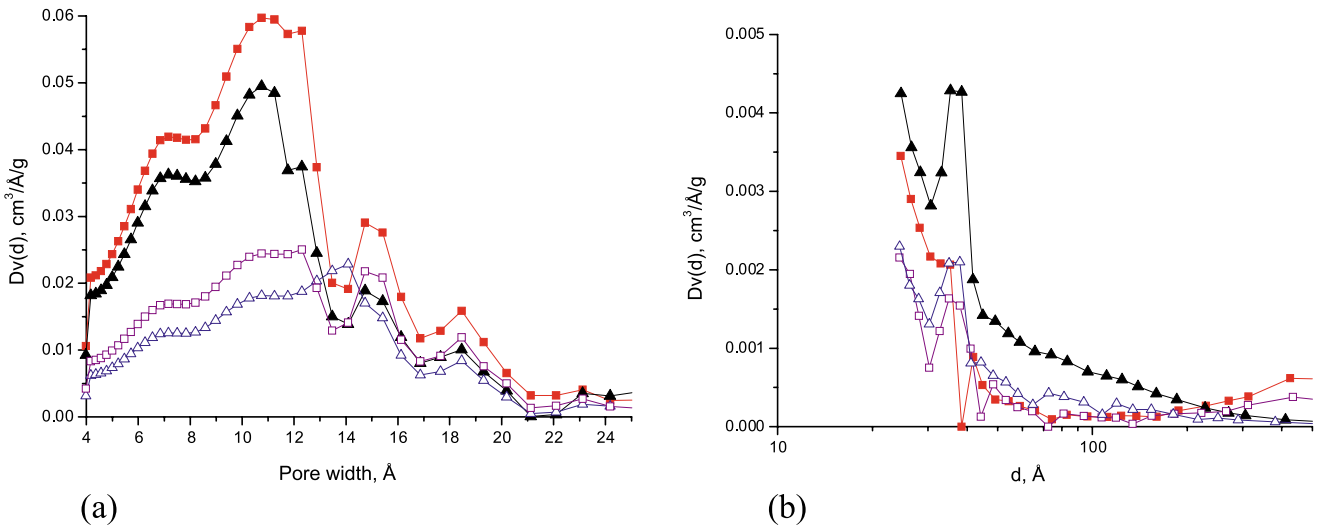

Fig. 5 **a** NLDFT **b** BJH PSDs of SC (■), F400 (▲), SC/Cu (□) and F400/Cu (△)

Table 5 Structural parameters from low temperature N_2 adsorption measurements for the SCOX carbons with different loading

Sample (Cu loading, mmol/g)	S_{BET} (m^2/g)	V_{TOT} (cm^3/g)	W_0 (cm^3/g)	w (Å)	W_0/V_{TOT} (%)	d_{ave} (Å)
SCOX	1176	0.55	0.46	7.8	84	9.35
SCOX/Cu (0.62)	956	0.47	0.39	9.5	83	20
SCOX/Cu (1.43)	734	0.38	0.30	10.5	79	21
SCOX/Cu (2.24)	128	0.12	0.06	15.9	50	38

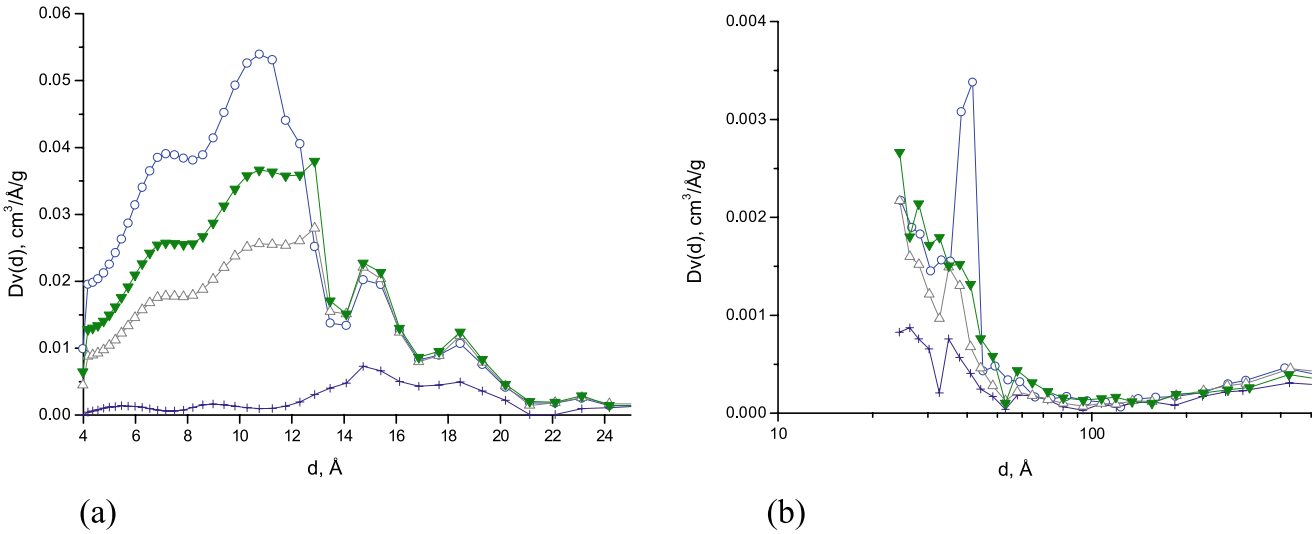

Fig. 6 **a** NLDFT, **b** BJH PSDs of metal-free SCOX (○) compared to SCOX after loading with 0.62 (▼), 1.43 (△) and 2.24 (+) mmol/g copper

face. However, part of the copper is reduced, forming copper wire, as shown in the electron micrographs of Fig. 8. This makes the mass determination of the sample uncertain.

The effect of Cu^{2+} and Sn^{2+} treatment is compared in Figs. 9–10 and in Table 7. These samples were prepared under identical conditions using copper acetate and tin chloride solutions. Uptake of tin is twice as high as that of copper, which is reflected in the reduced porosity and, as before, the loss is the most significant in the region of narrowest pores. The uptake is the result of a complex mechanism, which also involves (de)hydration and redox processes [17]. (The role of the anions was addressed previously.) The interaction between the carbon surface and the cations may be influenced by the geometrical constraints, i.e., size, electronegativity, effective charge and state of hydration of the ionic species (Table 8). Although ion exchange may be the dominant effect in the sorption mechanism, redox processes, even catalyzed by the solid surface, also may occur [18, 19]. A redox reaction seems to take place when $SnCl_2$ is used, which results in the appreciably rougher surface visible in the corresponding micrographs of Fig. 10b.

Table 6 Structural parameters from low temperature N_2 adsorption measurements for the SCOX carbons loaded with different copper salts

Anion	Cu uptake (mmol/g)	S_{BET} (m^2/g)	V_{TOT} (cm^3/g)	W_0 (cm^3/g)	w (Å)	W_0/V_{TOT} (%)	d_{ave} (Å)
–	0	1176	0.55	0.46	7.8	84	9.4
CH_3COO^-	0.62	956	0.47	0.39	9.5	83	20
NO_3^-	0.15	971	0.48	0.39	9.9	81	20
SO_4^{2-}	0.12	1280	0.61	0.52	9.0	85	19

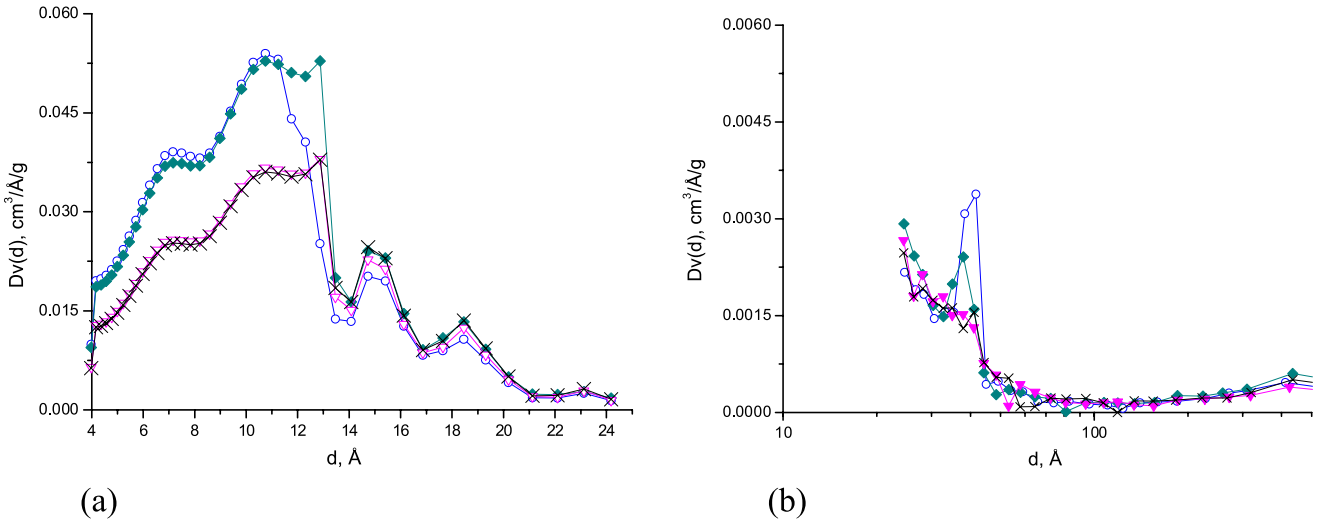

Fig. 7 **a** NLDFT, **b** BJH PSDs of metal-free SCOX (○) compared to SCOX after loading with $Cu(NO_3)_2$ (×), $CuSO_4$ (◆) and $Cu(CH_3COO)_2$ (▽)

Table 7 Structural parameters from low temperature N_2 adsorption measurements for the SC carbons loaded with copper and tin

Sample (cation loading, mmol/g)	S_{BET} (m^2/g)	V_{TOT} (cm^3/g)	W_0 (cm^3/g)	w (Å)	W_0/V_{TOT} (%)	d_{ave} (Å)
SC	1457	0.69	0.58	9.1	84	9.47
SC/Cu (0.29)	712	0.37	0.30	11.3	81	20.74
SC/Sn (0.62)	533	0.30	0.21	11.5	70	22.58

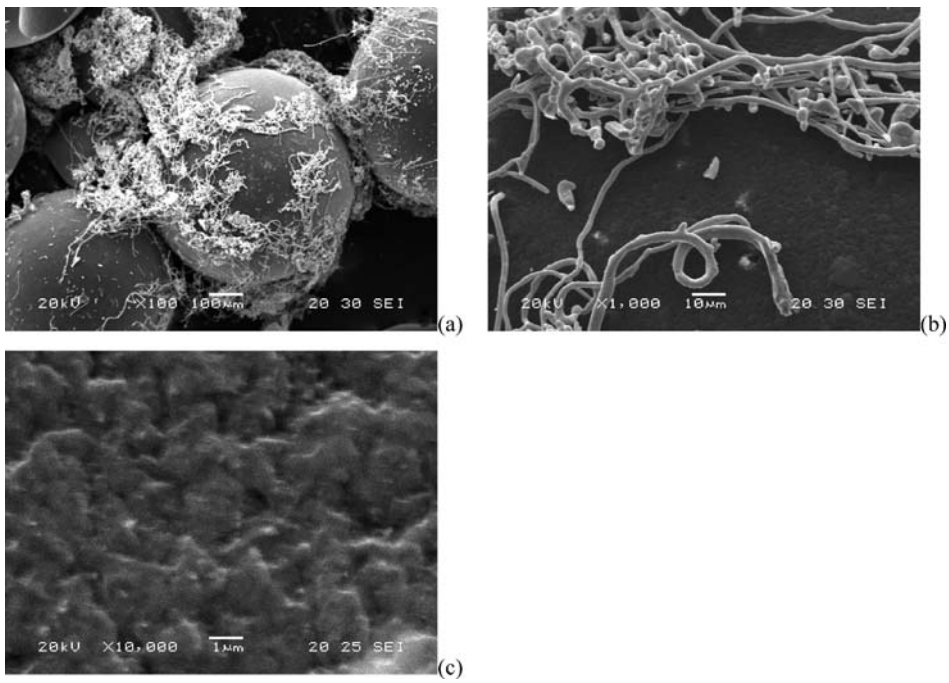

Fig. 8 Scanning electron micrographs of SC/Cu^+ at different magnifications. **a** 100 ×; scale bar: 100 µm **b** 1000 ×; scale bar: 10 µm; copper wires on the surface of SC **c** 10000 × times magnification of the carbon surface; scale bar: 1 µm

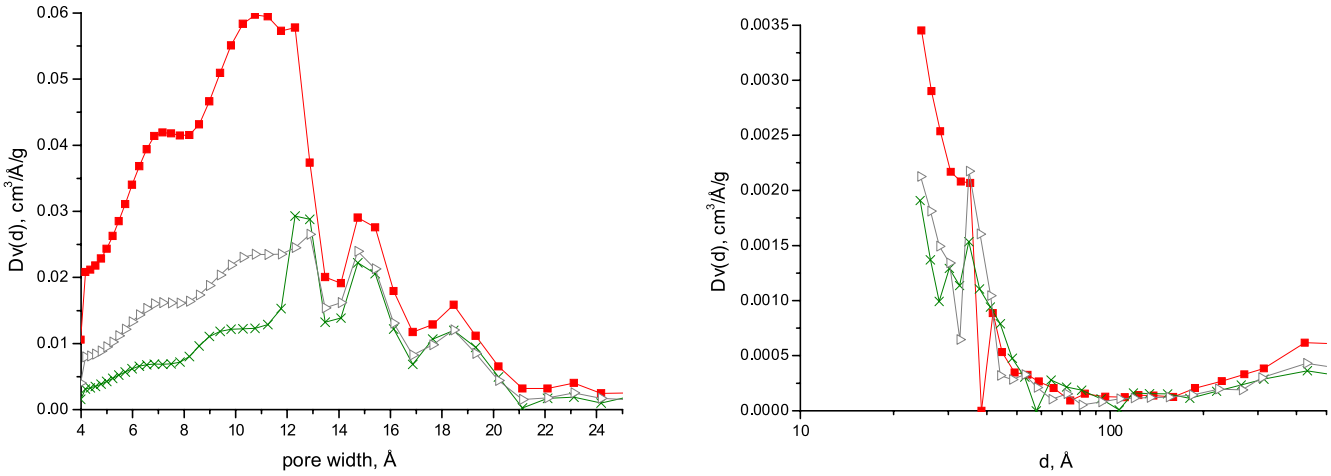

Fig. 9 **a** NLDFT, **b** BJH PSDs of metal-free (■), copper (0.29 mmol/g) (▷) and tin (0.62 mmol/g) (×) loaded SC

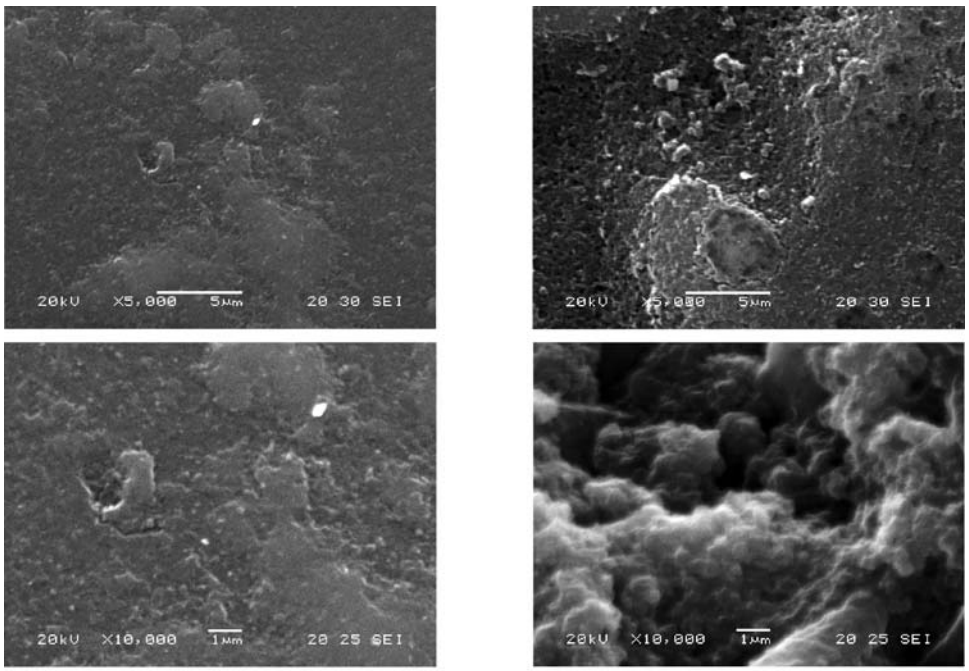

Fig. 10 Scanning electron micrographs of SC/Cu (**a**) and SC/Sn (**b**) at different magnifications (*upper row*: 5000 ×, scale bar: 5 μm; *lower row*: 10 000 ×, scale bar: 1 μm)

Table 8 Properties of the cations

	Standard electrode potential E^0 (V)	Electronegativity (Pauling)	Ionization energies (kJ/mol)	Polarizability (10^{-24} cm^3)	Ionic radius (Å)	Hydrated ionic radius (Å)
Cu [20]	+0.3419	1.90	1958	6.10	Cu^{2+}: 0.72	2.07 6.00 [21] 4.19 [22]
Sn [23]	−0.1364	1.96	1412	7.7 [24]	Sn^{2+}: 0.93	6.00 [21]

Conclusions

Porous carbon samples of different surface chemistry were produced by oxidation and metal impregnation. Oxidation by nitric acid substantially decreased the pH and slightly reduced the accessible porosity, but no significant changes were observed either in the morphology or in the Cu^{2+} adsorption capacity. Metal impregnation from aqueous phase was found to depend not only on the chemistry but also on the porosity of the carbon surface as well as the species of the anion and of the metal. The main structural changes were caused by blocking of pores of size smaller than 14 Å. Cu^{2+} loadings below the saturation capacity produced a corresponding decrease of the apparent surface area, proportional to the loading. No metal was detected on the surface of the particles. When the samples were treated with solid CuCl, a practically complete CuCl film covered the surface of the particles, but metallic copper was formed as a by-product. When $SnCl_2$ was used instead of Cu^{2+} salts in aqueous phase, a redox reaction appeared to take place, resulting in an appreciably rougher surface that is visible in SEM micrographs.

Acknowledgement The spherical carbon (SC) was kindly provided by the INSIDE PORES Network of Excellence. Access to the CRG beam line BM2 at the European Synchrotron Radiation Facility, Grenoble, is gratefully acknowledged. We extend our thanks to G. Bosznai for sample preparation. This research was performed in the framework of the Hungarian – Greek Intergovernmental S&T Cooperation Programme (GR-43/03) and supported by the EU – Hungarian Government joint fund (GVOP -3.2.2-2004-07-0006/3.0).

References

1. László K (2005) Microporous Mesoporous Mater 80:205
2. Tamon H, Kitamaru K, Okazaki M (1996) AIChE J 42:422
3. Mohamad AB, Iyuke SE, Daud WRW, Kadhum AAH, Fisal Z, Al-Khatib MF, Shariff AM (2000) J Mol Struct 550–551:511
4. Xie Y, Zhang J, Qiu J, Tong X, Fu J, Yang G, Yan H, Tangz Y (1996) Adsorption 3:27
5. Al-Khatib MF, Iyuke SE, Mohamad AB, Daud WRW, Kadhum AAH, Shariff AM, Yarmo MA (2002) Carbon 40:1929
6. Strelko VV, Kartel NT, Dukhno IN, Kuts VS, Clarkson RB, Odintsov BM (2004) Surf Sci 548:281
7. László K, Marthi K, Rochas C, Ehrburger-Dolle F, Livet F, Geissler E (2004) Langmuir 20:1321
8. Tessmer CH, Vidic RD, Uranowski LJ (1997) Environ Sci Technol 31:1872
9. Boehm HP (1966) Chemical Identification of Surface Groups. In: Eley DD, Pines H, Weisz PB (eds) Advances in Catalysis, vol 16. Academic Press, New York, pp 179–274
10. Hasmy A, Anglaret E, Foret M, Pelous J, Jullien R (1994) Phys Rev B 50:6006
11. Porod G (1983) In: Kratky O, Glatter O (eds) Small Angle X-ray Scattering. Academic, London
12. László K, Czakkel O, Josepovits K, Rochas C, Geissler E (2005) Langmuir 21:8443
13. Giles C, Mc Ewan T, Nakhwa S, Smith DJ (1960) J Chem Soc p 3973
14. Petit C, Bandosz T (2007) Reactive Adsorption of Ammonia on Modified Activated Carbons. CARBON 2007, Seattle, USA, CD-ROM of Extended Abstracts
15. Molina-Sabio M, Pérez V, Rodríguez-Reinoso F (1994) Carbon 32:1259
16. Santafé-Moros A, Gozálvez-Zafrilla JM, Lora-García J (2007) Desalination 204:63
17. Iyuke SE, Daud WRW, Mohamad AB, Kadhum AAH, Fisal Z, Shari AM (2000) Chem Eng Sci 55:4745
18. Fu RW, Zeng HM, Lu Y (1993) Carbon 31:1089
19. Kobya M, Demirbas E, Senturk E, Ince M (2005) Bioresour Technol 96:1518
20. Magini M, Licheri G, Paschina G, Piccaluga G, Pinna G (1988) X-ray Diffraction of Ions in Aqueous Solutions: Hydration and Complex Formation. CRC Press Inc, Boca Raton
21. Kielland J (1937) J Am Chem Soc 59:1675
22. Semmens MJ, Seyfarth M (1978) The Selectivity of Clinoptilolite for Certain Heavy Metals. In: Sand LB, Mumpton FA (eds) Natural Zeolites: Occurance, Properties, Use. Pergamon Press Ltd, Oxford, pp 517–526
23. Weast RC, Astle MJ (eds) (1982) CRC Handbook of Chemistry and Physics, 63rd edn. CRC Press, Boca Raton
24. http://www.chemicool.com; Accessed 12 Aug 2008

Progr Colloid Polym Sci (2008) 135: 148–156
DOI 10.1007/2882_2008_105

Published online: 30 August 2008

Ajna Tóth
Csaba Novák
Krisztina László

The Effect of Ionic Environment on the Adsorption of Phenol

Ajna Tóth · Krisztina László (✉)
Department of Physical Chemistry and Materials Science, Budapest University of Technology and Economics, Pf 92, 1521 Budapest, Hungary
e-mail: klaszlo@mail.bme.hu

Csaba Novák
Hungarian Academy of Sciences, Budapest University of Technology and Economics, Research Group of Technical Analytical Chemistry,
Szt. Gellért tér 4, 1111 Budapest, Hungary

Abstract The effect of the ionic environment on the adsorption of phenol from aqueous solutions was investigated in a predominantly microporous carbon and in a commercial carbon designed for wastewater treatment. It was found that not only the pH of the solution but also the method of its setting affects the adsorption capacity. Setting the pH with a buffer solution instead of HCl/NaOH results in a reduced adsorption capacity, owing to the increased number of competing species for adsorption sites, and also to pore blocking. The latter is less critical for the commercial carbon with wider pores. Thermal desorption of phenol exhibits an even stronger dependence on pH setting than adsorption. Upon heating, a mass equivalent to 10–35% of the adsorbed phenol is retained by the surface as a carbon-rich residue, which may modify not only the chemistry but also the pore volume and the pore size distribution of the carbon.

Keywords Activated carbon · Adsorption/desorption · pH dependence · Surface properties · Thermal analysis

Introduction

Growing awareness of the potential hazard of pollution by veterinary and human pharmaceuticals in aquatic environments has renewed concern for the treatment of both wastewater and drinking water. Although biological methods are the most widely employed, they cannot overcome the problem of the non-biodegradable organic, mainly aromatic compounds, that even at low concentration may act as inhibitors for biological treatment. For this reason, adsorption by activated carbons (AC) is still among the most extensively used technologies, owing to their high affinity for a wide variety of chemicals. Their outstanding performance stems from a unique combination of geometrical and chemical properties. The latter mainly depend on heteroatoms and their chemical forms, which are defined by the origin and the prehistory of the carbon. The most frequent heteroatom is oxygen, which bonds along the edges of the turbostratic layers. These functional groups and the delocalized electrons of the graphitic structure define the apparent acid/base character of the carbon surface [1–7].

When AC is used in an aqueous medium, the distribution of the surface functionalities is of fundamental importance, as these exhibit a pH dependent behaviour when they interact with water and the dissolved species [8]. This also results in the transformation of the active sites [9, 10]. Recent reviews of sorption by AC of aromatics from aqueous solution [11–14] unanimously conclude that the specific mechanism of the interaction of many organic compounds on the amphoteric surface of the carbon is still uncertain.

Phenol and its derivatives appear in wastewater by way of degradation of organic compounds in widespread use as intermediates for the synthesis of dyes, pesticides, insecticides, explosives, etc. Phenol is carcinogenic and, even at

low concentrations, imparts a bad taste and odour to drinking water. Being aromatic, its biological degradation is not straightforward, and therefore the most frequent method for its removal is still sorption-related. In water, phenol may be present as a weak acid, either in molecular or ionic form, depending on the pH. The fundamental interactions between the carbon surface and phenols are a) dispersion effect between the aromatic ring and the π electrons of the graphitic structure; b) electrostatic attraction and repulsion if ions are present [12]. The interaction between the water molecules and the surface sites cannot be excluded either, and their competitive adsorption results in depletion of the amount adsorbed. Electron donor – acceptor interaction between the aromatic ring and the basic surface oxygens does not play a significant role if the concentration of the surface oxygen atoms is relatively low.

Since the first paper of Coughlin and Ezra, published exactly 40 years ago [15], it has become universally accepted in the scientific community that pH has a determining influence on the sorption behaviour of carbon surfaces with respect to weak organic acids or bases. pH controls the mechanism of the interaction and, by localizing the adsorbates, influences the effective utilization of the carbon capacity. If sorption takes place in an electric field, polarization of the electrodes and anodic decomposition of water may enhance or reduce sorption [16].

In this paper the performance of a laboratory-made microporous carbon produced by recycling poly(ethyleneterephthalate) (PET) is compared to a commercial product F400, specifically designed for waste water treatment. Our purpose is to show that the manner of setting the pH may also play an important role in the sorption processes.

Experimental

Activated Carbons and their Characterization

Microporous granular activated carbon (APET) was prepared from PET pellets by two-step physical activation [17]. F400, a commercial pelleted porous carbon produced for water purification (Calgon Carbon Corp. Pittsburg, PA, USA) was used for comparison. Nitrogen adsorption/desorption isotherms were measured at 77 K, using a Quantachrome Autosorb-1 computer controlled apparatus. The apparent surface area S_{BET} was obtained from the BET model. The total pore volume V_{tot} was calculated from the amount of nitrogen vapour adsorbed at a relative pressure close to unity, on the assumption that the pores are then filled with liquid nitrogen. An average pore width d_{ave} ($= 2V_{tot}/S_{BET}$) was derived from S_{BET} and the total pore volume V_{tot}, assuming slit-shaped geometry, as revealed by the hysteresis loops. The micropore volume W_0 and the characteristic energy E_0 were deduced from the intercept and slope of the Dubinin–Radushkevich (DR) plot, respectively ($\beta = 0.34$). The pore width w of the slit-shaped micropores is taken to be $2kE_0^{-1}$ ($k = 13\,\mathrm{kJ\,nm\,mol^{-1}}$). The pore size distribution (PSD) in the micropore range was calculated with the DFT/Monte Carlo differential PSD program of the AUTOSORB apparatus.

The carbons studied are characterized by the pH of their aqueous suspension, detected under standardized conditions [18]. The pH of the point of zero charge pH_{PZC} was measured by the so-called drift method [18, 19]. As the carbon surfaces are decorated only with O-containing heteroatoms, the functional groups of different pK_a range were determined by Boehm titration [2]. Carbon samples were immersed in 0.05 M solutions of HCl, $NaHCO_3$, Na_2CO_3 and NaOH, respectively. The vials were sealed and shaken for 72 h at ambient temperature. The filtrates were titrated with NaOH and HCl, depending on the original titrant. The number of basic sites was calculated from the amount of HCl that reacted with the carbon. The various free acidic groups were derived using the assumption that NaOH neutralizes carboxyl, lactone and phenolic groups, Na_2CO_3 neutralizes carboxyl and lactone and $NaHCO_3$ neutralizes only carboxyl groups, respectively.

Sorption from Dilute Aqueous Solutions of Phenols

Solutions of phenol (Merck, 99.5%) were prepared using doubly distilled water. The pK_a value of phenol is 9.89 (20 °C) and its solubility is 82 g/l (25 °C).

For the adsorption isotherms, ca. 0.05 g of carbon was shaken with 50 ml of unbuffered phenol (1–10 mM) solutions for 24 hrs in sealed vials at ambient temperature. The contact times needed to reach equilibrium were deduced from preliminary kinetic measurements. The initial and equilibrium concentrations c_0 and c_e, respectively, were determined by UV absorption.

For the preparation of the phenol-loaded samples 5 mM phenol solutions were used. For one sample set the phenol was dissolved in Britton–Robinson (BR) buffer solutions in the pH range 3–11. The BR buffers are mixed from 0.04 M acetic acid ($pK_a = 4.76$, 25 °C), 0.04 M phosphoric acid ($pK_a = 2.12, 7.21, 12.76$, 25 °C), 0.04 M boric acid ($pK_a = 9.14, 12.74, 13.80$, 20 °C) and 0.2 M NaOH. For the second set, aqueous HCl or NaOH solutions in the same pH range ($pH_{solvent}$) were used as solvent. The calibration diagrams for UV absorption measurements were determined at each pH for both pH settings.

Thermal Analysis

Thermal analysis was carried out in nitrogen atmosphere (10 l/min), using a simultaneous DTA-TGA TA Instruments STD 2960 unit. The heating rate was 10 °C/min. In the temperature range investigated the mass loss of the carbon itself was negligible compared to the phenol desorption.

Results and Discussion

Characterization of the Porous Carbons

The low temperature nitrogen adsorption isotherms in Fig. 1 reveal the different porosities of the two carbons. The PSD in the micropore range in the insert of Fig. 1 confirms the higher microporosity of the PET-based carbon. The characteristic parameters calculated from the isotherms are listed in Table 1.

This information shows that the fundamental difference in the morphology of these carbons appears in the micropore range. APET is highly microporous, while F400 possesses a larger amount of mesoporosity.

The acid/base properties of the carbons were characterized under wet conditions. The difference in pH_{PZC}, in spite of the similar pH listed in Table 2, indicates that the distribution of the surface functionalities is different, as shown in Table 3.

Table 1 Data from low temperature nitrogen adsorption isotherms*

Sample	S_{BET} (m^2/g)	V_{tot} (cm^3/g)	d_{ave} (nm)	w (nm)	W_0 (cm^3/g)	W_0/V_{tot} (%)
F400	1122	0.66	2.4	0.69	0.42	64
APET	2025	1.02	2.0	1.79	0.78	76

* S_{BET} apparent surface area from the BET model;
V_{tot} total pore volume;
d_{ave} ($= 2V_{tot}/S_{BET}$) average pore width;
w pore width of the micropores;
W_0 micropore volume

Adsorption of Phenol in Unbuffered Condition

The adsorption isotherms from unbuffered aqueous phenol were measured at room temperature (Fig. 2). The isotherms, of type L according to Giles's classification [20], were fitted by the linearized Langmuir equation

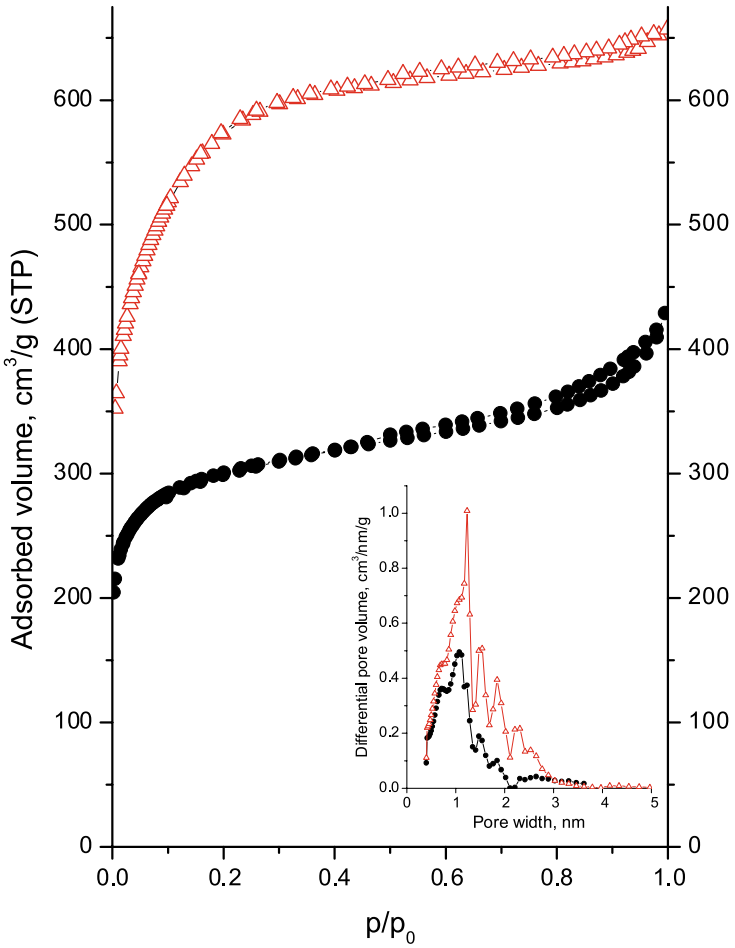

Fig. 1 Low temperature N_2 adsorption/desorption isotherms and micropore PSD of the carbon samples; △: APET, ●: F400

Table 2 pH and pH_{PZC} of the carbon samples

	pH, 25 °C	pH_{PZC}
F400	7.8	8.4
APET	7.9	9.8

to obtain the adsorption capacities n_m and the equilibrium constants K (Table 4). The surface area occupied by a single aromatic molecule was calculated as $S_{BET}/(n_m \times N_A)$, where N_A is Avogadro's number. It should be mentioned, however, that although the fit is not bad, the initial conditions of the Langmuir model are not properly satisfied owing to the chemical and morphological heterogeneity of the carbon surface. The advantage of our approach, however, is that the Langmuir parameters possess a physical meaning, thus offering a basis for further interpretation.

The high surface area APET sample exhibits greater monolayer capacity and a smaller K interaction parameter than the commercial carbon. Comparison of the surface area available for the phenol with its cross-sectional area (0.30–0.42 nm^2/molecule, [18]) leads to the conclusion that the surface of both carbons is only partially covered by the aromatic compound. The microporous character of the APET produces a less efficient surface coverage than F400, since about 60% (compared to ca. 50%) of the surface is not available for phenols, as a result of water adsorption or blocked porosity [21].

Table 3 Distribution of surface functional groups

Sample		Acidic groups					Basic groups (HCl)	Acidic + basic
		Carboxyl	Lactone	Phenol	Total acidicity (NaOH)	% of the acidic groups		
F400	μeq/g	65	58	87	210	–	not measurable	
	group/100 nm^2	3.6	3.2	4.8	11.8			
APET	μeq/g	below detection limit	5.6	82.6	88.2	27	328.2	416.4
	group/100 nm^2	0	0.17	2.5	2.6		9.7	12.3

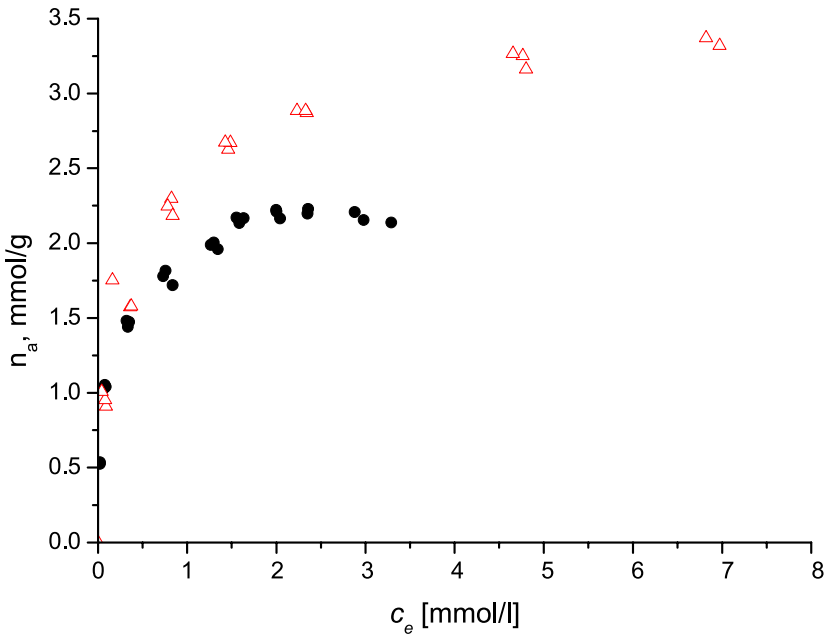

Fig. 2 Phenol adsorption isotherms in unbuffered condition at ambient temperature; △: APET, ●: F400

Table 4 Parameters obtained from the linear Langmuir fit to the aqueous phenol isotherms

	n_m (mmol/g)	K (l/mmol)	R^2	Surface area available per adsorbate molecule (nm^2/molecule)
F400	2.28	7.80	0.996	0.79
APET	3.52	2.31	0.999	0.96

Influence of the pH and the Buffer on the Adsorption of Phenol

When the simple acidic or basic (i.e., buffer-free) solutions were used as solvent, the pH (pHsolvent) changed when the phenol was added (pHsolution) (triangles in Fig. 3), in accordance with the weak acid character of phenol. For solvent pH values between 5 and 9 the pH of the solution is practically constant. This effect stems from the low-capacity buffer-like behaviour of the (phenol/HCl)aq or (phenol/NaOH)aq systems. When carbon is added to the system and the state of adsorption equilibrium is established, there is a measurable shift in the corresponding pH. Depending on the pH of the solution and the pK_a of the surface functional groups the overall basic properties of the surface slightly increase the pH. In the case of Britton–Robinson no such differences were detected.

The adsorption capacities obtained with the two sets of phenol solutions were related to the values measured in the unbuffered medium and are compared in Table 5. Below pH ≈ 5 the phenol is protonated, while at higher pH values molecular and ionic phenol species coexist. At low pH the surface is positively charged due to protonation, which has a complex effect. Protonated functional groups act as centres for water cluster formation [21, 22] and attract anions. Both water and the anions may compete for the adsorption sites and, furthermore, blocking of the micropore entrances by the adsorbed species may reduce access for the aromatics. Protonation of the basal plane also disturbs the π–π interaction with the aromatic ring of the pollutants. Incomplete coverage of the surface is a sign that the hydrogen bonding energy with oxygen-containing surface groups may be weak, and even water is able to interact with the basal planes [23]. Hydrogen bonds forming between phenol molecules and the surface groups

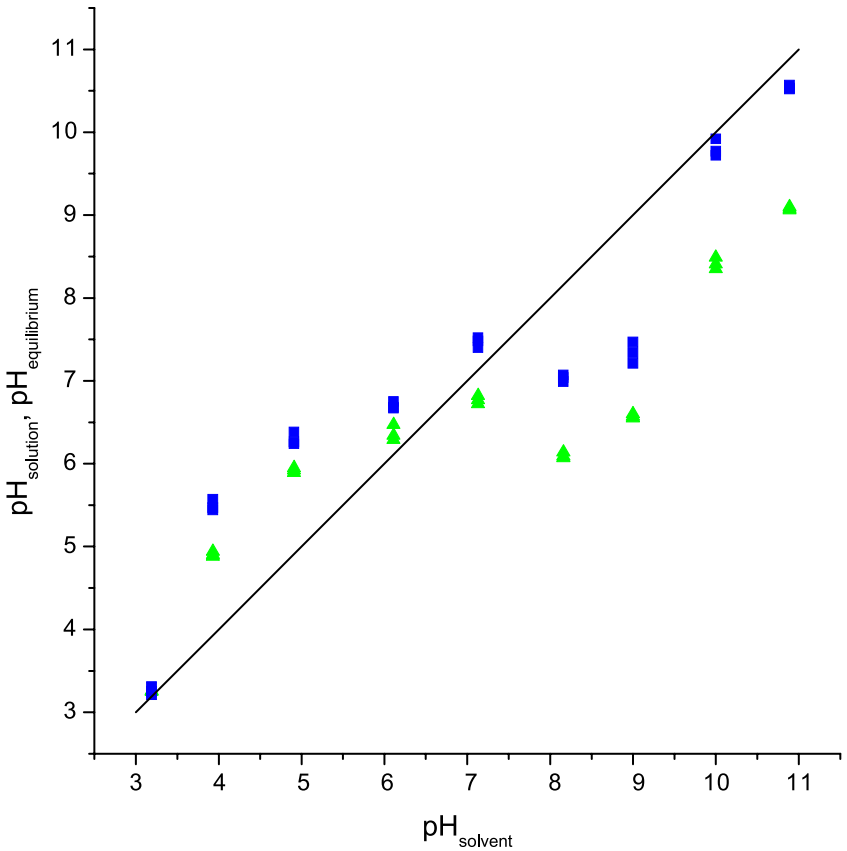

Fig. 3 Variation of the pH of the phenol solution with HCl/NaOH adjustment; pH of the phenol solution *triangles*: before contact with APET carbon, *squares*: after adsorption equilibrium was reached. *Solid black line* corresponds to a pH unaffected by the presence of phenol

Table 5 Equilibrium phenol uptake from 5 mM phenol solutions

pH	Relative phenol uptake* (%)		
	APET		F400
	HCl/NaOH	BR	BR
3	93.7	77.5	82.5
4	93.4	90.1	–
5	86.1	84.9	–
6	93.7	91.1	–
7	94.1	91.1	–
8	99.3	93.8	86.8 (pH = 8.4)
9	92.0	88.7	–
10	85.4	86.6	–
11	92.0	87.8	108.3
Unbuffered	100		100

* Relative phenol uptake = 100 × (maximum uptake at the given pH/maximum uptake in unbuffered solution)

also may block the entrances of the fine pores [24]. Above the pH_{PZC} of the carbon the surface is negatively charged, and the electrostatic repulsion could therefore reduce the adsorption of the phenolate ions.

With HCl or NaOH solutions the chlorine or sodium ions interact with the charged surface. In the case of the multi-ionic buffer solution, however, the ionic interaction can be much more complex since molecules or ionic derivates of the buffer components, as well as the solvent molecules, also compete for the sites. Inspection of the relative phenol adsorption in APET at pH 11 shows that in the buffered case, because the inorganic anions also con-

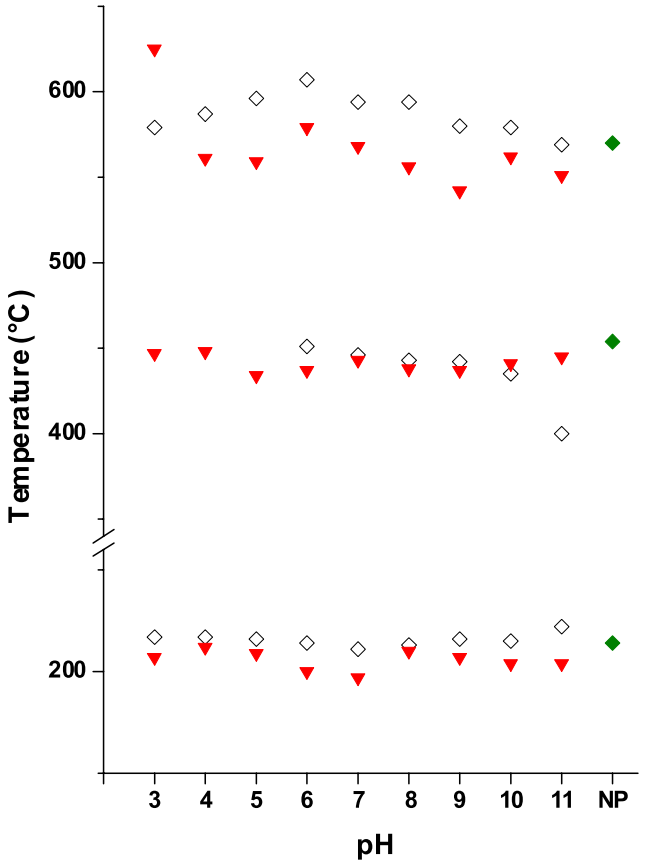

Fig. 5 Temperature of the peaks of the DTG curves depending on pH: (◇) BR buffer; (▼) HCl/NaOH; (◆) unbuffered

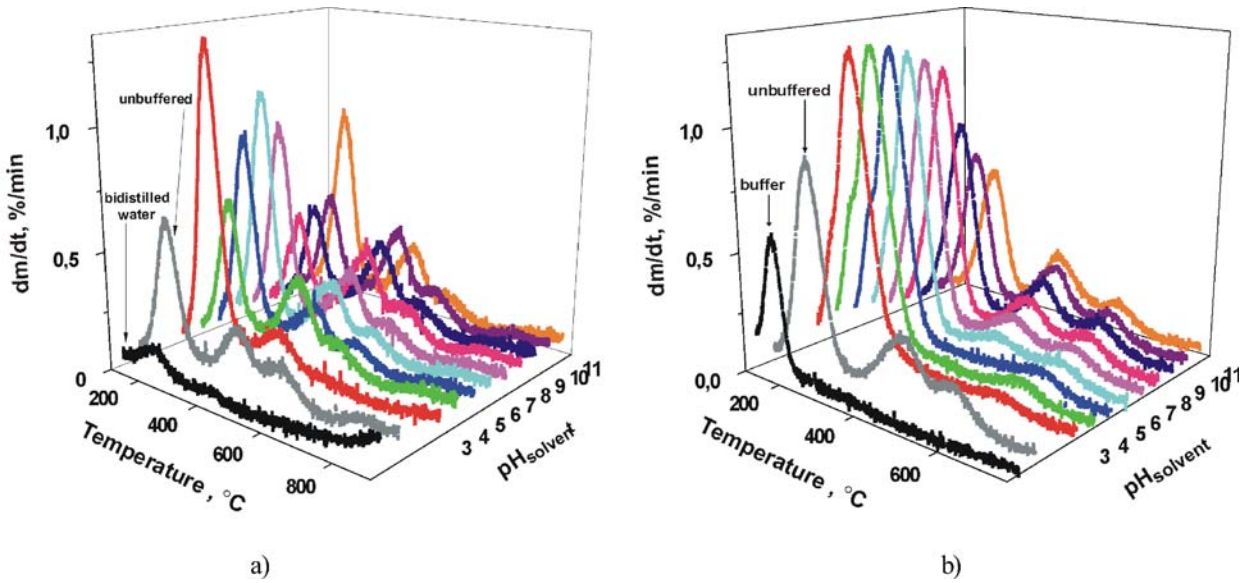

Fig. 4 DTG curves of phenol loaded samples buffered **a** by HCl/NaOH and **b** by BR buffer

tribute to the diffuse electric double layer, the uptake of phenolate ions is reduced with respect to the other sample.

The results from APET and F400 in the BR buffer indicate that the surface functionalities as well as the pore structure affect the pH dependence of the phenol adsorption. In F400 the pore blocking effect is less critical than in the predominantly microporous APET carbon, because wider pores can accommodate a thicker double layer.

When the pH is set with HCl/NaOH, the results in APET reveal no particular trend. It is noteworthy, however, that in the pH range 5–9, where the pH of the aqueous phase in the equilibrium state is practically constant, the adsorption capacity varies. With the BR buffer a well-defined maximum in the adsorption was detected at pH = 8, while a minimum in adsorbed amount was found at pH = 3. On comparing these results it can be concluded that ions present in the aqueous phase, e.g., inorganic salts in wastewater, may significantly influence the pollutant uptake of the carbon adsorbent.

The interaction forces prevailing during the sorption processes were compared by thermal desorption. The position of the peaks in the differential thermogravimetry (DTG) curves, and their integral, are related to the interaction and to the material released in that particular temperature range.

The derivatives of the TG runs in Fig. 4 show that the thermal desorption of phenol depends on pH even more strongly than the adsorption. Three different peak regions can be distinguished, which implies three separate types of interaction. Peak 1, around 210 °C, may be attributed to desorption of physisorbed species. The mass loss at this peak, which is the largest [25], thus also involves physisorbed phenol. The other two peaks above 300 °C belong to chemisorbed phenol. In the buffered samples, peaks 2 and 3 are fully resolved, while in the other sample set peak 3 appears as a shoulder following peak 2. The desorption from carbon itself is significant only in the first peak and is negligible at higher temperatures. Figure 5 shows that, although the positions of the peaks at different pH are practically identical, the results are systematically higher for the buffered samples.

The relative mass loss with respect to the adsorbed phenol is compared in Figs. 5 and 6. In the first set of samples (Fig. 6), the non-monotonic mass loss can be explained by the variable water-content of the sample, because the curve of the total mass loss and that at the first temperature range are similar. The loss in the second stage is twice as high as in the third. The DTG curves of the buffered samples display a systematic change as pH increases, i.e., the buffer stabilizes the chemistry of the surface processes. In the second set of samples (Fig. 7), the mass loss is greatest in peak 1, and it decreases monotonically with increasing pH. The relatively sudden drop in the peak area above the pH_{PZC} may stem from reduced physisorption due to electrostatic repulsion. The second stage, starting only at pH = 6, involves a mass loss of 10–20%, which increases with increasing pH. In the third stage the loss is 5–9%, and the physisorbed and the "chemisorbed" amounts are practically equal at pH = 11.

10–35% of the adsorbed phenol, which remains on the surface as a residue rich in carbon, may modify not only

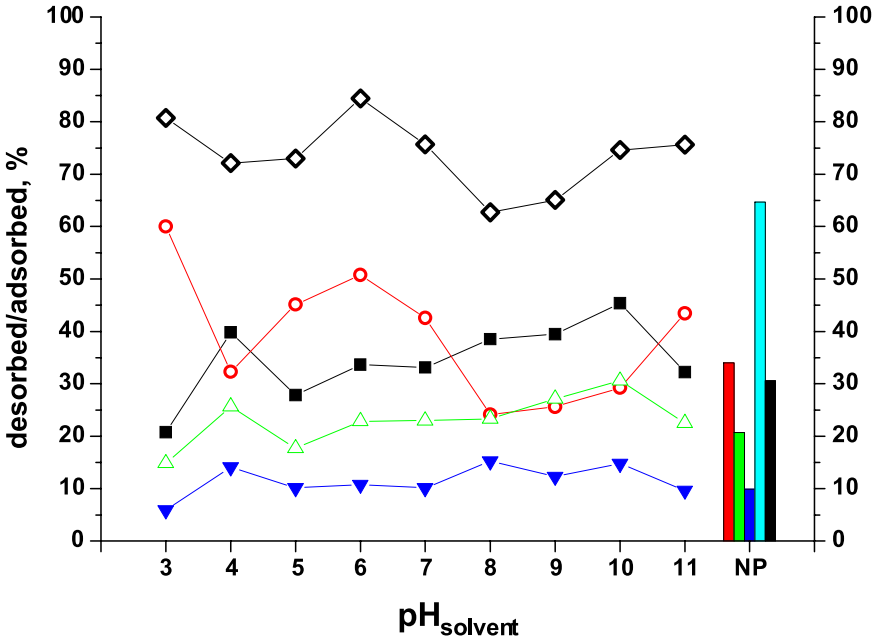

Fig. 6 Relative mass loss of the HCl/NaOH set. The *bar chart* shows the loss in the unbuffered samples. (○) peak 1; (△) peak 2; (▼) peak 3; (◇) total mass loss; (■) total "chemisorbed"

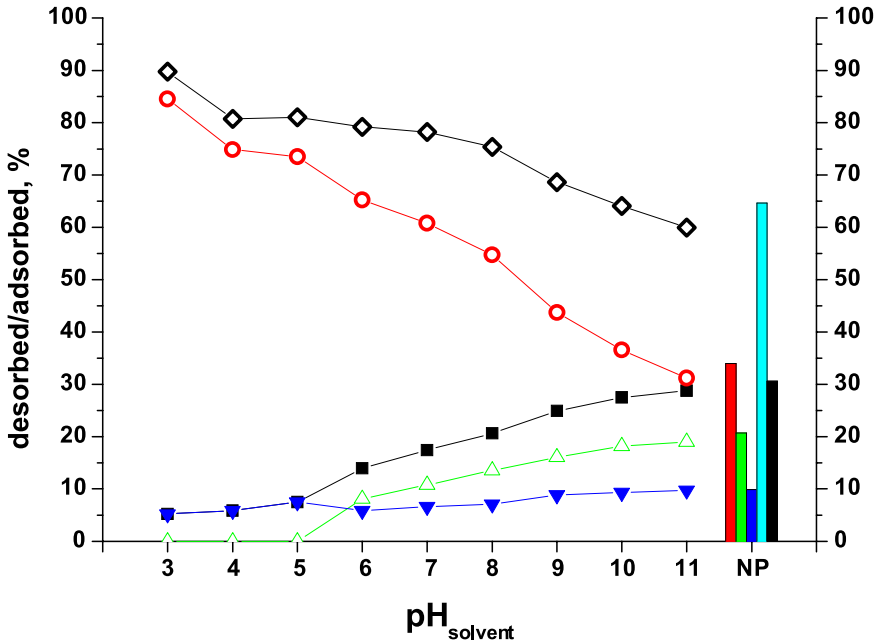

Fig. 7 Relative mass loss in BR-buffered set. *Bar chart* shows the loss in the unbuffered samples. (○) peak 1; (△) peak 2; (▼) peak 3; (◇) total mass loss; (■) total "chemisorbed"

the chemistry but also, by blocking some of the pores, the porosity of the surface [25, 26]. In addition, it can modify the pore size distribution of the carbon.

Conclusions

The method of the setting of the pH and its influence on the sorption behaviour from aqueous phenol on porous carbon surfaces was studied. Results from a predominantly microporous carbon (APET) and from a commercial carbon (F400) designed for wastewater treatment were compared. In unbuffered conditions in both cases only part of the surface area is occupied by phenol, indicative of competition between phenol and water. Since the pH of the solution affects the surface chemistry and the dissociation of the phenol, the adsorption itself is controlled by the pH. When the pH was set with aqueous HCl or NaOH by adding phenol to the system, limited buffer capacity was observed. Setting the pH with BR buffer solution reduced the adsorption capacity owing to enhanced competitive adsorption and pore blocking. When the carbon surface is negatively charged the contribution of the buffer anions to the electric double layer diminishes the phenol uptake. This effect is less critical in the F400 carbon, which, due to its wider pores, can accommodate a thicker double layer.

Thermal desorption of phenol depends on pH even more strongly than adsorption. Even at the highest temperature, a mass equivalent to 10–35% of the adsorbed phenol is retained by the surface as a carbon rich residue. This may modify not only the chemistry but also the pore volume and the pore size distribution of the carbon.

Acknowledgement We extend our thanks to G. Bosznai, P. Kerepesi and E. Tóth for technical assistance. This research was supported by the EU–Hungarian joint fund (GVOP – 3.2.2-2004 – 07-0006/3.0) and the DAAD-MÖB project (#33/2006).

References

1. Leon y Leon CA, Radovic LR (1994) Interfacial Chemistry and Electrochemistry of Carbon Surfaces. In: Thrower PA (Ed.) Chemistry and Physics of Carbon, Vol 24. Marcel Dekker, New York, pp 213–310.
2. Boehm H P (1966) Chemical Identification of Surface Groups. In: Eley DD, Pines H, Weisz PB (eds) Advances in Catalysis, Vol 16. Academic Press, New York, pp 179–274
3. Bismarck A, Wuertz C, Springer J (1999) Carbon 37:1019
4. López-Ramón MV, Stoeckli F, Moreno-Castilla C, Carrasco-Marin F (1999) Carbon 37:1215
5. Papirer E, Li S, Donnet JB (1987) Carbon 25:243
6. Suárez D, Menéndez JA, Fuente E, Montes-Morán MA (1999) Langmuir 15:3897
7. Fabish TJ, Schleifer DE (1984) Carbon 22:19
8. László K, Tombácz E, Novák C (2007) Colloids Surf A 306:95

9. Radovic LR, Moreno-Castilla C, Rivera-Utrilla J (2001) In: Radovic LR (ed) Chemistry and Physics of Carbon, A Series of Advances, Vol 27. Marcel Dekker, New York, pp 227
10. Contescu A, Vass M, Contescu C, Putyera K, Schwarz JA (1998) Carbon 36:247
11. Radovic LR, Moreno-Castilla C, Rivera-Utrilla J (2001) Carbon Materials as Adsorbents in Aqueous Solutions. In: Radovic LR (ed) Chemistry and Physics of Carbon, Vol 27. Marcel Dekker, New York, pp 227–405
12. Dąbrowski A, Podkościelny P, Hubicki Z, Barczak M (2005) Chemosphere 58:1049
13. Moreno-Castilla C (2004) Carbon 42:83
14. Terzyk AP (2004) J Colloid Interface Sci 275:9
15. Coughlin RW, Ezra FS (1968) Environ Sci Technol 2:291
16. Ania CO, Béguin F (2007) Water Res 41:3372
17. László K, Bóta A, Nagy LG (1997) Carbon 35:593
18. Tessmer CH, Vidic RD, Uranowski LJ (1997) Environ Sci Technol 31:1872
19. Newcombe G, Hayes R, Drikas M (1993) Colloids Surf A 78:65
20. Giles C, Mc Ewan T, Nakhwa S, Smith DJ (1960) J Chem Soc 3973
21. Franz M, Arafat HA, Pinto NG (2000) Carbon 38:1807
22. Villacanas F, Pereira MFR, Órfao JJM, Figueiredo JL (2006) J Colloid Interface Sci 293:128
23. Salame II, Bandosz TJ (2003) J Colloid Interface Sci 264:307
24. Terzyk AP (2003) J Colloid Interface Sci 268:301
25. Ania CO, Parra JB, Pevida C, Arenillas A, Rubiera F, Pis JJ (2005) J Anal Appl Pyrolysis 74:518
26. Cooke S, Labes MM (1994) Carbon 32:1055

Progr Colloid Polym Sci (2008) 135: 157–159
DOI 10.1007/2882_2008_118

Published online: 30 August 2008

István Pászli
Katalin F. Csáki
Zoltán Hórvölgyi

On the Magnitude of Line Tension

István Pászli · Katalin F. Csáki (✉)
Laboratory of Colloid and Supramolecular Systems, Institute of Chemistry, Eötvös Loránd University, P.O. Box 32, 1518 Budapest 112, Hungary
e-mail: fcsk@chem.elte.hu

Zoltán Hórvölgyi
Department of Physical Chemistry, Budapest University of Technology and Economics, Budafoki út 6–8, 1111 Budapest 112, Hungary

Abstract It was shown in our analysis of the internal energy determining the state of the capillary system that the magnitude of the intensive and non-canonical line tension depends on the size of the penetrating zone. Therefore, its effect is negligible for macroscopic systems.

Keywords Line tension · Parametric theory · Surface tension · Young equation

Introduction

Investigating the contact lines forms a relevant part of wetting theory research. Contact line analysis can mostly be connected with the analysis of the measurements and the corrections of the Young equation, respectively [1]. However, theoretical problems closely related with capillarity theory – e.g. fundamental relation describing equilibrium – cannot be disregarded. The apparatus of thermostatics containing Gibbs excess quantities contains only the deformation quantities instead of the variables characteristic to the geometry of the system (e.g. volumes, areas of surfaces, etc.). Thus the extensities connected with line length can be interpreted only indirectly. The importance of the practical and theoretical questions being "heavy" in themselves depends on the magnitude of the actual effect caused by the contact line. The extent of the latter is determined by its thermodynamic characteristics – the value of the so-called contact line tension [2]. However there are many kinds of notions – mostly dissimilar – connected with the meaning of this quantity [1–5]. The aim of this study is to encourage the clarification of this question.

Interpretation of Line Tension

Only one collective capillary variable can be interpreted on the basis of thermostatics, namely surface tension according to Bakker [6]. This quantity is determined theoretically by relations with similar algebraic form for each phase boundary layer. The surface tension of the boundary layers of phases ϕ and ψ with thickness τ is

$$\gamma_{\varphi\psi} = \int_{Q_\varphi^0}^{Q^\sigma} \left| u(Q) - u(Q_\varphi^0) \right| \mathrm{d}\tau + \int_{Q^\sigma}^{Q_\psi^0} \left| u(Q) - u(Q_\psi^0) \right| \mathrm{d}\tau \,, \tag{1}$$

where $u(Q)$ is the potential belonging to point Q of the layer, $u(Q_\phi^0)$ and $u(Q_\psi^0)$ are the potentials in the bulk phases, the Q^σ is the point where the value of the expression is minimal.

In this manner the internal point Q of the layer is identical with point $Q = Q^{\sigma}$ corresponding to the arithmetic average of the adjacent phase bulk potentials

$$u(Q^{\sigma}) = \left[\frac{u(Q^0_{\varphi}) + u(Q^0_{\psi})}{2}\right], \tag{2}$$

(the relation expresses the formula of the Stefan's ratio [7]; the tension area according to Gibbs is generated by points Q^{σ} dividing the layer into two "half layers"). Therefore the value of the scalar surface tension depends on both the potential of the bulk phase rounding the layer and the form of the potential curve belonging to the layer. Namely, different values belong to the homogenous part of the layer or – in case of osculating with several phase boundary layers – to the contact region of the common zone. (Therefore the contact line is the union of mutually perturbed surface parts, with width δ_s, length L, and area $\delta_s L$ at each layer.) Therefore each non-self-closing layer consists of two parts; thus the average quantities characteristic to the individual surfaces can be decomposed as well for the sake of simplifying such calculations.

Three-phase contacts can be described by the Young equation; besides homogenous surface parts the system contains a torus-shaped traversing zone as well. The condition of the equilibrium is determined by two types of data expressed by the (differential) Curie equation – on the one hand unperturbed surface tensions $\tilde{\gamma}_s$ and total area A_s of the layers s, on the other hand the sum of the quantities $(\gamma_i - \tilde{\gamma}_i)\delta_i$ and the length of contact line L

$$\sum_s \gamma_s \,\mathrm{d}\, A_s = \sum_s \tilde{\gamma}_s \,\mathrm{d}\, A + \left\{\sum_s (\gamma_s - \tilde{\gamma}_s)\delta_s\right\} \mathrm{d}\, L\,. \tag{3}$$

The scalar, non-canonical quantity denoted in {} arising from the decomposition can be identified as the line tension according to Pethica τ_s [2]. The magnitude of this quantity can be only estimated if a fair estimation can be given for the quantities of the perturbed surface tensions.

The Estimated Magnitude of the Perturbed Line Tensions

The magnitude of the perturbed line tensions cannot be determined based on the traditional theory of capillarity. (Namely: dependence on chemical-material quality is not expressed by their relations.) Conversely, their value can be determined directly by applying the parametric theory – also containing material equations – of surface tension [8, 9].

According to this theory, the potentials $u_{\phi} = u_{\phi}(\ldots {}_{\phi}x_i \left[Q^0_{\phi}\right], \ldots)$ determining surface tension are the functions of the independent fundamental variables ${}_{\phi}x_i\ (y_i, n_{\phi})$ expressing the scaling law of interactions [8]. These functions – together with the universal exponents v_i of individual interactions – determine the substantial parameters

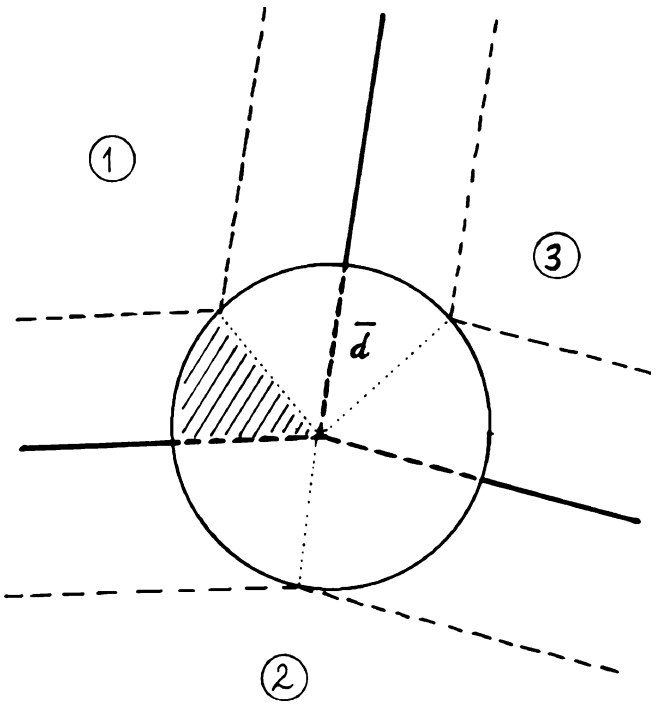

Fig. 1 Section of the three-phased penetrating zone

characteristic to the capillary properties of phases, whose tensor order is the scalar

$$\chi_{\phi}\left(\ldots, {}_{\phi}x_i\left[Q^0_{\phi}\right], \ldots\right) := \prod_i \left|{}_{\phi}x_i\left(Q^0_{\phi}\right)\right|^{v_i} > 0\,. \tag{4}$$

The product

$$\gamma_{\varphi\psi} = \chi_{\varphi}\left(Q^0_{\varphi}\right)\chi_{\psi}\left(Q^0_{\psi}\right), \tag{5}$$

of individual state variables of adjacent phases is the surface tension of the common layer $s_{\phi\psi}$ (thus substantial parameters are the multiplicative components of $\gamma_{\varphi\psi}$). The layer ranges of phases are characterized by the local parameters with different values – in consequence of the potential change due to the perturbation of the adjacent phase. If the parameter χ^{σ} belongs to the Gibbs tension surface of the boundary layer $s_{s\phi}$ with a continuous potential, the contributions of the surface tension of half layers $s_{s\phi(\phi)}$ separated with it will be in the order $\chi_s\chi^{\sigma}$ and $\chi_{\phi}\chi^{\sigma}$, respectively. Their sum will be the total layer quantity $\chi_s\chi_{\phi} = (\chi_s + \chi_{\phi})\chi^{\sigma}$, therefore the tension value of the half layer will be

$$\gamma_{s\phi(\phi)} = \frac{1}{2}\chi_{\phi}\frac{\chi_s\chi_{\phi}}{(1/2)(\chi_s + \chi_{\phi})} = A(\chi_{\phi})H(\chi_s;\, \chi_{\phi})\,, \tag{6}$$

(A and H are the arithmetic and the harmonic mean, respectively, of the argument).

Accordingly, the half layer tensions are changed depending on the quality of the adjacent phase – all this characterizes the different parts of the penetrating zone, the sectional drawing orthogonal to the mid-line is shown in Fig. 1.

To adapt the formula we should consider that each half layer of a phase is perturbed by both the other two phases. (The "average" distance $\overline{d}$ is the radius of the circular section of the torus-shaped penetrating zone because $\overline{d} \approx \delta_1 \approx \delta_2 \approx \delta_3$.) According to Eq. 6 the contribution of the magnitude of the surface tension arising from the presence of the phases 1 and 2, shown by shaded domain in the diagram, is

$$\chi_1^2 \frac{\chi_2}{\chi_1 + \chi_2} \,. \tag{7}$$

Considering the third phase, the contribution becomes

$$\gamma^{(1)} = \chi_1^2 \left(\frac{\chi_2}{\chi_1 + \chi_2} + \frac{\chi_3}{\chi_1 + \chi_3} \right) \,. \tag{8}$$

Since analogous expressions are valid for all sectors, according to the contribution of the summarized perturbation

$$\sum_s \gamma_s' = 2(\gamma_{12} + \gamma_{13} + \gamma_{23}) \,, \tag{9}$$

of the penetrating zone, the line tension is finally

$$\tau_2 \approx (\gamma_{12} + \gamma_{13} + \gamma_{23})\overline{d} \,. \tag{10}$$

It was shown that the expression in the curly bracket in Eq. 3 – line tension – is positive. According to Eq. 10 the magnitude order of the line tension is determined by the radius of the penetration zone. Its experimentally determined value is in order of magnitude 10^{-10} (J/m) [10].

Conclusions

The effect of intensive and non-canonical line tension characteristic to the contact lines of the system usually negligible for macroscopic systems because its magnitude is proportional to the radius of the penetrating zone. Similarly, the effect of tips of crystals and ragged surfaces are negligible as well.

References

1. Rusanov AI (1992) Pure Appl Chem 64(1):111
2. Pethica BA (1961) Rep Prog Appl Chem 46:14
3. Boruvka L, Neumann AW (1977) J Chem Phys 66:5464
4. Xia F, Gray WG, Chen P (2003) J Colloid Interface Sci 261:464
5. Tosev BV, Platikanov D, Sheludko A (1988) Langmuir 4:489
6. Bakker G (1926) Kapillarität und Oberflächenspannung. In: Wien W, Harms F (eds) Handbuch der Experimentalphysik, Bd 6. Akademische Verlagsgesellschaft, Leipzig
7. Stefan J (1886) Wiedemanns Ann Phys Chem 29:655
8. Pászli I (1986) Z Phys Chem (Leipzig) 267(3):433
9. Pászli I, László K (2004) Magy Kém Folyóirat 76:109
10. Pompe T, Herminghaus S (2000) Phys Rev Lett 85:1930

Progr Colloid Polym Sci (2008) 135: 160–162
DOI 10.1007/2882_2008_119

Published online: 11 September 2008

István Pászli
Katalin F. Csáki
János Bódiss

Autophobic Wetting and Captation

István Pászli · Katalin F. Csáki (✉)
Laboratory of Colloid and Supramolecular Systems, Institute of Chemistry, Eötvös Loránd University, P.O. Box 32, 1518 Budapest 112, Hungary
e-mail: fcsk@chem.elte.hu

János Bódiss
Department of Physical Chemistry, Budapest University of Technology and Economics, Budafoki út 6–8, 1111 Budapest, Hungary

Abstract Not all cases of spreading equilibrium can be described by the Young equation. However, assuming that the wetting is achieved in two steps – the equilibrium state is developed not directly on the solid surface but on the liquid film formed on the solid surface – the Young equation perfectly describes this latter state.

Keywords Capitation · Parametric representation · Scaling law · Stick-slip motion · Young equation

Introduction

"Wetability" is a collective property of solid/liquid/vapor systems, which is characterized unambiguously by its contact angle of a fixed value. However, the shapes of contacted phases can vary during the observation period (e.g. methanol firstly completely spreads out on freshly cleaved mica surfaces, then it forms a drop shape – i.e. an equilibrium characterized by finite contact angle $\tilde{\theta}_L$; but it immediately forms an acute contact angle on surfaces having been submerged in methanol vapor [1]). Thus the liquid does not spread out completely even on its own film. It behaves in an "autophobic" manner. The contact angle is determined by the Young equation – although this description of the spreading effects and contact is only a theoretical possibility. In fact, the validity of the expression cannot be checked either, because surface tensions of solid surfaces cannot be determined experimentally. Therefore, the interpretation of autophobia is not possible within the framework of traditional theory.

The aim of studies connected with autophobia – among other things – is to answer the question: How can the Young equation indicate the state which is to be realized in the end? Considering the parametric representation of capillarity the question can probably be clarified.

Characteristic Features of Parametric Representation

The collective variables of phase boundary layers (e.g. surface tension) are necessarily functions of the quantities individually characteristic of the properties of phases. The collective properties of adjacent phases $\phi \in \{\varphi; \psi\}$ are determined by the potentials u_ϕ of the volumetric (e.g. internal) forces. The latter is a function $u_\phi = u_\phi(\ldots {}_\phi x_i\left[Q_\phi^0\right], \ldots)$ of the union of the independent fundamental quantities ${}_\phi x_i(y_i, n_\phi)$ (so-called scaling laws [2, 3]) generated by the canonical intensities of i types of interactions $\{\ldots y_i, \ldots\}$ (e.g. thermal, electromagnetic etc.) and the individual material constants n_ϕ of phases (Q_ϕ^0 is a point of the bulk range of the phase ϕ). The specific substantial parameters

$$\chi_\phi\left(\ldots, {}_\phi x_i\left[Q_\phi^0\right], \ldots\right) := \prod_i \left|{}_\phi x_i\left(Q_\phi^0\right)\right|^{v_i} > 0\,, \qquad (1)$$

of phases being scalar in their tensor order, are determined by the cumulated value of the fundamental variables and the universal exponents v_i of the individual interactions. The product of the individual state variables of adjacent phases

$$\gamma_{\varphi\psi} = \chi_\varphi \left(Q_\varphi^0\right) \chi_\psi \left(Q_\psi^0\right) , \tag{2}$$

is the surface tension of the common layer $s_{\varphi\psi}$. According to the transformation formula, the substantial parameters are the multiplicative components of $\gamma_{\varphi\psi}$.

The phases of equilibrium pairs are characterized by global individual parameters in total volume depending on the state of bulk ranges enclosed by surfaces.

Their apparatus provides for the determination of the quantities of solid surfaces as well.

Interpretation of Autophobia

The shapes of the equilibrium phases can be expressed by parameters – i.e. individual variables. The Young equation is the bilinear relation of the actual parameters in its individual representation

$$\tilde{\chi}_\mathrm{S}(\tilde{\chi}_\mathrm{V} - \tilde{\chi}_\mathrm{L}) = \tilde{\chi}_\mathrm{L}\tilde{\chi}_\mathrm{V} \cos\tilde{\theta}_\mathrm{L}. \tag{3}$$

The conditions of spreading can be obtained from this expression by rearranging. For example – according to the equation derived from the former – complete spreading can occur only based on the covariant relation, when the inequality

$$\chi_\mathrm{S} \geq \chi_\mathrm{s}^{\otimes} = \left(\frac{1}{|(1/\chi_\mathrm{V}^0) - (1/\chi_\mathrm{L}^0)|}\right) \tag{4}$$

is valid for subphases (the index ^{0} denotes phases with constant composition). The condition is satisfied directly for mercury (its parameters are $\chi_\mathrm{L} = \{53.9\}$, $\chi_\mathrm{V} = \{9.1\}$ in $(\mathrm{mN/m})^{1/2}$ unit [4]), indeed, on its surface most liquids completely spread out. However, partial spreading is achieved in stationary state for systems with "pure" water (beside the quantities $\chi_\mathrm{L} = \{7.16\}$, $\chi_\mathrm{V} = \{10.1\}$ given in the former unit); whereas they form an acute contact angle on glass surfaces (as expected) but an obtuse angle on Teflon surfaces. Thus, the equilibrium arrangement is not always shaped according to the respective parameters of phases.

Completely and partially spread states of solid/liquid/vapor systems cannot be interpreted by single-valued parameters.

In the parametric theory the quantities of phases can be reversed (so-called reversal transformation) – corresponding to the principle of minimum energy. Thus, the equilibrium can be achieved by reversed parameters as well – in a so-called reversal state. In this manner – besides the ordinate state – reversal states (*LV*) or (*SL*) or (*SV*) can exist as well, corresponding to the reversed parameters (at the state (*LV*) fluid parameters are reversed in the relations, the latter are characterized by the actual parameters $\tilde{\chi}_\mathrm{V} = \chi_\mathrm{L}$ or $\tilde{\chi}_\mathrm{L} = \chi_\mathrm{V}^0$, or $\tilde{\chi}_\mathrm{S} = \chi_\mathrm{s}(\chi_\mathrm{L}/\chi_\mathrm{S}) \equiv \chi_\mathrm{L}$ or $\tilde{\chi}_\mathrm{L} = \chi_\mathrm{L}(\chi_\mathrm{S}/\chi_\mathrm{L}) = \chi_\mathrm{L}(\chi_\mathrm{L}^0/\chi_\mathrm{L}) \equiv \chi_\mathrm{L}^0$). On one hand, only obtuse angles can be assigned to aqueous systems in reversed state (*LV*), on the other hand the reversed states (*SL*) and (*SV*) are characterized in turn by the expressions

$$\cos\theta_\mathrm{L}^{(\mathrm{SL})} = \frac{1}{\gamma_\mathrm{LV}^\mathrm{ord}} \frac{\chi_\mathrm{L}}{\chi_\mathrm{V}} \left(\frac{\chi_\mathrm{L}}{\chi_\mathrm{S}} [\chi_\mathrm{V}]^2 - \gamma_\mathrm{LV}^\mathrm{ord}\right) \tag{5}$$

$$\cos\theta_\mathrm{L}^{(\mathrm{SV})} = \frac{1}{\gamma_\mathrm{LV}^\mathrm{ord}} \frac{\chi_\mathrm{V}}{\chi_\mathrm{S}} \left(\frac{\chi_\mathrm{S}}{\chi_\mathrm{V}} [\chi_\mathrm{V}]^2 - \gamma_\mathrm{LV}^\mathrm{ord}\right) , \tag{6}$$

being non-covariant (i.e. describing non-existing systems) according to its algebraic form.

However, the Young equation does not ensure an acute contact angle in equilibrium for an arbitrarily chosen system – not even in the case of reversed parameters.

Nevertheless, a new phase collective can be formed from input phases before partial spreading. A strongly bounded layer of varying thickness – a so-called captured film – can be formed on the surface of the subphase from liquids producing either a pure or a mixture phase. (Experiments prove that from cyclohexane–ethanol mixture a cluster consisting of pure ethanol can build up on silica surfaces [6]). The captation is achieved by phase segregation – theoretically according to the Gibbs' phase rule. Accordingly, the parameter χ_L^0 belongs to the enveloping surface of the captured layer as well. Thus the remaining (non-captured) liquid spreads out on this layer – instead of the solid surface. Therefore χ_S should be replaced by χ_L^0 in the Young equation.

Instead of a solid subphase the system contains a "captured phase" of an identical shape which consists of a liquid. The captation system of two states (captured and "free") containing liquid too, is at this point characterized by the parameters $\{\chi_\mathrm{L}, \chi_\mathrm{L}, \chi_\mathrm{V}\}$ – i.e. the quantities of an other phase collective instead of the parameters $\{\chi_\mathrm{S}, \chi_\mathrm{L}, \chi_\mathrm{V}\}$ of the input system. Accordingly, equilibrium state can be achieved – lacking other possibilities – only indirectly by consecutive processes. Special relations are applied for the system because respective equations $\chi_\mathrm{S} \equiv \chi_\mathrm{L}$ and $\chi_\mathrm{S} \equiv \chi_\mathrm{V}$, are valid for the parameters. However, the equations determine exactly the relations of the reversed states (*SL*) and (*SV*), which are now covariant owing to the replacement. These equations can be identified with the relations concerning the unit slope of the ordinary state. Thus in the case of captation the equilibrium of the aqueous systems in the domain of total surface tension is achieved with an acute contact angle according

to the relations

$$\cos\theta_{\mathrm{L}}^{\mathrm{ord}} = \gamma_{\mathrm{LV}}\left([1/\gamma_{\mathrm{LV}}] - \left[1/\left\{\chi_{\mathrm{V}}^{0}\right\}^{2}\right]\right) \tag{7}$$

$$\cos\theta_{\mathrm{L}}^{(\mathrm{SL})} = \gamma_{\mathrm{LV}}\left([1/\gamma_{\mathrm{LV}}] - \left[1/\left\{\chi_{\mathrm{V}}^{0}\right\}^{2}\right]\right)\ , \tag{8}$$

being identical for both ordinary and reversed (*SV*) states.

The special state – besides aqueous systems – can be achieved for other fluid pairs as well; and it is not impossible that the contact angle hysteresis is connected with the forming of a captured film. Spreading can be interpreted by the assumption of consecutive processes – forming a liquid film on a solid surface, followed by partial wetting. According to the assumed mechanism, special effects can be explained as well.

The presence of the captured film originating from adsorption – during a gradual immersion into a liquid – has an influence on the spreading mechanism which manifests in the stick-slip advancement of the three-phase contact line [7, 8]. The autophobic wetting of the surface takes place in a "regular" manner according to the modification of the parameter alongside the surface following the movement.

The adequacy of the former interpretation based on captation can be proved also by the theorems of thermostatics.

Conclusions

The equilibrium of spreading can be achieved not only directly but also indirectly (in consecutive steps). Autophobia is connected with the latter effect. Partial spreading is direct, if the contact is formed immediately, in one step. In the case of indirect spreading first a captured layer is achieved on the surface, i.e. the liquid spreads out completely, and then the remaining liquid – in reversed state (SL) – partially spreads out on the film (systems containing two liquids are determined by analogous relations). During the autophobic wetting the system changes compared to its original one – the solid phase is only a carrier of the captured film.

References

1. Bangham DH, Mosallam F, Saweris Z (1937) Nature 140:237
2. Pászli I, László K (2006) Magy Kém Folyóirat 112(1):25
3. Pászli I, László K (2004) Colloid Polym Sci 282:243
4. Pászli I (1986) Z Phys Chem (Leipzig) 267:3
5. Pászli I (1987) Die Parameter-Theorie der Kapillarität (33. Hauptversammlung der Kolloid-Gesellschaft, Graz) Abst. PAS 1–3
6. Mizukami M, Kurihara K (2000) Chem Lett 29(3):256
7. Kwok D, Neumann AW (1999) Adv Colloid Interf Sci 81:167
8. Tavana H, Neumann AW (2007) Adv Colloid Interf Sci 132:1

Progr Colloid Polym Sci (2008) 135: 163–168
DOI 10.1007/2882_2008_101

Published online: 11 September 2008

Roman Maršálek
Boleslav Taraba

Adsorption of the SDS on Coal

Roman Maršálek (✉) · Boleslav Taraba
Department of Chemistry, Ostrava University, 30.dubna 22, 70103 Ostrava 1, Czech Republic
e-mail: roman.marsalek@osu.cz

Abstract Simultaneous measurements of the sodium dodecyl sulphate (SDS) adsorption on coal and zeta potential determination of the (adsorption) suspensions were carried out. Three samples of sub-bituminous, bituminous and oxidative altered bituminous coal were investigated. The adsorption isotherms were found to be of typical Langmuir type, values of the SDS adsorption capacities have been calculated. Shape of the adsorption isotherms was correlated with zeta potential values of the suspensions in (adsorption) equilibrium. The results indicate that adsorption of SDS on coal is going mainly through hydrophobic interactions between the surfactant molecules and the coal surface.

Keywords Adsorption of SDS · Carbons · Zeta potential

Introduction

Surfactants are used widely in many industrial and commercial products and processes over the world. For example, surfactants are in demand for industrial processes requiring colloid stability, metal treatment, mineral flotation, oil production, emulsion polymerization, pesticides, pharmaceutical formulation. The application of surfactants can produce environmental pollution and raises a series of problems for wastewater treatment plants [1].

Several materials have been investigated as surfactant adsorbents. Different adsorption mechanisms and models have been proposed, depending on the adsorbent-adsorbate system. Below the critical micelle concentration, ionic surfactants behave as a single amphiphilic ions that can be retained on the adsorbent through hydrophobic interactions, by their hydrocarbon coil, or through electrical forces, by their ionic groups. The predominance of one kind of interaction adsorbent ionic surfactant in the adsorption process is determined by the surface characteristic of the adsorbent. Various techniques were used for description of surfactant adsorption on the carbonaceous materials, e.g. calorimetry, contact angle, electrophoresis [2–5].

The carbon matrix contains oxygen, nitrogen, phosphorus and/or sulfur. Oxygen is an important element that can form surface functional groups. Many different oxygenated species can be found on the surface of carbonaceous materials. Some of them are of the acidic quality (phenolic hydroxyl, carboxyl, anhydrides or lactones) and have cationic exchange properties. Basic surface oxides are always present on carbon surfaces (e.g. γ-pyrone-like structure). The π-electron system of graphene layers is also basic enough to bind protons from solutions. The presence and concentration of surface functional groups affect the relative hydrophobicity of carbonaceous materials and play important role in influencing the adsorption capacity and the mechanism of the adsorption process [2, 6].

The zeta potential is one of the few effective techniques for characterization of surface chemical properties of carbonaceous materials in solution. The zeta potential values correspond to the quantity and quality of functional groups on the surface [7]. The aim of this work is to carry out zeta potential measurement for the adsorption of sodium dodecyl sulphate (SDS) from aqueous solutions onto coal and to describe the impact of oxygen content on it.

Experimental

Materials and Methods

Coal Samples. Three different coal samples were investigated: the bituminous coal (denoted as BC), the bituminous oxidative altered coal (BO) and the sub-bituminous coal (SB). The elemental compositions and the proximate analysis data of the studied samples are shown in Table 1.

Various techniques were used for texture and structure characterization of coal samples.

Characterization of Surface. Adsorption isotherms of nitrogen at −196 °C and carbon dioxide at 25 °C were measured.

Surface areas of the samples from adsorption isotherms of nitrogen (S_{BET}) were evaluated according to the BET theory, using a molecular area of 0.162 nm^2 for the calculation.

For adsorption isotherms of carbon dioxide, the Medek's equation was applied to the evaluation of micropores surface area (S_{micro}, Medek 1977).

Dubinin–Radushkevich theory was used for calculation of the micropores volume (V_{micro}).

To estimate hydrophilic/hydrophobic character of the coal surfaces, enthalpies of the immersion of the dried samples with water, H^{im}, were determined at 30 °C using a SETARAM C80 calorimeter provided with a mixing cell.

Equilibrium amount of the coal moisture content (W^{eq}) was measured at laboratory temperature and relative humidity of air ≈ 60%. The W^{eq} values can be related to the abundance of the hydrophilic sites on coal surface.

Infrared Spectroscopy. Diffuse reflectance infrared Fourier transform (DRIFT) spectra of the samples were measured by Nicolet 7600 FTIR spectrometer (Thermo Nicolet Instruments Co., Madison, USA). Each spectrum averaged 512 scans per sample and all of them were recorded with the resolution of 2 cm^{-1}. Two ratios were calculated for characterization of coal structure I_{al} ($I_{2920}/(I_{2920}+I_{1610})$) and I_{CO} ($I_{1725}/(I_{1725}+I_{1610})$).

Index I_{al} denotes the existence of aliphatic carbohydrates in coal structure. Index was determined as a ratio between integrated areas of the aliphatic C–H bands (2920 cm^{-1}) and areas of both aromatic and aliphatic C=C absorption bands (1600 cm^{-1}).

Index I_{CO} denotes the existence of carbonyl function groups in coal structure. It was determined as a ratio between integrated areas of the carbonyl groups (1700 cm^{-1}) and areas of carbonyl groups and aromatic C=C absorption bands (1600 cm^{-1}).

Solid-state ^{13}C CP/NMR Spectroscopy. ^{13}C CP/MAS NMR spectra of the samples were measured by Bruker Avance 500 WB/US (Karlsruhe, Germany, 2003) at 125 MHz frequency. Samples rotated below magnetic angle. Glycin was used as an external standard. For quantitative evaluation, carbon aromaticity, f_A, was determined as a ratio between content of carbon in aromatic part of structure and total amount of carbon. Results are summarized in Table 2.

Surfactant Adsorption. The coal samples were diminished and sieved to a particle size smaller than 32 μm. For each sample, 0.05 g of coal was weighed in the flask and 50 ml of an SDS solution of known concentration was added. Flasks

Table 1 Proximate and ultimate analyses of samples

Sample	Ash^{dry} (%)	VM^{daf} (%)	C^{daf} (%)	H^{daf} (%)	N^{daf} (%)	O^{daf} (%)	S^{dry}_{total} (%)
BC	6.6	35.3	85.6	5.4	1.1	6.5	1.2
SB	22.7	55.6	71.9	6.4	1.0	20.5	1.2
BO	11.5	31.2	76.6	4.1	1.8	17.5	2.4

VM – volatile matter content

Table 2 Texture and structure parameters of samples

Sample	S_{BET} m^2/g	S_{micro} m^2/g	V_{micro} cm^3/g	$H^{im}_{(H_2O)}$ J/g	$W^{eq}_{(60\%)}$ %	I_{CO}	$I_{C-H_{alip}}$ f_A	Aromaticity
BC	1.5	133	0.049	2.7 ± 0.3	2.7	0.05	0.30	0.68
SB	49	152	0.055	26.5 ± 1.5	12.5	0.26	0.36	0.50
BO	1.5	235 ± 15	0.084	81 ± 2	14.3	0.27	0.05	0.96

were occasionally shaken. The time needed to reach equilibrium was 24 h, as determined in previous experiments. The zeta potential of samples was measured. Then, the coal sample was removed by filtering through paper filter.

The amount of SDS adsorbed (a) was determined from the change in the solution concentration before and after equilibrium, according to:

$$a = \frac{(c_0 - c_e)V}{m}, \quad (1)$$

where c_0 is the initial concentration of SDS solution, c_e the concentration of SDS solution at the adsorption equilibrium, V the volume of SDS solution and m the mass of the coal.

The SDS concentration of the filtered solutions was determined by UV/VIS spectrophotometry using colored complex of SDS with methylene blue extracted with chloroform. Critical micelle concentration of SDS (8.5 mmol/l) was determined by conductivity measurement.

Zeta Potential Measurements. Zeta potential measurements was performed by analyzing 0.05 g of coal in 50 ml of the Britton–Robinson buffer (or in the SDS solution) using the Coulter Delsa 440 SX (Coulter Electronic, USA). Delsa 440 SX uses the scattering effect of Doppler light to determine the electrophoretic mobility. The zeta potential was obtained from the electrophoretic mobility by the Smoluchowski equation:

$$\zeta = \frac{\mu\eta}{\varepsilon}, \quad (2)$$

ζ is the zeta potential (V), η represents dynamic viscosity (Pa s), and ε_0 stands for the dielectric constant. The fixed conditions of measuring were the following ones: temperature (298 K), electric field (15 V), frequency (500 Hz), and the properties of the samples – viscosity ($0.0089\ \mathrm{kg\,m^{-1}\,s^{-1}}$), refraction index (1.333), and dielectric constant (78.36).

The pH of the solution was measured using a combination of a single-junction pH electrode with an Ag/AgCl reference cell (LP Prague, model MS 22 pH meter).The samples were sonicated for 1 min before the analysis. All zeta potential measurement was at least duplicated; the mean relative standard deviation of the values reported usually did not exceed 5%. All the solutions were made in distilled water. Analytical grade chemicals were used.

Results and Discussion

Characterization of the Samples

Results (see Tables 1 and 2) indicate differences between study samples.

Sample BC represents typical bituminous coal. Its proximate and ultimate compositions as well as values of texture parameters correspond to the degree of coalification. Both surface area and concentration of polar sites of the coal are of the lowest value from the samples to be studied.

Sample SB represents low-rank coal and sample BO represents oxidative altered bituminous coal. The oxygen content in both coals is very similar as well as amount of carbonyl groups as deduced from infrared spectroscopy (Tables 1 and 2). Values of equilibrium moisture content $W^{eq}_{(60\%)}$ are comparable too. These facts confirm hydrophilic character of the coal surfaces, comprising mainly oxygen functional groups. Carbon content of SB and BO samples is similar too, however, there are significant differences in carbon aromaticity (see Table 2). Coal BO demonstrates mainly aromatic structure, while the SB sample is approximately of the same proportion between aromatic and aliphatic parts.

Values of S_{BET} and S_{mikro} indicate differences in pores system of coals. Low-rank coal SB contains mainly mesopores, on the contrary, oxidative altered coal BO includes mainly micropores. The value of immersions enthalpie is three times higher for sample BO in comparison with sample SB. Possible explanation (respecting quite comparable content of oxygen) can be find in higher volume of micropores in coal BO.

As a result, samples of oxidative altered coal BO and low-rank coal SB are obviously hydrophilic in character.

The Zeta Potential of Coals – Influence of the pH

Dependence of pH on the zeta potential of the samples is shown on Fig. 1.

From the Fig. 1, more negative values of the zeta potential are generally obvious with increasing pH level. Also, more negative values of zeta potential with increasing content of oxygen of the coal can be deduced. (cf. Table 1).

The isoelectric point is about at pH = 3.5 and pH = 1, for bituminous coal (BC) and oxidative altered coal (BO), respectively. Concerning sub-bituminous coal (SB), the pH value of the isoelectric point < 1 and could not be determined. These results correspond well with known facts about floatability of coals [8]. When hydroxyl (OH^-) ions are added to the flotation pulp, the coal surface becomes more negative. On the contrary, when the pH of the water-coal suspension decreases, the hydronium (H_3O^+) ions are adsorbed until the negative charge is neutralized. The flotation ability decreases for highly acidic or highly basic pulps. In general, the flotation of coals shows an optimum near the electrically neutral point known as the isoelectric point [9].

Adsorption of SDS onto Coals

Figure 2 depicts typical adsorption isotherms obtained from the experimental data. The shape of isotherms indicates that the adsorption data could be well fitted by

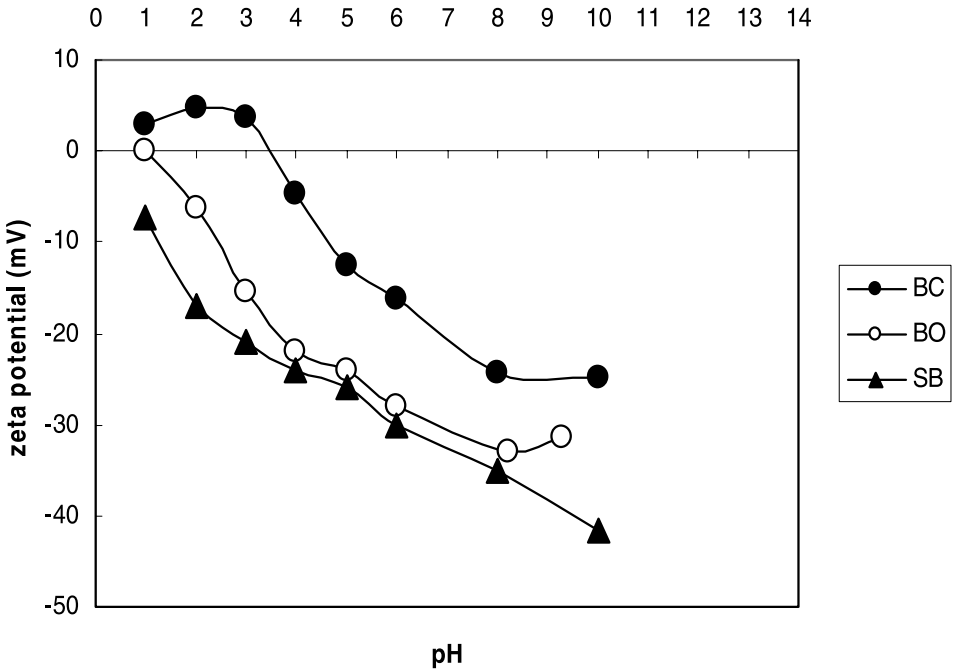

Fig. 1 Zeta potential of coal samples as a function of pH

the Langmuir adsorption model of monolayer coverage. In a linear form, the Langmuir equation is given by

$$\frac{c_e}{a} = \frac{c_e}{a_m} + \frac{1}{a_m b}, \tag{3}$$

where a is the amount of SDS adsorbed, c_e is an equilibrium concentration of SDS in solution, b represents a monolayer binding constant and a_m is the monolayer adsorption capacity.

All adsorption isotherms proved to be consistent with the Langmuir model as deduced from calculated r-square values close to 1. The most informative parameter in the Langmuir equation is a_m, providing information on adsorbed amount at monolayer surface coverage. These values are compiled in Table 3 as found for studied samples.

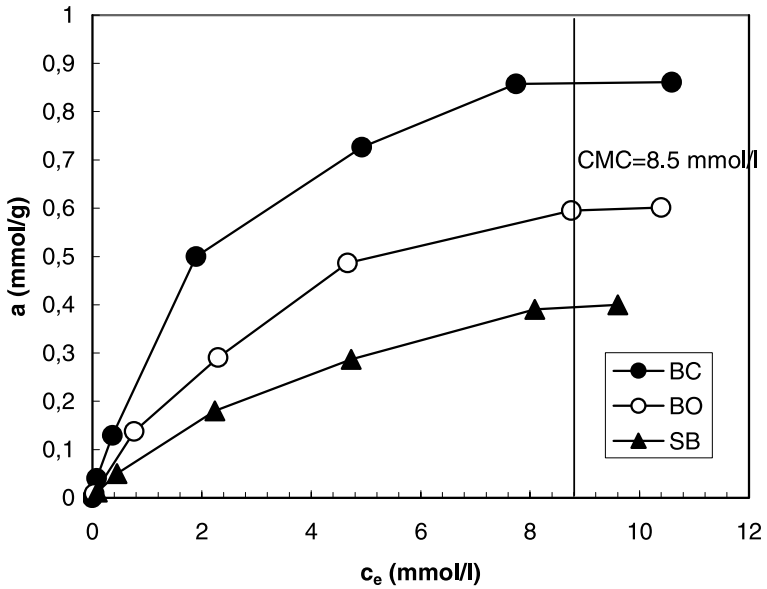

Fig. 2 Surfactant adsorption isotherms on coal

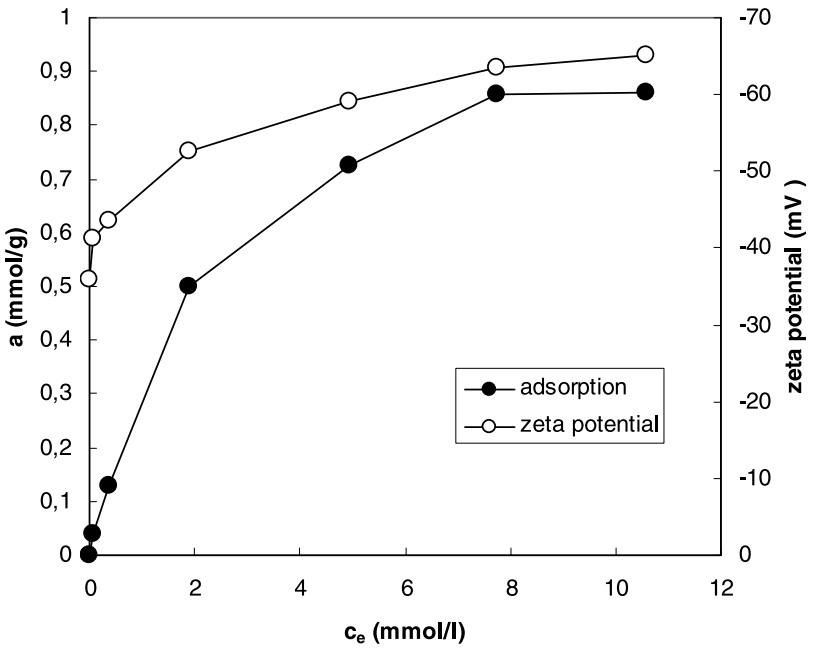

Fig. 3 Dependence of zeta potential (*white circles*) and adsorption of SDS, *a* (*black circles*), on bituminous coal (BC) with the equilibrium concentration of the surfactant solution (c_e)

Table 3 Langmuir data obtain from adsorption measurement

Sample	a_m (mmol/g)	b	r^2	Langmuir equation
BC	1.07	0.50	0.99	$a = \frac{0.53c_e}{1+0.50c_e}$
SB	0.61	0.07	0.99	$a = \frac{0.05c_e}{1+0.07c_e}$
BO	0.83	0.19	0.99	$a = \frac{0.15c_e}{1+0.19c_e}$

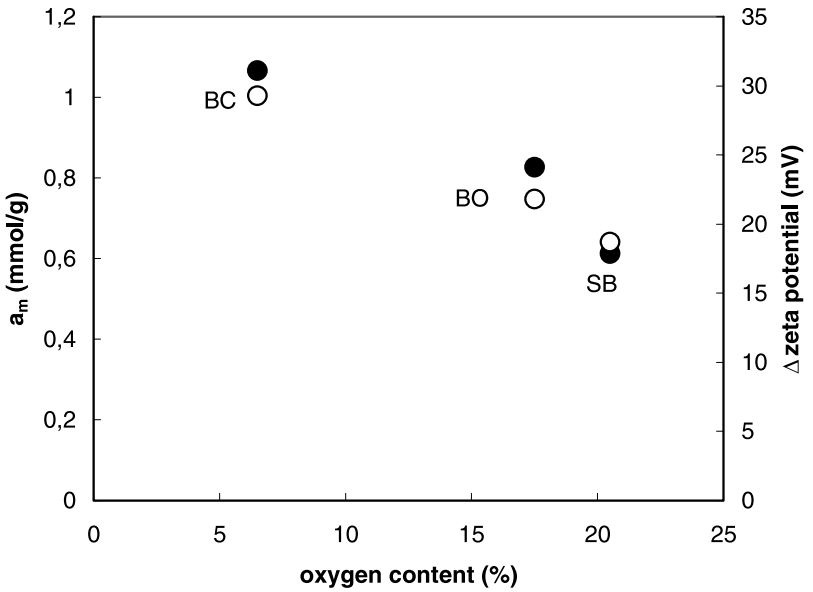

Fig. 4 Dependence of zeta potential change – absolute value (*white circles*) and adsorption capacity of SDS, a_m (*black circles*), on coals with the equilibrium concentration of the surfactant solution c_e

Modification of surface characteristics of solids using surfactants has practical implications in industrial and environmental applications, coal processing being one of them. Surfactants are added during the flotation process to increase productivity. Surfactants can change the surface properties of the coal grains. Generally, surfactants have hydrophilic (head) and hydrophobic (tail) parts and the question is which of them creates the connection with the surface of the coal grain. Hydrophilic adsorption of surfactants was found in three Australian coals [3]. However, measurements of the zeta potential of active coal and carbon blacks in the presence of surfactants led to the idea that the interactions are mainly of hydrophobic character [2, 10]. Such a type of the interactions was also supported by calorimetric measurements of natural and activated coals [11].

The following findings can be deduced from experimental data:

1. Addition of the anionic surfactant (SDS) affects the value of ξ-potential, making the zeta potential values more negative (Fig. 3);
2. There is no marked change in adsorbed amount of SDS at concentrations exceeding level of the critical micelle concentration (CMC, Fig. 2);
3. The most significant change of the ξ-potential in the presence of SDS was observed for bituminous coal (BC, Fig. 4), i.e. for sample of the most hydrophobic surface;
4. There is relationship between oxygen content of the coal, its adsorption capacity for SDS and change in the zeta potential of (adsorption) suspension (Fig. 4). Decrease in oxygen content (= increase in hydrophobicity) of the coal leads to the *increase* in its adsorption capacity for SDS, the adsorption being accompanied by the most significant changes in the zeta potential values of the suspensions.

Conclusions

Adsorption of anionic surfactant (SDS) on coal samples was confirmed to exhibit typical Langmuir-type behavior. From the zeta potential measurements as well as from surface characteristics of the coals, sorption mechanism of SDS on coal surface was deduced to be connected mainly with interactions between hydrophobic tail of surfactant and coal surface.

Acknowledgement Our work was supported by Czech Science Foundation (105/07/P041) and Ministry of Industry and Trade of the Czech Republic (2A-1TP1/083).

References

1. Wu HS, Pendleton P (2001) J Colloid Interf Sci 243:306
2. Gallardo-Moreno AM, Gonzáles-Garcia CM, González-Martín M, Bruque JM (2004) Colloid Surf 249:57
3. Crawford RJ, Mainwaring DE (2001) Fuel 80:313
4. Mishra SK, Kanungo SB, Rajeev J (2003) Colloid Interf Sci 267:42
5. Singh BP (1999) Fuel 78:501
6. Boehm HP (1994) Carbon 32:759
7. Wu SF, Yanagisawa K, Nishizawa T (2001) Carbon 39:1537
8. Bolat E, Saglam S, Pskin S (1998) Fuel Process Technol 55:101
9. Sarikaya M, Ozbayoglu G (1995) Fuel 74:291
10. Basar CA (2003) Appl Surf Sci 1–4:218
11. Taraba B, Kula P, Gúcka M (2001) International Slovak and Czech calorimetric seminar. pp 49–50

Progr Colloid Polym Sci (2008) 135: 169–173
DOI 10.1007/2882_2008_109

Published online: 9 September 2008

M. Kolsofszki
Á. Karsai
K. Soós
B. Penke
M.S.Z. Kellermayer

Thermally-Induced Effects in Oriented Network of Amyloid β25–35 fibrils

M. Kolsofszki · Á. Karsai · M.S.Z. Kellermayer (✉)
Department of Biophysics, University of Pécs, Faculty of Medicine, Szigeti u. 12, 7624 Pécs, Hungary
e-mail: miklos.kellermayer.jr@aok.pte.hu

K. Soós
Department of Medical Chemistry, University of Szeged, Dóm tér 8, 6720 Szeged, Hungary

B. Penke
Supramolecular and Nanostructured Materials Research Group of the Hungarian Academy of Sciences, Dóm tér 8, 6720 Szeged, Hungary

Abstract Amyloid fibrils are filamentous protein deposits in the extracellular space of various tissues in neurodegenerative and protein misfolding diseases. They may be used in nanotechnology applications because of their self-assembly properties and stability. Recently we have shown that amyloid beta 25–35 (Aβ25–35) forms a highly oriented, K^+-dependent network on mica, and its mutant form (Aβ25–35_N27C) may be chemically addressed for functionalization in dedicated applications. In the present work we investigated thermally-induced changes in the morphology of the oriented Aβ25–35 fibril network. The fibrils maintained a high orientation stability in the temperature range of 30–70 °C, suggesting that orientational rearrangement of Aβ25–35 fibrils on mica is an unfavorable process. Above ~ 45 °C a gradual decrease in fibril length and dissociation from the surface could be observed. Furthermore, at high temperatures (45–70 °C) the average fibril thickness increased, indicating changes in the underlying structure or structural dynamics. Possibly, a thermally induced transition in the Aβ25–35 peptide around 45 °C leads to structural changes in the fibril as well. The temperature-dependent changes need to be considered in the use of amyloid fibrils in nanotechnology applications.

Keywords Amyloid fibril · Atomic force microscopy · Heat stability · Intrafibrillar interactions · Structural transition

Introduction

Amyloid fibrils are nanoscale proteinaceous filaments found in extracellular tissue deposits accumulated in various degenerative disorders [1–4]. Amyloid peptides have been suggested to self-assemble into specific nanostructures such as nanosensors and conductive nanowires [5–8]. A special advantage of amyloid peptides is that variants suitable for a particular application may be generated by chemical [9] or biotechnological methods [8]. Once the fibrils are formed, they possess high stability under relatively harsh physical and chemical conditions. For nanotechnology applications, well-controlled orientation and growth of the fibrils would be desired in addition. Recently we have shown that amyloid β25–35 (Aβ25–35), a toxic fragment of Alzheimer's beta peptide, forms trigonally oriented fibrils on mica [10]. Oriented binding depends on an apparently cooperative interaction of a positively-charged moiety on the Aβ25–35 peptide with the K^+-binding pocket of the mica lattice. The formation of oriented fibrils is the result of epitaxial polymerization [11], and the growth rate and the mesh size of the oriented amyloid fibril network can be tuned by varying the K^+ concentration. In principle, such a fibril network may be used in nanotechnology applications, provided that a specific chemical labeling of the fibrils is available. We have also

demonstrated that Aβ25–35_N27C, in which Asp27 of the wild-type peptide was replaced with cysteine that carries a reactive sulfhydryl side chain, forms epitaxially growing fibrils on mica which evolve into a trigonally oriented branched network [12]. The oriented network of Aβ25–35_N27C fibrils could be specifically labeled and used for constructing nanobiotechnological devices. Because of the potential applicability of the oriented Aβ25–35 network, a detailed characterization of its physical and chemical properties is necessary.

In the present work we investigated, under aqueous buffer conditions, the effect of increasing temperatures on the morphology and structure of Aβ25–35 fibril network formed on mica. The fibrils displayed a pronounced orientation stability across the investigated temperature range (30–70 °C). Above ~ 45 °C, fibril length became reduced, fibrils gradually dissociated from the surface, and, interestingly, their average thickness became increased. The changes are most likely related to thermally-induced structural changes which are manifested in altered intrafibrillar and fibril-surface interactions.

Materials and Methods

Sample Preparation

Aβ25–35 (^{25}GSNKGAIIGLM^{35}-amide) peptide was produced by solid-state synthesis as documented previously [9]. Lyophilized peptides were dissolved in DMSO (50.0 mg/ml) and diluted in 10 mM potassium phosphate buffer ("PBSA", 10 mM K_2HPO_4/KH_2PO_4, pH 7.4, 140 mM NaCl, 0.02% NaN_3) to a final concentration ranging between 0.5 and 2 mg/ml. 20 µl aliquots of such samples were stored at −80 °C for later use. Peptide concentration was measured with the quantitative bicinchoninic acid assay [13].

Atomic Force Microscopy

A 150 µl sample of Aβ25–35, diluted typically 200–300-fold in PBSA buffer, was applied to freshly cleaved mica surface. We used high-grade mica sheets (V2 grade, #52-6, Ted Pella, Inc., Redding, CA) attached to the bottom of the closed fluid chamber of the BioHeater module of our AFM instrument (MFP3D, AsylumResearch, Santa Barbara, CA). After 10 min of incubation at room temperature, the surface was washed gently with PBSA buffer to remove unbound fibrils. The fluid chamber was then filled with 2 ml PBSA buffer so as to fill it completely. Non-contact mode AFM images were acquired using silicon-nitride cantilevers (Olympus BioLever, typical resonance frequency in buffer 9 kHz). 512 × 512-pixel images were collected at a typical scanning frequency of 1 Hz and with a high set point (0.8–1 V). The temperature of the closed fluid chamber was adjusted with close-loop control in 5 °C steps between 30–70 °C.

Image Processing and Data Analysis

AFM images were analyzed using algorithms built in to the MFP3D driving software. Fibril length was measured from the surface topography along a line positioned in the longitudinal axis of the respective fibril. Height histogram peak ratio (r) versus temperature (t) data (see Fig. 2b) were fitted with the sigmoid function

$$r = r_{\min} + \frac{r_{\max}}{1 + e^{(t_{1/2} - t)/k}}, \quad (1)$$

where $t_{1/2}$ is the temperature at the half-maximal ratio and k is a rate constant. For data analysis, we used IgorPro (v.5.1, Wavementrics, Lake Oswego, OR) and KaleidaGraph (v.4.0.2, Synergy Software, Reading, PA) software packages.

Results and Discussion

Global Morphology of Aβ25–35 Fibrils at Increasing Temperatures

Aβ25–35 peptide formed a trigonally oriented fibrillar network on mica surface. The finding is identical to our previous observations reported in several recent works [10–12]. The oriented amyloid fibrillar network was exposed to thermal effects by raising the temperature of the fluid chamber containing the sample (Fig. 1). The measurements were carried out under aqueous buffer conditions in the temperature range of 30–70 °C. The fibrils maintained their orientation across the examined temperature range. The observation suggests that either the angular reordering on mica is a highly unfavored process, or it might occur via a path that involves dissociation and reassociation. Considering that fibril dissociation is a highly non-equilibrium process due to the lack of Aβ25–35 peptides in the buffer solution, the probability of reassociation is extremely low. Thus, deviant fibril orientations are absent even at high temperatures.

Although there were no changes in the main fibril orientation directions, the number and length of fibrils became reduced at increasing temperatures. While at low temperatures the mica surface was densely packed with fibrils as long as several hundred nanometers, above 60 °C large surface areas devoid if fibrils appeared, and the presence of very short fibrils became more obvious (Fig. 1). The reduction in fibril density is the result of the dissociation of fibrils from the mica surface. It has previously been suggested that the association of Aβ25–35 fibrils to mica surface involves an apparently cooperative mechanism due to the coupling of numerous fibril-surface interactions [10]. In this arrangement the probability that all of the bonds holding a fibril on the mica surface become ruptured is extremely low. The observation that entire fibrils dissociated from mica at high temperatures suggests that thermal activation at these temperatures was sufficient to

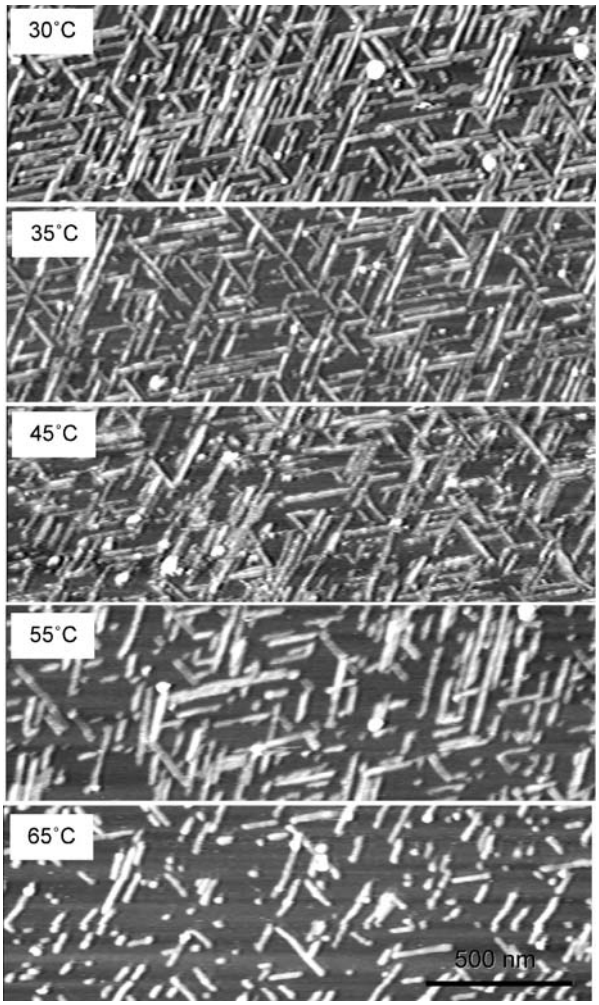

Fig. 1 Effect of increasing temperature on mica-associated Aβ25–35 fibril network. Non-contact mode, height contrast atomic force microscopic images recorded during a gradual increase of sample temperature in 5 °C steps in a range of 30–70 °C. Selected images are displayed for temperatures indicated in the *upper left corner* of the images.

disrupt all of the bonds holding the fibril on the surface. Additionally, it might also be possible that coupling within the fibril became disrupted at high temperatures due to a thermally induced conformational change. Inhibition of intrafibrillar coupling is also expected to increase the probability of dissociation [14, 15]. The observation that short fibrils became prevalent at high temperatures supports this idea and indicates that the interactions between the peptide units within the fibril also became altered.

Quantitative Assessment of Heat-Induced Effects

To explore the details behind the morphological changes of Aβ25–35 fibrils, quantitative analyses of the images were carried out. By following the distribution of image pixels according to absolute height, we could monitor the heat-induced changes in relative occupancy of the mica surface by Aβ25–35 fibrils (Fig. 2). Two peaks were observed in the height histogram at each temperature value. The peak at lower absolute height contains the image pixels of the substrate surface. The peak at the greater absolute height contains the pixels corresponding to amyloid fibrils (Fig. 2a). There was a marked shift between the two peaks as a function of temperature. While at low temperatures the two peaks were of similar height, at increased temperature levels the substrate surface peak became dominant (Fig. 2b). The analysis supports the visual observation that the mica surface occupancy becomes reduced at high temperatures (Fig. 1). Notably, the reduction in mica surface occupancy as a function of temperature was not continuous, but occurred as a transition between 45–55 °C (Fig. 2b). A sigmoidal fit to the data revealed an inflection point at a temperature of 48.8 ± 1.5 °C. Conceivably, a structural change may have occurred within the fibrils. Thermally induced conformational changes have been shown to occur within β-peptides around 45 °C [14, 15]. It is possible that the changes in fibril morphology ob-

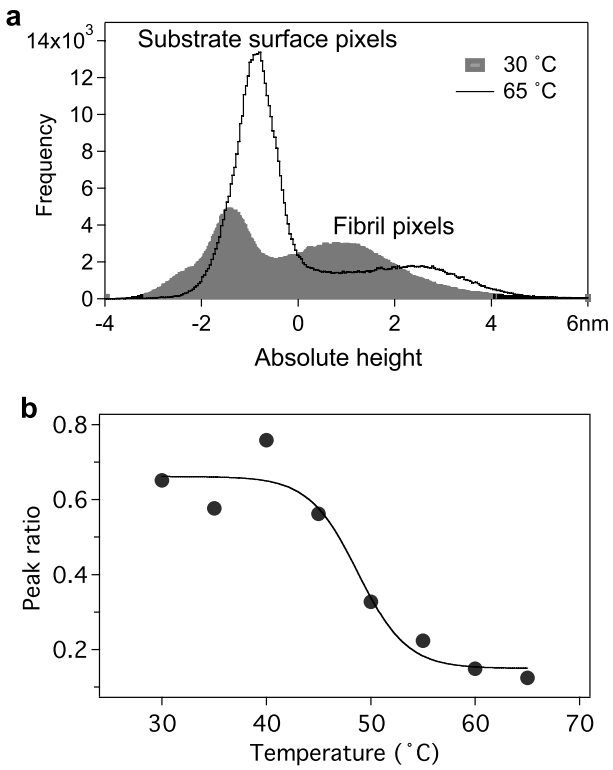

Fig. 2 Changes in relative substrate surface occupancy by amyloid fibrils as a function of temperature. (**a**) Height image pixel histograms at 30 and 65 °C. The *peak* at lower absolute height corresponds to the substrate surface pixels, whereas the one at the greater height to the fibril pixels. (**b**) Ratio of the heights of the surface and fibril peaks as a function of temperature. Data were fitted with Eq. 1

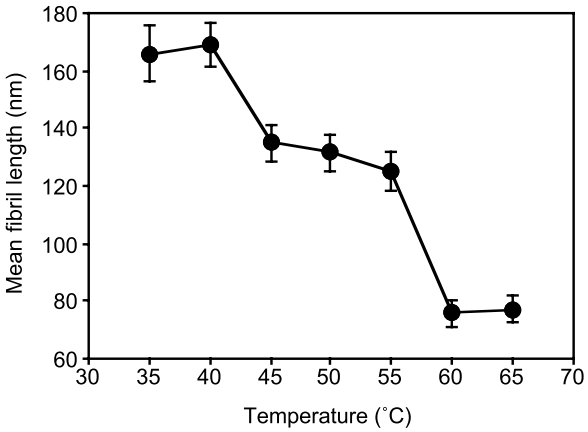

Fig. 3 Mean fibril length as a function of temperature. Lengths were measured at each temperature value for 50 fibrils randomly selected across the AFM images. *Error bars* correspond to standard error of the mean

served here are related to these thermally-induced structural changes.

Average fibril length also became reduced at increasing temperatures (Fig. 3). The initial length of Aβ25-fibrils on the mica surface, at room temperature, is limited not by equilibrium factors but by mechanical effects, because an individual fibrils may grow only until it hits another fibril that lies across its path [10]. Upon increasing temperature, average fibril length did not change significantly until 40 °C was reached. Increasing temperature above 60 °C, however, resulted in $\sim 60\%$ reduction of average fibril length. The results of the analysis correspond well with the morphological observations that revealed the appearance of short fibrils at high temperatures (Fig. 1).

Heat-Induced Microstructural Changes in Aβ25–35 Fibrils

In order to reveal mechanisms behind the heat-induced structural changes, we analyzed the distribution of fibril thickness as a function of temperature. The peak in the absolute height histogram (Fig. 2a) that corresponds to the fibril pixels shows wide, Gaussian distribution. Because of tip convolution, the peak does not exactly correspond to fibril height. Rather, it represents the fibril cross-sectional topography convolved with tip geometry. To obtain fibril thickness statistics with precision, we measured the local height along a line positioned in the longitudinal axis of individual fibrils. Data are shown in Fig. 4. Between 30–45 °C we observed a multimodal distribution of fibril height. The histogram peaks most likely correspond to β-sheets or protofilaments which are positioned above one another. The greater the number of β-sheets or protofilaments superpositioned, the greater the apparent fibril thickness. The average fibril thickness gradu-

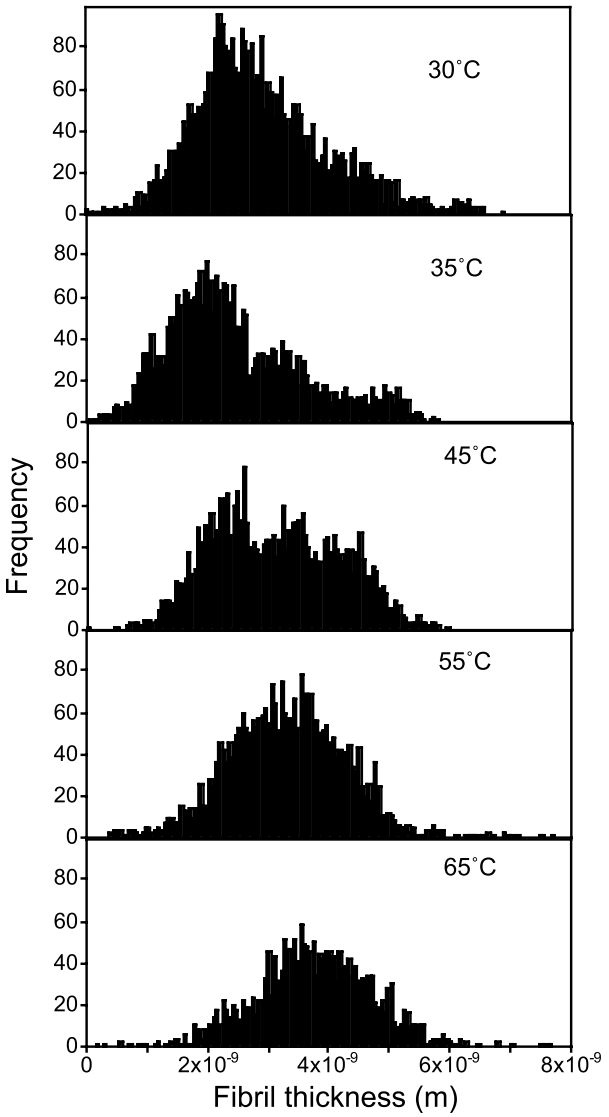

Fig. 4 Effect of temperature on amyloid fibril thickness distribution. Fibril thickness data were obtained by measuring the height along the longitudinal axis of the fibrils. 50 fibrils randomly selected across the AFM images were analyzed, for which all the pixels along the axis were included. Fibril height data were corrected with the average absolute sample height obtained from the height image histograms (see Fig. 2a)

ally shifted to lower values upon increasing the temperature from 30 to 35 °C. Probably the elevation of temperature resulted in the dissociation of the upper, superficial layers of β-sheets or protofilaments, leaving behind only the underlying, fundamental layer directly associated with the mica surface. In addition to the decrease in average thickness, we also observed a gradual loss in multimodality. Upon reaching 55 °C, only a single-mode histogram could be observed. The gradual loss of mul-

tiple modes supports the idea that superficial layers of the Aβ25–35 fibrils became dissociated, and only a single fibrillar layer remained. Finally, in the temperature range of 45–65 °C the average fibril thickness gradually increased with increasing temperatures. We may invoke two possible alternative mechanisms to explain the surprising, thermally-induced increase in fibril thickness. The first possibility is that a conformational transition of the β25–35 peptide around 45 °C induced structural changes in the fibril as well, resulting in increased apparent thickness. The second possibility is that there are no structural changes, but intrafibrillar structural fluctuations became greatly enhanced at the elevated temperatures. The increased fluctuations then result in the observation of apparently thicker fibrils. Because structural changes may occur in the β-peptide at ~ 45 °C [14, 15], the conformationally driven effect is more plausible. However, further experiments are needed to sort out the exact mechanisms.

Conclusions and perspectives

In the present work we investigated the heat stability and temperature-induced morphological changes in Aβ25–35 fibrils associated with mica in the form of an oriented network. Orientation stability was high in the temperature range of 30–70 °C, but fibril dissociation and a possible intrafibrillar structural change occurred at elevated temperatures. Because the oriented amyloid network may be important in nanotechnological and nanoelectronic applications, temperature-dependent effects need to be taken into consideration and further investigated.

Acknowledgement This work was supported by grants from the Hungarian Science Foundation (OTKA T049591, TS049817 and PU50134), Hungarian National Office for Research and Technology (OMFB-01600/2006, OMFB-01627/2006, OMFB-00198/2007, KFKT-1-2006-0021, RET 08/2004), and the Hungarian Ministry of Health (ETT-506/2006).

References

1. Hardy J, Selkoe DJ (2002) The Amyloid Hypothesis of Alzheimer's Disease: Progress and Problems on the Road to Therapeutics. Science 297:353–356
2. Selkoe DJ (2001) Alzheimer's disease: Genes, proteins and therapy. Physiol Rev 81(2):741–766
3. Selkoe DJ (2003) Folding proteins in fatal ways. Nature 426(6968):900–904
4. Serpell LC (2000) Alzheimer's amyloid fibrils: structure and assembly. Biochim Biophys Acta 1502(1):16–30
5. Gazit E (2006) Use of biomolecular templates for the fabrication of metal nanowires. FEBS J 274: 317–322
6. Hamada D, Yanagihara I, Tsumote K (2004) Engineering amyloidogenicity towards the development of nanofibrillar materials. Trends Biotechnol 22:93–97
7. Reches M, Gazit E (2003) Casting metal nanowires within discrete self-assembled peptide nanotubes. Science 300:625–627
8. Scheibel T, Parthasarathy R, Sawicki G, Lin XM, Jaeger H, Lindquist SL (2003) Conducting nanowires built by controlled self-assembly of amyloid fibers and selective metal deposition. Proc Natl Acad Sci USA 100(8):4527–4532
9. Zarándi M, Soós K, Fülöp L, Bozsó Z, Datki Z, Tóth GK, Penke B (2007) Synthesis of Aβ(1-42) and its derivatives with improved efficiency. J Pept Sci 13(2):94–99
10. Karsai Á, Grama L, Murvai Ü, Soós K, Penke B, Kellermayer MSZ (2007) Potassium-dependent oriented growth of amyloid β25–35 fibrils on mica. Nanotechnology 18:345102
11. Kellermayer MSZ, Karsai Á, Benke M, Soós K, Penke B (2008) Stepwise assembly dynamics of single amyloid fibrils revealed by scanning force kymography. Proc Natl Acad Sci USA 105:141–144
12. Karsai Á, Murvai Ü, Soós K, Penke B, Kellermayer MSZ (2008) Oriented epitaxial growth of amyloid fibrils of the N27C mutant β25–35 peptide. Eur J Biophys PMID: 18189132. doi: 10.1007/s00249-007-0253-0
13. Smith PK, Krohn RI, Hermanson GT, Mallia AK, Gartner FH, Provenzano MD, Fujimoto EK, Goeke NM, Olson BJ, Klenk DC (1985) Measurement of protein using bicinchoninic acid. Anal Biochem 150(1):76–85
14. Chu H-L, Lin S-Y (2001) Temperature-induced conformational changes in amyloid β(1-40) peptide investigated by simultaneous FT-IR microspectroscopy with thermal system. Biophys Chem 89:173–180
15. Lin S-Y, Chu H-L, Wei YS (2003) Secondary conformations and temperature effect on structural transformation of amyloid beta (1-28), (1-40) and (1-42) peptides. J Biomol Struct Dyn 20(4):595–601

Progr Colloid Polym Sci (2008) 135: 174–180
DOI 10.1007/2882_2008_106

Published online: 10 September 2008

Alfredo González-Pérez
Sanja Bulut
Ulf Olsson
Björn Lindman

Temperature Induced DNA Compaction in a Nonionic Lamellar Phase

Alfredo González-Pérez (✉) ·
Sanja Bulut · Ulf Olsson · Björn Lindman
Physical Chemistry 1, Center for Chemistry and Chemical Engineering, Lund University, 124, 221 00 Lund, Sweden
e-mail: alfredo@memphys.sdu.dk

Abstract A nonionic lamellar phase was prepared using $C_{10}E_3$ in buffer solution at pH = 7.6. A suitable T4DNA concentration around 5 wt % was immobilized in a lamellar phase with 40 wt % $C_{10}E_3$. The mixed system was investigated at two temperatures, 25 and 5 °C by using cryo-fracture TEM direct imaging, fluorescence microscopy and small-angle X-ray scattering. The surprising results where obtained showing that the DNA conformation can be tuned to compacted and extended state at 25 and 5 °C, respectively. Additionally, DNA is aligned with a preferential orientation in the direction of the flow by simply injecting the sample in a capillary.

Keywords DNA – compaction – decompaction · Mesh phase – lamellar phase · Nonionic surfactant – $C_{10}E_3$

Introduction

Liquid crystalline materials have been a subject of many fundamental studies. In particular, lyotropic liquid crystalline phases that are formed by amphiphilic molecules in aqueous solution [1]. The understanding of the phase behaviour of the rich variety of morphologies and how to control the intrinsic ordering by external parameters is vital for numerous industrial applications [2, 3]. In particular, liquid crystalline materials have been used combined with biomolecules as a tool in order to build new biological soft materials in drug delivery and as artificial matrices for tissue engineering [4, 5].

One of the most interesting self-assembly structures is the lamellar phase or L_α. In this phase the surfactants are organized into planar bilayers with a characteristic spacing between them. This ideal two-dimensional environment between bilayers can be used to immobilize biomacromolecues and to aligned them [6]. The alignment can be induced by e.g. a magnetic field or shear flow. Macromolecules like proteins or DNA have previously been successfully immobilized in L_α structures. DNA and oppositely charged cationic lipids may form liquid crystalline structures usually with lamellar structure [6–8]. Biological macromolecules have also been incorporated into nonionic liquid crystals [9]. The use of nonionic surfactant based lamellar phases has the additional interest because charged molecules, as DNA can not interact electrostaticaly with the bilayers. This gives us some additional freedom to manipulate molecules in two-dimensional arrangements. They can be easily aligned under of flow or in a magnetic field without restriction of the electrostatic interactions with the bilayers.

It is well know that nonionic surfactants form a rich variety of self-assembled structures that can be tuned by varying temperature or concentration [10]. In particular, $C_{10}E_3$ ($C_{10}H_{21}(OCH_2CH_2)_3OH$) forms a lamellar phase with water at 25 °C which can be transformed into a random lamellar mesh phase upon decreasing temperature. The mesh phase is characterized by the presence of perforated domains [11, 12]. These perforations can be a mimic of many natural processes occurring in the living cell [13]. Additionally, in combination with alcohols the spacing in the lamellar phase can range from several hundred nanometers (1 wt %) to a few nanometers in the more concentrated regime (> 5 wt %) [14]. Polyethylene glycol moieties (PEG) are water soluble, non-toxic, and non immunogenic. These properties can enhance biocompati-

bility. Liquid crystalline materials composed of PEG are also uncharged, insensitive to pH, fairly insensitive to salt and more important have no binding capacity for charged macromolecules [9].

In the present work we investigate the mixture of T4DNA with a nonionic lamellar phase of $C_{10}E_3$ in buffer solution and the corresponding mesh phase using small-angle X-ray scattering, fluorescence microscopy and cryo-fracture TEM. Interestingly, both extended and compacted DNA conformations can be observed as a function of temperature.

Experimental

Materials and Sample Preparation

$C_{10}E_3$ was supplied by Nikko Chemical Co. Ltd., Tokyo, with purity $> 98\%$. Coliphage T4DNA 166kbp was supplied by wako Nippon Gene. Fluorescent dye GelStar® nucleic acid gel stain was from Cambrex and is supplied as a $10,000\times$ concentrated stock solution in DMSO. All stock solutions were prepared in a 10 mM Tris-Cl buffer (pH 7.6). DNA molecules were diluted in the 10 mM Tris-Cl buffer. The final concentration of DNA was 0.5 μM in nucleotide units. All 40 wt % samples of $C_{10}E_3$ have been prepared by gently mixing the appropriate amount of surfactant and millipore filtered H_2O. The experiments of fluorescence microscopy where made with GelStar.

Fluorescent Microscopy

The samples were illuminated with a UV-mercury lamp, the fuorescence images of single DNA molecules were observed using a Zeiss Axioplan microscope, equipped with a 100U oil-immersed objective lens, and digitized on a personal computer through a high-sensitive SIT Cvideo camera and an image processor, Argus-20 (Hamamatsu Photonics, Japan). The observations were carried out at 5 and 25 °C. Special care was taken to clean the microscope glasses (No. 0, Chance Propper, England) thoroughly before the observation to prevent DNA degradation, as well as precipitation to the glass surface.

Cryo-Fracture TEM

A drop of the sample was put on a glow-discharged carbon grid (Lacey Carbon filmed grid). The specimens were made using a standard cryo-TEM procedure [15]. The setup was a Philips CM120 cryo electron microscope operated at 120 kV. Images were recorded with a GIF 100 (Gatan Imaging Filter), using a CCD camera and a low mode dose, giving low beam intensity. The lamellar phase was frozen on the carbon grid. Fractures of the frozen specimen can be formed by using a new procedure of breaking the carbon grid with the tweezers [16]. The thickness of the sample does not allow observing the whole sample, but only the edges of the fractures where the sample is thin enough so that the lamellar phase can be observed and directly imaged using the electron microscope.

Small-Angle X-ray Scattering (SAXS)

Small-angle X-ray scattering where performed in MaxLab laboratory, Lund, Sweden on the beam line I711. The wavelength range is 0.8–1.55 Å. The instrument utilizes a 13-period, 1.8 T, multipole-wiggler designed to operate in the 0.85 (14.6 keV) to 1.55 Å (8.0 keV) region. The beamline has a single crystal monochromator, giving a high photon flux at the sample but sacrificing easy tunability and high energy resolution. For detailed information about the instrument, see Cerenius et al. [17]. The capillaries were filled with the samples shortly before the measurements. During the measurement, the samples were kept in an evacuated sample chamber with a thermostated capillary holder. The samples have been thermostated at a given temperature for 2 h before any measurement was performed. Scattering was accumulated for 150 s.

Results and Discussion

The phase behavior of $C_{10}E_3$ in aqueous solutions is well known and have been reported in the earlier studies by Ali and Mulley [18]. In particular the lamellar phase region as well the transition to a mesh lamellar phase has been studied as a function of temperature and concentration [11]. Also different topological transformations of surfactant bilayers have been investigated under shear flow [19, 20]. The general information about the phase behavior of $C_{10}E_3$ in water is shown on Fig. 1.

A 5 wt % concentration of T4DNA has been added to the original lamellar phase prepared at 40 wt % of $C_{10}E_3$ in buffer solution. The sample was gently mixed in order to insure homogenization of the mixture. The sample was stored at room temperature for 24 h, imaged at 25 °C and after that kept at 5 °C for another 24 h. After this, the sample was used in the cryo-fracture TEM experiment. The imaging of the $C_{10}E_3$ 40 wt % and DNA is shown in Fig. 2.

The results show the presence of perforated domains, as in the lamellar phase prepared without DNA. This is an indication that the structure of the lamellar phase is not significantly affected by the presence of DNA. However, DNA should be present in the lamellar phase, between the lamellae. In Fig. 2 we show two possible orientations of the lamellar phase, with respect to the electron beam, denoted a) and b). The orientation a) corresponds to the lamellar phase normal being parallel with the beam, and in this position, the presence of perforated domains characteristic of the mesh lamellar phase can be observed. Similar perforations where observed with the lamellar phase prepared in pure water and the same concentration [16].

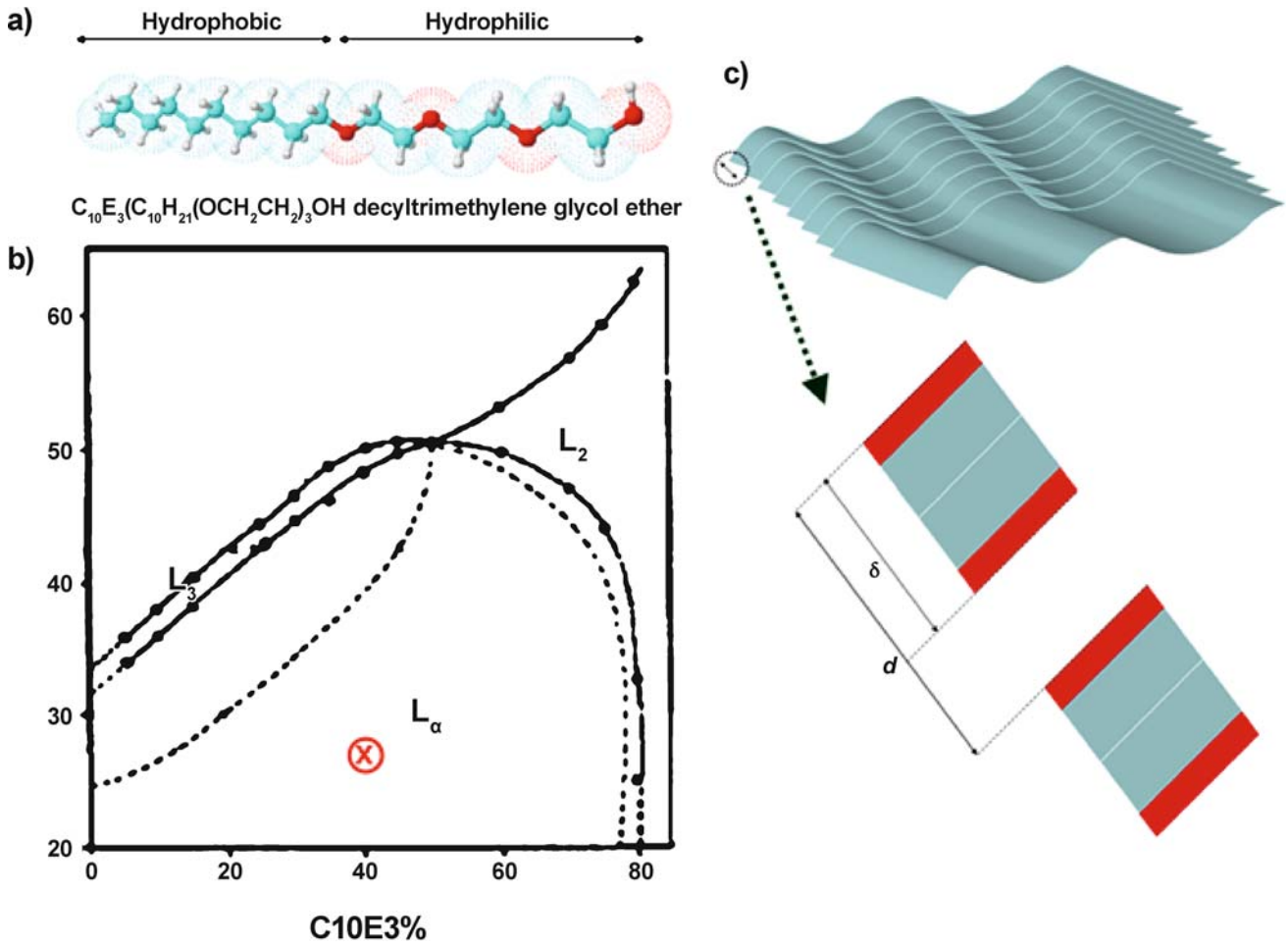

Fig. 1 (**a**) Molecular structure of $C_{10}E_3$ indicating the hydrophobic and hydrophilic moieties. (**b**) Phase diagram of $C_{10}E_3$ in water solutions from [18] and (**c**) represent the lamellar phase with the characteristic distances *d*-spacing and δ the thickness of the bilayer

The perpendicular b) orientation of the lamellar phase corresponds to a cut through the several layers. This image informs us about the spacing of the lamellae.

In order to investigate the DNA conformation in the lamellar phase we have performed fluorescence microscopy experiments using T4DNA stained using GelStar. In Fig. 3 we show the fluorescence microscopy images of individual T4DNA molecules immobilized in the lamellar phase at 25 and 5 °C, respectively.

The apparent size of the compacted DNA observed in the Fig. 3 at 25 °C is approximately $0.7 \pm 0.2\,\mu$m. This result is in good agreement with previous findings for T4DNA in buffer solution when this is compacted by using different types of cationic surfactants [21]. At this temperature we can not observe the presence of DNA in the coil conformation, hence no coexistence between coils and globules was found. The results at 5 °C show that DNA is present in the elongated coil conformation with no presence of globules in the solution. We note that the DNA appear to be more extended compared to the same DNA in bulk solution, possibly due to a two dimensional confinement. Similar has been observed with DNA immobilized on surfaces [21]. What is particular interesting here is the possibility to control the DNA conformation by simply changing the temperature of the system. The kinetics of the process is currently under investigation.

Finally, in order to obtain additional information about the influence of DNA on the lamellar phase as well as the DNA alignment we have performed SAXS experiment at 25 and 5 °C. All the samples were kept at approximately 5 °C for several days before measurements. The capillaries were filled at 5 °C using a cooled syringe and immediately put in the SAXS sample chamber cooled to 5 °C. The samples are then left to equilibrate at 5 °C for 2 h before the measurements. After the measurement at 5 °C, the temperature was raised to 25 °C and left to equilibrate for two hours before the measurements. In Fig. 4 we show the two-dimensional pattern obtained using SAXS instrument for a lamellar phase in buffer with and without T4DNA at 25 and 5 °C.

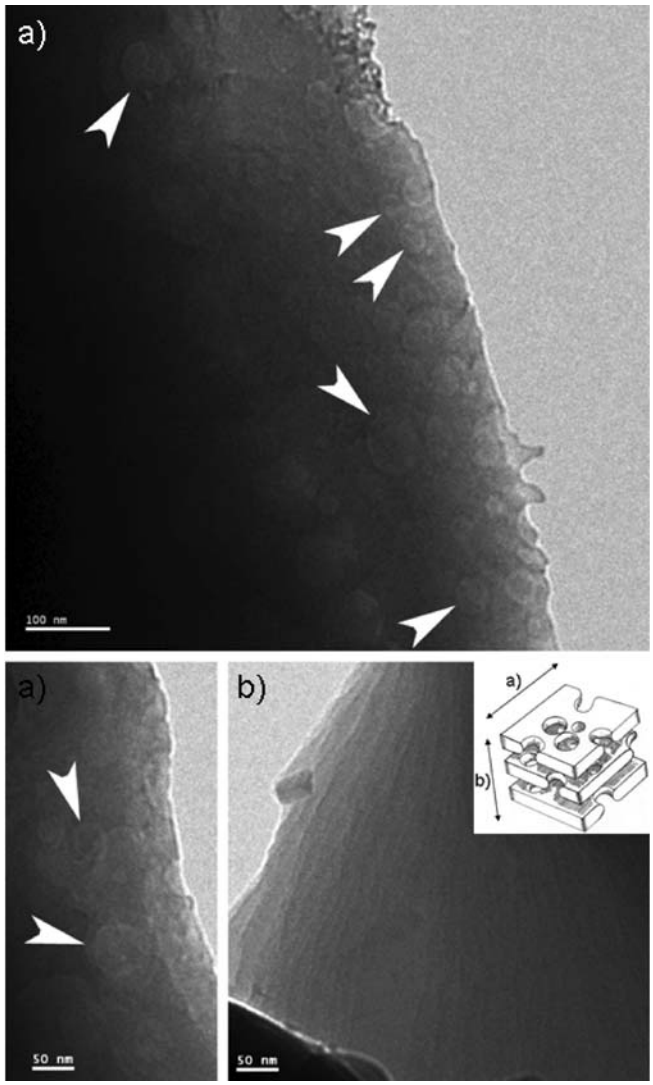

Fig. 2 Cryo-fracture TEM imaging of 40 wt % $C_{10}E_3$ in buffer solution in presence of T4DNA at 5 wt % at 5 °C. (**a**) and (**b**) represent the two different orientation of the lamellar phase as is indicated on the *inset*

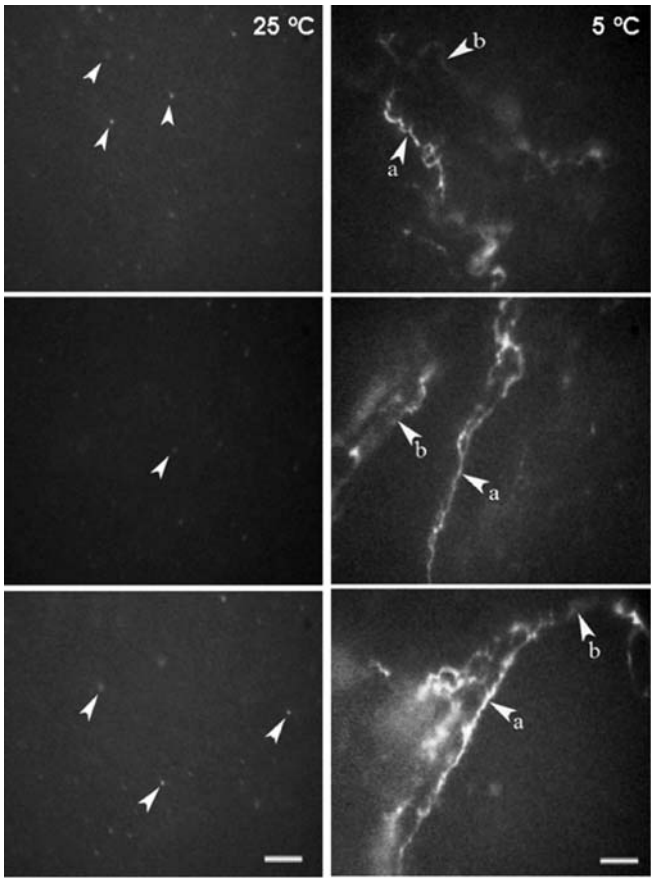

Fig. 3 Fluorescence imaging of T4DNA immobilized in a lamellar phase $C_{10}E_3$ at pH 7.6 at 25 and 5 °C. a and b show the transition between different layers

In Fig. 4a the typical two-dimensional pattern characteristic of a poly-crystalline or powder lamellar phase is shown. The rings resulting form the Bragg reflections on the q space show only a weak preferred orientation in one direction. This can be a consequence of the preferential orientation of the bilayers on the direction of the flow when the sample is injected into the capillary. In the presence of DNA, we instead observe a strong alignment of the lamellar phase in the capillary. This is probably due to DNA being aligned in the flow direction.

Looking at the temperature effect we can easily observe that the patterns at 25 °C are better defined than at 5 °C, for both the first and the second peak. It was reported for other nonionic systems that the temperature has an effect on the repeat distance and this effect was be more pronounced as the surfactant concentration is decreased [22]. However there is more pronounced effect on the topology of the lamellar phase under shear [23, 24]. Working at 40 wt % the effect of temperature in our systems is negligible and the position of the Bragg peaks does not shift towards higher q when the temperature drops from 25 to 5 °C. However the decrease in temperature suppresses the undulations that can affect the regularity of the lamellar arrangement. It is accepted that in nonionic surfactants the lamellar phase is stabilized by the long-ranged Helfrich repulsion that is a result of the thermal undulation [25]. Undulation forces dominate when the membranes are flexible or the electrostatic forces are absent or screened out [26]. This condition is satisfied in our system and it is expected that undulation forces can be dominant at 25 °C and very week at 5 °C.

The addition of T4DNA gives us a substantially different picture of our system as we can observe in Fig. 4b. We know that DNA is present in an extended conformation at 5 °C, hence looking at the two-dimensional pattern from SAXS experiments we can observe a strong prefer-

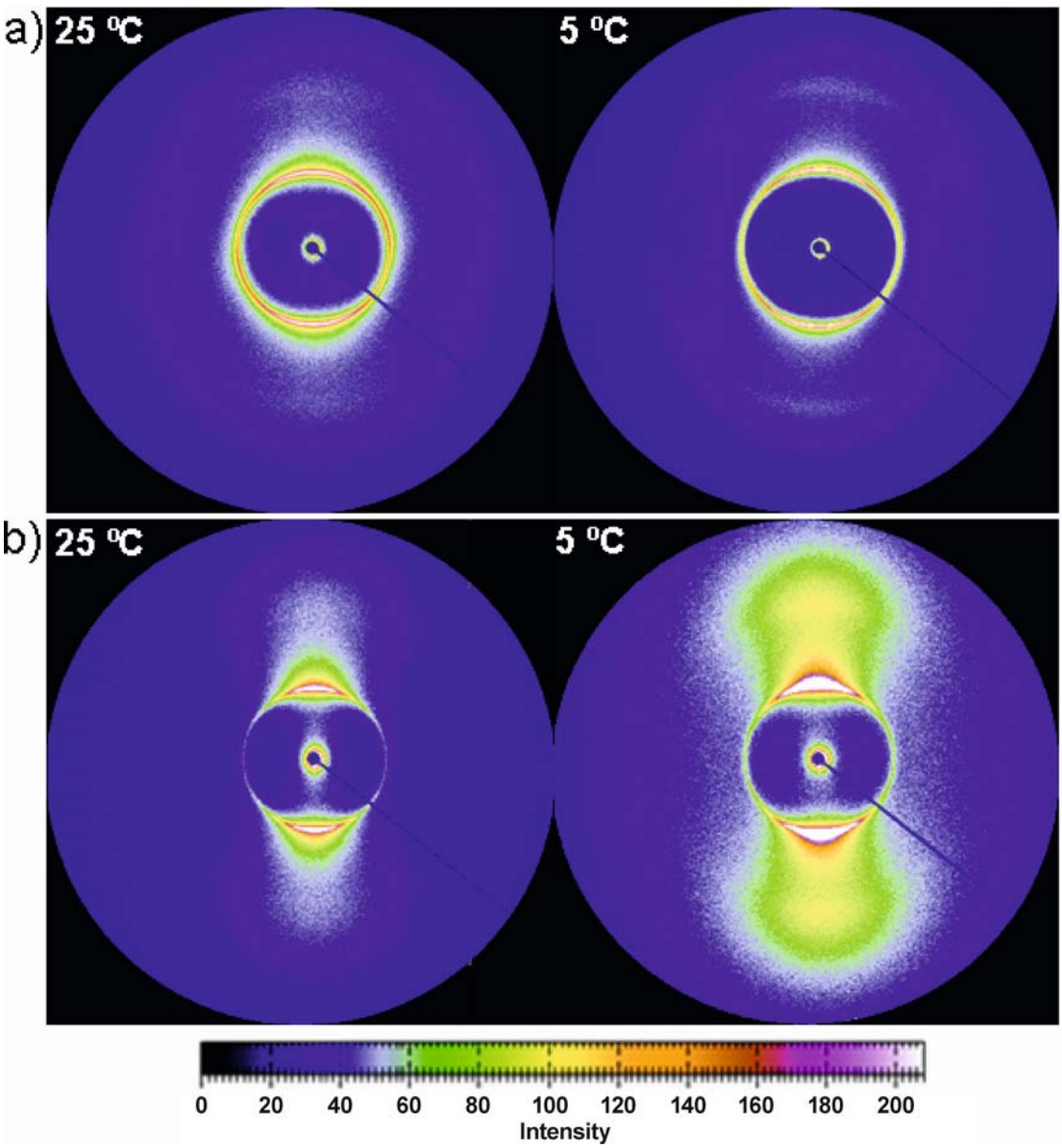

Fig. 4 Two-dimensional SAXS patterns for $C_{10}E_3$ at 40 wt % in buffer pH 7.6 at 5 and 25 °C without (**a**) and with (**b**) T4DNA at a concentration 5 wt %

ential orientation of the mixed system $C_{10}E_3$ + T4DNA. The extended DNA is expected to be immobilized with different degrees of extension, meaning different apparent long axis lengths. As the DNA is a polyelectrolyte, here confined in an ideal 2D box, we can expect partial orientation between the bilayers because of the repulsion between DNA macromolecules. The effect of the flow when the sample is injected on the capillary should affect mainly the different groups of stacked bilayers but not substantially the individual molecules of DNA between bilayers. At 25 °C the DNA is present in a compact conformation and can be treated ideally as a dot. In this case there is no preferential orientation of the DNA, hence the slight effect observed on the two-dimensional patters is mainly due to the orientation of the lamellar phase itself and the diminished anisotropy or order of the system induced by the presence of DNA in a compact conformation.

Summarizing the substantially different two-dimensional pattern shown at 5 °C in the presence of DNA gives us an indication about the DNA conformation in the lamellar phase. The preferential orientation of the sample at 5 °C is the result of the orientation of the lamellar arrangement under flow when the sample is injected in the capillary. The results from SAXS are in agreement with the ob-

servations from fluorescence microscopy experiments and confirm the different conformations of the DNA in the lamellar phase.

A different DNA condensing agents can induce compaction by a variety of mechanism, in particular when compaction is achieved by using cationic surfactant the compaction mechanism goes through the formation of a surface micelles that exist only in the presence of DNA or other charged polyelectrolyte. Using nonionic surfactants, Budker et al. [27] showed that reversed micelles formed by $C_{12}E_4$ in an organic solvent can induce DNA compaction on the small inner space of the isotropic micellar phase. Forming a lamellar phase at higher surfactant concentration they found the presence of DNA structures reminiscent of "nanowires" that they interpret as partially condensed DNA within the lamellar phase. Also there is some evidences that the state of water can affect the DNA packing [28].

The results obtained from SAXS gave a constant q position for all the samples. This means that the d-spacing between the bilayers is the same and independent of changes in the temperature or addition of DNA. Previous studies on the mixture of simple polyelectrolyte and nonionic surfactant in lamellar phase revealed insolubility of the polyelectrolyte in the nonionic lamellar phase and preference for phase separation [29]. One phase consists of a pure polyelectrolyte and water, while the other phase consists of a pure (and more concentrated) lamellar phase essentially free from polyelectrolyte. In this case the lamellar phase is "squeezed" by electrolyte solution leading to shorter d-spacing between lamellae is shorter. This would give a shift in q to higher values, which we do not observe from the SAXS pattern. Thus, no phase segregation is present in our system. If, on the other hand, the polyelectrolyte was hydrofobically modified by grafting hydrophobic chains on the polyelectrolyte bone, the polyelectrolyte becomes soluble in the lamellar phase and no phase separation is observed. According to this, we could treat the DNA as a polyelectrolyte with hydrophobic patches. Also, it is important to point out that the changes in the structure of the DNA molecule with temperature can be due to a strong temperature dependence of properties of the nonionic surfactant. It is well known that the solubility of a nonionic surfactants in water decrease with increase in temperature. This is believed to be the origin of this intriguing phenomenon that allows tuning DNA compaction with temperature.

Conclusions

The lamellar phase conformation seems not to be affected by the presence of DNA in buffer solution. The presence of perforation domains on the bilayers characteristic of a mesh lamellar phase have been observed at 5 °C using the new cryo-fracture TEM direct imaging technique. The DNA conformation seems to be controlled by changing temperature form 25 to 5 °C. Additionally, the alignment of DNA molecules immobilized on the lamellar phase can be induced by flow when the sample is injected in a capillary. The mechanism of DNA compaction controlled by temperature is for the present not understood. Additional experiments in order to understand the mechanism and the kinetics of the process will be carried out in our lab in order to achieve a better understand of these interesting phenomena.

Acknowledgement The authors are grateful to Gunnel Karlsson for the valuable help with cryo-TEM imaging experiments and fruitful discussion about the implementation of the present protocol. A. González-Pérez is grateful to the EU Research Training Network, CIPSNAC (contract No.: MRTN-CT-2003-504932) and U. Olsson thanks the Swedish Research Council (VR) for financial support.

References

1. Matthew LL, Spicer PT (2005) Bicontinuous liquid crystals. Taylor & Francis, New York
2. Chernik GG (1999) Curr Opin Colloid Interf Sci 4:381
3. Kato T (2002) Science 295:2414
4. Goldberg M, Langer R, Jia XQ (2007) J Biomater Sci Polym Ed 18:241
5. Hamley IW, Castelletto V (2007) Angew Chem Int Ed 46:4442
6. Radler JO, Koltover I, Salditt T, Safinya CR (1997) Science 275:810
7. Artzner F, Zantl R, Rapp G, Radler JO (1998) Phys Rev Lett 81:5015
8. Salditt T, Koltover I, Radler JO, Safinya CR (1997) Phys Rev Lett 79:2582
9. Ruckert M, Otting G (2000) J Am Chem Soc 122:7793
10. Mitchell DJ, Tiddy GJT, Waring L, Bostock T, McDonald MP (1983) J Chem Soc Faraday Trans I 79:975
11. Baciu M, Olsson U, Leaver MS, Holmes MC (2006) J Phys Chem B 110:8184
12. Imai M, Saeki A, Teramoto T, Kawaguchi A, Nakaya K, Kato T, Ito K (2001) J Chem Phys 115:10525
13. Mecke A, Dittrich C, Meier W (2006) Soft Matter 2:751
14. Salamat G, Kaler EW (1999) Langmuir 15:5414
15. Danino D, Bernheim-Groswasser A, Talmon Y (2001) Colloids Surf A: Physicochem Eng Asp 183:113
16. Bulut S, González-Pérez A, Olsson U (2008) Langmuir 24:22
17. Cerenius Y, Stahl K, Svensson LA, Ursby T, Oskarsson A, Albertsson J, Liljas A (2000) J Synchrotron Radiat 7:203
18. Ali AA, Mulley BA (1978) J Pharm Pharmacol 30:205
19. Medronho B, Miguel MG, Olsson U (2007) Langmuir 23:5270
20. Nettesheim F, Zipfel J, Olsson U, Renth F, Lindner P, Richtering W (2003) Langmuir 19:3603
21. Dias RS, Pais A, Miguel MG, Lindman B (2004) Colloids Surf A: Physicochem Eng Asp 250:115

22. Minewaki K, Kato T, Yoshida H, Imai M, Ito K (2001) Langmuir 17:1864
23. Le TD, Olsson U, Mortensen K (2000) Physica B 276:379
24. Le TD, Olsson U, Mortensen K, Zipfel J, Richtering W (2001) Langmuir 17:999
25. Von Berlepsch H, De Vries R (2000) Eur Phys J E 1:141
26. Von Berlepsch H, Burger C, Dautzenberg H (1998) Phys Rev E 58:7549
27. Budker VG, Slattum PM, Monahan SD, Wolff JA (2002) Biophys J 82:1570
28. Osfouri S, Stano P, Luisi PL (2005) J Phys Chem B 109:19929
29. Baggerjorgensen H, Olsson U, Iliopoulos I (1995) Langmuir 11:1934

Progr Colloid Polym Sci (2008) 135: 181–187
DOI 10.1007/2882_2008_095

Published online: 29 August 2008

Lívia B. Pártay
Marcello Sega
Pál Jedlovszky

A Two-step Aggregation Scheme of Bile Acid Salts, as Seen From Computer Simulations

Lívia B. Pártay · Pál Jedlovszky (✉)
Laboratory of Interfaces and Nanosize Systems, Institute of Chemistry, Eötvös Loránd University, Pázmány Péter stny. 1/a, 1117 Budapest, Hungary
e-mail: pali@chem.elte.hu

Marcello Sega
Dipartimento di Fisica, Università degli Studi di Trento, 14 via Sommarive, 38050 Povo (Trento), Italy

Marcello Sega
Frankfurt Institute for Advanced Studies, Ruth-Moufang Str. 1, 60438 Frankfurt, Germany

Pál Jedlovszky
HAS Research Group of Technical Analytical Chemistry, Szt. Gellért tér 4, 1111 Budapest, Hungary

Abstract The concentration dependence of the aggregation scheme of two bile anions, i.e., cholate and deoxycholate is investigated in aqueous environment on the basis of molecular dynamics computer simulations. The distribution of the probability that a bile ion belongs to a cluster of a given size is determined. In the analysis we distinguish between hydrogen bonding connections and links of hydrophobic origin. The results show that at low concentrations the systems contain small primary micelles, built up by no more than 10 ions. For cholate, these primary micelles are either kept together by hydrophobic interactions, or by hydrogen bonds, whereas in the case of deoxycholate the number of the hydrogen bonded aggregates is negligibly small. At high concentrations large secondary micelles are formed by the attachment of primary hydrophobic micelles to each other by hydrogen bonds.

Keywords Bile acids · Computer simulation · Micelles · Primary-secondary micelle model

Introduction

Aggregation and self-assembly behavior of amphiphilic molecules is one of the key issues of colloid chemistry for many decades. Simple surfactants, typically built up by a long apolar hydrocarbon tail and a small, ionic or strongly polar head are usually forming spherical micellar objects in aqueous environment above a certain concentration, called the critical micellar concentration (cmc), whereas below this concentration value they do not aggregate. The main thermodynamic driving force of this micelle formation is the free energy gain due to the drastic decrease of the water-apolar contacts, letting the water molecules participate in their hydrogen bonded network instead.

The aggregation mechanism of the amphiphilic molecules can be, however, considerably different from the above picture if the molecular structure of the surfactant is largely different from the long apolar tail – small polar head scheme. Amphiphils of this type frequently occur in biological systems. Bile acids, acting as solubilizers of cholesterol, bilirubin, and various fat-soluble vitamins in the intestine of vertebrates are probably the best known examples for such biological amphiphils. The structure of these molecules, biosynthetized from cholesterol in the liver, is characterized by a large, rigid, quasi-planar tetracyclic ring system. The amphiphilic character of the bile acids comes from the fact that the polar (usually OH) and apolar (usually CH_3) groups are attached to the opposite sides of the ring system. Thus, these molecules are char-

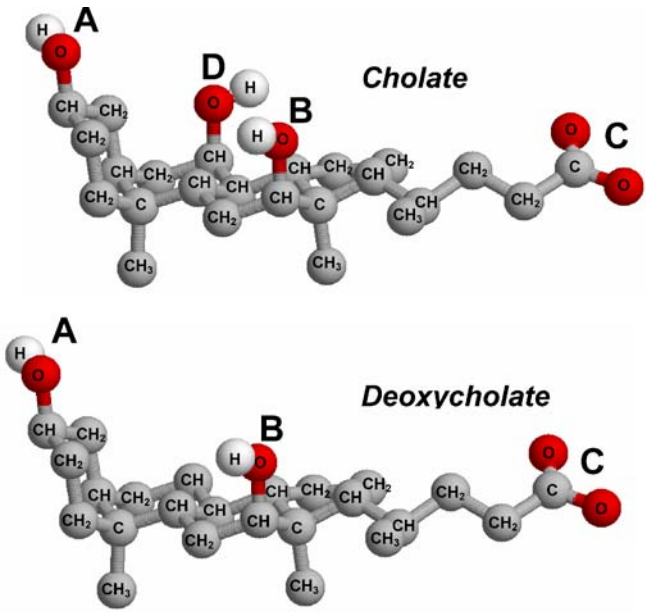

Fig. 1 Spatial structure of the cholate (*top*) and deoxycholate (*bottom*) ions. The notation used to mark the oxygen atoms of different positions (i.e., A–D) throughout the paper is also indicated.

acterized by a hydrophilic and a hydrophobic face. These faces are usually referred to as the α and β face of the molecule, respectively. The spatial structure of two bile ions, i.e., cholate and deoxycholate is shown in Fig. 1. The cholate ion has O atoms in four different positions, marked here by the letters A–D. The difference between these two bile ions is that deoxycholate lacks the oxygen atom in position D, which makes this ion less hydrophilic than cholate.

The unusual arrangement of the polar and apolar groups leads to a peculiar aggregation behavior of these ions. First, the aggregation number of the bile salt micelles just above the cmc is much smaller, and the cmc itself occurs at considerably lower concentrations than in the case of the widely studied aliphatic surfactants. For instance, the cmc value of both cholate and deoxycholate is below 10 mM, and the mean aggregation number of their micelles in the concentration range of 10–50 mM is about 2–5 [1]. A more striking feature of the aggregation scheme of bile acid salts is that it is characterized by at least two cmc values. At the vicinity of the higher cmc value the aggregation number increases rather sharply, whilst it shows only a rather weak dependence on the surfactant concentration between the two cmc values and above the higher value. Thus, the aggregation number of both the cholate and the deoxycholate ion is about 20 above the concentration value of 100 mM [1].

The aggregation of bile salts was first explained by the primary–secondary micelle model of Small [2]. According to this model, at low concentrations the bile ions are forming small, primary micelles. In these micelles the bile ions turn toward each other by their hydrophobic β face. Thus, similarly to the conventional spherical micelles, these primary micelles are also characterized by a hydrophobic core and a hydrophilic outer surface. The low aggregation number can simply be explained by the fact that these ions possess a hydrophobic face rather than just a hydrophobic tail. Above the second cmc these primary micelles are attached together forming large secondary micelles by hydrogen bonding interactions acting between their hydrophilic outer surfaces.

In spite of its plausibility and elegance, the primary–secondary aggregation model of Small has later been challenged several times. Thus, Oakenfull and Fisher found by conductometry measurements that both cholate and deoxycholate ions can hydrogen bond to each other, forming even hydrogen bonded trimers and tetramers just above the first cmc [3–5]. Similar results were obtained by Venkatesan et al., who found that by attaching more hydrophilic groups to the α side of the bile ion the first cmc shifts to lower concentrations, indicating that hydrogen bonds between the bile ions probably play an important role in the formation of the micelles even between the first and second cmc's [6]. Results of molecular mechanics calculations of Li and McGown were, however, in contradiction with these conclusions, indicating that in sodium taurocholate aggregates hydrogen bonding interactions do not play an important role even above the second cmc [7]. All these results indicate that the details of the primary-secondary micelle model of Small has to be refined, and also that the small differences between the chemical structure of the various bile ions can lead to certain differences in their aggregation mechanism.

To investigate this problem computer simulation methods can be very efficient tools. In a computer simulation the intermolecular interactions are described by appropriate model functions, and a set of sample configurations, representing the required equilibrium statistical mechanical ensemble (i.e., canonical, isothermal-isobaric, grand canonical, etc.) of the model system investigated is generated. In these sample configurations the system is seen at atomistic resolution, and therefore any structural characteristic of the equilibrium system can, in principle, be accessed. The choice of the used model has, of course, to be validated, which can be done by demonstrating that the model system is able to sufficiently well reproduce various experimentally obtained properties of the real system.

In spite of the suitability of computer simulation methods in studying the properties of bile ions in aqueous solutions, such studies have only been performed a handful of times. In their pioneering paper Marrink and Mark studied the solubilization of cholesterol by bile ions [8]. Later, Nakashima et al. simulated sodium chenodeoxycholate at infinite dilution (i.e., placing one single ion pair in the simulation box) [9]. Recently, we performed molecular dynamics simulations of the aqueous solutions of sodium cholate and sodium deoxycholate at various different concentrations [10, 11]. In these papers we demonstrated that the systems simulated indeed reached ther-

modynamic equilibrium (i.e., the size of the individual aggregates are fluctuating, whereas the cluster size distribution does not change with the time, and the clusters are in a dynamical equilibrium with the monomers) [10], analyzed the pair correlation functions, dynamics of the bile ions, cluster size distributions [10], relative orientation of the neighboring ions, and characterized the morphology of the various aggregates [11]. We also demonstrated that the model system studied sufficiently reproduces the experimental properties of the bile acid aggregates. The first cmc value of the cholate and deoxycholate ions was found to be 2.7 and 4.1 mM, respectively, and the second cmc appeared between 30 and 90 mM in the case of sodium cholate, and between 90 and 300 mM for sodium deoxycholate. The average size of the aggregates was found to be between 4 and 5 for both ions at 30 mM (i.e., between the two cmc's), and 20 and 7–8 for cholate and deoxycholate, respectively, at 300 mM, i.e., above the second cmc.

In this paper we focus our attention to the problem of what is the probability that a bile ion belongs to an aggregate of a certain size. This analysis provides us a more precise description of the aggregation scheme than what can be obtained simply by calculating the cluster size distribution, as done in the previous paper [10]. This analysis provides us the opportunity to test the validity of the primary-secondary aggregation model of Small for our systems, and also to refine this model appropriately in the light of the present findings.

Molecular Dynamics Simulations

The molecular dynamics simulations performed have been described in detail in our previous paper [10], thus, only a brief summary of their details is presented here. Aqueous solutions of sodium cholate and sodium deoxycholate have been simulated on the isothermal-isobaric (N, p, T) ensemble at 298 K and 1 atm at three different concentrations, i.e., 30, 90 and 300 mM. These systems have contained 10, 27 and 124 ion pairs, hydrated by 18 000, 16 000 and 20 000 water molecules, respectively. Cubic simulation box and standard periodic boundary conditions have been applied. The bile ions have been described by the potential model of Höltje et al., developed originally for cholesterol [12]. Since this potential model is based on the GROMOS87 force field [13, 14], the ligands attached to the tetracyclic ring system as well as the Na^+ counterions have also been described by this force field. The CH, CH_2 and CH_3 groups have been treated as united atoms. Water molecules have been modeled by the SPC/E potential model [15].

The simulations have been performed by the GROMACS program package [16]. The length of the bonds have been kept fixed by employing the LINCS [17] and SETTLE [18] algorithms for the bile ions and water molecules, respectively. The temperature and pressure of the systems have been kept constant using the weak coupling algorithms of Berendsen [19]. Lennard–Jones interactions have been truncated to zero beyond the cut-off distance of 9.0 Å. The long-range part of the electrostatic interactions has been treated by the smooth particle mesh Ewald method [20].

The integration time step of 2 fs has been used in the simulations. The equilibration part of the simulations has been 20–50 ns long. During this time even the slowest varying observables relevant to our study have been found to converge to their equilibrium values [10]. Then, 1000 sample configurations per system, separated by 20 ps long trajectories each, have been saved for the analysis. This length of 20 ns of the production period was shown to be at least an order of magnitude longer than the average lifetime of both the monomers and of the connected state of two bile ions [10], indicating that the samples collected in this period can indeed provide relevant statistics for the cluster size distribution analyses.

Results and Discussion

In analyzing the properties of any kind of aggregates one has to specify first when two monomeric units are regarded as linked to each other. The situation is further complicated here by the fact that two bile ions can be linked together in two different ways: they can either hydrogen bond to each other, or can be attached to each other in a hydrophobic way, by expelling the water molecules from the region between them. Based on the detailed analysis of the pair correlation functions of the various atomic groups of the bile ions we created three linking definitions [10]. Thus, two bile ions are defined to be (i) connected (C-bonded) to each other if their centers-of-mass are closer to each other than 10.75 Å, (ii) hydrogen bonded (H-bonded) to each other if the distance of two O atoms belonging to the two different ions is smaller than 3.35 Å, and, at the same time, the distance of one of these O atoms from the H atom chemically bound to the other O atom is less than 2.45 Å, and (iii) hydrophobically bound (P-bonded) to each other if the distance of two CH_3 groups attached to the tetracyclic ring systems of the two ions is less than 5.5 Å. Based on these linking criteria, we can define the following three types of aggregates. Hydrogen bonded primary micelles (CH clusters) are the assemblies of bile ions from any of which one can reach any other one by a chain of bile ion pairs that are both C- and H-bonded to each other. Similarly, hydrophobically bound primary micelles (CP clusters) are the assemblies of bile ions from any of which one can reach any other one by a chain of bile ion pairs that are both C- and P-bonded to each other. Finally, secondary micelles (CPH clusters) are the assemblies of bile ions from any of which one can reach any other one by a chain of bile ion pairs that

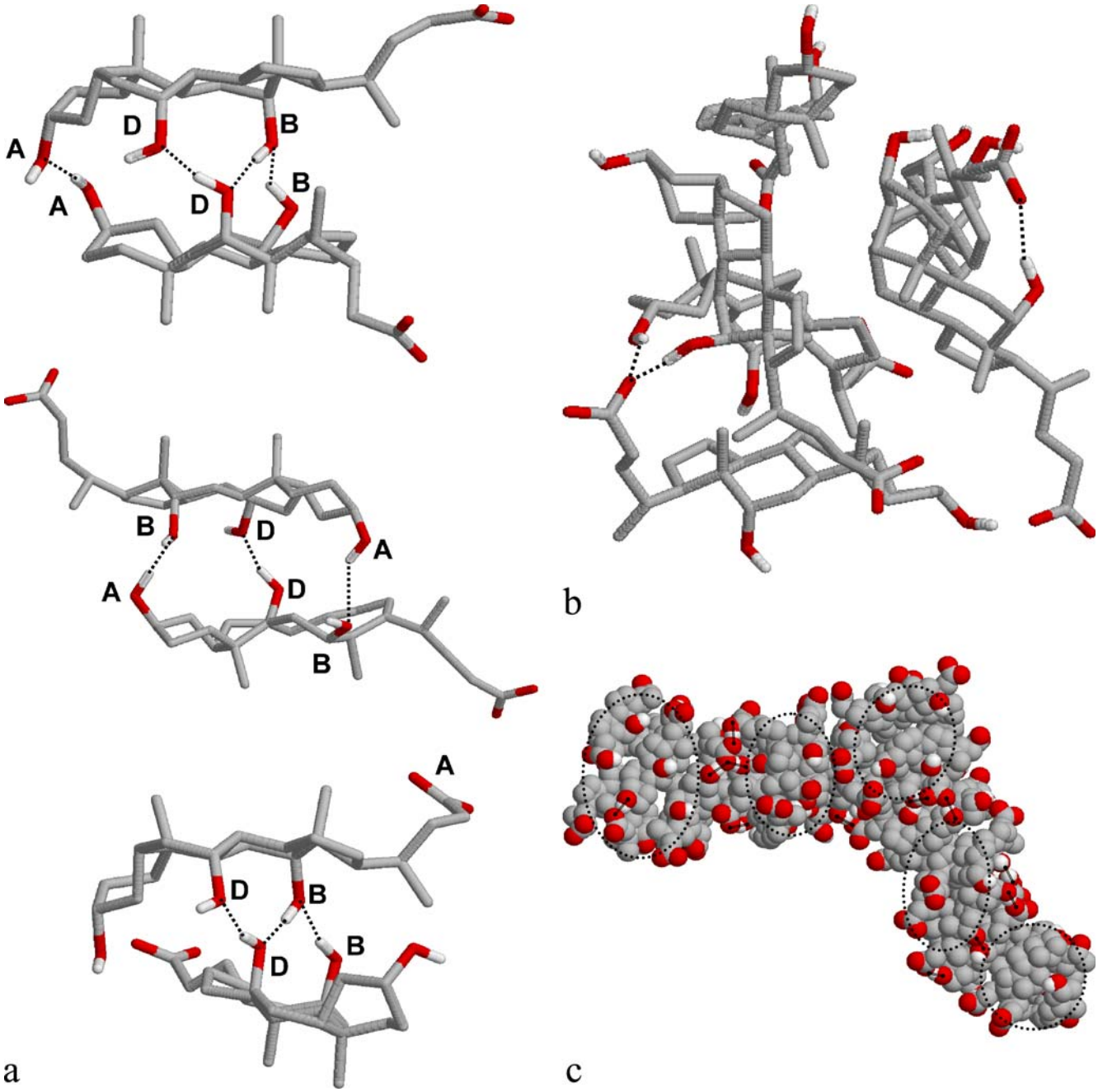

Fig. 2 Examples for **a** neighboring H-bonded cholate ions, **b** a small hydrophobic primary micelle built up by four deoxycholate ions, and **c** a large secondary deoxycholate micelle, formed by five hydrophobic primary ones that are attached together by hydrogen bonds, as taken out from instantaneous equilibrium configurations of the simulations. For the hydrogen bonded pairs the type of the O atoms participating in the hydrogen bond is also indicated. The hydrophobically bound deoxycholate cluster is additionally stabilized by hydrogen bonds between the C-type O atoms located at the end of the flexible hydrocarbon tail and OH groups located at the outer surface of the aggregate. In order to illustrate the presence of the two different types of structural elements in the secondary micelle, the elemental hydrophobic aggregates and the hydrogen bonded oxygen pairs are marked by *circles* and by *double lines*, respectively.

are both C- and either H- or P-bonded to each other. Examples for CH, CP and CPH clusters are shown in Fig. 2, as taken out from equilibrium configurations of the simulations.

In order to characterize the size of the various aggregates that are present in the systems we have calculated the distribution of the probability p_i that a bile ion belongs to a cluster built up by exactly i ions. Clearly, if the number of

the i-size clusters is n_i, the p_i probability can be calculated as

$$p_i = \frac{in_i}{\sum_{i=1}^{N} in_i} = \frac{in_i}{N}, \quad (1)$$

where N is the total number of the bile ions in the system. The p_i distribution is a much more sensitive characteristic of the clustering properties than the simple cluster size distribution $s_i = n_i / \sum n_i$, used in our previous paper [10]. Namely, the role of the small aggregates and, in particular, monomers is overemphasized by s_i, which can be avoided by using the p_i distribution instead. As a simple example, if in a system of 100 particles all but one of the particles belong to the same cluster the values of p_1 and p_{99} are 0.01 and 0.99, respectively (i.e., 1% of the particles are monomers), but the s_1 and s_{99} values are both 0.5 (since 50% of the clusters are monomers). It is also clear that the mean value of the p_i distribution, calculated as

$$\langle p \rangle = \frac{\sum_{i=1}^{N} ip_i}{\sum_{i=1}^{N} p_i} = \frac{\sum_{i=1}^{N} i^2 n_i}{N} = \frac{\sum_{i=1}^{N} i^2 n_i}{\sum_{i=1}^{N} in_i} \quad (2)$$

is exactly the weight average of the cluster size distribution, and hence it detects the formation of large secondary aggregates in a system that contains only a small number of particles (as, unavoidably, in the case of any computer simulation) more sensitively than the simple number average of the cluster size $\langle s \rangle = \sum is_i / \sum s_i = \sum in_i / \sum n_i$.

The distribution of the p_i probability that a bile ion belongs to a cluster of the size i is shown in Fig. 3 as obtained in the six different systems simulated for the CH and CP primary as well as for the CPH secondary micelles. The corresponding cluster size weight average values are summarized in Table 1. As is seen from Fig. 3a, the p_i distribution of the hydrogen bonded clusters does not show a considerable dependence on the bile salt concentration. In the case of sodium cholate about half of the ions do not have any hydrogen bonded cholate partner, whereas the rest of the ions belong to small hydrogen bonded oligomers, built up by only a few cholate ions. In the case of deoxycholate, however, the vast majority of the ions are isolated monomers as far as only hydrogen bonding interactions are concerned. A similar picture is seen when only the hydrophobic links are considered (Fig. 3b). The hydrophobically bound clusters are typically larger than the hydrogen bonded ones, but the fraction of the bile ions that belong to CP clusters built up by more than 10 ions is small in every case. However, if both hydrogen bonding and hydrophobic connections are taken into account the resulting p_i distribution (Fig. 3c) shows strong concentration dependence. At low concentration (i.e., 30 mM) the p_i distribution of the CPH and CP clusters are rather similar to each other. At intermediate concentration (90 mM) the distribution obtained for cholate is already shifted to higher values, whereas in the case of deoxycholate this distribution is still rather similar to the one obtained at 30 mM. However, at high enough concentration (i.e., 300 mM) the p_i distribution is extended to rather large values (i.e., above 50 for cholate and up to about 40 for deoxycholate). The p_i distribution of the cholate ions shows a very nice periodic structure. Its first peak appears at 10–15, followed by another ones at about 25–30, 40 and 50, respectively. This finding indicates that smaller clusters built up by 10–15 monomers frequently merge to larger ones. Considering also the behavior of the p_i distribution of the CH and CP clusters we can conclude that hydrophobically bound primary (CP) micelles are stuck here together by hydrogen bonds to form large secondary aggregates.

In the light of the present findings we can refine the primary–secondary micelle model of Small [2] in the following way. The role of the hydrogen bonding interaction in the formation of primary micelles strongly depends on the hydrophilicity of the bile ion. Thus, in the case of deoxycholate, which lacks the OH group at position D (see Fig. 1), and hence can be characterized by a hydrophilic edge rather than a hydrophilic face, the aggregation mechanism can be well described by the model of Small. At low concentrations only primary micelles, kept together by hydrophobic interactions are present in the system, whereas at higher concentrations these primary micelles are attached together via hydrogen bonding to form secondary aggregates. The structure of such a large secondary aggregate is illustrated in Fig. 2c. However, in the case of the cholate ion, which

Table 1 Cluster size weight average of the CH, CP and CPH clusters as obtained in the six simulations performed

	30 mM		90 mM		300 mM	
	Sodium Cholate	Sodium Deoxycholate	Sodium Cholate	Sodium Deoxycholate	Sodium Cholate	Sodium Deoxycholate
CH clusters	1.44	1.04	1.88	1.11	2.65	1.26
CP clusters	2.76	3.91	5.75	5.13	6.49	5.03
CPH clusters	4.26	4.01	9.49	5.60	12.48	9.01

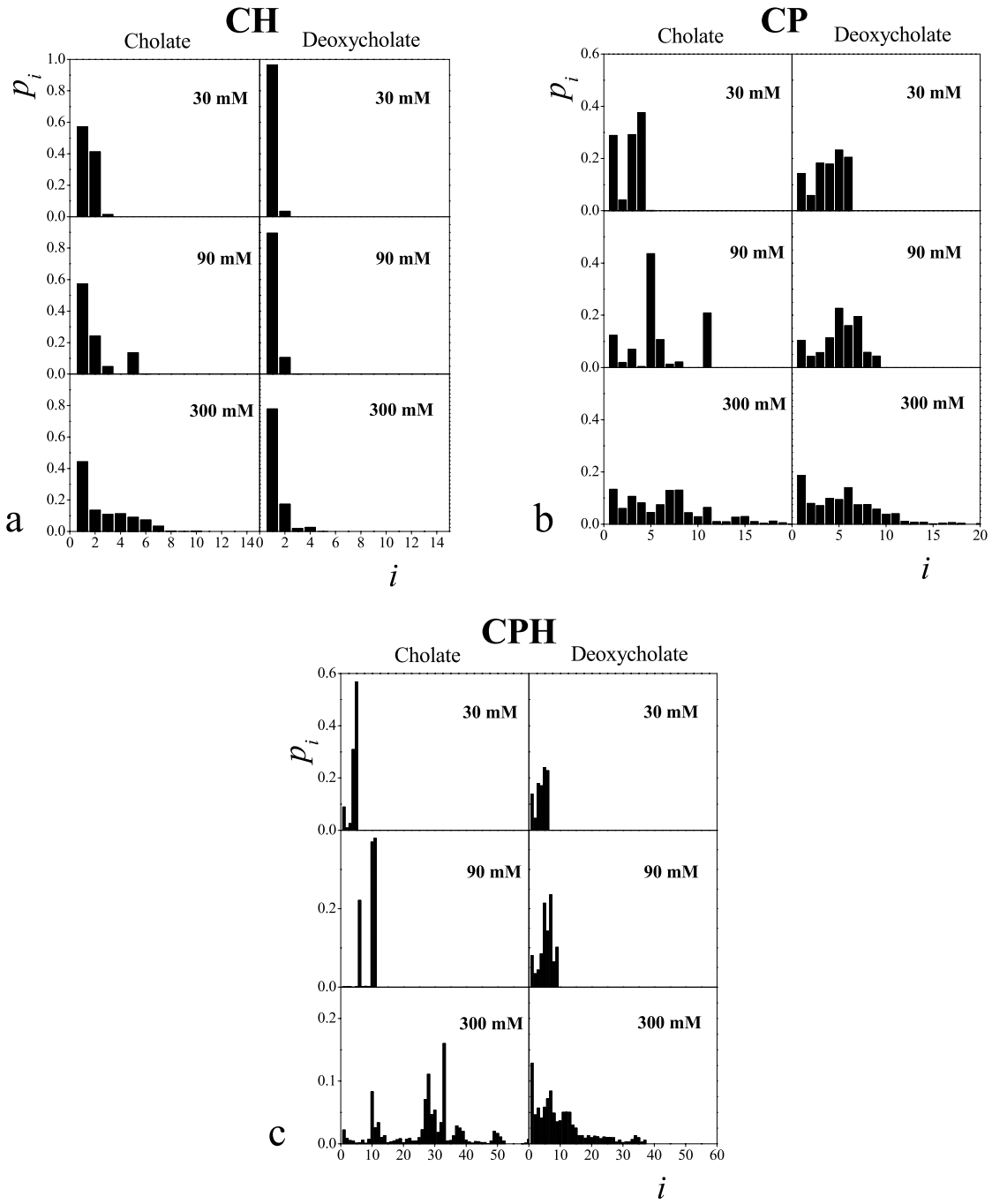

Fig. 3 Distribution of the probability p_i that a bile ion belongs to a cluster built up by exactly i ions, if the cluster is kept together by **a** solely hydrogen bonds, **b** solely hydrophobic links, and **c** both of these two types of bonds in the six different systems simulated

is certainly more hydrophilic than deoxycholate, hydrogen bonding interactions also play a non-negligible role even in the formation of the primary micelles. Thus, at low concentrations the system contains both hydrogen bonded primary aggregates and hydrophobically bound primary micelles. The structure of the large secondary micelles, occurring at high enough concentrations, is similar to those of deoxycholate, however, it should be noted that here the role of the hydrogen bonding and hydrophobic links is symmetric. Thus, secondary cholate micelles can equally be described as hydrophobically bound primary micelles that are linked to each other by

hydrogen bonds, and as hydrogen bonded primary aggregates that are linked to each other by hydrophobic interactions.

Acknowledgement This work has been supported by the Hungarian–Italian bilateral collaboration program between MTA and CNR, and partly by the Hungarian OTKA Foundation under project No. T049673. P.J. is an Eötvös fellow of the Hungarian State, which is gratefully acknowledged. The simulations have partly been performed using the HPC facility of the Physics Department of the University of Trento. The authors are grateful to Dr. Éva Kiss (ELTE University, Budapest) for discussions initiating this study.

References

1. Fontell K (1965) The Micellar Structure of Bile Salt Solutions. In: Ekwall P, Groth K, Runnström-Reio V (eds) Surface Chemistry. Munksgaard, Copenhagen, pp 252–267
2. Small DM (1971) The Physical Chemistry of Cholanic Acids. In: Nair PP, Kritchevsky D (eds) Chemistry; The Bile Acids. vol 1. Plenum Press, New York, chap 8
3. Oakenfull DG, Fisher LR (1977) J Phys Chem 81:1838
4. Oakenfull DG, Fisher LR (1978) J Phys Chem 82:2443
5. Oakenfull DG, Fisher LR (1980) J Phys Chem 84:936
6. Venkatesan P, Cheng Y, Kahne D (1994) J Am Chem Soc 116:6955
7. Li G, McGown LB (1994) J Phys Chem 98:13711
8. Marrink SJ, Mark AE (2002) Biochemistry 41:5375
9. Nakashima T, Iwahashi K, Okazaki S (2006) Chem Phys Lett 420:489
10. Pártay LB, Sega M, Jedlovszky P (2007) J Phys Chem B 111:9886
11. Pártay LB, Sega M, Jedlovszky P (2007) Langmuir 23:12322
12. Höltje M, Forster T, Brandt B, Engels T, Von Rybinski W, Höltje HD (2001) Biochim Biophys Acta 1511:156
13. Hermans JW, Berendsen HJC, Van Gunsteren WF, Postma JPM (1984) Biopolymers 23:1513
14. Van Gunsteren WF, Berendsen HJC (1987) Groningen Molecular Simulation (GROMOS) Library Manual. Biomos, Groningen
15. Berendsen HJC, Grigera JR, Straatsma TP (1987) J Phys Chem 91:6269
16. Lindahl E, Hess B, Van der Spoel D (2001) J Mol Mod 7:306
17. Hess B, Bekker H, Berendsen HJC, Fraaije JGEM (1997) J Comput Chem 18:1463
18. Miyamoto S, Kollman PA (1992) J Comput Chem 13:952
19. Berendsen HJC, Postma JPM, Di Nola A, Haak JR (1984) J Chem Phys 81:3684
20. Essman U, Perera L, Berkowitz ML, Darden T, Lee H, Pedersen LG (1959) J Chem Phys 103:8577

Progr Colloid Polym Sci (2008) 135: 188–193
DOI 10.1007/2882_2008_114

Published online: 13 September 2008

Attila Borsos
Roberta Acciaro
Róbert Mészáros
Tibor Gilányi

Interaction of Cetyl Trimethylammonium Bromide With Poly-(*N*-Isopropylacrylamide-*Co*-Acrylic Acid) Copolymer Nanogel Particles

Attila Borsos · Roberta Acciaro · Róbert Mészáros · Tibor Gilányi (✉)
Laboratory of Interfaces and Nanosize Systems, Institute for Chemistry, Eötvös Loránd University, P.O. Box 32, 1518 Budapest 112, Hungary
e-mail: gilanyi@chem.elte.hu

Abstract The interaction between the cetyl trimethylammonium bromide cationic surfactant and the negatively charged poly-(N-isopropylacrylamide-*co*-acrylic acid) copolymer nanogels was investigated by dynamic light scattering, electrophoretic mobility and potenciometric surfactant activity measurement. The interaction can be divided into three characteristic surfactant concentration ranges. At low surfactant concentration range the nanogel dipersion is stable, the size of the latex particles markedly decreases and the electrophoretic mobility tends to zero with the surfactant concentration. The surfactant binds to the nanogel in form of monomers. Above a certain concentration the nanogel dispersion coagulates. With a further increase of the surfactant concentration a charge reversal of the particles occurs and the nanogel dispersion becomes stable again. The size of the particles increases and the surfactant binding accelerates with increasing equilibrium surfactant concentration, i.e. the binding isotherm shows a new step reflecting collective surfactant binding. In this concentration range the features of the interaction is significantly different from the physical picture previously observed for the mixtures of poly(ethylenimine) and sodium dodecyl sulfate in which case the excess of the surfactant results in a stable colloid dispersion but the particles do not re-swell.

Keywords Nanogels · Polyelectrolyte/surfactant complex · Poly-(*N*-isopropylacrylamide-*co*-acrylic acid) copolymer

Introduction

Several studies have been reported in the past decade on stimuli-responsive hydrogels that can swell or shrink in response to external stimuli. The discovery of a discontinuous volume phase transition in gels, which is often called collapse transition, has rendered such soft materials technologically useful [1–4]. The stimuli that have been investigated to induce changes in polymer gels are diverse, and they include temperature, pH, solvent and ionic composition, electric field, light intensity and an introduction of specific molecules such as surfactants. Poly-(*N*-isopropylacrylamide) hydrogel, abbreviated as pNIPAM gel, is one of the most frequently studied temperature-responsive hydrogels. pNIPAM gels have negative thermosensitivity resulting in a remarkable shrinking with increasing temperature. A non-continuous collapse transition takes place around 34 °C. The interaction of surfactants (mainly sodium dodecyl sulfate, NaDS) with pNIPAM has been studied in polymer solutions [5–10], in macrogels [11–15] and in microgel latexes [16–21]. Ionic surfactants bind to the polymer (either the polymer is in the form of polymer coils or cross-linked gel) above a critical concentration (cac) resulting in the formation of a polyelectrolyte type polymer-surfactant complex. The electrostatic interactions between the bound

surfactant ions result in an increase of the hydrodynamic volume [5, 7] and the cloud point [5] of the polymer as well as the swelling and the increase of the critical collapse temperature [16, 18, 19, 21] of the gel.

The polymer/surfactant systems are essentially important since macromolecules and surface-active agents are usually the main components of cosmetic, detergent, and other industrial applications. Therefore, an intensive effort has been made to characterize the nature of these interactions as well as their impact on phase separation, rheological and interfacial properties with special relevance to the various commercial applications [22–25]. Among these mixtures the oppositely charged polyelectrolyte/surfactant systems attracted special attention [23]. While the non-ionic polymer-surfactant interactions are well-described in terms of a cooperative binding process of the surfactant, the situation in the oppositely charged systems is more complex. There is a growing trend to consider these interactions as basically cooperative in nature and as a sort of surface charge neutralization of micelles via the oppositely charged flexible polymers, supported by theoretical simulations and experiments [23, 24]. On the other hand, there is also evidence of non-cooperative surfactant binding [26, 27] and also a specific binding mechanism involving cooperative and non-cooperative steps as well [28]. The key factors determining the cooperativity of the binding of an ionic surfactant to oppositely charged polyelectrolytes are not clearly understood yet but might include the chemical nature, rigidity, charge density, and molecular architecture of the polymer and also the chemical nature of the surfactant molecules [22].

The aim of this work was to prepare electrically charged nanogel particles with narrow size distribution which allow to manipulate the characteristics of the stimuli responsive gel. Furthermore, such a system with well defined particle shape and size distribution serves an ideal model to study the interaction of the polyelectrolytes with oppositely charged ionic surfactants.

Experimental

Preparation of the Charged Copolymer Nanogel Latex

For the preparation of the copolymer poly(*N*-isopropylacrylamide-*co*-acrylic acid), *N*-isopropylacrylamide (NIPAM), acrylic acid (AAc), methylene bisacrylamide (BA), ammonium persulfate (APS) and sodium dodecyl sulfate (SDS) were used. The chemicals were provided by Aldrich and were used for the preparation without further purification. Our procedure was based on a modified method developed by Wu et al. [29] for the preparation of monodisperse pNIPAM nanogel particles. 2.61 g NIPAM, 57 mg of BA and 38 mg SDS were dissolved in 190 ml of distilled water. The temperature of the reactor was kept at 80 °C and the solution was intensively stirred. In order to remove oxygen, nitrogen gas was purged through the solution for 30 min. Then 2 ml of a 2.80 wt. % aqueous APS solution and 0.187 g AAc (solved in 8 ml water) were added to the solution, followed by intensive stirring for 4 h. The pNIPAM-*co*-AAc latex was purified from un-reacted monomers and surfactant by dialysis against distilled water for 6 weeks.

Determination of the Analytical Charge

The total analytical charge of the gel particles was determined by potenciometric pH-titration with NaOH solution. The charge of the nanogel particles was found to be 0.87 mmol/g dry gel. This value corresponds to 10 mol % AAc content which is theoretically expected if all the NIPA and AAc monomers are reacted during the synthesis.

Electrophoretic Mobility Measurements

Malvern Zetasizer NanoZ equipment from Malvern Instruments was used to measure the electrophoretic mobility of the PEI/SDS complexes at different pH values. The instrument uses a combination of laser Doppler velocimetry and phase analysis light scattering (PALS) in a technique called M3-PALS. Prior to the measurements the instrument was always tested with Malvern Zeta Potential Transfer Standard. All the measurements were performed at 25 °C. The standard error in the values of the electrophoretic mobility was found to be around 10%.

Dynamic Light Scattering Measurements

The dynamic light scattering measurements were performed by means of a Brookhaven dynamic light scattering equipment consisting of a BI-200SM goniometer and a BI-9000AT digital correlator. An argon-ion laser (Omnichrome, model 543) operating at 488 nm wavelength and emitting vertically polarized light was used as the light source. The signal analyser was used in the real-time "multi tau" mode. In this mode the time axis was logarithmically spaced over a time interval ranging from 0.1 μs to 0.1 s and the correlator used 218 time channels. The pinhole was 100 μm. The nanogel samples were cleaned of dust particles by filtering through a 0.8 μm pore-size sintered glass filter.

In the dynamic light scattering experiments the intensity–intensity autocorrelation function was measured (homodyne method) and was converted into the normalized electric field autocorrelation function g by means of the Siegert relation g is related to the distribution of relaxation rates $G(\Gamma)$ through a Laplace transformation:

$$g(q, \tau) = \int_0^\infty G(q, \Gamma) \exp(-\Gamma\tau)\, \mathrm{d}\Gamma\,, \qquad (1)$$

where Γ is the relaxation rate, $q = (4\pi n/\lambda_0)\sin(\theta/2)$ is the scattering vector in which n is the refractive index of the solution, λ_0 is the wavelength of the incident light in vacuum and θ is the scattering angle. Since the recovery of $G(\Gamma)$ from the experimentally determined g is an ill-posed problem, several numerical methods have been developed for the analysis of the measured autocorrelation function. In this work we used the cumulant expansion which gives reliable results in the case of narrow distribution of Γ. This method has the advantage of getting $\langle\Gamma(q)\rangle$ and $p = \int(\Gamma - \langle\Gamma(q)\rangle)^2 G(\Gamma)\,\mathrm{d}\Gamma$ (the so-called first and second cumulants) without any knowledge about $G(\Gamma)$. The first cumulant refers to the mean and the second relates to the width of the relaxation time distribution (polydispersity).

If the intensity fluctuation of the scattered light is due to the translational motion of the particles the collective diffusion coefficient D_m can be calculated from the mean relaxation rate as

$$D_\mathrm{m} = \langle\Gamma\rangle/q^2 = D_0(1+kc)\,, \tag{2}$$

where c is the concentration of the particles. In case of spherical particles D_0 is related to the hydrodynamic diameter of the particles d through the Stokes–Einstein relation:

$$D_0 = \frac{kT}{3\pi\eta d}\,, \tag{3}$$

where k is the Boltzmann constant, T is the temperature and η is the viscosity of the medium.

Determination of the Surfactant Binding Isotherm

2 g polyvinyl chloride ($M_\mathrm{w} = 1\times10^5$) was dissolved in 50 cm^3 THF. 20 cm^3 of this solution, 40 cm^3 THF and 2.97 g tritolyl phosphate was used as membrane forming solution. It was poured on a clean flat glass surface and dried for two days at 40 °C. The membrane was conditioned in 1 mM cetyl trimethyl ammonium bromide, CTAB, solution for a day then washed out with distilled water. A piece of membrane was placed in a plastic membrane holder [30]. The response time of the membrane was dependent on its thickness. The thick membranes were slow, the very thin ones could easily hurt when managed. The optimal thickness of the membrane was found to be 0.3–0.5 mm. Ones a peace of membrane was successfully prepared and fixed in the holder the electrode worked for very long time. The response time of the electrode was within 1–3 min depending on the measured concentration range.

The electromotive force (EMF) values of the Ag/AgBr/0.1 M NaBr/membrane/c_latex, c_CTAB/Ag/AgBr galvanic cell were determined by means of a Radelkis research pH-meter at 25.00 ± 0.1 °C. 10 cm^3 c_latex nanogel latex solution was placed into the measuring cell and titrated with a CTAB stock solution (of the same latex concentration). The equilibrium EMF values were read at each titration step. The EMF values were converted into surfactant monomer concentration (c_e) by means of a calibration curve. The EMF vs. $\log c_\mathrm{CTAB}$ function was found to be linear up to the cmc (with a slope of 54 mV) if there was no latex in the solution.

The binding isotherm of the surfactant on the nanogel $B(c_\mathrm{e})$ was calculated from the expression

$$c = c_\mathrm{e} + Bc_\mathrm{latex} + c_\mathrm{mic}\,, \tag{4}$$

where c and c_e are the total and equilibrium monomer surfactant concentration, respectively, c_mic is the concentration of the micelles in monomer unit and c_latex is the nanogel latex concentration. The $c - c_\mathrm{e}$ difference gives the sum of the micelle concentration and bound surfactant concentration. The other calculation of the binding isotherm was restricted to the range $c_\mathrm{e} <$ cmc when $c_\mathrm{mic} \approx 0$.

Results and Discussion

In Fig. 1 the apparent hydrodynamic diameter (calculated at finite concentrations from D_m) is plotted against the (dry weight) nanogel latex concentration. The apparent diameter shows strong dependence on the concentration reflecting significant interaction between the particles, especially at neutral pH when the carboxyl groups in the nanogel particles are fully dissociated. The strong interaction can be visually observed because at higher concentrations the solutions become viscous and show irisation, which is a consequence of the diffraction of the visible light on an ordered (liquid-like crystalline) nanogel latex. By stirring the system this structure can by mechanically

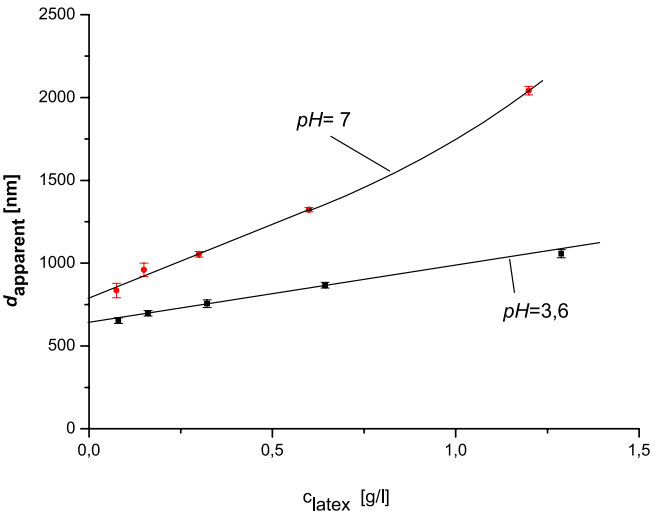

Fig. 1 Apparent diameter of the nanogel particles against the latex concentration

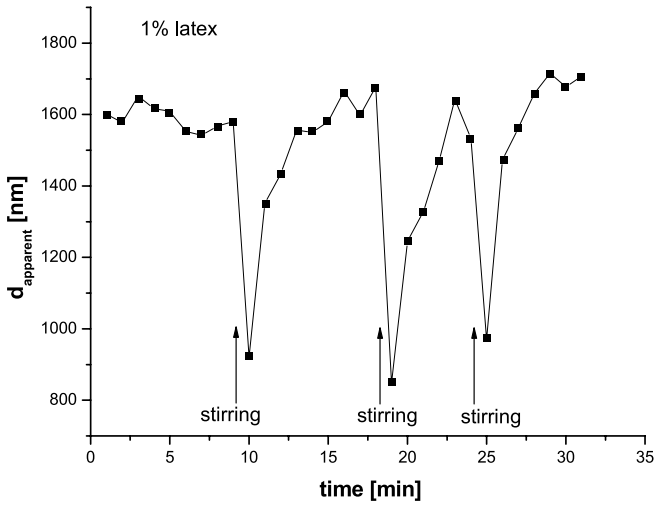

Fig. 2 Effect of the stirring of the latex on the apparent particle diameter

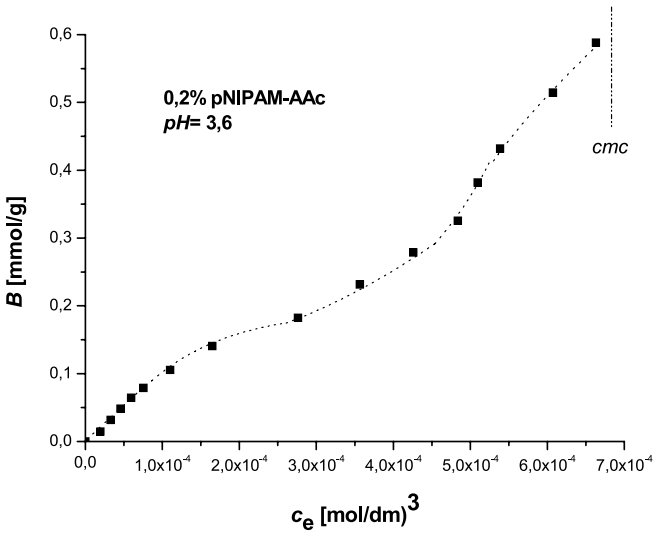

Fig. 3 Binding of the CTAB on the nanogel latex

easily destroyed. Due to the stirring the irisation disappears and the apparent diameter drops down to low value then leaving to stand the system the ordered structure reforms in about 10 min (see Fig. 2). In order to get the true particle diameters the data must be extrapolated to zero latex concentration or to perform the dynamic light scattering measurement at least 0.02% latex concentration when the particle–particle interactions can be neglected.

The cumulant analysis of the intensity–intensity autocorrelation function indicates a very narrow size distribution of the nanogel particles (the second cumulant $p = 0.02$, which means practically monodisperse latex). The appearance of the irisation in the ordered structure is possible only in the case of monodisperse particles, indeed, in case of the ordinary (polydisperse) polyelectrolytes such an effect can not be observed. The prepared copolymer nanogel latex is an ideal model in this respect to investigate the ordered/disordered structure formation and the interaction between the polyelectrolytes and oppositely charged ionic surfactants.

In Fig. 3 the binding of the CTAB on the nanogel is plotted against the equilibrium (free surfactant monomer) concentration. The isotherm can be characterized with two binding steps. The binding starts from zero surfactant concentration according to a Langmuir-like isotherm and accelerates from 0.2–0.3 mM equilibrium surfactant concentration showing a second binding step. The binding isotherm can be determined only below the critical micelle formation concentration ($c_e < \text{cmc}$) because above the cmc both the bound surfactant and the free micelles formed in the system is involved in the calculated B values.

In the case of electrically neutral nanogel/ionic surfactant interaction (such as e.g. pNIPAM homopolymer nanogel interaction with sodium dodecyl sulfate [31]) the interaction starts at a finite surfactant concentration (at the critical aggregation concentration, cac) indicating collective interaction of the surfactant with the polymer. In the case of the investigated nanogel there is no cac, the surfactant binds in the charged nanogel particles in form of monomers at the first binding step. This can be interpreted by the contribution of the electrostatic interaction to the hydrophobic interactions. The polyelectrolyte/ionic surfactant interaction starts from zero surfactant concentration and shows a two step binding process in case of the branched polyelectrolytes [32] as well.

In Fig. 4 the hydrodynamic size of the nanogel/surfactant complex is plotted against the surfactant concentration. The concentration axis also corresponds to the equilibrium surfactant concentration because the experiments were performed at such low latex concentration that the bound surfactant is negligible as compared to the free monomer concentration. The d vs. c_{CTAB} function can be divided into three characteristic surfactant concentration ranges. First the size of the complex decreases and the system is stable then in a second concentration range the latex coagulates (the particle size can not be measured in this range) and finally the particles re-swell and the systems becomes stable again with further increasing surfactant concentration. In this surfactant concentration range the nanogel latex is still monodisperse indicating that the measured increase in the nanogel size is a real re-swelling and not an aggregation process of the particles. The size of the complex particles remained unchanged within the experimental error (checked for three months). The system seems to be a true solution of the nanogel/surfactant complex in thermodynamic equilibrium.

In Fig. 5 the electrokinetic mobility of the nanogel particles is plotted. The negative mobility values decrease (to zero) with increasing surfactant binding and after

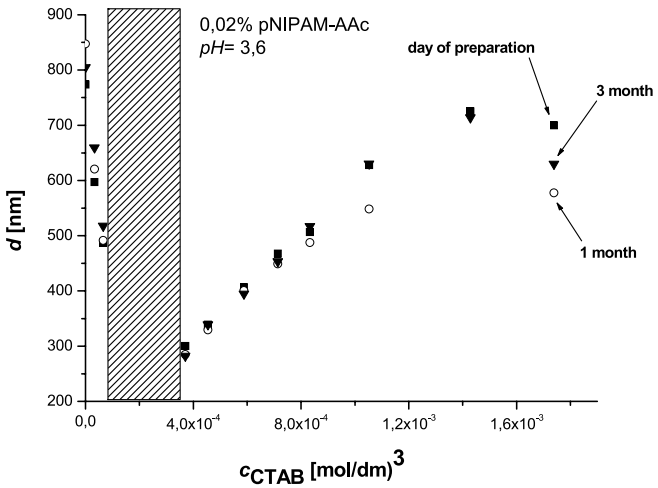

Fig. 4 Size of the nanogel particles against the CTAB concentration

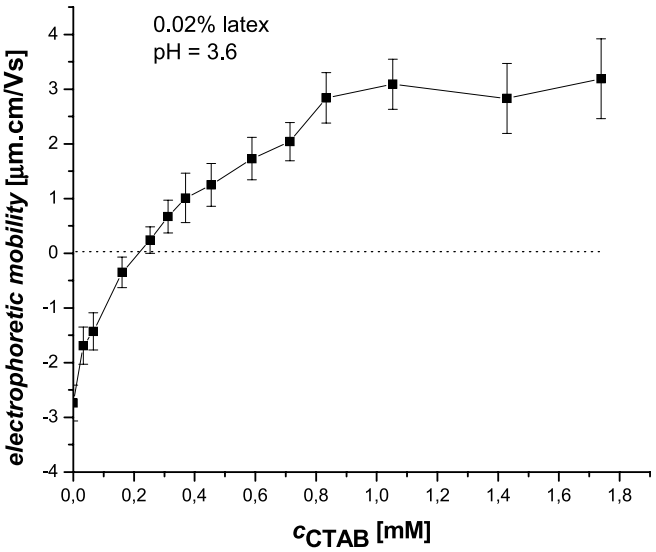

Fig. 5 The electrokinetic mobility of the nanogel particles against the CTAB concentration

the charge reversal the mobility tends to high positive values. The charge reversal corresponds to the coagulation range of the latex and coincides with the starting of the second binding step in the surfactant binding isotherm (see Fig. 3).

Conclusions

Electrically charged monodisperse nanogel latex was synthetized and the interaction of the nanogel with an oppositely charged ionic surfactant was investigated. The binding of the surfactant occurs in two steps. At low surfactant concentrations the surfactant binds in form of monomers. The size of the latex particles and their electrophoretic mobility decreases than the system coagulates. After the charge reversal the mobility increases again and the particles re-sweel forming a stable solution. In this range a second step appears in the surfactant binding isotherm.

Comparing the copolymer nanogel/surfactant interaction to that of the linear and branched polyelectrolytes it can be concluded that difference in the interaction appears only if the surfactant is in excess amount. While the linear and branched polyelectrolytes form a kinetically stable dispersion of collapsed particles in the surfactant excess, the nanogel/surfactant complex form a thermodynamically stable true solution.

Acknowledgement This work was supported by the Hungarian Scientific Research Fund (OTKA No. K 68434 and NKTH-OTKA K 68027) and by the Marie Curie Network "Self-Organization under Confinement, SOCON".

References

1. Gandhi MV, Thompson BS (1992) Smart materials and structures. Chapman & Hall, London
2. Harland RS, Prud'homme RK (eds) (1992) Polyelectrolyte Gels: Properties, Preparation, and Applications. ACS Symposium Series 480. American Chemical Society, Washington, DC
3. Osada Y (1987) Adv Polym Sci 82:1
4. DeRossi D, Kajiwara K, Osada Y, Yamauchi A (eds) (1991) Polymer Gels: Fundamentals and Biomedical Applications. Plenum Press, New York
5. Eliassaf SJ (1978) J Appl Polym Sci 22:873
6. Wu XY, Pelton RH, Tam KC, Woods DR, Hamielec AE (1993) J Polym Sci A 31:957
7. Tam KC, Wu RH, Pelton RHJ (1993) Polym Sci A 31:963
8. Schild HG, Tirrell DA (1990) J Phys Chem 94:4352
9. Schild HG, Tirrell DA (1991) Langmuir 7:665
10. Mylonas Y, Staikos G, Lianos P (1999) Langmuir 15:7172
11. Kokufuta E, Zhang YQ, Tanaka T, Manada A (1993) Macromolecules 26:1053
12. Kokufuta E, Suzuki H, Sakamoto D (1997) Langmuir 13:2627
13. Yoshida M, Asano M, Omochi H, Kamimura W, Kumakura M, Katakai R (1997) Macromolecules 30:2795
14. Suzuki H, Kokufuta E (1999) Colloids Surf 147:233
15. Okuzaki H, Osada Y (1994) Macromolecules 27:502
16. Tam KC, Ragaram S, Pelton RH (1994) Langmuir 10:418

17. Mears SJ, Deng Y, Cosgrove T, Pelton R (1997) Langmuir 13:1901
18. Abuin E, Leon A, Lissi E, Varas JM (1999) Colloids Surf 147:55
19. Gao Y, Auyeung SCF, Wu C (1999) Macromolecules 32:3674
20. Wang G, Pelton R, Zhang J (1999) Colloids Surf 153:335
21. Wu C, Zhou S, Auyeung SCF, Jiang S (1996) Angew Makromol Chem 240:123
22. Goddard ED, Ananthapadmanabhan KP (eds) (1993) Interactions of Surfactants with Polymers and Proteins, Chap 4. CRC Press, Boca Raton
23. Wei YC, Hudson SM (1995) J Macromol Sci Rev Macromol Chem Phys C 35:15
24. Hansson P, Lindman B (1996) Curr Opin Colloid Interface Sci 1:604
25. Zana R (1998) Polymer-Surfactant Systems. In: Kwak JCT (ed) Surfactant Science Series, Chap 10. Marcel Dekker, New York
26. Ohbu K, Hiraishi O, Kashiwa I (1982) J Am Oil Chem Soc 59:108
27. Hajakawa K, Kwak JCT (1982) J Phys Chem 86:3866
28. Li Y, Ghoreishi SM, Bloor DM, Holzwarth JF, Wyn-Jones E (2001) Langmuir 6:3093
29. Wu C, Zhou SQ, Auyeung SCF, Jiang SH (1996) Angew Makromol Chem 240:123
30. Davidson CJ, Meares P (1988) J Membrane Sci 36:511
31. Gilányi T, Varga I, Mészáros R, Filipcsei G, Zrinyi M (2001) Langmuir 17:4764
32. Mészáros R, Thompson L, Bos M, Varga I, Gilányi T (2003) Langmuir 19:609

Progr Colloid Polym Sci (2008) 135: 194–199
DOI 10.1007/2882_2008_108

Published online: 12 September 2008

Árpád Némethy
András Szilágyi
Genovéva Filipcsei
Etelka Tombácz
Miklós Zrínyi

Characterization of Poly(*N*-isopropylacrylamide) and Magnetic Poly(*N*-isopropylacrylamide) Latexes

Árpád Némethy · András Szilágyi · Genovéva Filipcsei (✉) · Miklós Zrínyi
Department of Physical Chemistry and Materials Science, Budapest University of Technology and Economics, Budafoki street 6, 1111 Budapest, Hungary
e-mail: gfilipcsei@mail.bme.hu

Genovéva Filipcsei
Materials Structure and Modeling Research Group of the Hungarian Academy of Sciences, Budapest University of Technology and Economics, Budafoki street 6, 1111 Budapest, Hungary

Etelka Tombácz
Department of Colloid Chemistry, University of Szeged, Aradi V. t. 1, 6720 Szeged, Hungary

Abstract Monodisperse poly(*N*-isopropylacrylamide) (PNIPA) nanogel latexes with temperature and magnetic field sensitivity were prepared and characterized. The phase transition of the latex was characterized by dynamic light scattering. Electrokinetic measurements revealed that the particles have a negative surface charge, which depends on the pH of the swelling medium. Incorporation of magnetite nanoparticles facilitates the separation of the gel beads and their application in targeted delivery in an external magnetic field. The incorporation of magnetic material does not modify the temperature sensitivity of the PNIPA latex.

Keywords Magnetic particle · Phase transition · Polymer gels · Temperature sensitive latex

Introduction

Novel polymer gels that respond to various external stimuli, e.g., temperature, solution chemistry, electric field, light , etc. were developed in the past decades [1–3]. The discovery of a discontinuous volume phase transition in gels, which is often called collapse transition, has rendered such soft materials technologically useful [4, 5]. These gels can be utilized in mechanical devices, controlled release delivery and separation systems [1, 2, 5].

Among the synthetic responsive polymer gels the best known and studied are those which have hydrophobic side chains like poly(*N*-isopropylacrylamide) (PNIPA) gels [4, 5]. The main characteristic property of fully or partially hydrophobic network chains is that at lower temperature they are more hydrated and more expanded than at higher temperature. Hence, they can convert thermal energy directly into mechanical work by swelling or collapsing. The temperature range in which this conversion abruptly occurs can be adjusted by the chemical composition of the network backbone. The lowest temperature above which the network chains are still in the collapsed state is called lower critical solution temperature, LCST. For PNIPA gels swollen in water, LCST has been found to be 34 °C. Several other gels also display a reversible swelling and shrinking transition with different LCST. These gels are often used for immobilizing enzymes or as carriers of certain functional groups important for biochemical or biomedical applications [5–7].

It is possible to prepare magnetic field sensitive gels, so called ferrogels, using ferrofluid as swelling agent [8–16]. Ferrofluids or magnetic fluids are colloidal dispersions of monodomain magnetic particles with a typical size of less than 10 nm. In the ferrogel, the finely distributed ferromag-

netic particles are attached to the flexible network chain by adhesive forces, which results in a unique magnetoelastic behavior. When a ferrogel is placed in a magnetic field gradient external forces act on the filler particles and the magnetic interaction is enhanced. The polymer network follows the motion of the particles. Depending on the geometrical arrangement, elongation, contraction, bending and rotation can be achieved [9].

The synthesis of stimuli-responsive polymer gel nano- and microspheres is receiving growing attention. The manufacture of polymer nano- and microspheres that combine both temperature and pH-sensitivity has been reported by several authors [17–22].

Magnetic nano- and microspheres made of cross-linked polymers have been studied extensively for a wide range of applications. Owing to their relatively rapid and easy magnetic separation, thermosensitive polymer magnetic microspheres could be widely used in biomedication and bioengineering, such as enzyme immobilization and immunoassay, cell separation and clinical diagnosis. Magnetic separation of labeled cells and other biological entities, therapeutic drug, gene and radionuclide delivery, radio frequency methods for the catabolism of tumors via hyperthermia and contrast enhancement agents for magnetic resonance imaging are the most important examples [17]. In addition, owing to their sensitivity to both magnetic field and temperature, thermosensitive polymer magnetic microspheres offer a high potential for applications in targeted drug delivery systems, which is considered as a safe and effective way for tissue-specific release of drugs. A small amount of magnetic thermoresponsive polymer microspheres is sufficient to deliver a large amount of drug to the selected site.

In this paper we report the preparation of monodisperse PNIPA latexes filled with magnetic nanoparticles in different experimental conditions. The size, the size distribution and phase transition of the temperature and magnetic field sensitive latex were studied. The surface charge was characterized by electrokinetic measurement and potentiometric titration.

Experimental

Preparation of PNIPA Latex

For the preparation of poly(*N*-isopropylacrylamide) latex, *N*-isopropylacrylamide (NIPA), *N*,*N*′-methylenebisacrylamide (BA), ammonium persulfate (APS) and sodium dodecyl sulfate (SDS) were used (Aldrich) without further purification. The preparation of PNIPA latex was based on the method developed by Wu et al. [23]; 14 g NIPA, 1.4 g BA and 94 mg SDS were dissolved in 470 ml distilled water. To remove the residual oxygen, nitrogen gas was bubbled through the solvents for 30 min. The temperature of the reactor was kept at 80 °C and the solution was vigorously stirred. Then 0.28 g APS dissolved in 30 ml water was mixed with the solution and the reaction mixture was vigorously stirred for a further 4 h. The PNIPA latex was purified from the unreacted monomers and surfactant by dialysis against distilled water for 4 weeks. The monomer/cross-linker ratio ($r = [\text{NIPA}]/[\text{BA}]$) was used to characterize the cross-linking ratio of the gels. In case of the prepared PNIPA latex it was varied between 13.6 and 300.

Preparation of Magnetic NIPA Latex

Preparation of magnetic PNIPA gels (MPNIPA) is similar to other filler-loaded elastomer networks. The ferrofluid, which contains magnetite (Fe_3O_4) nanoparticles, was formed by a conventional co-precipitation method. Identical volumes of aqueous $FeCl_3$ (1.2 M) and $FeCl_2$ (0.7 M) solution were mixed together. Magnetite particles were flocculated with concentrated NaOH solution (pH = 11). After removing supernatant liquid, the resulting magnetite slurry was washed with water, adjusting the pH to 5.5. The sediment was dispersed with 1 M HCl, which induced peptization. Then the purified and stabilized magnetite sol, of concentration 17.2 wt %, was used for further preparative work. More detailed descriptions of the preparation procedure can be found in our earlier papers [10, 24]. 10 ml of the ferrofluid was used to prepare MPNIPA latex, according to the previously described method. The molar ratio (r) between monomer and cross-linker molecules was 200.

Particle Size Analysis

The hydrodynamic diameter of the PNIPA latex particles was determined by dynamic light scattering (DLS) measurements using a Brookhaven BI-200SM goniometer and a BI-9000AT digital correlator. The pinhole was 100 μm. The light source was an argon-ion laser (Omnichrome, model 543AP) operating at 488 nm wavelength and emitting vertically polarized light. The signal analyzer was used in the real-time multi-tau mode.

Electrokinetic Measurements

Electrophoretic mobility of the latex particles was measured at 25 and 37 °C in a capillary cell (ZET5104) with a Malvern ZetaSizer4 apparatus.

Potentiometric Titration

The pH-dependent surface charge was determined by acid-base titration under a CO_2 free atmosphere using an indifferent background electrolyte (KNO_3) to maintain constant ionic strength. Before the titration the latex suspensions were stirred and bubbled with purified nitrogen for 1 h. Equilibrium titration was performed by means of a home-built titration system (GIMET1) with 665 Dosimat (Metrohm) burettes, magnetic stirrer, high performance potentiometer. The hydrogen ion activity versus concentration was determined from the reference solution titration, thus allowing the electrode output to be converted directly to hydrogen ion concentration.

The net proton surface excess amount (Δq) can be defined as

$$\Delta q = n^{\sigma}_{H^+} - n^{\sigma}_{OH^-}\,, \tag{1}$$

where $n^{\sigma}_{H^+}$, $n^{\sigma}_{OH^-}$ are the surface excesses amount referred to the mass unit.

The surface excess amount defined for the adsorption [25, 26] can be determined directly from the initial (c_i^0, [mol/l]) and equilibrium (c_i^e, [mol/l]) concentration of solute for adsorption from dilute solution

$$n_i^{\sigma} = \frac{\left(c_i^0 - c_i^e\right) V}{m}\,, \tag{2}$$

where V is volume of the latex, m is the mass of the gel in the latex.

The values of $n^{\sigma}_{H^+}$ and $n^{\sigma}_{OH^-}$ were calculated at each titration point from the electrode output.

Results and Discussion

Size and Size Distribution of PNIPA Latex Particles

The size of the PNIPA latex particles was determined by DLS. The homodyne intensity function $g_2(q, \tau)$ was converted to the normalized electric field autocorrelation function $g_1(q, \tau)$ by means of the Siegert relation

$$b[g_1(q, t)]^2 = [g_2(q, t) - A]/A\,, \tag{3}$$

where A is the experimentally determined baseline, b ($0 < b < 1$) is a constant that depends on the number of coherence areas seen by the detector and $q = (4\pi n/\lambda_0)\sin(\vartheta/2)$ is the scattering vector in which n is the refractive index of the solution, λ_0 is the wavelength of the incident light in vacuum and ϑ is the scattering angle. $g_1(q, \tau)$ is related to the distribution of relaxation rates ($G(\Gamma)$) through the Laplace transform:

$$g_1(q, \tau) = \int_0^{\infty} G(q, \Gamma)\exp(-\Gamma\tau)\,\mathrm{d}\Gamma\,, \tag{4}$$

where Γ is the relaxation rate. In this work, evaluation of $G(q, \Gamma)$ was performed using the CONTIN program supplied with the correlator [27].

If the intensity fluctuation of the scattered light is due to the translational motion of the particles the mutual diffusion coefficient ($D_m(q)$) can be calculated from the mean relaxation rate by the following relation:

$$D_m(q) = \bar{\Gamma}(q)/q^2 = D_0\left(1 + CR_g^2q^2\right) \quad (c \to 0)\,, \tag{5}$$

in which R_g is the radius of gyration and C is a constant. D_0 is related to the equivalent hydrodynamic diameter of the particles (d_h) through the Stokes–Einstein relation

$$D_0 = \frac{k_B T}{3\pi\eta d_h}\,, \tag{6}$$

where k_B is the Boltzmann constant, T is the absolute temperature and η is the viscosity of the medium.

In Fig. 1 the size distribution of the NIPA latex particles can be seen below and above the phase transition temperature. It can be clearly seen that the PNIPA particles are monodisperse both at 25 and at 37 °C. The phase transition of the particles does not influence the size distribution. Irisation of the latex was observed providing visible evidence of the monodispersity.

Characterization of the Phase Transition of Monodisperse PNIPA Latex by DLS

Dynamic light scattering also offers the possibility of investigating the phase transition of PNIPA latex. To de-

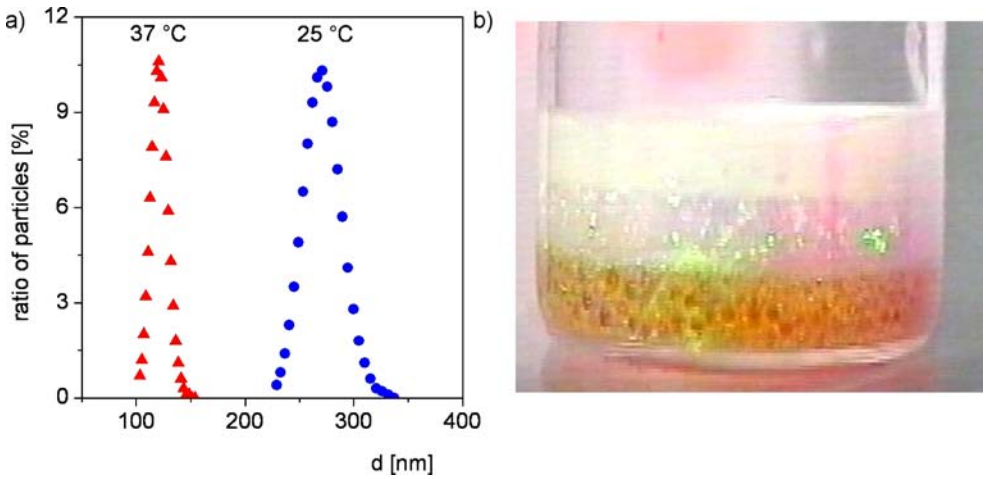

Fig. 1 **a** Size distribution of NIPA latex particles ($r = 13.6$) at 25 and 37 °C, below and above the phase transition temperature; **b** irisation of latex sample

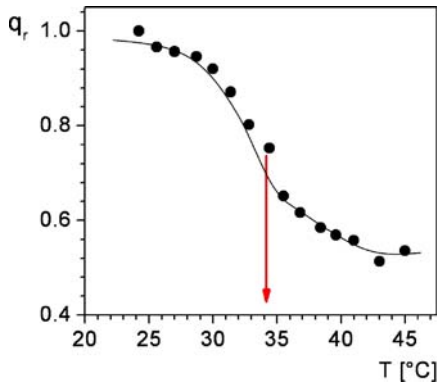

Fig. 2 Relative swelling degree of the NIPA latex ($r = 13.6$) as a function of temperature

termine the phase transition temperature (PTT) a relative swelling degree (q_r) was defined:

$$q_r = \frac{d_T}{d_{25\,^\circ C}}, \tag{7}$$

where $d_{25\,^\circ C}$ the diameter of the latex particles at 25 °C and d_T the diameter of the latex particles at a given temperature.

The relative swelling degree of latex particles was measured in the temperature range 25–45 °C. Figure 2 shows the relative swelling degree q_r of the NIPA latex as a function of temperature. Above a certain temperature the relative swelling degree strongly decreased, as is expected. Analysis of the q_r–T curve shows that the PTT occurs close to 34 °C. To determine the PTT the inflection point of the curve was used. The result correlates well with data from the literature [5, 14, 23, 28].

The effect of the cross-linking ratio on the particle size of the PNIPA particles was also investigated by DLS measurements, the results are shown on Fig. 3. At 25 °C the particle size of the latex increased with the cross-linking ratio (r). At 37 °C, above the PTT, the cross-linking ratio did not affect the particle size, and no temperature dependence of the relative swelling degree was observed. This result can be explained by the preparation conditions. The latex particles were synthesized at 80 °C, above their PPT. At this temperature the PNIPA chains were in the collapsed state, the cross-linking reaction took place in these globules. At 25 °C, i.e., below the PPT, the latex particles swelled according to their crossling density. The swelling degree of the highly cross-linked particles is smaller that the weakly cross-linked latex particles.

Characterization of the Phase Transition of Monodisperse NIPA Latex by Electrokinetic Measurements

To determine the surface charge and the electrophoretic mobility of the NIPA latex, electrokinetic measurements were performed above and below the PPT. In Fig. 4 the electrophoretic mobility of the latex particles is plotted against the cross-linking ratio at 25 and 37 °C, respectively. The electrophoretic mobility of the latex particles was negative, which means, the latex particles were negatively charged. This finding conflicts with the notion that PNIPA gels are composed of neutral polymers [29]. The surface charge probably originated from initiator molecules linked to the end groups of the polymer chains on the surface layer. We cannot, however, ignore the role of the SDS molecules. Surfactant molecules with long alkyl chains can bind to polymers through the hydrophobic interaction and can practically transform the polymer chains into polyelectrolytes [30, 31].

Figure 4 clearly shows that the electrophoretic mobility (u) increases drastically at 37 °C. Increasing the temperature above the PTT the particle size decreased significantly, but the amount of fixed charges on the latex particle did not change, and the surface charge density (σ) increased as the particle size decreased. This increased

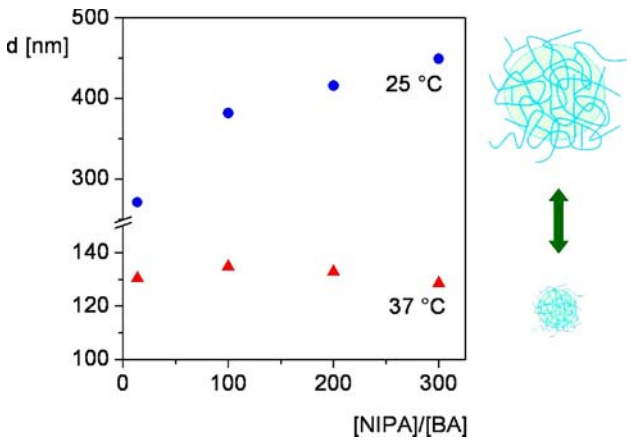

Fig. 3 Effect of the cross-linking ratio on the particle size of the latex below and above the phase transition temperature

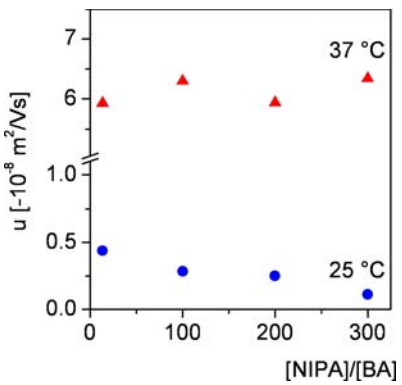

Fig. 4 The electrokinetic mobility of the latex particles as a function of cross-linking ratio below and above the phase transition temperature

surface charge density caused by the increment in the electrophoretic mobility. The electrophoretic mobility became 12–24 times higher with the temperature. Result could be interpreted by the following equation:

$$\sigma = \frac{Q}{\pi a^2} = \varepsilon\kappa\phi_0 \left(1 + \frac{1}{\kappa a}\right), \quad (8)$$

where Q is the electric charge, ε is the dielectric permittivity of the medium, κ is the inverse Debye–Hückel screening length, ϕ_0 is the surface potential and a is the radius of the particle. The electrophoretic mobility is:

$$u = \frac{2\varepsilon\zeta}{3\eta} f(\kappa a), \quad (9)$$

where η is the viscosity of the medium.

If the radius of the particles is the hydrodynamic radius ($a = d_h/2$) in Eqs. 8 and 9, the value of ϕ_0 is the electrokinetic potential. According to this, the electrophoretic mobility varies inversely as the square of the hydrodynamic diameter of the particle. Figure 4 shows that absolute value of the electrophoretic mobility decreased at 25 °C with increasing cross-linking ratio; while at 37 °C the electrophoretic mobility remained the same within the experimental accuracy.

Potentiometric Titration

In Fig. 5 the titration curves of PNIPA latex are displayed for different cross-linking ratios. The negative value of the surface charge was found by the electrokinetic measurements which is in a good agreement with the potentiometric titration result. The pH of the PNIPA latex with different cross-linking ratios changed in the range 6.7–7.3. According to the titration curves, the values of the net proton surface excess amount were negative for pH = 6.7–7.3, which implies that the sulfate groups ($R–SO_4^-$) on the surface of latex particles were dissociated. The zero net surface proton excess concentration was found to be in the pH range 5.2–6.2 for the latexes of different cross-linking ratios. In the acidic pH range (pH < 5.2) the PNIPA latex particles have a small amount of pH-dependent positive surface charge. This can be explained by the protonation of the amide groups on the polymer backbone ($R_1–NH–R_2 + H^+ \rightleftharpoons R_1–NH_2^+–R_2$).

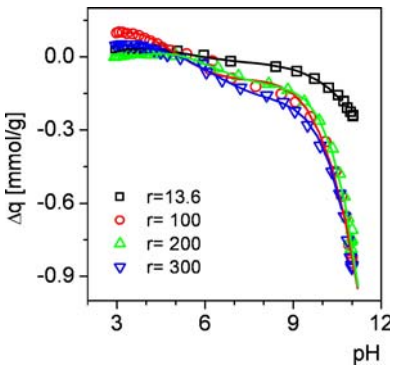

Fig. 5 Potentiometric titration curves of NIPA latex at different cross-linking ratios

Size and Size Distribution of Magnetic PNIPA Latex Particles

The size and the size distribution of the PNIPA and MPNIPA latex particles were measured by DLS. The results are shown in Fig. 6. We conclude that the PNIPA latex as well as the MPNIPA latex have a narrow size distribution. The particle size of the unloaded latex (214 nm) is more than two times smaller than the magnetic latex (589 nm) despite the same preparation conditions. The magnetic latex particles may take the form of clusters with a well-defined aggregation number.

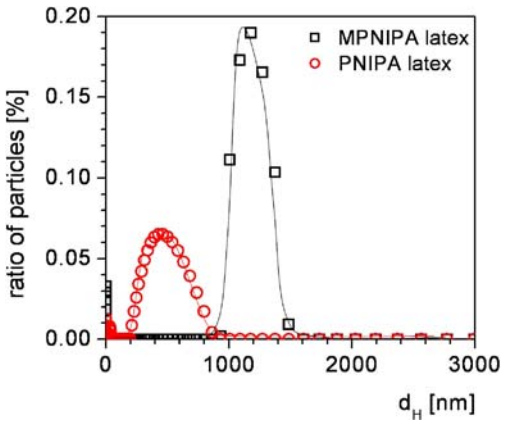

Fig. 6 Size distribution of the PNIPA ($r = 200$) and magnetic PNIPA ($r = 200$) latex

Conclusion

We prepared temperature responsive poly(*N*-isopropyl acrylamide) (PNIPA) latex with different particle sizes. Irisation was observed, which lends support to the finding that the latex is monodisperse. The size of the latex particle could be easily influenced by the cross-link density. The surface charge density depends on the particle size which could be controlled by the temperature.

Magnetic field sensitive PNIPA latex was also prepared. The peculiar magnetic properties of the latex may be used to target and orient the temperature responsive particles and are expected to be applicable in separation by using non-uniform magnetic field.

Acknowledgement This research was supported by the Intel KKK (GVOP-3.2.2-2004-07-0006/3.0), NKFP-3A/081/04 and by the Zoltán Magyary Postdoctoral Fellowship.

References

1. Peppas NA, Korsmeyer RW (eds) (1987) Hydrogels in Medicine and Pharmacology. CRC Press, Boca Raton
2. De Rossi D, Kawana K, Osada Y, Yamauchi A (1991) Polymer Gels, Fundamentals and Biomedical Applications. Plenum Press, New York, London
3. Harland RS, Prud'homme RK (eds) (1992) Polyelectrolyte Gels. ACS Symposium Series 480
4. Tanaka T (1978) Phys Rev Lett 40:820
5. Okano T (Ed.) (1998) Biorelated Polymers and Gels. Academic Press, Boston, San Diego, New York, London, Sydney, Tokyo, Toronto
6. Takahashi F, Sakai Y, Mizutani Y (1997) J Ferment Bioeng 83(2):152
7. Kato N, Takizawa Y, Takahashi F (1997) J Intell Mater Syst Struct 8:588
8. Barsi L, Büki A, Szabó D, Zrínyi M (1996) Progr Colloid Polym Sci 102:57
9. Zrínyi M, Barsi L, Büki A (1996) J Chem Phys 104:20
10. Zrínyi M, Barsi L, Szabó D, Kilian HG (1997) J Chem Phys 106:5685
11. Zrínyi M (1997) Trends Polym Sci 5(7):277
12. Zrínyi M, Barsi L, Büki A (1997) Polym Gels Netw 5:415
13. Szabó D, Szeghy G, Zrínyi M (1998) Macromolecules 31:6541
14. Filipcsei G, Szilagyi A, Csetneki I, Zrínyi M (2006) Macromol Symp 239:130
15. Filipcsei G, Csetneki I, Szilágyi A, Zrínyi M (2007) Magnetic field-responsive smart polymer composites. In: Oligomers, Polymer Composites, Molecular Imprinting, Advances in Polymer Science, vol 137. Springer, Berlin Heidelberg
16. Rosenweig RE (1985) Ferrohydrodynamics. Cambridge University Press,
17. Filipcsei G (2008) eXPRESS Polym Lett 2(2):77
18. Chatterjee J, Haik Y, Chen CJ (2003) J Appl Polym Sci 91:3337
19. Deng Y, Yang W, Wang C, Fu S (2003) Adv Mater 15:1729
20. Sauzedde F, Elaissari A, Pichot C (1999) Colloid Polym Sci 277:846
21. Kondo A, Fukuda H (1999) Colloids Surf A 153:435
22. Zhou SQ, Chu B (1998) J Phys Chem B 102:1364
23. Wu XY, Pelton RH, Tam KC, Woods DR, Hamielec AE (1993) J Polym Sci Part A: Polym Chem 31:957
24. Zrínyi M, Szabó D, Barsi L (1999) in: Osada Y, Rossi DE (eds) Polymer Sensors and Actuators. Springer, Berlin Heidelberg, p 385
25. Everett DH Pure (1986) Appl Chem 58:967
26. Tombácz E, Szekeres M (2001) Langmuir 17:1411
27. CONTIN Provencher SW (1985) Makromol Chem 82:632
28. László K, Kosik K, Geissler E (2004) Macromolecules 37:10067
29. Pelton RH, Pelton HM, Morfesis A, Rowell RL (1989) Langmuir 5:816
30. Schild HG, Tirrel DA (1991) Langmuir 7:665
31. Sakai M, Satoh M, Tsujii K (1995) Langmuir 11:2493

Progr Colloid Polym Sci (2008) 135: 200–208
DOI 10.1007/2882_2008_112

Published online: 2 September 2008

Z. Nagy
L. Novák
C. Kozma
M. Berka
I. Bányai

NMR Study of Poly(γ-Glutamic Acid) and Partially Benzylated Poly(γ-Glutamic Acid): Nanoparticles in Solution

Z. Nagy · L. Novák · C. Kozma · M. Berka · I. Bányai (✉)
Department of Colloid and Environmental Chemistry, Faculty of Science, University of Debrecen, H4032 Egyetem t.1, Hungary
e-mail: ibanyai@delfin.unideb.hu

Abstract Poly(γ-glutamic acid) (γ-PGA) and its partially benzylamidated (hydrophobized) derivatives were prepared and studied in solution by means of dynamic light scattering (DLS), 1D, 2D and PGSE NMR in order to determine the structure, size and aggregation in solution. By pH potentiometric titrations in aqueous solution the apparent p$K \approx 4$ of γ-PGA was determined. The measured diffusion coefficients as a function of pH showed the swelling of γ-PGA by deprotonation of carboxyls. DLS measurements showed a certain degree of aggregation even in dilute solution. The degree of aggregation is increased in the presence $H_2PO_4^-$ and HPO_4^{2-} buffer anions. Benzylamidation of 30–50% of caboxylates resulted in folded structure of the BzPGA, probably spherical like nanoparticles, verified by NMR diffusiometry and 2D NOE spectroscopy.

Keywords Aggregation · Amphipatic polymers · NMR diffusiometry · Poly(γ-glutamic acid) · Self-assembly

Introduction

Poly(γ-glutamic acid) (γ-PGA) is a biotechnologically produced anionic polymer. It was discovered by Ivánovics and Bruckner who obtained it from the capsule of *Bacillus anthracis* and later from a culture of *Bacillus subtilis* (*Bacillus mesentericus*) [1, 2]. More important observation is the presence of γ-PGA in "natto" (fermented soybeans) produced by *Bacillus natto* which is a basic ingredient of traditional Japanese and Korean kitchen [3, 4]. In the past two decades many papers were dealing in details with different aspects of effective biotechnological production of γ-PGA [4–8]. γ-PGA as a member of microbially produced poly(amino acids) is a water soluble, biodegradable and functionalizable non-toxic polymer of potential interest in a wide range of industrial and biomedical applications [3, 6, 7, 9, 10].

Amphipatic polymers, usually poly-ions functionalized with hydrophobic groups received a wide interest because they can form micelles, vesicles therefore are good candidates for nano-sized drug deliverers [11–13]. Akashi and his co-workers developed the idea of further functionalizing poly (amino acids) with hydrophobic groups in order to gain amphipatic biodegradable macromolecules with well controlled size [14]. Using water soluble carbodiimides (WSC) as catalyst they synthesized partially amidated γ-PGA with L-phenyl-alanine ethyl ester (PEA 10–60%) and L-leucine methyl ester (25–30%). By analyzing TEM micrographs they found that from fiber-like γ-PGA by 40–60% amidation with PEA spherical nanoparticles formed with a diameter of 200 nm. These nanoparticles were successfully tested with ovalbumin as protein carrier [14, 15]. Independently of their work but governed by same idea we worked out a new synthetic process for producing benzylamine functionalized γ-PGA without using WSC [16]. With this process we can prepare well characterized amphipatic poly (amino acids) in one-pot reaction without introducing WSC to the reaction mixture, therefore no care is needed for the subsequent elimination of the catalyst.

While for the preparation of γ-PGA derivatives extensive research has been done, much less efforts seem

to be made for characterization of the product [4, 8]. Although there are industrial scale producers of γ-PGA all around the world one cannot purchase it as a fine chemical with controlled molecular weight and well characterized chemical properties. In the published papers the authors use γ-PGA either donated by supporter companies or prepared by themselves. The molecular weight data are accepted as provided by the manufacturer or determined by the authors usually with gel permeation chromatography. There is also much less information in the literature about the size in solution and acid-base properties of γ-PGA although these properties usually play key roles in different applications [17–19].

When nanoparticles are prepared from γ-PGA the proofs of the formation are mainly electron microscopic images, TEM or SEM pictures. However these methods require solid, precipitated or dried samples. During the drying or precipitation processes the size may change because of aggregation and loss of hydration. The size measured in dry state is not always informative on the size in solution, in other words, on the size of nanoparticles in action [20–22]. In the literature the size of the nanoparticles prepared from γ-PGA are reported to lie between 40–300 nm for particles synthesized from γ-PGA of $M_w = 1 \times 10^5$–1.6×10^6 g/mol. The size of γ-PGA itself is not always characterized or mentioned although it is important, otherwise the origin and the mechanism of the formation of the nanoparticles prepared from γ-PGA cannot be explored. In solution, usually dynamic light scattering (DLS) is employed for determination of mean size and size distribution. With the advent and extended use of z-gradient NMR probe heads, nowadays NMR diffusiometry is also a possible choice. Neither of these methods can be considered to be less or more appropriate, both of them have advantages and considerable disadvantages.

In the literature no unambiguous relation could be found between the declared molecular weight of the starting γ-PGA and the determined size of the prepared nanoparticles from that. Akagi et al. reported no detectable nanoparticle formation from γ-PGA of $M_n = 380$ kDa unless hydrophobic groups were introduced into it [10]. However, when they prepared γ-PGA-L-PAE (γ-PGA grafted with phenyl alanine) nanoparticles of 305 to 150 nm could be obtained with increasing the degree of grafting from 43 to 61% from γ-PGA. They encapsulated a protein (ovalbumin) into these grafted nanoparticles, prepared from γ-PGA of $M_n = 300$ kDa in another series of experiments [15]. Application of different solvents did not affect the mean diameters but rather the size distribution. The reason of formation of nanoparticles was explained by self-assembly caused by the appearance of PAE hydrophobic groups. Another example is a Pb-γ-PGA complex prepared from a much larger γ-PGA of $M_w = 1200$ kDa. The size distribution of nanoparticles determined by DLS was found to be bimodal with a hydrodynamic diameter of 40–100 nm for individual nanoparticles while the larger particles were considered as aggregates. According to the authors hypothesis lead ions cross-linked the γ-PGA fibers to form nanoparticles by coordinative bond resulting in smaller nanoparticles [19].

The size and the degree of aggregation in aqueous solution may depend on pH, therefore the knowledge of the protonation equilibrium (or equilibria) of γ-PGA is vital. Surprisingly enough we could not find potentiometric or other type of studies for γ-PGA, only pK values were reported without indicating the source of the data. One of these is in a feature article as p$K = 2.3$ with $M_n =$ 380 kD [10]; the other is in an US patent as p$K = 3.6$ with $M_n = 1500$ kDa [23]. The first value is close to the pK of the α-carboxylate group of monomeric glutamic acid, the second one is similar to that of the triglutamate (α tripeptide, which has one COOH similar to that of γ-PGA) indicating that the pKcan be different for larger molecules [24].

As a summary, there are a large number of papers dealing with γ-PGA but mainly from the practical side. According to this wide interest, γ-PGA seems to be a very promising macromolecule for medical and environmental applications. However, we believe that for the next successful steps of R&D projects an extensive basic research is also needed. This paper reports results from experiments for structure and size determination of γ-PGA in different solvents, as well as changes of the size and the structure by hydrophobization and interaction with different ions in solution. We also describe the results of pH-potentiometric titration of γ-PGA with discussion of the average pK value we calculated from the titration data.

Materials and Methods

Materials

γ-PGA was produced by bacterial fermentation using *Bacillus licheniformis* ATC 9945A grown aerobically on medium "E" at 37 °C [25]. The product was purified and obtained in H-form solid material as described before [16]. Another batch of γ-PGA was kindly provided by NonStoptec Inc. Solvents D_2O (Cambridge), DMSO (Scharlau, Spain) and DMSO-d_6 (Cambridge) were used without further purification. Reagents HCl, KCl and KOH of analytical grade were purchased from Sigma-Aldrich. KOH was standardized by titration of weighted amount of potassium hydrogen phtalate (Sigma). BzPGA was synthesized by direct amidation and analyzed by SEC and ^{1}H and ^{13}C NMR according to the literature [16].

Methods

Size Exclusion Chromatography. Periodically, samples were drawn from the reaction mixtures of benzylamine and

PGA in DMSO, diluted with HPLC eluent, then analyzed by size exclusion chromatography (SEC) on an HP 1090 liquid chromatograph (formerly Hewlett-Packard, now Agilent Technologies, Santa Clara, CA), equipped with a Waters Ultrahydrogel Linear (Waters Kft, Budapest, Hungary) column ($300 \times 7.8\,\mathrm{mm}^2$). The eluent contained 5 mM NaH_2PO_4, 7.5 mM Na_2HPO_4, 140 mM NaCl, and 20% (v/v) acetonitrile in water. The flow rate was set to 0.7 ml/min and the column thermostated at 40 °C. The effluent was monitored with the built-in diode array detector of the HP 1090, allowing to record chromatograms simultaneously at several wavelengths.

NMR Measurements. Between 6 and 40 mg of γ-PGA and BzPGA were dissolved in 600 μL of hexadeuterated DMSO (DMSO-d_6) or in a mixture of H_2O and D_2O and analyzed with Bruker DRX 360 MHz and DRX 500 MHz NMR spectrometers equipped with inverse broadband z-gradient probe head. The temperature of the probe heads were regulated by Eurotoherm controller unit using electric heating and room temperature air cooling. Routine ^{1}H NMR and ^{13}C NMR measuring programs were used to record spectra in 1D J-modulated (^{13}C) and 2D (COSY, NOESY and HETCOR) mode at room temperature. The diffusion coefficient was measured at 300 K by pulse field gradient spin echo (PGSE) using standard *ledbpgp2s* (Bruker) 2D sequence. This is a stimulated spin echo pulse program designed especially for large molecules using bipolar gradient pulses for diffusion, two spoil gradient pulses (1 ms) and longitudinal eddy current delay (LED) for suppression of artifacts [26]. Usually 16 gradient steps were employed with full gradient power applying 3–5 ms gradient pulse length and 75–150 ms diffusion time. The NMR spectra were post-processed by means of 1D and 2D WinNMR software (Bruker©). The diffusion coefficients were calculated by non-linear least square method (Origin©) from attenuation of signals at increasing gradient power (G) according to the following equation:

$$I = I_0 \exp[-DG^2\gamma^2\delta^2(\Delta - \delta/3)]\,, \qquad (1)$$

where I and I_0 (when $G = 0$) are the integrated intensities of NMR signals; γ is the magnetogyric ratio; δ is the duration of gradient pulse; D is the diffusion coefficient and Δ is the diffusion time. The method was calibrated on D_2O using $D = 1.93 \times 10^{-9}\,\mathrm{m^2\,s^{-1}}$ at 300 K [27]. D was determined from integrated intensities of separated protons as a function of G^2. Normally three combinations of different diffusion times and gradient pulse durations were used.

The NOESY experiments were evaluated quantitatively by means of WinNMR software. 1D slices were selected and after the appropriate phase and baseline corrections the integrated intensities of the cross peaks and diagonal peak were determined at different mixing time. In order to determine the rate of cross relaxation the ratio of the integral of cross peaks and the diagonal peak was calculated and plotted against the mixing time. Numerical derivation of these curves at zero mixing time gave the cross relaxation rate.

Potentiometry. pH-potentiometric titrations were performed in 25-ml samples in the concentration range of 0.08–0.12mg/ml γ-PGA. The solid sample was dissolved in potassium hydroxide solution, and after dilution it was re-acidified using 0.2 M HCl solution. The measurements were carried out at constant temperature (298 K). A carbonate-free potassium hydroxide of known concentration was used [28] for the titration with the help of an automatically controlled Radiometer ABU 91 titration system equipped with a Metrohm 6.0234.110 combined electrode. Argon was bubbled through the samples to ensure the absence of oxygen and carbon dioxide and to stir the solution. pH readings were converted into hydrogen ion concentration and the protonation constant was calculated by means of a general computational program (SUPERQUAD) as it was described earlier [29, 30]. The concentration of COOH functional groups and the pK values were determined from the titration.

The experimental data as input data were also evaluated by the FITEQL program for the pK of γ-PGA [31]. The parameter adjustment procedure is based on minimizing the weighted sum of squares of the difference functions of mass balance equation for hydrogen ion, in other words, on the difference between the measured and calculated concentration of hydrogen ions. The value of WSOS/DF (WSOS/DF weighted sum of squares divided by degrees of freedom) depends on the estimates for the standard deviation in the experimental data. The experience has shown that values of WSOS/DF < 20 are common for a reasonable good fit. Our result can be thought as fair fit with WSOS/DF $= 41$–47.

Light Scattering. Scattering experiments were performed with Brookhaven Research Laser Light Scattering instrument with standard pinhole optics with a High Speed Research Grade Digital Autocorrelator (BI-9000AT). The light source was a NdYAg solid state laser, the wavelength of the vertically polarized light was $\lambda = 532$ nm. In typical experiments the scattering angles were between 30–60°. The concentrations of the PGA solutions were 10 mg/ml (Count rates 50–80 kcnts/s, duration time minimum 300 s). The measurements were carried out in optically homogeneous quartz cylinder cuvettes. DLS measurement yields the particle's diffusion coefficient, from which the spherical particle size is calculated using the Stokes–Einstein equation. The autocorrelation functions of DLS experiments were fitted with Contin method [32]. The light scattering measurement is very sensitive to the presence of large particles because the primary results are intensity weighted mean diameters. In a polydispersed system the final results depend on the condition (scattering

angles, delay times) and the fitting method. The scattering of the large particles (which may be dust or aggregates as well) is very intensive, therefore a very small amount of those can be detected.

Results and Discussion

Protonation Constant of γ-PGA

The titration curves of γ-PGA solution are shown in Fig. 1. The titration curves between pH = 2 and 9 could be described well with one pK value as 4.2 ± 0.1 by Superquad and 4.0 ± 0.1 by FITEQL. These relatively large difference and large standard deviations can be explained with the quality of titration data, the very simple model and the consequence of the different parameter fitting procedures.

The lack of size and shape data prevented us to refine the model using electrostatic double layer models. However we can state that γ-PGA can be characterized by a p$K \approx 4$. This pK value is larger than both values we could find in the literature (without published experimental details) [10, 23]. It is also higher than that of α-amino carboxylates which are usually around 2–3. A possible explanation is that the protonated γ-PGA forms very stable helical structure with 19-membered rings as observed experimentally and confirmed by theoretical calculations [33, 34]. Additional hydrogen bonds between carboxylate side chain and NH groups, although they are weak, can be responsible for the stability of the helix. Deprotonation may cause distortion of this structure by electrostatic repulsion and additional hydration, resulting in the relatively high pK for γ-PGA.

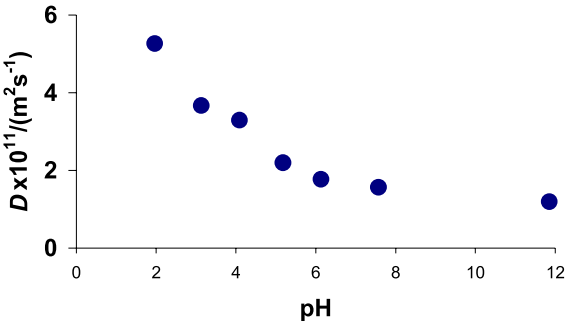

Fig. 2 Dependence of the apparent diffusion coefficient of γ-PGA on pH; $c = 10$ mg/ml, $T = 300$ K

The NMR diffusiometry supports the results of pH potentiometry. In Fig. 2 the variation of the diffusion coefficient of γ-PGA with pH is shown in aqueous solution (50% D_2O). The diffusion is slower progressing from acidic medium to basic medium indicating the repulsion of deprotonated carboxylates, which are not completely compensated by the shielding effect of K^+ ions present. Also, the hydration of the negatively charged carboxylates must be more effective in increasing further the size of γ-PGA. The steepest change in D with pH happens at pH about 4 indicating the reality of the pK value obtained from potentiometry. However, the diffusion coefficient of γ-PGA in the most acidic sample is somehow higher than expected.

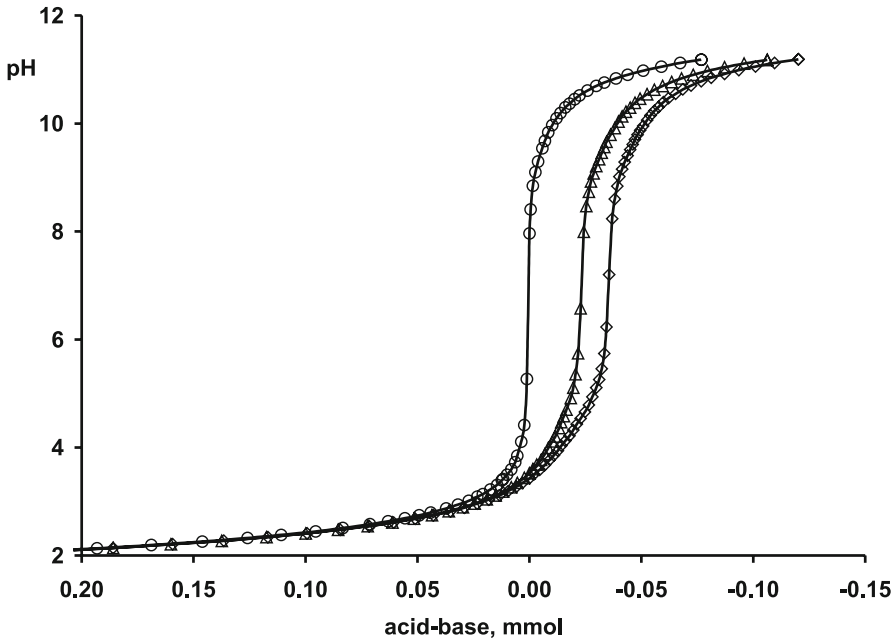

Fig. 1 Titration curves of γ-PGA: the measured pH as a function of the added acid (positive) and base amount (negative values). (○) acid solution without γ-PGA; (△) acid solution with 0.08 mg/ml γ-PGA; (◇) 0.12 mg/ml γ-PGA

Basically one expects constant value after the complete protonation. We have no explanation of this accelerated diffusion. The salt concentration is the highest in the acidic sample (no constant ionic medium was kept, because we added first KOH for higher pH and then HCl to lower the pH) and the substitution of H_3O^+ with K^+ counter ions somehow may cause a shrinking in the structure. Detailed studies with rigorously controlled salt concentration will help to clear this problem.

Characterization of Molecular Weight and Size of γ-PGA

When γ-PGA is a precursor for the preparation of nanoparticles, usually the molecular weight either is not given e.g. [16] or given by size exclusion chromatography (SEC or GPC) but the reference material is not always specified, e.g. [15]. In general, for SEC standardized polymers more or less similar to γ-PGA are used as standards, for example poly(acrylic amide) [3], poly(styrene sulfonic acid) [18] or in the present case poly(acrylic acid) (PAA) with known molecular mass. We found that the γ-PGA we prepared had a $M_p = 125$ kDa (peak molecular weight) while the γ-PGA from NonStoptec had $M_p = 89$ kDa. Of course it means that the retention time of γ-PGA corresponds to the retention time of PAA of M_n 125 and 89 kDa respectively.

The size determination of γ-PGA in aqueous solution has proven to be difficult. Size patterns derived from DLS were multimodal with wide distributions. The main peak had a radius about about 170 ± 30 nm. In the case of SLS (static light scattering) applying the Guinier-method [35] the average radius of gyration of $R_g = 126 \pm 13$ nm was obtained. Both light scattering techniques indicate the presence of aggregates of larger size than expected in solution considering proteins with same polymerization degree. By addition of excess amount of carbamide or guanidinium chloride as H-bond breakers [36] a smaller size of 10–20 nm has been found. However, these results are not relevant for dilute aqueous medium because of the large organic electrolyte concentration (6 M).

NMR diffusiometry seemed to be another promising choice because of the presence of measurable covalently bonded protons on γ-PGA. Typical NMR spectra of γ-PGA is shown as a function of applied pulse field gradient in Fig. 3 in DMSO-d_6. Scheme 1 shows a part

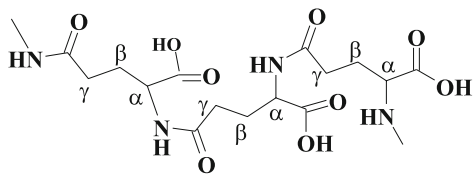

Scheme 1 Part of γ-PGA chain and the symbols used for citing in the text

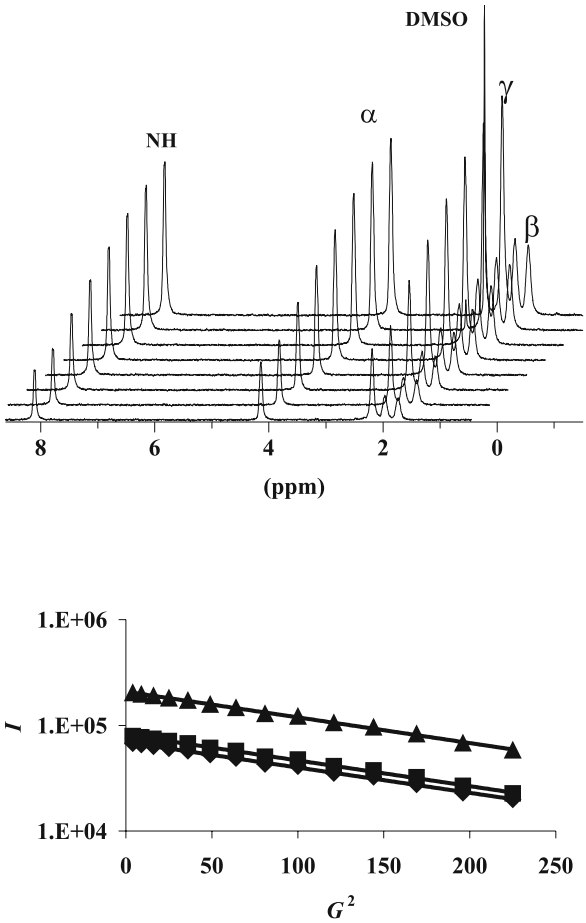

Fig. 3 Change of ^{1}H NMR spectra of γ-PGA as function of power of gradient (*upper part*). The logarithmic plot of integrated intensity against square of gradient (in arbitrary units). The three *lines* are integrals of the three separate parts of the spectrum as NH, α and $\beta + \gamma$ protons. $T = 300$ K, solvent is DMSO-d_6

of the polymer chain and the assignment of protons. According to Eq. 1 D_{PGA} can be calculated from the slope of the straight lines shown in Fig. 3. In all cases we used a non-linear least square analysis for obtaining D values in a more precise way. Straight lines in Fig. 3 serve an illustration about the quality of the data. From the measured diffusion coefficients the apparent hydrodynamic radius can be calculated using the Einstein–Stokes equation:

$$R_H = \frac{k_B T}{6\pi\eta D}, \tag{2}$$

where R_H is the hydrodynamic radius, k_B is the Boltzmann constant, T is the temperature, η is the viscosity of the solvent. This equation, as it is well known, has a restricted validity for spherical particles in continuum, but it is generally used in NMR diffusiometry, as well as in DLS technique, supposing that the size of water molecules is much smaller than that of the γ-PGA. The measured values are collected in Table 1.

Table 1 The measured diffusion coefficients and the calculated apparent hydrodynamic radii of γ-PGA and benzylamidated γ-PGA (BzPGA) in different solutions, determined by PGSE NMR at 300 K

Compound	c [mg/mL] (solvent)	D $\times 10^{12}$ [m^2/s]	R_H [nm]	Note
γ-PGA	42 (DMSO)	3.5_2	32	298 K
γ-PGA	10 (DMSO)	10.3_4	12	300 K
γ-PGA	9.7 (D_2O, KCl)	20.9_2	9.7	300 K
γ-PGA	10 (D_2O, 0.15 M PB)	8.4_5	24	300 K, pH = 6.2
BzPGA	22 (DMSO)	45.6_3	2.7	298 K, 30% Bz
BzPGA	10 (DMSO)	47.1_7	2.6	300 K, 50% Bz
BzPGA	10 (D_2O, 0.15 PB)	58.0_3	3.45	300 K 50% Bz, pH = 6.2

For γ-PGA the apparent R_H is probably far from the reality. This size is rather large comparing to bioproteins with similar molecular weight, e.g. HAS of M_n = 66.4 kDa has $R_H = 3.5$ nm [37, 38]. γ-PGA has an α-helix secondary structure as it is known from the literature [33, 34] however no hydrophobic core is available for a folding process therefore the shape can hardly be approximated with sphere. There is also a clear indication of aggregation because the diffusion becomes slower if the concentration is higher in DMSO. The faster diffusion of γ-PGA in water is probably due to the difference of viscosities of the two solutions. In this case PGSE NMR proved to be better choice over DLS because it gave the number average of the diffusion constant. Since the decay of integrated intensity of NMR peaks showed a single exponential but DLS indicated significant polydispersity, the fast exchange between the monomers and aggregates should have been held. However, the small amount aggregates contributes to the mean of diffusion constant in smaller degree in the case of NMR than in the case of DLS. This latter method gives an intensity weighted mean radius where the large particles dominate the average value.

It is an interesting observation that the diffusion is much slower in phosphate buffer (PB) which is usual medium both in SEC analysis or in biological applications. The most probable reason is the H-bond interaction between the dominant $H_2PO_4^-$ and HPO_4^{2-} anions at pH = 6.2 and the side chain (α) COO^- ions. The diprotonated phosphate ion may form a bridge between two side chain carboxylates of two single particles γ-PGA. In the case of benzylamidated PGAs the number of carboxylates available for this interaction is 30–50% less, therefore this effect is much less pronounced supporting the above explanation.

The most important consequence, can be drawn from Table 1, is that the BzPGA diffuses faster than γ-PGA. If no fragmentation happens during the preparation the molar weight of BzPGA and the size as well must be larger than that of γ-PGA. The possible explanation of the faster diffusion and the calculated smaller R_H is that, the shape of BzPGA is different. The difference in shape is probably the consequence of a structural modification of BzPGA, that is the formation of spherical nanoparticles as in the case of γ-PGA-PEA reported by Akashi et al. [14, 15].

Size and Structure of Benzylamidated γ-PGA (BzPGA)

Preparation of BzPGA was performed at high temperature in DMSO therefore fragmentation during the synthesis cannot be closed out without investigation. Fragmentation may result in smaller molecules and as a consequence faster diffusion in average [16]. By careful analysis of 2D NOESY NMR spectra either γ-PGA or BzPGA, we can prove that this is not the case here. In Fig. 4 the 2D NOESY spectrum of BzPGA of 30% functionalized is shown.

While the interpretation of cross peak intensities in NOESY is not straightforward in the case of small organic compounds for large molecules it seems to be easier [39]. The appearance of cross peaks in NOESY spectrum is the consequence of cross relaxation between the given protons, in other words they relax each other by means of dipole–dipole coupling. The intensity of the cross peak depends on the mixing time it goes through a maximum with that. The first, increasing part called "NOE build-up" depends on the nuclear distances and the rotation correlation time of the molecule (see below). The second, decreasing part is determined by the rate of longitudinal relaxation of the protons between which the cross peak is observed. The total analysis of the intensity vs. mixing time curves is difficult it requires a parameter fitting on bi-exponential theoretical function. However, this fitting procedure is very sensitive to the quality of experimental data. Another, more usable approach is to analyze the initial rate of build up of the intensity of cross peaks during the mixing period. For this calculation the relative intensity of the cross peak to diagonal peak can be used at different mixing time, taken from 1D slice. The intial rate of cross relaxation is inversely proportional to sixth power of distance between the protons which relax each other (i and j) and depends on the rotation correlation time of

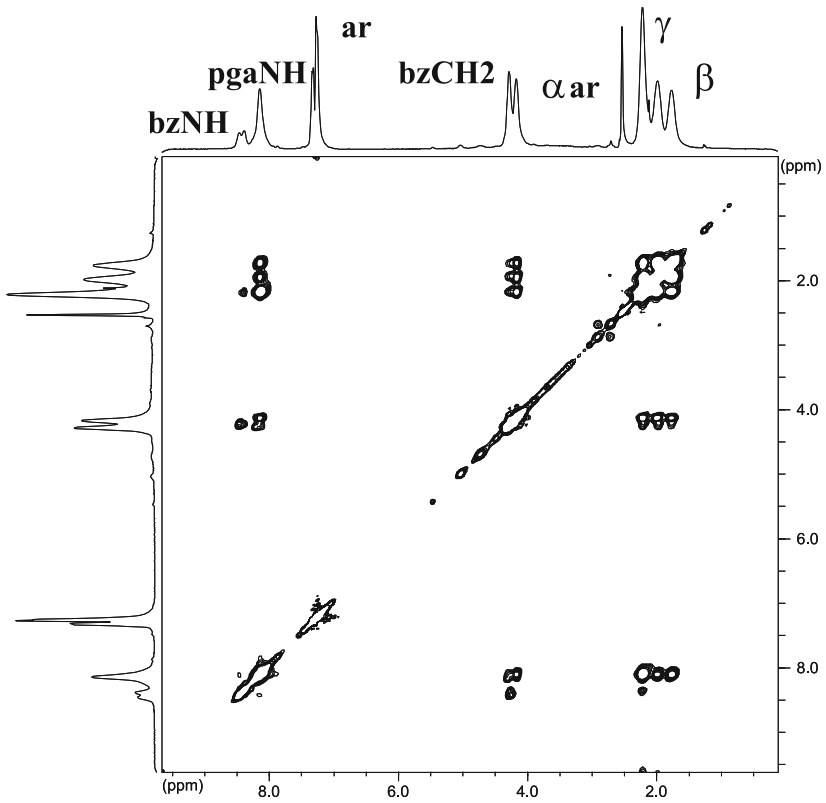

Fig. 4 500 MHz 2D NOESY spectrum of BzPGA functionalized in 30%; $c = 22$ mg/ml. The mixing time is 150 ms. $T = 300$ K

the molecule [39]:

$$\sigma_{i,j} = f(\tau_c) r_{i,j}^{-6} , \tag{3}$$

where τ_c is the global rotation correlation time of the molecule, $r_{i,j}$ is the distance between i-th and j-th protons which relax each other, $\sigma_{i,j}$ is the rate of cross relaxation which determines the rate of build up of cross peaks. $f(\tau_c)$ is the spectral density function expressed as follows

$$f(\tau_c) = q \left(\frac{6}{1 + 4\varpi_0^2 \tau_c^2} - 1 \right) \tau_c . \tag{4}$$

In case of large molecules at high resonance frequency ($\omega_0 = 500$ MHz in our case) and slow tumbling, (long τ_c) the cross relaxation rate is directly proportional to the correlation time through $f(\tau_c)$ and inversely proportional to the sixth power of distance between protons in space see Eq. 3. Usually the rotation correlation time is taken from independent experiments or considerations and the proton–proton distances are calculated. We show now another application. Since both in γ-PGA and BzPGA there are two protons which are at the same distance for sure, i.e. the two protons of AB doublet of β CH_2 group at 1.87 and 2.01 ppm. Between these two peaks of γ-PGA or BzPGA, the rate of the cross relaxation will be different if τ_c is different of the two molecules [39, 40]. Therefore a series of 2D NOESY spectra were recorded at different mixing times and rate of the cross relaxation (from NOE build-up) was determined. Figure 5 shows the change of cross peak intensities relative to the diagonal peak between the protons β CH_2 groups as a function of mixing time. It is seen that the initial rate is higher for BzPGA than that for γ-PGA therefore the rotation correlation time of BzPGA must be longer. Comparing with diffusion data it means that the BzPGA on one hand diffuses faster on the other hand rotates or tumbles slower than γ-PGA.

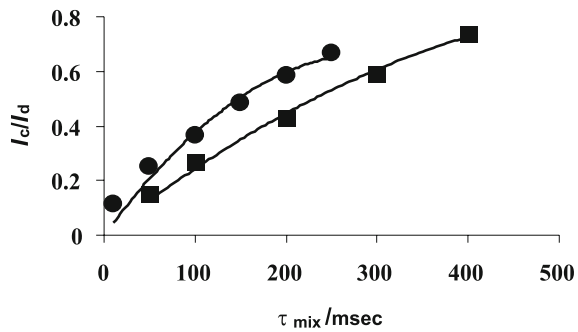

Fig. 5 Change of cross-peak intensity relative to the appropriate diagonal as a function of mixing for γ-PGA (■) and BzPGA (●). The *lines* are the best fitted second order polynoms

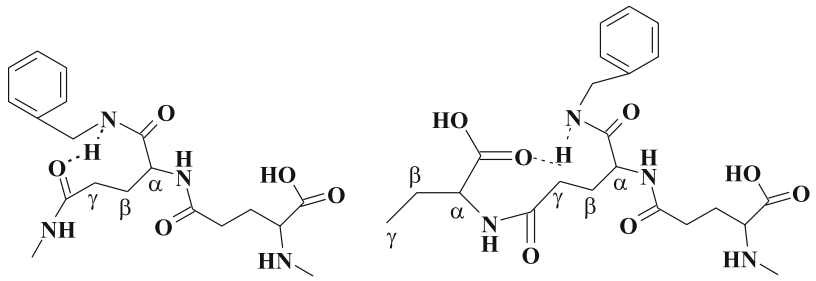

Scheme 2 The formation of ternary (folded) structure of BzPGA through H-bond between the new NH group and γ carbonyl (*left*) and the N atom of the new NH group and non-amidated α carbonyl (*right*)

A probable explanation of slower tumbling but faster linear diffusion of BzPGA is the appearance of hydrophobic benzyl groups on the side chain that makes the folding possible.

The folded BzPGA molecule (some authors call it as "molecular micelle" [14]) is more spherical than the helical (random coiled) γ-PGA, therefore its diffusion is faster. The faster rotation of γ-PGA can be explained with that the random coil cannot be characterized by one global rotation correlation time but rather by the average of faster local rotation correlation times from the inside dynamics of the molecule.

The 2D NOESY experiment also provides qualitative information about the nature of folding of BzPGA. The reaction with benzyl amide resulted in a new amide group (BzNH see Fig. 4 and Scheme 2) which may be able to make hydrogen bond to some skeleton carbonyls breaking the helix, or to α COOH group not amidated as Scheme 2. shows. Both H-bond can bring close in space the γ protons (2.19 ppm) and the new bzNH group (8.39 ppm) resulting in cross-peaks in NOESY spectrum (Fig. 4). It is also seen that the benzyl CH_2 protons (4.28 ppm) give cross peaks with both β and γ protons but definitely more intense cross-peaks with γ protons. This latter is hardly seen in Scheme 2 but can very easily be imagined if the benzyl group turns down into another position behind the scheme.

The lack of cross-peaks between phenyl group and either of the protons on the chain may be the consequence of small degree of the solvation of phenyl groups either in water or in DMSO. As a consequence, in the formed "molecular micelle" the hydrophobic phenyl side-chain is in large distance from the hydrophilic (liophilic) strongly hydrated (solvated) peptide chain turning into the internal part of the macromolecule.

Conclusions

In conclusion, γ-PGA is a weaker acid ($pK = 4$) than α amino acids probably because in acidic medium there is a structural stabilization of the protonated form therefore the release of protons are thermodynamically hindered. The γ-PGA molecule has no well defined ternary structure because of the lack of hydrophobic segments in the chain to allow folding and making a globular structure. On the other hand γ-PGA is disposed to aggregation even in dilute solution. The presence of small molecules and ions which tend to form H-bond enhance this ability of γ-PGA for making aggregates. Hydrophobic functionalization of γ-PGA results in a formation of a folded poly(amino acid) (BzPGA) which yields a more compact, smaller molecule which can be characterized with one global rotational correlation time. The shape of the particle is probably spherical with hydrodynamic radius 3–4 nm determined by NMR diffusiometry. The decrease in size may also be the consequence of the reduced degree of hydration or solvation in water or in DMSO.

Acknowledgement This work was supported by Hungarian Scientific Foundation (OTKA 49044) and GVOP 3.2.1 0154/3. One of the authors (M.B.) thanks Scholarship Békésy, the other (Z.N.) thanks Scholarship Öveges (Hungarian National Office of Research and Technology, NKTH) for financial supports. NonStoptec Inc. and Bogdany Petrol Ltd. are kindly acknowledged for continuous providing of chemicals and instrumental supports.

References

1. Iványovics G, Bruckner V (1937) Z Immunitätsforsch 90:304
2. Iványovics G, Erdös L (1937) Z Immunitätsforsch 90:5
3. Sung M-H, Park C, Kim C-J, Poo H, Soda K, Ashiuchi M (2005) Chem Rec 5:352
4. Shih I-L, Van YT (2001) Bioresour Technol 79:207
5. Shi F, Xu ZN, Cen PL (2006) Appl Biochem Biotechnol 133:271
6. Shi F, Xu ZH, Cen PL (2007) Sci China Ser B: Chem 50:291
7. Chen X, Chen S, Sun M, Yu Z (2005) Bioresour Technol 96:1872
8. Ashiuchi M, Kamei T, Misono H (2003) J Mol Catal B 23:101
9. Taniguch M, Kato K, Shimauchi A, Ping X, Nakayama H, Fujita K, Tanaka T, Tarui Y, Hirasawa E (2005) J Biosci Bioeng 99:245
10. Akagi T, Baba M, Akashi M (2007) Polymer 48:6429

11. Nishikawa T, Akiyoshi K, Sunamato J (1994) Macromolecules 27:7654
12. Harada A, Kataoka K (1999) Science 283:65
13. Kukula H, Schlaad H, Antonietti M, Förster S (2002) J Am Chem Soc 124:1658
14. Matsusaki M, Hiwatari K, Higashi M, Kaneko T, Akashi M, Chem Lett 33:398
15. Akagi T, Kaneko T, Kida T, Akashi M (2005) J Control Drug Rel 108:226
16. Novák L, Bányai I, Fleischer-Radu ÉJ, Borbély J (2007) Biomacromolecules 8:1624
17. Yao J, Xu H, Wang J, Jiang M, Ouyang P (2007) J Biomater Sci Polym Ed 19:193
18. Kunioka M (2003) Macromol Biosci 4:324
19. Bodnár M, Kjoniksen A-L, Monár RM, Hartman JF, Daróczi L, Nyström J, Borbély J (2008) J Hazard Mater 153:1185
20. Thill A, Spalla O (2003) Colloid Surf A: Physicochem Eng Asp 217:143
21. Thill A. Spalla O (2005) J Colloid Interf Sci 291:477–488
22. Jin H. Nishiyama Y, Wada M, Kuga S (2004) Colloid Surf A: Physicochem Eng Asp 240:63
23. Dilorio A, Mark S, Tongue PA (2003) US Pat. 6 533 938 B1, Worchester Polytechnic Institute, USA
24. Kállay C, Várnagy K, Micera G, Sanna D, Sóvágó I (2005) J Inorg Biochem 99:1514
25. Borbély M, Nagasaki Y, Borbély J, Fan K, Bhogle A, Sevoian M (1994) Polym Bull 32:127
26. Wu D, Chen A, Johnson CSJ (1995) J Magn Reson A 115:260
27. Mills J (1973) J Phys Chem 77:685
28. Gran G (1950) Acta Chem Scand 4:559
29. Irving HM, Miles MG, Pettit LD (1967) Anal Chim Acta 38:475
30. Gans V, Sabatini A, Vacca A (1985) J Chem Soc Dalton Trans 1196
31. Herbelin A, Westall J (1996) Oregon State University, Oregon, FITEQL 3.2. Computer program
32. Provencher SW (1982) Comput Phys Commun 27:213
33. Rydon HN (1964) J Chem Soc 1328
34. Zanuy D, Alemán C, Munoz-Guerra S (1998) Int J Biol Macromol 23:175
35. Guinier A (1939) Ann Phys 12:161
36. Strucksberg KH, Rosenkranz T, Fitter J (2007) Biochim Biophys Acta 1774:1591
37. Tayyab S, Haq SK, Aziz MA, Khan MM, Muzammil S (1999) Int J Biol Macromol 26:173
38. Rusoa JM, Taboadaa P, Varelaa LM, Attwood D Mosqueraa V (2001) Biophys Chem 92:141
39. Juranic N, Zsolnai Z, Macura S, in: Batta G, Kövér KE, Szántay CJ (Eds.) Methods for Structure Elucidation ny High-Resolution NMR. Vol. 8, Elsevier, Amsterdam, Lausanne, New York, Oxford, Shannon, Singapore, Tokyo p. 265
40. Macura S, Farmer II BT, Brown LR (1986) J Magn Reson 70:493

Progr Colloid Polym Sci (2008) 135: 209–217
DOI 10.1007/2882_2008_092

Published online: 29 August 2008

E. Fleit
Z. Melicz
D. Sándor
M. Zrínyi
G. Filipcsei
K. László
I. Dékány
Z. Király

IASON – Intelligent Activated Sludge Operated by Nanotechnology – Hydrogel Microcarriers in Wastewater Treatment

E. Fleit (✉) · Z. Melicz · D. Sándor
Department of Sanitary and Environmental Engineering, Budapest University of Technology and Economics, Műegyetem rkp 3, 1111 Budapest, Hungary
e-mail: fleit@vkkt.bme.hu

G. Filipcsei
Materials Structure and Modelling Research Group of the Hungarian Academy of Sciences at the Budapest University of Technology and Economics, 1521 Budapest, Hungary

M. Zrínyi · G. Filipcsei · K. László
Department of Physical Chemistry and Materials Science, Budapest University of Technology and Economics, Műegyetem rkp. 3, 1111 Budapest, Hungary

I. Dékány · Z. Király
Department of Colloid Chemistry, University of Szeged, Aradi vértanuk tere 1, 6720 Szeged, Hungary

Abstract Performance of biological wastewater treatment depends to a large extent on mechanical strength, size distribution, permeability and other textural properties of the activated sludge flocs. A novel approach was developed in applying synthetic polymer materials to organize floc architecture instead of spontaneously formed activated sludge floc. Developed microcarrier polymer materials were used in our experiments to mitigate technological goals. Preliminary results suggest that the PVA–PAA (polyvinyl alcohol–polyacrylic acid copolymer) is a feasible choice for skeleton material replacing "traditional" activated sludge floc. Use of PVA–PAA hydrogel material as microreactors and methods for biofilm formation of wastewater bacteria on the carrier material are described. Laboratory scale experimental results with microscopic size bioreactors and their potential application for simultaneous nitrification and denitrification are presented.

Keywords Activated sludge · Biofilm development · Hydrogels

Introduction

The driving forces for international efforts during the past few decades in the field of wastewater treatment technologies were the recognition of environmental problems with respect to surface waters (oxygen depletion, eutrophication, etc.) as well as more stringent environmental legislation (such as the 91/271/EEC directive). Apart from biologically degradable organic compounds, nitrogen forms, such as ammonium ion (nitrification), nitrate (denitrification) as well as phosphorus compounds and various micropollutant materials (heavy metals, oil derivates, hormone residues, etc.) have to be removed in biological and/or combined wastewater treatment technologies. As the results of these requirements and consequent technological developments the layout, design and process control of biological wastewater treatment plants have become highly diversified and complex.

The tendency of increasing technological complexity has remained the same during the past few decades. The question remains, however, whether this is the only right tendency to follow. In biological wastewater treatment technologies the majority of systems are based on activated sludge technology. In these systems the population structure and dynamics of the activated sludge microbial community is largely governed by indirect regulatory

mechanisms, such as aerated/non-aerated, reactor configurations and sludge recycling ratios. Yet, despite all the R + D efforts, the build-up of activated sludge flocs (bacterial aggregates) that is the key elements of the wastewater treatment process remains uncontrolled. Their morphology, microscopic architecture and biochemical build-up could only controlled by indirect methods. Furthermore, a design tendency is that for each particular functions (i.e., ammonium oxidation, nitrate reduction, etc.) a separate reactor space is provided, thus making nutrient removal costly.

In the framework of the IASON (*Intelligent Activated Sludge Operated by Nanotechnology*) project we introduced a non-traditional concept by utilizing the results of nanotechnological development in biological wastewater treatment process. Artificially constructed microreactors could perform complex tasks within a single aerated basin, as the biochemical processes are regulated by the responses of the microenvironment of IASON structures. These are governed directly by the build-up of the nanostructures constructed within. The new concept of IASON changes the traditional wastewater treatment approach. Hitherto, wastewater treatment plants and technologies were designed on the basis of the spontaneously formed activated sludge floc.

In biological wastewater treatment the biomass consists of multiple species, complex microbial communities either in suspended or immobilized form. The traditional activated sludge flocs, commonly called as suspended biomass in reality are also organized by immobilized bacterial consortia [1]. The heterogeneous multiple layered flocs (or biofilm) consist of several strata having an average size of several hundreds of μm, with porous structure, embedded EPS materials (extracellular slime materials). The knowledge to regulate or furthermore to design the microenvironment of activated sludge community is largely missing. Typical examples are the spontaneously occurring simultaneous nitrification/denitrification phenomena either in bioreactors or in secondary clarifiers or in both. The same bacterial layer within a spontaneously formed activated floc might have aerobic, anoxic or anaerobic microenvironment depending on the prevalent shear stresses, mixing and aeration regime. Should oxygen penetration depth change into the immobilized cell layers (irrespective to floc or biofilm structure) the consortia of microorganisms might switch from anaerobic fermentation pathways to the aerobic TCA cycle or could use the ammonium ion as energy source (i.e., nitrification) or depend on nitrate as final electron acceptor [2]. The heterogeneity of bacteria with respect their biochemical repertoire as well as their microscopic structure expressed in biofilm build up makes the predictions, modeling and process control difficult [3].

Activated sludge flocs used in biological wastewater treatment could be regarded as a sort of self-immobilized system where the carrier material itself consists of living and dead cell biomass. Self carrying biofilms are also used in several full-scale wastewater treatment applications (e.g., UASB – *upflow anaerobic sludge blanket reactors*). Similarly to suspended cell immobilized systems (activated sludge) the mechanisms of biofilm formulation, maturation and final structure formation (density, microchannels, other textural properties) are largely unknown and directly could not be controlled [4]. To overcome these drawbacks a novel concept has been developed (IASON) where biofilm development and final microstructure is directly controlled on the surface and within the inner layer of hydrogel materials in the same particle size dimensions of spontaneously formed activated sludge flocs.

Establishment of heterogeneous layers in biofilm developing on the PVA–PAA carriers was the most difficult step in the multifunctional reactor. The structure of the biofilm depends on many environmental conditions and biotic factors (inoculation of the gels, composition of influent (raw) wastewater, diurnal changes of influent wastewater, flow conditions and apparent shearing forces in the reactor, the continuously changing density and average thickness of the biofilm, texture and 3D structure of the biofilm. Two papers report various effects of presence or absence of microscopic channels and voids, dosing of the methanol, buffer solutions on biofilm structure [6, 7].

Laboratory scale results of artificial microcarriers (IASON) to which the activated sludge bacteria adhere and function in a designed and controlled microenvironment are presented in the paper. The objective of our laboratory scale research is to explore on how the hydrogel carrier materials can be designed and test their environmental reaction with and without wastewater bacteria. Technological results with the newly developed hydrogel materials (PVA–PAA (*polyvinyl alcohol–polyacrylic acid copolymer*) for nitrification and denitrification are detailed in the paper.

Materials and Methods

Synthesis and Treatment of Microcarrier Hydrogel Materials

Several batches of new hydrogel materials were tested and selected on the basis of their durability, size distribution (Fig. 1), density, surface properties regarding bacterial adherence as illustrated by Fig. 2. where the steps of the selection process of the technologically appropriable hydrogels materials are depicted. Some examples of investigated hydrogel beads are: PVA–PAA (polyvinyl alcohol–polyacrylic acid copolymer), modified starch and cellulose materials, ferromagnetic PVA, NIPA (*N*-isopropyl-acrylamide) gels. Technical details were discussed elsewhere [5]. In this paper the results with the PVA–PAA copolymer hydrogel beads are presented. In this carrier the regulation of the porosity (inner structure) of hydrogel pearls was achieved by the addition of fine

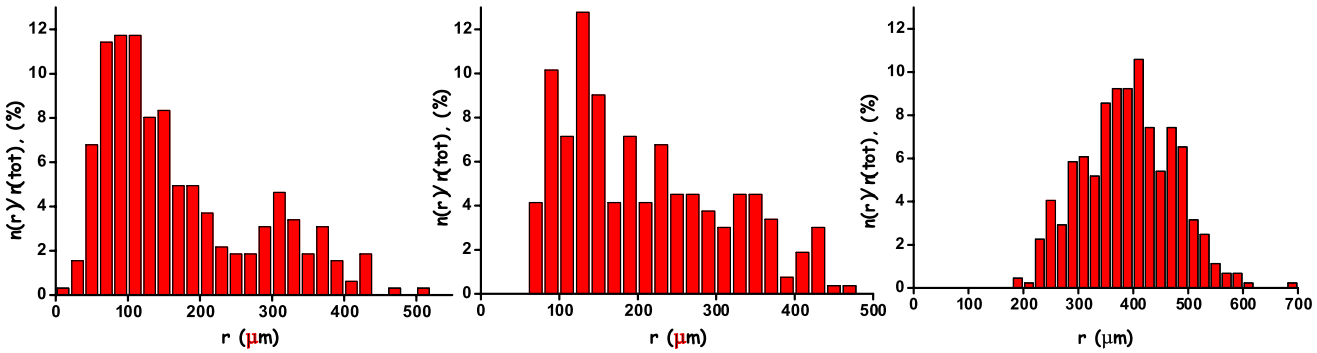

a) Non-treated PVA/PAS b) NaOH treated PVA/PAS c) NaOH treated PVA/PAS with fully developed biofilm attached to surface

Fig. 1 Size distribution of non-treated (**a**), NaOH treated (**b**) and biofilm covered (**c**) PVA/PAA gels with starch based on measurements of 350–400 particles (disappearance of small sized fraction is due to separation steps in preparation)

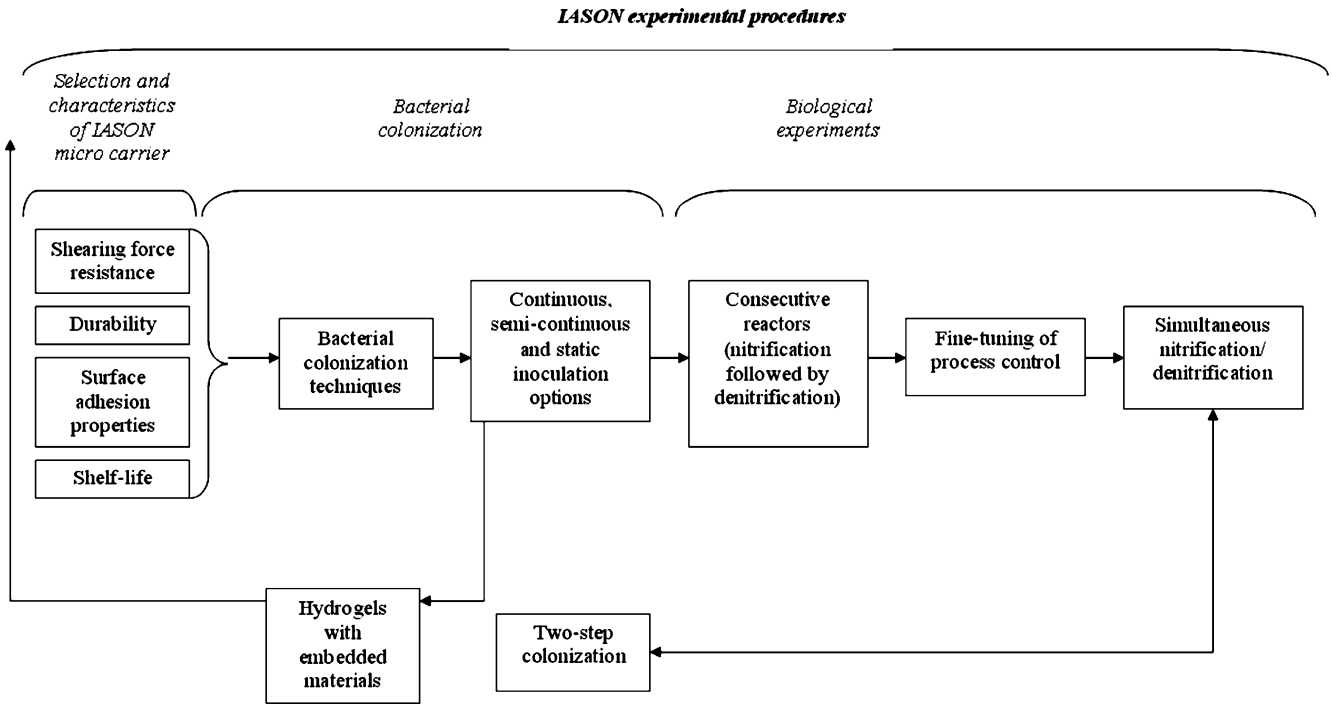

Fig. 2 Flow scheme of experimental procedures in selecting the technologically feasible hydrogel type(s)

starch suspension into the gelifying liquor hence embedding easily biodegradable substrate into the inner structure of the gels.

The starch contents of the gels was partially removed by simple method (heat and chemical treatment for 120 min, at 60 °C in 10 N NaOH solution) prior to bacterial colonization. Heat treatment and partial removal of starch from the polymer matrix did not alter the particle size distribution of the original gels beads (Fig. 1a,b). Presence of residual starch was checked by KI tests (potassium iodine solution staining and visual observation under microscope). KI test showed that starch was removed from the polymer matrix in the depth of 20–30 μm from the surface. Removal of near-to-surface embedded starch granules from the polymer matrix provided surface roughness and microholes for the wastewater bacteria for initial adherence. After the preliminary treatment with NaOH the process of bacterial colonization on the outer surface started. Further biodegradation of the inner starch particles within the gel beads provided additional adhesion surfaces to bacterial cells.

Previous experimental results focusing on the selection of adequate microcarrier for biofilm development [5] revealed that PVA–PAA gels concerning their durability, surface properties, resistance against mechanic strength were found to be the most favorable carrier material. On

the basis of these preliminary experimental results, various types of breeding and inoculation techniques were conducted on laboratory scale to investigate bacterial colonization processes. Investigations included the rate of biofilm attachment/detachment, as a function of hydraulic properties (turbulence) and loading conditions (i.e., substrate and nutrient loads per volume of gel) for wastewater microbial consortia in batch tests.

Tests with colonized hydrogels were carried out in continuously fed sequential biological reactors: the system was designed for complete nitrogen removal by the implementation of nitrifying (aerated and mixed tank, see Fig. 3.) and a post-denitrifying (mixed only) reactor. Methanol was dosed as external carbon source into the non-aerated tank to fulfill electron donor requirements of denitrification. Adjustment of methanol addition and aeration served for fine control of nitrogen removal processes.

Laboratory Scale Experimental Systems

The outline of the laboratory scale series of biological reactors for full nitrogen removal is depicted on Fig. 3. The system consisted of two consecutive reactors, reactor "A" (hydraulic volume $4.5–6.3 \times 10^{-3}$ m^3) for nitrification, aerated and mixed and consequent reactor "H" (hydraulic volume $6.3–7 \times 10^{-3}$ m^3) for denitrifying bacteria. Methanol dosage was adjusted to the varying nitrate concentration (40–70 g/m^3). The dissolved oxygen concentration was measured at sampling points 2, 3 and 5, on Fig. 3.

Wastewater analyses (at the sampling points on Fig. 3) were focused on traditional wastewater parameters (COD (*chemical oxygen demand*), SS (*suspended solids*), N and P forms) and biomass concentration parameters. pH and DO measurements were conducted at daily intervals.

Wastewater Composition and Origin

During the experimental period (3 months) wastewater of the effluent of secondary clarifiers from the South Budapest Wastewater Treatment Plant was utilized as inflow water to the system. Adjustment of water quality was needed according to the experimental objectives, such as dosing surplus ammonium ion, etc. At sampling point 1 (Fig. 3) ammonium concentration was raised to be around 60 g/m^3 (by dosing NH_4Cl solution into the raw wastewater), and pH was set and maintained by dosing 0.5 kg/m^3 $NaHCO_3$ to provide the necessary buffering capacity to influent wastewater. Influent wastewater composition in experimental system is given in Table 1.

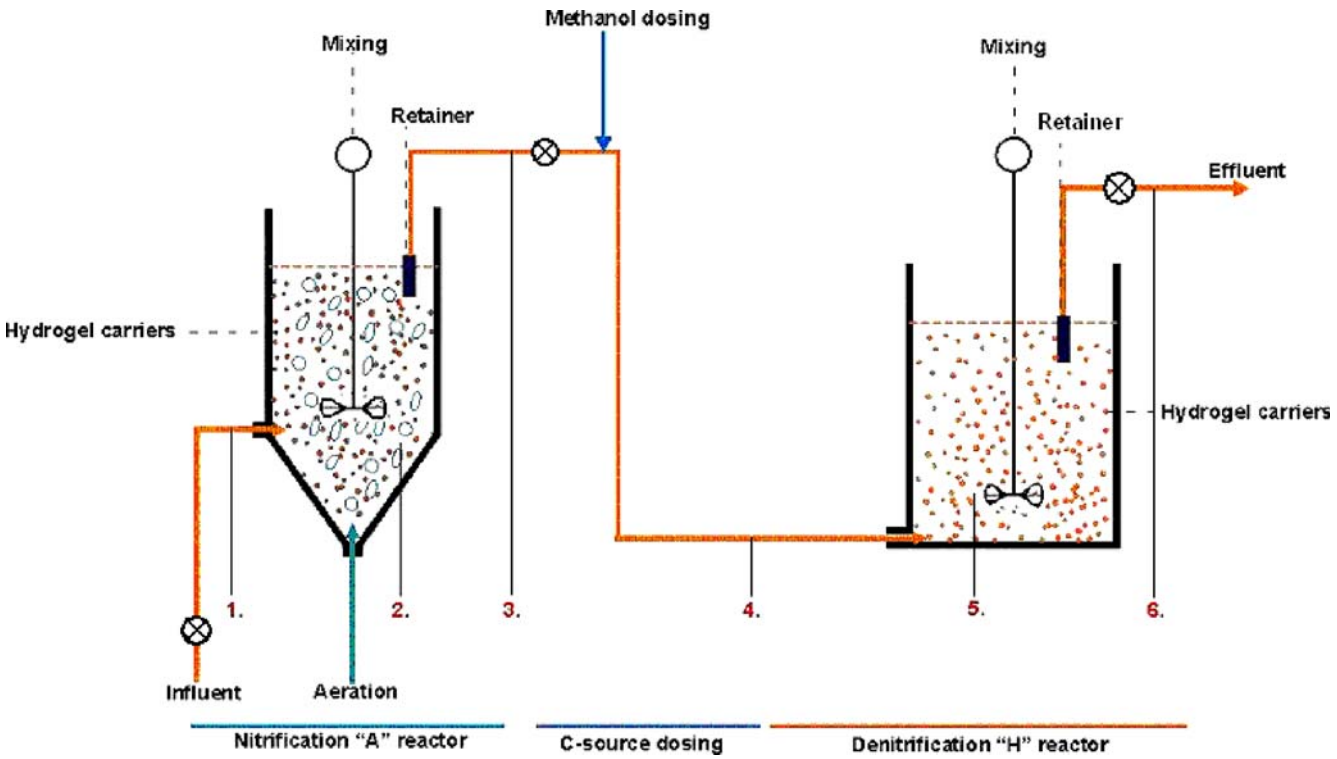

Fig. 3 Lay-out of laboratory scale experimental treatment system for nitrification and denitrification with C-source dosing. (Sampling points are numbered. Flow rates were regulated by PLP 66 peristaltic pumps)

Table 1 Composition of the influent wastewater used in consecutive reactors

Parameter	Average	Minimum	Maximum
pH	7.89	7.56	8.06
o-PO_4-P g/m^3	1.6	0.16	3.2
NH_4-N g/m^3	57	54	71
NO_2-N g/m^3	3.66	1.27	7.8
NO_3-N g/m^3	4.26	1.2	7.3
Kjeldahl N g/m^3	58	57	60
org N g/m^3	0.75	0.5	1
Total N g/m^3	64	62	66
SS g/m^3	4.1	3.5	5
COD g/m^3	71	55	87

Results and Discussion

Bacterial Colonization and Biofilm Maturation of Autotrophic and Heterotrophic/Denitrifying Bacteria

Biofilm establishment on microcarrier surfaces was achieved by using the natural attachment processes of the suspended wastewater bacteria into hydrogel carriers. Inoculation of the initial 500 ml gel material per reactor (A and H) was conducted by using wastewater bacterial consortia from the same plant from where the influent was originated. Suspended biomass (activated sludge) was ultrasonicated for disaggregating the flocs that was followed by a filtration step on 50 μm glass fiber filter. Initial biomass concentration measured as SS (suspended solids as g/m^3) was in the range of 5–10 g/m^3. Biomass development was monitored by regular microscopic investigations, SS measurement, and dry material contents determination of gels and attached biomass.

Results indicated that biofilm development and establishment of solid biofilm layers on the surface of PVA–PAA gels requires about 10–12 days (for heterotrophic bacteria) and more than 21 days in case of nitrifyers (autotrophic bacteria). The stages of the autotrophic bacterial growth on the carrier material were started initially by protobiofilm patch formation (approx. 3 days) that is followed by the slow appearance (see Fig. 4.) of single and multiple cell Proto- and Metazoa organisms (14–21 days). Upon the completion of the formation of the good textured, solid biofilm surface technological and environmental stress experiments were started. During the process of biofilm formation continuous care was taken for the removal of the spontaneously formed activated sludge flocs (detached biofilm particles in stirred and aerated reactors). Figure 4a–d illustrate the different stages of biofilm development.

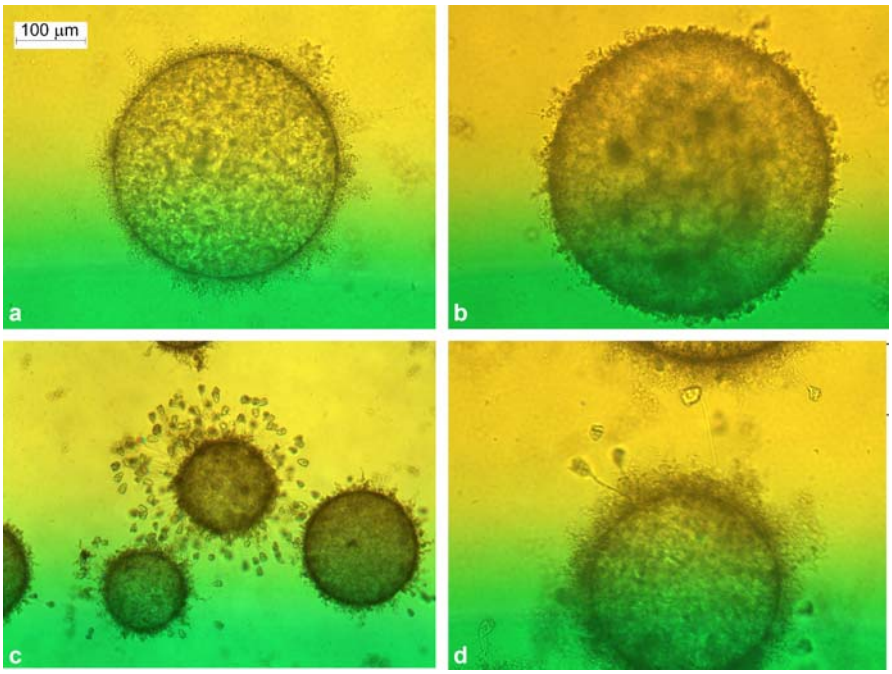

Fig. 4 Biofilm development on NaOH treated starch containing PVA–PAA hydrogel beads. **a** State of heterotrophic biofilm development on the 18th day. At this time the second stage of the inoculation was started. **b** Multiple layered biofilm on the 22nd day. 3 days after the inoculation with autotrophic (nitrifying) bacteria. **c** Fully developed multiple layer mature biofilm on the 25th day. *Epistylis* spp. and *Vorticella* spp. started to grow on the surface of the autotrophic biofilm indicating non-toxic environmental conditions and high sludge retention time. **d** Heterotrophic biomass from deeper biofilm layer starts to overgrow the upper autotrophic biofilm

Simultaneous Nitrification and Denitrification

Simultaneous nitrification and denitrification was achieved by the establishment of multiple strata protobiofilm formed by wastewater bacterial culture. The biofilm was spontaneously attached to the surface of the PVA–PAA hydrogels beads embedded with starch. Suspended growth activated sludge flocs and in our experiments the biofilm on hydrogel surfaces as well have the average diameter of several hundreds μm (see also Fig. 1 regarding the changes of particle size distribution). On microscopic scale there are steep concentration gradients within such entities, at a given dissolved bulk oxygen concentration in the deeper layers of the biofilm anoxic or anaerobic conditions could develop. The upper layer of the protobiofilm was dominated by the autotrophic nitrifyer bacteria as this layer was well aerated, nearest to bulk solution. The deeper layers of the established biofilm were supposed to be composed predominantly by the heterotrophic bacteria (facultative anaerobic microorganisms) hence denitrification was expected to occur in this zone.

Inoculation Procedures

The multiple layered biofilm was established by using double step inoculation process. At starting suspension of heterotrophic bacterial cells was dosed to the reactor twice at 24 h intervals. Prior to inoculation the suspended biomass was treated by ultrasonication for disaggregating the flocs followed by a filtration step on 50 μm glass fiber filter. In the second step of inoculation autotrophic nitrifying bacteria were dosed into the reactor on the 18th day of the inoculation process. Pretreatment and inoculation technique of the bacterial suspension was the same as described above. Wastewater characteristic during the inoculation period is shown in Table 2.

Indirect Control of Biofilm Composition and Structure by the Wastewater Parameters

The texture of the double layers biofilm could be controlled indirectly by the concentration levels of various electron acceptors and donors in influent wastewater and aeration intensity. Environmental conditions in bulk solution (i.e., within the reactor volume) can be finely tuned by regulating aeration intensity (fine and coarse bubble aeration) and methanol dosing that effects indirectly the dissolved oxygen concentration via the oxygen utilization of microorganisms. Conditions favoring the growth of heterotrophic biomass having higher growth rate than autotrophic counterparts could be altered by organic carbon source (methanol) dosage as evidenced by microscopic observation during the experiments. These observations were supported by regular nitrification and denitrification activity measurements (see also Fig. 5).

Spontaneous Growth of Suspended Flocs in Bioreactor

The presence of spontaneously suspended flocs (truly "planktonic" biomass fraction) in the bioreactor might cause false results as well as structural alterations in biofilm used in these small-scale laboratory experiments. Spontaneously formed suspended planktonic flocs were removed constantly from the bioreactor by thorough washing and withdrawal of the not polymergel-bound biomass at every second day.

Flow Conditions in the Bioreactor and Biofilm Density and Thickness

Environmental conditions such as temperature, exposure time, concentration of suspended bacteria (initial inoculum concentration) and most notably reactor hydraulics effect bacterial adhesion and the ultimate structure of formed biofilm. Shearing forces as dominant factors [8] effect the structure and hence technological performance of immobilized cell bioreactors [9]. As a general rule supported by many experimental evidence it is stated that higher shearing forces result in more compact but less tenuous biofilm structures [10].

Control of Dissolved Oxygen Concentration

The efficiency of denitrification in the lower layers of biofilm depends on the bulk level of dissolved oxygen

Table 2 Influent wastewater quality during the multiple step inoculation

Parameter	Unit	Heterotrophic biofilm			Double layered biofilm		
		Minimum	Maximum	Average	Minimum	Maximum	Average
NH_4-N	g/m^3	13.7	24	21	23.8	52.2	30
NO_2-N	g/m^3	0.1	3.9	1.8	0.05	0.7	0.14
NO_3-N	g/m^3	21	63	44	17	52	28.5
pH		7.8	8.2	8.1	7.86	8.26	8.04
Conductivity	μS/cm	1765	1862	1800	2110	2120	2110
Temperature	°C	20	21	20.5	20	21	20.5

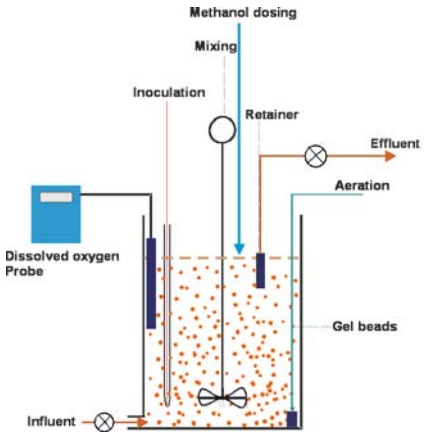

Hydraulic reactor volume: 6.3-7 * 10^{-3} m^3
Volume of the PVA-PAA gels: 0.6 * 10^{-3} m^3
Hydraulic loading: 0.5-0.7 * 10^{-3} m^3/hour
Methanol dosing: 0.3 g/m^3 of influent wastewater (corresponding to 415 g/m^3 COD value)

Dissolved oxygen level was measured at every 15 minutes (see also Fig 6a and 6b).
The required DO levels were set by the intensity of aeration.

Fig. 5 Laboratory scale experimental system for simultaneous nitrification and denitrification with additional C-source dosing

and the diffusion through the upper layers of fully grown biofilm. Structural changes of biofilm were monitored microscopically at daily intervals, while technological performance of the biomass was continuously checked. Should nitrification efficiency drop throughout the experimental period dissolved oxygen concentration in the bioreactor was increased to favor autotrophic growth (i.e., stepwise increase of bulk oxygen concentration).

Dosage of the Methanol (Organic Carbon Source for Denitrification)

Growth rate of heterotrophic denitrifying bacteria had to be controlled to maintain the depth and texture of the deeper layers of biofilm. During development period of the biofilm the growth rate of heterotrophic bacteria was limited by the concentration of organic carbon source (methanol). The background COD concentration of methanol in influent wastewater was kept constant throughout the experimental period. The continuously aerated and methanol dosed system containing the biofilm covered PVA–PAS hydrogel beads is shown on Fig. 5. The hydraulic retention time was set to 9.5–10.5 h close to the normal operating range of full-scale wastewater treatment systems.

Technological Results

Influent and effluent wastewater quality of the laboratory system was measured daily to obtain information on the technological capabilities of the system and its temporal changes. Figure 6 depicts the daily removal efficiencies for N compounds upon the development of multiple layered biofilm. In this biofilm the upper layer consisted of mostly autotrophic bacteria able to oxidize ammonium ion in the presence of oxygen (nitrification) and the lower layer consisting of predominantly heterotrophic bacteria able to reduce nitrate to nitrogen gas in the absence of oxygen

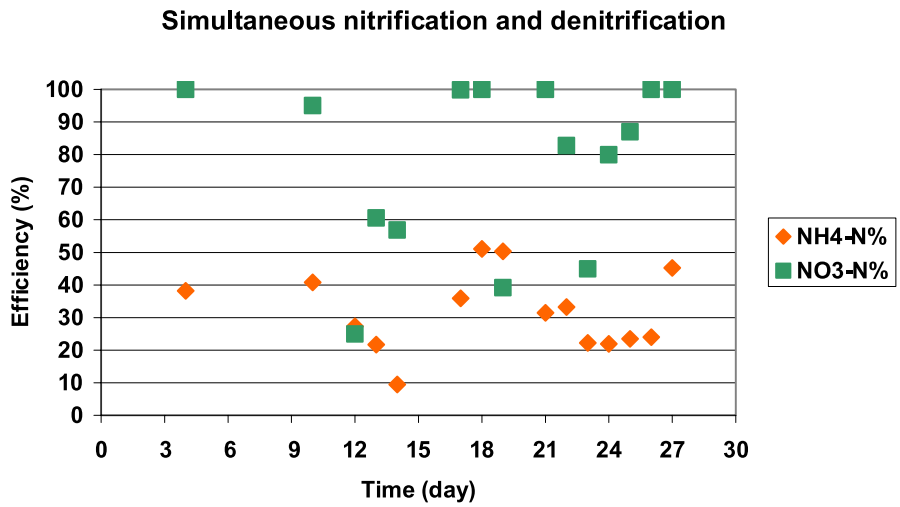

Fig. 6 Removal efficiencies of NH_4-N and NO_3-N in the simultaneous nitrification/denitrification system

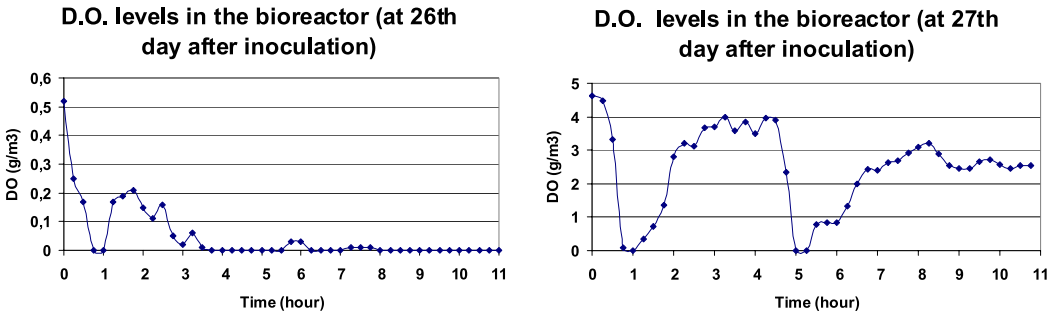

Fig. 7 Dissolved oxygen concentration profiles in the bulk solution during simultaneous nitrification/denitrification experiments

by utilizing methanol as electron donor for the reduction process (denitrification). Figure 6. shows the removal efficiency fluctuations in terms of ammonium ion and nitrate that are largely due to altered oxygen concentrations, inoculations and formation of spontaneous flocs. In the volume of the reactor the mixing was always complete as evidenced by DO levels checked at various points. This might indicate along with the measured ammonium and nitrate removal rates (Fig. 6) that spatial heterogeneity of DO was established within the microscopic layers of the biofilm enabling to form anoxic zones for denitrifier bacteria.

As the oxygen requirement of these microbiologically mediated processes is contradicting it is of interest to monitor closely the bulk DO level across the experiments as depicted on Figs. 7a and 7b. Considering the low dissolved oxygen concentrations on Fig. 7a nitrification would not be expected to occur under these conditions. The corresponding results on Fig. 6 however clearly indicate the opposite (days 26 and 27). Nitrification activity of autotrophic bacteria was observed at DO level below 0.2 g/m^3 on the 26th day (23%), while it was 45% on the 27th day. Removal efficiency of denitrification was close to 100% irrespective to bulk DO levels (in the range of 0.2 g/m^3 and higher than 2 g/m^3). It is noted that efficiency of nitrification increased slightly by elevated DO concentration levels.

Conclusions

In biological wastewater treatment technologies most of the full-scale systems are based on activated sludge technology. In these systems the population dynamics of the activated sludge microbial community cannot be regulated directly. The architecture of activated sludge flocs (bacterial aggregates) that are the key elements of the wastewater treatment process remains uncontrolled. The IASON project aimed to overcome these problems by the introduction of microscopic carrier structures to which the activated sludge bacteria adhere and meet technological objectives. In this paper the results of the preliminary laboratory experiments of simultaneous nitrification and denitrification are presented.

On the basis of the preliminary durability checks we selected the PVA–PAS hydrogel material with embedded starch particles for further testing and to address wastewater technological problems. We developed colonization techniques for the establishment of multiple species biofilm structures on hydrogel surfaces having different biochemical potential (auto- and heterotrophic populations). Application of two steps inoculation techniques (in consecutive manner) made possible the coexistence of ammonia oxidizer (nitrification) and nitrate reducer (denitrification) bacteria in the same bioreactor volume. The layered biofilm structures were able to proceed with the simultaneous removal of nitrogen forms (NH_4^+, NO_2^- and NO_3^-) in a single, aerated biological reactor.

Acknowledgement The present research was funded by the National Office for Research and Technology of Hungary grant No. 3/081/04. Technical assistance of Ms. Ildikó Musa, Head of the Laboratory of Wastewater Treatment Technology (Department of Sanitary and Environmental Engineering BME) is gratefully acknowledged.

References

1. Moussa MS, Hooijmans CM, Lubberding HJ, Gijzen HJ, Van Loosdrecht MCM (2005) Modelling nitrification, heterotrophic growth and predation in activated sludge. Water Res 39:5080–5098
2. Stoodley MP, Sauer K, Davies DG, Costerton JW (2002) Biofilms as complex differentiated communities. Annu Rev Microbiol 56:187–209
3. Picioreanu C, Kreft J-U, Klausen M, Haagensen JAJ, Tolker-Nielsen T, Molin S (2007) Microbial motility involvement in biofilm structure formation – a 3D modelling study. Water Sci Technol 55(8–9):337–343
4. Van Loosdrecht MCM, Heijnen JJ, Eberl H, Kreft J, Picioreanu C (2002) Mathematical modelling of biofilm structures. Antonie van Leeuwenhoek 81:245–256
5. Fleit E, Somlyódy L, Pőcze K, Melicz Z (2007) Intelligent Activated Sludge Operated by Nanotechnology –

IASON. Poster presentation at 2007 IWA Leading Edge Technologies Conference, Singapore
6. Mascari L, Ymele-Leki P, Eggleton CD, Speziale P, Ross JM (2003) Fluid shear contributions to bacterial cell detachment initiated by a monoclonal antibody. Biotechnol Bioeng 83:65–74
7. Eberl HJ, Parker DF, Van Loosdrecht MCM (2001) A new deterministic spatio-temporal continuum model for biofilm development. J Theor Med 3:161–175
8. Isberg RR, Barnes P (2002) Dancing with the host: flow-dependent bacterial adhesion. Cell 110:1–4
9. Klapper I, Rupp CJ, Cargo R, Purvedorj B, Stoodley P (2002) Viscoelastic fluid description of bacterial biofilm material properties. Biotechnol Bioeng 80:289–296
10. Chang HT, Rittmann BE, Amar D, Heim R, Ehrlinger O, Lesty Y (1991) Biofilm detachment mechanisms in a liquid fluidised bed. Biotechnol Bioeng 8:499–506

Progr Colloid Polym Sci (2008) 135: 218–224
DOI 10.1007/2882_2008_102

Published online: 11 September 2008

Béla Pukánszky Jr.
Kristóf Bagdi
Zsuzsa Tóvölgyi
József Varga
Lajos Botz
Stephan Hudak
Tamás Dóczi
Béla Pukánszky

Effect of Interactions, Molecular and Phase Structure on the Properties of Polyurethane Elastomers

Béla Pukánszky Jr. · Kristóf Bagdi · József Varga · Stephan Hudak · Béla Pukánszky (✉)
Laboratory of Plastics and Rubber Technology, Department of Physical Chemistry and Materials Science, Budapest University of Technology and Economics, P.O. 91, 1521 Budapest, Hungary
e-mail: bpukanszky@mail.bme.hu

Béla Pukánszky Jr. · Kristóf Bagdi · Béla Pukánszky
Institute of Materials and Environmental Chemistry, Chemical Research Center, Hungarian Academy of Sciences, P.O. 17, 1525 Budapest, Hungary

Zsuzsa Tóvölgyi · Lajos Botz
Department of Pharmaceutics and University Pharmacy, Medical School, University of Pécs, P.O. 99, 7601 Pécs, Hungary

Tamás Dóczi
Department of Neurosurgery, Medical School, University of Pécs, P.O. 99, 7601 Pécs, Hungary

Abstract Linear polyurethanes with various stoichiometry were prepared from 4,4′-methylenebis(phenyl isocyanate), 1,4-butanediol and poly(tetrahydrofuran) in melt reaction. The molecular weight of the polymers was estimated from the equilibrium torque measured during the reaction, mechanical properties were characterized by tensile testing and DMA measurements, while phase separation by the determination of transparency. Changes in the NCO/OH ratio led to the expected changes in molecular weight. Both strength and elongation-at-break increased with increasing isocyanate content up to the equimolar ratio of the two functional groups, but decreased only slightly at larger NCO/OH ratios. On the other hand, modulus assumed minimum value in the same composition range. The extent of phase separation is the smallest and the number of mobile soft segments the largest at around the equimolar ratio of the two functional groups. While viscosity depends only on molecular weight, strength and deformability are strongly influenced also by interactions, which on the other hand drive phase separation and completely determine stiffness.

Keywords Medical applications · Phase separation · Polyurethane elastomer · Structure–property correlations

Introduction

Polyurethanes (PU) are very versatile materials used in a large variety of application areas [1, 2]. Their properties depend on several factors and can be varied in a wide range by the proper selection of components and composition [3–7]. Depending on these factors polyurethanes can be cross-linked rigid or elastic foams or linear elastomers, but they are also applied as adhesives, paints, etc. [8–12]. One of the most important areas of their use is the preparation of medical devices; the excellent properties of PU makes possible to meet the stringent conditions of such applications [13–16]. Compatibility with tissue and blood, stability, appropriate mechanical properties and other conditions can be all satisfied by the proper adjustment of composition [17–19]. However, fine tuning of properties

to meet a specific application requires the deep knowledge of structure–property correlations and the factors influencing them [20].

The final properties of polyurethanes are determined by many factors. Molecular weight and molecular architecture have the same importance like in all other polymers. Bifunctional monomers yield linear polymers, segmented polyurethane elastomers. However, the distribution of structural elements and the end groups formed may result in strongly differing properties even at the same composition [21–23]. Polyurethanes contain several polar groups which enter into various interactions with each other usually leading to phase separation, to the formation of soft and hard phases. The extent of phase separation, the size of the structural units and their properties may have strong effect on the final properties of the polymer [24–27]. The various factors, i.e. molecular characteristics, interactions and phase structure influence each property of the polymer in a different way [28–30], thus the knowledge of these relationships is essential to achieve the desired combination of properties.

The goal of our research was to prepare a segmented polyurethane elastomer for medical application. In order to meet the stringent requirement of the application, a wide range of polymers were prepared with various compositions, structure and properties. In one series of experiments we prepared polyurethanes with varying stoichiometric ratio of the isocyanate and the hydroxyl groups to change the molecular weight of the polymer. However, the modification of composition changed also interactions and phase structure. In this communication we report the effect of various factors on the properties of the segmented polyurethanes prepared.

Experimental

The polyurethanes were prepared from 4,4′-methylenebis(phenyl isocyanate) (MDI), 1,4-butanediol chain extender (BD) and poly(tetrahydrofuran) polyether polyol with a molecular weight of 1000 (PTHF). All three ingredients were purchased from Aldrich and used as received. The –OH functional group ratio of polyol/total diol was kept constant at 0.4 in all experiments. In this study the variable was the ratio of the isocyanate and the hydroxyl groups (NCO/OH), which changed between 0.940 and 1.150. Polymerization was carried out by melt reaction in an internal mixer (Brabender W 50 EH) at 150 °C, 50 rpm for 30 min. For characterization purposes the polymer was compression molded into 1 mm plates at 200 °C and 5 min using a Fontijne SRA 100 machine.

Several techniques were used for the characterization of the samples. The torque and temperature of mixing was recorded during polymerization, which give information about the kinetics of polymerization and the molecular weight of the final product. An attempt was made to determine molecular weight also by GPC. Measurements were done in tetrahydrofurane using a Waters 201 chromatograph with 5 UltraStyragel columns. Polystyrene samples of narrow molecular weight were used for calibration. DMA spectra were recorded on samples with $20 \times 10 \times 1\ mm^3$ dimensions between −120 and 200 °C at 2 °C/min heating rate in N_2 atmosphere in tensile mode using a Perkin Elmer Pyris Diamond DMA apparatus. The mechanical properties of the samples were characterized by tensile testing on dog bone type specimens with $50 \times 10 \times 1\ mm^3$ dimensions at 100 mm/min cross-head speed using an Instron 5566 apparatus. Tensile strength and elongation-at-break were derived from recorded force vs. elongation traces, while Young's modulus was determined from the initial, linear section of the traces. The transparency of the samples was measured by a Spekol UV-Vis apparatus at 500 nm wavelength.

Results and Discussion

The various aspects of the structure and properties of the polyurethanes prepared are discussed in separate sections. Molecular weight, mechanical properties and phase structure are presented first, followed by the discussion of structure–property correlations.

Molecular Weight

According to the rules of stepwise polymerization, the molecular weight of the polymer decreases with the changing stoichiometric ratio of the two functional groups; it drops

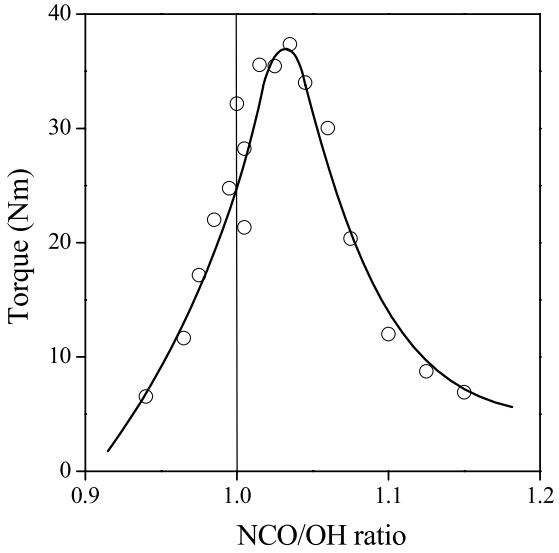

Fig. 1 Effect of composition on the equilibrium torque of the melt at the end of the polymerization reaction

drastically with increasing deviation from equimolar stoichiometry. The torque of the polymer melt in the internal mixer is proportional to viscosity, which on the other hand depends on molecular weight. Accordingly, torque is a good indicator of changes in molecular weight if all other conditions are the same. The torque measured at the end of the reaction is plotted against the NCO/OH ratio in Fig. 1. The expected correlation is obtained, molecular weight decreases drastically with changing stoichiometry. The maximum of the correlation is not at equimolar ratio of the two components probably because of side reactions, some impurities or the effect of moisture, which cannot be avoided in spite of all efforts done.

We must call the attention here to a few important facts. The polymer flows freely and the sample could be compression molded into plates even at large isocyanate/hydroxyl ratios indicating that considerable cross-linking did not take place. The determination of possible cross-linking was difficult by any other means since the solubility of the samples is rather poor in all common solvents. Although we made an attempt to determine molecular weight by GPC and we obtained a similar correlation to the one presented in Fig. 1, we do not trust the results obtained, because most of the samples could not be dissolved completely without residue.

We found it also important that the correlation is almost completely symmetrical, viscosity is only slightly higher on the side of isocyanate excess than at large OH content. The slight difference might result from the different effect of chain ends and the stronger interaction of the urethane moieties. In further consideration we assume that the polymer consists of mainly linear chains.

Mechanical Properties

The tensile strength of the samples is plotted against the stoichiometric ratio of the components in Fig. 2, while the corresponding elongation-at-break values in Fig. 3. The two correlations are very similar to each other, but unlike the torque vs. NCO/OH correlation they are highly asymmetric. Ultimate tensile properties are strongly influenced by molecular weight. Increasing length of the molecules makes possible the formation of multiple entanglements and strongly increases tensile strength and the ultimate deformation of the samples.

This effect is clearly demonstrated in the left hand side of the correlations, where excess number of –OH groups were added to the reaction mixture. On the isocyanate side larger strengths and elongations were measured, which cannot result from cross-linking or longer chains, because viscosity changed symmetrically with changing stoichiometry. The asymmetry of the correlation is probably caused by the stronger interactions prevailing at large isocyanate content; both the urethane and the amine end groups formed may enter into stronger interactions with each other than the free –OH end groups. These results clearly indicate that interactions have a stronger influence on properties in the solid than in the melt state.

The composition dependence of stiffness is presented in Fig. 4. The correlation differs very strongly from those shown previously (see Figs. 1–3). Stiffness decreases almost linearly with increasing NCO/OH ratio until a minimum, which more or less corresponds to the maximum observed in Figs. 1–3, and then increases also linearly with further increase in isocyanate content. The figure clearly

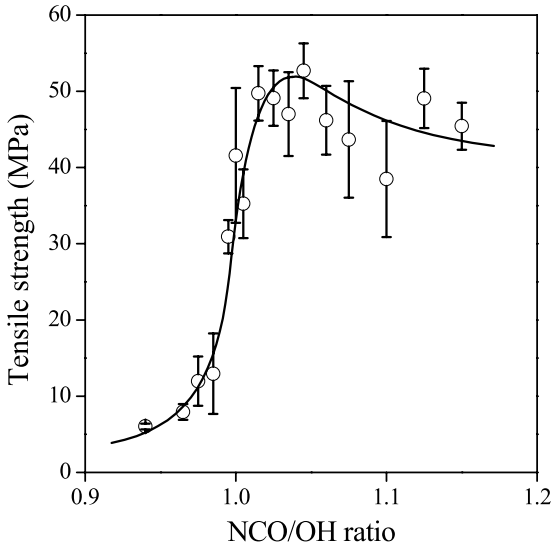

Fig. 2 Dependence of the tensile strength of segmented polyurethanes on the NCO/OH ratio of the reaction mixture

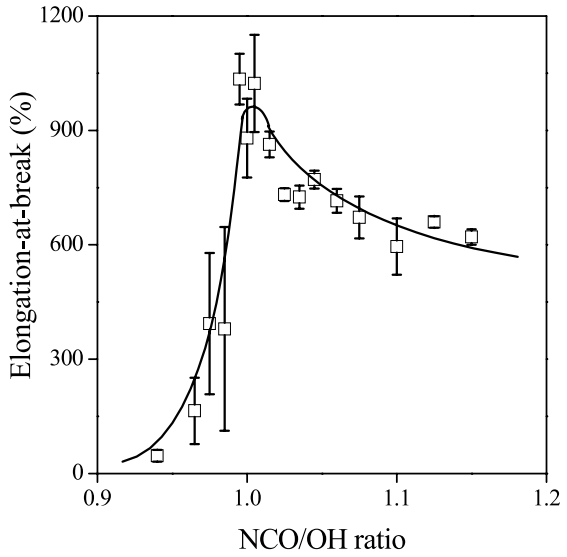

Fig. 3 Changes in the elongation-at-break values of segmented polyurethanes as a function of the relative number of functional groups

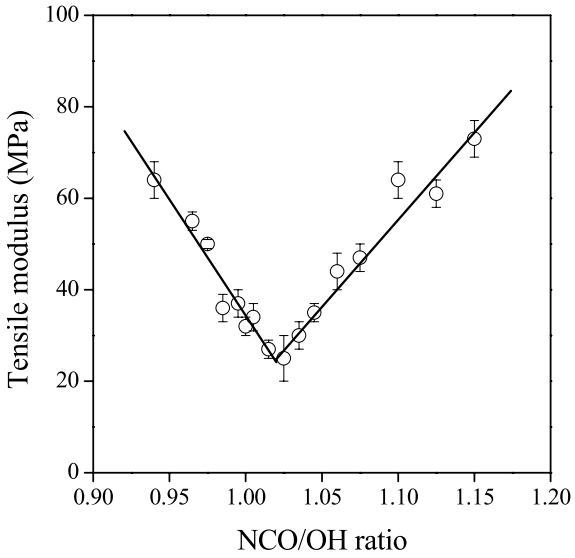

Fig. 4 Tensile modulus of polyurethanes vs. the stoichiometric ratio of the functional groups

shows that modulus does not depend on molecular weight practically at all, but on some other factor, which also changes with composition. Based on the other results presented up to now, a trivial explanation cannot be given for the correlation.

Relaxation, Mobility

DMA is a powerful tool for the characterization of the molecular structure of polymers; it reveals the number of relaxing units and offers some information also about their size and mobility. A typical DMA spectrum is presented in Fig. 5. Three relaxation transitions of various intensities can be observed on the traces of storage and loss modulus as well as on the temperature dependence of loss tangent. The first appears at around −75 °C with a relatively low intensity. The exact identification of the relaxing species is relatively difficult; it might belong to the aliphatic units of the polytetrahydrofurane segments. The second transition detected at around −13 °C is obviously the relaxation transition of the soft segments of the PU chains. The intensity of this transition is considerable and dominates the spectrum. The third, weak transition appears at higher temperature, at around 75 °C indicating the movement of larger, less mobile structural units. We may assume that this transition belongs to the movement of the hard segments. The small intensity of this transition can be explained by the stiffness of these segments, which does not change much during the transition from the glassy to the rubbery state.

Varying composition and sequence distribution as well as changing interactions modify the mobility of the structural units and influence transition temperatures. The composition dependence of the transition temperature of the soft and hard segments is presented in Fig. 6. The T_g of the soft segments increases relatively steeply with increasing isocyanate content, the total increase of T_g is about 15 °C, which is considerable, then slightly decreases after reaching a maximum ($\Delta T_g \cong 4$ °C). The continuous decrease of mobility can be explained with the effect of the increasing amount of isocyanate groups which hinder the movement of the soft segments. The T_g of the

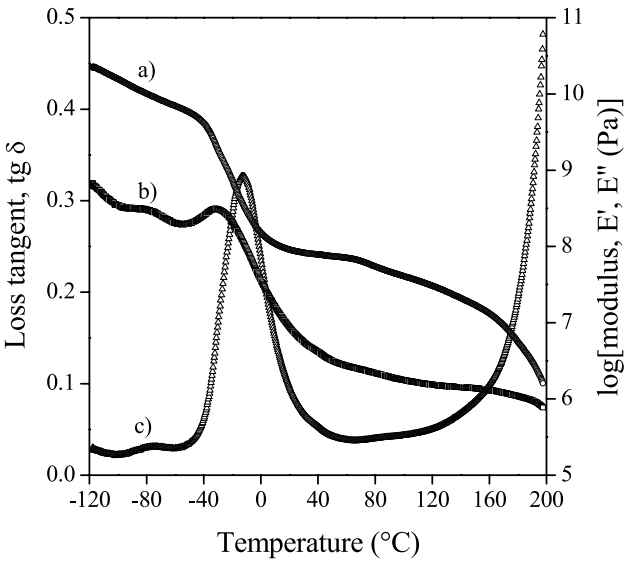

Fig. 5 DMA spectrum of a polyurethane sample with the NCO/OH ratio of 1.045. (a) storage modulus, E', (b) loss modulus, E'', (c) loss tangent, tg δ

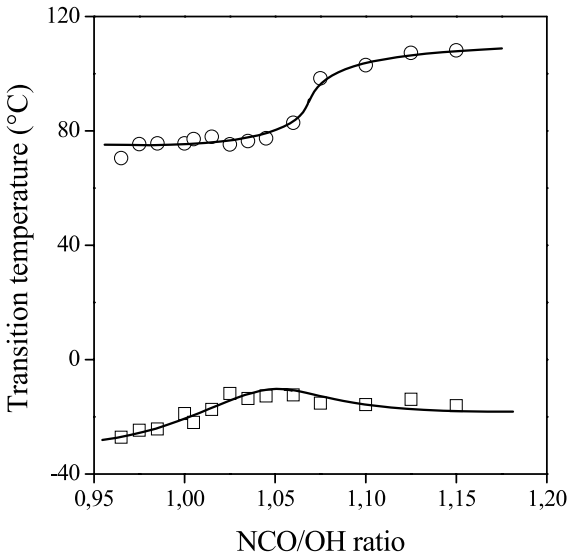

Fig. 6 Effect of composition on the temperature dependence of the glass transition temperature of the soft and hard segments of PU; (□) soft segments, (◯) hard segments

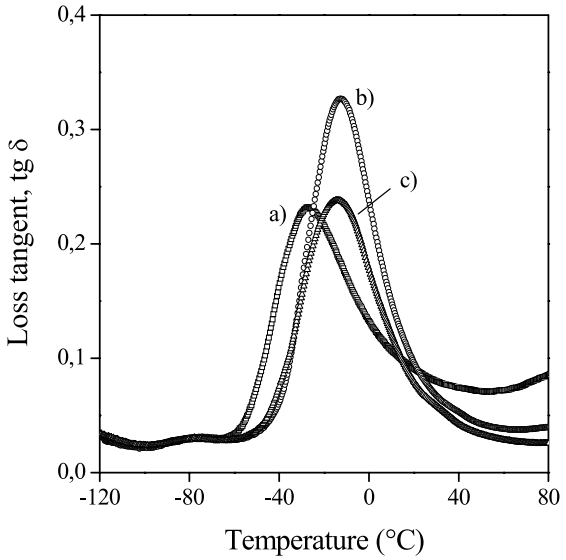

Fig. 7 Changes in the relaxation intensity of the soft segments with composition; NCO/OH ratio: (a) 0.965, (b) 1.045, (c) 1.125

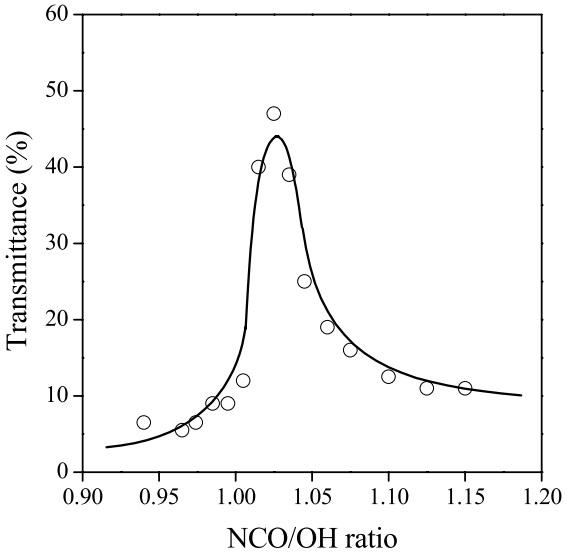

Fig. 8 Changes in light transmittance indicating the extent of phase separation with changing composition

hard segments increases at a slower rate at low NCO/OH ratio, but much sharper at around the equimolar ratio of the two components. T_g continues to increase at a slower rate again at large NCO/OH ratios. The strong increase of slope observed in the range of equimolar stoichiometry suggests that besides the interaction of individual groups, also phase structure might influence the behavior of the chains and the properties of the polymer. Unfortunately, the correlations presented in Fig. 5 do not explain the decrease of modulus presented in Fig. 4. The mobility of both soft and hard segments decreases continuously, which should result in the continuous increase of polymer stiffness as well. Further information and considerations are needed for the reliable explanation of the contradiction.

Transition temperatures indicate the mobility of the relaxing moieties, while the intensity of the transition depends on the number of relaxing units. The loss tangent of three samples is compared to each other in Fig. 7. The three samples were prepared with different NCO/OH ratios. It is obvious from the figure that the intensity of the transition of the soft segment is significantly larger at the NCO/OH ratio of 1.045 than in the two other cases. Besides larger intensity, the width of the relaxation peak also becomes larger in these two latter cases indicating more hindrance and a wider distribution of relaxing moieties. Although it is rather difficult to explain that the intensity of the relaxation increases when the mobility of the units decreases as the increasing T_g indicates, this larger intensity explains the minimum observed in the stiffness of the samples. A larger amount of soft segments will definitely result in smaller modulus.

Phase Structure

Segmented polyurethanes are known to undergo phase separation during their polymerization, which result in the formation of soft and hard phases [20–30]. The relative amount of the two phases as well as their characteristics determine the properties of the polymer. A relatively simple way to study phase separation is the measurement of the transparency of the polymer. Completely homogeneous polymers produce transparent samples, while phase separation leads to a loss of light transmission. The degree of transparency depends on the extent of phase separation and on the size of the phases. The transparency of the various samples is presented in Fig. 8. A maximum appears in light transmission around the equimolar ratio of the functional groups. Obviously the surplus of either functional groups results in a larger extent of phase separation and a stiffer material. The relatively small extent of phase separation observed at around equimolar stoichiometry results in a larger amount of flexible chains which on the other hand leads to a decrease of stiffness. Obviously modulus is determined mainly by the phase separated morphology of the polymer.

Discussion

The results presented above indicate that different factors influence each property of segmented polyurethanes. Viscosity and the related torque are determined mainly by the molecular weight of the polymer. Mechanical properties are influenced by molecular weight, but interactions also play a role in their determination. The stiffness of the

samples, i.e. modulus is mainly determined by phase separation, by the heterogeneous structure of the polymer.

The extent of phase separation and the properties of the phases formed are determined by competitive interactions acting among various groups. The results of DMA experiments indicated that the mobility of both the soft and the hard segments decrease with increasing isocyanate content. The change in the slope of glass transition temperature of both phases as well as the changing amount of relaxing soft segments indicate that phase separation plays a considerable role in the determination of properties. Apparently the dominating interaction, the properties and also the size of the phases change with composition.

At small isocyanate content we have short chains and a relatively large number of chain-end –OH groups which strongly interact with each other through the formation of hydrogen bridges. These interactions lead to phase separation, as well as to the decreased mobility and smaller number of relaxing soft segments. With increasing isocyanate content, the chains become longer and the number of –OH groups decreases leading to an increase in the number of relaxing soft segments, but with a decreased mobility due to the larger number of isocyanate groups, which decrease the flexibility of the connecting soft segments. Less phase separation and increasing number of mobile soft segments lead to increased transparency and decreased stiffness.

A further increase in the NCO/OH ratio results in the association of the urethane groups and the dominating role of the hard segments. This interaction seems to be stronger than that of the –OH groups, shown by the larger strength and elongation-at-break of the polymers formed. At very high isocyanate content also the amine end groups forming seem to enter into interaction and influence phase separation and properties. The smaller molecular weight achieved at these extreme compositions also influence phase separation and properties. The strong interaction of the hard segments excludes soft segments, which leads to the decrease of the T_g of these latter in this composition range. The combined effect of molecular weight, interaction and phase separation determine properties, but the influence of these factors is different on each property. The proper consideration of these relations explains the apparent contradictions observed.

Conclusions

Changes in the NCO/OH ratio of the segmented polyurethanes prepared in this study led to the expected changes in molecular weight. Other properties, however, did not depend only on molecular weight, and composition dependence showed apparent contradictions. Both strength and elongation-at-break increased with increasing isocyanate content up to the equimolar ratio of the two functional groups, but decreased only slightly at larger NCO/OH ratios, i.e. the correlations were asymmetric. On the other hand, modulus assumed minimum value in the same composition range. The analysis of various interactions developing in the polymer showed that phase separation plays an important role in the determination of properties. The interaction of chain end –OH groups dominates at small NCO/OH ratio, while the interaction of hard segments at large isocyanate content. The extent of phase separation is the smallest and the number of mobile soft segments the largest at around the equimolar ratio of the two functional groups. While viscosity depends only on molecular weight, strength and deformability are strongly influenced also by interactions, which on the other hand drive phase separation and completely determine stiffness. Taking into account these considerations makes possible the design of polymers with targeted properties.

Acknowledgement The project was financed by the National Bureau of Research and Development (NKFP Grant No. 1/0027/2005) and the National Scientific Research Fund of Hungary (OTKA Grant No. K 68748); their support is highly appreciated.

References

1. Randall D, Lee S (2003) The Polyurethanes Book. Wiley, New York
2. Gum W, Riese W, Ulrich H (1992) Reaction Polymers. Hanser, Munich
3. Li F, Zuo J, Dong L, Wang H, Luo J, Han W, Huo Y (1998) Eur Polym J 34:59
4. Sekkar V, Gopalakrishnan S, Devi KA (2003) Eur Polym J 39:1281
5. Sekkar V, Bhagawan SS, Prabhakaran N, Rao M, Ninan KN (2000) Polymer 41:6773
6. Subramani S, Cheong IW, Kim JH (2004) Prog Org Coat 51:329
7. Crawford DM, Bass RG, Haas TW (1998) Thermochim Acta 323:53
8. Sánchez-Adsuar MS (2000) Int J Adhes Adhes 20:291
9. Król P (2007) Prog Mater Sci 52:915
10. Sarier N, Onder E (2007) Thermochim Acta 90:454
11. Kabir ME, Saha MC, Jeelani S (2006) Mater Sci Eng A 429:225
12. Mills NJ (2007) Polymer Foams Handbook. Elsevier, New York
13. Kavlock KD, Pechar TW, Hollinger JO, Guelcher SA, Goldstein AS (2007) Acta Biomater 3:475
14. Andrews KD, Feugier P, Black RA, Hunt JA (2008) J Surg Res 149:39
15. Urbano J, Manzarbetia F, Caramelo C (2008) J Vasc Interv Radiol 19:189
16. Chandran KB, Kim S-H, Han G (1991) J Biomech 24:385
17. Lyu S, Grailer T, Belu A, Schley J, Bartlett T, Hobot C, Sparer R, Untereker D (2007) Polymer 48:6049
18. Yeganeh H, Hojati-Talemi P (2007) Polym Degrad Stab 92:480
19. Phaneuf MD, Dempsey DJ, Bide MJ, Quist WC, LoGerfo FW (2001) Biomaterials 22:463

20. Macosko CW (1989) RIM, Fundamentals of Reaction Injection Molding. Hanser, Munich
21. Elwell MJ, Ryan AJ, Grünbauer HJM, Lieshout HCV (1996) Polymer 37:1353
22. Pompe G, Pohlers A, Pötschke P, Pionteck J (1998) Polymer 39:5147
23. Garrett JT, Xu R, Cho J, Runt J (2003) Polymer 44:2711
24. Ayres L, Orefice RL, Yoshida MI (2007) Eur Polym J 43:3510
25. Kojio K, Nakashima S, Furukawa M (2007) Polymer 48:997
26. Zheng J, Ozisik R, Siegel RW (2006) Polymer 47:7786
27. Chen C-P, Dai SA, Chang HL, Su W-C, Wu T-M, Jeng R-J (2005) Polymer 46:11849
28. Sonnenschein MF, Lysenko Z, Brune DA, Wendt BL, Schrock AK (2005) Polymer 46:10158
29. Jena KK, Raju KVSN (2007) Ind Eng Chem Res 46:6408
30. Qi HJ, Boyce MC (2005) Mech Mater 37:817

Progr Colloid Polym Sci (2008) 135: 225–230
DOI 10.1007/2882_2008_110

Published online: 30 August 2008

Daisaku Kaneko
Hidemitsu Furukawa
Yoshimi Tanaka
Yoshihito Osada
Jian Ping Gong

Flower Petal-like Pattern on Soft Hydrogels during *Vodka* Spreading

Daisaku Kaneko
School of Materials Science, Japan Advanced Institute of Science and Technology, Japan
e-mail: daisaku@jaist.ac.jp

Hidemitsu Furukawa · Yoshihito Osada · Jian Ping Gong (✉)
Division of Biological Sciences, Graduate School of Science, Japan Hokkaido University, 060-0810 Sapporo, Japan
e-mail: gong@sci.hokudai.ac.jp

Yoshimi Tanaka
CRI Sousei, Hokkaido University, Japan

Jian Ping Gong
SORST, Japan Science and Technology Agency, Japan

Abstract Flower petal-like pattern has been observed during *Vodka* spreading on gel surfaces. Since the spreading kinetics vanishes within a few seconds, the flower petal-like pattern is extremely impressive like shooting-up of fireworks. This pattern can be formed when ethanol/water mixtures having more than 25 vol. % of ethanol are used as spreading liquid and soft gels with storage modulus less than 10^4 Pa are used as underlying substrates. The origin of this phenomenon is discussed in terms of instability of leading edge of spreading liquid on soft hydrogels.

Keywords Instability · Hydrogels · Pattern formation · Spreading · Thin film

Introduction

Snow crystals form beautiful patterns, however, each crystal of snow is said to be different one by one. Most of the patterns in nature, e.g. a milk crown, and cloudscapes, appear in their growth or motion. Many researchers have discussed their enchanting spatio-temporal features, about symmetry or its breaking, self-similarity, periodicity, and so forth [1–11]. The pattern formation sometimes appears in polymeric systems, as typified by Liesegang phenomena [1], viscous fingering phenomena [2–4], and also various kinds of phase separations [11]. Despite intensive work devoted to understand such kind of phenomena, experimental observations have not been sufficiently explained in the theoretical point of view. Preceding theoretical works, patterning on material based on self-organization has gripped the attentions for the bottom-up type devices with practical application of electronics fields [13, 14].

In this paper, we will report a novel pattern formation on polymer gels like flower petal during *Vodka* spreading. When a small amount of *Vodka* is put on the soft gel surface, the droplet starts to spread immediately on the surface. Soon the petal-like pattern appears transiently with altering its shape drastically, and then loses it gradually.

Understanding the transient phenomena observed over gel surfaces is important not only for scientific interesting but also practical gel-based applications [15–18].

Experiment

Chemically cross-linked poly(2-acrylamido-2-methylpropanesulfonic acid) (PAMPS) gel and poly acrylamide (PAAm) gel were prepared by radical polymerization from an aqueous solution of 0.5 M AMPS monomer and AAm monomer, respectively, in the presence of a calculated

amount of cross-linking agent, *N*-*N*′-methylenebisacrylamide (MBAA), and 3 mM initiator, 2-oxoglutaric acid. Before polymerization, the monomer solution was purged by nitrogen for 10 min to eliminate the inhibition effect of oxygen.

The polymerization was conducted under irradiation by a UV lamp (ENF-260C/J, Spectronics Co., USA) with wavelength 365 nm, at 20 °C for about 12 h. These gel samples were prepared between two parallel glass plates separated by a silicone spacer with a thickness 5 mm, to obtain sheet-shaped gels. Before using them, the glass plates were carefully washed with 0.5 M hydrochloric acid and special detergent (Extran MA02, Merck Inc.), then cleaned with a large amount of deionized water. After the polymerization, sheet-shaped PAMPS gels were immersed into a large amount of water for a week in order to reach their equilibrium state. Equilibrated PAMPS gels having various thicknesses according to their swelling degree were cut into rectangular solid shape having 50 mm in horizontal and vertical length.

Agarose gels having rigid networks were prepared by dissolving agarose powder (Invitrogen Corp., Carlsbad, CA, USA) into pure hot water (90 °C) in a beaker. After that, it was poured into a Petri-dish and left it in a low temperature room (4 °C) for 24 h.

Ethanol (98%), Nippon Alcohol Co., Ltd) and *Vodka* were used as received from manufacturer. The drop volume of spreading liquids is 8 μl to avoid the gravity effect. Excessive water layer over gel surface was removed with a Kimwipe (S-200, Crecia Co., Ltd.) prior to droplet deposition. The experiments were performed in a Petri-dish of 6 cm diameter and 1.5 cm depth. A small droplet of spreading liquid ejected from a micro syringe was placed right above on the gel surfaces. The contour of the spreading liquid was visualized and blown up by a digital video camera. In order to improve the visual observation of the spreading, a small amount of methylene blue trihydrate (10^{-2} M, Kanto Chemical Co., Ltd.) was added into the ethanol. The effect of dye on the spreading is confirmed to be negligible. The experimental setup was sensitive to small deflection of the transmitted light caused by the variation of surface curvature, therefore the location of the leading edge of the spreading fluid was well visualized.

The time evolution of the spreading leading edge was recorded by the digital video camera (time resolution: 1/30 s, NV-GS70K-S, Matsushita Electric Industrial Co., Ltd.) or high speed digital camera (time resolution: 1/1000, NAC Image Technology), and each photograph was evaluated by digital image analysis (Adobe, Photoshop 6.0). The experimental data were fitted by Origin 6.1J (OriginLab Corporation, USA).

Parallel-plate geometry was used for dynamic oscillatory measurements of the gels. Cylindrical gel samples equilibrated in distilled water with a thickness of ca. 10 mm and a diameter of 15 mm were embedded and glued between parallel plates with a diameter of 20 mm.

Results

The *Vodka* is one of the most favorite liquor over the world and it is distilled liquor containing ca. 40% ethanol. When a small amount of liquid containing ethanol like *Vodka* is dropped on a soft hydrogel surface, *Vodka* spreads immediately over a gel surface due to surface tension difference between spreading liquid and hydrogel. During this spreading process, beautiful flower petal-like patterns appear and their successive snapshots are shown in Fig. 1a. In this figure, *Vodka* with small amount of methylene blue for well visualization and chemically cross-linked poly(2-acrylamido-2-methylpropanesulfonic acid) (PAMPS) gel swollen by 0.1 M KCl aqueous solution were used as spreading liquid and underlying substrate, respectively. The spreading droplet volume was fixed as 8 μl to avoid a gravitational effect and addition of methylene blue to the spreading liquid was found to be negligible for pattern formation by preceding experiment [19, 20]. The leading edge of the spreading liquid becomes dim after at ca. 0.08 s and flower petal-like patterns appear suddenly at ca. 0.1 s from the liquid starting to spread. Each petal of pattern coalesces with neighbors increasing its size with time advancing and consequently, the number n_p of petal gradually reduces as 36 pieces (250 ms), 26 pieces (500 ms), 22 pieces (1.0 s), and 17 pieces (1.5 s) as shown in Fig. 1b, showing a scaling relation of $n_p \propto t^{-0.4\pm0.1}$. From 1.0 to 1.5 s, petal-like patterns begin to lose their beautiful alignments and shapes. This fusion of petal is similar to "coarsening" of phase separation. Clearly visible capillary wave of *Vodka* like "river terrace" also can be observed inside of patterns. Although there are reports that evaporating effects of spreading liquid influences the spreading dynamics [21] or pattern formation [22], the effect of ethanol evaporation in this study can be negligible since the spreading process occurs within a few seconds. These beautiful patterns were never observed on water, glass substrate, and polymer solutions.

Time evolution of leading edge R and spreading velocity v of *Vodka* spreading over the gel surfaces are plotted in Fig. 1c. The leading edge R is defined as the distance shown in Fig. 1a and the spreading velocity v was calculated as change in R at each measuring intervals. As shown in Fig. 1c and earlier work [19, 20], spreading process on viscoelastic surface contains 3 stages (denoted as *stage I*, *II,* and *III*) and the kinetic equation of the leading edge R during *stage I* and *stage II* can be collectively expressed as follow

$$R = K\left(\frac{t+c}{t_0}\right)^{\alpha}, \tag{1}$$

where α is the spreading exponent, K is the prefactor, and c is a constant depending on the initial conditions such as the initial shape of spreading liquid. The parameter α characterizes the inclination of the spreading curve in *stage II* that can be considered as practical spreading kinetics of

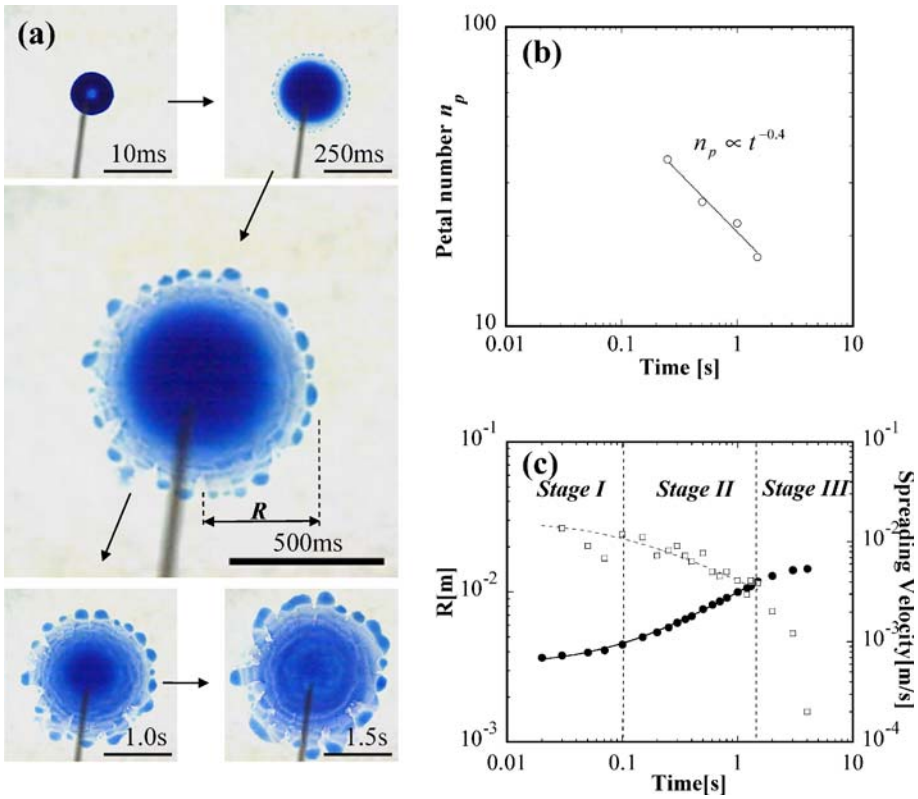

Fig. 1 (**a**) Successive snapshots of pattern formation during the *Vodka* spreading on soft PAMPS gel (swollen by 0.1 M KCl aqueous solution) having storage modulus $G' \sim 10^2$ Pa. The *numbers* in the figure are spreading times and *scale bars* indicate 10^{-2} m. (**b**) The petal number n_p as a function of spreading time. (**c**) Time evolution of spreading radius R (●) and velocity v (□) of *Vodka* spreading on PAMPS gel swollen by 0.1 M KCl aqueous solution. *Solid line* and *dotted line* are the non linear fitting results by Eqs. 1 and 2, respectively

Vodka without any noises. From the fitting of spreading curve of R by Eq. 1 and setting $t_0 = 1$ s, spreading parameters, K, c, and α were found to be 9.6×10^{-3} m, 0.090 s, and 0.45, respectively, by the least square method. We found that during *Vodka* spreading on soft gel surface, the flower petal-like patterns firstly appear at the end of *stage I* ($t \sim 0.1$ s), and disappear at the end of *stage II* ($t \sim 1.5$ s).

The spreading velocity v can be obtained by differentiating Eq. 1 with the spreading time t,

$$v = K\frac{\alpha}{t_0}\left(\frac{t+c}{t_0}\right)^{\alpha-1}. \qquad (2)$$

We denote the critical spreading velocity and time at the end of *stage I* when the petal patterns appear as v_s and t_s, respectively. The spreading velocity gradually reduces from the v_s with petal size growing up and petal number reducing during *stage II*. At the end of *stage II*, the petal-like patterns disappear. We denote this terminal spreading velocity and time as v_e and t_e, respectively. Using experimental result of $K = 0.96 \times 10^{-2}$ m, $c = 0.090$ s and $\alpha = 0.45$ to Eq. 2, we found that $v_s = 1.1 \times 10^{-2}$ m/s and $v_e = 0.33 \times 10^{-2}$ m/s.

As demonstrated earlier [19], spreading on gel surface shows the intermediate behavior between liquids and solids due to their soft natures. To study the pattern forming condition, we have carried out the spreading experiments by changing 1) the viscoelasticity of various gel substrates and 2) ethanol concentration of spreading liquid.

Spreading on Various Gel Substrates Having Different Viscoelasticity

To investigate the effect of softness of gel substrates to the pattern formation, we have tried to observe the change of pattern formation by varying the storage modulus G' of gel substrates, such as polyacrylamide (PAAm) gels composed of neutral soft networks, PAMPS gels composed of strong polyelecrolyte networks, and agarose gels composed of rigid network. Measurement of G' was carried out by dynamic oscillating mode using rheometer at a wide angler frequency range from 0.1 to 50 rad/s, applying a strain $\varepsilon = 0.01$ that is within the linear deformation region of gels. (Since the gel samples for oscillating measurement were cut into cylindrical shape having 1.5×10^{-2} m in

diameter and ca. 10^{-2} m in thickness, $\omega \approx 1$ rad/s of oscillating angular frequency provides the maximum oscillation velocity at external side of gel as $\sim 10^{-2}$ m/s, which is comparable to the order of spreading velocity. Storage modulus G' of gels showed little frequency dependence in the angular frequency range from the 0.1 to 50 rad/s. 98% ethanol as received with small amount of methylene blue was used as spreading liquid in these experiments.

It was found that the spreading leading edge becomes slightly unclear until at 0.067 s and very small petal-like patterns were confirmed until 0.1 s in all pattern-forming case, independently of the gel substrates. This critical time, t_s, most likely, corresponds to the boundary between *stage I* and *stage II*. The terminal time, t_e, when the propagating spreading liquid begins to converge, depends on the substrates, showing values in a range of $t_e \approx 0.67 \sim 1.67$ s. The kinetics parameters c, K, and α determined by Eq. 1 and the critical and terminal spreading velocity v_s, v_e calculated using $t_s = 0.1$ s and the corresponding t_e are summarized in Table 1. For the non-pattern-forming cases, $t_s = 0.1$ s was used to calculate v_s in order to make a comparison to pattern forming cases.

Figure 2 shows v_s and v_e as a function of G', and the typical snapshots of pattern formation on various gel substrates at spreading time 0.67 s when the petal-like pattern were clearly confirmed from the snapshots. It was found that the leading edge becomes obscure during spreading on relatively soft gel substrate with a storage modulus G' less than ca. 10^5 Pa and petal-like patterns clearly appear only on soft gel substrates with a storage modulus G' less than ca. 10^4 Pa and the petal number n_p increasing with decreasing G', consequently pattern becomes beautiful with decreasing G'. As shown in inset of Fig. 2, we have obtained following relation, $n_p \propto G^{-0.1\pm0.05}$ at a certain spreading time. It was also found that when pattern forms, the critical spreading velocity v_s exceeds a value $\sim 1.0 \times 10^{-2}$ m/s and terminal velocity v_e below a value $\sim 0.5 \times 10^{-2}$ m/s.

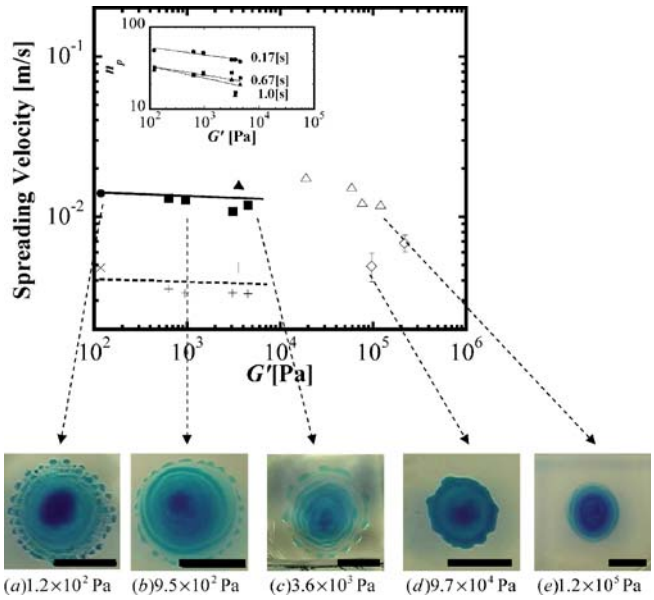

Fig. 2 The critical spreading velocity v_s and terminal velocity v_e on various gel substrates having various storage modulus G'. The v_s of pattern forming case are denoted by *filled symbols* (●: PAMPS gel swollen by 0.1 M KCl aqueous solution, ■: PAAm gels, ▲: PAMPS gels) and non-pattern forming case are denoted by *open symbols* (△: PAMPS gels, ◇: Agarose gels). The v_e of pattern forming case are denoted by ×: PAMPS gel swollen by 0.1 M KCl solution, +: PAAm gels, |: PAMPS gel. *Inset figure* indicates petal number n_p as a function of G' at spreading time 0.167 s (●), 0.67 s (■) and 1.0 s (▲) and *solid lines* indicate fitting curves of 0.167 s ($n_p = 85 \times G'^{-0.09}$), 0.67 s ($n_p = 55 \times G'^{-0.11}$) and 1.0 s ($n_p = 64 \times G'^{-0.14}$). Snapshots are typical spreading pattern of 98% ethanol at 0.67 s on **a** PAMPS gel swollen by 0.1 M KCl aqueous solution, $G' = 1.2 \times 10^2$ Pa, **b** PAAm gel, $G' = 9.5 \times 10^2$ Pa, **c** PAMPS hydrogel, $G' = 3.6 \times 10^3$ Pa, **d** Agarose hydrogel, $G' = 9.7 \times 10^4$ Pa, and **e** PAMPS hydrogel, $G' = 1.2 \times 10^5$ Pa. *Scale bars* indicate 10^{-2} m

Changing the Ethanol Concentration of Spreading Liquid

The driving force of spreading on gel surface is the surface tension difference between spreading liquid and gel substrate. Surface tension effects of the spreading liquid to the pattern formation also have been investigated by changing the ethanol volume fraction of ethanol-water mixture used as spreading liquid. Experiments were performed on the PAMPS hydrogel having the same storage modulus $G' = 3.6 \times 10^3$ Pa. Kinetics parameters c, K, and α determined by Eq. 1 and calculated v_s and v_e are listed in Table 2. v_s and v_e are estimated by the same manner as in Table 1 at $t_s = 0.1$ s and corresponding t_e that decreases with decreasing ethanol volume fraction, in a range of ca. $t_e \approx 0.67 \sim 1.67$ s. Figure 3 shows the critical spreading velocity v_s and terminal velocity v_e as a function of ethanol volume fraction and the typical snapshots of pattern formation at spreading time 0.67 s. It is obviously confirmed that flower petal-like pattern becomes clear with increasing ethanol volume fraction and the critical value for pattern formation is ca. 25% and the critical spreading velocity v_s of pattern formation was above ca. 1.0×10^{-2} m/s, coincides with the results of Fig. 2.

Discussion

Our observed flower petal-like pattern is similar to fingering instabilities of driven spreading films. According to the Joanny's theory [23], stability limit of wavelength λ_m to the spreading direction of leading edge is given by

$$\lambda_m = 8h_0(3Ca)^{-1/3}, \tag{3}$$

where h_0 is a thickness of fluid and Ca is a capillary number defined by $Ca = \eta V/\gamma$, where η, V and γ are viscosity,

Table 1 The critical spreading velocity v_s ($t_s = 0.1$ s) and terminal velocity v_e ($t_e \approx 0.67 \sim 1.67$ s) of ethanol spreading on various kinds of substrates having various storage modulus G'. The velocities were calculated by Eq. 2 using the listed parameters c, K, and α which were determined by experimental data of time evolution of spreading radius R fitted by Eq. 1. The non-pattern forming case of v_s at $t_s = 0.1$ s are denoted in parenthesis for comparison

Gel	G' [Pa]	c [s]	K $\times 10^{-2}$ [m]	α	R^2	$v_s \times 10^{-2}$ [m/s] ($t_s = 0.1$ [s])	$v_e \times 10^{-2}$ [m/s] (t_e [s])
PAMPS swollen by KCl aq	1.2×10^2	0.030	1.01	0.48	0.999	1.40	0.48(1.00)
PAAm	6.3×10^2	0.052	1.03	0.46	0.998	1.31	0.35(1.67)
	9.5×10^2	0.039	0.96	0.44	0.999	1.28	0.33(1.50)
	3.1×10^3	0.090	0.96	0.45	0.999	1.08	0.33(1.50)
	4.5×10^3	0.053	0.95	0.42	0.991	1.19	0.33(1.33)
PSMPS	3.6×10^3	0.059	1.28	0.45	0.998	1.58	0.48(1.33)
	1.9×10^4	0.040	1.33	0.44	0.998	(1.76)	–
	5.9×10^4	0.047	1.18	0.47	0.998	(1.53)	–
	7.7×10^4	0.033	0.91	0.40	0.998	(1.22)	–
	1.2×10^5	0.042	0.91	0.43	0.998	(1.19)	–
Agarose	9.7×10^4	0.157	0.61	0.32	0.993	(0.49)	–
	2.2×10^5	0.067	0.66	0.29	0.993	(0.68)	–

velocity and surface tension of a fluid, respectively. In our system, capillary number Ca can be estimated as $\sim 10^{-3}$ using fluid parameters, $\eta \sim 10^{-3}$ Pa s, $\gamma \sim 10^{-2}$ N/m and $V \sim 10^{-2}$ m/s which is a typical pattern forming velocity. If we assume the volume conservation of fluid, mean fluid thickness h_0 can also be estimated as a few dozen of micrometers depending on the spreading radius. From Eq. 3 with these parameters, one can estimate the stability limit of wavelength of leading edge as $\lambda_m \sim 1.1$ mm.

On the other hand, our results obtained from Fig. 1, we can roughly estimate the disturbance wave length λ_d in our case from the petal-like pattern intervals when they start to appear, $\lambda_d = 2\pi R(t)/n_p \approx 1$ mm, where n_p is the observed petal number at this moment. This value of λ_d should be comparable to the Joanny's prediction.

However, this explanation is not satisfactory to the flower petal-like pattern formation. For example, in the cases of spreading on PAMPS gels with storage modulus G' around 10^5 Pa (Fig. 2), although spreading velocities exceeds 10^{-2} m/s, they did not show the flower petal-like patterns. (For pattern formation, there should be other factors).

We think this discrepancy arises from the specific nature of polymer gels such as a surface fluctuation of gel substrates due to their soft nature. Kumaran et al. predicted the flow induced instability between a fluid and a gel interface [24]. The instability is caused by the energy transfer from the mean flow to the surface fluctuation due to the work done by the mean flow at the interface. When a thin fluid layer flows on a gel surface with a thickness much thicker than that of the fluid, unstable modes appear above a critical liquid velocity [24]

$$v_c = \frac{H^2 G'}{\eta H_g} \tag{4}$$

Table 2 The critical spreading velocity v_s ($t = 0.1$ s) and terminal velocity v_e ($t_e \approx 0.67 \sim 1.67$ s) of ethanol/water mixture spreading on PAMPS gel. The velocities were calculated by Eq. 2 using the listed parameters c, K, and α which were determined by experimental data of time evolution of spreading radius R fitted by Eq. 1. The non-pattern forming case of v_s at $t_s = 0.1$ s are denoted in parenthesis for comparison

Ethanol concentration [vol.%]	c [s]	$K \times 10^{-2}$ [m]	α	R^2	$v_s \times 10^{-2}$ [m/s] ($t_s = 0.1$ [s])	$v_e \times 10^{-2}$ [m/s] (t_e [s])
0	0.001	0.407	0.05	0.961	(0.17)	–
15	0.072	0.780	0.39	0.998	(0.89)	–
25	0.029	1.03	0.38	0.998	1.39	0.38(1.00)
50	0.030	1.02	0.43	0.998	1.40	0.32(1.67)
75	0.023	1.06	0.40	0.997	1.49	0.31(1.67)
98	0.059	1.28	0.45	0.998	1.58	0.43(1.67)

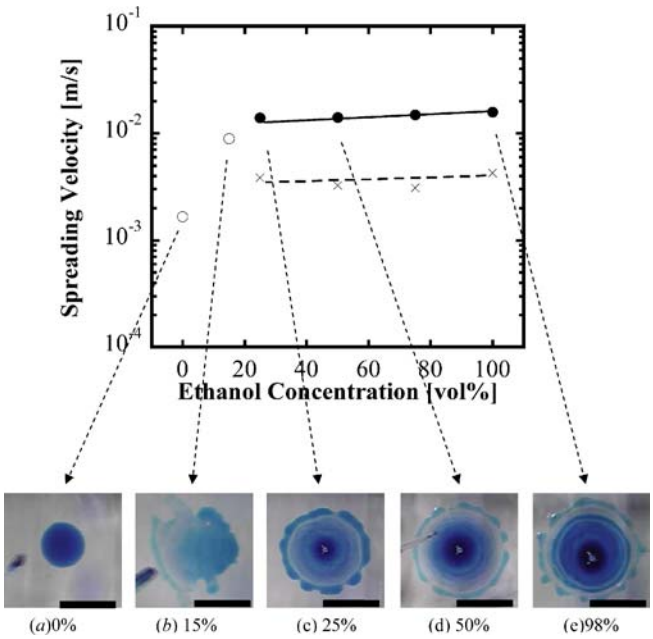

Fig. 3 The critical spreading velocity v_s and terminal velocity v_e of various ethanol volume concentrations on PAMPS gels. The v_s of pattern forming case are denoted by *filled circles* and non-pattern forming case are denoted by *open circles*. The v_e of pattern forming case are denoted by *cross symbols*. Snapshots are typical spreading pattern at 0.67 s of different ethanol volume concentration **a** 0%, **b** 15%, **c** 25%, **d** 50%, and **e** 98%, respectively, used as spreading liquid on PAMPS hydrogel having $G' = 3.6 \times 10^3$ Pa. *Scale bars* indicate 10^{-2} m. *Solid* and *dotted lines* are guide for eyes

Here, H and H_g are thickness of fluid layer and gel, respectively, η is the viscosity of the fluid. From Eq. 4, if we set the $v_c \sim 10^{-2}$ m/s, $\eta = 10^{-3}$ Pa s, $H \sim 10\,\mu$m and $H_g \sim 10^{-2}$ m, critical storage modulus G' for pattern formation can be estimated as $G' = 10^3$ Pa. Although this order estimation is somewhat smaller than what we obtained, we think disturbance of soft gel substrates should be an essential factor to flower petal-like pattern formation.

Summary

When a droplet of ethanol is placed on a hydrogel surface, ethanol starts to spread over the gel surface with a certain initial spreading velocity depending on the surface tension difference between them. During this spreading process, we have found the novel pattern formation on polymer gels like flower petals. Pattern forming conditions were found to be as follows:

1. Initial spreading velocity should exceed ca. 10^{-2} m/s
2. Storage modulus of gel substrates should be less than ca. 10^4 Pa.
3. Ethanol concentration of spreading liquids should be above ca. 25%.

Although this phenomenon is basically similar to the fingering instability, there may be other factor concerning soft nature of hydrogels. We have interpreted that this is from the surface fluctuation of soft gel surface during fluid spreading. We think this fluctuation energy may couple with the spreading kinetics and enhance the instability of leading edge.

At present stage, our finding has remained at phenomenological level, this pattern formation can be reproducible if one has only has a soft gel and a small amount of strong alcoholic liquor.

References

1. Liesegang RE (1896) Naturwiss Wochenschr 11:353
2. Saffman PG, Taylor G, FRS (1958) Proc R Soc London A 245:312
3. Matar OK, Troian SM (1999) Phys Fluids 11:3232
4. Waner MRE, Craster RV, Matar OK (2004) J Fluid Mech 510:169
5. Darhuber AA, Troian SM (2001) J Appl Phys 90:3602
6. Kotonis MA, Muthukumar M (1992) Macromolecules 25:1716–1724
7. Tong P, Goldburg WI, Huang JS, Witten TA (1990) Phys Rev Lett 65(22):2780
8. Smith DE, Wu XZ, Libchaber A, Moses E, Witten T (1992) Phys Rev A 45(3):R2165
9. Yamazaki S, Kawaguchi M, Kato T (2002) J Colloid Interf Sci 254:396
10. Antal T, Droz M, Magnin J, Racz Z (1999) Phys Rev Lett 83(15):2880
11. Lebedeva MI, Vlachos DG, Tsapatsis M (2004) Phys Rev Lett 92(8):088301-1
12. Nicolis G, Prigogine I (1977) Self-Organization in Nonequilibrium Systems. Wiley, New York
13. Nishikawa T, Nonomura M, Arai K, Hayashi J, Sawadaishi T, Nishiura Y, Hara M, Shimomura M (2003) Langmuir 19:6193
14. IBM Research News (2003) http://www.research.ibm.com/resources/news/20031208_selfassembly.shtml
15. Kaneko D, Tada T, Kurokawa T, Gong JP, Osada Y (2005) Adv Mater 17(5):535
16. Gong JP, Osada Y (1998) J Chem Phys 109:8062
17. Gong JP, Kurokawa T, Narita T, Kagata G, Osada Y, Nishimura G, Kinjo M (2001) J Am Chem Soc 123:5528
18. Kagata G, Gong JP, Osada Y (2002) J Phys Chem B 106:4596
19. Kaneko D, Gong JP, Zrínyi M, Osada Y (2005) J Polym Sci B 43:562–572
20. Szabo D, Akiyoshi S, Matsunaga T, Gong JP, Osada Y, Zrinyi M (2000) J Chem Phys 113:8253
21. Poulard C, Guena G, Cazabat AM, Boudaoud A, Ben Amar M (2005) Langmuir 21:8226
22. Deegan RD (2000) Phys Rev E 61:475
23. Trolan SM, Herbolzheimer E, Safran SA, Joanny JF (1989) Europhys Lett 10:25
24. Kumaran V, Fredrickson GH, Pincus P (1994) J Phys II France 4:893

Progr Colloid Polym Sci (2008) 135: 231–232

AUTHOR/TITLE INDEX

Progr Colloid Polym Sci (2008) 135: 233–234

KEY WORD INDEX